

Brandenburg  
University of Technology  
Cottbus - Senftenberg

# Slow Wave Resonator Based Tunable Multi-Band Multi-Mode Injection-Locked Oscillators

## Habilitationsschrift

der Fakultät Maschinenbau, Elektrotechnik und Wirtschaftsingenieurwesen der  
Brandenburgischen Technischen Universität Cottbus-Senftenberg zur  
Erlangung des akademischen Grades  
Doktor der Ingenieurwissenschaften habilitatus (Dr.-Ing. habil.) vorgelegt

von

**Dr.-Ing. Ajay Kumar Poddar**  
geboren am 01.03.1967 in Dhamdaha, India

Datum der Eröffnung des Habilitationsverfahrens: 23.10.2013

Datum des Fakultätsbeschlusses über die Zuerkennung der Lehrbefähigung: 22.10.2014

Vorsitzender: Professor Dr.-Ing. Gerhard Lappus

Gutachter: Professor Dr.-Ing. habil. Wolfgang Heinrich, TU Berlin  
Professor Dr.-Ing. Thomas Eibert, TU München  
Professor Dr.-Ing. Matthias Rudolph, BTU Cottbus-Senftenberg

Weiteres Mitglied des Habilitationsausschusses:  
Professor Dr.-Ing. Dirk Killat, BTU Cottbus-Senftenberg



Brandenburg  
University of Technology  
Cottbus - Senftenberg

Author contact data:

Dr.-Ing. Ajay K. Poddar.

2 River Drive

Elmowood Park, NJ 07407, USA

Email: [akpoddar@synergymwave.com](mailto:akpoddar@synergymwave.com)

Phone: (001)-201-791-9605

# Table of Contents

## Summary

## Preface, Appreciation, and Acknowledgement

	<b>Page</b>	
<b>1.0</b>	<b>Introduction</b>	<b>1</b>
1.1	Abstract	1
1.2	Motivation	1
1.3	Problem Statement	2
1.4	Definition of the Task and Oscillator Figure of Merit (FOM)	2
1.5	Overview of the Thesis	4
1.6	Publications Arising from the Present Work	8
<b>2.0</b>	<b>General Comments on Oscillators</b>	<b>9</b>
2.1	Theory of Operation	9
2.2	Specifications of Tunable Oscillators	14
2.2.1	Frequency Range and Tuning Characteristics	14
2.2.2	Tuning Linearity	14
2.2.3	Tuning sensitivity, Tuning Performance	14
2.2.4	Tuning Speed	14
2.2.5	Post-Tuning Drift	14
2.2.6	Phase Noise	15
2.2.7	Output Power	16
2.2.8	Harmonic Suppression	17
2.2.9	Output Power as a Function of Temperature	17
2.2.10	Spurious Response	17
2.2.11	Frequency Pushing	17
2.2.12	Sensitivity to Load Changes	18
2.2.13	Power Consumption	18
2.3	History of Microwave Oscillators	18
2.4	Resonator Choice	22
2.4.1	LC Resonator	22
2.4.2	Transmission Line Resonator	23
2.4.3	Integrated Resonator	23
2.5	Large Signal S-Parameter Analysis	27
2.6	Conclusion	32
<b>3.0</b>	<b>Noise Analysis of the Oscillators</b>	<b>33</b>
3.1	Oscillator Noise	33
3.1.1	Source of Noise	33
3.1.2	Oscillator Noise model Comments	35
3.2	Leeson's Phase Noise Model	39
3.2.1	Leeson's Phase Noise Model (Linear Time Invariant Approach)	40
3.2.2	Lee and Hajimiri's Noise Model (Linear Time Variant Model)	49
3.2.3	Kaertner and Demir's Noise Model (Nonlinear Time Variant)	55
3.2.4	Multiple Threshold Crossing Noise Model	56
3.2.5	Conclusion on Phase Noise Models	57

<b>4.0</b>	<b>Phase Noise Measurement Techniques and Limitations</b>	<b>58</b>
4.1	Introduction	58
4.2	Noise in Circuits and Semiconductors	58
4.2.1	Johnson Noise	59
4.2.2	Planck’s Radiation Noise	59
4.2.3	Schottky/Shot Noise	59
4.2.4	Flicker Noise	60
4.2.5	Transit Time and Recombination Noise	60
4.2.6	Avalanche Noise	60
4.3	Phase Noise Measurement Techniques	60
4.3.1	Direct Spectrum Technique	61
4.3.2	Frequency Discriminator Method	62
4.3.2.1	Heterodyne (Digital) Discriminator Method	65
4.3.3	Phase Detector Technique	65
4.3.3.1	Reference Source/PLL Method	66
4.3.4	Residual Method	69
4.3.5	Two-Channel Cross-Correlation Technique	69
4.3.6	Conventional Phase Noise Measurement System	72
4.4	Prediction and Validation of Oscillator PN Measured on Different Equipments	75
4.4.1	Verification of 100MHz Crystal Oscillator Using CAD simulation tool	76
4.4.2	Verification of 100MHz Crystal Oscillator (LN XO100) using Analytical Model	79
4.4.3	Verification of 100 MHz Crystal Oscillator using PN Measurement Equipments	80
4.4.3.1	Experimental Verification of 100 MHz Crystal Oscillator using Agilent E5052B PN Measurement Equipment	81
4.4.3.2	Experimental Verification of 100 MHz Crystal Oscillator using R&S FSUP 26)	82
4.4.3.3	Experimental Verification of 100 MHz Crystal Oscillator using Anapico (APPH6000-IS)	83
4.4.3.4	Experimental Verification of 100 MHz Crystal Oscillator using Holzworth (HA7402A)	83
4.4.3.5	Experimental Verification of 100 MHz Crystal Oscillator using Noise XT DCNTS	84
4.5	Phase Noise Measurement Evaluation and Uncertainties	84
4.6	Uncertainties in Phase Noise Measurement:	89
4.6.1	Measurement	90
4.7	Factors Influence Phase Noise Measurement	91
4.8	Conclusion	92
<b>5.0</b>	<b>Resonator Dynamics and Applications in Oscillators</b>	<b>93</b>
5.1	Microwave Resonators	93
5.2	Linear Passive 1-Port	93
5.3	Resonator Networks	94
5.4	Resonator Q-Factor	97
5.4.1	Definition of Q Factor for Passive Resonant Circuit	98
5.4.1.1	Fractional 3-dB Bandwidth	98
5.4.1.2	Phase to Frequency Slope	98
5.4.1.3	Stored-to-Dissipated Energy Ratio	99
5.4.2	Definition of Q Factor for Active Resonant Circuit: Sensitive for Oscillation	99
5.4.2.1	Active NISO Circuit Q-Factor (Noise Spectrum Basis)	101
5.4.2.2	Active NISO Circuit Q-Factor (Reflection Coefficient Basis)	102
5.4.2.3	Active NISO Circuit Q-Factor (Energy Basis)	102
5.4.2.4	Active SISO Circuit Q-Factor (Source-Push and Load-Pull Basis)	104
5.4.2.5	Active SIBO Circuit Q-Factor (Injection Locking Basis)	107

5.5	Resonator Design Criteria for Low Phase Noise Oscillator Applications	108
5.5.1	Passive Lumped LC Resonator	109
5.5.2	Planar Transmission Line Resonator	109
5.5.2.1	Microstripline Resonator	110
5.5.3	Active Resonator	110
5.6	Conclusion	113
<b>6.0</b>	<b>Printed Coupled Slow-Wave Resonator Oscillators</b>	<b>114</b>
6.1	Introduction	114
6.1.1	Lossless Transmission Line	115
6.1.2	Capacitive Loaded Transmission Lines (CTL)	115
6.2	Slow Wave Resonator (SWR)	116
6.2.1	Slow Wave Evanescent Mode (SWEM) Propagation	119
6.2.2	SWEM Resonator Modes and Noise Dynamics	119
6.3	Slow Wave Resonator Oscillator	120
6.3.1	Slow Wave Resonator Coupling Characteristics and Q-factor	120
6.3.2	Loaded Open Loop Printed Resonator Coupling and Mode Characteristics	126
6.4	Tunable Low Phase Noise Oscillator Circuits	129
6.4.1	Examples: Slow Wave Resonator Based Tunable Oscillator Circuits	130
6.4.1.1	Tunable (2000-3200 MHz) Oscillator Circuits [US Patent No. 7,365,612 B2]	130
6.4.1.2	Hybrid Tuned Wideband Circuit (1600-3600 MHz) with Coarse and Fine Tuning	133
6.4.1.3	Power Efficient Wideband Oscillator (SWRO) Circuits (2000-3000 MHz)	136
6.4.1.4	User-Defined Ultra Low Phase Noise Oscillator Circuits [US Patent No. 7,586,381]	138
6.4.1.5	Multi-Octave Band SWRO Circuit [US Patent No. 7,605,670]	141
6.4.1.6	High Frequency Push-Push VCO Topology [US Patent No. 7,292,113]	147
6.4.1.7	Multi-Octave Band Push-Push VCO Topology [US Patent No. 7,292,113]	152
6.4.1.8	Substrate Integrated Waveguide (SIW) Resonator Based Oscillators	154
6.4.1.9	OEO using Metamaterial Resonator	167
6.5	Conclusion	169
<b>7.0</b>	<b>Printed Coupled Mobius Resonator Oscillators</b>	<b>170</b>
7.1	Introduction	170
7.2	Planar Mobius strip Resonator	170
7.3	MCPR Oscillator: Inexpensive Alternative of DRO	173
7.3.1	Synthesized Frequency Sources using Mobius coupled resonator VCOs	177
7.4	Mobius Coupled Resonator: Applications	177
7.4.1	Mobius Resonator Strips for RTRD Applications	178
7.4.2	Mobius Coupled Resonator Strips: Discussion	182
7.5	Conclusion	182
<b>8.0</b>	<b>Printed Coupled Metamaterial Resonator Based Frequency Sources</b>	<b>183</b>
8.1	Metamaterial	183
8.2	The Electromagnetic Wave Propagation Dynamics of Metamaterial	185
8.2.1	Backward Wave Propagation Dynamics in Left-Handed Material	188
8.2.2	Evanescent Wave Propagation Dynamics	189
8.2.3	Phase Velocity, Group Velocity, Energy Density	191
8.2.3.1	Phase Velocity	191
8.2.3.2	Group Velocity	191
8.2.3.3	Energy Density	192
8.3	Realization of NRM Components	192

8.3.1	Split Ring Resonator (SRR) s NRIM	193
8.3.2	Coupled Wire Sets NRIM	193
8.3.3	Dielectric Material Resonator NRIM	194
8.4	Metamaterial NRIM Model	194
8.4.1	Resonator Model	194
8.4.2	Transmission Line Model (TLM)	194
8.5	Physical Realization of Metamaterial Component for Oscillator Circuits	196
8.6	CSRR (Complementary Split Ring Resonator) for Oscillator Circuit Applications	199
8.7	Slow Wave Metamaterial Resonator (SWMR)	200
8.8	Examples: Tunable Oscillators Using SWMR	201
8.8.1	Tunable 2-4 GHz Oscillator using SWMR	203
8.8.2	Multi-band Oscillators using Printed Slow Wave Metamaterial Resonator	203
8.8.3	MCSWMR (Mode Coupled Slow Wave Metamaterial Resonator) VCO	208
8.8.4	Example: Compact Size MCSWMR VCOs	209
8.8.4.1	Example: 3.385 GHz Evanescent Mode Metamaterial Resonator Oscillator	212
8.8.4.2	Example: 7 GHz Evanescent Mode Phase-Injection Mode Coupled Oscillator	213
8.8.4.3	Example: Tunable EMPIMC Oscillator	216
8.9	High Performance Frequency Synthesizer Using MCSWMR VCO	218
8.10	Conclusion	227
<b>9.0</b>	<b>High Performance X-band Oscillators</b>	<b>228</b>
9.1	Introduction	228
9.2	DRO Circuit Topology	228
9.3	Dielectric Resonator (DR)	229
9.4	Design Methodology of Parallel Feedback 10GHz DRO Circuit	231
9.5	Conclusion	240
<b>10.0</b>	<b>High Performance Opto-Electronic Oscillators (OEOs)</b>	<b>242</b>
10.1	Introduction	242
10.2	Opto-Electronic Oscillator (OEO) System	242
10.3	Conclusion	249
<b>11.0</b>	<b>Conclusion</b>	<b>250</b>
11.1	Summary of Work	250
11.2	Futuristic Work	250
<b>Symbols</b>		S1-S8
<b>References</b>		R1-R24

## Summary

In modern information technology, increasingly powerful electronic circuits are required for the targeted generation of complex signals with well-defined amplitudes and phases. In circuits of this type, oscillators frequently form the central element because of its phase noise and stability, which essentially determines the achievable precision in the signal generation. Further requirements are derived from the electronic definability of the signal properties and the operational behavior of the oscillators. Conventional oscillator circuit models autonomous circuits, mainly consist of a passive frequency-selective or phase-selective network and an active amplifier element, which together produce an oscillatory circuit via a suitable feedback. At first glance, the circuit topology seems to be quite simple and can often be explained quite visibly. However, when it comes to describing in particular the very important phase noise dynamics and stability of oscillators, it very soon becomes apparent that highly complex structures are involved. A fundamental difficulty in the theoretical description arises due to the non-linear behavior of oscillators, the understanding of which is crucial for a reliable description of jitter and oscillator phase noise. The resonant condition of oscillators arises due to the fact that the noise in the oscillator circuit is always present in the system for  $T > 0$  degree Kelvin, which is amplified in a frequency-selective manner to the extent that a stable oscillation arises at most at a fixed frequency because of non-linear limitation of the amplification. The frequency selectivity arises due to the frequency selectivity or phase selectivity of the mainly passive feedback path. The non-linear limitation of the amplification in the oscillator normally results in a very reliable control of the amplitude noise of the output oscillation. It is well understood that any particular oscillator's phase noise could be improved by increasing the generated signal amplitude or increasing the quality factor of the resonant network. Increasing the signal level is limited by the utilized supply voltage or the break down limits of transistors and cannot be increased further to improve the phase noise. Accordingly, the remaining phase noise, which can normally be minimized via resonating circuits with pronounced phase selectivity and therefore a high quality factor resonator, is of great importance for oscillators. Traditional high Q-factor resonators (ceramic resonator, surface acoustic wave, bulk acoustic wave, dielectric resonator, YIG resonator, Whispering gallery mode resonator, Optoelectronic resonator, etc.) are usually 3-dimensional structures and bulky for both handheld and test-measurement equipments and does not offer integration using current foundry technology. The 4<sup>th</sup> generation wireless communication market is pushing the need for miniaturization to its limits. Printed coupled transmission line resonator is a promising alternative due to its ease of integration and compatibility with planar fabrication processes but limited by its large physical size and low quality factor, making it a challenging choice to design low phase-noise oscillators. This problem is more prominent in integrated circuits (ICs) where high degrees of thin conductor losses reduce the quality factor by orders of magnitude compared to hybrid circuit technologies.

This thesis describes the design and investigation of a variation of printed resonators using Möbius slow-wave structures for the applications in oscillator circuits. A novel Möbius slow-wave mode-coupled structure offers additional degrees of freedom (higher Q-factor and multi-band characteristics) as compared to conventional transmission line printed resonators. A design study has been carried out to optimize the phase noise performance by using the novel resonant structures (mode-coupled, slow-wave, Möbius strips, evanescent mode, negative index metamaterial) in conjunction with mode coupling, and injection locking for improving the overall performances, beyond the limits imposed by conventional limitations. The thesis also covers a broad spectrum of research on DRO and OEO ranging from practical aspects of circuit implementation and measurement through to sophisticated design and the modeling of complex circuits and resonator structures. This thesis is research work carried out from 2004-2014, organized in 11 chapters, theoretical and experimental

results documented by a range of specific measurement results and substantiated by over 150 publications in scientific conferences and over dozen patents approved, which are listed below:

1. *Metamaterial Resonator Based Oscillators, US Patent applications No. 61976185, April 2014*
2. *BALUN, US Patent applications No. 61976199, April 2014*
3. *Integrated production of self injection locked self phase loop locked Opto-electronic Oscillators", US Patent application no. 13/760767 (Feb 06, 2013).*
4. *User-definable, low cost, low phase hit and spectrally pure tunable oscillator, European Patent No. 1 783 893 - January, 9, 2013*
5. *Self Injection Locked Phase Locked Looped Optoelectronic Oscillator, US Patent application No. 61/746, 919 (Dec 28, 2012).*
6. *Wideband Voltage Controlled Oscillator Employing Evanescent Mode, Japanese Patent No. 5102019 - October 5, 2012*
7. *Passive Reflection Mixer, CA. Patent No. 2524751 - March 1, 2010*
8. *Tunable Oscillator, CA. Patent No. 2533623 - March 1, 2010*
9. *Tunable Frequency, Low Phase Noise and Low Thermal Drift Oscillator, CA. Patent No. 2534370 - February 9, 2010*
10. *Low Noise And Low Phase Hits Tunable Oscillator, US Patent No: 7,636,021 - December 22, 2009*
11. *Visually Inspectable Surface Mount Device Pad, US Patent No: 7,612,296 - November 3, 2009*
12. *User-Definable Low Cost, Low Noise, and Phase Hits Insensitive (Multi-Octave-Band Tunable Oscillator), US Patent No: 7,605,670 - October 20, 2009*
13. *User-Definable Low Cost, Low Phase Hits and Spectrally Pure Tunable Oscillator, US Patent No: 7,586,381 - September 8, 2009*
14. *User-Definable Low Cost, Low Noise, and Phase Hits Insensitive Multi-Octave-Band Tunable Oscillator, CA. Patent No. 2568244 - September 24, 2009*
15. *Passive Reflection Mixer, U.S. Patent No. 7,580,693 - August 25, 2009*
16. *Integrated Low Noise Microwave Wideband Push-Push VCO, CA. Patent No– 2548311, Aug 2009*
17. *User Definable Thermal Drift Voltage Oscillator, CA. Patent No. 2548317 - August 5, 2009*
18. *Low Noise, Hybrid Tuned Wideband Voltage Controlled Oscillator, US. Patent 7365612, April 2008*
19. *Multi-Octave Band Tunable Coupled - Resonator Oscillator, US Patent No. 7292,113, NoV. 2007*
20. *User-Definable Thermal Drift Voltage Controlled Oscillator, US Patent No. 7265,642, Sept. 2007*
21. *Low Thermal Drift, Tunable Frequency VCO, US Patent No. 7262670 Aug. 2007*
22. *Tunable Frequency, Low Phase Noise and Low Thermal Drift Osc. US Patent 7196591 March 2007*
23. *Wideband Voltage Controlled Oscillator Employing Evanescent Mode Coupled-Resonators U.S. Patent No. 7,180,381 - February 20, 2007*
24. *Oscillator Circuit Configuration, U.S Patent No. 7,102,453 - September 5, 2006*
25. *Integrated Low Noise Microwave Wideband Push-Push VCO U.S. Patent No. 7088189, Aug. 2006*



## **Preface, Appreciation, and Acknowledgement**

This work is the result of my research in the area of microwave oscillators and my desire to replace the expensive resonators (ceramic resonator, SAW resonators, Dielectric Resonators, YIG resonators) with new class of printed slow-wave mode-coupled resonator that minimizes microphonics and yet optimizes phase noise, output power, harmonics, and size. The novel injection-mode-locking approach is validated in 100 MHz Crystal oscillator, X-band DRO, X-band Opto-electronic oscillator (OEO), and X-band printed resonator oscillator solution for applications in current and later generation communication systems. This work is a continuation of my Dr.-Ing dissertation in TU-Berlin, Germany. The related research work was only possible based on many measurements and tests performed at Synergy Microwave Corporation. I am thankful for the support of Anisha Apte for doing the required proofreading of the manuscript.

### **Slow Wave Resonator Based Tunable Multi-Band Multi-Mode Injection-Locked Oscillators**

Submitted in February 2013 to the Technischen Universität Cottbus-Senftenberg

The possibility to use this research topic for habilitation made available by Prof. Dr.-Ing. habil Ulrich L. Rohde (BTU-Germany) who made himself available for many discussions on this novel technology. Prof. Dr.-Ing. habil Wolfgang Heinrich (TUB-Germany), Prof. Dr.-Ing. Matthias Rudolph (BTU-Germany), Prof. Ignaz Eisele (UniBW-Germany), Prof. Dr.-Ing. Thomas Eibert (TUM-Germany), Prof. Dr.-Ing. Gerhard Lappus, Prof. Tatsuo Itoh (UCLA-USA), Prof. Afshin Daryoush (DU-USA), Prof. Shiban Koul (IITD-India), Prof. Takashi Ohira (TUT-Japan), Prof. Dr.-Ing. Frank Küppers and Prof. Hans Hartnagel (TUD-Germany) were always available for technical discussions and useful recommendations.

My acknowledgements would not be complete without expressing gratitude towards Mother Nature, our creator and redeemer.

# Chapter 1

## Introduction

### 1.1 Abstract

The current generation radio communication market has been experiencing tremendous growth and will continue to do so in the next decade. Future radio communication units will require higher speed for faster data transmit rate, higher operating frequency to accommodate more channels and users, more functionality, light weight, lower power consumption, and low cost. Oscillators are vital components of any radio frequency (RF) communications system. They are necessary for the operation of phase-locked loops commonly used in frequency synthesizers and clock recovery circuits, and are present in digital electronic systems, which require a reference clock signal in order to synchronize operations. Phase noise is of major concern in oscillators, as it affects adjacent channel interference and bit-error-rate, ultimately limiting the overall performance of communications systems. In general, an oscillator's phase-noise determines the overall communications system's capability and places inflexible requirements on the performance of other transceiver modules.

The oscillator theory is complex and mystifying. It is still an open issue despite significant gains in practical experience and modern CAD tools for design. To this end, the oscillator noise theory, on how the resonant circuit builds the transient and stable resonance condition, resonator structure, active device noise mechanism, optimum drive level and conduction angle, the nature of signals generated, and the effect of flicker noise are often considered as research topics. Rohde [1] has formulated a unified noise equation for predicting the phase noise within reasonable degree of accuracy for a given resonator Q-factor and circuit operating condition. However, improving the resonator Q-factor is a challenging task under the given constraints of planar and integrable solutions in miniaturized size and cost. The design of low noise octave-band VCOs is challenging and difficult because maintaining uniform Q of the resonator/tuning network for wideband is a complex phenomenon. It is a major challenge to find ways to realize low phase noise with low Q-factor components at higher operating frequency that supports multi-octave-band tunability.

This thesis describes the design and investigation of a variation of printed resonators using Möbius slow-wave structures for the applications in tunable low phase noise oscillator circuits, including design basis of optical fiber delay resonator based Opto-electronic Oscillators. A novel Möbius slow-wave mode-coupled structure offers additional degrees of freedom (higher quality factor, multi-band characteristics, compact size, and phase-hits insensitivity) as compared to conventional transmission line printed resonators.

### 1.2 Motivation

The need for miniaturization of signal sources for application in modern communication systems has presented new challenges to the design of high quality factor compact resonators. The miniaturization of electronic components has received a lot of attention in the last decades due to the rapid development of the telecommunications industry. Traditional high Q-factor resonators (ceramic resonator, dielectric resonator, YIG resonator, Whispering gallery mode resonator, Optoelectronic resonator, etc.) are usually too heavy and bulky for both, the handheld and test-measurement equipments and does not offer integration using current foundry technology. The 4<sup>th</sup> generation wireless communication market is pushing the need for miniaturization to its limits. Printed coupled transmission line resonator is a promising alternative due to its ease of integration and compatibility with planar fabrication processes but limited by its large physical size and low quality factor, making it a

challenging choice to design low phase-noise oscillators. This problem is more prominent in integrated circuits (ICs) where high degrees of thin conductor losses reduce the quality factor by orders of magnitude compared to hybrid circuit technologies.

Different techniques have been developed to achieve miniaturization of printed resonators, such as negative index resonator network, Möbius coupled resonator network, and slow wave mode-coupling methods using capacitively loaded transmission lines (CLTL) [2]. The CLTL concept has been explored to reduce the size of printed coupled resonator circuits for low cost high performance signal source solutions [3]. The research work done is towards developing mode-coupled slow-wave Metamaterial resonator (MCSWMMR) topology for multi-band multi-mode resonance condition for switchable band modern radio architecture.

In multi-band multi-mode radio architectures, a number of local oscillator (LO) frequencies are required in order to process the information in various frequency bands. Since oscillators consume a substantial part of the IC chip area, and battery power the design approach of slow-wave resonator based tunable multi-band multi-mode injection-locked oscillator offers concurrent multiple frequencies with the user having an option of choosing a frequency or combination of them that eliminate the need of lossy switches for switching the frequency band, thereby improves the throughput. Various techniques, such as switching between VCOs for separate bands, utilizing inter-modal multiple frequency, using switched resonators for band selection have been proposed in past for the realization of multi-octave-band oscillators. However, these result in large size of the circuit, current hungry, narrow band, and poor phase noise performances. Switched inductors or capacitor banks suffer from the resistive and capacitive parasitics associated with the switches [4].

### **1.3 Problem Statement**

The definition of problem undertaken in this research work is to investigate the complex resonant structures (mode-coupled, slow-wave, Möbius strips, evanescent mode, negative index Metamaterial), including active and high-order resonant circuits, capable of overcoming the limited quality-factor of current planar hybrid and IC fabrication technologies. The research described here explores a different novel topology for both narrowband (<5% tuning) and wideband oscillators (>50% tuning), including the optimization of the performance for low phase-noise signal source applications. The proposed methods can be applied and suited for miniaturized low phase-noise voltage controlled-oscillator solutions at microwave and mm-wave frequencies using hybrid or integrated circuit fabrication technologies.

Furthermore, this work examines systems of coupled oscillators using N-push/push-push configuration in conjunction with slow-wave planar resonator networks, and points out the realization of integrated SiGe HBT/GaAs HBT based MMIC solutions at higher frequencies (2-40 GHz). For millimeter wave application, the active devices are often pushed near to their physical limits of operation, resulting in degraded noise performance of the integrated oscillator/VCOs circuit. The N-push/push-push oscillator basically enhances the even mode harmonics and suppresses the odd mode output, doubling the frequencies, so higher oscillating frequencies can be obtained beyond the limitation caused by the cut-off frequency of the available three terminal active devices and the tuning diodes. The monolithic VCO implementations suffer from poor phase noise performance partly due to the low quality factor Q of the resonator networks. A design study has been carried out to optimize the phase noise performance that incorporates the N-push/push-push approach to compensate for the low Q-factor in the integrated VCO implementation.

### **1.4 Definition of the Task and Oscillator Figure of Merit (FOM)**

Tunable oscillators are considered as most important RF module, used in portables and test & measurement equipments (spectrum analyzers, frequency sweepers, network analyzers, etc.). The

demand of broadband oscillators is increasing in modern communications systems for enabling 4G features. Frequency domain test and measurement systems pose design challenges for wideband VCOs design due to the constraint of size, cost, power-consumption, and phase noise performance. The phase noise performance of the oscillator is very critical, and it is the governing figure of merit for overall system performances. The challenge is to build an ultra-low phase noise signal source; but the difficulties related with measurement of low phase noise oscillators using modern phase noise measurement equipments are paramount. Chapters 3 & 4 are dedicated for oscillator phase noise dynamics and phase noise measurement related issues with concluding remarks about the noise model and measurement techniques.

The monolithic VCO implementations suffer from poor phase noise performance partly due to the low quality factor  $Q$  of the printed resonator at high frequencies. It is a common-practice to design oscillators using single resonators. However, in this case, the achievable oscillator  $Q$  is determined and limited by the resonator technology used. In particular, planar resonators suffer from excessive conductor and substrate losses limiting their achievable quality-factor. Therefore, conventional low phase-noise oscillator design techniques rely on reducing the losses in single resonators by manipulating their circuit designs and layouts. A design study has been carried out to optimize the phase noise performance by incorporating the resonant structures (mode-coupled, slow-wave, Möbius strips, evanescent mode, negative index Metamaterial) for high performance signal source applications.

It will be investigated as to how the  $Q$ -factor of resonator can be improved, and identifying the effects that limit the tuning range, which leads to the development of the several electromagnetic coupling scheme towards improving the phase noise performance. The objective is to realize low cost, tiny and high performance signal sources using novel planar resonator oscillator for the applications of current and later generation communication systems. Several design examples are discussed in Chapters 5-11 for the validation of the new approaches based on the following tasks listed as follows:

- general closed form expression for quality factor of active and passive resonators
- exploring architecture of high quality factor slow-wave planar resonator
- exploring architecture of Möbius strips planar resonator for low phase noise
- exploring architecture of Metamaterial resonator for multi-band operation
- exploring architecture and design methodology of Opto-Electronic Oscillator (OEO)

This dissertation deals with the design, fabrication, and testing of various wideband VCOs using slow-wave multi-coupled resonators based oscillators. A miniaturized printed coupled transmission line resonator using slow wave structure is developed and the methodology for obtaining high quality factor resonator is discussed. The new resonator structure is characterized for various oscillator topology using Metamaterial resonators. The tunable oscillators considered in this work are based on the commercially available discrete Si and SiGe HBTs using abrupt and hyper abrupt varactor diodes for wideband tuning. The manufacturers S-parameters data available for the transistor is valid for small-signal cases but oscillator circuits are large signal circuit operations. As most designers do not have elaborate and expensive equipment for device parameter extraction, the large signals S-parameters are generated using a synthesis-based approach. The high performance oscillators proposed in this thesis offers significant improvement in figure of merit (FOM) for a given phase noise, tuning range, and power consumption. A spot phase noise number is difficult to compare, unless it is compared at the same frequency offset from the carrier and the same carrier frequency for a given tuning range and output power. Comparing oscillators operating at different frequencies, tuning range, and output power levels, a figure of merit (FOM) with a single number has long been desired. In order to make a fair comparison

of performances of VCOs (voltage-controlled oscillators) at different operating frequencies are given by *FOM* (figure-of-merit) in  $\left(\frac{dBc}{Hz}\right)$  and PFTN (power-frequency tuning-normalized) in dB, defined as [5]

$$FOM|_{f_{offset}} = \left[ \mathcal{E}(f_{offset}) - 20 \log_{10} \left( \frac{f_o}{f_{offset}} \right) + 10 \log_{10} \left( \frac{P_{DC}}{1mW} \right) \right] \left( \frac{dBc}{Hz} \right) \quad (1.1)$$

$$PFTN = - \left[ \mathcal{E}(f_{offset}) - 20 \log_{10} \left( \frac{\Delta f}{f_{offset}} \right) - 10 \log_{10} \left( \frac{P_{DC}}{kT} \right) \right] (dB) \quad (1.2)$$

where  $f_o$  is the oscillation frequency,  $\mathcal{E}(f_{offset})$  is the phase-noise at the offset frequency  $f_{offset}$ ,  $k$  is the Boltzmann constant,  $\Delta f = f_{max} - f_{min}$  is tuning range,  $T$  is temperature in Kelvin, and  $P_{DC}$  is the total consumed DC power in milli-watts.

From [5], larger values of  $|FOM|$   $\left(\frac{dBc}{Hz}\right)$  and *PFTN* (dB) values relates to superior oscillators. From (1.1) and (1.2), the FOM for integrated phase noise in dBc from 1 kHz to 1 MHz can be given by  $FOM|_{Integrated(1kHz-1MHz)}$

$$FOM|_{Integrated(1kHz-1MHz)} = 10 \log(P^2(\emptyset)) + 10 \log \left( \frac{P_{RF}}{P_{DC}} \right) - 20 \log \left( \frac{2\Delta f}{f_{max} + f_{min}} \right) \quad (1.3)$$

where

$$\Delta f = f_{max} - f_{min}$$

$f_{max}$  = maximum oscillation frequency

$f_{min}$  = minimum oscillation frequency

$P^2(\emptyset)$  = integrated phase noise from 1 kHz to 1 MHz

$P_{RF}$  = signal output power averaged over frequency

$P_{DC}$  = DC power consumption of the oscillator

The novel Möbius coupled slow wave resonator based X-band oscillator proposed in the thesis (Chapter-10) allows for the design of oscillator with state-of-the-art phase-noise performance, close to the phase-noise of the expensive high Q-factor DROs (shown in Table 1.1), while providing compact and planar structures compatible with hybrid and integrated circuit fabrication technologies.

Table 1.1 shows the state-of-the-art oscillators using different fabrication technologies for comparative analysis. Table 1.2 shows the printed resonator based oscillators for comparative analysis. Table 1.3 shows the comparative analysis for tunable voltage controlled oscillator circuits based on *FOM* (figure-of-merit) in  $\left(\frac{dBc}{Hz}\right)$  and PFTN (power-frequency tuning-normalized) parameters. As shown in Tables 1.1, 1.2, and 1.3, this work shows superior FOM and PFTN performance of tunable voltage controlled oscillators (VCOs) compared to published result to date for a given class and topology [6]-[32].

## 1.5 Overview of the Thesis

This thesis organized in 11 chapters. The scientific chapters structured in such a way that graduate students and engineers can easily follow the state-of-the art oscillator technology and phase noise measurement scheme for the validation of the approach and techniques discussed.

**Chapter 1** – briefly discusses a short introductory abstract, motivation, problem statement, defines the task and oscillator figure of merit (FOM) in order to make a fair comparison of performances of different oscillator topologies operating at different frequencies and DC bias condition, and provides an overview of the contents of this thesis.

References	Oscillator	Technology	$f_o$ (GHz)	$P_o$ (dBm)	DC-RF Efficiency	$L(f)$ $\left(\frac{dBc}{Hz}\right)$ @1MHz	$FOM$ $\left(\frac{dBc}{Hz}\right)$ @1MHz
ref [6]	DRO	Non Planar	23.8	3.3	3.4%	-146@ 1 MHz	-215.6
ref [7]	DRO	Non Planar	6.7	14	3.1%	-155 @ 1 MHz	-202.5
ref [8]	DRO	Non Planar	8	14.5	2%	-162 @ 1 MHz	-208.6
ref [13]	DRO	Non Planar	25.9	6.5	3.4%	-122@ 1 MHz	-188.9
<b>This work Ch-4: Fig. 4-23</b>	Ocxo	Non Planar	0.1	15	11.2%	-183.4 @ 100kHz	-218.9
<b>This work Ch-9: Fig. 9-21</b>	DRO	Non Planar	10	11	2.58%	-162@ 1 MHz	-215.1
<b>This work Ch-10: Fig. 10-12</b>	OEO	Non Planar	10	10	1%	-170@ 1 MHz	-220

Reference	Resonator	Technology	$f_o$ (GHz)	$P_o$ (dBm)	DC-RF (Efficiency)	$L(f)$ $\left(\frac{dBc}{Hz}\right)$ @ 1MHz	$FOM$ $\left(\frac{dBc}{Hz}\right)$ @1 MHz
ref [9]	Microstrip ring	Planar	12	5.3	48.7%	-116.2	-189.3
ref [10]	Microstrip hair-pin	Planar	9	9	4.5%	-129	-185.6
ref [11]	IC- FBAR	Quasi-Integrated	2.4	-2.5	1.9%	-144	-195.7
Ref [12]	Ring	CMOS IC	10	-15	1%	-110	-185.2
<b>This work Ch-5: Fig. 5-21</b>	Active Resonator	Planar	3.2	5	2.1%	-162	-210.3
<b>This work Ch -6: Fig. 6-22c</b>	Slow Wave Resonator (SWR)	Planar	0.622	5	3.16%	-170	-205.8
<b>This work Ch -6: Fig. 6-22c</b>	Slow Wave Resonator (SWR)	Planar	2.488	4.2	2.63%	-155	-202.9
<b>This work Ch -6: Fig. 6-22c</b>	Slow Wave Resonator (SWR)	Planar	4.2	3.3	2.14%	-150	-202.4
<b>This work Ch -7: Fig. 7-8</b>	Hybrid Coupled Resonator	Planar	10	2.88	1.2%	-138	-195.9
<b>This work Ch -7: Fig. 7-8</b>	Möbius Coupled Resonator	Planar	10	3.3	1.3%	-145	-202.9
<b>This work Ch -7: Fig. 7-8</b>	Mode-Locked Möbius Resonator	Planar	10	4.5	1.7%	-147	-204.9
<b>This work Ch -8: Fig. 8-27b</b>	Mode-Coupled Slow-Wave Metamaterial	Planar	10.24	10.05	1.3%	-160	-215

	Resonator						
<b>This Work Ch-8: Fig. 8-31d</b>	EMPIMC Oscillator	3.85	300	5	1.5%	-168	-215

Table 1.3: Comparison of tunable oscillator circuits performance published and this work

Reference	Technology	$f_o$ (GHz)	$P_{DC}$ (mW)	$P_o$ (dBm)	Tuning Range	$L(f)$ $\left(\frac{dBc}{Hz}\right)@$ 1MHz	$FOM$ $\left(\frac{dBc}{Hz}\right)@1$ MHz	PFTN (dB)
ref [14]	CMOS (0.18- $\mu$ m)	25.1	11	-4.2	3.01 GHz (12%)	-99.94	-177.5	-14.7
ref [15]	CMOS (0.18- $\mu$ m)	20.9	40.32	-6.83	2.17 GHz (10.4%)	-111.67	-181.5	-11.5
ref [16]	CMOS (0.18- $\mu$ m)	19.9	39	-3	0.51 GHz (2.6%)	-111	-181.06	-24.6
ref [17]	CMOS (0.18- $\mu$ m)	20.7	10.8	-21.12	1.8 GHz (8.7%)	-108.67	-181.06	-24.6
ref [18]	CMOS (0.18- $\mu$ m)	40	6		1.12 GHz (2.8%)	-109	-193.26	-14.44
Ref [19]	CMOS (0.13- $\mu$ m)	28	12		1.87 GHz (6.7%)	-113	-191.151	-6.304
ref [20]	CMOS (90-nm)	20.9	6.3		0.647 GHz (3.1%)	-117.2	-195.61	-8.540
ref [21]	CMOS (0.18- $\mu$ m)	18.95	3.3		0.678 GHz (3.58%)	-110.82	-191.187	-11.712
ref [22]	CMOS (0.18- $\mu$ m)	21.37	3.5		1.089 GHz (5.1%)	-109.8	-190.955	-8.8704
ref [23]	CMOS (0.12 $\mu$ m SOI)	44	7.5		4.312 GHz (9.8%)	-101	-185.118	-9.034
ref [24]	CMOS (65-nm)	38.4	80		6.873 GHz (17.9%)	-97.5	-170.156	-18.764
ref [25]	RTD/HBT	17.65	1.42	-9.0	0.37 GHz (2.1%)	-112	-195	-12.13
ref [26]	SiGe HBT	41	280		10.78 GHz (26.3%)	-110	-177.784	-7.794
ref [27]	SiGe BiCMOS	22.1	11.1	-11.3	4.552 GHz (20.6%)	-109	-181.435	-2.265
<b>This Work Ch-6: Fig. 6-19b</b>	Si- Bipolar	2.615	240	3	1390 MHz (53.1%)	-150	-194.4	15.08
<b>This Work Ch-6: Fig. 6-20b</b>	Si- Bipolar	2.6	400	4	2000 MHz (76.9%)	-135	-177.2	1.02
<b>This Work Ch-6: Fig. 6-21c</b>	Si- Bipolar	2.5	150	-3	1000 MHz (40%)	-156	-202.1	20.26
<b>This Work Ch-6: Fig. 6-26a</b>	Si- Bipolar	1.341	200	3	1543MHz (115%)	-148	-187.6	16.02

<b>This Work Ch-6: Fig. 6-26b</b>	Si- Bipolar	1.5	200	-3	2041 MHz (136%)	-157	-197.5	26.20
<b>This Work Ch-6: Fig. 6-28e</b>	SiGe HBT	7.92	300	-3	4644 MHz (58.5%)	-118	-171.2	-7.41
<b>This Work Ch-8: Fig. 8-22b</b>	SiGe HBT SWMR	3	120	3	2000 MHz (66.6%)	-142	-190.75	13.25

**Chapter 2** – summarizes important principles of oscillator theory and describes oscillator topologies and important properties of oscillators such as selection of resonator networks and performance matrices (frequency range and tuning characteristics, tuning linearity, tuning sensitivity, tuning speed, post-tuning drift, phase noise, output power, harmonic-suppression, spurious response, pushing and pulling). For the device characterization, large signal S-parameter measurements performed on bipolar and JFET for the validation of low phase noise oscillators are discussed in Ch 6, Ch 7, Ch 8, and Ch 9.

**Chapter 3** – devoted to the principles of oscillator noise dynamics including different noise models. To supplement this, different methods for the Phase noise measurements noise are presented and evaluated in Chapter 4.

**Chapter 4** – describes the phase noise measurement techniques and limitations, prediction and validation of oscillator phase noise measured on commercially available different PN equipments ((Agilent E5052B, R&S FSUP, Holzworth, Noise XT-DCNTS, and Anapico APPH6000-IS), phase noise measurement evaluation in Faraday Cage, CAD simulation and phase noise measurement of 100 MHz OCXO circuits. The selection of 100 MHz OCXO was done based on on-going demand of low phase noise reference frequency sources, measurement was carried out at IEEE sponsored 2012 IMS Symposium in Canada, 2013 IMS Symposium in Seattle, USA, 2014 IMS Symposium in Tampa, USA for giving understanding about the uncertainty involved in phase noise measurement.

**Chapter 5** – an overview of microwave resonator and its characteristics (resonator quality factor, figure-of-merit), resonator design criteria for oscillator application discussed. The options for the implementation of passive and active resonators and the normal procedures for their characterization are set out and evaluated in the light of the thesis research work.

**Chapter 6** – describes printed transmission line resonator networks, resonant properties of capacitively loaded transmission line resonator, and slow wave resonator dynamics, and the discussion focuses on how the phase speed on the line structures can be reduced via capacitive load. The key element of this chapter is the use of evanescently coupled resonance modes, wherein an increased phase selectivity of the resonance modes can be achieved using slow wave resonator (SWR) through the coupling of different modes. Different coupling methods are investigated and implemented for comparative analysis. The novel oscillator structure using slow wave resonator (SWR) shows significant advantages in terms of size, power consumption and frequency tunability, prototype examples are validated and built over million for radio applications. The state-of-the-art technology is disclosed in public domain (IEEE publications and patent applications)

**Chapter 7** – deals with printed planar resonators according to the Möbius principle, characterizes the Q and coupling coefficient of the newly developed Möbius resonator structure, presents a range of oscillator implementations with excellent properties for this purpose. Furthermore, use of Möbius strips for microwave sensors and RFID (real time signal retention device) applications is discussed.



**Chapter 8** –deals with artificial negative index material that has been highly newsworthy for a number of years and investigates the possibility of appropriately using these materials (Metamaterial) to implement microwave resonators with advantageous properties. The chapter begins with an introduction to the fundamental properties of Metamaterials, describes the evanescent mode propagation for improving the storing of the energy and improving the group delay of the resonator used within microwave oscillators. A brief description of slow wave characteristics in resonators is discussed; the thesis is focused on slow-wave planar resonators; a common type namely the multiple-coupled slow wave resonator is explored and used. The complex oscillator circuits are subsequently shown and characterized with measurement and simulation results. Very impressive results from specific microwave oscillator implementations in building high performance 10.24 GHz frequency synthesizer are presented.

**Chapter 9** – high-performance oscillators for the X-band are presented which are essentially based on dielectric resonators. The design methodology and implementations of low noise 10 GHz DRO (Dielectric Resonator Oscillators) circuit is described for RADAR applications. The step-by-step procedure of high performance X-band DRO is presented for giving good insights about Disc resonator based oscillator circuits.

**Chapter 10** – this Chapter briefly discusses OEO (Opto-Electronic Oscillator) circuits' topology, and novel design concepts using SILPLL techniques for the realization of stable frequency source for high performance application in modern communication systems. The OEO configuration is amenable for MMIC in silicon, enabling compact, low noise and low cost solution in which it is possible to synthesize any precise RF frequency by adjusting the optical source wavelength, leading to satisfying stable oscillation conditions for a new RF frequency in highly dispersive photonic bandgap fibers. The detailed discussion and validation examples are given in the extended version of this thesis [ref. 33, Appendix F-I).

**Chapter 11** – concludes the thesis and suggests future works (IC fabrication at microwave and millimeter-wave frequencies based on patented techniques) for the benefit of research engineers.

**Symbols** – acronyms and their description is listed for the abbreviations used throughout the thesis

**References** – the list of Publications are listed Chapter wise (Ch-1 to Ch-10) for a quick reference.

## **1.6 Publications and Patent Applications arising from this research work**

This thesis covers a broad spectrum of research ranging from practical aspects of circuit implementation and measurement through to sophisticated design and the modeling of complex circuits and resonator structures. The chapters are primarily structured in such a way that certain principles providing an introduction to the subject are presented in very concise form, and In most cases, the relationship between the oscillator circuits and the previously introduced principles is not explained in detail and must be deduced by the reader himself. The detailed analysis and validation examples are given in [33]. Based on this research work, over 150 technical papers have been published in IEEE journals, conferences, workshops, and over dozen patent applications filed.

## Chapter 2

### General Comments on Oscillators

#### 2.1 Theory of Operation

An oscillator is an autonomous circuit consisting of a frequency selective positive feedback network. The noise present in the active device or power supply turn on transient leads to the initial oscillation build-up [1]-[2]. As a basic requirement for producing a self-sustained, near-sinusoidal oscillation, an oscillator must have a pair of complex-conjugate poles on the imaginary axis i.e. in the right half of an s-plane with  $\alpha > 0$  [3].

$$P(p_1, p_2) = \alpha \pm j\beta \quad (2.1)$$

While this requirement does not guarantee an oscillation with a well-defined steady state (squeaking), it is nevertheless a necessary condition for any oscillator. When subjected to an excitation due to the power supply turn-on transient or noise associated with the oscillator circuit, the right half plane RHS-poles in the equation above produce a sinusoidal signal with an exponentially growing envelope given as

$$v(t) = V_0 \exp(\alpha t) \cos(\beta t) \quad (2.2)$$

$$v(t)|_{t=0} \rightarrow V_0 \quad (2.3)$$

$V_0$  is determined by the initial conditions and the growth of the signal amplitude  $v(t)$  is eventually limited by the associated nonlinearities of the oscillator circuit.

Oscillators are fundamentally a feedback amplifier with a resonator in the feedback path and if enough gain exists for given oscillation conditions, noise will be amplified sufficiently enough to eventually stabilize the gain via non-linearity effects and create an output signal that consists of narrow band noise. This narrow-band profile of the noise characteristics in the oscillator is the prime issue of the oscillator design. The two methods used for analyzing and understanding noise issues for oscillators are the feedback model approach and the negative resistance model. Using either the feedback model approach or the negative resistance model, one can perform the analysis of the oscillator. Depending on the oscillator topology and characteristics, one approach is preferred over the other. The condition of oscillation build-up and steady state oscillation will be discussed using both approaches. The application of either the feedback model or the negative-resistance model is sufficient for analyzing the linear behavior of the oscillator circuit, and it must be unstable about its bias point or, equivalently, have poles in the RHP if an oscillation buildup is to take place.

The feedback model is shown in Figure 2-1, where an oscillator circuit is decomposed into a frequency-dependent forward loop gain block  $H_1(j\omega)$  and a frequency-dependent feedback network  $H_2(j\omega)$ , both of which are typically multi-port networks. If the circuit is unstable about its operating point (poles in the right half of the s-plane), it can produce an expanding transient when subject to an initial excitation. As the signal becomes large, the active device in the circuit behaves nonlinearly and limits the growth of the signal. When oscillation starts up, the signal level at the input of the amplifier (forward loop gain block) is very small, and the amplitude dependence of the forward amplifier gain can be initially neglected until it reaches saturation. The closed loop transfer function (T.F) and output voltage  $V_o(\omega)$  are given by [4]

$$[TF(j\omega)]_{closed-loop} = \frac{[Y(j\omega)]_{output}}{[X(j\omega)]_{input}} = \frac{V_o(\omega)}{V_{in}(\omega)} = \frac{H_1(j\omega)}{1+H_1(j\omega)H_2(j\omega)} \quad (2.4)$$

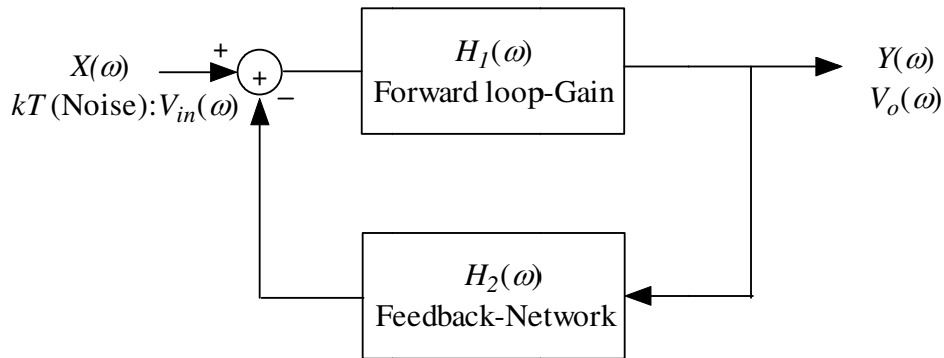


Figure 2-1: Block diagram of basic feedback model-oscillator [4]

$$[Y(j\omega)]_{output} = V_o(\omega) = \left[ \frac{H_1(j\omega)}{1 + H_1(j\omega)H_2(j\omega)} \right] V_{in}(\omega) \quad (2.5)$$

For an oscillator, the output voltage  $V_o$  is nonzero even if the input signal  $V_i = 0$ . This is only possible if the forward loop gain is infinite (which is not practical), or if the denominator  $1 + H_1(j\omega)H_2(j\omega) = 0$  at some frequency  $\omega_o$ ; that is the loop gain is equal to unity for some values of the complex frequency  $s=j\omega$ . This leads to the well-known condition for oscillation (the *Nyquist criterion*), where at some frequency  $\omega_o$ ,  $H_1(j\omega_o)H_2(j\omega_o) = -1$  and can be mathematically expressed as

$$|H_1(j\omega_o)H_2(j\omega_o)| = 1 \quad (2.6)$$

and 
$$Arg|H_1(j\omega_o)H_2(j\omega_o)| = (2n + 1)\pi, \text{ where } n = 0,1,2 \dots \quad (2.7)$$

When the above *criterion* is met, the two conjugate poles of the overall transfer function are located on the imaginary axis of  $s$ -plane, and any departure from that position will lead to an increase or a decrease of the oscillation amplitude of the oscillator output signal in time domain, which is shown in Figure 2-2.

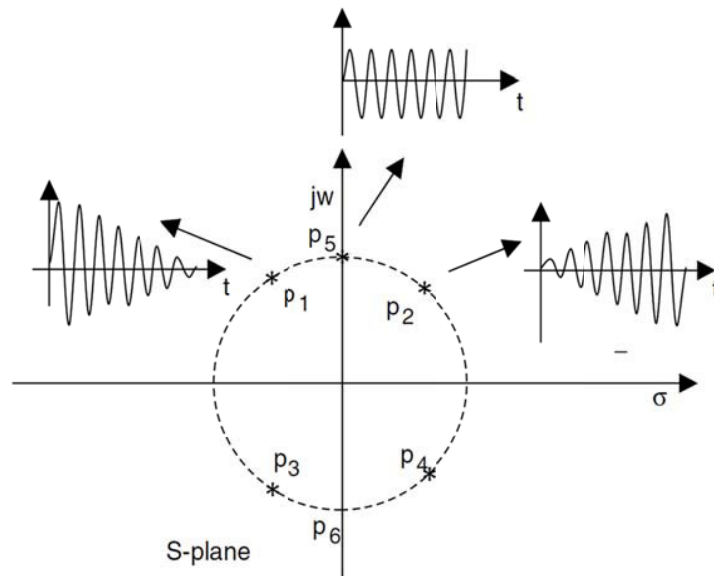


Figure 2-2: Frequency domain root locus and the corresponding time domain response [4]

In practice, the equilibrium point cannot be reached instantaneously without violating some physical laws. As an example, high Q oscillators take longer than low Q types for full amplitude. The oscillator output sine wave cannot start at full amplitude instantaneously after the power supply is turned on. The design of the circuit must be such that at start-up condition, the poles are located in the right half plane, but not too far from the Y-axis. However, the component tolerances and the nonlinearities of the amplifier will play a role. This oscillation is achievable with a small signal loop gain greater than unity, and as the output signal builds up, at least one parameter of the loop gain must change its value in such a way that the two complex conjugate poles migrate in the direction of the Y-axis and that the parameter must then reach that axis for the desired steady state amplitude value at a given oscillator frequency. Figure 2-3 shows the general schematic diagram of a one-port negative resistance model.

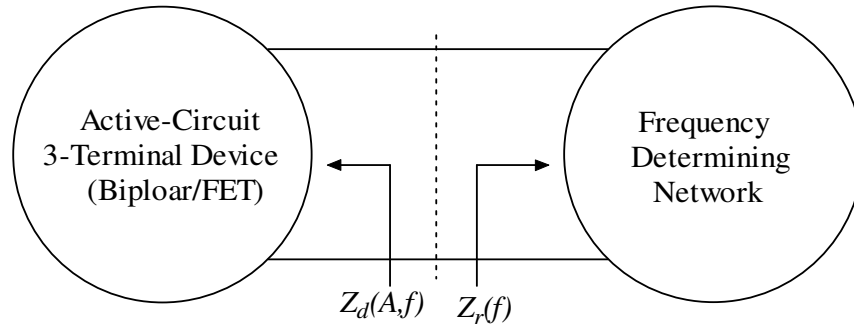


Figure 2-3: Shows the 1-port negative resistance model for the realization of resonant condition using impedance function (compensating the loss resistance associated with the frequency-determining network) [4]

The oscillator circuit is separated into a one-port active circuit, which is a nonlinear time variant (NLTV) and a one-port frequency determining circuit, which is a linear time invariant (LTIV) system. The frequency determining circuit, or resonator, sets the oscillation frequency, and it is signal-amplitude independent.

The function of the active-circuit is to produce a small-signal negative resistance at the operating point of the oscillator and couple it with the frequency-determining circuit while defining the oscillation frequency. Assuming that the steady state current at the active circuit is almost sinusoidal, the input impedance  $Z_d(A, f)$  can be expressed in terms of a negative resistance and reactance as

$$Z_d(A, f) = R_d(A, f) + jX_d(A, f) \quad (2.8)$$

where  $A$  is the amplitude of the steady state current and  $f$  is the resonance frequency.  $R_d(A, f)$  and  $X_d(A, f)$  are the real and imaginary parts of the active circuit and depend on the amplitude and frequency. Since the frequency determining circuit is amplitude-independent, it can be represented as

$$Z_r(f) = R_r(f) + jX_r(f) \quad (2.9)$$

where  $Z_r(f)$  is the input impedance of the frequency determining circuit,  $R_r(f)$  and  $X_r(f)$  are the loss resistance and reactance associated with the resonator/frequency determining circuit.

To support the oscillator build-up,  $R_d(A, f) < 0$  is required so the total loss associated with the frequency determining circuit can be compensated. Oscillation will start build-up if the product of the input reflection coefficient  $\gamma_r(f_0)$ , looking into the frequency determining circuit and the input reflection coefficient  $\gamma_d(A_0, f_0)$  of the active part of the oscillator circuit is unity at  $A = A_0$  and  $f = f_0$ . The steady state oscillation condition can be expressed as

$$\gamma_d(A, f) \gamma_r(f)|_{f=f_0} \Rightarrow \gamma_d(A_0, f_0) \gamma_r(f_0) = 1 \quad (2.10)$$

Figure 2-4 shows the input reflection coefficient  $\gamma_d(A_0, f_0)$  and  $\gamma_r(f_0)$ , which can be represented in terms of the input impedance and the characteristic impedance  $Z_0$  as

$$\gamma_d(A_0, f_0) = \frac{Z_d(A_0, f_0) - Z_0}{Z_d(A_0, f_0) + Z_0} \quad (2.11)$$

$$\gamma_r(f_0) = \frac{Z_r(f_0) - Z_0}{Z_r(f_0) + Z_0} \quad (2.12)$$

$$\gamma_d(A_0, f_0) \gamma_r(f_0) = 1 \Rightarrow \left[ \frac{Z_d(A_0, f_0) - Z_0}{Z_d(A_0, f_0) + Z_0} \right] \left[ \frac{Z_r(f_0) - Z_0}{Z_r(f_0) + Z_0} \right] = 1 \quad (2.13)$$

$$[Z_d(A_0, f_0) - Z_0][Z_r(f_0) - Z_0] - [Z_d(A_0, f_0) + Z_0][Z_r(f_0) + Z_0] = 0 \quad (2.14)$$

$$\Rightarrow Z_d(A_0, f_0) + Z_r(f_0) = 0 \quad (2.15)$$

The characteristic equation  $Z_d(A_0, f_0) + Z_r(f_0) = 0$  can be written as

$$R_d(A_0, f_0) + R_r(f_0) = 0 \quad (2.16)$$

$$\text{and } X_d(A_0, f_0) + X_r(f_0) = 0 \quad (2.17)$$

This means that the one-port circuit is unstable for the frequency range ( $f_1 < f < f_2$ ), where  $R_d(A, f)|_{(f_1 < f < f_2)} < 0 \Rightarrow R_d(A, f)|_{(f_1 < f < f_2)} > R_r(f)$

At the start-up oscillation, when the signal amplitude is very small, the amplitude dependence of the  $R_d(A, f)$  is negligible and the oscillation build-up conditions can be given as

$$[R_d(f) + R_r(f)] \Rightarrow R_d(f_x) + R_r(f_x) \leq 0 \quad (2.18)$$

$$\text{And } [X_d(f) + X_r(f)]_{f=f_x} \Rightarrow X_d(f_x) + X_r(f_x) \leq 0 \quad (2.19)$$

where  $f_x$  denotes the resonance frequency at which the total reactive component equals zero.

The conditions above are necessary, but are not sufficient conditions for oscillation build-up, particularly in a case when multiple frequencies exist to support the above- shown conditions. To guarantee the oscillation build-up, the following condition at the given frequency needs to be met [1]:

$$\frac{\partial y}{\partial f} [X_d(f) + X_r(f)]_{f=f_x} > 0 \quad (2.20)$$

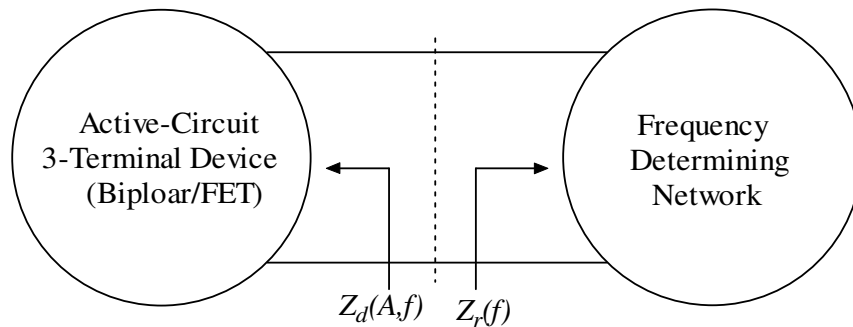


Figure 2-4: Shows the oscillator model for the realization of resonant condition using reflection coefficient  $\gamma$  ( $\gamma_d(A_0, f_0)$  is input reflection coefficient for active circuit which depends on the signal amplitude  $A_0$  and operating frequency  $f_0$ ;  $\gamma_r(f_0)$  is reflection coefficient for resonator depends mainly on the oscillating frequency  $f_0$ ) [4]

$$R_d(f_x) + R_r(f_x) < 0 \quad (2.21)$$

$$X_d(f_x) + X_r(f_x) = 0 \quad (2.22)$$

Alternatively, for a parallel admittance topology [3],

$$Y_d(f_x) + Y_r(f_x) = 0 \quad (2.23)$$

$$G_d(f_x) + G_r(f_x) < 0 \quad (2.24)$$

$$B_d(f_x) + B_r(f_x) = 0 \quad (2.25)$$

$$\frac{\partial}{\partial f} [B_d(f) + B_r(f)]_{f=f_x} > 0 \quad (2.26)$$

Figure 2-5 shows the start-up and steady state oscillation conditions.

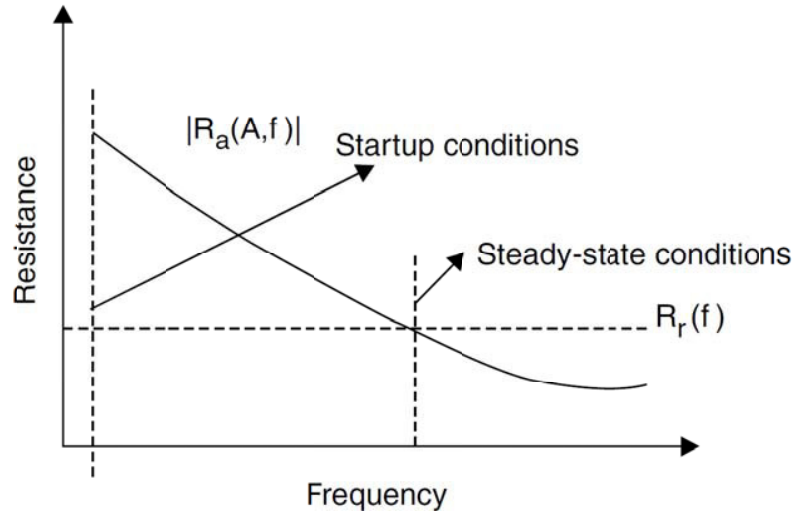


Figure 2-5: Plot of start and steady state oscillation conditions [3]

As discussed earlier, if the closed-loop voltage gain has a pair of complex conjugate poles in the right half of the s-plane, close to the imaginary axis, then due to an ever-present noise voltage generated in the circuit or power-on transient, a growing, near-sinusoidal voltage appears. As the oscillation amplitude grows, the amplitude-limiting capabilities, due to the change in the transconductance from a small signal  $[g_m]$  to the large signal  $[g_m(t)=G_m]$  of the amplifier, produce a change in the location of the poles. The changes are such that the complex-conjugate poles move towards the imaginary axis and at some value of the oscillation amplitude; the poles reach to the imaginary axis giving steady-state oscillation as [2]:

$$|G(j\omega)H(j\omega_0)| = 1 \quad (2.27)$$

In the case of the negative resistance model, the oscillation will continue to build as long as  $R_d(A, f)|_{f_1 < f < f_2} < 0 \Rightarrow |R_d(A, f)|_{f_1 < f < f_2} > |R_r(f)|$ . The frequency of oscillation determined by  $R_d(A_0, f_0) + R_r(f_0) = 0$ , and  $X_d(A_0, f_0) + X_r(f_0) = 0$  might not be stable because  $Z_d(A, f)$  is frequency and amplitude-dependent. To guarantee stable oscillation, the following condition is to be satisfied as [1]

$$\frac{\partial}{\partial A} [R_d(A)|_{A=A_0}] \times \frac{\partial}{\partial f} [X_r(f)|_{f=f_0}] - \frac{\partial}{\partial A} [X_d(A)|_{A=A_0}] \times \frac{\partial}{\partial f} [R_r(f)|_{f=f_0}] > 0 \quad (2.28)$$

$$\frac{\partial}{\partial A} [R_d(A)|_{A=A_0}] \times \frac{\partial}{\partial f} [X_r(f)|_{f=f_0}] > \frac{\partial}{\partial A} [X_d(A)|_{A=A_0}] \times \frac{\partial}{\partial f} [R_r(f)|_{f=f_0}] \quad (2.29)$$

In the case of an LC resonant circuit,  $R_r(f)$  is constant and the equation above can be simplified to [5]

$$\frac{\partial}{\partial A} [R_d(A)|_{A=A_0}] \times \frac{\partial}{\partial f} [X_r(f)|_{f=f_0}] > 0 \quad (2.30)$$

Alternatively, for a paralleled tuned circuit, the steady-state oscillation condition is given as  $Y_d(f_0) + Y_r(f_0) = 0$  (where  $Y_d$  and  $Y_r$  are respective admittances of active circuitry and resonator networks) [5]

$$G_d(f_0) + G_r(f_0) = 0 \quad (2.31)$$

$$B_d(f_0) + B_r(f_0) = 0 \quad (2.32)$$

$$\frac{\partial}{\partial A} [G_d(A)|_{A=A_0}] \times \frac{\partial}{\partial f} [B_r(f)|_{f=f_0}] > 0 \quad (2.33)$$

## 2.2 Specifications of Tunable Oscillators

Today, oscillators are used in test and measurement equipment and communication equipment. The largest group of users is for the use of two-way radios and “handies” (cell phones). For these applications, oscillators have to meet a variety of specifications, which affect the quality of the operational system. The properties of an oscillator can be described in a set of parameters [6]. The following is a list of the important and relevant parameters, as they need to be discussed with oscillators.

### 2.2.1 Frequency Range and Tuning Characteristics

The output frequency of Voltage Controlled Oscillators (VCOs) can vary over a wide range. The frequency range is determined by the architecture of the oscillator. A standard tunable oscillator has a frequency range typically less than 2:1; multi-octave-band slow-wave resonator (SWR) oscillator can have 4:1 tuning range (Figure 2-6). This specification shows the relationship, depicted as a graph, between the VCO operating frequency and the tuning voltage applied. Ideally, the correspondence between operating frequency and tuning voltage is linear.

### 2.2.2 Tuning Linearity

For stable oscillator, a linear deviation of frequency versus tuning voltage is desirable. It is also important to make sure that there are no breaks in tuning range, for example, that the oscillator does not stop operating with a tuning voltage of 0V.

### 2.2.3 Tuning Sensitivity, Tuning Performance

This datum, typically expressed in megahertz per volt (MHz/V), characterizes how much the frequency of a VCO changes per unit of tuning voltage change.

### 2.2.4 Tuning Speed

This characteristic is defined as the time necessary for the VCO to reach 90% of its final frequency upon the application of a tuning voltage step. Tuning speed depends on the internal components between the input pin and the tuning diode, including, among other things, the capacitance present at the input port. The input port’s parasitic elements, as well as the tuning diode, determine the VCOs maximum possible modulation bandwidth.

### 2.2.5 Post-tuning Drift

After a voltage step is applied to the tuning diode input, the oscillator frequency may continue to change until it settles to a final value. The post-tuning drift is one of the parameters that limit the bandwidth of the VCO input and the tuning speed.

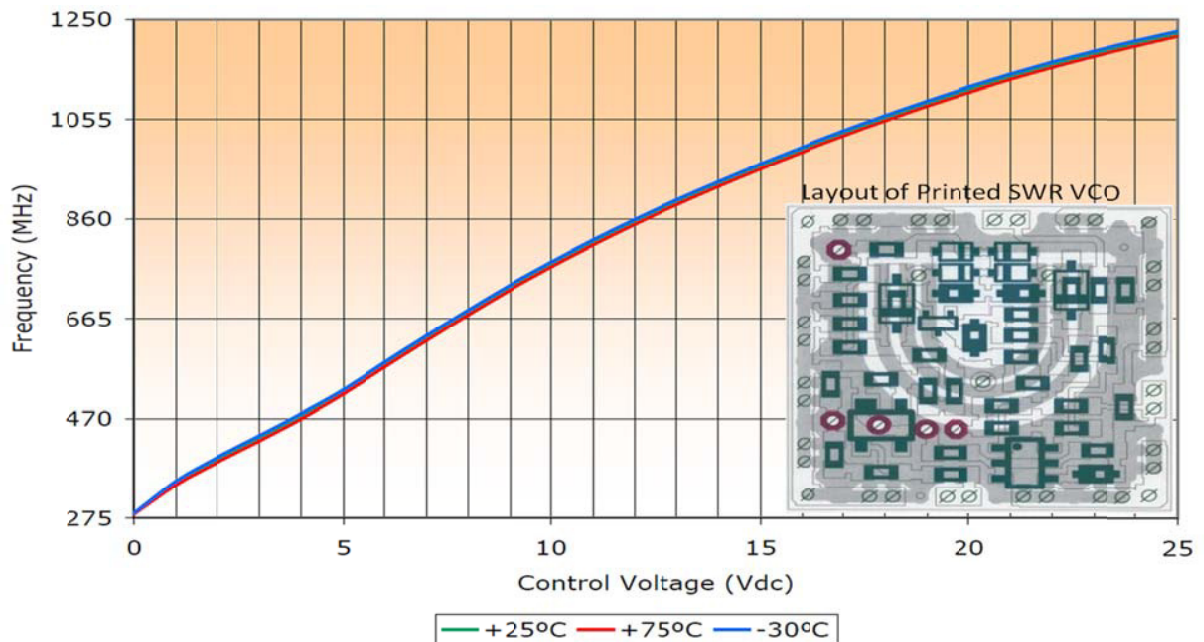


Figure 2-6: Plot of tuning range (300-1200 MHz) of SWR VCO (0.75X0.75X0.18 inches)

### 2.2.6 Phase Noise

An important feature is the stability of the oscillator (low phase noise) and its freedom from spurious signals and noise. While the oscillator is used as a voltage-controlled oscillator (VCO) in a frequency synthesizer system, its free-running noise performance outside the loop is still extremely important and solely determined by the oscillator. Unfortunately, oscillators do not generate perfect signals. The various noise sources in and outside of the active device (transistor) modulate the VCO, resulting in energy or spectral distribution on both sides of the carrier due to modulation and frequency conversion. AM and FM noise is expressed as the ratio of noise power in a 1 Hz bandwidth divided by the output power. It is measured at frequency offset of the carrier.

Figure 2-7 shows a typical measured phase noise plot of a VCO (300-1200 MHz) using printed slow-wave coupled resonator (SWR) in compact size (0.75X0.75X0.18 inches). The x-axis is the frequency offset from the carrier on a logarithmic scale. The y-axis is the phase noise in dBc/Hz. The stability or phase noise of an oscillator can be determined in the time or frequency domain.

Phase noise is a short-term phenomenon and has various components. Figure 2-8 (a) shows the typical illustration of the stability and phase noise in the time and frequency domain. The major noise contributors are thermal noise, Schottky noise and the flicker noise from the active device. Flicker noise depends on the transistor type and its biasing. The noise contribution from the resonator is mainly thermal noise. The minimum phase noise is at far offsets from the carrier, the best number being  $-P_{out}(dBm) + kT_o (-174dBm) + NF$  (large-signal noise figure of the oscillator transistor in dB); all per 1Hz bandwidth.



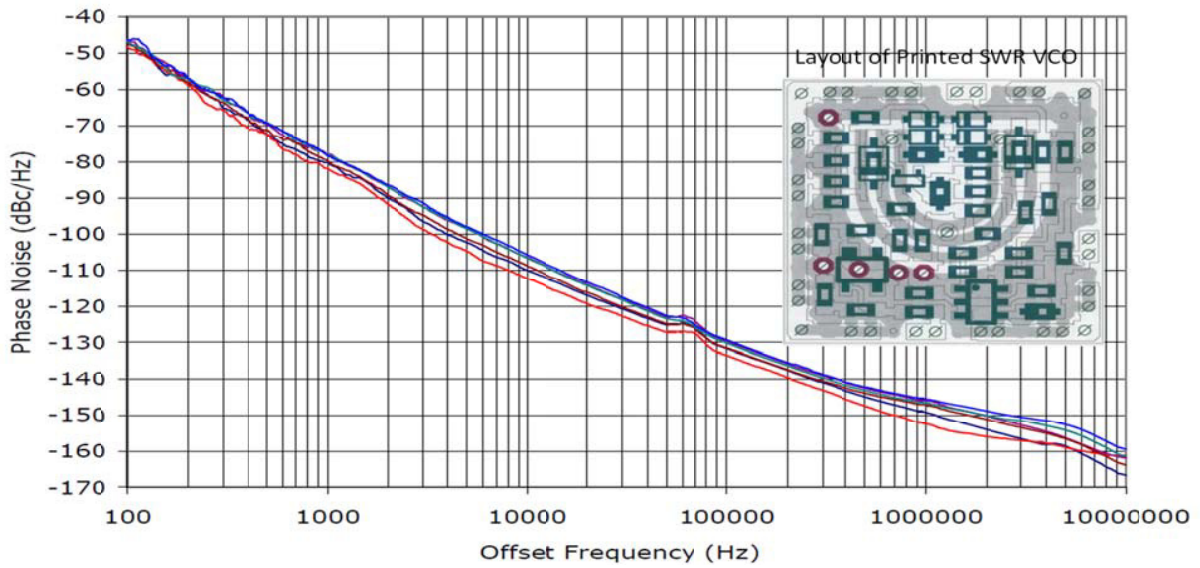


Figure 2-7: Measured phase noise of SWR VCO (300-1200 MHz) (0.75X0.75X0.18 inches)

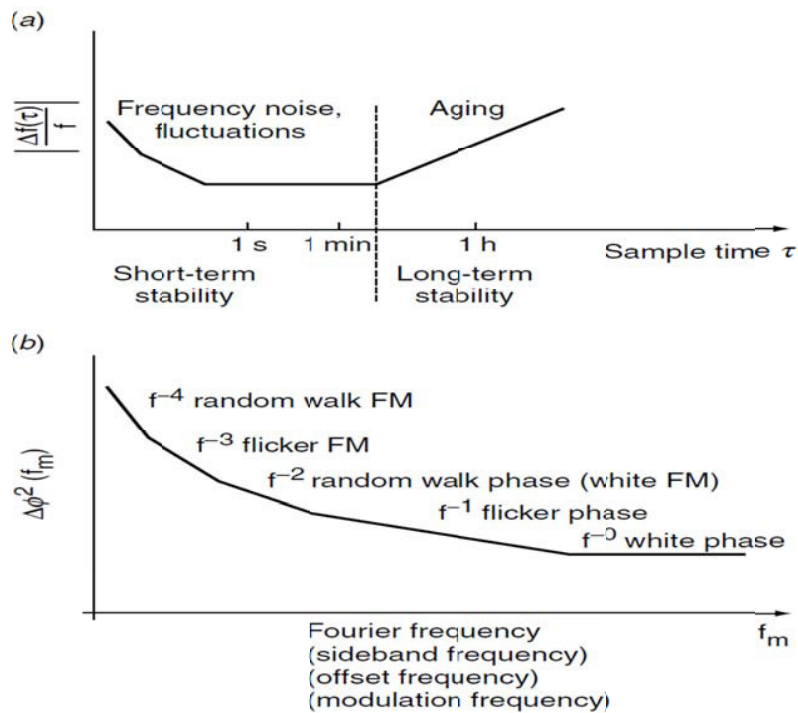


Figure 2-8 typical characterization of the noise sideband in the time and frequency domain and its contributions: (a) time domain and (b) frequency domain. Note that two different effects are considered, such as aging in (a) and phase noise in (b) [2].

### 2.2.7 Output Power

The output power is measured at the designated output port of the oscillator circuit. Practical designs require one or more isolation stages between the oscillator and the output. The VCO output power can vary as much as  $\pm 2$  dB over the tuning range. A typical output levels ranges from 0 to +10 dBm.

### 2.2.8 Harmonic Suppression

The oscillator/VCO has a typical harmonic suppression of better than 15 dB. For high performance applications, a low pass filter at the output will reduce the harmonic contents to a desired level. Figure 2-9 shows a typical second harmonic suppression plot of a 300-1200 MHz) using printed slow-wave coupled resonator (SWCR) in compact size (0.75X0.75X0.18 inches).

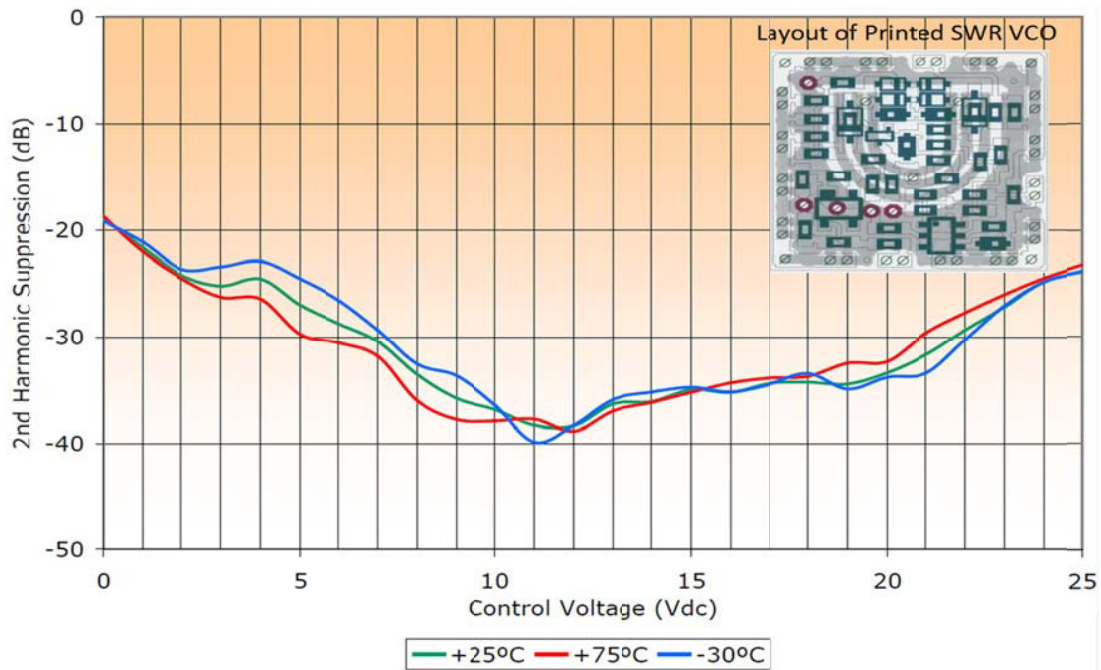


Figure 2-9: Measured harmonics at the output of a slow-wave coupled resonator (SWCR) VCO

### 2.2.9 Output Power as a Function of Temperature

All active circuits vary in performance as a function of temperature. The output power of an oscillator over a temperature range varies for broadband SWR VCO (300-1200 MHz) as shown in Figure 2-10. Therefore tracking filter with buffer amplifier is needed to enable less than a specified value variation, such as 1 dB over multi-octave-band tuning ranges.

### 2.2.10 Spurious Response

Spurious outputs are signals found around the carrier of an oscillator, which are not harmonically related. A good, clean oscillator needs to have a spurious-free range of 90 dB, but these requirements make it expensive. Oscillators typically have no spurious frequencies besides possibly 60 Hz and 120 Hz pick-up. The digital electronics in a synthesizer generates many signals, and when modulated on the VCO, are responsible for these unwanted output products.

### 2.2.11 Frequency Pushing

Frequency pushing characterizes the degree to which an oscillator's frequency is affected by its supply voltage. For example, a sudden current surge caused by activating a transceiver's RF power amplifier may produce a spike on the VCOs DC power supply and a consequent frequency jump. Frequency pushing is specified in frequency/voltage form and is tested by varying the VCOs DC supply voltage (typically  $\pm 1V$ ) with its tuning voltage held constant. Frequency pushing must be minimized, especially in cases where power stages are close to the VCO unit and short pulses may affect the output frequency. Poor isolation can make phase locking impossible.

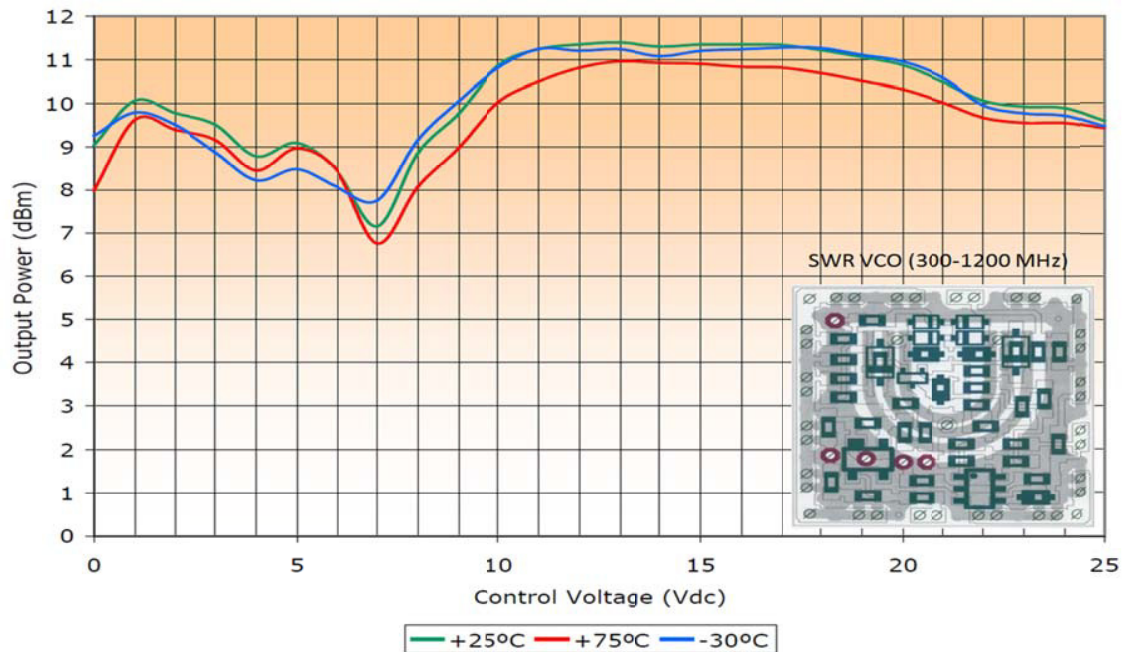


Figure 2-10: Measured output power as a function of temperature of SWR VCO (300-1200 MHz)

### 2.2.12 Sensitivity to Load Changes

To keep manufacturing costs down, many wireless applications use a VCO alone, without the buffering action of a high reverse-isolation amplifier stage. In such applications, frequency pulling, the change of frequency resulting from partially reactive loads is an important oscillator characteristic. Pulling is commonly specified in terms of the frequency shift that occurs when the oscillator is connected to a load that exhibits a non-unity VSWR (such as 1.75, usually referenced to  $50\Omega$ ), compared to the frequency that results with unity-VSWR load (usually  $50\Omega$ ).

### 2.2.13 Power Consumption

This characteristic conveys the DC power, usually specified in mill watts and sometimes qualified by operating voltage, required by the oscillator to function properly.

## 2.3 History of Microwave Oscillators

Early microwave oscillators were built around electron tubes and great efforts were made to obtain gain and power at high frequencies [8]-[12]. Starting from simple glass triodes (lighthouse tubes) and coaxial ceramic triodes, a large number of circuits designed to obtain reasonable performance were built. After using the Lecher lines (quarter-wave length U-shaped parallel wires, shorted at the end, with a few centimeters spacing), the next step was the use of coaxial systems, which became mechanically very difficult and expensive. At higher frequencies, cavities dominated the application and many publications dealt with the various resonant modes. For special applications such as microwave ovens and radar applications, magnetrons and reflex klystrons were developed. Today, the good understanding of the planar structures, such as microstrip, stripline, and coplanar waveguide have been instrumental in extending the practical frequency range up to 100 GHz and higher [13]-[20].

Early transistors followed the same trend. Siemens at one time produced a coaxial microwave transistor, Model TV44 and Motorola offered similar devices. Today, microwave transistors, when packaged, are also in microstrip form or are sold as bare die, which can be connected via bond wires to the circuit. These bond wires exhibit parasitic effects and can be utilized as part of the actual circuit. The highest form of integration

is RFICs, either in gallium arsenide (GaAs) or in silicon germanium (SiGe) technology. The SiGe circuits are typically more broadband because of lower impedances and GaAs FETs are high impedance at the input. From an application point of view, in oscillators, SiGe seems to be winning. From a practical design, both transistor types can be considered a black box with a set of  $S$  parameters, which are bias and frequency dependent [2]. For autonomous circuit operation, the transistor operates in large-signal condition, and historically, people have used FETs to demonstrate that there is little change in parameters from small to large-signal operation. Bipolar transistors have much more pronounced changes. Early pioneers have invented a variety of oscillator circuits, which are named after them. The following picture, Figure 2-11, shows a set of schematics, applicable for both bipolar and field-effect transistors [7].

Oscillator type	Bipolar transistor RF circuit	FET RF circuit
Hartley		
Colpitts		
Clapp (GOURIET)		
Transformer feedback		
Meissner		
Tuned input/ tuned output		

Figure 2-11: Six different configurations, which can be built either around bipolar transistors or around FETs [7].

The ones using magnetic coupling are not useful for microwave applications. For Frequencies above 400 MHz resonators are built around helical resonators, ceramic resonators (CR), dielectric resonators (DR), or resonant transmission lines (microstrip or coplanar waveguides) to name a few. Constraints on high-Q resonators used in high performance VCO circuits are particularly demanding, and a MMIC integrable solution has been the dream for decades [13]. In general, a high Q resonator element is required in order to achieve low phase noise characteristics in a VCO, but the realization of planar high-Q resonators is difficult due to the higher loss characteristics of the resonator at high frequency.

The DR (Dielectric resonator) offers high Q factor, and well known for high spectral purity signal sources at radio and microwave frequencies [14]-[19]. However, a VCO employing a DR has a narrow tuning range, is sensitive to vibration, costly, and not suited for current fabrication process in MMIC technology [20]-[27]. One cost-effective and alternative way to eliminate the DR is to use a printed resonator, which is appropriate for current semiconductor manufacturing processes. However, phase noise characteristics of a VCO using a printed resonator is inferior to that of the VCO using a DR (DR Q factor is much higher than the printed resonator) [28]-[34].

Planar resonators, such as ring, hairpin, spiral, and coupled resonators, are implemented easily in practical MMIC fabrication process at the cost of large size and low Q in comparison to the commercially available DR [35]-[40]. Figure 2-12 shows the typical DR for giving brief insights about the possible resonant condition for given parameters ( $L, a, \epsilon_r$ ), where L is the length of DR, a, is the radius, and  $\epsilon_r$  is the relative permittivity. Figure 2-13a shows the typical high performance DRO circuit using the DR in Push-Push configuration. It offers low phase noise but limited in tuning and poor sub-harmonic rejection [16]-[18]. As depicted in Figure 2-13 (b), the exact placement of the DR disc between the two parallel microstripline is critical and slight variation may lead to higher harmonics and poor phase noise performance.

In addition to this, DR resonant frequencies may differ from the measured result due to the slight variation in temperature that causes problems in integration and mass production [21]. The above problems limit the utility of DRs and the frequency drift is not a straightforward function of the temperature changes (due to different thermal expansion coefficients for the cavity and the dielectric puck. To overcome the above problems and reduce the thermal sensitivity of the DRO, temperature compensation and frequency locking using a PLL (phase locked loop) circuit are needed [19]. However, it is still not a cost-effective solution or suitable for integration [30].

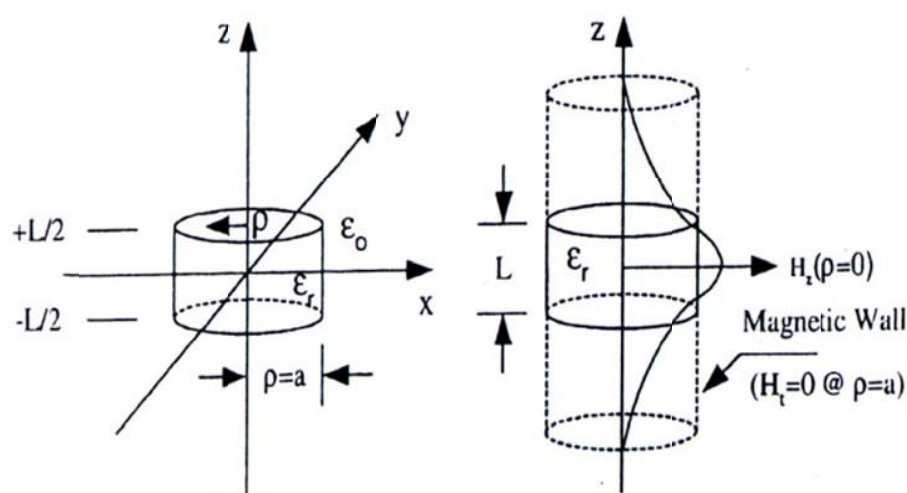


Figure.2-12: A typical DR TE<sub>01δ</sub> mode and H<sub>z</sub> field distribution [21]

Standard integrated circuits are planar circuits, so only those resonators having a planar structure are suitable in a MMIC/RFIC environment. However, integrable planar resonators lack sufficient Q (quality factor) and therefore are a limiting factor of the VCO's phase noise performance. The reason for the poor phase noise performance is due to the slow rate of phase change, and associated group delay characteristics of the resonator over the desired tuning range. Recent publications explore the possibility of replacing the DR with techniques to improve the Q factor of the planar resonators for VCO applications, which have advantages for low cost, low phase noise, wide tuning range, and suited for on-chip realization [19]-[22].

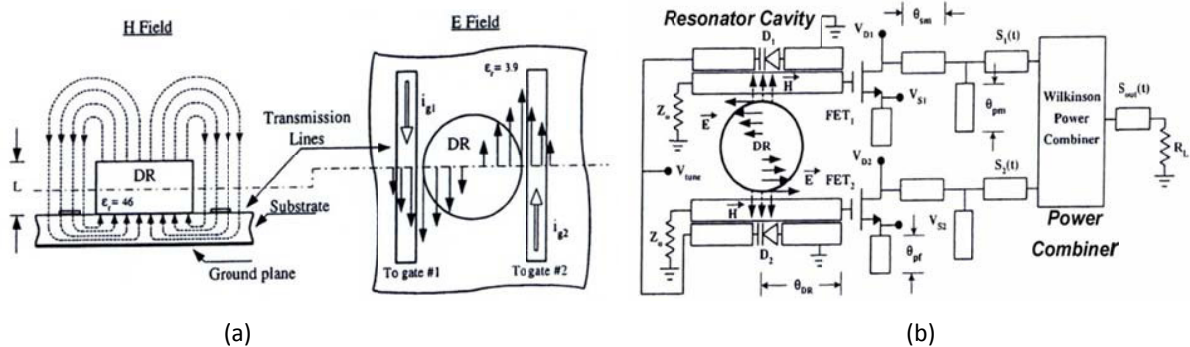


Figure 2-13: (a) DR microstrip coupling EM field distribution, (b) Tunable 12 GHz Push-Push DRO circuit [21]

The low temperature co-fired ceramic (LTCC) resonator (Figure 2-14) is a possible alternative. It exhibits high-Q factor, and is amenable for integration in MMIC process, but is very difficult to integrate in a compact system configuration [14]. Printed helical resonators at microwave frequencies exhibit high Q factor for a given size, and are a strong contender for low phase noise VCO applications [36]-[39]. Figure 2-15 depicts a typical 3-D layout of the inductively coupled helical resonator with two  $\frac{3}{4}$  turn loops connected together using a via-hole [37].

Edward [36], proposed a novel high-Q compact multilayer integrable printed helical resonator that offers optimum  $Q_L/Q_0$  ratio (loaded quality factor/unloaded quality factor) for minimum phase noise for a given VCO topology. Figure 2-16 illustrates the integrable planar helical resonator coupled to coplanar waveguide (CPW) line for high performance VCO applications [6]. The drawbacks of the reported [37]-[38] high-Q helical resonators are limited tuning capability for a given phase noise, size, and cost requirement.

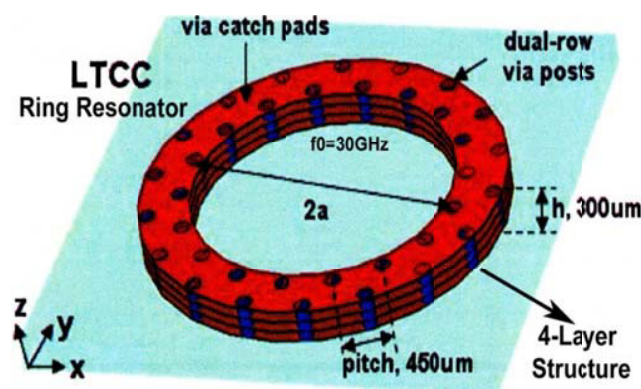


Figure 2-14: Layout of LTCC resonators (resonators are embedded in multilayer LTCC blocks for implementing integrated system in package) [38]

For low cost, broadband tunability, and integrable solutions, a new approach is discussed, which is based on the tunable active inductor where total dimensions of the resonator are unaltered while

exhibiting wider tuning and improved  $Q$  factor. The solution is reconfigurable and reduction in the number of manufacturing process steps.

## 2.4 Resonator Choice

Extensive research work is being done in the area of resonator networks such as passive and active resonator for the applications as the frequency selective element in voltage controlled oscillator applications.

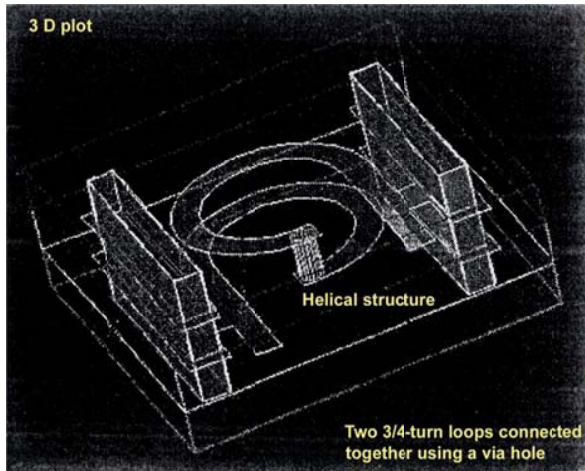


Figure 2-15: 3-D layout of helical resonator [36]

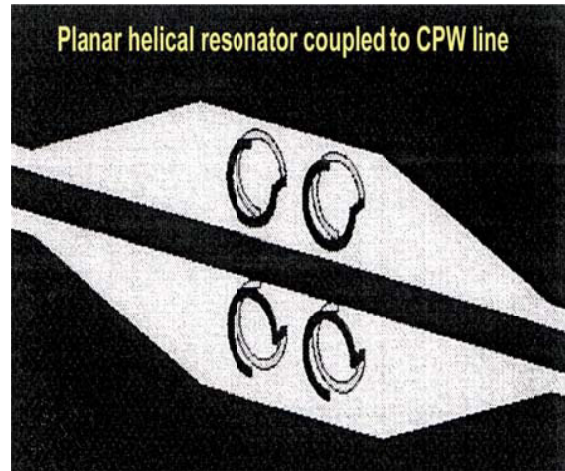


Figure 2-16: Planar helical resonator [37]

### 2.4.1 LC Resonator

Figure 2-17 shows the circuit diagram of a simple resonator. The coupling to the port is accomplished by a very small capacitor. The lumped resonator consists of a lossy  $2\text{pF}$  capacitor and a lossy  $1.76\text{nH}$  inductor with a  $0.2\text{pF}$  parasitic capacitor. The capacitor has a lead inductor of  $0.2\text{nH}$  and  $0.2\ \Omega$  losses. Likewise, the inductor has the same value loss resistor. To measure the operating quality factor  $Q$  (definition of quality factor is discussed in Ch-5), the simplified method is connect the tuned network as shown in Figure 2-17 to a network analyzer, which determines  $S_{11}$ .

For passive network, the quality factor  $Q$  is calculated by dividing the center frequency by the 3 dB bandwidth of  $S_{11}$ . Alternatively, the quality factor  $Q$  is defined as the ratio of stored energy to the dissipated energy. If there is no energy loss or resonator loss is 100% compensated, resulting  $Q$  is infinite, therefore new definition of quality factor needed for analyzing an active resonator networks (see Ch-5, section 5.4).

To determine the operating quality factor  $Q$  of the circuit as shown in Figure 2-17, let us calculate the  $Q$  of the individual branches representing the resonator. The equivalent quality factor  $Q$  of the circuit can be calculated by combining the two individual  $Q$  values ( $Q_1$  and  $Q_2$ ) using the equation [2]:

$$Q = \frac{Q_1 \times Q_2}{Q_1 + Q_2} \quad (2.34)$$

$Q_1 = 2 \times \pi \times 2.4\ \text{GHz} \times 1.76\text{nH}/0.2\ \Omega = 133$ ,  $Q_2 = 165$ ,  $Q = 73$ . The reason for the low  $Q$  is due to the  $0.2\ \Omega$  loss resistor. It should be possible to reduce this by more than a factor of two.

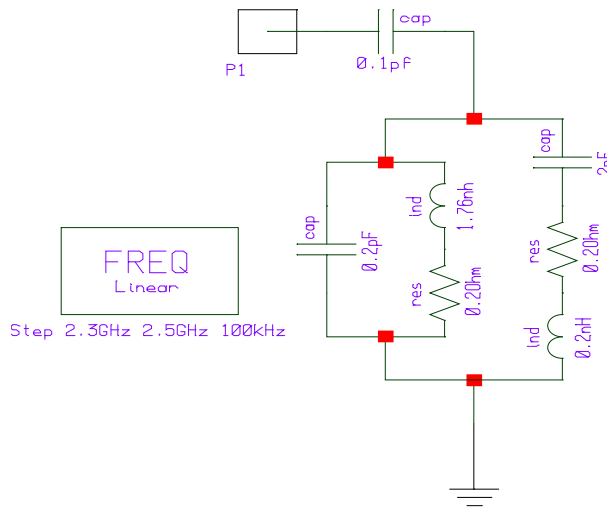


Figure 2-17: A typical circuit diagram of a parallel tuned circuit with lossy components and parasitic loosely coupled to the input [3]

### 2.4.2 Transmission Line Resonator

The same parallel-tuned circuit shown in Figure 2-17 can be generated by using a printed transmission line instead of the lumped inductor and maintain the same capacitance. This is shown in Figure 2-18. Since the transmission line has losses due to the material, they need to be considered. It is not practical to calculate these by hand, but rather use a CAD program (Ansys-Nexxim 7, ADS 2013, AWR, and CST) which does this accurately.

The Q can be determined from the 3dB bandwidth  $\left(\frac{\Delta f}{f_0}\right)$  shown in Figure 2-19 and was determined to be 240. This is also valid if the Y or Z parameters are used. This is a typical value for a microstrip resonator. Values up to 300 are possible if the appropriate layout and material is used [1].

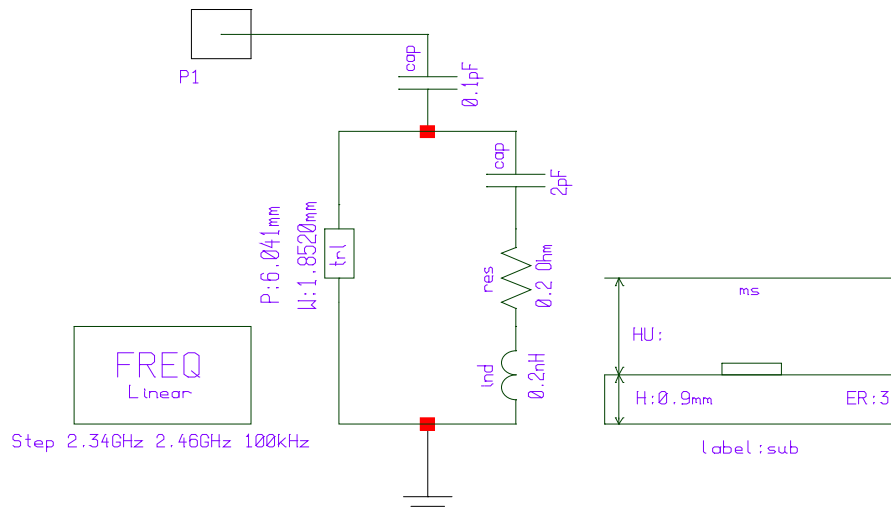


Figure 2-18: Shows a typical 2.4 GHz resonator using both lumped and distributed components [7]

### 2.4.3 Integrated Resonator

The circuit of Figure 2-17 can be generated not only using printed circuit board material, but also in GaAs or silicon.



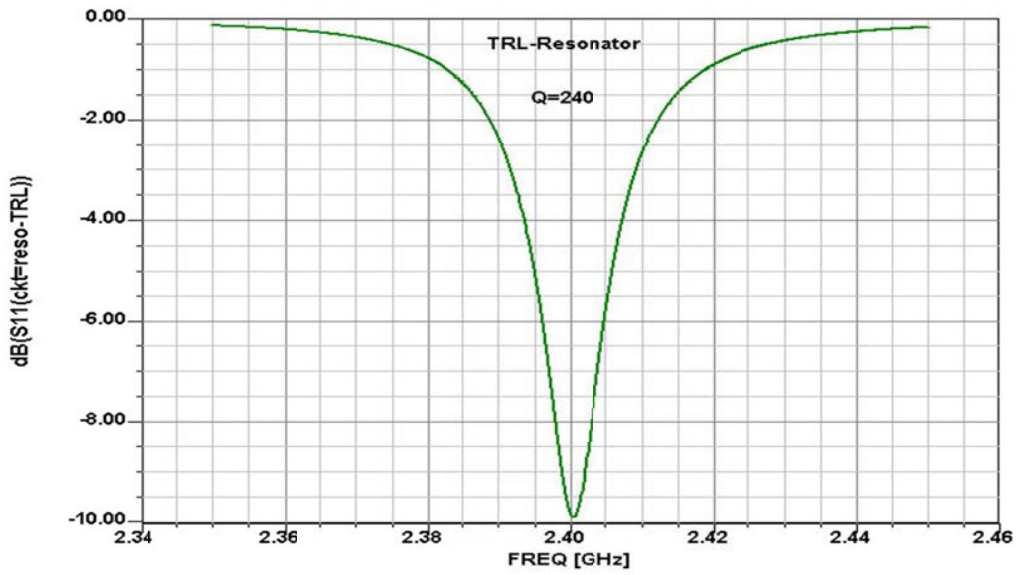


Figure 2-19: A typical CAD simulated reflection coefficient  $S_{11}$  to determine the operating Q. Since this material has high losses, an operating Q of only 240 was achieved [3].

Figure 2-20 shows the schematic of a parallel tuned circuit using a rectangular inductor and an inter-digital capacitor. The ground connection is achieved through via. At 2.4 GHz, the number of turns and size of the inductor would be significant. The same applies to the capacitor. This arrangement should be reserved for much higher frequencies, above 5 GHz. The inductor losses, both in GaAs and silicon, are substantial and this case is only shown for completeness [7].

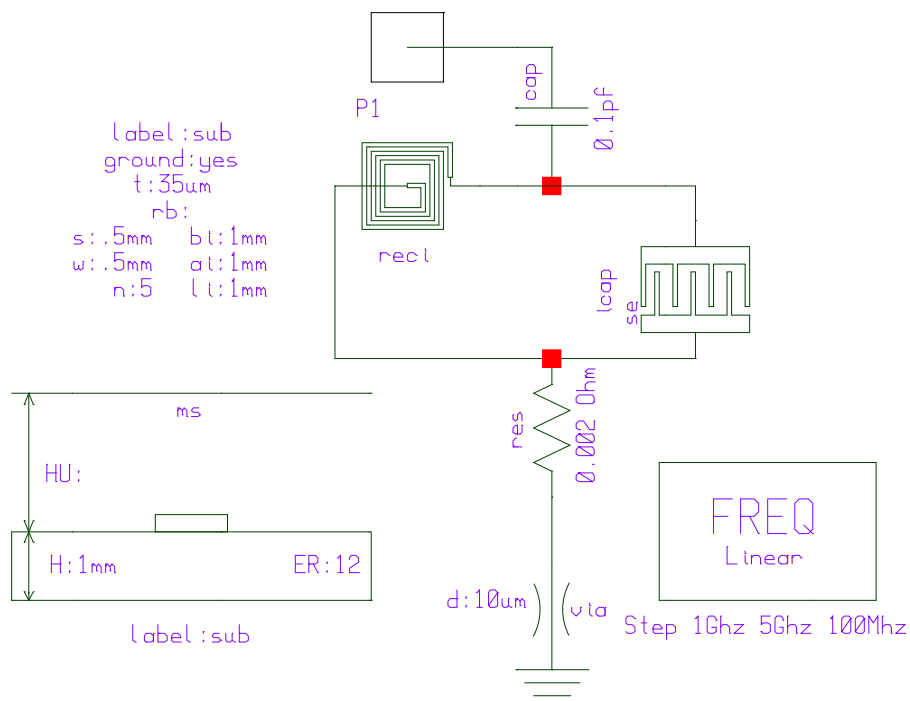


Figure 2-20: Parallel tuned circuit using a rectangular inductor (spiral could also be used) and an interdigital capacitor. If implemented on GaAs or silicon, it exhibits low Q [7].

For optimum performance, wherever possible an external resonator should be used. Referring to integrated resonators, a high Q resonator consisting of two coupled inductors has been developed. Figure 2-21 shows a three-dimensional array where the two-coupled resonators are easily identifiable. One side of the resonator is connected to ground through via. The 3-D layout can be reduced to a two-dimensional layout as shown in Figure 2-22, which gives further details about the resonator. The resonator analysis was done using Ansoft Designer (now known as Ansys Nexxim), specifically the 2.5-D simulator. A more conventional resonator analysis can be performed, using the S-parameters obtained from the structure. Figure 2-23 shows the electrical equivalent circuit of the coupled microstrip line resonator [4, 7].

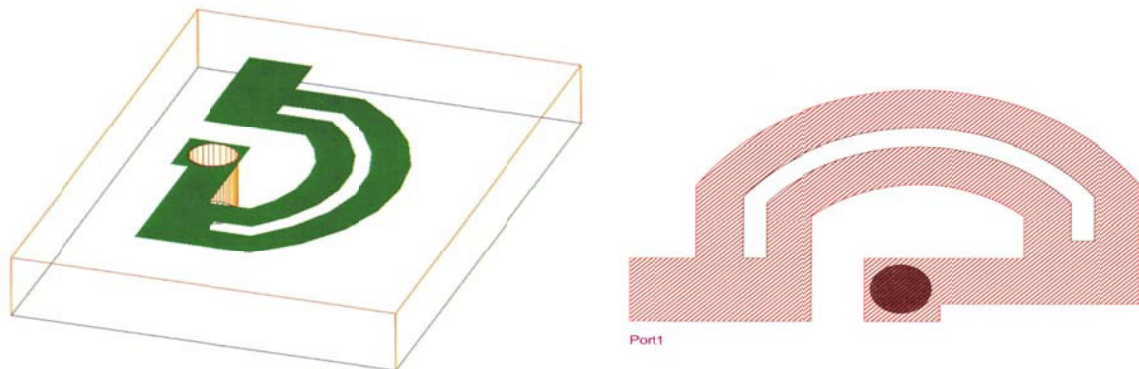


Figure 2-21: 3-D view of the coupled resonator [4]      Figure 2-22: 2-D view of the coupled microstrip resonator [4]

Finally, the  $S_{11}$  resonant curve is analyzed. The curve seen in Figure 2-24 shows a coupled micro-stripline resonator response, and the resulting Q is determined to be 560. This structure and application is covered by U.S. patents 7,088,189 B2 and 7,292,113 B2 [4, 7]. This type of resonator, as shown in Figure 2-21, plays a major role in the design of ultra-wide-band oscillators. Figure 2-25 shows the typical circuit layout of a coupled resonator oscillator as it is built on a multi-layer printed circuit board. It is a 1.1-4.5 GHz multi-octave, low-noise oscillator, and this was achieved in our patented approach, US copyright registration No.VAU 603984 [3, 4, and 7]. Besides the coupled resonator, which determines the resonant frequency, there is an additional resonator used for noise filtering.

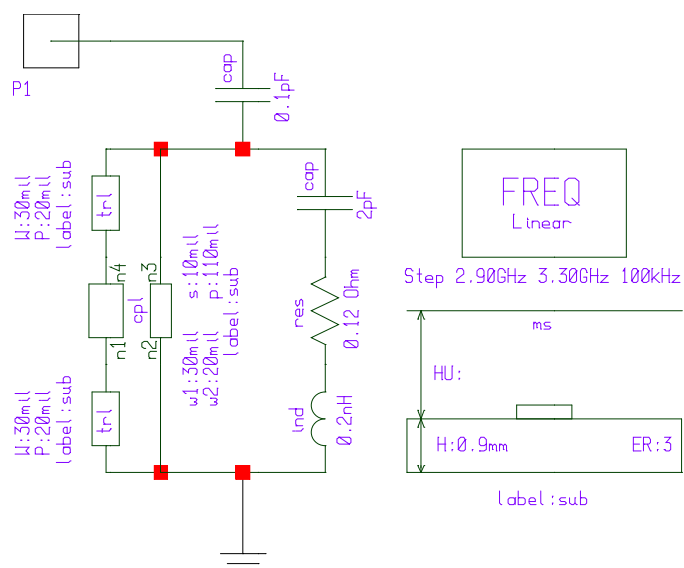


Figure 2-23: Electrical equivalent of the coupled microstrip line resonator [7]

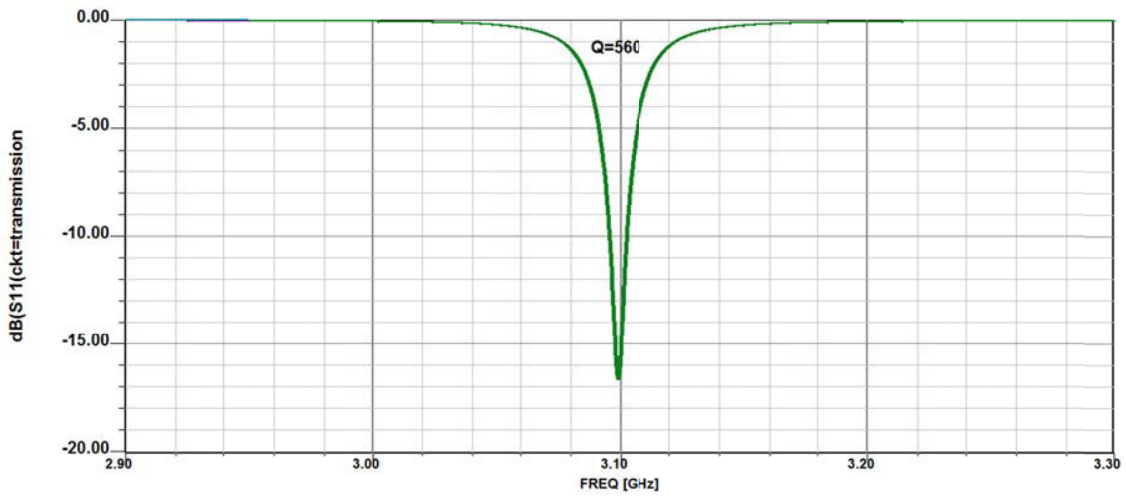


Figure 2-24: Frequency response of the coupled microstrip line resonator

Figure 2-26 shows the achievable phase noise for this oscillator. Oscillators operate under large-signal conditions. Under large-signal conditions, the RF currents and voltages are of the same magnitude as the DC values. The most accurate result will be obtained by switching from linear to nonlinear analysis. Besides the coupled resonator, which determines the resonant frequency, there is an additional resonator used for noise filtering [4, 7].

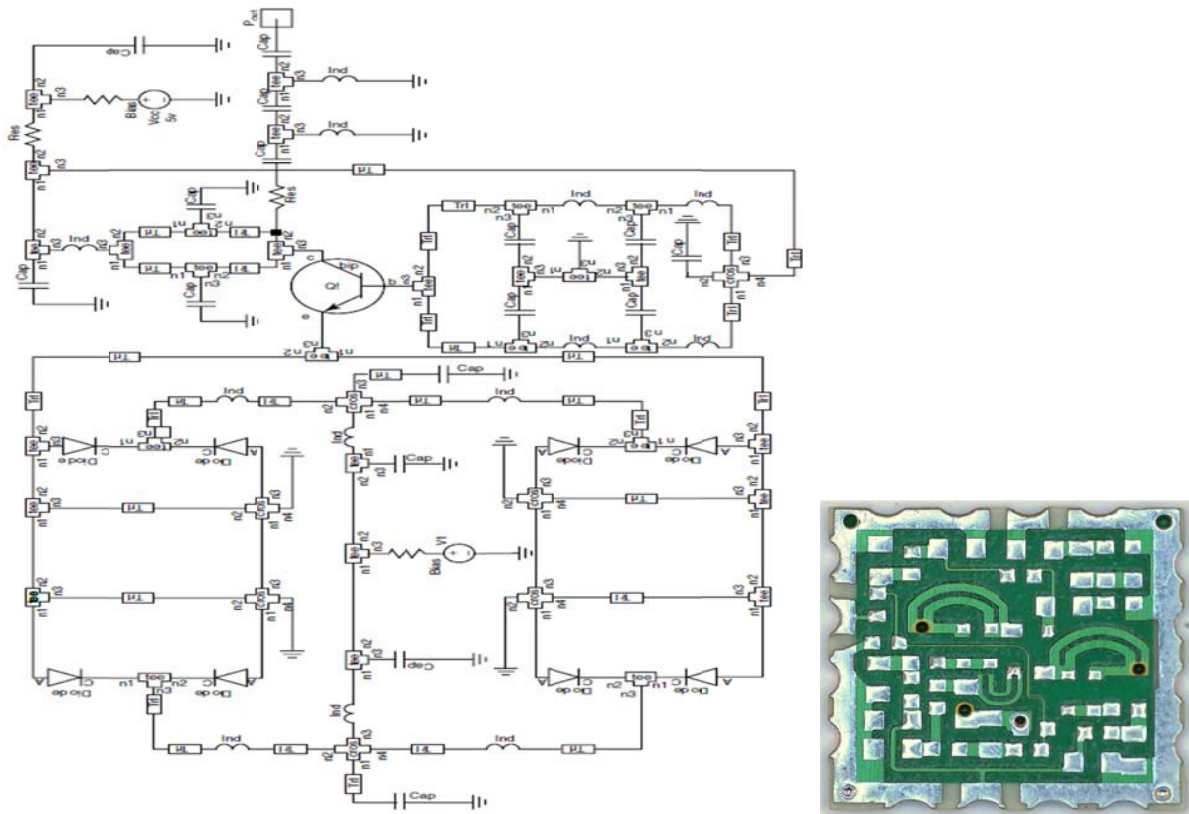


Figure 2-25: An example of a 1.1-4.5 GHz VCO with coupled resonators on a 0.5 X 0.5 inch<sup>2</sup> PCB [U.S. patent Nos. 7,088,189 B2 and 7,292,113 B2] [4, 7]

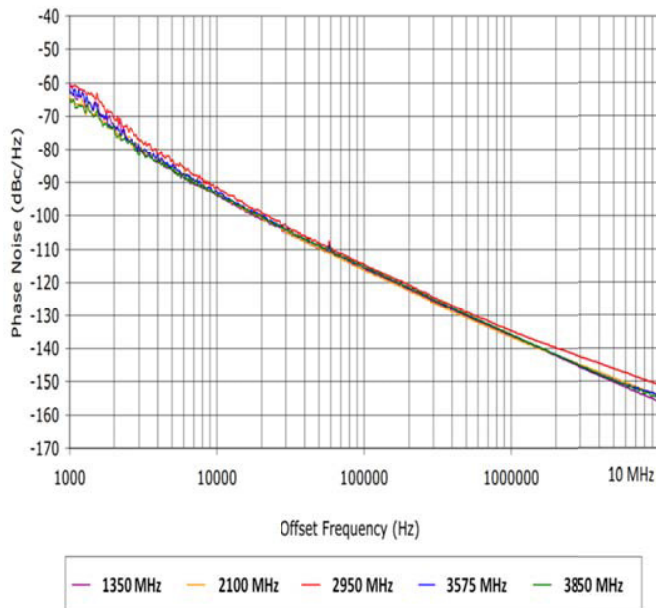


Figure 2-26: Measured phase noise plots

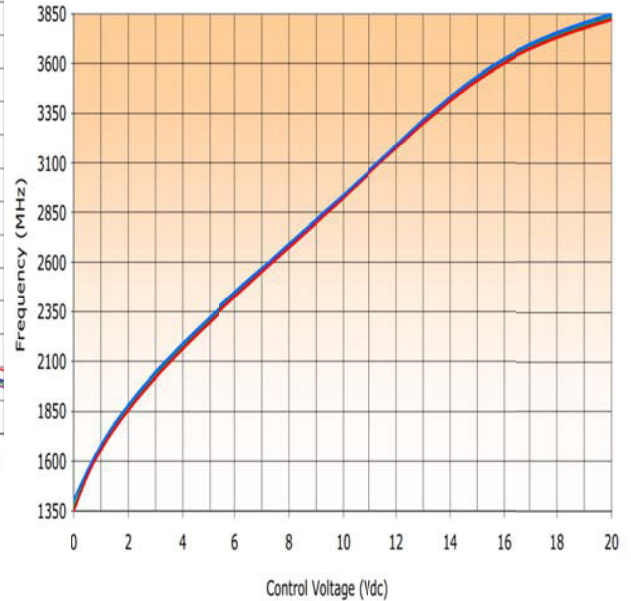


Figure 2-27: Measured tuning characteristics

Figures 2-26 and 2-27 show the measured phase noise and operating tuning range of the wideband oscillator circuit shown in Figure 2-25. The circuit operates at 5V, 18 mA, and delivers output power better than 3dBm over operating frequency range (1350MHz-3850 MHz). Over few million pieces produced on pick & place machine and commercialized for the applications in Radio and test & measurement equipments, the design layout is stable over temperature and vibration.

## 2.5 Large Signal S-Parameter Analysis

The description of linear, active or passive 2-ports can be explained in various forms. In the early days Z-parameters were commonly used which then were replaced by the Y-parameters. Z-parameters are open-ended measurements and Y-parameters are short circuit measurements relative to the output or input depending on the parameter. In reality, however, the open circuit condition does not work at high frequencies because it becomes capacitive and results in erroneous measurements. The short-circuit measurements also suffer from non-ideal conditions as most “shorts” become inductive. Most RF and microwave circuits, because of the availability of 50Ω coaxial cables, are now using 50Ω impedances. Component manufacturers are able to produce 50Ω termination resistors, which maintain their 50Ω real impedance up to tens of GHz (40 GHz). The 50Ω system has become a defacto standard. While the Z- and Y-parameter measurements were based on voltage and currents at the input and output, the S-parameters refer to forward and reflected power [2]-[5]. For low frequency applications, one can safely assume that the connecting cable from the source to the device under test or the device under test to the load plays no significant role [7]. The wavelength of the signal at the input and output is very large compared to the physical length of the cable. At higher frequencies, such as microwave frequencies, this is no longer true.

If the signal from the signal generator is increased in power, it essentially has no impact on passive devices until a level of several hundred watts is reached where intermodulation distortion products can be created due to dissimilar alloys. However, active devices, depending on the DC bias point, can only tolerate relatively low RF levels to remain in the linear region. In the case of the oscillator, there is a large RF signal, that is, a large voltage and current, imposed on the DC voltage/current. Assuming an RF output power from 0dBm to 10dBm, and assuming 10-15 dB gain in the transistor, the RF power level driving the emitter/source or base/gate terminal is somewhere in the vicinity of -15dBm. An RF drive of -15dBm will change the input and

output impedance of the transistor, even if the transistor operates at large DC currents. It is important to note that the input and output impedances of field-effect transistors are much less RF voltage-dependent or power-dependent than the bipolar transistor. The generation of “large-signal  $S$ -parameters” for bipolar transistors is, therefore, much more important than for FETs. Figure 2-28 shows the test fixture, which was used to measure the large-signal  $S$ -parameters for the device under test (DUT). The test fixture was calibrated to provide  $50\Omega$  to the transistor leads. The test set-up shown in Figure 2-29 consists of a DC power supply and a network analyzer for combined  $S$ -parameter measurements. The R&S ZVR network analyzer, as shown in Figure 2-29, was chosen because its output power can be varied between  $-60\text{dBm}$  and  $+10\text{dBm}$ . This feature is necessary to perform these measurements. The picture shown in Figure 2-28 demonstrates the experimental setup for large signal  $S$ -parameter measurement. The experimental set up is very simple, but unfortunately, very expensive. Currents and voltages follow Kirchhoff’s law in a linear system. A linear system implies that there is a linear relationship between currents and voltages. All transistors, when driven at larger levels show nonlinear characteristics. The FET shows a square law characteristic, while the bipolar transistor has an exponential transfer characteristic. The definition of  $S$ -parameters in large-signal environment is ambiguous compared to small-signal  $S$ -parameters. When driving an active device with an increasingly higher level, the output current consists of a DC current and RF currents: the fundamental frequency and its harmonics. When increasing the drive level, the harmonic content rapidly increases.  $S_{12}$ , mostly defined by the feedback capacitance, now reflects harmonics back to the input. If these measurements are done in a  $50\Omega$  system, which has no reactive components, then we have an ideal system for termination.

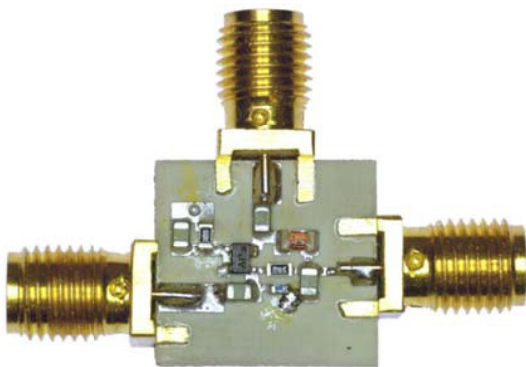


Figure 2-28: Test fixture to measure large signal  $S$ -parameters. A proper de-embedding has been done (DC Operating condition, 2V, 20mA) [7]

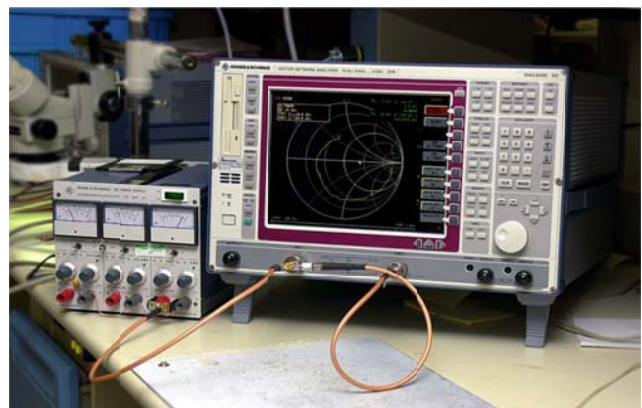


Figure 2-29: Rohde & Schwarz 3 GHz network analyzer to measure the large-signal  $S$ -parameters at different drive levels (DC Operating condition, 2V, 20mA) [7].

In practical applications, however, the output is a tuned circuit or matching network, which is frequency selective. Depending on the type of circuit, it typically presents either a short circuit or an open circuit for the harmonic. For example, say the matching network has a resonant condition at the fundamental and second harmonic frequency or at the fundamental and third harmonic frequency (quarter wave resonator). Then a high voltage occurs at the third harmonic, which affects the input impedance, and therefore,  $S_{11}$  (Miller effect). This indicates that  $S$ -parameters measured under large-signal conditions in an ideal  $50\Omega$  system may not correctly predict device behavior when used in a non- $50\Omega$  environment. A method called “load pull”, which includes fundamental harmonics, has been developed to deal with this issue [5]. In the case of an oscillator, however, there is only one high-Q resonator, which suppresses the harmonics of the fundamental frequency (short circuit). In this limited case, the  $S$ -parameters, measured in a  $50\Omega$  system are

useful. Since the oscillator operates in quasi-large-signal operation, we will need the large-signal  $S$ -parameters as a starting condition for the large-signal design (output power, harmonics, and others). The following four plots, Figures 2-30, 2-31, 2-32, 2-33, show  $S_{11}$ ,  $S_{12}$ ,  $S_{21}$ , and  $S_{22}$  measured large-signal of the Infineon BFP 520 transistor, frequency sweeping from 50 MHz to 3000 MHz with driving levels from  $-20\text{dBm}$  to  $5\text{dBm}$ . The DC operating conditions were  $2\text{V}$  and  $20\text{mA}$  as shown in Figure 2-29 [3].

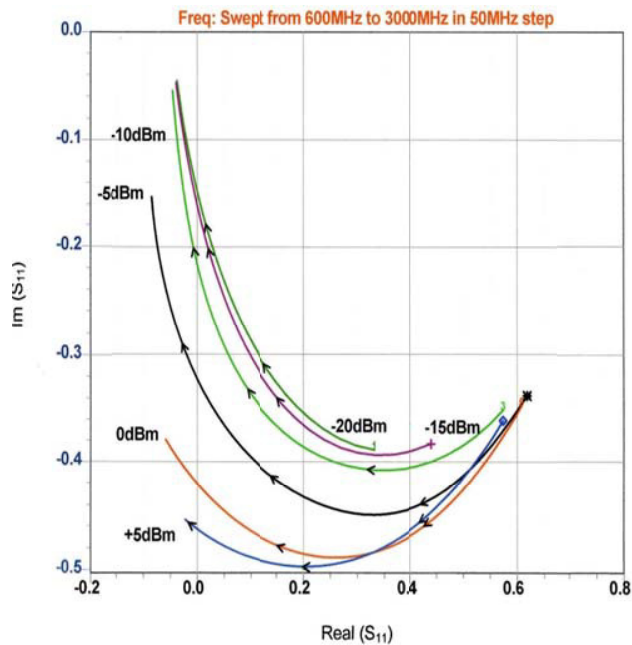


Figure 2-30: Measured large-signal  $S_{11}$

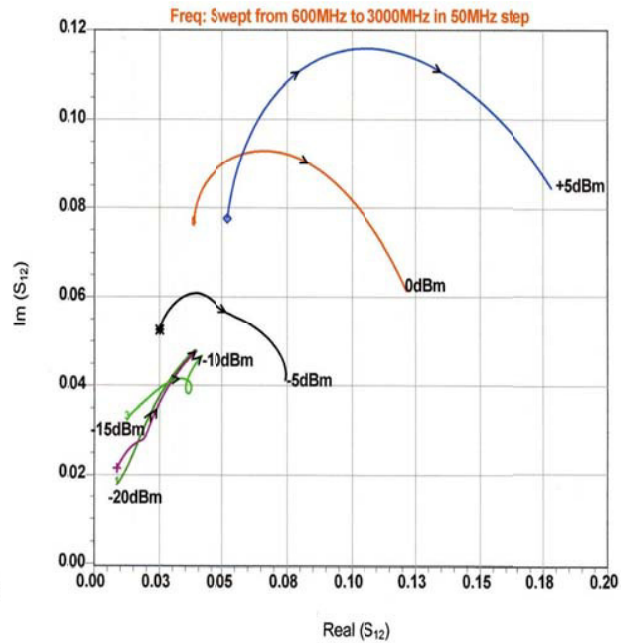


Figure 2-31: Measured large-signal  $S_{12}$

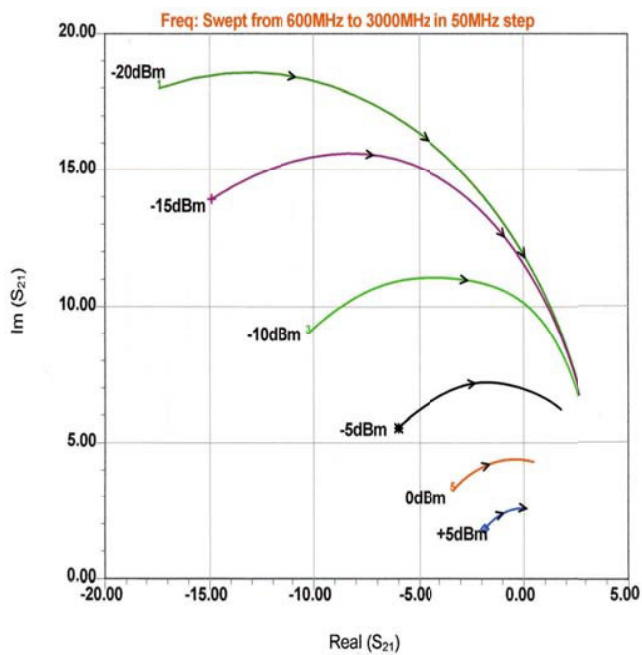


Figure 2-32: Measured large-signal  $S_{21}$

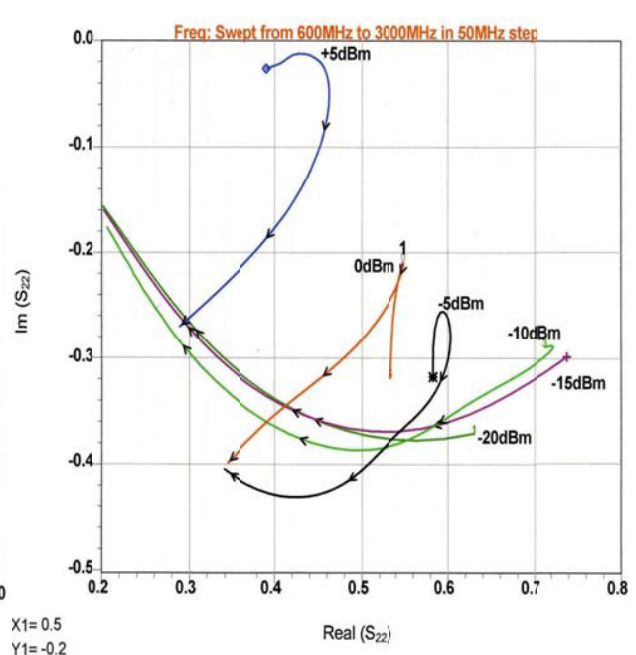


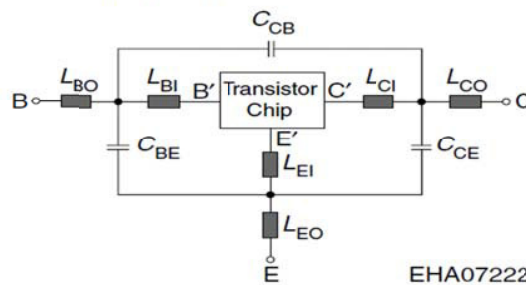
Figure 2-33: Measured large-signal  $S_{22}$

When using a SPICE type simulator, or a harmonic balance simulator, then one must use the non-linear model parameters as shown in Figure 2-34. Modern foundries supply relevant data for GaAs and for BiCMOS devices. The choice of which model to use is not always simple: for bipolar transistors, here the advanced Gummel Poon model [40]-[41] is preferred similar to Figure 2-35 [42]. A modification to the base-emitter diffusion capacitance is preferred. Recent publications address this issue in detail. For GaAs devices, the modified Materka model gives very good results.

**Transistor Chip Data:**

IS = 15	aA	BF = 235	-	NF = 1	-
VAF = 25	V	IKF = 0.4	A	ISE = 25	fA
NE = 2	-	BR = 1.5	-	NR = 1	-
VAR = 2	V	IKR = 0.01	A	ISC = 20	fA
NC = 2	-	RB = 11	$\Omega$	IRB = -	A
RBM = 7.5	$\Omega$	RE = 0.6		RC = 7.6	$\Omega$
CJE = 235	fF	VJE = 0.958	V	MJE = 0.335	-
TF = 1.7	ps	XTF = 10	-	VTF = 5	V
ITF = 0.7	A	PTF = 50	deg	CJC = 93	fF
VJC = 0.661	V	MJC = 0.236	-	XCJC = 1	-
TR = 50	ns	CJS = 0	fF	VJS = 0.75	V
MJS = 0.333	-	XTB = -0.25	-	EG = 1.11	eV
XTI = 0.035	0	FC = 0.5	-	TNOM = 298	K

**Package Equivalent Circuit:**



$L_{BI}$	=	0.47	nH
$L_{BO}$	=	0.53	nH
$L_{EI}$	=	0.23	nH
$L_{EO}$	=	0.05	nH
$L_{CI}$	=	0.56	nH
$L_{CO}$	=	0.58	nH
$C_{BE}$	=	136	fF
$C_{CB}$	=	6.9	fF
$C_{CE}$	=	134	fF
Valid up to 6 GHz			

Figure 2-34: SPICE parameters and package equivalent circuit of the Infineon transistor BFP520 [42].

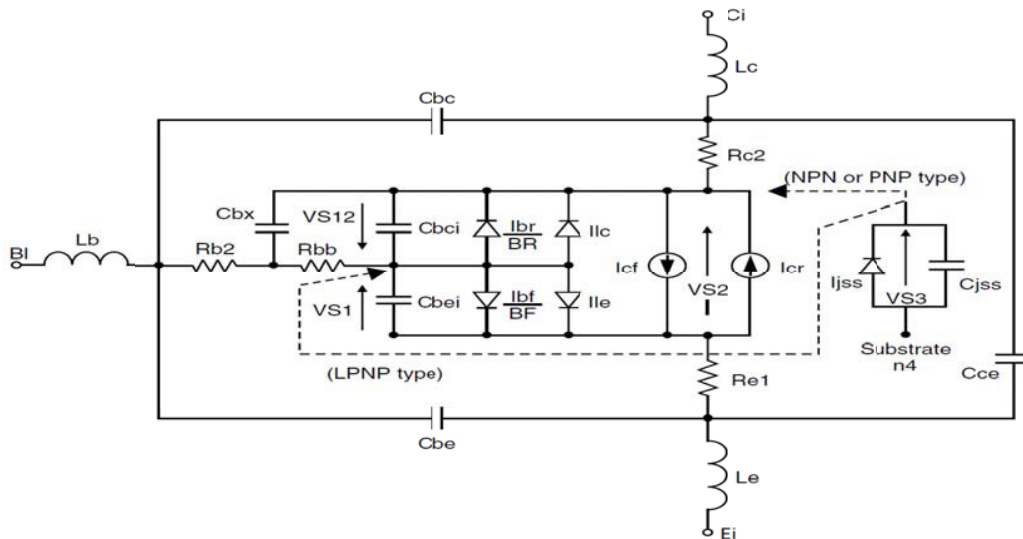


Figure 2-35: A modern equivalent circuit of a bipolar transistor [42]

Modeling a JFET using the Materka model also yields very accurate RF results. For oscillator circuits a well-documented MOS level-3 models and the EKV3 model can provide accurate simulation. For RF applications, the final optimum model is still undefined [3]. The accompanied parameter extraction to measure the model parameters is similarly complex.

Recently JFETs have found many applications in the higher microwave frequencies and hence their large-signal measurement seems important and useful. The large-signal measurement for Vishay-Siliconix U310 device [4] has been done for the comparative analysis. Figure 2-36 shows the test fixture for the measurement of the large-signal  $S$ -parameters for the device under test (DUT). The test fixture was calibrated to provide  $50\Omega$  to the transistor leads. The test set-up consists of a DC power supply and a network analyzer for combined  $S$ -parameter measurements.

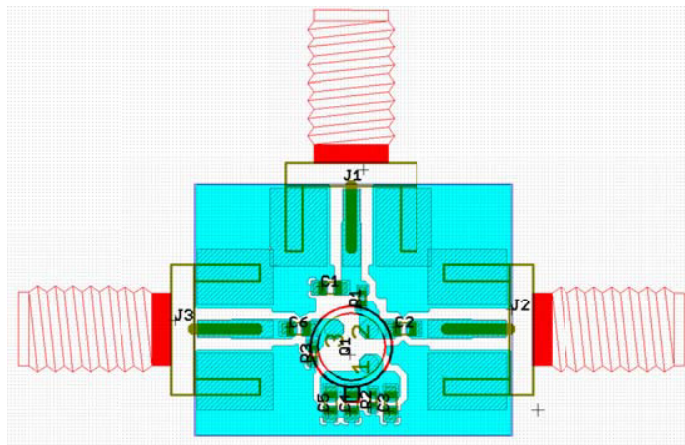


Figure 2-36: Test Fixture to measure large signal  $S$ -parameters (A proper de-embedding has been done) using Vishay-Siliconix U310 device [5].

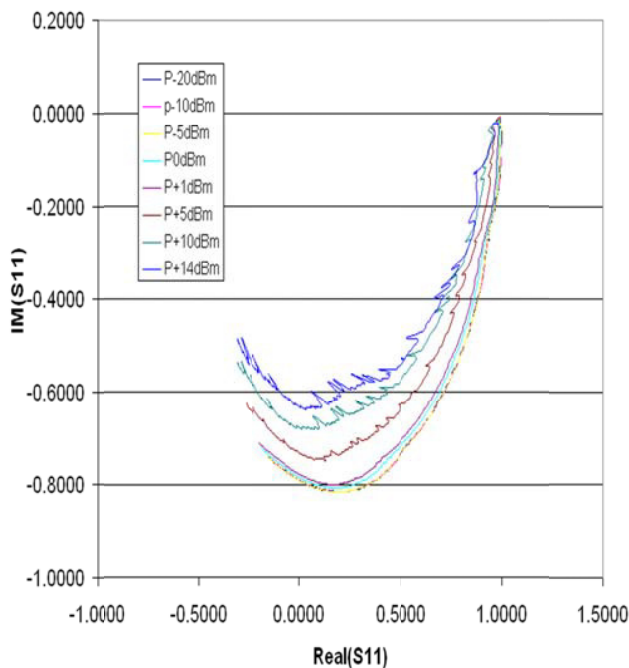


Figure 2-37: Measured large-signal  $S_{11}$  JFET U310

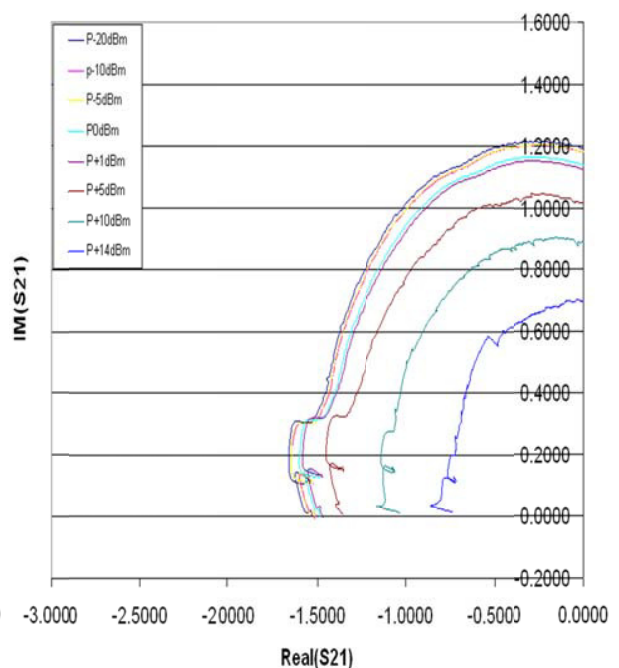


Figure 2-38: Measured large-signal  $S_{21}$  JFET U310



The following four plots, Figures 2-37, 2-38, 2-39, 2-40, show  $S_{11}$ ,  $S_{12}$ ,  $S_{21}$ , and  $S_{22}$  measured from 1 MHz to 250 MHz with driving levels from  $-20\text{dBm}$  to  $14\text{dBm}$ .

The DC operating conditions were  $V_d = 11.08\text{V}$  and  $I_{\text{dss}} = 29.9\text{mA}$ . Using bipolar and JFET models, the basic topology of frequency selective RF components such as active inductor for the application of oscillator circuits has been developed.

The flicker corner frequency for JFET is very small and lends itself for the oscillator application [5].

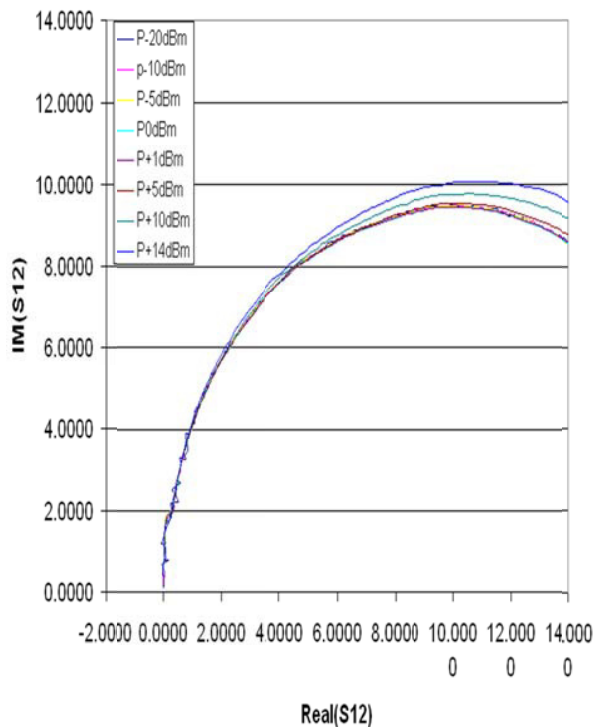


Figure 2-39: Measured large-signal  $S_{12}$  for JFET U310

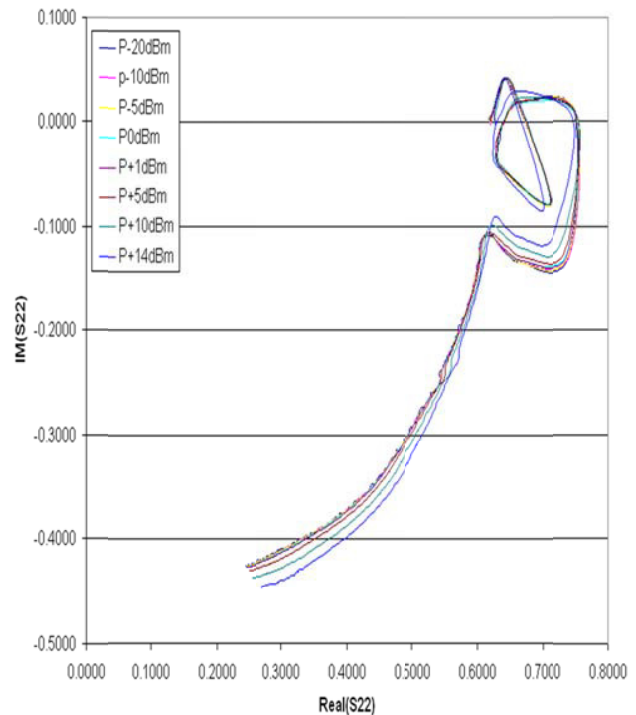


Figure 2-40: Measured large-signal  $S_{22}$  for JFET U310

## 2.6 Conclusion

In this chapter, brief oscillator theory is discussed, including the selection of resonator networks, and performance matrices (frequency range and tuning characteristics, tuning linearity, tuning sensitivity, tuning speed, post-tuning drift, phase noise, output power, harmonic suppression, spurious response, pushing and pulling). For the device characterization, large signal S-parameter measurements carried out for bipolar and JFET for using these transistors as negative resistance generating devices for compensating the loss of resonator tank in oscillator circuits discussed in Chapter 6, Chapter 7, Chapter 8, and Chapter 9 for the validation. The detailed description and validation examples are described in e-book [43].

## Chapter 3

### Noise Analysis of the Oscillators

#### 3.1 Oscillator Noise

Noise is associated with all the components of the oscillator circuit; however, the major contribution of the noise in an oscillator is from the active device, which introduces AM (amplitude modulation) noise and PM (phase modulation) noise. The conventional wisdom is to ignore AM component of the noise because the gain limiting properties of the active device operating under saturation, allows very little variation in the output amplitude in comparison to PM noise component, which directly affects the frequency stability of the oscillator and creates noise sidebands [1]. But in reality, many oscillator topologies create significant AM noise, therefore effective noise contribution is the combination of  $1/f$  spectrum with the  $1/f^2$  effect in all phase modulation makes the low-frequency noise much greater, and that's where the information in most modulated signals reside [2]-[4].

##### 3.1.1 Sources of Noise

There are mainly two types of noise sources in bipolar oscillator circuit: broadband noise sources due to thermal and shot noise effects and the low-frequency noise source due to  $1/f$  (flicker noise effects) characteristics. In FET oscillator, high-field diffusion noise is dominant source of noise generation.

The current flow in a transistor is not a continuous process but is made up of the diffusive flow of large number of discrete carriers and the motions of these carriers are random and explains the noise phenomenon up to certain degree, however many of them are unknown. In conventional terms, the thermal fluctuation in the minority carrier flow and generation-recombination processes in the semiconductor device generates thermal noise, shot noise, partition-noise, burst noise and  $1/f$  noise [4]. But in reality, this is not the case, the source of  $1/f$  noise is still a subject of research, physicists are still arguing about what causes it. Figure 3-1(a) shows the equivalent schematic of the bipolar transistor in a grounded emitter configuration, and the high frequency noise of a silicon bipolar transistor in common emitter configuration can be modeled by using the three noise sources as shown in equivalent schematic (hybrid- $\pi$ ) in Figure 3-1(b) [4]. The emitter junction in this case is conductive and this generates shot noise on the emitter. The emitter current is divided into a base ( $I_b$ ) and a collector current ( $I_c$ ) and both these currents generate shot noise. There is the collector reverse current ( $I_{cob}$ ), which also generates shot noise. The emitter, base and collector are made of semiconductor material and have finite value of resistance associated with them, which generates thermal noise. The value of the base resistor is relatively high in comparison to resistance associated with emitter and collector, so the noise contribution of these resistors can be neglected.

For noise analysis three sources are introduced in a noiseless transistor and these noise generators are due to fluctuation in DC bias current ( $i_{bn}$ ), DC collector current ( $i_{cn}$ ) and thermal noise of the base resistance ( $v_{bn}$ ). In Silicon transistor the collector reverse current ( $I_{cob}$ ) is very small and noise ( $i_{con}$ ) generated due to this can be neglected. For the evaluation of the noise performances, the signal-driving source should also be taken into consideration because its internal conductance generates noise and its susceptance affects the noise figure through noise tuning. The mean square values of the noise generator in a narrow frequency interval  $\Delta f$  is given by [4]

$$\overline{i_{bn}^2} = 2qI_b\Delta f \quad (3.1)$$

$$\overline{i_{cn}^2} = 2qI_c\Delta f \quad (3.2)$$

$$\overline{i_{con}^2} = 2qI_{cob}\Delta f \quad (3.3)$$

$$\overline{v_{bn}^2} = 4kTr_b'\Delta f \quad (3.4)$$

$$\overline{v_{sn}^2} = 4kTR_s\Delta f \quad (3.5)$$

$I_b$ ,  $I_c$  and  $I_{cob}$  are average DC current over  $\Delta f$  noise bandwidth.

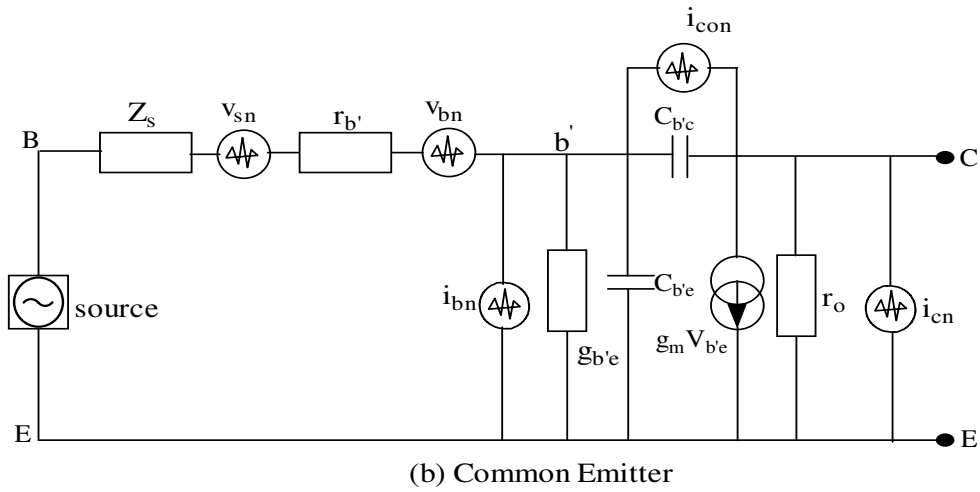
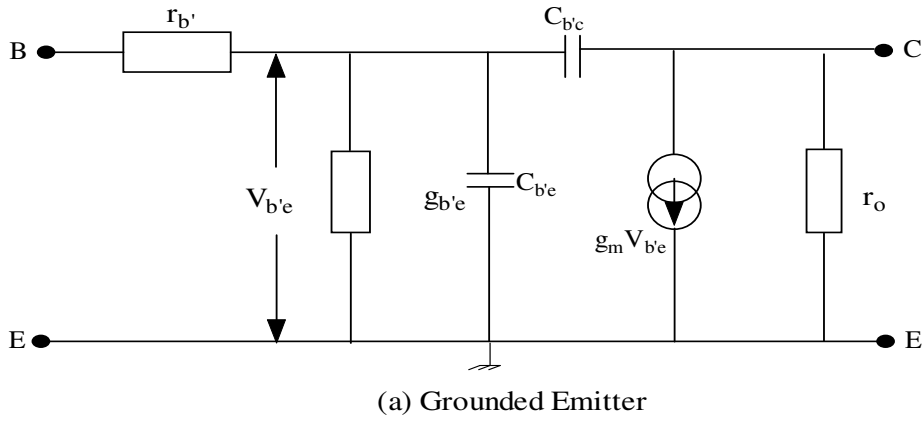


Figure 3-1: (a)  $\pi$ - configuration of the GE-bipolar transistor and (b)  $\pi$ - configuration of CE-bipolar transistor with noise sources [4]

The noise power spectral densities due to noise sources is given as [4]

$$S(i_{cn}) = \frac{\overline{i_{cn}^2}}{\Delta f} = 2qI_c = 2KTg_m \quad (3.6)$$

$$S(i_{bn}) = \frac{\overline{i_{bn}^2}}{\Delta f} = 2qI_b = \frac{2KTg_m}{\beta} \quad (3.7)$$

$$S(v_{bn}) = \frac{\overline{v_{bn}^2}}{\Delta f} = 4KTr_b' \quad (3.8)$$

$$S(v_{sn}) = \frac{\overline{v_{sn}^2}}{\Delta f} = 4KTR_s \quad (3.9)$$

$r_b'$  and  $R_s$  are base and source resistance and  $Z_s$  is the complex source impedance.

### 3.1.2 Oscillator Noise Model Comments

The phenomenon of phase noise generation in oscillators/VCOs has been the focus of important research efforts, and it is still an open issue despite significant gains in practical experience and modern CAD tools for design. In the design of VCOs, minimizing the phase noise is usually an important task and these objectives have been accomplished using empirical rules or numerical optimizations, and to this end, are often held as trade secrets by many manufacturers [5]-[12]. The ability to achieve optimum phase noise performance is paramount in most RF design and the continued improvement of phase noise in oscillators is required for the efficient use of frequency spectrum.

The degree to which an oscillator generates constant frequency throughout a specified period is defined as the frequency stability of the oscillator and the cause of the frequency instability is due to the presence of noise in the oscillator circuit that effectively modulates the signal, causing a change in frequency spectrum commonly known as phase noise. Phase noise and timing jitter are both measures of uncertainty in the output of an oscillator. Phase noise defines the frequency domain uncertainty of an oscillator, whereas timing jitter is a measure of oscillator uncertainty in the time domain [13]-[19]. However, in reality, phase noise and time jitter correlate each other and tells same thing. The main distinction is just that "jitter" is applied primarily to digital sources [20]-[33]. The Equation for ideal sinusoidal oscillator in time domain is given by [18]

$$V_{out}(t) = A \cos(2\pi f_0 t + \varphi) \quad (3.10)$$

where  $A$ ,  $f_0$  and  $\varphi$  are the amplitude, frequency and fixed phase of the oscillator. The Equation of the real oscillator in time domain is given by [18]

$$V_{out}(t) = A(t) \cos[\omega_0 t + \varphi(t)] = [A + \alpha(t)] \cos[2\pi f_0 t + \varphi(t)] \quad (3.11)$$

where  $A(t)$ ,  $\varphi(t)$ , and  $f_0$  are the time variable amplitude fluctuation, time variable phase fluctuation, frequency of the respectively.

Because of the fluctuations, the spectrum of a practical oscillator is broadened near the carrier frequency. In practice, amplitude noise (AM noise) is smaller than phase-noise (PN) due to the amplitude-restoring mechanism in LC oscillators, this is illustrated by the limit cycle of an ideal LC oscillator as shown in Figure 3-2 [34]-[37]. As shown in Figure 3-2, the current noise perturbs the signal and causes its phasor to deviate from the stable trajectory, producing both amplitude and phase-noise. The amplitude deviation is resisted by the stable limit cycle, whereas the phase is free to drift. Therefore, oscillators almost exclusively generate phase-noise near the carrier [38]-[42].

Figures 3-3 (a), (b), and (c) illustrate the frequency spectrum and time jitter of ideal and real oscillators, and the typical oscillator phase noise plot. From Equations (3.10) and (3.11), the fluctuation introduced by  $A(t)$  and  $\varphi(t)$  are functions of time and lead to sidebands around the center frequency  $f_0$ . In the frequency domain, the spectrum of the oscillator consists of Dirac-impulses at  $\pm f_0$ . The SSB phase-noise  $\mathcal{L}(f)$  is usually expressed in the frequency domain and described in units of dBc/Hz, representing the noise power relative to the carrier contained in a 1 Hz bandwidth centered at a certain frequency offset from the carrier [43]-[46].

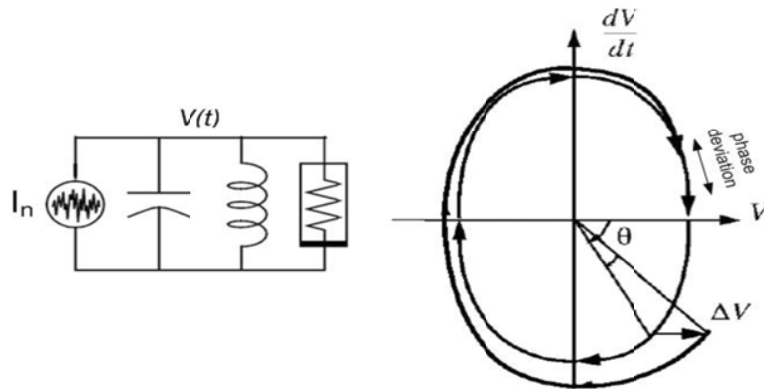


Fig. 3-2 A typical limit cycle of an ideal LC oscillator (The current noise perturbs the oscillator's voltage by  $\Delta V$  and the perturbed signal restores its stable amplitude whereas its phase is free to drift, causing strong random phase variations) [34].

In the order of increasing complexity, noise models are grouped into one of the three categories as: (i) linear time invariant (LTIV) model, (ii) linear time variant model (LTV), and (iii) nonlinear time variant model (NLTV) [47]-[68]. The first noise model is proposed by Leeson [1], based on LTIV (Linear-time-invariant) properties of the oscillator, such as resonator Q, feedback gain, output power, and noise figure; a second model is proposed by Lee and Hajimiri [35], based on time-varying properties of the oscillator RF current waveform (LTV); and a third is proposed by Kaertner, Demir, and Ngova using a perturbation model based on numerical techniques (NLTV) [38, 39, 46, 47].

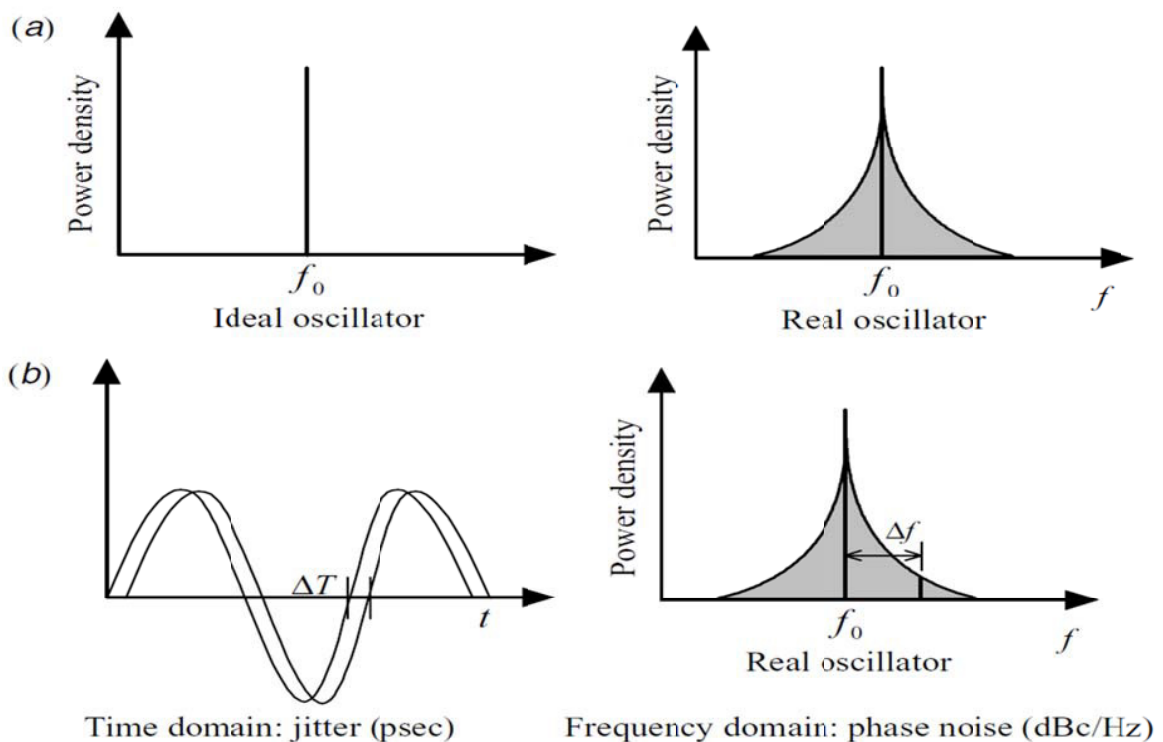


Fig 3-3: (a) A typical frequency spectrum of ideal and real oscillators, (b) Jitter in time domain relates to phase noise in the frequency domain [4]

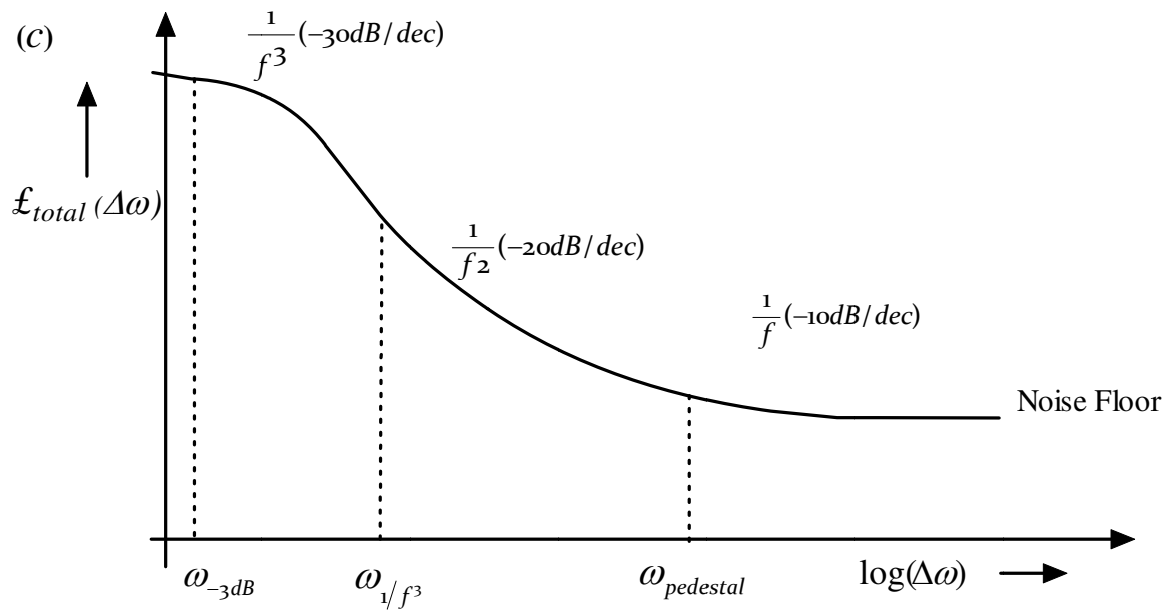


Fig 3-3: (c) a typical phase noise plot of real oscillator

Nallatamby et al. [6] revisited the Lesson's noise model, providing a detailed and enlightening analysis, demonstrating its applicability to several oscillator circuits. The theories proposed by Hajimiri and Lee, and from Kaertner and Demir are based on time-domain approaches for harmonic oscillator circuits (like LC resonator) [40]-[48]. The approach from Hajimiri and Lee can be seen as a particular case of the theory of Kaertner [46] and Demir [38, 42, 47], as it can be shown in the analytical comparison between time and frequency-domain techniques for phase noise analysis, carried out by Suárez et al. [7]. The Impulse Sensitivity Function (ISF) proposed by Hajimiri [45] and Lee can be employed to optimize the phase noise performances of a given oscillator and ISF can be obtained from Harmonic Balance (HB) as shown by Ver Hoeye et al. [8]. More insight and improvements of phase noise analysis that can be implemented [49]-[66] using commercially available HB tools that can be found in the paper Rizzoli [9] and Sancho et al. [9]-[10].

It is important to distinguish noise dynamics in resonator-based oscillators (harmonic oscillators) with a sharply contrasting oscillator type, time/waveform based oscillator (like relaxation, ring, and multivibrator) [67]-[68]. Generically this comprises a single reactance, usually a capacitor, a regenerative memory element such as a flip-flop or Schmitt trigger, and a means of charging and discharging the capacitor as shown in Figure 3-4 [69].

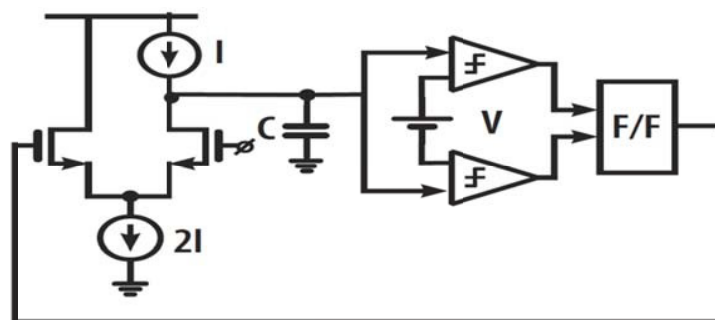


Figure 3-4: A typical simplified relaxation oscillator circuit [69]

Typically, harmonic oscillators can be characterized by equivalence to two energy storage reactive elements (inductor and capacitor), exchanging electrical and magnetic energy at resonance in order to give a periodic output signal. The actual LC resonant element can be high quality factor SAW (surface acoustic wave) resonator or Quartz Crystal resonator or Dielectric Resonator, YIG resonator or printed transmission line or lumped inductor-capacitor resonator [30]. The time/waveform based RC oscillator circuits (like relaxation, ring, and multivibrator) use one energy storage reactive element typically “capacitor” for determining oscillation frequency [68]. The single reactance is not frequency selective like the resonator, and the regenerative element makes this into a discrete-time feedback loop [69].

The basis of noise dynamics is fluctuation-dissipation theorem of thermodynamics in conjunction with probability viewpoints using the concept of Brownian motion (Wiener process), which dictates a lower limit for phase noise in RC oscillators [18]. Specifically, the phase noise due to the distinct characteristics of threshold crossing in RC oscillators can be expressed as functions of temperature, power dissipation, frequency of oscillation and the offset frequency [50]-[54].

In the family of inductor less oscillator, ring oscillator is most useful for current and later generation communication systems. As shown in Figure 3-5, the ring oscillator derives its frequency from the cumulative delay in the stages making up the ring. It follows by symmetry that if all the stages are identical, then as the sine wave traverses each stage of the ring, its amplitude remains unchanged, and it experiences a phase lag of  $45^\circ$  [69]. For simplification in analysis, one can assume that only one of the delay stages in the ring generates noise, and the other stages are noiseless so that at frequencies  $f_c$ , the ring oscillator can be characterized as a single noisy differential pair with negative feedback from the output to the input through an ideal delay line,  $t_d$  (as shown in Figure 3-5). Therefore, the unity gain delay line models the other three noiseless stages because its gain is one (at resonant frequency), and the effective delay of the entire ring is given by  $t_d = 1/(2f_c)$  [69].

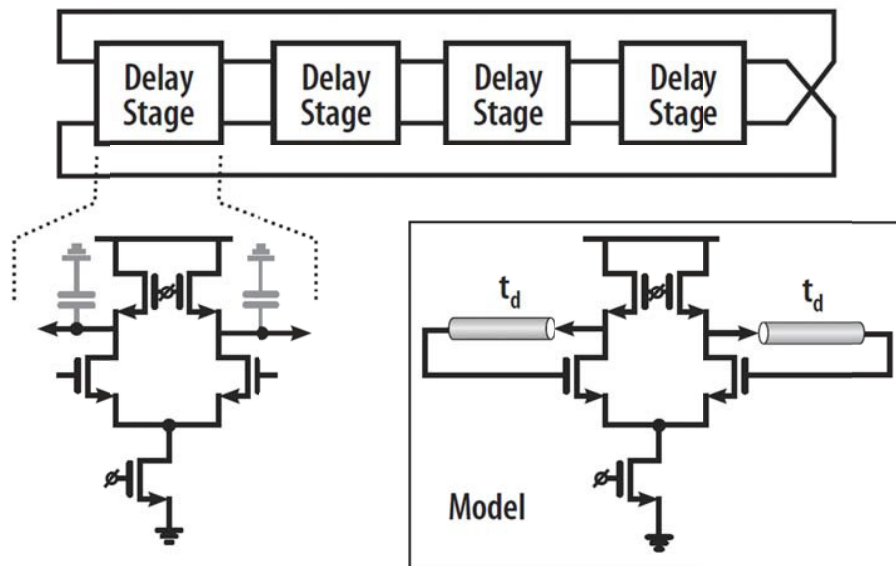


Figure 3-5: A typical simplified Ring Oscillator circuit using CMOS device and equivalent model to calculate the additive noise transfer function [69].

To have a better insight of the noise effects in the oscillator design, it is necessary to understand oscillator topologies how the noise arises in active (transistors) and passive devices. The designer has very limited control over the noise sources in a transistor, only being able to control the device selection and the operating bias point. However, using knowledge about how noise affects oscillator waveforms, the designer is able to substantially improve phase-noise performance of the oscillator circuits by the optimization of the key parameters (large signal noise factor, output waveform symmetry, circuit topology, drive-level, and noise filtering techniques) [4]-[11].

### 3.2 Leeson's Phase Noise Model

Phase noise is usually characterized in terms of the signal sideband noise spectral density. It has units of decibels below the carrier per hertz (dBc/Hz) and is defined as [4]

$$L_{\text{total}}\{\Delta\omega\} = 10 \cdot \log \left[ \frac{P_{\text{sideband}}(\omega_0 + \Delta\omega, 1\text{Hz})}{P_{\text{carrier}}} \right] \quad (3.12a)$$

where,  $P_{\text{sideband}}(\omega_0 + \Delta\omega, 1\text{Hz})$  represents the signal sideband power at a frequency offset of  $\Delta\omega$  from the carrier with a measurement bandwidth of 1Hz. Leeson's phase noise equation is given by [1]

$$\mathcal{L}(f_m) = 10 \log \left\{ \left[ 1 + \frac{f_0^2}{(2f_m Q_L)^2 \left(1 - \frac{Q_L}{Q_0}\right)^2} \right] \left( 1 + \frac{f_c}{f_m} \right) \frac{FkT}{2P_o} \right\} \quad (3.12b)$$

$\mathcal{L}(f_m)$  = ratio of sideband power in a 1Hz bandwidth at  $f_m$  to total power in dB

$f_m$  = frequency offset from the carrier

$f_0$  = center frequency

$f_c$  = flicker frequency

$Q_L$  = loaded Q of the tuned circuit

$Q_0$  = unloaded Q of the tuned circuit

$F$  = noise factor

$kT = 4.1 \times 10^{-21}$  at 300 K (room temperature)

$P_o$  = average power at oscillator output

It is important to understand that the Leeson model is based on linear time invariant characteristics (LTIV) and is the best case since it assumes the tuned circuit filters out of all the harmonics. Assuming the phase-noise as a small perturbation, Leeson linearizes the oscillator circuit around the steady-state point in order to obtain a closed-form formula for phase-noise. In all practical cases, it is hard to predict what the operating Q and noise figure will be. The predictive power of the Leeson model is limited due to the following, which is not known prior to measurement: the output power, the noise figure under large signal conditions, and the loaded Q [18].

This classic paper [1] is good design guide with the basic understanding that the "noise factor" as shown in Equation (3.12) is not what we understand; but a measure of the upconverted 1/f noise. Since Leeson's model does not try to account for this, it cannot possibly provide useful noise predictions. The drawback of this approach is the fact that the up-conversion of the low frequency flicker noise components to around carrier phase-noise, which is a necessary input to the equation; the RF output power, the loaded Q, and the noise factor of the amplifier under large signal condition, are not known. In addition to this Equation (3.12) predicts an infinite phase-noise power as  $f \rightarrow 0$ .



### 3.2.1 Leeson's Phase Noise Model (Linear Time Invariant Approach)

Since an oscillator can be viewed as an amplifier with feedback as shown in Figure 2-1 (Chapter 2), it is helpful to examine the phase noise added to an amplifier that has a noise factor  $F$ . With  $F$  defined as

$$F = \frac{(S/N)_{in}}{(S/N)_{out}} = \frac{N_{out}}{N_{in}G} = \frac{N_{out}}{GkTB} \quad (3.13)$$

$$N_{out} = FGkTB \quad (3.14)$$

$$N_{in} = kTB \quad (3.15)$$

$$\Delta\theta_{1peak} = \frac{V_{nRMS1}}{V_{savRMS}} = \sqrt{\frac{FkT}{P_{sav}}} \quad (3.16)$$

$$\Delta\theta_{RMS} = \frac{1}{\sqrt{2}} \sqrt{\frac{FkT}{P_{sav}}} \quad (3.17)$$

where  $N_{in}$  is the total input noise power to a noise-free amplifier,  $F$  is the noise factor,  $T$  is temperature in Kelvin,  $k$  is the Boltzmann constant ( $kT = 4.1 \times 10^{-21}$  at 300 K),  $P_{sav}$  is average output power.

Figure 3-6 shows the typical representation of noise power versus frequency of a transistor amplifier with an input signal applied. The input phase noise in a 1 Hz bandwidth at any frequency  $f_0 + f_m$  from the carrier produces a phase deviation as shown in Figure 3-7.

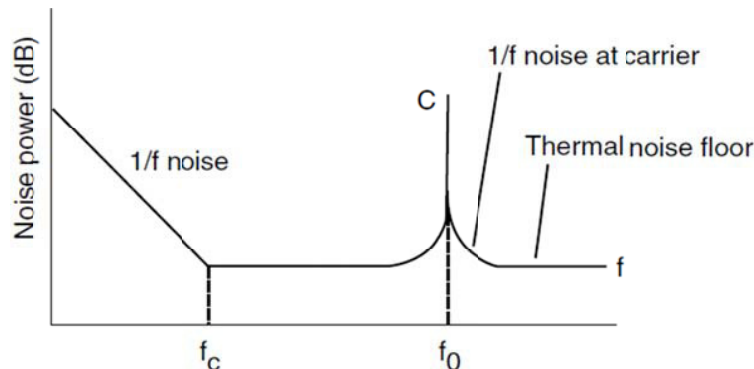


Figure 3-6: Noise power vs. frequency of a transistor amplifier with an input signal applied [4, pp. 124]

Since a correlated random phase noise relation exists at  $f_0 - f_m$ , the total phase deviation becomes

$$\Delta\theta_{RMStotal} = \sqrt{FkT/P_{sav}} \quad (\text{SSB}) \quad (3.18)$$

The spectral density of phase noise becomes

$$S_{\theta}(f_m) = \Delta\theta_{RMS}^2 = FkTB/P_{sav} \quad (3.19)$$

where  $B = 1$  for a 1 Hz bandwidth.

$$kTB = -174 \text{ dBm} \quad (B = 1 \text{ Hz}, T = 300\text{K}) \quad (3.20)$$

Using (3.20), allows a calculation of the spectral density of phase noise that is far away from the carrier (that is, at large values of  $f_m$ ). This noise is the theoretical noise floor of the amplifier. For example, an amplifier with +10 dBm power at the input and a noise figure of 6 dB gives

$$S_{\theta}(f_m > f_c) = -174 \text{ dBm} + 6 \text{ dB} - 10 \text{ dBm} = -178 \text{ dBm} \quad (3.21)$$

Only if  $P_{out}$  is  $> 0$  dBm can we expect L (signal-to-noise ratio) to be greater than -174dBc/Hz (1 Hz bandwidth.) For a modulation frequency close to the carrier,  $S_{\theta}(f_m)$  shows a flicker or  $1/f$  component, which is empirically described by the corner frequency  $f_c$ . The phase noise can be modeled by a noise-free amplifier and a phase modulator at the input as shown in Figure 3-8.

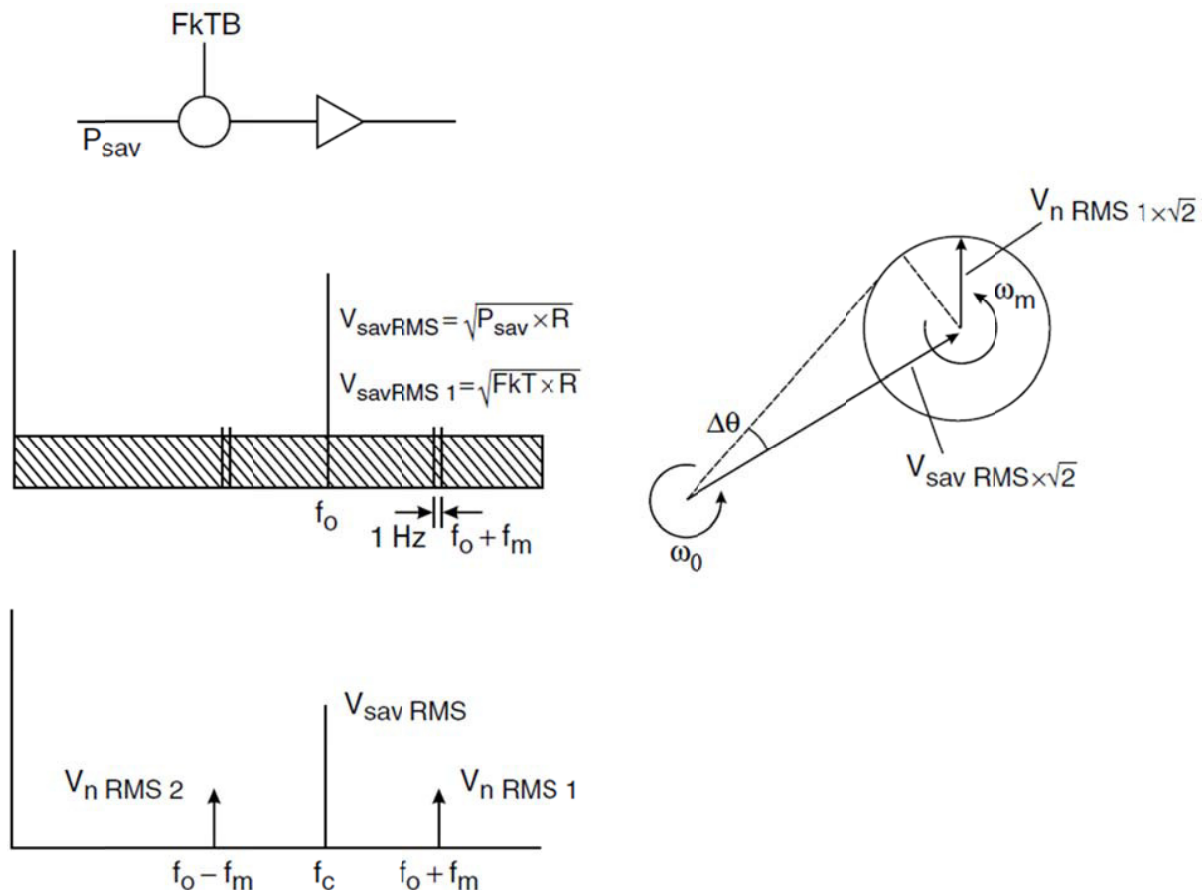


Figure 3-7: Phase noise added to the carrier (the input phase noise in a 1 Hz bandwidth at any frequency  $f_0 + f_m$  from the carrier produces a phase deviation) [4, pp. 125].

The purity of the signal is degraded by the flicker noise at frequencies close to the carrier. The phase noise can be described by

$$S_{\theta}(f_m) = \frac{FkTB}{P_{sav}} \left( 1 + \frac{f_c}{f_m} \right) \quad (B = 1) \quad (3.22)$$

No AM-to-PM conversion is considered in this equation. The oscillator may be modeled as an amplifier with feedback as shown in Figure 3-9 [4].

The phase noise at the input of the amplifier is affected by the bandwidth of the resonator in the oscillator circuit in the following way. The tank circuit or bandpass resonator has a low pass transfer function

$$H(\omega_m) = \frac{1}{1 + j(2Q_L \omega_m / \omega_0)} \quad \text{where} \quad \omega_0 / 2Q_L = 2\pi B / 2 \quad (3.23)$$

where  $\omega_0 / 2Q_L = 2\pi B / 2$ , is the half bandwidth of the resonator,  $Q_L$  is the loaded quality factor. These equations describe the amplitude response of the bandpass resonator; the phase noise is transferred unattenuated through the resonator up to the half bandwidth [4].

Leeson's phase-noise formula was derived for an oscillator using a single resonator with the transfer function given in (3.10); thus one might question its validity for oscillators using more complex resonant structures such as slow-wave-resonator (SWR) with different  $H(\omega_m)$ .

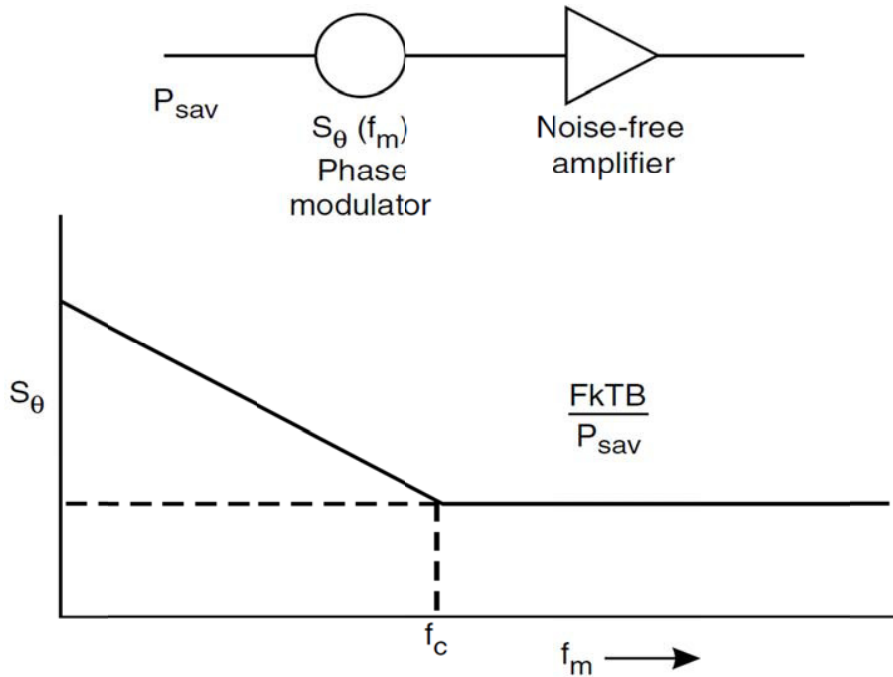


Figure 3-8 Phase noise modeled by a noise free amplifier and phase modulator [Ref. 4, pp. 126, Fig. 7-3]

In fact, by replacing  $H(\omega_m)$  in (3.23) with its Taylor series expansion around the resonant frequency, one can easily show that the Lesson's phase-noise formula remains valid and can be applied to oscillators with complex resonators, provided that the loaded quality-factor is defined as [39]-[41]

$$Q_L = \frac{\omega_0}{2} \sqrt{\left(\frac{\Delta A(\omega)}{\Delta \omega}\right)^2 + \left(\frac{\Delta \theta(\omega)}{\Delta \omega}\right)^2} \quad (3.24)$$

where  $A(\omega)$  and  $\theta(\omega)$  are the amplitude and phase of the resonator's transfer function  $H(\omega_m)$ .

The closed loop response of the phase feedback loop as shown in Figure 3-9 is given by

$$\Delta \theta_{\text{out}}(f_m) = \left(1 + \frac{\omega_0}{j2Q_L \omega_m}\right) \Delta \theta_{\text{in}}(f_m) \quad (3.25)$$

The power transfer becomes the phase spectral density

$$S_{\theta_{\text{out}}}(f_m) = \left[1 + \frac{1}{f_m^2} \left(\frac{f_0}{2Q_L}\right)^2\right] S_{\theta_{\text{in}}}(f_m) \quad (3.26)$$

where  $S_{\theta_{\text{in}}}$  was given by Equation (3.9).

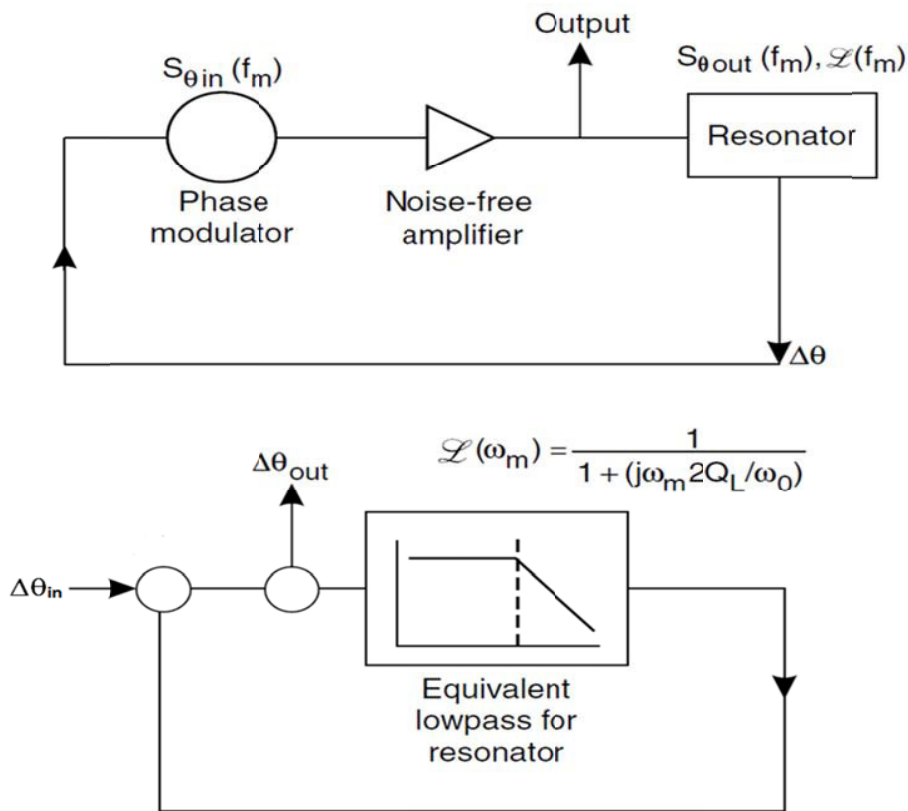


Figure 3-9: Equivalent feedback models of oscillator phase noise [4, pp. 126, Fig. 7-4]

Finally,  $\mathcal{L}(f_m)$ , which is the single sideband phase noise  $\frac{1}{2} [S_{\theta_{out}}(f_m)]$  [4, pp. 127]

$$\mathcal{L}(f_m) = \frac{1}{2} \left[ 1 + \frac{1}{f_m^2} \left( \frac{f}{2Q_L} \right)^2 \right] S_{\theta_{in}}(f_m) \quad (3.27)$$

This equation describes the phase noise at the output of the amplifier (flicker corner frequency and AM-to-PM conversion are not considered). The phase perturbation  $S_{\theta_{in}}$  at the input of the amplifier is enhanced by the positive phase feedback within the half bandwidth of the resonator,  $f_0/2Q_L$ . Depending on the relation between  $f_c$  and  $f_0/2Q_L$ , there are two cases of interest, as shown in Figure 3-10.

For the low  $Q$  case, the spectral phase noise is unaffected by the  $Q$  of the resonator, but the  $\mathcal{L}(f_m)$  spectral density will show a  $1/f^3$  and  $1/f^2$  dependence close to the carrier. For the high  $Q$  case, a region of  $1/f^3$  and  $1/f$  should be observed near the carrier. Substituting Equation (3.22) in (3.27) gives an overall noise of [4, pp.128]:

$$\mathcal{L}(f_m) = \frac{1}{2} \left[ 1 + \frac{1}{f_m^2} \left( \frac{f}{2Q_L} \right)^2 \frac{FkT}{P_{sav}} \left( 1 + \frac{f_c}{f_m} \right) \right] = \frac{FkT}{2P_{sav}} \left[ \frac{1}{f_m^3} \frac{f^2 f_c}{4Q_L^2} + \frac{1}{f_m^2} \left( \frac{f}{2Q_L} \right)^2 + \left( 1 + \frac{f_c}{f_m} \right) \right] \text{dBc/Hz} \quad (3.28)$$

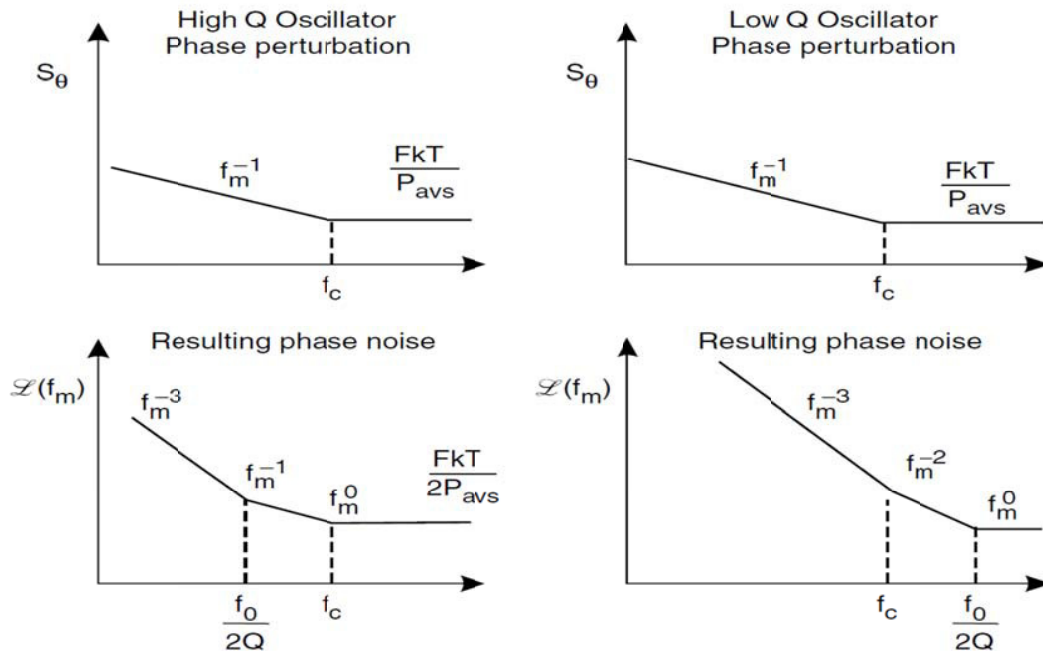


Figure 3-10: The representation of oscillator phase noise plots for high and low Q-factor resonator oscillator [4]

Examining Equation (3.27) gives the four major causes of oscillator noise: the up-converted  $1/f$  noise or flicker FM noise, the thermal FM noise, the flicker phase noise, and the thermal noise floor, respectively. The  $Q_L$  (loaded Q) can be expressed as [4, pp. 128]

$$Q_L = \frac{\omega_o W_e}{P_{diss, total}} = \frac{\omega_o W_e}{P_{in} + P_{res} + P_{sig}} = \frac{\text{reactive power}}{\text{total dissipated power}} \quad (3.29)$$

where  $W_e$  is the reactive energy stored in  $L$  and  $C$ ,

$$W_e = \frac{1}{2} CV^2 \quad (3.30)$$

$$P_{res} = \frac{\omega_o W_e}{Q_{unl}} \quad (3.31)$$

$$\mathcal{L}(f)_m = \frac{1}{2} \left[ 1 + \frac{\omega_0^2}{4\omega_m^2} \left( \frac{P_{in}}{\omega_0 W_e} + \frac{1}{Q_{unl}} + \frac{P_{sig}}{\omega_0 W_E} \right)^2 \right] \left( 1 + \frac{\omega_c}{\omega_m} \right) \frac{FkT_0}{P_{sav}} \quad (3.32)$$

More comments on the Leeson formula are found in [36]-[39]. The practical oscillator will experience a frequency shift when the supply voltage, is changed. This is due to the voltage and current dependent junction capacitances of the transistor. To calculate this effect, we can assume that the fixed tuning capacitor of the oscillator is a semiconductor junction, which is reverse biased. This capacitor becomes a tuning diode [4]. This tuning diode itself generates a noise voltage and modulates its capacitance by a slight amount, and therefore modulates the frequency of the oscillator by minute amounts. The following calculates the phase noise generated from this mechanism, which needs to be added to the phase noise calculated above. It is possible to define an equivalent noise  $R_{aeq}$  that, inserted in Nyquist's equation,

$$V_n = \sqrt{4kT_o R_{aeq} \Delta f} \quad (3.33)$$

where  $kT_o = 4.2 \times 10^{-21}$  at 300 K,  $R$  is the equivalent noise resistor,  $\Delta f$  is the bandwidth determines an open noise voltage across the tuning diode. Practical values of  $R_{aeq}$  for carefully selected tuning diodes are approximately 100Ω, or higher. If we now determine the voltage  $V_n = \sqrt{4 \times 4.2 \times 10^{-21} \times 100}$ , the resulting voltage value is  $1.265 \times 10^{-9} \text{ V} \sqrt{\text{Hz}}$ . This noise voltage generated from the tuning diode is now multiplied with the VCO gain, resulting in the rms frequency deviation:

$$(\Delta f_{rms}) = K_o \times (1.265 \times 10^{-9} \text{ V}) \text{ in 1 Hz bandwidth} \quad (3.34)$$

In order to translate this into the equivalent peak phase deviation,

$$\theta_d = \frac{K_o \sqrt{2}}{f_m} (1.265 \times 10^{-9} \text{ rad}) \text{ in 1 Hz bandwidth} \quad (3.35)$$

$$\text{Or, for a typical oscillator gain of 10 (MHz/V), } \theta_d = \frac{0.00179}{f_m} \text{ (rad in 1 Hz bandwidth)} \quad (3.36)$$

For  $f_m = 25$  kHz (typical spacing for adjacent channel measurements for FM mobile radios), the  $\theta_d = 7.17 \times 10^{-8}$ . This can be converted into the SSB signal-to-noise ratio

$$L(f_m) = 20 \log_{10} \frac{\theta_c}{2} = -149 \text{ dBc / Hz} \quad (3.37)$$

Figure 3-11 shows a plot with an oscillator sensitivity of 10 kHz/V, 10 MHz/V, and 100 MHz/V. The center frequency is 2.4 GHz [4]. The lowest curve is the contribution of the Leeson equation. The second curve shows the beginning of the noise contribution from the diode, and the third curve shows that at this tuning sensitivity, the noise from the tuning diode by itself dominates as it modulates the VCO. This is valid regardless of the Q. This effect is called modulation noise (AM-to-PM conversion), while the Leeson equation deals with the conversion noise. Rohde modified the Leeson phase noise Equation (3.12) with the tuning diode contribution, following Equation allows us to calculate the oscillator phase noise as [4, 98]

$$L(f_m) = 10 \log \left\{ \left[ 1 + \frac{f_0^2}{(2f_m Q_L)^2} \right] \left( 1 + \frac{f_c}{f_m} \right) \frac{FkT}{2P_{sav}} + \frac{2kTRK_0^2}{f_m^2} \right\} \quad (3.38)$$

where

$L(f_m)$  = ratio of sideband power in a 1 Hz bandwidth at  $f_m$  to total power in dB

$f_m$  = frequency offset

$f_0$  = center frequency

$f_c$  = flicker frequency

$Q_L$  = loaded Q of the tuned circuit

$F$  = noise factor

$kT = 4.1 \times 10^{-21}$  at 300 K<sub>0</sub> (room temperature)  
 $P_{sov}$  = average power at oscillator output  
 $R$  = equivalent noise resistance of tuning diode (typically 50 Ω - 10 kΩ)  
 $K_o$  = oscillator voltage gain

The limitation of this equation is that the loaded Q in most cases has to be estimated and the same applies to the noise factor. The microwave harmonic-balance simulator, which is based on the noise modulation theory (published by Rizzoli), automatically calculates the loaded Q and the resulting noise figure as well as the output power [40].

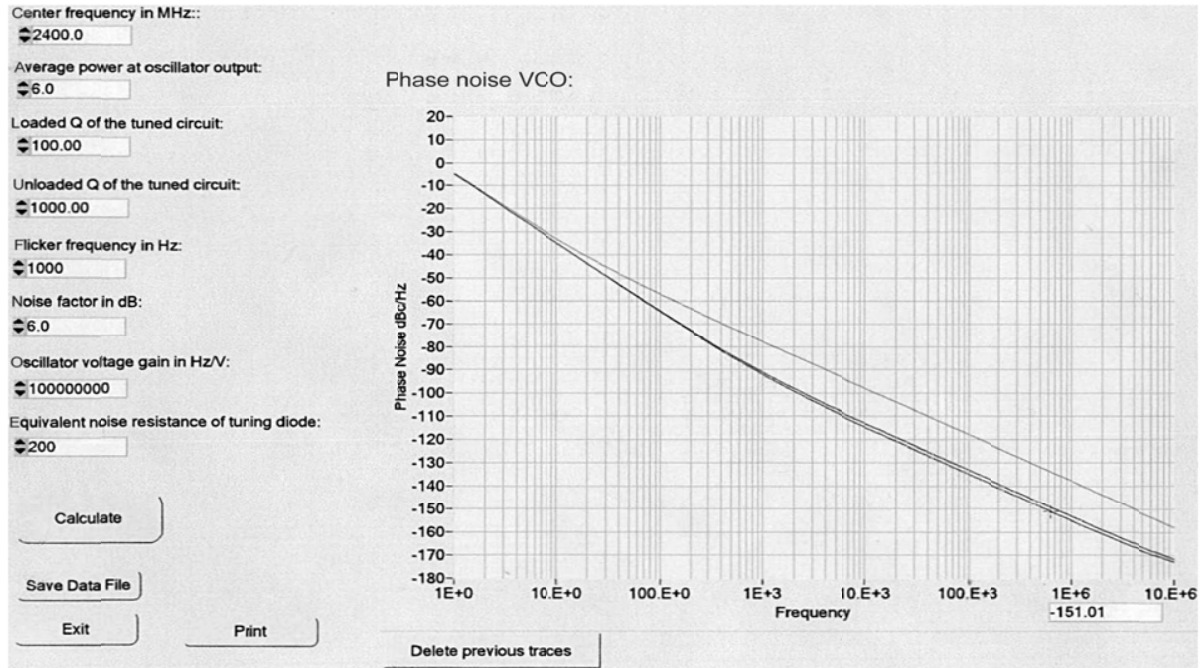


Figure 3-11 Simulated phase noise following Equation (3.24)

When adding an isolating amplifier, the noise of an LC oscillator system is determined by

$$\begin{aligned}
 S_{\phi}(f_m) = & \left[ a_R F_0^4 + a_E (F_0 / (2Q_L))^2 \right] / f_m^3 \\
 & + \left[ (2GFkT / P_0) (F_0 / (2Q_L))^2 \right] / f_m^2 \\
 & + (2a_R Q_L F_0^3) / f_m^2 \\
 & + a_E / f_m + 2GFkT / P_0
 \end{aligned} \tag{3.39}$$

where

- $G$  = compressed power gain of the loop amplifier
- $F$  = noise factor of the loop amplifier
- $k$  = Boltzmann's constant
- $T$  = temperature in Kelvins
- $P_0$  = carrier power level (in watts) at the output of the loop amplifier
- $F_0$  = carrier frequency in Hz
- $f_m$  = carrier offset frequency in Hz
- $Q_L = (\pi F_0 \tau_g)$  = loaded Q of the resonator in the feedback loop
- $a_R$  and  $a_E$  = flicker noise constants for the resonator and loop amplifier

From (3.38), resonator Q factor is an important parameter for low phase noise oscillator applications. Care must be taken to maximize the dynamic loaded Q-factor for improved phase noise performances. If the loaded Q is infinite at oscillator steady state condition that leads to “0Hz” noise bandwidth for the negative resistance oscillator circuit. Moreover, if this is the case then this oscillator would take infinite time to build the output transient waveform and reach at the stable state condition [42]. For practical condition, there is a net resistance at turn-on, and the start-up transient depends on the behavior of the nonlinearity associated with the oscillator circuits and the slope parameter of resonator establishes the noise spectrum [42].

Although Leeson’s phase-noise model provides a valuable insight into the oscillator design from engineering perspectives, it cannot explain some of the important phase noise phenomena [38]. This is due to simplifying assumptions made about the linearity and time-invariant behavior of the system. When comparing the measured results of oscillators with the assumptions made in Leeson’s Equation (3.28), one frequently obtains a *de facto* noise figure in the vicinity of 20 to 30 dB and an operating Q that is different than the assumed loaded Q, therefore must be determined from measurement; diminishing the predictive power of the Leeson’s phase noise model [4]. Leeson’s model observes the asymptotic behavior of phase-noise at close-to carrier offsets, asserting that phase-noise goes to infinity with  $1/f^3$  rate [1]. This is obviously wrong as it implies an infinite output power for oscillator. For noisy oscillators it could also suggest that  $L(f) > 0$  dBc/Hz, this singularity arises from linearity assumption for oscillator operation around steady-state point [38]-[43]. In fact, the linear model breaks down at close-to-carrier frequencies where the phase-noise power is strong [39]. Considering a nonlinear model for the oscillator in absence of flicker noise, these singularities can be resolved by expressing the phase noise in the form of a Lorentzian function [42]

$$L(\Delta f_m) \propto \frac{a^2}{a^2 + (\Delta f_m)^2} \quad (3.40)$$

where  $a$  is a fitting parameter.

Although Equation (3.40) models the spectrum and avoids any singularity at  $\Delta f_m=0$  while maintaining the same asymptotic behavior as illustrated in Figure 3-12, this is only an after-the-fact approach, but not a predictive one [41]-[43]. From Equation (3.40), the total power of phase-noise from minus infinity to plus infinity is 1, this means that phase-noise does not change the total power of the oscillator; it merely broadens its spectral peak.

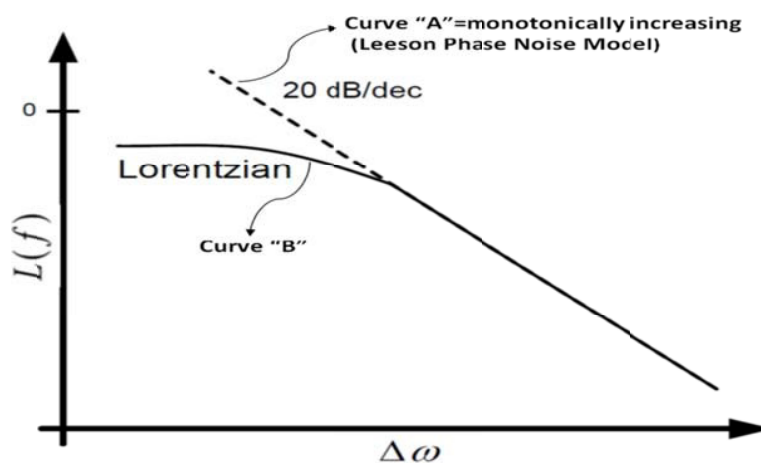


Fig. 3-12 Close-In phase-noise behavior due to white noise sources. Leeson’s model predicts phase-noise monotonically increases by approaching the carrier whereas in reality it takes the form of a Lorentzian shape [42]



Attempting to match the Leeson calculated curve “A” (Figure 3-12) considering the Equation (3.40), the measured curve requires totally different values than those assumed due to up-conversion and down-conversion of noise components from harmonically related frequencies to around carrier frequency as depicted in Figure 3-13 [37]-[39].

The influence of low frequency noise component in stable frequency sources is paramount and determining factor for phase hits due to time-jitter noise dynamics. Particularly, the effect of low-frequency flicker noise components on close-in phase-noise is not well defined in Leeson’s model. The model asserts that the phase-noise  $1/f^3$  corner frequency is exactly equal to the amplifier’s flicker-noise corner frequency ( $f_c$ ), but measurements do not clearly show such equality [38]. This is because Leeson models the oscillator as a time-invariant system, whereas oscillators are in general cyclostationary (cyclostationary process: Signal having statistical properties that vary cyclically with time) time-varying systems due to the presence of the periodic large-signal oscillation. This issue has been addressed by several authors [33]-[48]. Lee and Hajimiri [36] has shown that the oscillator’s phase-noise  $1/f^3$  corner frequency can be significantly lower than the device’s flicker corner frequency, provided that the oscillation signals at the output of the oscillator circuits are odd-symmetric.

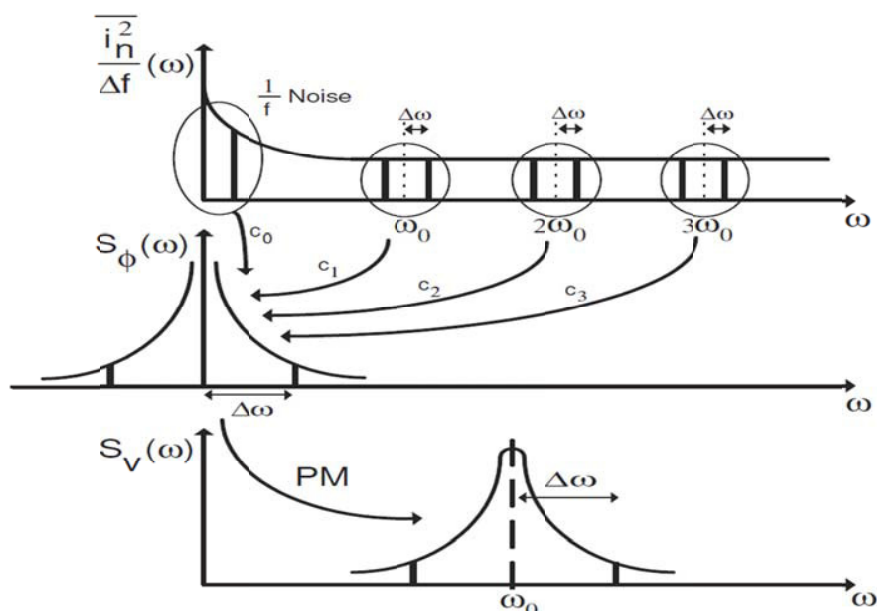


Fig. 3.13 Conversion process from noise ( $S_n(\omega)$ ) to phase-noise ( $L(\omega)$ ). Noise components from harmonically related frequencies are up/down-converted to around carrier phase noise, Leeson’s model fails to address this phenomenon [36].

The basic concept of the Leeson equation gives a quick approximate valuation of the phase noise performance for oscillator circuits, including the trend for the minimization of noise if following unknown terms are assumed and inserted properly; the computed results will agree within a reasonable degree of the accuracy but not the error free prediction. The information that is not known prior to the measurement is [4]:

- a) the output power,
- b) the noise figure under large-signal conditions, and
- c) the loaded (operational ) noise figure
- d) flicker up conversion dynamics
- e) singularity at close to carrier

In conclusion, Leeson's model assumes linear approach but oscillators are inherently nonlinear, it is expected that such a linear phase noise model would predict the phase noise of an oscillator with a significant error.

### 3.2.2 Lee and Hajimiri's Noise Model (Linear Time Variant Model)

To overcome the limitation of linear time invariant phase noise model (Leeson's phase noise model), Lee and Hajimiri proposed linear time varying [LTV] phase noise model to predict the noise properties of the oscillator output waveform [36, 43, 44, 45]. There were many LTV models around and before Lee and Hajimiri, explaining the phase noise dynamics of autonomous circuits (oscillators) for a given nonlinearity associated with the circuits in large signal conditions. Lee and Hajimiri's noise model is based on the linear time varying [LTV] properties of the oscillator current waveform, and the phase noise analysis is given based on the effect of noise impulse on a periodic signal. Figure 3-14 shows the noise signal in response to the injected impulse current at two different times, peak and zero crossing. As illustrated in Figure 3-14, if an impulse is injected into the tuned circuit at the peak of the signal, it will cause maximum amplitude modulation and no phase modulation whereas; if an impulse is injected at the zero crossing, there will be no amplitude modulation but maximum phase modulation. If noise impulses are injected between zero crossing and the peak, there will be components of both phase and amplitude modulation. Variations in amplitude are generally ignored because they are limited by the gain control mechanism of the oscillator. Therefore, according to this theory, to obtain the minimal phase noise, special techniques have to be adopted so that any noise impulse should coincide in time with the peaks of the output voltage signal rather than at the zero crossing or in between of zero-crossing and peak [18].

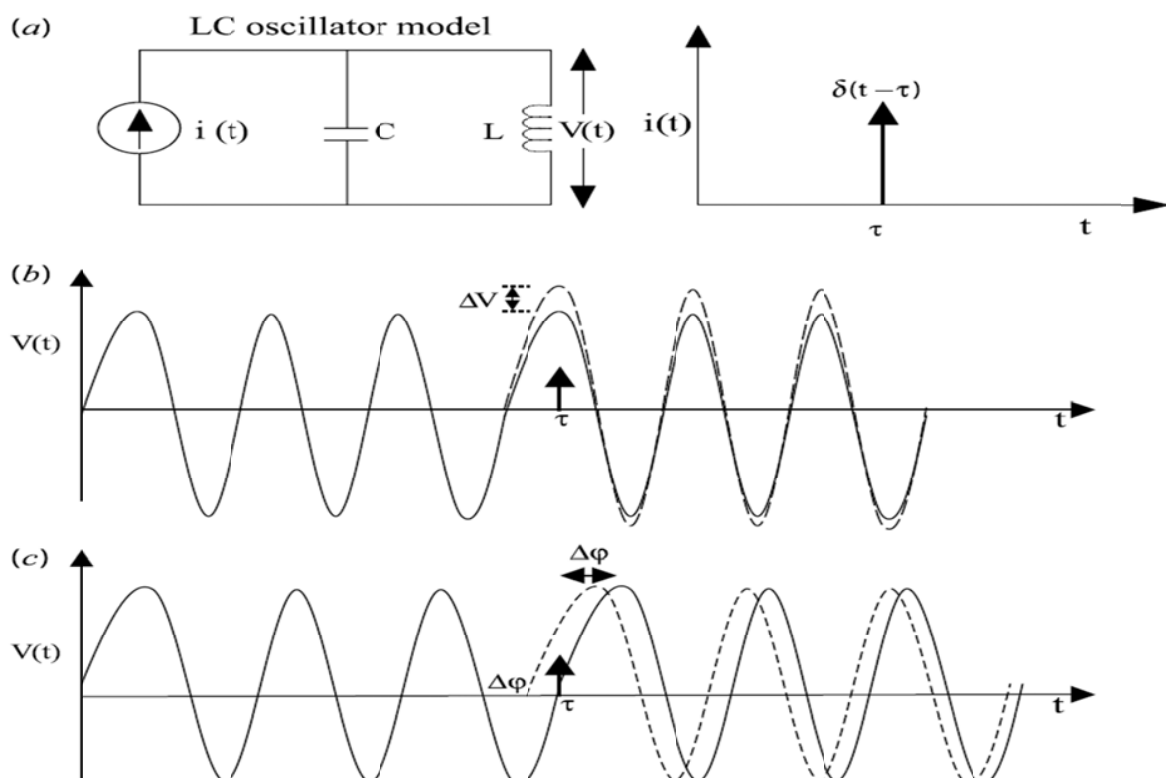


Figure 3-14: a) A typical LC oscillator excited by current pulse b) Impulse injected at peak of the oscillation signal and c) Impulse injected at zero crossing of the oscillation signal [4].

Lee and Hajimiri introduced an impulse sensitivity function (ISF) based on injected impulse, which is different for each topology of the oscillator [43]-[45]. It has its largest value when the most phase modulation occurs but has the smallest value when only amplitude modulations occur. This model is a kind of impulse response function that defines the phase noise versus device noise transfer function, in a manner similar to an impulse-response function in a linear circuit. The calculation of the ISF is tedious and depends upon the topology of the oscillator. Based on this theory, phase noise equation is expressed as [36]

$$\mathfrak{L}(f_m) = \begin{cases} 10 \log \left[ \frac{C_0^2}{q_{\max}^2} * \frac{i_n^2 / \Delta f}{8f_m^2} * \frac{\omega_{1/f}}{f_m} \right] & \frac{1}{f^3} \rightarrow \text{region} \\ 10 \log \left[ 10 \log \left[ \frac{\Gamma_{rms}^2}{q_{\max}^2} * \frac{i_n^2 / \Delta f}{4f_m^2} \right] \right] & \frac{1}{f^2} \rightarrow \text{region} \end{cases} \quad (3.41)$$

where

$i_n^2 / \Delta f$  = Noise power spectral density,  $\Delta f$  = Noise bandwidth

$\Gamma_{rms}^2 = \frac{1}{\pi} \int_0^{2\pi} |\Gamma(x)|^2 dx = \sum_{n=0}^{\infty} C_n^2$  = Root mean square (RMS) value of  $\Gamma(x)$

$\Gamma(x) = \frac{C_0}{2} + \sum_{n=1}^{\infty} C_n \text{Cos}(nx + \theta_n)$  = Impulse Sensitivity function (ISF)

$C_n$  = Fourier series coefficient,  $C_0$  = 0<sup>th</sup> order of the ISF (Fourier series coefficient)

$\theta_n$  = Phase of the n<sup>th</sup> harmonic,  $f_m$  = Offset frequency from the carrier

$\omega_{1/f}$  = Flicker corner frequency of the device,  $q_{\max}$  = Maximum charge stored across the capacitor in the resonator.

At first glance, it appears that LTV model overcomes the shortcomings of LTIV model presented by Leeson [1]. However, careful assessment of Lee and Hajimiri LTV model reveals that there are difficulties with its application to phase noise prediction. This follows since, apart from the ISF, the phase noise does not directly describe the effect of circuit parameters e.g. capacitance, inductances, resistance, transistor parameters, etc.). In order to obtain a quantitative phase noise solution for a circuit, the ISF is to be calculated by computer simulation on the oscillator circuit. Since analytical solutions for the ISF in terms of circuit parameters are mostly non-existent, it can only be done numerically. As a result, insight into how the physics of the oscillator circuit parameters can be manipulated to yield improved phase noise performance is lost. Equation (3.41) is a generalization of Leeson's model if it is evaluated at the hand of underlying assumptions (as shown in Figure 3-12 and Figure 3-13), but it is a step closer to the numerical computer simulation with the penalty of analytical insight bound to physical parameters. While Leeson's model retained the loaded quality factor of the resonator (a physical parameter), Lee and Hajimiri model gives up as many of the physical circuit parameters as possible (unifying the effect of such parameter into a single ISF). This result in losing valuable insight that its retention could have brought to the approach for minimization of phase noise dependence on such parameter is lost [7].

Various other conclusions are drawn that amount to manipulation of the ISF, but such conclusions are removed from what can be implemented through oscillator circuit design. Nevertheless LTV model does yield some insights that Leeson's model lack, first it reveals that if the active element in an oscillator were able to instantaneously restore the energy transferred to the resonator at precisely the right moment in the oscillation cycle, then it would in principle limit the phase noise to a minimum, which is

validated by the examination of the Colpitts oscillator circuit [36]. Second, the phase noise can be reduced by increasing the maximum charge displacement  $q_{max}$  in Equation (3.41), this can in some case be physically accomplished by increasing the output power level of the oscillation signal-although this insight is more specific; it is something already known from LTI based Leeson's model. Third, any phase noise present around integer multiples of the oscillation frequency is frequency translated to appear as phase noise sidebands around the oscillation signal. In conclusion, LTI based noise model gives good results once all the data is known, but does not lead to exact design rules. The Equation (3.41) using LTV theory though providing a good tool for explaining the phase noise spectrum in oscillators especially the  $1/f^3$  region, suffers from the following shortcomings [38]:

- a) assumes oscillators are inherently linear time variant, but does not give a reason for this
- b) based on the parameter impulse sensitivity function (ISF), which is very difficult to determine
- c) It does not provide insight into the factors affecting performance in oscillator design

As described above, the implication of Lee and Hajimiri's theory is that the designer does not have much control in terms of the oscillator circuit component parameters over the timing of the noise impulse injected into the oscillator circuit. The noise analysis based on the signal drive level and the conduction angle of the time-varying properties of the oscillator current waveform can overcome partly the drawback associated with Lee and Hajimiri's Noise Model [33].

As shown in Figure 3-15, the drive-voltage ( $v_{resonator}$ ) produces an output current  $i_c$  consisting of a series of current pulses, its shape and conduction angle depends upon the strength of the signal drive level [18, 98]. Figure 3-15 (c) shows the typical noise current  $i_{noise}$  relative to the RF current  $i_c$  as depicted in Figure 3-15 (b) for a LC-Colpitts oscillator in presence of resonator signal voltage  $v_{resonator}$ , Figure 3-15 (a). The natural operation of the oscillator will cause the current pulses to be centered on the negative peaks of the resonator tank voltages and the associated noise components depend on the conduction angle (width of the RF current pulse). From Rohde's noise model [98], the conduction angle  $\varphi$  ( $\varphi \propto 1/C_2$ ) is inversely proportional to the feedback capacitor  $C_2$ , and directly proportional to the drive-level  $x$  ( $x \propto C_2$ ). The following example given in the Figure 3-16 illustrates the typical circuit diagram of the 100 MHz LC Colpitts oscillator for giving insight into the relationship between the drive level, the current pulse, and the phase noise [4].

As shown in Figure 3-15, the majority of noise current exists only during collector current pulses and the oscillator output current will be negligible or zero during the time between output current pulses, and therefore, aside from thermal noise, the noise sources, which depend on current such as shot, partition, and  $1/f$ , exist only during the conducting angle of output current pulses. If the signal drive level is increased, the oscillator output current pulse will be narrower, and consequently, noise pulse during conduction angle becomes narrowed, and thereby, has less PM noise contribution than the wider pulse.

Table 3-1 shows the drive level for different values of  $C_2$  for a 100 MHz oscillator. The collector current of the circuit shown in the Figure 3-16 plotted in Figure 3-17 using CAD simulator (Ansys: Ansoft Designer 8), becomes narrower as the drive level  $x$  increases, and the corresponding base voltage  $V_{base}$  swing increases as illustrated in Figure 3-18 [18, 98].

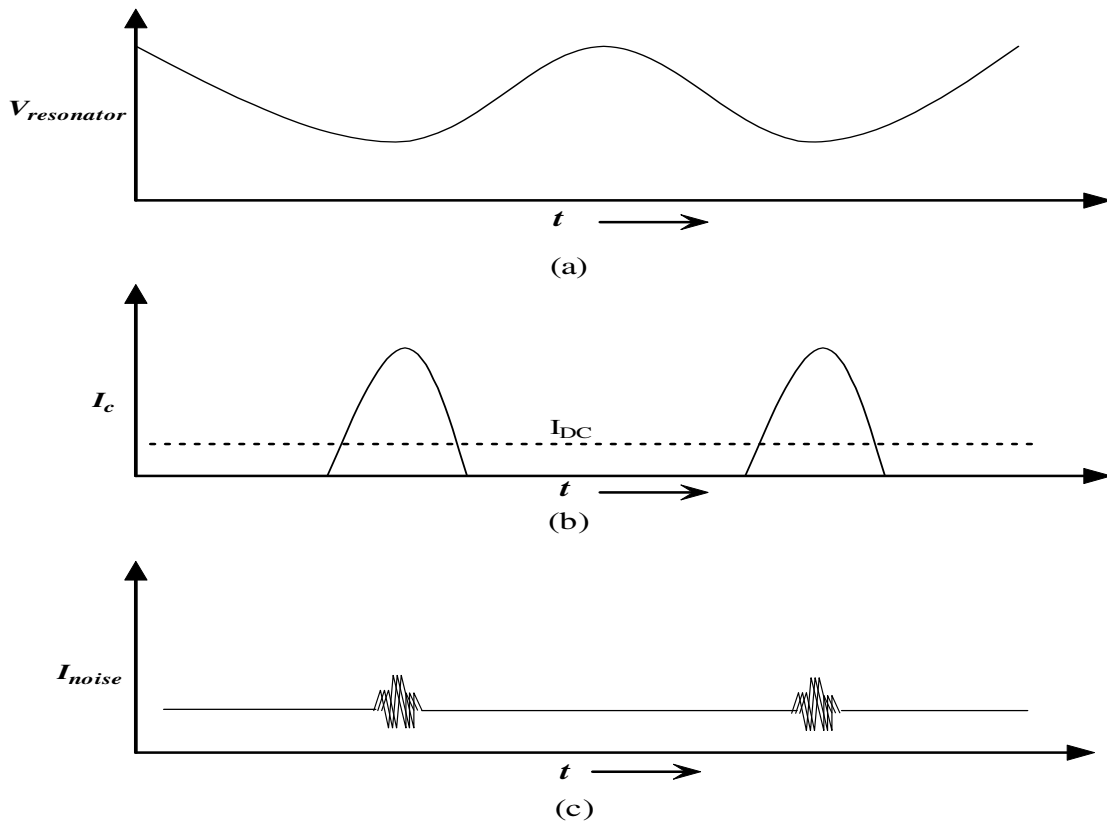


Figure 3-15: The plots show (a) voltage across resonator, (b) oscillator output RF current, and (c) noise current.

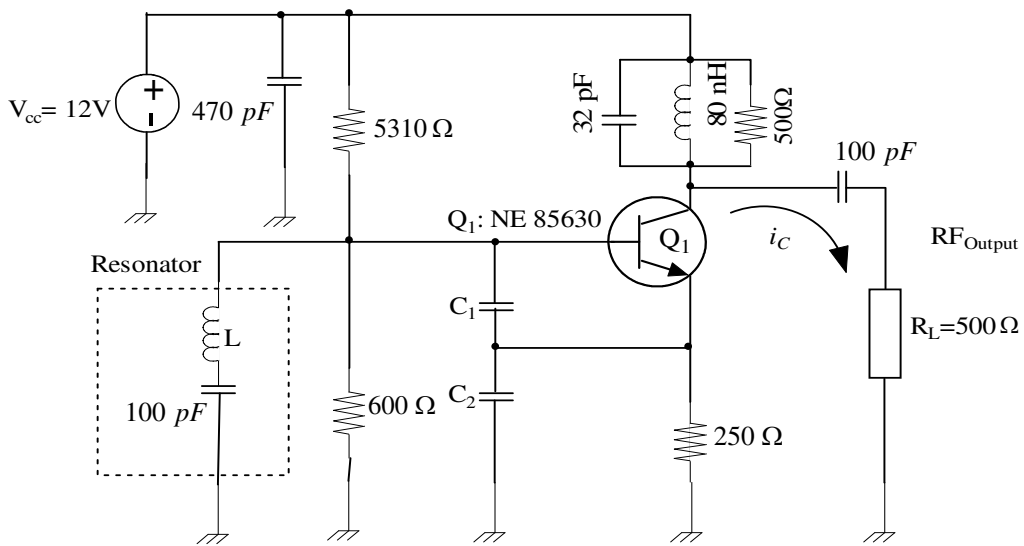


Figure 3-16: Schematic of 100 MHz LC Colpitts oscillator [18]

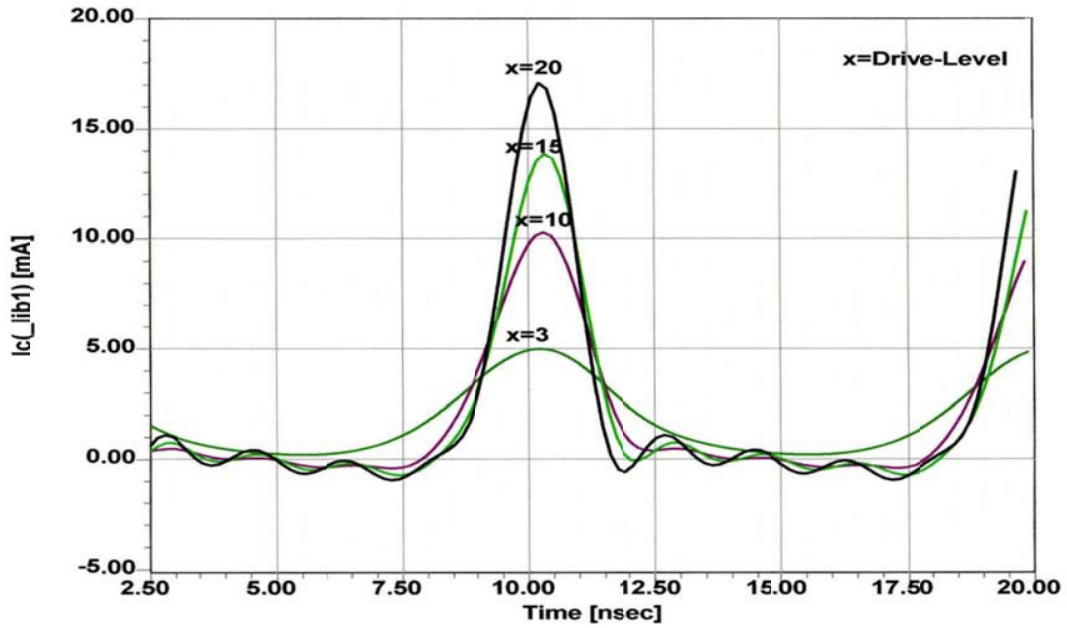


Figure 3-17: RF current as a function of the normalized drive level  $x$  for the oscillator circuit (as shown in the Figure 3-16) [98]

Table 3-1: Drive level for different values of  $C_2$  for a 100MHz Oscillator

$x = \frac{qV_{base}}{kT}$	$C_1$	$C_2$	L	Phase Noise @10 kHz offset	Frequency
3	500pF	50pF	80nH	-98dBc/Hz	100MHz
10	500pF	100pF	55nH	-113dBc/Hz	100MHz
15	500pF	150pF	47nH	-125dBc/Hz	100MHz
20	500pF	200pF	42nH	-125dBc/Hz	100MHz

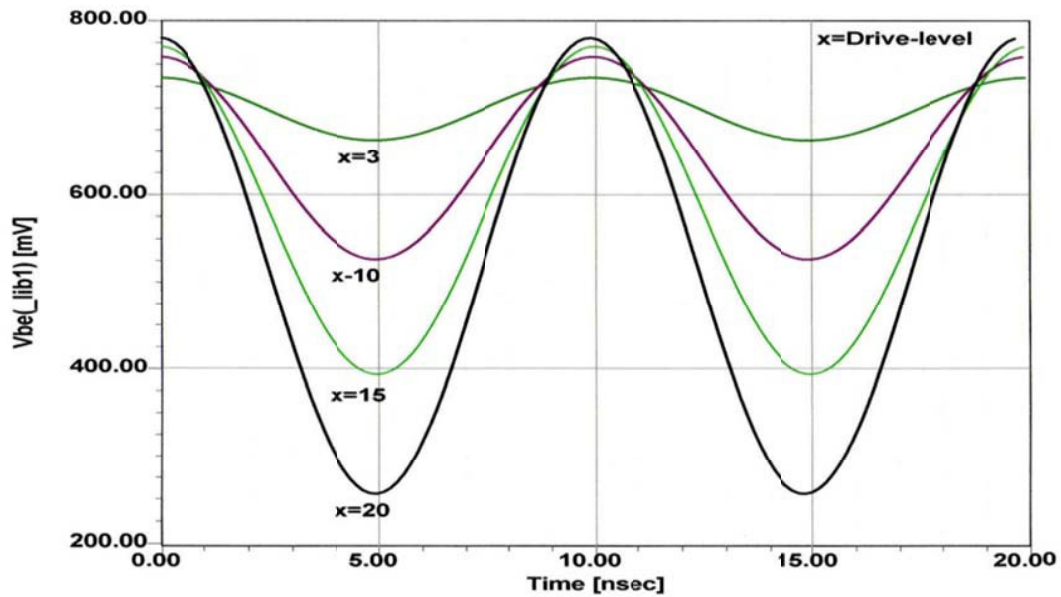


Figure 3-18: RF voltage  $V_{be}$  across the base emitter as a function of the normalized drive level  $x$  [98].

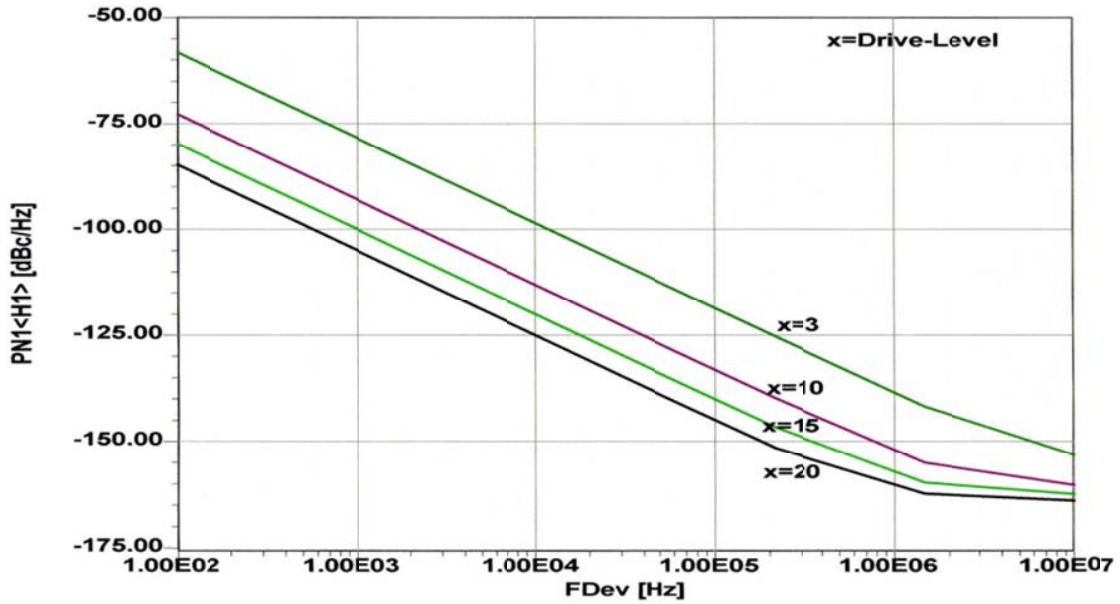


Figure 3-19: Phase noise as a function of the normalized drive level  $x$  for the circuit shown in Figure 3-18 [98].

The improvement in the phase noise, with respect to the drive level, is shown in Figure 3-19, and it is limited by the strong harmonic content due to the large signal drive level. Introducing the signal drive level concept in conjunction with oscillator output current conduction angle, the phase noise Equations (3.28) can be expressed as [4, pp. 180]:

$$\mathcal{L}(\omega) = 10 \text{Log} \left\{ \left[ 4kTR + \frac{4qI_c g_m^2 + \frac{4K_f I_b^{AF}}{\omega} g_m^2}{\omega_0^2 C_1^2 (\omega_0^2 (\beta^+)^2 C_2^2 + g_m^2 \frac{C_2^2}{C_1^2})} \right] \left[ \frac{\omega_0^2}{4\omega^2 V_{cc}^2} \right] \left[ \frac{Q_o^2}{Q_L^2} + \frac{[C_1 + C_2]^2}{C_1^2 C_2^2 \omega_0^4 L^2 Q_L^2} \right] \right\} \quad (3.42)$$

where  $\beta^+ = \left[ \frac{Y_{21}^+}{Y_{11}^+} \right] \left[ \frac{C_1}{C_2} \right]^p$ ,  $g_m = \left[ Y_{21}^+ \right] \left[ \frac{C_1}{C_2} \right]^q$ ; values of  $p$  and  $q$  depends upon the drive level ( $x$ )

$Y_{21}^+$ ,  $Y_{11}^+$  = large signal [Y] parameter of the active device

$K_f$  = flicker noise coefficient,  $AF$  = flicker noise exponent

$\mathcal{L}(\omega)$  = ratio of sideband power in a 1Hz BW at  $\omega$  to total power in dB

$\omega$  = frequency offset from the carrier,  $\omega_0$  = center frequency

$Q_L$  = loaded  $Q$  of the tuned circuit,  $Q_o$  = unloaded  $Q$  of the tuned circuit

$kT$  =  $4.1 \times 10^{-21}$  at 300 K (room temperature)

$R$  = equivalent loss resistance of the tuned resonator circuit

$I_c$  = RF collector current

$I_b$  = RF base current

$V_{cc}$  = RF collector voltage

$C_1, C_2$  = feedback capacitor as shown in the Figure 3-16.

Equation (3.42) gives clear insight and apriori estimation of the phase noise in terms of the operating condition and circuit parameters (validation examples and numerical results are described in Ref. 4, pp. 181-199). However, all three noise models discussed above linear and quasi-linear free-running

oscillator circuit, do not explain in detail about the chaotic condition witnessed in presence of strong linearity of autonomous circuits. Therefore, suggesting the need for noise analysis for nonlinear time variant noise model for oscillator circuits [47]-[62].

### 3.2.3 Kaertner, Demir, Ngova's Noise Model (Nonlinear Time Variant)

Even though the LTV method is able to explain how the device noise around the oscillator's harmonics affects the phase noise, it is a matter of fact that the oscillator behavior is nonlinear by nature. Therefore, it can be expected that the results obtained from Linear Time Variant (LTV) noise model will not take into account, the associated nonlinearity in the oscillator circuits, hence cannot offer unified solution. For simplification in analysis, some approximations employed in the LTV method, turn out to be false assumption [48] even though it provides design flow for noise dynamics. To overcome the limitation of LTV noise model, there have been several attempts to analyze the phase noise using nonlinear time variant (NLTV) techniques, perhaps the most acknowledged of these is presented by Kaertner and Demir in [38, 39, 46, and 47].

Kaertner and Demir pointed out the flaws of LTIV and LTV models that both the total integrated power and the noise power density at the carrier are infinite—a physical impossibility. To overcome these discrepancies, nonlinear time variant (NLTV) phase noise model was proposed from the fundamental differential equation description for a general oscillator by taking noise perturbation signals into account [39]. The proposed NLTV phase noise model is based on orbital asymptotic stability theory using white and modulated-white noise sources with power spectrum falling  $1/f^k$  for any  $k \in \mathbb{N}$ , it is proved that such white and modulated-white noise sources led to a phase deviation,  $\phi(t)$ , which is characterized as a stochastic process with characteristic function,  $F(\omega, t)$ , described by a mean,  $\mu(t)$ , and a variance,  $\sigma(t)$ .

Stability theory addresses the following questions: will a nearby orbit indefinitely stay close to a given orbit? Will it converge to the given orbit? In the former case, the orbit is called stable and in the latter case, asymptotically stable, or attracting. Figure 3-20 illustrates the stability planes for asymptotically stable, marginally stable, and unstable conditions.

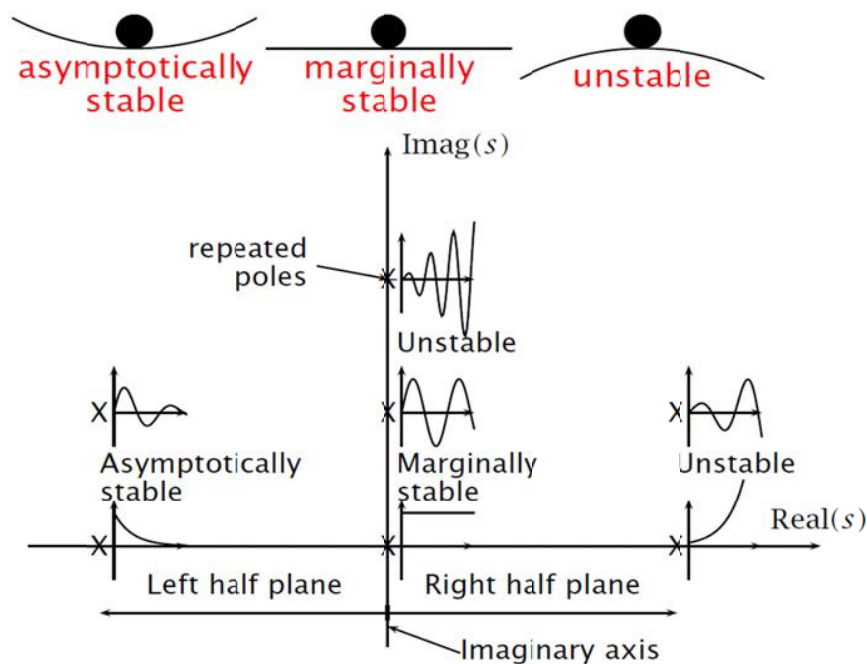


Figure 3-20: shows the stability plane for asymptotically stable, marginally stable, and unstable condition [39]



For such white noise and modulated white noise sources, the phase noise power spectrum is analytically derived for angular frequency  $\omega_0$  of carrier signal as:

$$S(\omega) = \sum_{k=-\infty}^{\infty} X_k X_k^* \frac{4\omega_0^2 k^2 p}{\omega_0 k^4 p^2 + 4(\omega + k\omega_0)^2} \quad (3.43)$$

Where  $X_k$  is Fourier coefficient of the asymptotically (as shown in Figure 3-20) orbitally stable periodic solution. This implies that n-dimensional stable limit cycle solution based on standard nonlinear analysis technique of linearizing around a nonlinear stable limit cycle solution, implies that  $x_s(t)$  is simply the unperturbed oscillation signal to the oscillation  $x_s(t)$ , as:

$$x_s(t) = \sum_{k=-\infty}^{\infty} X_k e^{jk\omega_0 t} \quad (3.44)$$

$p = \frac{d}{dt} [\sigma^2(t)]$ , which physically translates to the rate of change of the squared variance,  $\sigma$ , to the Gaussian solution of the characteristic function,  $F(\omega, t)$ , of the phase deviation  $\phi(t)$ . The Equation (3.43) is so general that it does not even need to be an electrical system and valid for any physically realizable system (electrical, mechanical, biological, etc.) that exhibits stable oscillatory behavior. The NLTV phase noise model proposed by Kaertner and Demir using differential equations for describing the frequency and amplitude response of oscillators through perturbation techniques is unequalled in its generality, accuracy and efficient computational complexity, but the physics of the circuit is completely lost by a pure statistical characterization of the system [37]-[49]. The solution of Equation (3.43) is derived by computer but poorly suited to analytical computation by hand on paper (It is just like anything else that is useful, correct, and accurate in the world of nonlinearity). Initial guess of Equation (3.43) is the  $1/f^2$  phase noise reduction with frequency and so qualitatively reveals nothing more than what can be learned from linear phase noise models [50]-[61].

The noise model is based on differential equations describing the amplitude and phase deviations of the oscillator in terms of Taylor series expansions, assuming that the underlying device noise can be completely described stochastically [62]-[82]. The stochastic differential equations so obtained are solved to obtain the final expression of phase noise. Since flicker noise is difficult to characterize in time domain, Kaertner and Demir obtain approximate series solutions. The time domain phase noise algorithm for Equation (3.43) becomes numerically unstable when the concerned oscillator employs a high Q resonator (Crystal resonator,  $Q \cong 10^6$ ). Similarly, the frequency domain phase noise algorithm for Equation (3.43) depends on the numerical method of harmonic balance using CAD simulator (AWR, Agilent ADS 2013, Ansys-Ansoft Designer 8) - a method which is similarly known to be problematic (convergence and accuracy) when applied to oscillators with high Q resonators [83]-[92]. The phase noise models depend on complex parameters, have no circuit focus, and require special tools and efficient algorithms to evaluate the model parameters. The main drawbacks of this model is noise analysis, mainly takes into account white noise sources, hence only phase noise with a  $1/f^2$  characteristic, and it is therefore not straightforward to use their result in practical design and also numerical characterization of phase noise, breaks down when extremely low phase noise Crystal oscillators are considered. It mainly attempts to establish a foundation theory for the description of phase noise in nonlinear systems, which has been lacking earlier [93]-[98]. Ngova et.al proposed phase noise model based on envelope transient simulation technique for arbitrary circuit topology [96]. The frequency conversion and modulation effects taking place in a free running oscillator because of noise perturbation are intimately linked within a single equation however; phase noise model is not free from convergence problems for high Q resonator oscillator circuits.

### 3.2.4 Multiple Threshold Crossing Noise Model

The noise model (LTIV, LTV and NLTV) discussed in section (3.2.1)-(3.2.3) explains the noise dynamics of LC resonator based "Harmonic Oscillators". The LTIV, LTV and NLTV model (all are frequency based) are good for resonant based (like LC resonator, Crystal resonator, Surface Acoustic Wave resonator,

Dielectric resonator, printed transmission line resonator) but not suitable for RC relaxation and ring oscillator circuits. In particular, relaxation oscillator has noise jump/spikes (chaos/bifurcation) due to regeneration during transition, which cannot be easily modeled by frequency-based method. The poor phase noise performance of time/waveform based oscillator (like relaxation, ring, and multivibrator) limits the figure of merit (FOM) in RF systems as compared to harmonic oscillator (LC tank oscillator).

There is a need to improve the phase noise performance of single energy storage reactive element (capacitor) oscillator such as RC oscillator (like relaxation and ring oscillators) for taking the advantage of integrated solution using existing MMIC technologies. The noise model based on threshold crossing is ideal for time/waveform based oscillator (relaxation and ring) [93]-[96].

### 3.2.5 Conclusion on Phase Noise Models

Table 3-2 describes the relative strength and weakness of the three-phase noise models discussed above for the characterization of oscillator circuits [97]-[101]. All the three models discussed above and shown in Table 3-2 for harmonic oscillators, one can argue the superiority of any of the three models based on accuracy, reliability, simulation time, and convergence for a given oscillator circuit topologies. The noise model for non-harmonic oscillator circuits (proposed by A. Abidi, A. Hajimiri, B. Razavi, R. Navid, T. Lee, R. Dutton, and B. Leung) such as relaxation and ring oscillator circuits, Leung highlighted the inadequacy of traditional first passage time (FPT) model and the need for the last passage time (LPT) model in representing the threshold crossing behavior of time/waveform based oscillator [68]-[84].

The noise model discusses the timing jitter based on the LPT model. Leung's noise model is based on multiple thresholds crossing concept, which considers the impact caused by both noise and slew rate changing as transistors change between triode/saturation. It also develops a link between the last passage and FPT model and indicates when the difference between the two models becomes significant. Using multiple thresholds crossing concept, a new and more accurate way of handling such a regional change is formulated and developed [99]-[101]. For a typical ring oscillator with an arbitrary voltage swing, core transistors in delay cells move between saturation and triode region, resulting timing jitter accumulated within a particular region. Leung's LPT model for the threshold crossing offers more accurate description than the conventional FPT model when the noise/ramp ratio is not small.

Comparing the noise models discussed for harmonic (LC resonator type) and non-harmonic oscillator circuits (RC oscillator type), it is up to the designers to choose noise models for analyzing the autonomous circuits because none of the models allow closed form solution for phase noise—a unified solution needed for any typical oscillator circuit for an optimum figure of merit (FOM) as discussed in Chapter 1 (Equation 1.1-1.3) [101].

Table 3-2: Describes the relative strength and weakness of the 3-noise models [97]-[101]

Model	Leeson	Lee and Hajimiri	Kaertner and Demir
Assumptions	LTIV	LTV	NLTV
Perturbing noise Source	white noise (KTB)	Cyclostationary $1/f^k$ for any $k \in N$	Modulated $1/f^k$ for any $k \in N$
Accuracy	Reasonable	Good	Exact
Simplicity	Simple	Moderate	Involved
Computer dependence	Independent (Calculation by hand)	Computer to evaluate ISF	Computer dependent (no closed form solutions)
Predicts close-in phase noise	No	Yes	Yes
Retained circuit parameters	Loaded Q-factor ( $Q_L$ ), output power ( $P_o$ )	$q_{max}$	None

# Chapter 4

## Phase Noise Measurement Techniques and Limitations

### 4.1 Introduction

Accurate measurement of phase noise is one of the most difficult measurements tasks in the field of electrical engineering [1]-[5]. The biggest challenge is the huge dynamic range required in phase noise measurements [6]-[11]. There are several methods to measure phase noise and the right one must be chosen to make the necessary measurements [12]. To properly select among the various methods it is necessary to know and appreciate the weaknesses and strengths of each of the different techniques, because none of these methods is perfect for every situation [8]. This chapter focuses on key phase noise measurement techniques for oscillators and reviews their advantages and disadvantages.

In general, measuring phase noise is more difficult than measuring amplitude or frequency related properties [13]. Different signal sources, whether it is an oscillator alone or a synthesizer, have widely varying phase noise performances [14]-[23]. Higher noise sources do not work well with phase noise measurement equipments that are optimized to measure very low noise levels. An ability to measure the phase noise performance of ultra-low phase noise oscillators drives the specifications of the best performing phase noise analyzers [15]. Phase noise is usually expressed in units of dBc/Hz at some specific offset frequency  $f$ , from the carrier, the value of the noise level relative to the carrier level calculated in 1Hz bandwidth. Most often only single sideband (SSB) noise is considered. Some measurement set-ups measure both noise sidebands and a conversion factor is required to report SSB noise. The pioneer in Phase Noise measurement unquestionably was Hewlett Packard [1, 8, 32, and 34].

Once adequate for advanced designs, a noise floor dictated by SSB thermal noise (Johnson Noise at  $kT$ ) of -174 dBm for zero dBm output power is not enough anymore for some special requirements and also marketing of these reference frequency sources [36]. The noise correlation technique allows us to look below  $kT$  level ( $< -174$  dBm). However, the usefulness of the noise contribution below  $kT$  is debatable in the perspective of overall system performance [37]. To achieve a very low measurement noise floor, many modern phase noise measurement instruments use the correlation principle, with all its pros and cons as described in the subsequent sections [38]-[48]. The modern test equipments using the cross-correlation methods are at least 20 times faster [49]-[58].

### 4.2 Noise in Circuits and Semiconductors

In general, phase noise describes how the frequency of an oscillator varies in short time scale. The level of phase noise is deterministically related to the carrier frequency, increasing by 6dB for every doubling in frequency. The long-term frequency stability is called frequency drift, and it must be considered during the measurement process. The output frequency of an oscillator takes finite time to stabilize after the oscillator has been started and this drift can be up to few MHz. The output frequency also usually drifts noticeably during the measurements, especially in the case of free running oscillators. This drift is a real problem, because during the measurements the system must be able to lock to the carrier or carrier must be stable enough, therefore without the carrier tracking-mechanism measurement process is difficult exercise. Therefore, understanding the frequency drift caused due to noise contributions from the active and passive devices, is important.

Any type of amplifier in the test signal chain will also serve as a source of noise. While the main purpose of the amplifier is to increase the power level of a weak carrier signal, it also adds its own noise to the signal and boosts any input noise. The net result is that the amplifier, thermal noise, and flicker

noise continue to give any phase-noise plot a characteristic shape and, more significantly, reduce the theoretical lower limit of sensitivity for any phase-noise measurement. These effects appear in the phase-noise characteristics of any high-performance signal generator.

#### 4.2.1 Johnson noise

- The Johnson noise (thermal noise) is due to the movement of molecules in solid devices called Brown's molecular movements.
- This noise voltage is expressed as  $v_n^2 = 4kT_0RB$  (emf) (volt<sup>2</sup>) (4.1)
- The power of thermal noise can thus be written as

$$\text{Noise Power} = \frac{v_n^2}{4R} = kT_0B \text{ (W)} \quad (4.2a)$$

- It is most common to do noise evaluations using a noise power density, in Watts per Hz. We get this by setting B=1Hz. Then we get:

$$\begin{aligned} \text{For } B = 1\text{Hz, Noise Power} &= kT_0 \\ T &= 290\text{K and } k - \text{ Boltzmann's constant} = 1.38 \times 10^{-23} \text{ J/K} \\ \text{by Thevinin, Noise Power} &= 1.38 \times 10^{-23} \times 290 = 4 \times 10^{-21} \text{W} \end{aligned} \quad (4.2b)$$

- Noise floor below the carrier for zero dBm output is given by

$$L(\omega) = 10 \log \left( \frac{v_n^2/R}{1\text{mW}} \right) = -173.97\text{dBm or about } -174\text{dBm} \quad (4.2c)$$

In order to reduce this noise, the only option is to lower the temperature, since noise power is directly proportional to temperature.

- The Johnson noise sets the theoretical noise floor.

#### 4.2.2 Planck's Radiation Noise

- The available noise power does not depend on the value of resistor but it is a function of temperature T. The noise temperature can thus be used as a quantity to describe the noise behavior of a general lossy one-port network.
- For high frequencies and/or low temperature, a quantum mechanical correction factor has to be incorporated for the validation of equation. This correction term results from Planck's radiation law, which applies to blackbody radiation.

$$P_{av} = kT \cdot \Delta f \quad (4.3a)$$

$$P_{av} = (kT\Delta f) \times p(f, T), \text{ with } p(f, T) = \left[ \frac{hf}{kT} / \left( e^{\left( \frac{hf}{kT} \right)} - 1 \right) \right] \quad (4.3b)$$

- where  $h = 6.626 \times 10^{-34}$  Joule – sec (Planck's Constant)

#### 4.2.3 Schottky/Shot noise

- The Schottky noise occurs in conducting PN junctions (semiconductor devices) where electrons are freely moving. The root mean square (RMS) noise current is given by

$$\overline{i_n^2} = 2qI_{dc} \quad (4.4a)$$

$$P = i_n^2 [Z] \quad (4.4b)$$

- Where,  $q$  is the charge of the electron,  $P$  is the noise power, and  $I_{dc}$  is the dc bias current,  $[Z]$  is the termination load (can be complex load, comprised of real and reactive load).
- Since this noise process is very different from other noise processes, this noise is independent from all others.

#### 4.2.4 Flicker noise

- The electrical properties of surfaces or boundary layers are influenced energetically by states, which are subject to statistical fluctuations and therefore, lead to the flicker noise or  $1/f$  noise for the current flow.
- $1/f$  - noise is observable at low frequencies and generally decreases with increasing frequency  $f$  according to the  $1/f$  - law until it will be covered by frequency independent mechanism, like thermal noise or shot noise.

**Example:** The noise for a conducting diode is bias dependent and is expressed in terms of AF and KF. 
$$\langle i_{Dn}^2 \rangle_{AC} = 2qI_{dc}B + KF \frac{I_{DC}^{AF}}{f} B$$

The AF term is a dimensionless quantity and a bias dependent curve fitting parameter. This term has a value generally within the range of 1 to 3 and a typical value of 2.

The KF value ranges from  $1E^{-12}$  to  $1E^{-6}$ , and defines the flicker corner frequency.

#### 4.2.5 Transit time and Recombination Noise

- When the transit time of the carriers crossing the potential barrier is comparable to the periodic signal, some carriers diffuse back and this causes noise. This is really seen in the collector area of NPN transistor.
- The electron and hole movements are responsible for this noise. The physics for this noise has not been fully established.

#### 4.2.6 Avalanche Noise

- When a reverse bias is applied to semiconductor junction, the normally small depletion region expands rapidly.
- The free holes and electrons then collide with the atoms in depletion region, thus ionizing them and produce spiked current called the avalanche current.
- The spectral density of avalanche noise is mostly flat. At higher frequencies the junction capacitor with lead inductance acts as a low-pass filter.
- Zener diodes are used as voltage reference sources and the avalanche noise needs to be reduced by big bypass capacitors!

### 4.3 Phase Noise Measurement Techniques

The usual goal for measuring phase noise in an R&D environment is to achieve the lowest measurement noise floor possible. As we shall see, this is not necessarily the best choice, depending on the signal source being measured. In a production environment, the objective is fast throughput for product phase noise performance testing. Again, this is best achieved by using a method that is appropriate for the source being measured.

There are some very capable general-purpose phase noise measurement instruments available on the market, including the Agilent-E5052B, Rohde & Schwarz-FSUP, Holzworth-HA7402A, Noise XT-DCNTS, Anapico-APPH6000-IS, and OE Wave-PHENOM™. With the growing demand for improved dynamic range and lower noise floor, equipment companies are introducing general purpose phase noise analysis software driven tools for extracting far out (offset frequency > 1MHz) noise below the kT floor even though claims of -195dBc/Hz or lower lack the practical utility. Modern phase noise test equipment addresses these issues, but one must understand the limitations of measurement techniques so that a suitable method can be chosen. The Direct Spectrum Method, PLL method, delay line discriminator method, and cross-correlation method are frequently used to measure the oscillator phase noise. The first one is the simplest and has the biggest limitation. The last one requires the most complex

measurement system but useful and can measure oscillator phase noise performance better than that of its reference oscillator. Here we present the following primary phase noise measurement techniques, listed in the order of increasing precision:

- Direct Spectrum Technique
- Frequency discriminator method
  - Heterodyne (digital) discriminator method
- Phase detector techniques
  - (Reference source/PLL method)
- Residual Method
- Two-channel cross-correlation technique

#### 4.3.1 Direct Spectrum Technique

This is the simplest technique for making phase noise measurements. Using this technique, measurements are valid as long as the analyzer's phase noise is significantly lower than that of the measured device (DUT). Figure 4-1 shows the basic block diagram of a Direct Spectrum Measurement Technique. As shown in Figure 4-1, the signal from the device under test (DUT) is input into a spectrum/signal analyzer tuned to the DUT frequency, directly measuring the power spectral density of the oscillator in terms of  $\mathcal{L}(f_m)$ . Because the spectral density is measured with the carrier present, this method is limited by the spectrum/signal analyzer's dynamic range. Though this method may not be useful for measuring very close-in phase noise to a drifting carrier, it is convenient for qualitative quick evaluation on sources with relatively high noise. For practical application, the measurement is valid if the following conditions are met:

The spectrum/signal analyzer's internal SSB phase noise at the offset of interest must be lower than the noise of the DUT. It is therefore essential to know the internal phase noise of the analyzer we are using. Because the spectrum/signal analyzer measures total noise power without differentiating amplitude noise from phase noise, the amplitude noise of the DUT must be significantly below its phase noise (typically 10 dB will suffice). This can be assured by first passing the DUT signal through a limiter. The presence of amplitude noise is suggested if the sidebands of the signal are not symmetrical. It is very important to adjust the noise measurement from the spectrum analyzer.

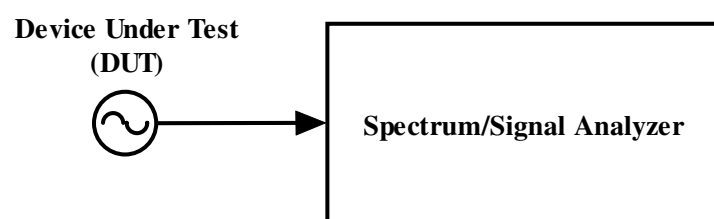


Figure 4-1: A typical simplified representation of Direct Spectrum Measurement Technique

All spectrum analyzers pass signals through a logarithmic amplifier (logamp) before detection and averaging. This distorts the noise waveform, essentially clipping it somewhat from the logarithmic transfer function. A 2.5dB error on the low side results from this average-of-log process. The details of this measurement techniques can be found in Agilent application note AN1303, "Spectrum and Signal Analyzer Measurements and Noise" [1].

#### Advantages:

- Simple, frequency based measurement
- Fast measurement, for relatively noisy sources

- Relatively low cost
- Suitable for measurements of oscillators that drift slightly (less than the resolution filter bandwidth) during measurement.

**Drawbacks:**

- Not suitable for measuring oscillators with ultra-low phase noise performance, because the noise floor of the instrument is comparatively high.
- Not suitable for measuring the phase noise within 1 kHz carrier frequency, mostly because spectrum analyzers have their own noise properties that can degrade the measurement results.
- Limited measurement dynamic range
- One of the major drawbacks of the Direct Spectrum technique is its dynamic range limitation due to the presence of the carrier power. All of the following measurement techniques eliminate this limitation by separating the sideband noise from the carrier power, using a variety of techniques.

**4.3.2 Frequency discriminator method**

In the frequency discriminator method, the frequency fluctuations of the source are translated to low frequency voltage fluctuations, which can then be measured by a baseband analyzer. There are several common implementations of frequency discriminators including cavity resonators, RF bridges and a delay line.

**Delay Line Frequency Discriminator:**

The delay-line measurement system is often chosen for the flexibility in measuring a free-running oscillator between 1 GHz and 10 GHz. The delay-line technique has sufficient sensitivity to measure most microwave oscillators with loaded Q-factors of several hundred and does not require a second reference oscillator. The expression of delay can be calculated as

$$t_{delay} = \sqrt{\epsilon_r} \left( \frac{l_{cable}}{c} \right) \tag{4.5}$$

Where  $\epsilon_r$  is the relative dielectric constant in a coaxial cable.

The primary advantage of this method is that it can be used to measure noisy sources but on the other hand, it does not work with low noise sources, because the noise performance of this method is the limiting factor. Delay-line discriminators are limited by the loss of the delay-line due to the power requirements for the mixer. Using lower power than required will lead to degraded performance of the system. The noise floor depends on the length of the cable (delay), the longer the delay the lower the noise floor, but it will also mean higher losses and lower offset frequency. The highest usable offset frequency depends mostly on the length of the delay. There is a null at  $f=1/t_{delay}$  offset frequency, and the recommendation is to use offset frequencies up to  $f=1/ (4t_{delay})$ . With a 500ns delay, the usable offset frequency range is from 0 to 500 kHz.

As shown in Figure 4-2, the signal power from the DUT is split into two channels. The signal in one path is delayed relative to the signal in the other path. The delay line converts the frequency fluctuation to phase fluctuation. The mixer requires phase quadrature at its two inputs at the carrier frequency, which is achieved by either adjusting the delay line (not likely) or using a small phase shifter in the through-path. As shown in Figure 4-2, the mixer (acting as phase detector) converts the phase difference between the delayed and undelayed paths into a DC voltage related by the phase discriminator constant  $K_{\phi}$ . The output of this frequency discriminator is then read on the baseband spectrum analyzer as frequency noise. This frequency noise is converted to phase noise using the well-known relationship between FM and PM, and reported as phase noise measurement.

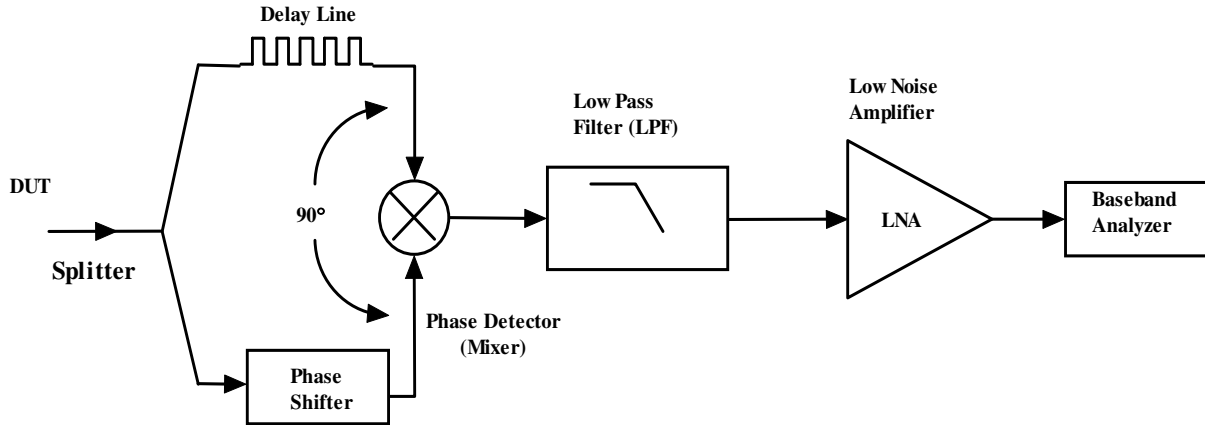


Figure 4-2: Shows the basic block diagram of frequency discriminator method (Courtesy: Agilent Company)

The frequency fluctuations of the oscillator in terms of offset frequency  $f_m$  are related to the phase detector constant  $K_\phi$  and the delay  $\tau_d$  by [31]:

$$\Delta V(f_m) = [K_\phi 2\pi\tau_d] \Delta f(f_m) = K_d \Delta f(f_m) \quad (4.6)$$

Since frequency is the time rate change of phase we have:

$$S_\phi(f_m) = \frac{S_{\Delta f}(f_m)}{f_m^2} = \frac{\Delta f^2(f_m)}{f_m^2} \quad (4.7)$$

The voltage output is measured as a double sideband voltage spectral density  $S_v(f_m)$ .

From (4.6) and (4.7), phase noise  $S_\phi(f_m)$  is related to the measured  $S_v(f_m)$  by:

$$S_\phi(f_m) = \frac{\Delta V^2(f_m)}{K_d^2 f_m^2} = \frac{S_v(f_m)}{K_d^2 f_m^2} \quad (4.8)$$

The single sideband phase noise is given by

$$\mathcal{L}_\phi(f_m) = \frac{S_v(f_m)}{2K_d^2 f_m^2} \quad (4.9a)$$

$$\mathcal{L}_\phi(f_m)[dBc/Hz] = S_v(f_m) - 3 - 20 \log(K_d) - 20 \log(f_m) \quad (4.9b)$$

With a single calibration of the mixer as a phase detector,  $K_\phi$  and known delay  $\tau_d$ , the phase noise of an oscillator can be measured using FFT (baseband) analyzer. The phase discriminator constant  $K_\phi$  is in V/rad and is determined by measuring the DC output voltage change of a mixer while in quadrature (nominally 0V DC) for a known phase change in one branch of discriminator. The value of  $K_d$  is dependent upon the RF input power of the mixer that in turn is directly proportional to the noise floor shown in Figure 4-3 [31]. Using Z-parameters the sensitivity of the delay line discriminator can be determined first by introducing the Q-factor defined with respect to the phase of the open-loop transfer function  $\phi(\omega)$  at the resonance of parallel RLC circuit [31-33]:

$$\phi(j\omega) = \tan^{-1} \frac{\text{Imag}(Z(j\omega))}{\text{Real}(Z(j\omega))} \quad (4.10)$$

$$Q = \frac{1}{R} \sqrt{\frac{L}{C}} = \frac{\omega \delta_\phi}{2\delta\omega} \quad (4.11)$$

A typical coaxial delay-line exhibits a linear phase relation with frequency across the usable bandwidth of the transmission line.



The linear phase relationship in a coaxial line to the derivative of the phase change in a resonator results in an effective Q,  $Q_E$  for a transmission line with time delay  $\tau_d$ :

$$Q_E = \pi f_0 \tau_d \quad (4.12)$$

From (4.12), the effective Q-factor increases linearly with both delay line length and frequency of operation. Using  $Q_E$  as the Q-factor in the Leeson's equation and using an approximate mixer noise floor of -175 dBc. The Flicker corner is set at 10 kHz, typical for silicon (Si) diode mixer. The measurement phase noise floor is calculated:

$$\mathcal{L}_\phi(f_m) = 10 \log \left[ \left( 1 + \frac{1}{(2\pi\tau_d f_m)^2} \right) \left( 1 + \frac{f_c}{f_m} \right) \right] + N_{mixer\ floor} \quad (4.13)$$

A plot of (4.13) is shown in Figure 4-3.

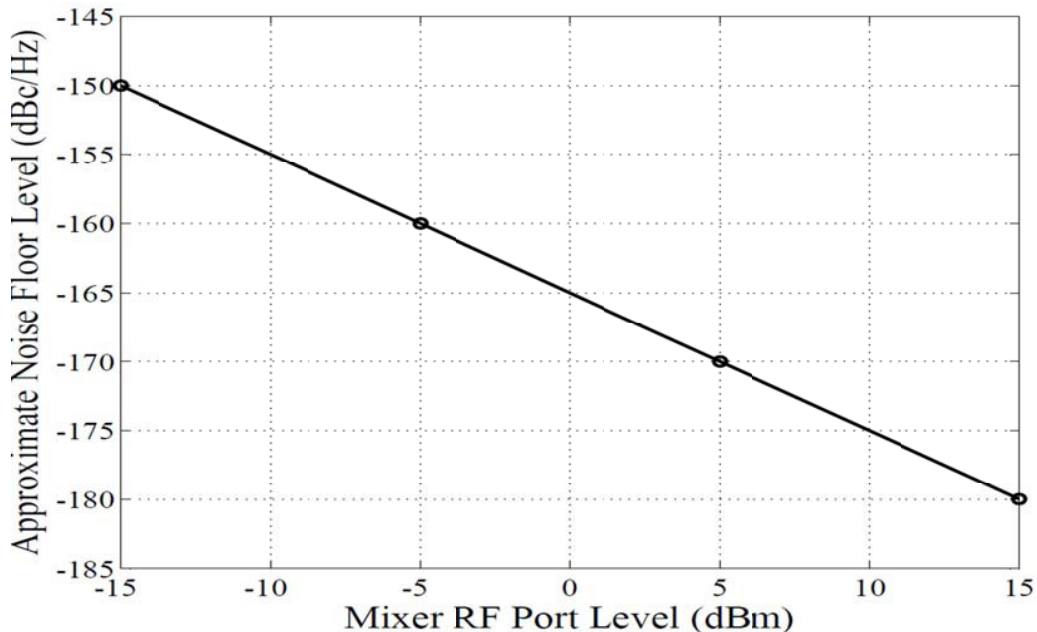


Figure 4-3: The ideal phase detector sensitivity in terms of RF power (assuming LO power is great than RF) and phase detector constant  $K_\phi$ . The noise floor sensitivity is 1:1 to mixer power input [31]

**Advantages:**

- Better Sensitivity than Direct Spectrum Methods
- Good for free running sources such as LC oscillators or cavity oscillators
- Appropriate when the DUT is a relatively noisy source with high-level, low rate phase noise or high close-in spurious sideband

**Drawbacks:**

- Significantly less sensitivity than phase detector methods
- A longer delay line will improve the sensitivity but the insertion loss of the delay line may exceed the source power available and cancel any further improvement.
- In addition, longer delay lines limit the maximum offset frequency that can be measured. This method is best used for free running sources such as LC oscillators or cavity oscillators, although the frequency discriminator method degrades the measurement sensitivity, particularly at close to the carrier frequency.

### 4.3.2.1 Heterodyne (Digital) Discriminator method

As shown in Figure 4-4, the heterodyne (digital) discriminator method is a modified version of the analog delay line discriminator method and can measure the relatively large phase noise of unstable signal sources and oscillators. Unlike the analog discriminator method, here the input signal is down-converted to a fixed intermediate frequency  $f_{IF}$  using a separate local oscillator. The local oscillator is frequency locked to the input signal. Working at a fixed frequency, the frequency discriminator does not need re-connection of various analog delay lines at any frequency. This method allows wider phase noise measurement ranges as compared to the PLL method. This option is available in commercially available in latest phase noise measurement equipments (Agilent E5052B, R&S FSUP).

#### Advantages:

- Offers easy and accurate AM noise measurements (by setting the delay time to zero) with the same setup and RF port connection as the phase noise measurement
- Frequency demodulation can be implemented digitally

#### Drawbacks:

- Dynamic range of Phase Noise measurement is further limited by the additional scaling amplifier and ADCs.

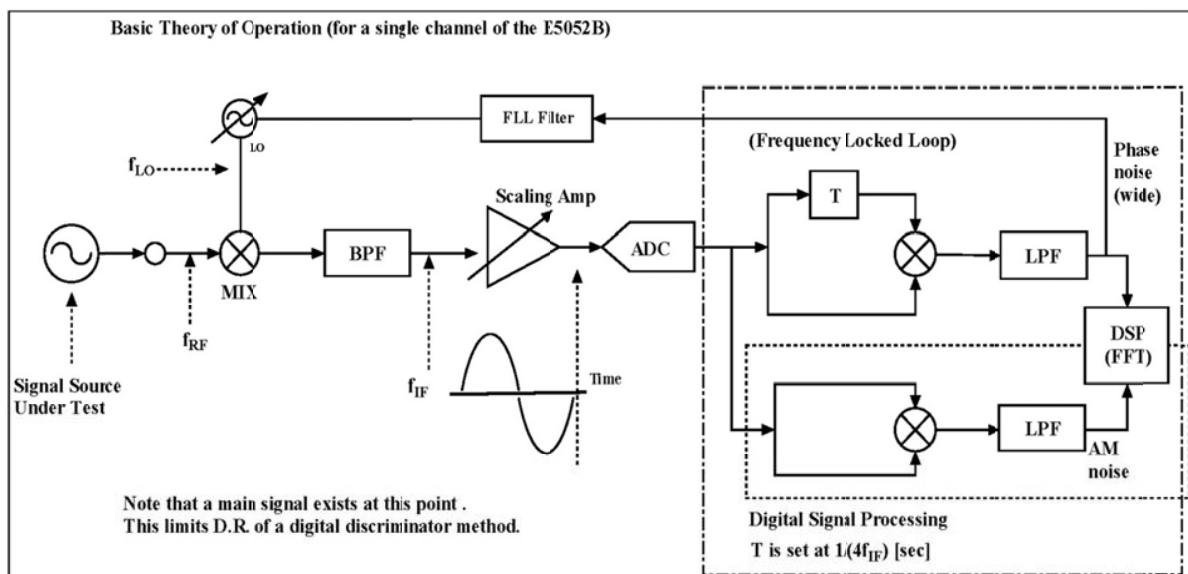


Figure 4-4: Basic block diagram of heterodyne (digital) discriminator method (Courtesy: Agilent) [9]

### 4.3.3 Phase Detector Technique

Figure 4-5 shows the basic concept for the phase detector technique. The phase detector method measures voltage fluctuations directly proportional to the combined phase fluctuations of the two input sources. To separate phase noise from amplitude noise, a phase detector (PD) is required. The (PD) converts the phase difference of the two input signals into a voltage at the output of the detector. When the phase difference between the two input signals is set to  $90^\circ$  (e.g. at quadrature), the nominal output voltage is zero volts and sensitivity to AM noise is minimized. Any phase fluctuation from quadrature results in voltage fluctuation at the output. This method has a very low noise floor and therefore has a very good measurement dynamic range.

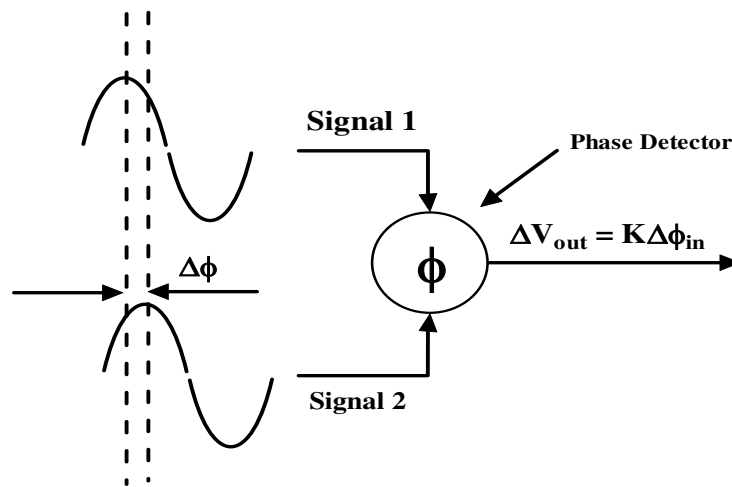


Figure 4-5: Basic concept of Phase detector techniques [1]

#### 4.3.3.1 Reference Source/PLL Method

Figure 4-6 shows the basic block diagram of the phase detector method using reference source/PLL techniques. The basis of this method is to use a phase lock loop (PLL) in conjunction with a double balanced mixer (DBM) used for the phase detector. The PLL compares the phases of two input signals and generates a third signal which is used to steer one of the input signals into phase quadrature with the other. When the phase of the input signals are aligned, the loop is said to be locked and the nominal output from the phase detector is zero. This voltage varies a little due to phase noise on the input signals. The noise present at the output of the mixer includes phase noise of both signals. If the noise from the reference oscillator is more than 20 dB lower than the noise from DUT, the main contributor for phase noise is the DUT.

As shown in Figure 4-6, two sources, one from the DUT and the other from the reference source, provide inputs to the mixer. Again the reference source is controlled such that it follows the DUT at the same carrier frequency ( $f_c$ ) and in phase quadrature ( $90^\circ$  out of phase) to null out the carrier power. The mixer sum frequency ( $2f_c$ ) is filtered out by the low pass filter (LPF), and the mixer difference frequency is 0 Hz (dc) with an average voltage output of 0 V when locked. The DC voltage fluctuations are directly proportional to the combined phase noise of the two sources. The noise signal is amplified using a low noise amplifier (LNA) and measured using a spectrum analyzer. The advantage of this method is broadband measurement capability for both fixed frequency and tunable oscillators. With only a few different double balanced mixers and suitable reference oscillators, noise on signals from 1MHz to several tens of GHz can be measured. If the DUT is a tunable oscillator, the reference oscillator will then be a free running one and the DUT would be controlled with the PLL, and need a suitable PLL amplifier after the low pass filter (LPF). The limitation of this method is that it is difficult to determine the contribution of noise, i.e. which part of the noise comes from the reference and which from the DUT. Nevertheless, this problem is true for most measurement systems. Usually, if the phase noise levels of the two signals are not that far from each other, a correction factor ( $P_{correction}$ ) from 0 to 3dB is subtracted from the measured result, where the highest number is used when the noise levels are equal [24]. The expression of the correction factor is given by [32]

$$P_{correction} = 10 \log_{10} \left( 1 + 10^{-\frac{\Delta P}{10}} \right) \quad (4.14)$$

Where  $\Delta P$  is the difference between the noises of the reference and the DUT in dB, Table 4-1 shows the correction factors for different noise level differences.

Table 4-1: Correction factor if the phase noise of the reference oscillator is near the phase noise of DUT

$\Delta P/Db$	0	2	4	6	8	10	15	20
$P_{\text{Correction}}/dB$	3	2.12	1.46	0.97	0.64	0.4	0.14	0.04

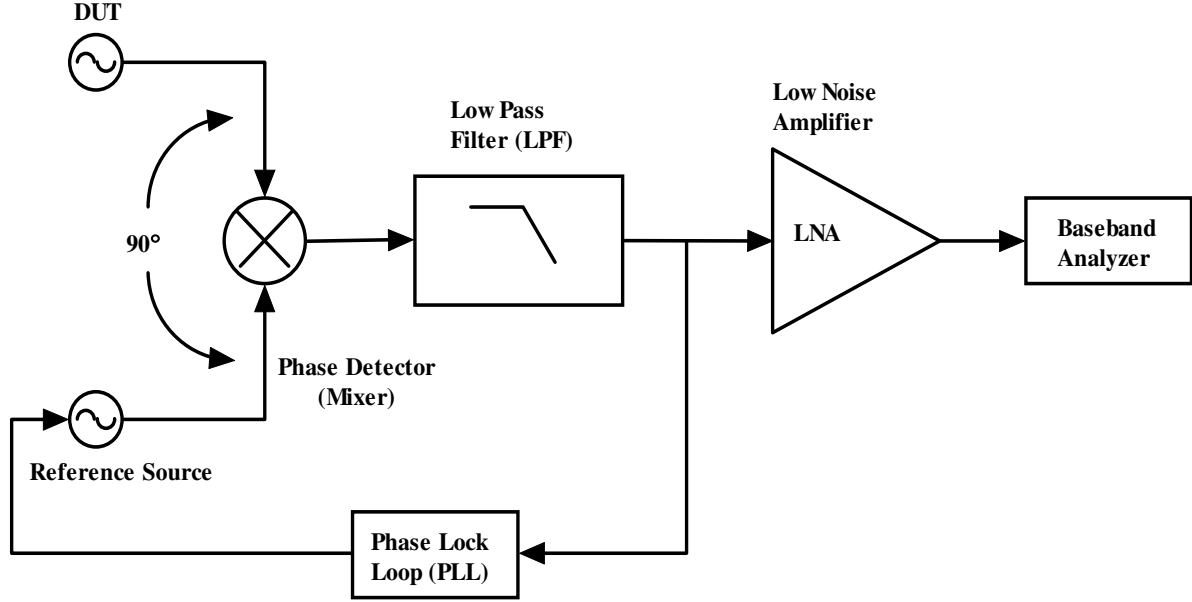


Figure 4-6: Shows the basic block diagram Phase Detector Method using reference source/PLL techniques). Small fluctuations from nominal voltages are equivalent to phase variations. The phase lock loop keeps two signals in quadrature, which cancels carriers and converts phase noise to fluctuating DC voltage (Courtesy of Agilent Technologies) [1]

This method exhibits promising noise floor but the performance is dependent on DBM and reference source characteristics. The selection of a mixer as a phase detector is critical to the overall system performance. The noise floor sensitivity is related to the mixer input levels; therefore high power level mixers are preferred. However, care must be taken to match mixer drive to available source power.

#### Choice of DBM as Phase Detector:

Figure 4-7 exhibits typical DBM phase detector response curve, where  $V_{IF}$  varies as the cosine of the phase difference  $\Delta\phi$  between LO and RF signals [31]. As shown in Figure 4-7, phase detector response ( $V_{IF}$ ) is reasonably linear in the region  $\Delta\phi$  where phase detector sensitivity ( $\frac{\partial V_{IF}}{\partial \phi}$ ) is maximum, represented by

$$\Delta\phi = (\phi_{LO} - \phi_{RF}) = \left(\frac{\pi}{2} + \delta\phi\right) \quad (4.15)$$

The phase detector output  $V_{IF}(t)$  is given by [5]

$$V_{IF}(t) = \pm V \cos[(\omega_R - \omega_L)t + \Delta\phi(t) + \pi] \quad (4.16)$$

For mixer's two input signals are at the same frequency,  $\omega_R = \omega_L$  and 90° out of phase,  $V_{IF}(t)$  is

$$\Delta V_{IF}(t) = \pm V \sin \delta\phi(t) \quad (4.17)$$

where  $V$  is the peak amplitude (at  $\Delta\phi = 0$  or  $\pi$ ),  $\Delta V_{IF}(t)$  is the instantaneous voltage fluctuations around DC, and  $\delta\phi(t)$  is the instantaneous phase fluctuation.

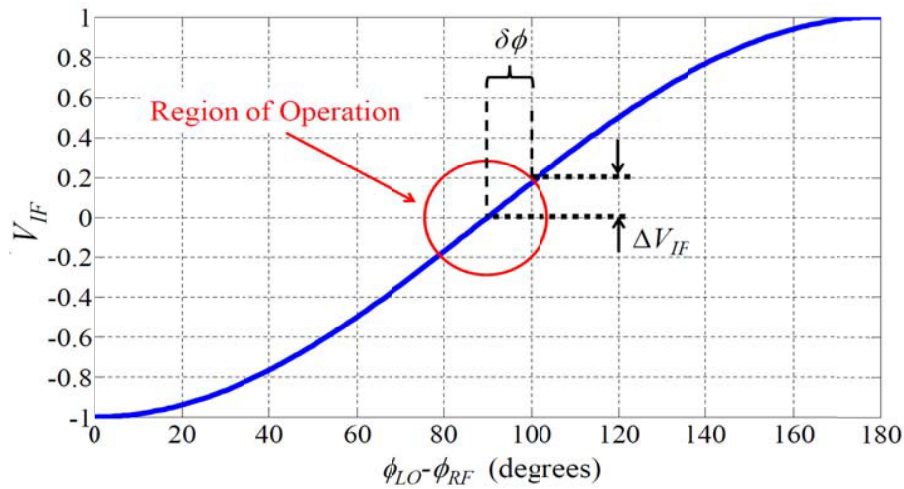


Figure 4-7: Shows the response of DBM as a phase detector varies as  $\cos(\Delta\phi + \pi)$ , ( $V_{IF}$ ) is reasonably linear in the region  $(\Delta\phi = \frac{\pi}{2} + \delta\phi)$  [31]

For  $\delta\phi(t) \ll 1 \text{ rad}$ ,  $\sin(\delta\phi(t)) \approx \delta\phi(t)$ , which describes a linear response region, the phase detector sensitivity varies linearly with maximum output voltage as

$$\Delta V_{IF}(t) = V \delta\phi = K_{\phi} \delta\phi \quad (4.18)$$

where,  $K_{\phi}$  is the phase detector gain constant (volts/radian), equal to the slope of the mixer sine wave output at the zero crossing.

#### Choice of Reference Sources:

The other critical component of the phase detector method is the reference source. As discussed in the Direct Spectrum technique section, a spectrum analyzer measures the sum of noise from both sources. Therefore, the reference source must have lower phase noise than device under test, DUT. For practical purposes 10 dB margin is sufficient to ensure correct measurements within reasonable degree of accuracy. When a reference source with lower phase noise is unavailable then it is appropriate to use a source with comparable phase noise to the DUT. In this case, each source contributes equally to the total noise and 3 dB is subtracted from the measured value.

#### Advantages:

- Excellent sensitivity for measuring low phase noise levels
- Wide signal frequency range
- Wide offset frequency range (0.01Hz to 100 MHz)
- Rejects AM noise
- Frequency tracks slowly drifting sources.

#### Drawbacks:

- Requires a very clean reference source that is electronically tunable,
- Measurement frequency bandwidth matched to the tuning range of the reference sources.
- Locking PLL bandwidth is very narrow, <10% of the minimum offset frequency used in the measurement.
- Narrow PLL bandwidth cannot track a noisy source.
- Expensive and complex

In conclusion, the phase detector method has excellent system sensitivity, but on the other hand its complexity (PLL and two oscillators are required) must be handled with care.

#### 4.3.4 Residual method

The methods shown thus far can be used to measure only oscillators. There are some methods for measuring 2-port devices, and the residual method is one of them. It can be used for example to measure amplifiers, mixers, cables, and filters. As shown in Figure 4-8, the output of a reference source is split with a power splitter. One branch is connected through the DUT to the mixer and the other branch through a phase shifter to the mixer. The phase shifter is adjusted until the phases are in quadrature, and the output of the mixer is measured with a spectrum analyzer. Because the noise from the reference source is coherent at the mixer input and the signals are in quadrature, it will be subject to some degree of cancellation. The degree of cancellation improves as the signal path delay in the two arms of the bridge is minimized. The remaining phase noise at the mixer output is thus added by the DUT. When the DUT is relatively broadband (i.e. low delay) device having equal input and output frequencies, the need for a second device in the other bridge arm is eliminated. When the device is either narrowband, or is one with unequal input and output frequencies (a mixer frequency multiplier or divider etc.) identical devices must be used in both arms of the phase bridge.

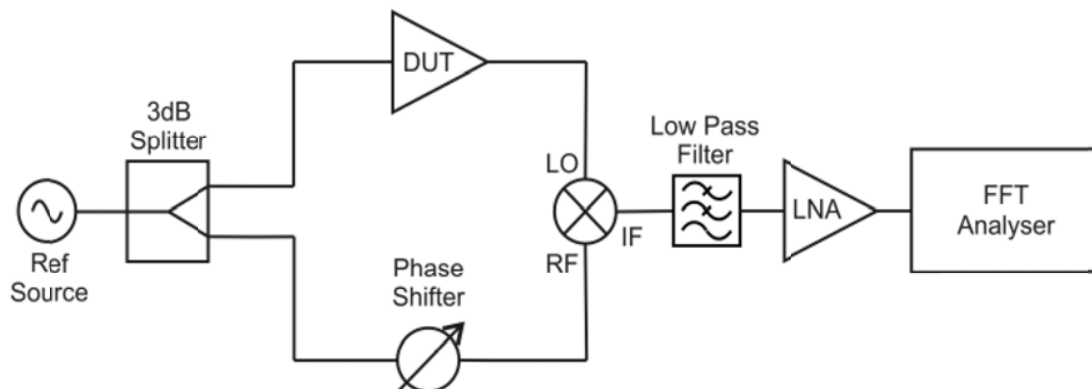


Figure 4-8: Residual method set-up (Simplified single channel residual phase noise measurement system)

The noise floor of a system utilizing this single channel measurement technique is highly dependent on and limited by the noise floors of the mixer, filters and low noise amplifier. This type of system can have a residual phase noise floor in the region of  $-180\text{dBc/Hz}$  at high offset frequencies [2].

In residual measurement system phase, the noise of the common source might be insufficiently canceled due to improperly high delay-time differences between the two branches. It is therefore vitally important to match the delay times very closely.

#### A Residual Phase Noise Measurement System

Figure 4-9 shows a system that automatically measures the residual phase noise of the 8662A synthesizer [4]. It is a residual test, since both instruments use one common 10MHz referenced oscillator. Quadrature setting is conveniently controlled by first offsetting the tuning of one synthesizer by a small amount, usually 0.1Hz. The beat signal is then probed with a digital voltmeter and when the beat signal voltage is sufficiently close to zero, matching the synthesizer tuning commands to stop the phase slide between the synthesizers.

#### 4.3.5 Two-Channel Cross-Correlation Technique

Figure 4-10 shows the diagram of the 2-channel cross-correlation technique from Agilent [1]; built around a similar measurement set-up as the PLL method except that there are three oscillators and the

measurement involves performing cross-correlation operations among the outputs from each channel. It can be seen that there are two reference oscillators, one power splitter, two mixer/amplifier/PLL circuits and a cross-correlation FFT analyzer. The cross-correlation technique is used to minimize the noise contribution from mixer, filter and LNA from the measurement results. This works because the noise from the DUT is common between both paths, but the noise contributed from each internal reference oscillator is independent. Thus over time, the noise contributions from the independent sources will show a zero cross-correlation. However, the noise from the DUT will correlate, and ultimately dominate the output measurement (as desired).

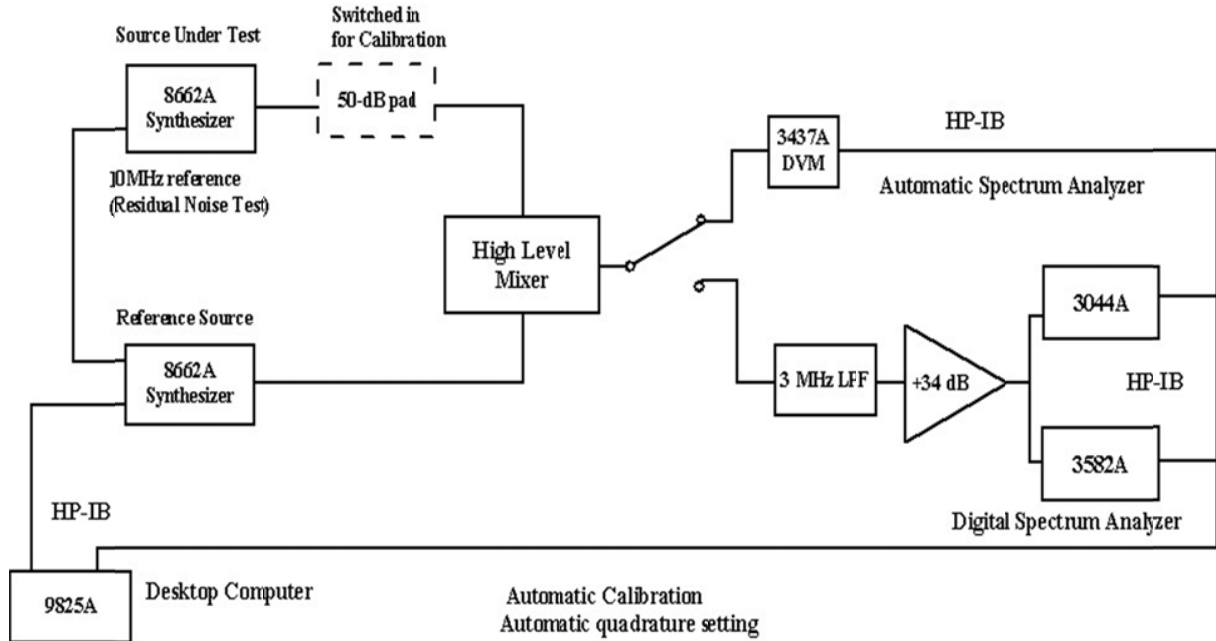


Figure 4-9: Automatic system to measure residual phase noise of two 8662A synthesizers (Courtesy of Hewlett-Packard Company) [32]

The noise from the first reference feeds into the first phase noise detector and ends up on channel 1 of the cross-correlation FFT analyzer. The noise from the second reference passes through in the second phase noise detector and appears on channel 2 of the cross-correlation FFT analyzer. The output of the DUT is connected through a high isolation inductive power splitter to two mixer circuits where it is mixed with the signal from these two reference oscillators. The outputs of the mixer circuits are used for PLL circuits to lock the internal references in phase quadrature to the DUT input signal, as in the PLL method. The mixer output signals are then amplified, the DC is filtered away and finally the signals are fed to two channels of the FFT analyzer to perform a cross-correlation measurement between the two output signals. The noise from output of each mixer can be modeled using two noisy signals [36]-[39]

$$x(t) = a(t) + c(t) \overline{FFT} X(f) = A(f) + C(f) \quad (4.19)$$

$$y(t) = b(t) + c(t) \overline{FFT} Y(f) = B(f) + C(f) \quad (4.20)$$

where  $a(t)$  and  $b(t)$  are uncorrelated equipment noise present in each channel and  $c(t)$  represents the correlated DUT noise. The cross-spectrum of these two signals after averaging over  $M$  samples is described by

$$\overline{S_{XY}} = \frac{1}{M} \sum_{m=1}^{m=M} [X_m \times Y_m^*] \quad (4.21)$$

where ' $m$ ' represents the sample index and (\*) implies the conjugate function.

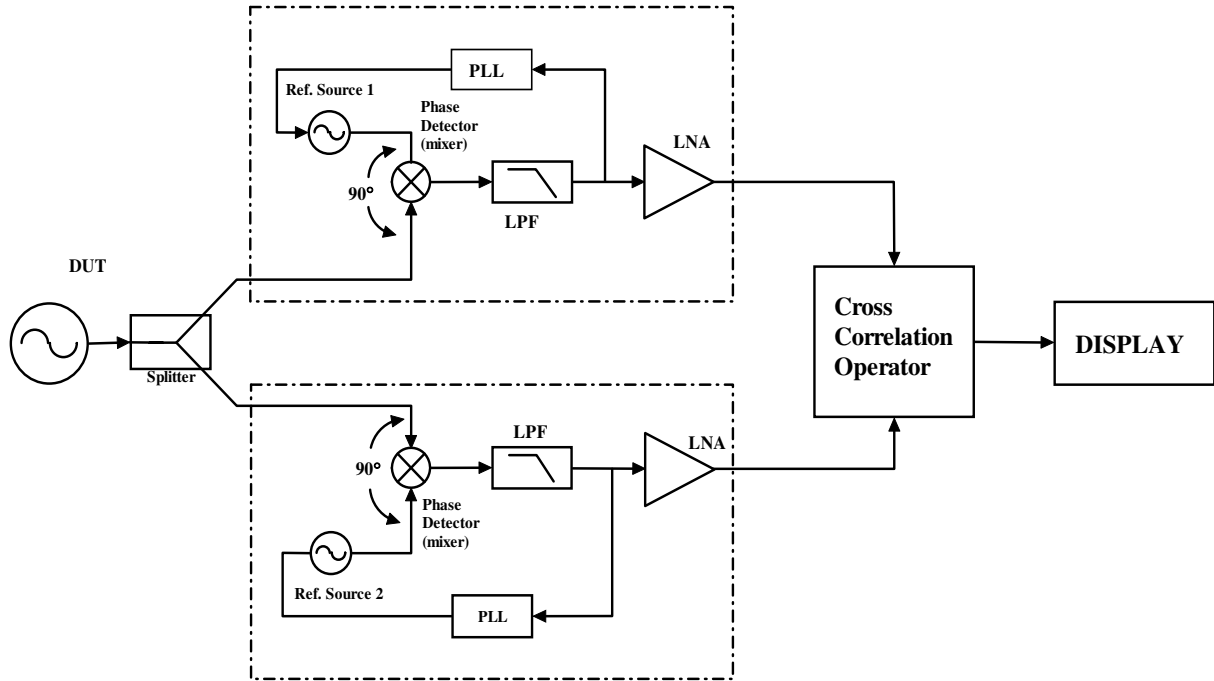


Figure 4-10: The basic block diagram of 2-channel cross-correlation technique (Courtesy: Agilent) [34]

From (4.19), (4.20) and (4.21) into (4.22) and (4.23),

$$\overline{S_{XY}} = \frac{1}{M} \sum_{m=1}^{m=M} [(A_m + C_m) \times (B_m + C_m)^*] \quad (4.22)$$

$$\overline{S_{XY}} = \frac{1}{M} \sum_{m=1}^{m=M} [(A_m B_m^*) + (A_m C_m^*) + (C_m B_m^*) + (C_m C_m^*)] \quad (4.23)$$

Considering that there is no correlation between the noisy signals  $a(t)$ ,  $b(t)$  or  $c(t)$  then as the number of averages increases the uncorrelated terms in the cross spectrum ( $AB$ ,  $AC$  and  $CB$ ) will tend toward zero. The only remaining term  $CC$  represents the power spectral density of the correlated DUT noise. When the analyzer is set to average, the common noise is kept, and the noise not common to both channels is attenuated and averaged away.

From (4.23) the DUT noise through each channel is coherent and is therefore not affected by the cross-correlation, whereas, the internal noises generated by each channel are incoherent and diminish through the cross-correlation operation at the rate of  $\sqrt{M}$  ( $M$ =number of correlations)

$$[Noise]_{meas} = [Noise]_{DUT} + \left( \frac{[Noise]_{channel\#1} + [Noise]_{channel\#2}}{\sqrt{M}} \right) \quad (4.24)$$

where  $[Noise]_{meas}$  is the total measured noise at the display;  $[Noise]_{DUT}$  the DUT noise;  $[Noise]_{channel\#1}$  and  $[Noise]_{channel\#2}$  are the internal noise from channels 1 and 2, respectively; and  $M$  the number of correlations.

From (4.24), the 2-channel cross-correlation technique achieves superior phase noise measurement capability but the measurement speed suffers when increasing the number of correlations. This method offers 15 to 20 dB improved phase noise measurement sensitivity when compared to the Reference source/PLL method described above, so it can be used to measure oscillators with ultra-low phase noise. It is even possible to measure oscillators with better noise performance than the reference oscillators, because phase noises from the reference oscillators are suppressed considerably [37].



The improved dynamic range and noise floor of the cross-correlation phase noise measurement technique comes at price. Usually many samples are needed in order to average out the uncorrelated noise. The measuring yardstick of the confidence interval of a phase noise detector is expressed by [26]:

$$S_{\phi}^s(f) = S_{\phi}^m(f) \left(1 \pm \frac{1}{\sqrt{n}}\right) = \mp 10\% \text{ (for } n = 100) \rightarrow \text{For single-channel} \quad (4.25)$$

$$S_{\phi}^x(f) = S_{\phi}^m(f) \left(1 \pm \frac{2S_{\phi}^s}{\sqrt{n}}\right) = \mp 10\% \text{ (for } n = 20,000) \rightarrow \text{For dual-channel} \quad (4.26)$$

where  $x$  = cross –correlation,  $m$  = measured (noise),  $s$  = single channel,  $n$  = number of samples

Equation (4.25) shows that for a single channel the confidence interval is  $\pm 10\%$  for 100 samples.

Equation (4.26) shows that to obtain the same confidence interval for a phase noise measurement 10 dB below the single channel noise floor 20,000 samples are required. Indeed, the dual channel or cross-correlation method of phase noise results in a lower floor than the standard single channel method but there is a cost of measurement speed [49]. From (4.25) and (4.26), more averages are required to achieve the same level of confidence in a measurement for dual-channel cross-correlation method. The advantage of lower noise floor using the cross-correlation method provides a level of characterization of extremely low noise Crystal oscillators, which was not possible using the single channel method. The practical value of the noise floor is given by [50]

$$[L(f)_{SSB}] = -177 + N_o - P_i \quad (4.27)$$

where  $N_o$  is the noise figure and  $P_i$  is the power available.

Today, the cross-correlation process is the only technique that allows close to thermal noise floor measurements below -177dBc/Hz at far offset from the carrier, and with 20dB of DUT output power can provide a noise floor better than -195dBc/Hz provided the DUT output buffer stage is low noise amplifier and can handle the 20dBm power. However, this improvement of 20 dB is based on 100,000 correlations, which results in a long measurement time [51]-[58].

#### Advantages:

- Best sensitivity for measuring low phase noise levels
- Wide signal frequency range
- Wide offset frequency range (0.01 Hz to 100 MHz)
- Frequency tracks slowly drifting sources
- Rejects AM noise

#### Drawbacks:

- Complexity: Requires two very clean reference sources that are electronically tunable
- Long measurement times when very low noise is being measured
- Measurement frequency bandwidth matched to the tuning range of the reference sources
- Phase Inversion and collapse of the cross-spectral function (condition when the detection of the desired signal using cross-spectral techniques collapses partially or entirely in the presence of second uncorrelated interfering signal).

### 4.3.6 Conventional Phase Noise Measurement System (Hewlett-Packard)

This section is based on published Hewlett-Packard material [1], described here to give brief insights about the working principle of the early, very low phase noise measurement equipment (during the 1980s) and subsequently the development of modern automated test systems [4].

The most sensitive method to measure the spectral density of phase noise  $S_{\Delta\theta}(f_m)$  requires two sources – one or both of them may be the device(s) under test – and a double balanced mixer used as a phase detector. The RF and LO input to the mixer must be in phase quadrature, indicated by 0 Vdc at the mixer IF port. Good phase quadrature assures maximum phase sensitivity  $K_\theta$  and minimum AM sensitivity. With a linearly operating mixer,  $K_\theta$  equals the peak voltage of the sinusoidal beat signal produced when both sources are frequency offset (Figure 4-11). When both signals are set in quadrature, the voltage  $\Delta V$  at the IF port is proportional to the fluctuating phase difference between the two signals.

$$\Delta\theta_{rms} = \frac{1}{K_\theta V_{rms}} \quad (4.28)$$

$$S_{\Delta\theta}(f_m) = \frac{(\Delta V_{rms})^2(1Hz)}{V_B^2 peak} \frac{1}{2} \frac{(\Delta V_{rms})^2(1Hz)}{V_B^2 rms} \quad (4.29)$$

$$\mathcal{L}(f_m) = \frac{1}{2} S_{\Delta\theta}(f_m) = \frac{1}{4} \frac{(\Delta V_{rms})^2(1Hz)}{V_B^2 rms} \quad (4.30)$$

where  $K_\theta$  is phase detector constant and  $V_{B peak}$  for sinusoidal beat signal

Calibrations required of the wave analyzer or spectrum analyzer can be read from the equations above. For a plot of  $\mathcal{L}(f_m)$  the 0-dB reference level is to be set 6 dB above the level of the beat signal. The -6-dB offset has to be corrected by +1.0 dB for a wave analyzer and by +2.5 dB for a spectrum analyzer with log amplifier followed by an averaging detector. In addition, noise bandwidth corrections likely have to be applied to normalize to 1Hz bandwidth.

Since the phase noise of both sources is summed together in this system, the phase noise performance of one of them needs to be known for definite data on the other source. Frequently, it is sufficient to know that the actual phase noise of the dominant source cannot deviate from the measured data by more than 3 dB. If three unknown sources are available, three measurements with three different source combinations yield sufficient data to calculate accurately each individual performance.

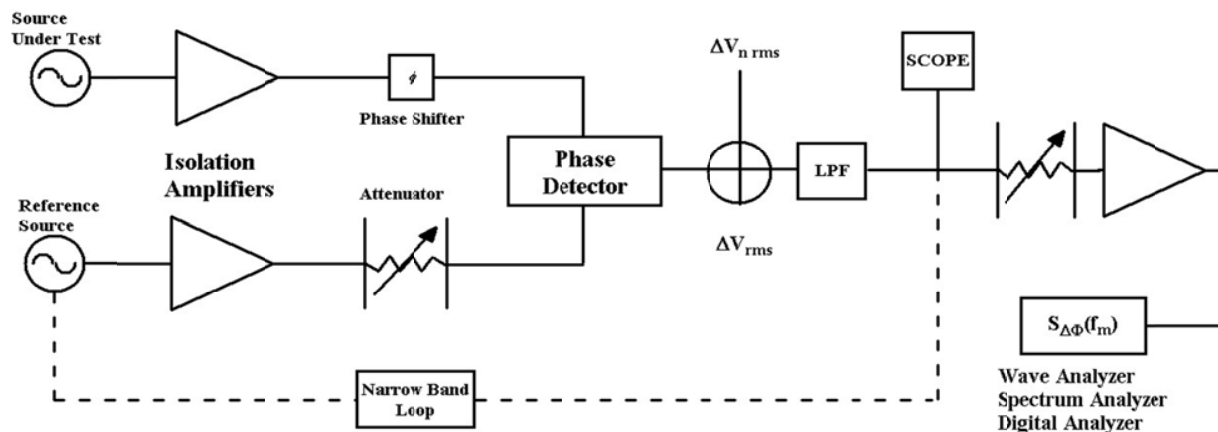


Figure 4-11: Phase Noise system with two sources maintaining phase quadrature

Figure 4-11 indicates a narrowband phase-locked loop that maintains phase quadrature for sources that are not sufficiently phase stable over the period of the measurement. The two isolation amplifiers are to prevent injection locking of the sources to each other.

The noise floor of the system is established by the equivalent noise voltage  $\Delta V_n$  at the mixer output. It represents mixer noise as well as the equivalent noise voltage of the following amplifier:

$$\mathcal{L}_{system}(f_m) = \frac{1}{4} \frac{(\Delta V_{n\,rms})^2 (1\text{Hz})}{V_B^2\,rms} \quad (4.31)$$

Wideband noise floors close to -180 dBc can be achieved with a high-level mixer and a low-noise port amplifier. The noise floor increases with  $f_m^{-1}$  due to the flicker characteristic of  $\Delta V_n$ . System noise floors of -166dBc/Hz at 1 kHz have been realized.

To get this excellent performance, the phase detector/PLL method is complex and requires significant calibration. In measuring low-phase-noise sources, a number of potential problems have to be understood to avoid erroneous data. These include:

- When two sources are phase locked to maintain phase quadrature, it has to be ensured that the lock bandwidth is significantly lower than the lowest Fourier frequency  $f_m$  of interest, unless the test set takes into account (as many do) the loop suppression response
- Even with no apparent phase feedback, two sources can be phase locked through injection locking, resulting in suppressed close-in phase noise and causing a measurement error. This can normally be avoided with the use of high isolation buffer amplifiers or frequency multipliers.
- AM noise of the RF signal can come through if the quadrature setting is not maintained accurately.
- Deviation from the quadrature setting also lowers the effective phase detector constant.
- Nonlinear operation of the mixer results in a calibration error.
- Need for low harmonic content: A non-sinusoidal RF signal causes  $K_\theta$  to deviate from  $V_{Bpeak}$
- The amplifier or spectrum analyzer input can be saturated during calibration or by high spurious signals such as line frequency multiples.
- Closely spaced spurious signals such as multiples of 60 Hz may give the appearance of continuous phase noise when insufficient resolution bandwidth and averaging are used on the spectrum analyzer.
- Impedance interfaces must remain unchanged when transitioning from calibration to measurement.
- Noise from power supplies for devices under test can be a dominant contributor of error in the measured phase noise.
- Peripheral instrumentation such as an oscilloscope, analyzer, counter, or DVM can inject noise.
- Microphonic effects may excite significant phase noise in devices.

Despite all these hazards, automatic test systems now exist and operate successfully [8].

Oscillator manufacturers and users who frequently need to evaluate the performance of ultra low phase noise oscillators, at some point, recognize that their phase noise test systems could be primarily improved in the following aspects: (i) Accuracy, (ii) Speed of test, (iii) Large dynamic range and lower noise floor, (iv) Reliability and repeatability of test data, (v) Range, (vi) ease of use and data retrieval, and (vi) Cost (though high performance test systems will never be cheap!)

#### **General Discussion:**

Characterizing the phase noise of a system or component is not necessarily very easy. Many different approaches are possible, but the key is to find the best approach for the measurement requirements at hand. Practically, it is advisable to use the cross-correlation approach for the best sources so that keeping them locked is easy during measurement cycle. In principle, each reference is locked to track the DUT, therefore PLL bandwidth needs to be monitored for reliable and accurate measurement.

Usually, corrections for PLL bandwidth works to some degree, but corrections beyond certain limit have more errors, leading to inaccurate phase noise measurement of the DUT. One of the weaknesses, with the cross-correlation method is that, many measurements must be made and the average calculated between them. Thus, the measurement takes longer, and the DUT must be kept locked for a longer time. Usually, 1-sweep takes approximately 10 seconds, and the required amount of sweep is  $2^m$  where  $m > 2$  but for a noisy source this may not be easy.

Hence, this method is most suitable for measuring low noise oscillators having a small frequency drift. A survey of some of the more common topologies along with some possible trouble spots helps one to review and keep in mind the advantages and limitations of each approach. Figure 4-12 Shows phase noise plots and noise floor for 3-phase noise measurement techniques (Delay line, PLL and cross-correlation).

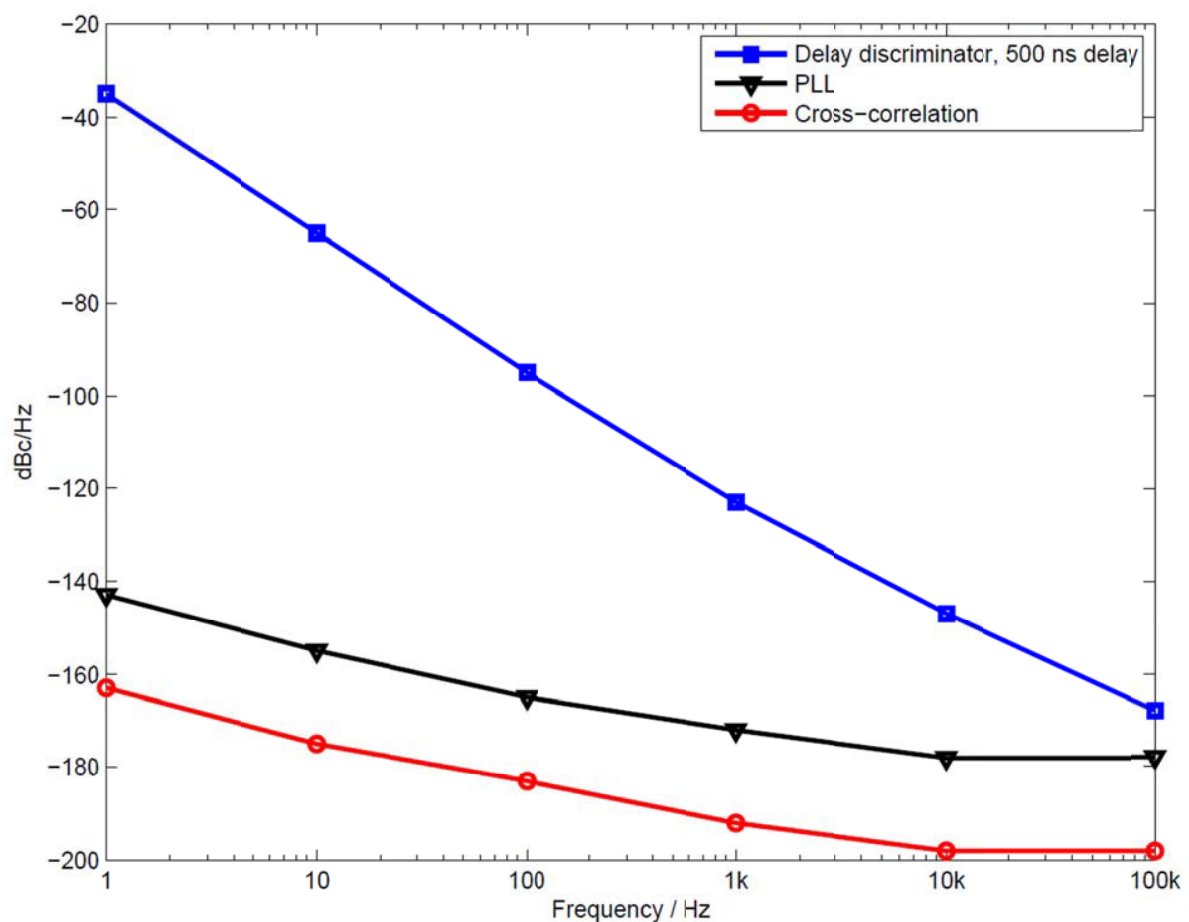


Figure 4-12: Shows phase noise plots and noise floor for 3-techniques (PLL, Delay line, and cross-correlation) [31]

#### 4.4 Prediction and validation of Oscillator Phase Noise measured on different Equipments

The phase noise equation for a Colpitts based oscillator circuit can be expressed as [3]

$$\mathcal{E}(\omega) = 10 \text{Log} \left\{ 4kTR + \frac{4qI_c g_m^2 + \frac{4K_f I_b^{AF}}{\omega} g_m^2}{\omega_0^2 C_1^2 (\omega_0^2 (\beta^+)^2 C_2^2 + g_m^2 \frac{C_2^2}{C_1^2})} \left[ \frac{\omega_0^2}{4\omega^2 V_{cc}^2} \right] \left[ \frac{Q_0^2}{Q_L^2} + \frac{[C_1 + C_2]^2}{C_1^2 C_2^2 \omega_0^4 L^2 Q_L^2} \right] \right\} \quad (4.32)$$

where  $\beta^+ = \left[ \frac{Y_{21}^+}{Y_{11}^+} \right] \left[ \frac{C_1}{C_2} \right]^p$   $g_m = [Y_{21}^+] \left[ \frac{C_1}{C_2} \right]^q$ ; Values of p and q depends upon the drive level

$Y_{21}^+, Y_{11}^+$  = large signal [Y] parameter of the active device

$K_f$  = flicker noise coefficient, AF = flicker noise exponent

$\mathcal{E}(\omega)$  = ratio of sideband power in a 1Hz BW at  $\omega$  to total power in dB

$\omega$  = frequency offset from the carrier,  $\omega_0$  = center frequency

$Q_L$  = loaded Q of the tuned circuit,  $Q_0$  = unloaded Q of the tuned circuit

$kT$  =  $4.1 \times 10^{-21}$  at 300 K (room temperature)

$R$  = equivalent loss resistance of the tuned resonator circuit

$I_c$  = RF collector current,  $I_b$  = RF base current

$V_{cc}$  = RF collector voltage

$C_1, C_2$  = feedback capacitor as shown in Figure 4-13

#### 4.4.1 Verification of 100 MHz Crystal Oscillator using CAD Tool (Ansoft Designer from Ansys)

Figures 4-13, 4-14, 4-15, 4-16 and 4-17 shows the typical simplified Colpitts 100 MHz Crystal oscillator circuit, grounded base buffer circuit, noise Figure plots, phase noise plots, and output power.

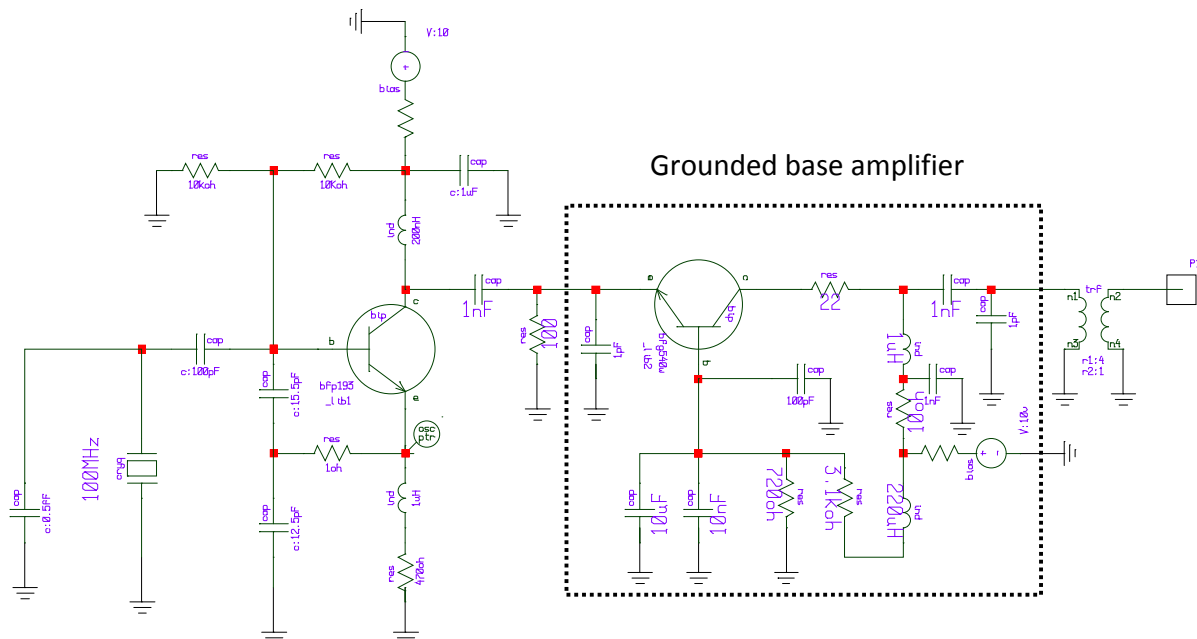


Figure 4-13: 100 MHz Crystal Oscillators with the Grounded-Base low noise Amplifier

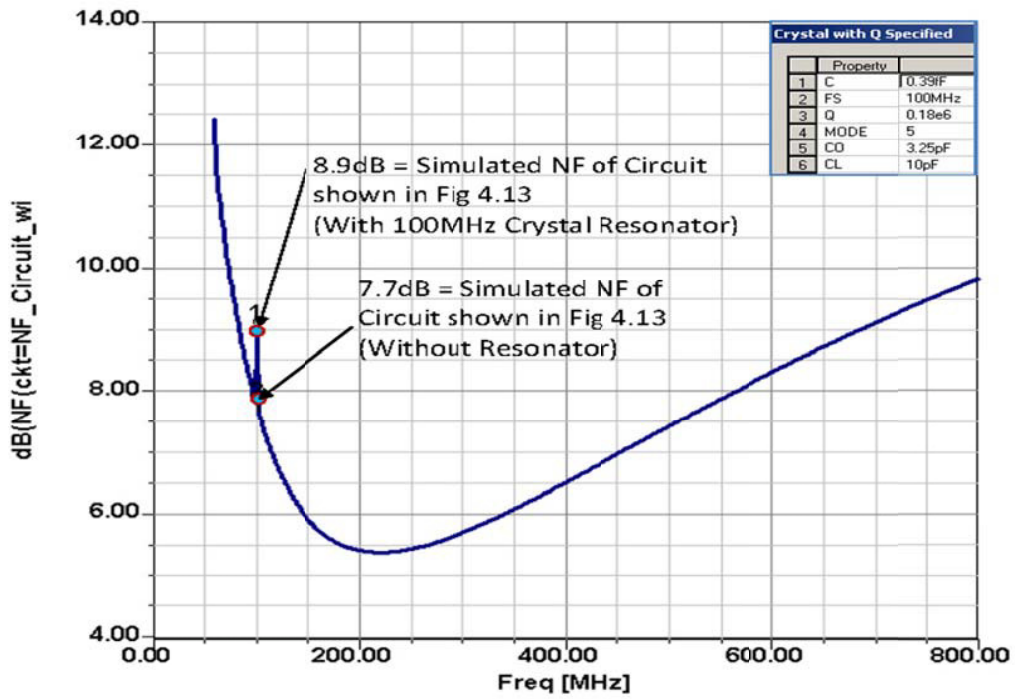


Figure 4-14: Simulated plot showing NF of 100 MHz Oscillator shown in Fig 4-13

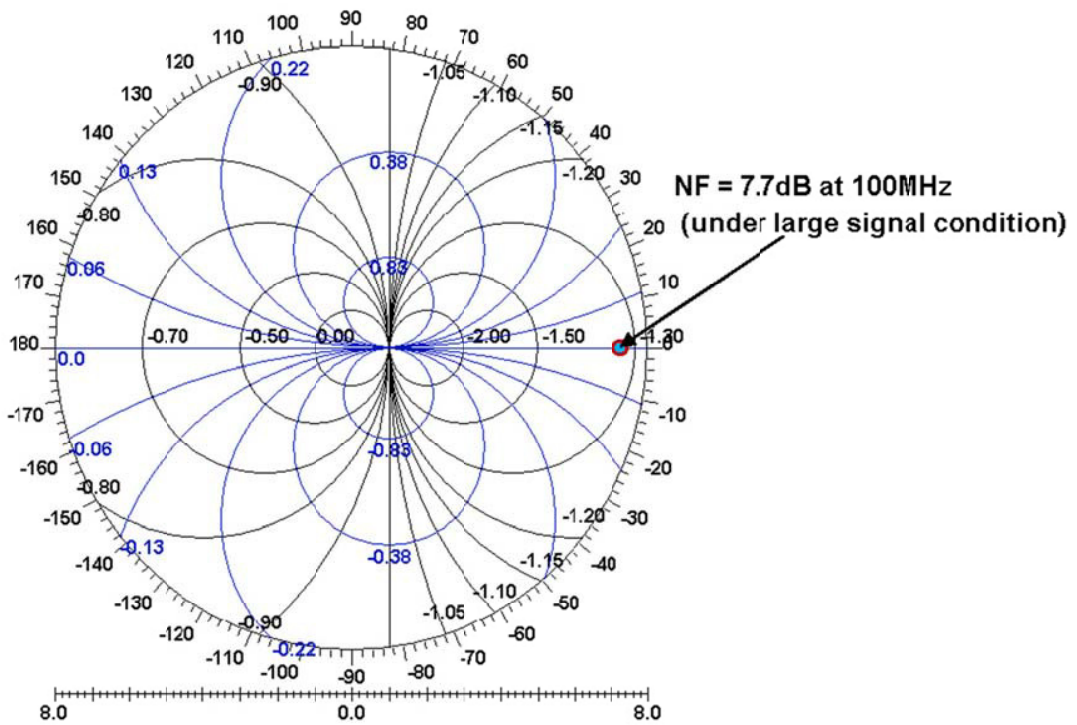


Figure 4-15: CAD simulated Polar Plot of Noise of the Oscillator Circuit shown in Figure 4-13

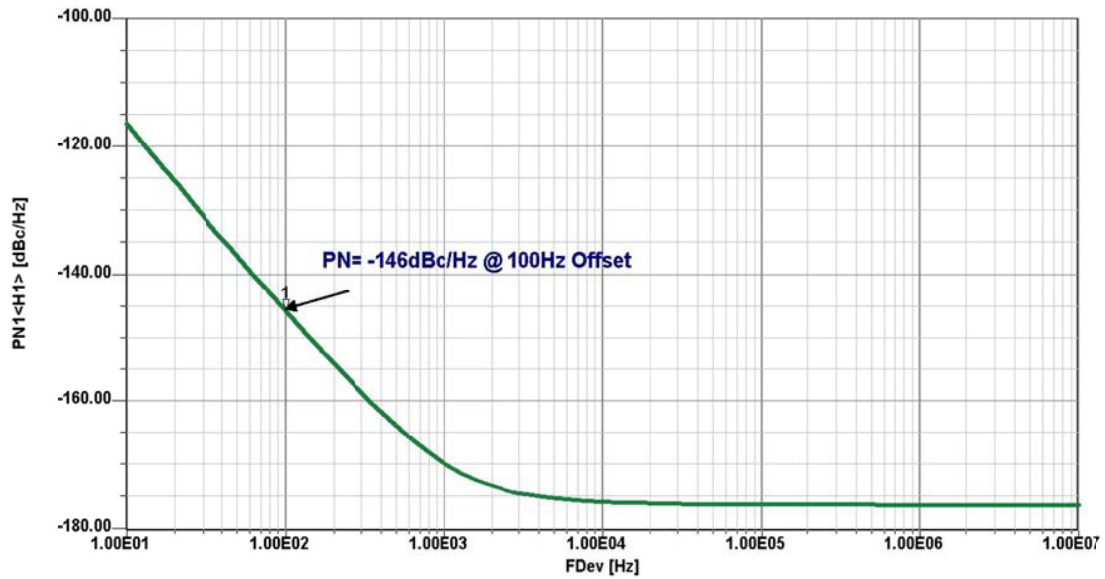


Figure 4-16: CAD simulated Phase Noise Plot of 100MHz Crystal Oscillator with Buffer Stage

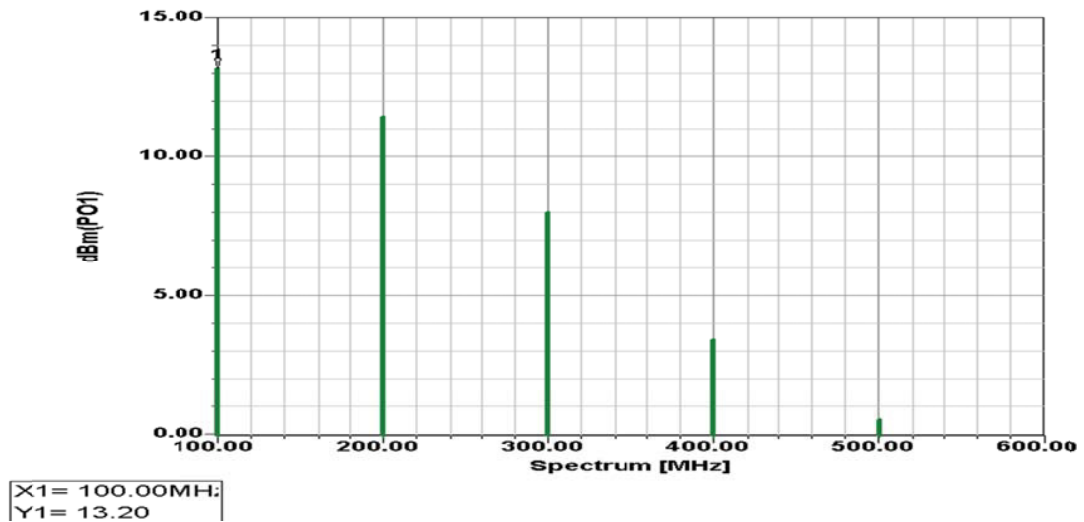


Figure 4-17: Simulated Power Output Plot of 100MHz Crystal Oscillator with Buffer Stage

The basic equation needed to predict the phase noise using CAD simulation for the circuit shown in Figures 4-13 and 4-14 is found in [3]

$$\mathcal{L}(f_m) = 10 \log \left\{ \left[ 1 + \frac{f_0^2}{[2f_m Q_0 m(1-m)]^2} \right] \left( 1 + \frac{f_c}{f_m} \right) \frac{FkT}{2P_0} + \frac{2kTRK_0^2}{f_m^2} \right\} \quad (4.33)$$

where  $\mathcal{L}(f_m)$ ,  $f_m$ ,  $f_0$ ,  $f_c$ ,  $Q_L$ ,  $Q_0$ ,  $F$ ,  $k$ ,  $T$ ,  $P_0$ ,  $R$ ,  $K_0$  and  $m$  are the ratio of the sideband power in a 1Hz bandwidth at  $f_m$  to total power in dB, offset frequency, flicker corner frequency, loaded  $Q$ , unloaded  $Q$ , noise factor, Boltzmann's constant, temperature in degree Kelvin, average output power, equivalent noise resistance of tuning diode, voltage gain and ratio of the loaded  $Q$ -factor ( $Q_0$ ) and unloaded  $Q$ -factor ( $Q_L$ ). In the past this was done with the Leeson formula, which contains several estimates, those being output power ( $P_0$ ), flicker corner frequency ( $f_c$ ), oscillator noise factor ( $F$ ), and the operating (or loaded)  $Q$ . Now, one can assume that the small signal linear estimation of noise factor ( $F$ ) can give

wrong estimation of phase noise when oscillator operates under large signal condition. The approximate formulae (considering quasi-nonlinear analysis) of the noise factor under the large signal condition can be given by the following equation [3, pp. 135].

$$F \cong 1 + \frac{Y_{21}^+ C_2 C_c}{(C_1 + C_2) C_1} \left[ r_b + \frac{1}{2r_e} \left( r_b + \frac{(C_1 + C_2) C_1}{Y_{21}^+ C_2 C_c} \right)^2 \left( \frac{1}{\beta^+} + \frac{f^2}{f_T^2} \right) + \frac{r_e}{2} \right] \quad (4.34)$$

where  $Y_{21}^+$  = large signal [Y] parameter of the active device.

Table 4-2: shows the calculated Noise Figure and Phase Noise for 100MHz Crystal Oscillator using (4.32), (4.33) and (4.34) for unloaded  $Q_0 = 180000$ , and time average loaded Q ( $Q < Q_0/4$ ) under large signal drive level condition is 25000.

Table 4-2: Calculated Noise Figure and Phase Noise for 100MHz Crystal Oscillator

Oscillator Frequency	Simulated Large Signal Noise Figure	Calculated Phase Noise at 100Hz offset
100 MHz	7.7 dB	-146 dBc/Hz

#### 4.4.2 Verification of 100 MHz Crystal Oscillator (LN XO 100) using Analytical Model

The calculated parameters of 100MHz crystal oscillator circuit are given below [ref. 3, pp.181], after defining all the values, the phase noise can be predicted for comparative analysis (shown in Figure 4-18).

Theoretical calculated parameters of 100MHz crystal oscillator circuit

$C1 := 15.6\text{pF}$	$C2 := 12.5\text{pF}$	$kT := 4.143 \cdot 10^{-21} \cdot \text{J}$	$R := 0.2 \cdot \Omega$
$q\text{charge} := 1.602 \cdot 10^{-19} \cdot \text{coul}$		$Ic := 8.2 \cdot \text{mA}$	$Ib := 220 \cdot \mu\text{A}$
$y11 := (0.000884 - 0.0000158j) \cdot \text{mho}$			
$y21 := (0.0105 - 0.00084j) \cdot \text{mho}$			
$L := 6.4949 \cdot 10^{-3} \cdot \text{henry}$	$af := 2$	$kf := 1 \cdot 10^{-10}$	$y := \frac{C1}{C2}$
$Vcc := 10\text{V}$	$i := 0.7$	$p := 1.45$	$q := 1.05$
$Q := 25000$	$Q0 := 180000$	$nfdB := 4.747$	$PoutdB := 13$
$fc := 100\text{MHz}$	$wc := 2\pi \cdot fc$	$gm :=  y21  \cdot y^q$	
$fo_i := 10^1 \cdot \text{Hz}$	$wo_i := 2\pi \cdot fo_i$	$B1_i := (wo_i)^2 \cdot L^2 \cdot Vcc^2$	
$k\text{constant} := \frac{KT \cdot R}{wc^2 \cdot C2^2}$	$k0_i := \frac{k\text{constant}}{B1_i}$	$b := \frac{ y21  \cdot y^p}{ y11 }$	
$k1\text{constant}_i := q\text{charge} \cdot Ic \cdot gm^2 + \frac{kf \cdot Ib^{af} \cdot gm^2}{wo_i}$			
$k1_i := \frac{k1\text{constant}_i}{wc^2 \cdot B1_i}$	$k3_i := wc^2 \cdot gm^2$	$k2_i := wc^4 \cdot b^2$	$k_i := \frac{k3_i}{k2_i \cdot C2^2}$
$t2_i := k0_i \frac{(1+y)^2}{y^2}$	$t1_i := \left[ \left( \frac{b^2}{gm^3} \right)^2 \cdot \frac{k_i^3 \cdot k1_i \cdot (wc)^2}{y^2 + k_i} \right] \cdot \frac{(1+y)^2}{y^2}$		$1_i := t1_i + t2_i$
$m_i := 10 \cdot \log \left[ 1_i \cdot (\text{kg}^{-2} \cdot \text{m}^{-4} \cdot \text{s}^5 \cdot \text{A}^2) \cdot \frac{Q0^2}{Q^2} \right]$			
$L_i := \text{if}[m_i < (-177 + Pout(dBm) - nfdB)], (-177 + PoutdB - nfdB), m_i$			



$m_i$	$f_{o_i}$	$L_i$
-88.581	$1 \cdot s^{-1}$	-88.581
-118.515	$10 \cdot s^{-1}$	-118.515
-147.901	$100 \cdot s^{-1}$	-147.901
-174.251	$1 \cdot 10^3 \cdot s^{-1}$	-174.251
-195.999	$1 \cdot 10^4 \cdot s^{-1}$	-185.253
-216.22	$1 \cdot 10^5 \cdot s^{-1}$	-185.253
-236.243	$1 \cdot 10^6 \cdot s^{-1}$	-185.253
-256.245	$1 \cdot 10^7 \cdot s^{-1}$	-185.253

Figure 4-18 shows the theoretical phase noise model expressed in (4.23)

#### 4.4.3 Verification of 100 MHz Crystal Oscillator using Phase Noise Measurement Equipments

For validation of the theoretical model described in section (4.4.2), 100 MHz Crystal oscillator was built and tested on different Phase Noise Measurement Equipments (Agilent E5052B, R&S FSUP, Holzworth, Noise XT, and Anapico APPH6000-IS) available on the market. Figure 4-19 shows the phase noise plot generated from theoretical calculations.

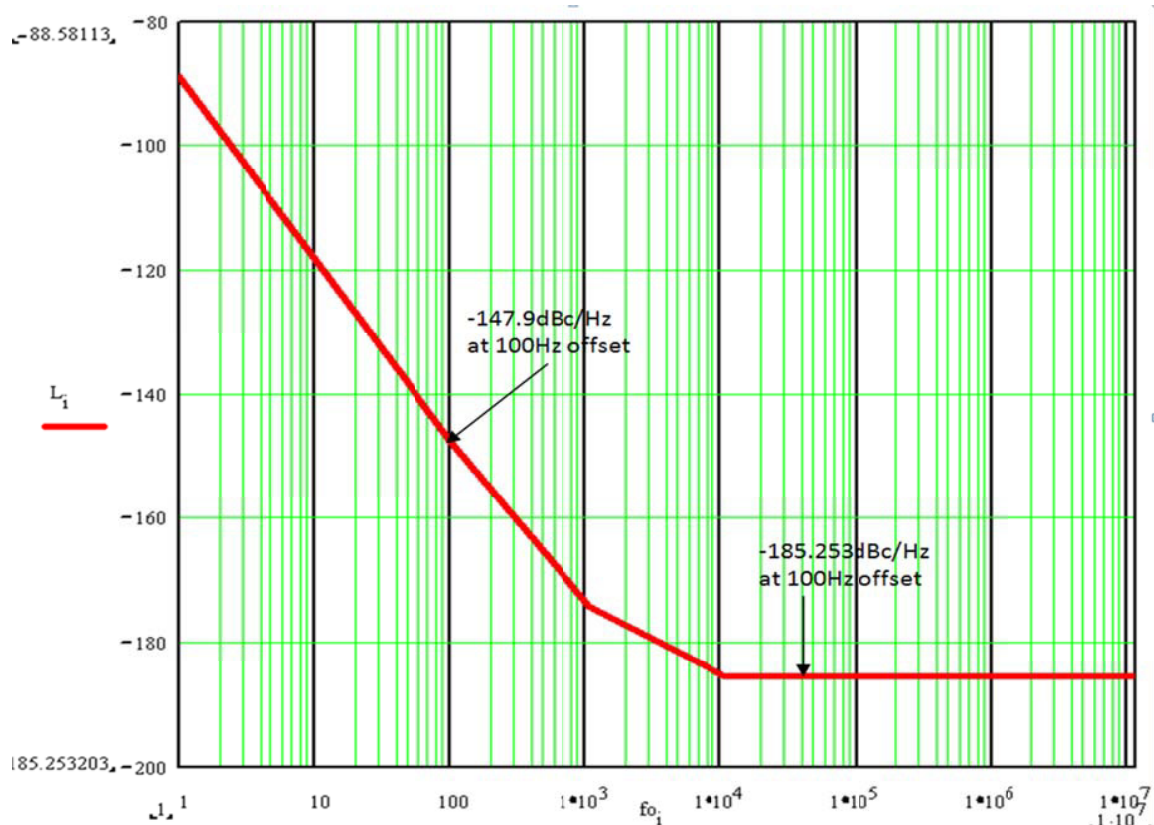


Figure 4-19: Theoretically calculated Phase Noise Plot for 100MHz Crystal Oscillator (LN XO 100)

#### 4.4.3.1 Experimental Verification of 100 MHz Crystal Oscillator using Agilent E5052B

The feature of cross-correlation techniques in Agilent E5052B satisfies the established criteria without additional references, nor calibration of the device under test (DUT) on exact frequency. Figures 4-20 and 4-21 show the picture of Agilent E5052B equipment and measured phase noise plot of 100 MHz crystal oscillator circuit for the purpose of the verification of measurement uncertainty.

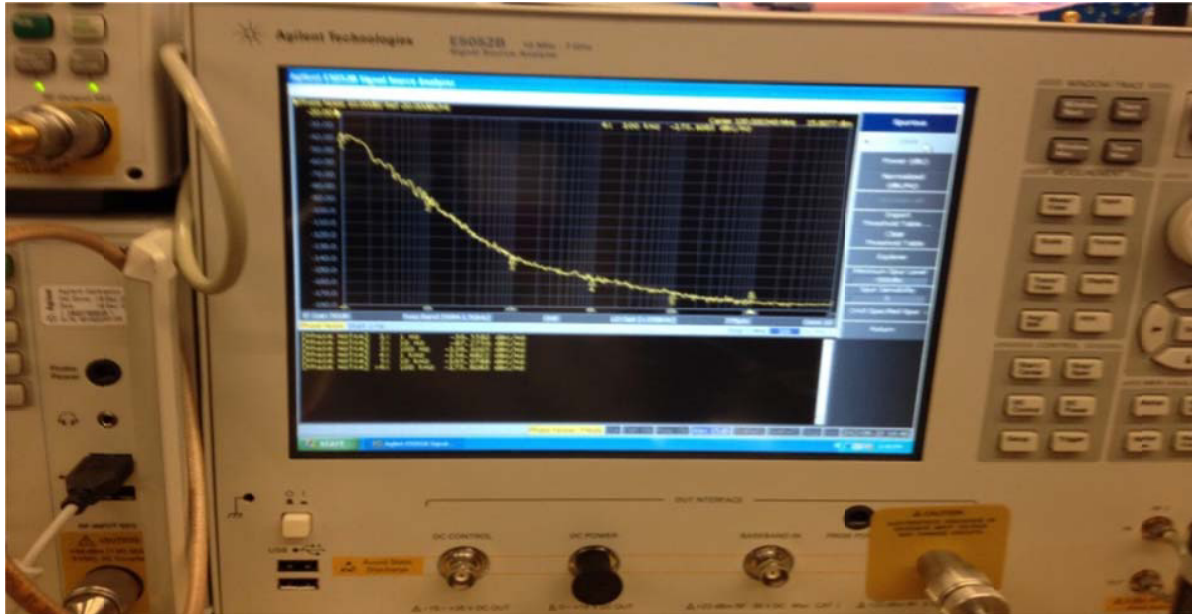


Figure 4-20 shows the picture of E5052B (Courtesy: Agilent) with the phase noise plot of 100 MHz crystal oscillator circuit for the purpose of the verification of measurement uncertainty (IMS show 2012, Montreal, Canada)

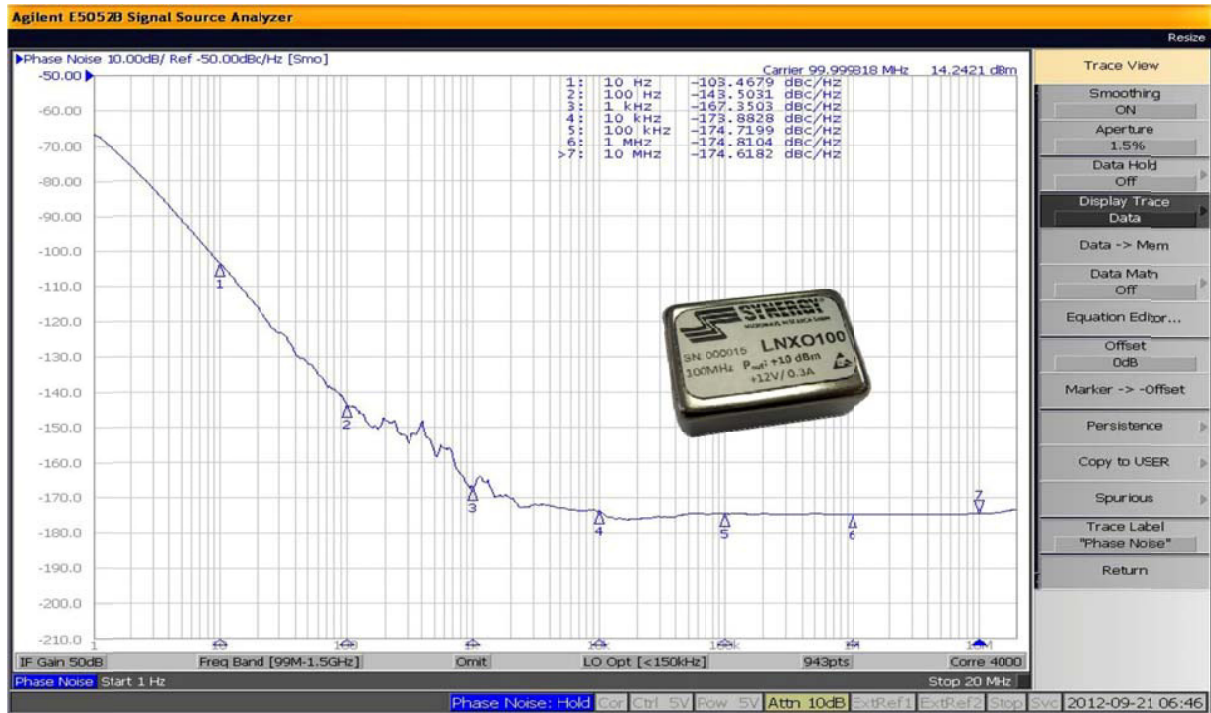


Figure 4-21: 100MHz Crystal Oscillator Measured on Agilent E5052B (Corr\_4000) [measurement performed in IMS show 2012, Montreal, Canada]

The measured phase noise at 100 Hz offset is -143 dBc/Hz for LNXO 100 (100MHz carrier frequency), this shows the capability of close-in measurement. The main concern is the dynamic range and noise floor of the equipment measured at large offsets from the carrier, the far offset noise floor is -174 dBc/Hz at offsets greater than 100 KHz. The theoretical expectations were closer to -191 dBc/Hz at 10 KHz offsets and beyond for 14 dBm output power. The other problem is that the mixer and the post amplifier can easily get into compression, which raises the noise floor.

#### 4.4.3.2 Experimental Verification of 100 MHz Crystal Oscillator using R&S (FSUP 26)

The feature of cross-correlation techniques in R&S (FSUP 26) satisfies the established criteria, and requires neither additional references, nor calibration of the device under test (DUT) on exact frequency. Figures 4-22 and 4-23 show the picture of R&S (FSUP 26) equipment and measured phase noise plot of 100 MHz crystal oscillator for the purpose of the verification of measurement uncertainty. The measured phase noise at 100 Hz offset is -140 dBc/Hz for LNXO 100 (100MHz carrier frequency), and the far offset noise floor is -174 dBc/Hz at offsets greater than 100 KHz. The theoretical expectations were closer to -191dBc/Hz at 100 KHz offsets and beyond for 14dBm output power.



Figure 4-22 shows the picture of R&S FSUP 26 (Courtesy: R&S) while taking measurement

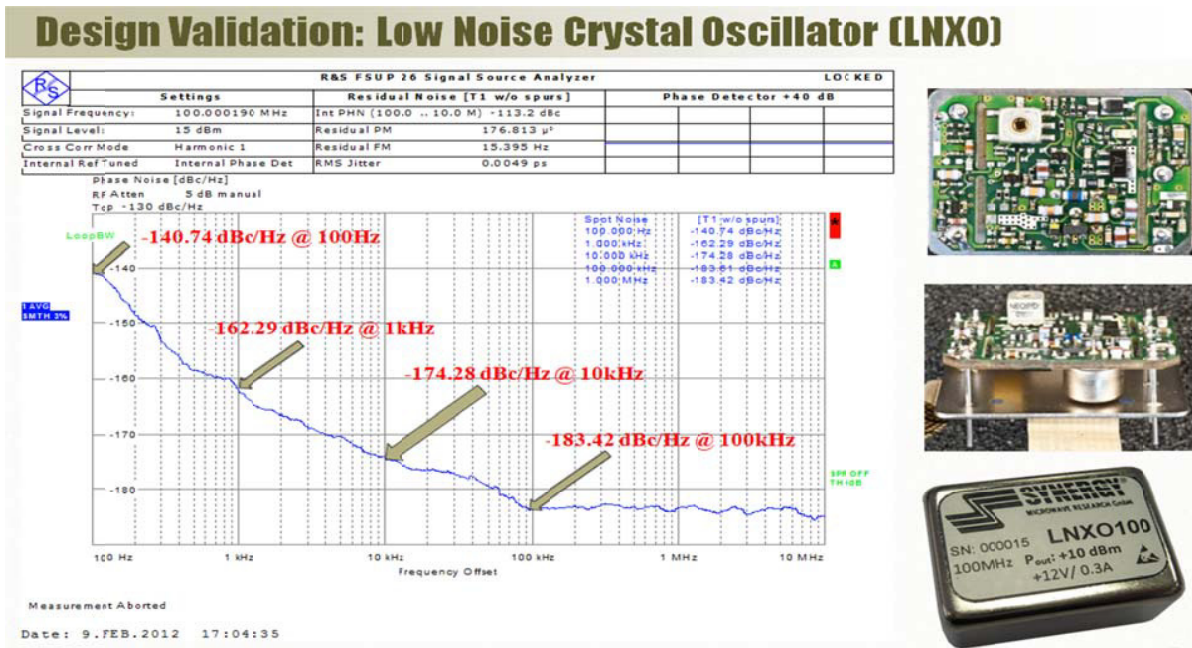


Figure 4-23: 100MHz Crystal Oscillator Measured on R&S FSUP

### 4.4.3.3 Experimental Verification of 100 MHz Crystal Oscillator using Anapico (APPH6000-IS)

The feature of cross-correlation techniques in APPH 6000 (Anapico) satisfies the established criteria, but require 2-additional references at exact frequency. Figures 4-24 shows the measured phase noise plot of 100 MHz crystal oscillator for the purpose of the verification of measurement uncertainty. The measured phase noise at 100 Hz offset is -146dBc/Hz for LNXO 100 (100MHz carrier frequency), this shows the capability of close-in measurement. The instrument's specification calls (conservatively) for -184dBc/Hz floor at offsets greater than 100 KHz. The theoretical expectations were closer to -191dBc/Hz at 100 KHz offsets and beyond for 14dBm output power. The main concern is the additional references at exact frequency of DUT.

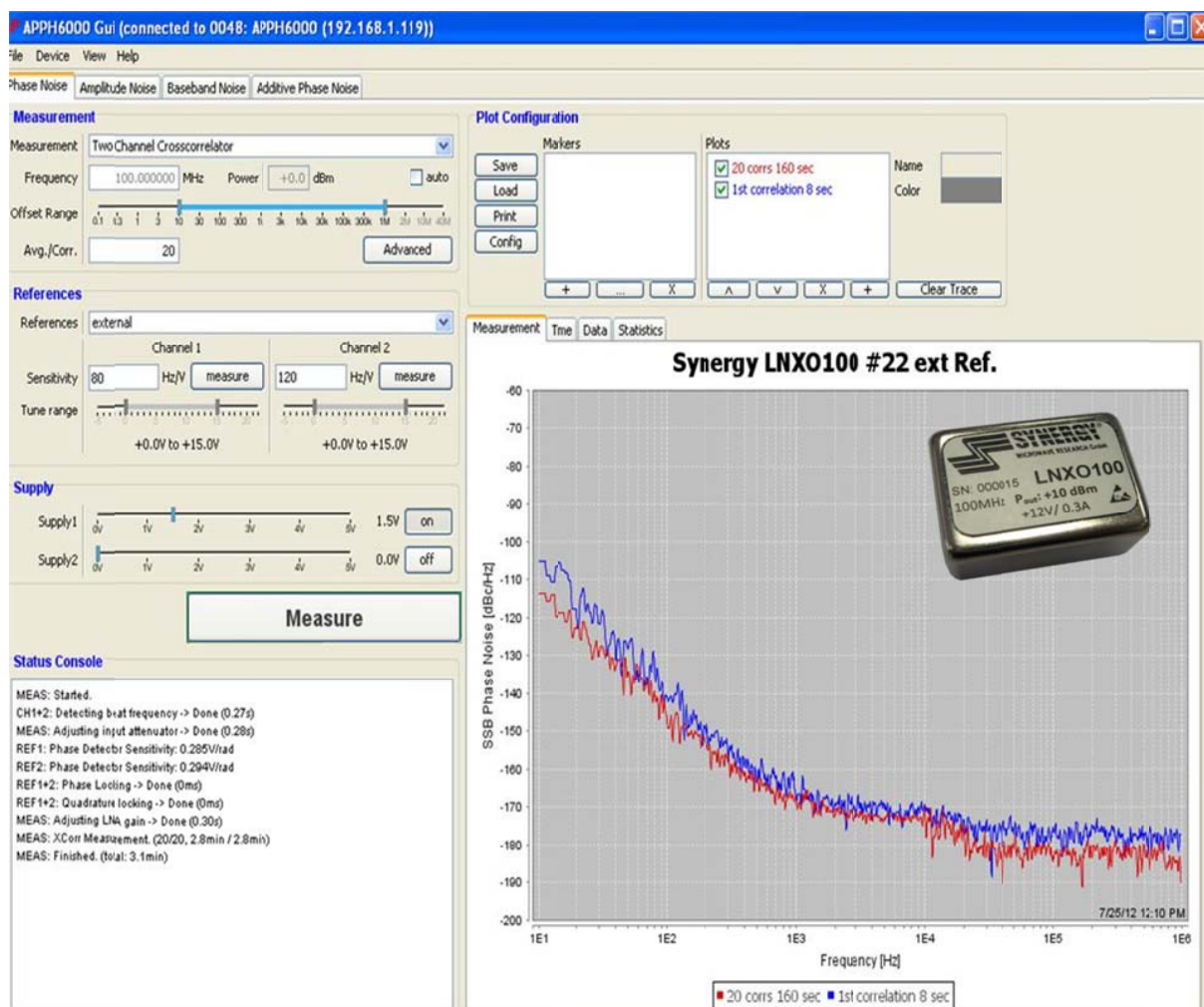


Figure 4-24 shows the picture of phase noise plots and equipment setting (Courtesy: Anapico APPH6000-IS) 100MHz Crystal Oscillator Measured on Anapico phase noise engine

### 4.4.3.4 Experimental Verification of 100 MHz Crystal Oscillator using Holzworth (HA7402A)

The feature of cross-correlation techniques in Holzworth satisfies the established criteria; require 2-additional references at exact frequency. Figure 4-25 shows the picture of Holzworth phase noise measurement equipment, including the measured phase noise plot of 100 MHz crystal oscillator for the

purpose of the verification of measurement uncertainty. The measured phase noise at 100 Hz offset is -147dBc/Hz for LNXO 100 (100MHz carrier frequency), this shows the capability of close-in measurement. The instrument's specification calls (conservatively) for -178dBc/Hz floor at offsets greater than 100 KHz. The theoretical expectations were closer to -191dBc/Hz at 100 KHz offsets and beyond for 14dBm output power. The main concern is the additional references at exact frequency of DUT.

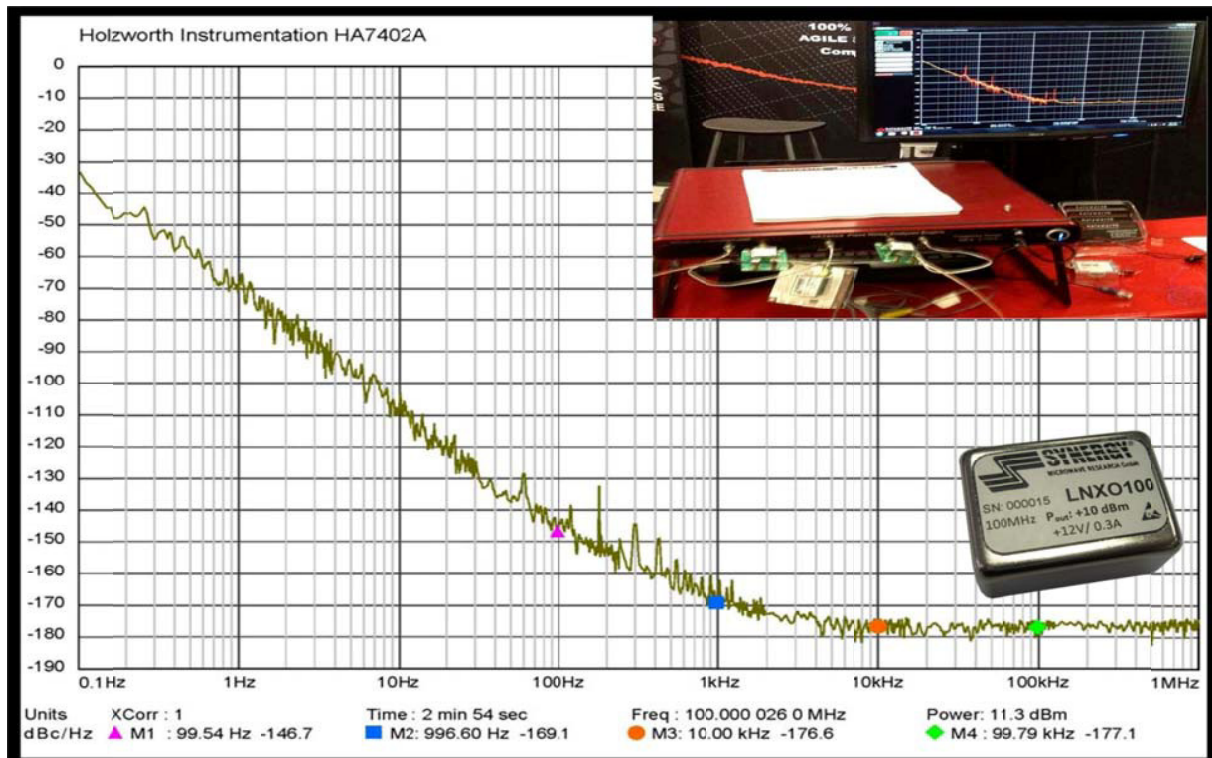


Figure 4-25 shows the picture of phase noise plots and equipment setting (Courtesy: Holzworth) 100MHz OXO Measured on Holzworth Phase Noise Engine [measurement performed at IMS show 2012, Montreal, Canada]

#### 4.4.3.5 Experimental Verification of 100 MHz Crystal Oscillator using Noise XT (DCNTS)

The feature of cross-correlation techniques in Noise XT satisfies the established criteria; require 2-additional references at exact frequency. Figures 4-26 shows the picture of NoiseXT phase noise measurement equipment, including the measured phase noise plot of 100 MHz crystal oscillator for the purpose of the verification of measurement uncertainty. The measured phase noise at 100 Hz offset is -140dBc/Hz for LNXO 100 (100MHz carrier frequency), this shows the capability of close-in measurement. The instrument's specification calls for -190 dBc/Hz floor at offsets greater than 1 MHz. The theoretical expectations of -191dBc/Hz noise floor closely met with this equipment for 14dBm output power. The main concern is the close-in phase noise, which is 7dB inferior as compared to Holzworth for identical correlations. As shown in Figure 4-26, Noise XT Dual Core Noise Test Set (DCNTS) [28] requires two references with similar performance as the DUT (the better the reference – the faster the test), the references must have voltage control (ability to change frequency with the change of the voltage on the control terminal), and be calibrated on the frequency of DUT.

#### 4.5 Phase Noise Measurement Evaluation and Uncertainties:

The rigorous measurement are conducted on 100 MHz Crystal oscillator using different Phase Noise Measurement Equipments (Agilent E5052B, R&S FSUP, Holzworth, Noise XT, and Anapico APPH6000-IS) commercially available on the market.

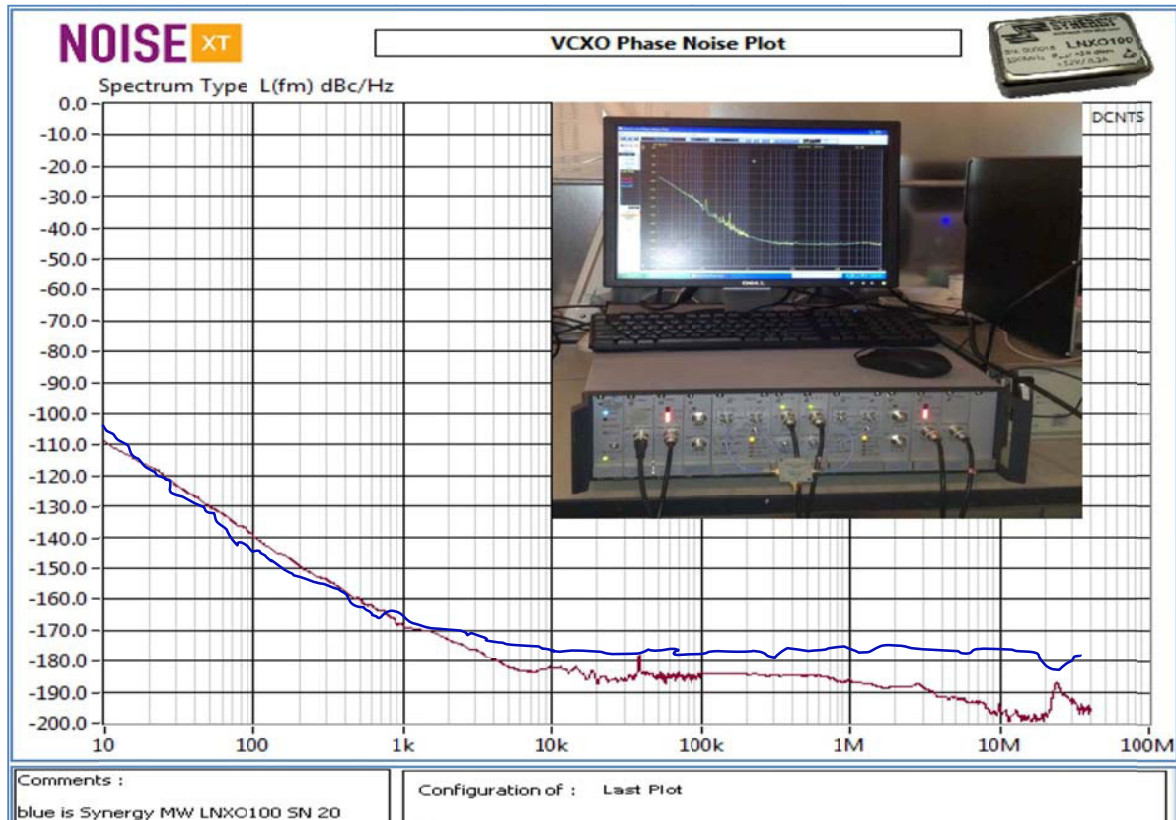


Figure 4-26: Phase noise measurement using cross-correlation techniques using Noise XT DCNTS Engine

Table 4-3 describes the theoretical and measured phase noise on different test equipment for comparative analysis of the measured data under similar test condition. The consequence is this set of equations gives the best possible phase noise. If the equipment in use, after many correlations gives out a better number, either it violates the laws of physics and if it gives a worse number, then the correlations settings needs to corrected or the dynamic range of the equipment is insufficient. This measurement is exhaustive, but it was necessary to explain how things fall in place.

At 20dBm output, the output amplifier certainly has a higher noise figure, as it is driven with more power and there is no improvement possible. Phase Inversion may lead to collapse of the cross-spectral function, failure to truly measured noise occurs when a special phase condition exists between the signals being offered to the cross-spectrum function [49]-[55]. This may be favorable condition to see optimistic but wrong phase noise measurement due to the established anti-phase condition of second uncorrelated interfering signal. Therefore, the detection of the desired signal using cross-spectral techniques collapses partially or entirely in the presence of the second uncorrelated interfering signal. Cross-spectral analysis is a mathematical tool for extracting the power spectral density of a correlated signal from two time series in the presence of uncorrelated interfering signals [55]. The cross-spectrum of two signals  $x(t)$  and  $y(t)$  is defined as the Fourier transform of the cross-covariance function of  $x$  and  $y$ .

For example,  $x(t) = a(t) + c(t) + d(t)$ ;  $y(t) = a(t) + c(t) - d(t)$ , where  $c(t)$  to be the desired signal,  $a(t)$  and  $b(t)$  are the uncorrelated interfering signals,  $d(t)$  is anti-correlated (phase inverted) in  $x$  and  $y$  then it leads to an unexpected negative hump (exhibits unexpected very low phase noise) in phase noise plot due to cancellation dynamics. This implies that at any frequency  $f$  where the average

magnitude of signal  $C(f)$  is equal to that of signal  $D(f)$ , the magnitude of the cross-spectrum collapses to zero [56].

Any contribution of the desired signal  $c(t)$ , or the interferer  $d(t)$ , to the cross spectral density is eliminated. This occurs even though signals  $c(t)$  and  $d(t)$  are completely uncorrelated. If  $C(f)$  and  $D(f)$  have the same shape or slope versus frequency, entire octaves or decades of spectrum can be suppressed and be grossly under-reported. If the PSD (power spectral density) of C and D are not exactly equal, a partial cancelation still occurs. These phenomena are demonstrated on 100 MHz OCXO, measured on different equipments, some of the measurements showing -198 dBc/Hz @ 20 MHz offset for 100 MHz OCXO (Figure 4-26, red plot).

The cross correlation technique allows us to look below  $kT$  ( $k$  is Boltzmann constant and  $T$  is temperature in degree Kelvin), however the usefulness of noise contributions below  $kT$  is a matter of discussion among scientific community because not understanding when and how this effect occurs can lead to dramatic underreporting of the desired signal [56]-[58].

Following is a set of measured results of 100MHz Crystal Oscillators with different test equipments shown in Table 4-3 for giving good understanding about the discrepancy in phase noise measurement performed on different commercially available equipments in the market [47]-[48].

Table 4-3 describes the theoretical and measured phase noise on different test equipments available in market

100 MHz OCXO O/P=14dBm, NF=7dB	Theoretical Model [1]	Agilent E5052B	R & S FSUP 26	Anapico APPH6000-IS	Holzworth HA7402-A	Noise XT DCNTS
PN @ 100 Hz offset	-147 dBc/Hz	-143 dBc/Hz	-143 dBc/Hz	-141 dBc/Hz	-147 dBc/Hz	-140 dBc/Hz
PN @ 1 kHz offset	-175 dBc/Hz	-167 dBc/Hz	-163 dBc/Hz	-170 dBc/Hz	-170 dBc/Hz	-170 dBc/Hz
PN @ 10kHz offset	-185 dBc/Hz	-173 dBc/Hz	-174 dBc/Hz	-172 dBc/Hz	-178 dBc/Hz	-181 dBc/Hz
PN @ 100kHz offset	-185 dBc/Hz	-174 dBc/Hz	-183 dBc/Hz	-181 dBc/Hz	-179 dBc/Hz	-183 dBc/Hz
PN @ 1 MHz offset	-185 dBc/Hz	-174 dBc/Hz	-184 dBc/Hz	-182 dBc/Hz	-179 dBc/Hz	-186 dBc/Hz
PN @ 10MHz offset	-185 dBc/Hz	-174 dBc/Hz	-185 dBc/Hz	-188 dBc/Hz	-178 dBc/Hz	-196 dBc/Hz

### **Phase Noise Measurement Issues**

There are important measurement issues that, if not well understood, can lead to erroneous results and interpretations [45]. They involve measurement bandwidth masking of, and accurate distinction between, true discrete spurious signals and narrowband noise peaks (typically encountered under vibration). Although the phase noise data displayed by phase noise equipment is usually normalized to 1Hz measurement bandwidth, most automated phase noise measurement equipment actually measure the phase noise in measurement bandwidths that increase with increasing carrier offset frequency. This is done for two reasons: (1) it results in shorter, overall measurement time, and (2) at high carrier offset frequency (i.e., > 100 kHz), many measurement systems employ analog spectrum analyzers that are not capable of 1Hz resolution. Noise measured in a 1 kHz bandwidth, for example, is 30dB higher than that displayed in a 1Hz bandwidth. That means that low-level discrete spurious signals (and narrowband noise peaks typically encountered under vibration as a result of high Q mechanical resonances) may not be detected. The second problem involves the software employed by the noise measurement system vendor used to discriminate between random noise and discrete spurious signals. Usually, when a reasonably sharp increase in noise level is detected, the system software assumes the increase marks the presence of a “zero bandwidth” discrete signal.

It therefore (when displaying the phase noise on a 1Hz bandwidth basis) applies a bandwidth correction factor to the random noise, but does not make a correction to what was interpreted as a discrete signal. This results in an erroneous plot if/when the detected “discrete” is really a narrowband noise peak. Figure 4-27 and Figure 4-28 attempt to depict the various situations that can result from these issues as described above. Figure 4-29 shows the picture of Faraday Cage, demonstrating the phase noise measurement setup using different equipments (Agilent E5052B, R&S FSUP, Holzworth HA7402-A, Noise XT DCNTS, Anapico APPH6000-IS) for the validation purpose. OEwaves -PHENOM™ and Agilent E5500 claim for improved dynamic ranges and capable of measuring noise floor below  $kT$  but these equipments were not made available for the validation in our Faraday Cage. The effort is in progress to validate the phase noise measurement using PHENOM™ and E5500 for broader acceptance of the fact and myth linked with variation in measurement phase noise data below the  $kT$ .

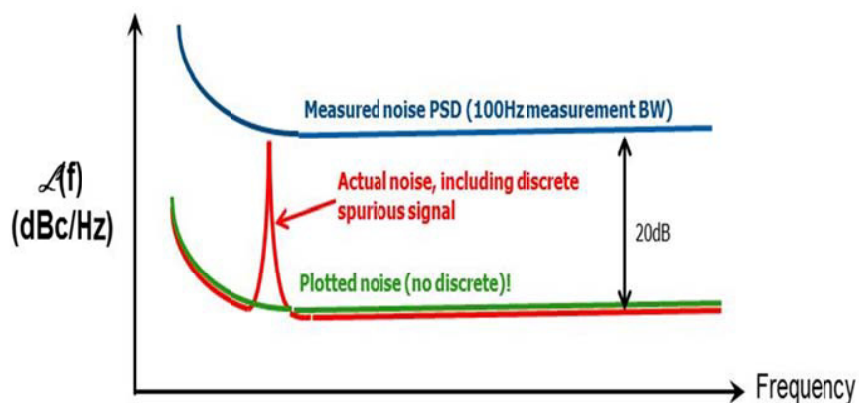


Figure 4-27: Undetected Discrete Spurious Signal [45]

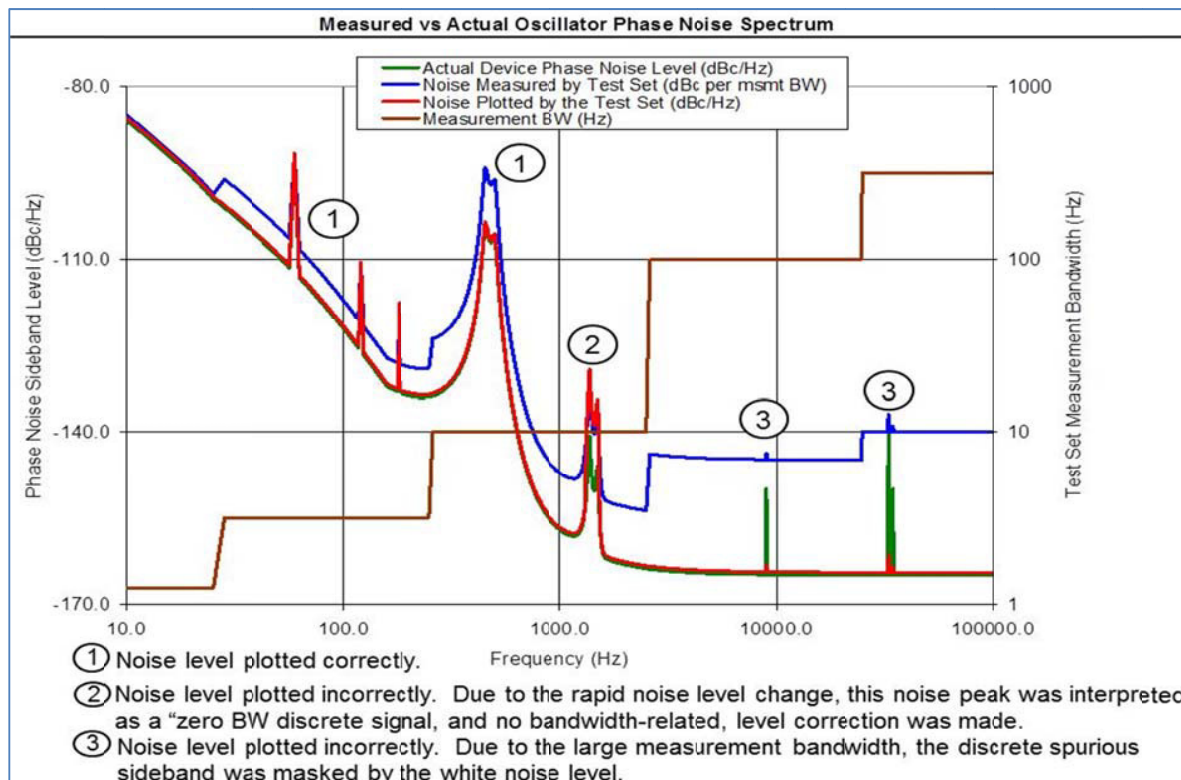


Figure 4-28: Correct and Erroneous Display of Phase Noise Data [45]



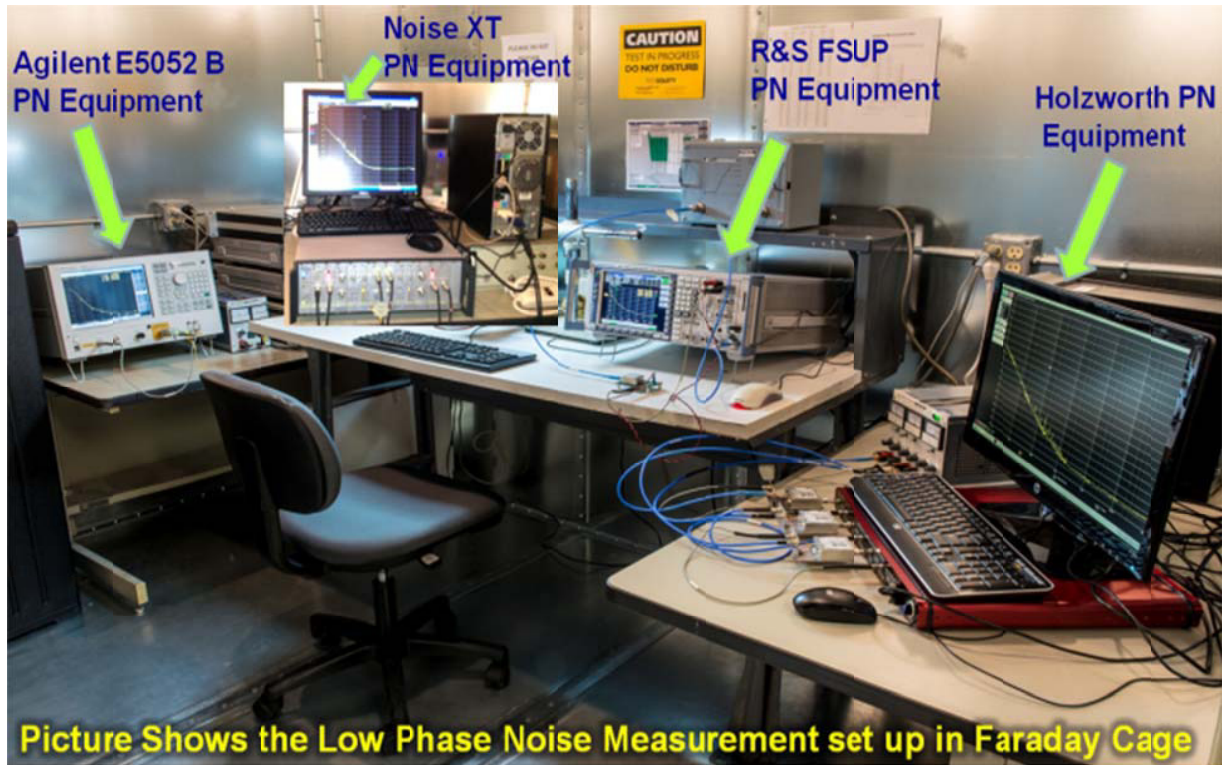


Figure 4-29 – Picture shows Low Phase Noise Measurement Setup in Faraday Cage

### Applying the Cross-Correlation

The old systems have an FFT analyzer for close-in calculations and are slower in speed. Modern equipments use noise-correlation method. The reason why the cross-correlation method became popular is that most oscillators have an output between zero to 15dBm and what is even more important is that only one single source is required. The method with a delay line (Figure 4-30 and Figure 4-31), in reality required a variable delay line to provide correct phase noise numbers as a function of offset. This is important and shown in ref. [3, pp. 148-153, Fig 7.25 and 7.26].

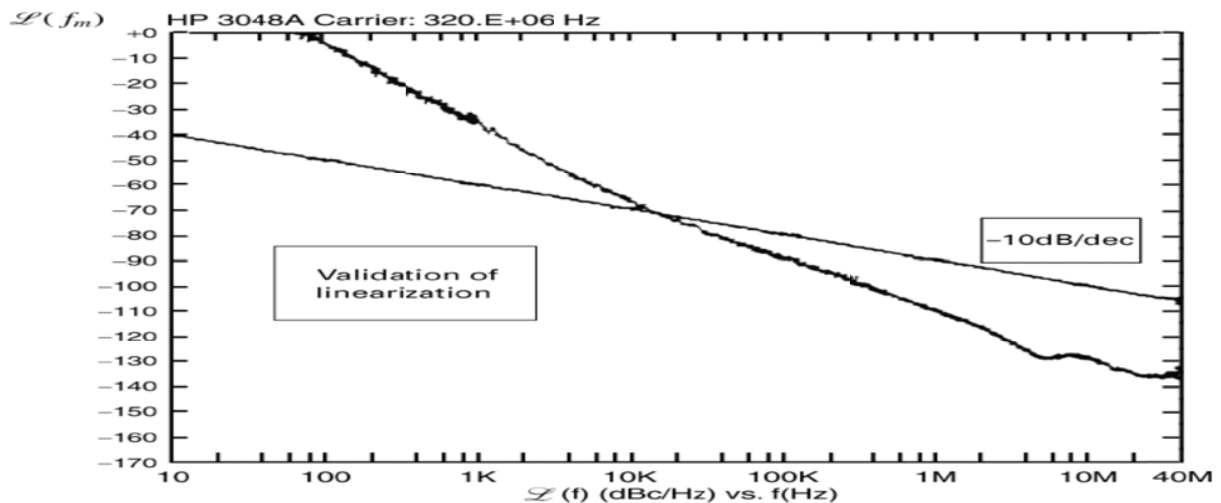


Figure 4-30: Display of a typical phase noise measurement using the delay line principle. This method is applicable only where  $x \ll \sin(x)$ . The measured values above the solid line violate this relationship and therefore are not valid

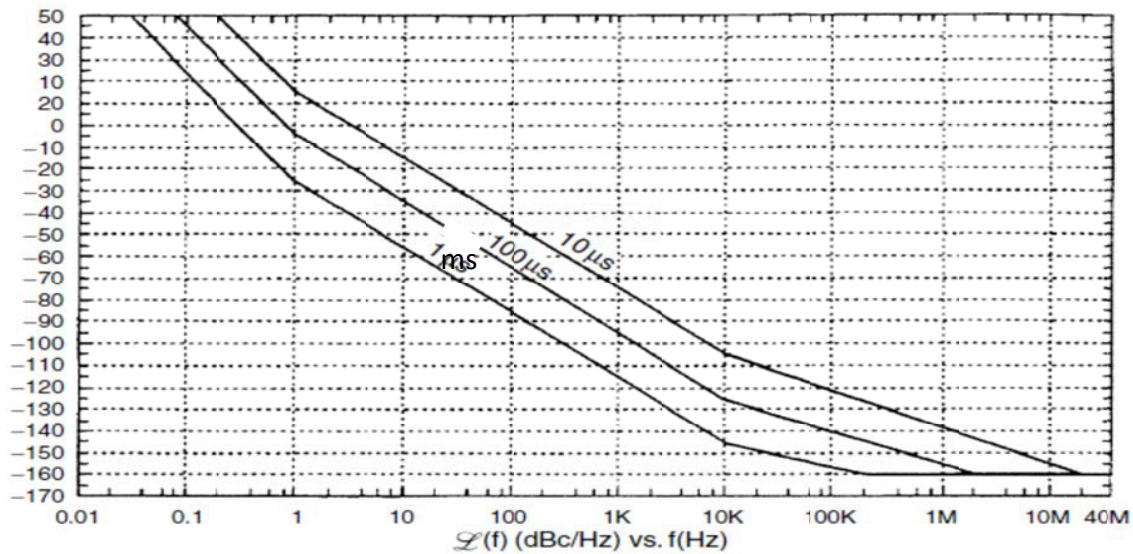


Figure 4-31: Dynamic range as a function of cable delay. A delay line of 1ms is ideal for microwave frequencies.

**Advantages of the noise correlation technique:** (i) Increased speed, Requires less input power, (ii) Single source set-up, (iii) Can be extended from low frequency 1 MHz to 100GHz depending on the internal synthesizer

**Drawbacks of the noise-correlation technique:**

- Different manufacturers have different isolation, so the available dynamic range is difficult to predict
- These systems have a “sweet-spot”, both R&S and Agilent start with an attenuator, not to overload the two channels; 1dB difference in input level can result in quite different measured numbers. These “sweet-spots” are different for each machine.
- The harmonic contents of the oscillator can cause an erroneous measurement [8], that’s why a switchable-low-pass filter like the R&S FSUP-26, Agilent 5052B or its equivalent should be used.
- Frequencies below 200MHz, systems such as Anapico or Holzworth using 2 crystal oscillators instead of a synthesizer must be used. There is no synthesizer good enough for this measurement. Example: Synergy LNXO100 Crystal Oscillator measures about -142dBc/Hz, 100Hz after carrier, limited by the synthesizer of the FSUP and -147dBc/Hz with the Holzworth system. Agilent results are similar to the R&S FSUP, just faster.
- At frequencies like 1MHz off the carrier, these systems gave different results. The R&S FSUP, taking advantage of the “sweet-spot”, measures -183dBc, Agilent indicates -175dBc/Hz and Holzworth measures -179dBc/Hz.

We have not researched the “sweet-spots” for Agilent and Holzworth, but we have seen publications for both Agilent and Holzworth showing -190dBc/Hz far-off the carrier. These were selected crystal oscillators from either Wenzel or Pascall [46]-[47]. Another problem is the physical length of the crystal oscillator connection cable to the measurement system. If the length provides something like “quarter-wave-resonance”, incorrect measurements are possible. The list of disadvantages is quite long and there is a certain ambiguity whether to trust these measurements or can they be repeated.

#### 4.6 Uncertainties in Phase Noise Measurement

The uncertainties in phase noise measurement due to following: Harmonics, Output Load Mismatch, Output Phase Mismatch, Cable Length (Delay), and Equipment Dynamic Range.

RF signals in VCOs, PLLs and synthesizers are characterized by signal power, harmonic content and phase noise; these parameters have to be accurately measured in order to guarantee the system performance. Phase noise measurement methods that use mixers to down-convert the signal to baseband are subject to uncertainty in presence of harmonics.

- Signal Source Analyzer topology
- The conversion characteristic of mixers
- Harmonic Measurement Set-Up
- Effects of fundamental and 3<sup>rd</sup> harmonic down-conversion on PN measurements
- Harmonic Injection Locking Mechanism
- Harmonic-Injection Locked VCO

**4.6.1 Measurement:** This work is to perform analysis of harmonics, phase, and delay and load variations during ultra-low phase noise measurement.

- Commercially available signal source analyzers (SSA) (Figure 4-32) use a phase detector method to measure the phase noise [29] and [30].
- The signal produced by the DUT is mixed with a reference generated by the instrument's internal oscillator and the result is filtered and sampled by an ADC.
- The ADC samples are analyzed and the information is used to extract the phase noise information and to synchronize the internal oscillator.
- Considering practical mixer and oscillator designs used inside the instrument; the harmonics produced by the DUT will also mix with the local oscillator's signal and will produce low frequency components.
- These low frequency components added to the fundamental components sampled by the ADC resulting in measurement errors.
- The phase detection measurement uses a mixer to down-convert the DUT signal.
- The phase noise is extracted from the ADC's samples
- A PLL locks the internal oscillators to the DUT frequency.
- Correlation between the 2 channels reduces the noise floor of the instrument.
- Because mixers are used, DUT harmonics will influence the measurements.

SSA#2 adjusted (harmonically tuned injection locked source): -152dBc/Hz @ 10 kHz (HFSO 100). The filtered signal on both instruments reported as -142.34 and -142.41dBc. The phase noise between 100Hz and 10 kHz offset show little variation (less than 1dB) when 1 filtered, SSA #2 measured on SSA # filtered or SSA#2 unfiltered (Figure 4-33).

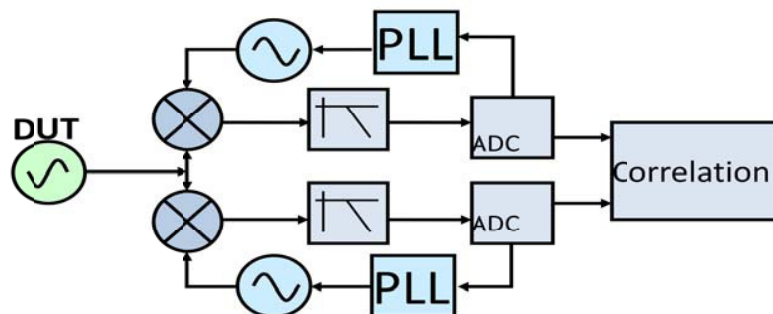


Figure 4-32: A typical Signal source analyzer

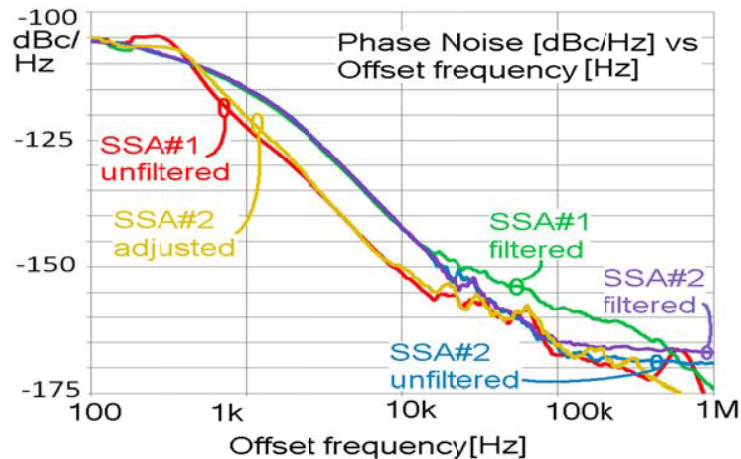


Figure 4-33: Phase noise measurement of 1GHz SAW Oscillator (SSA#1: -151.9dBc/Hz @ 10 kHz for 1GHz carrier frequency, SSA#2: -142.3dBc/Hz @ 10 kHz) HFSO 100

**Conclusion:**

- Phase noise measurement methods that use mixers to down-convert the signal to baseband are subject to uncertainty in presence harmonics.
- If the mixed signals have harmonics, the mechanism that converts the harmonics to baseband will degrade the measurement accuracy.
- We have demonstrated how the harmonics can alter the accuracy of the phase noise measurements based on the mixer characteristics in the test equipment.
- Based on our observations we recommend that phase noise measurements should be performed on clean signals, harmonics level should be kept below -20dBc.
- In the case where harmonic levels are high we recommend that low pass filters be used to suppress the third harmonic to the levels below 20 dBc to get reliable and repeatable phase noise measurements.
- We developed harmonics-injection mechanism to improve the phase noise of SAW, Crystal and Dielectric Resonator Oscillator, including high performance frequency synthesizers.

The low phase noise measurement requires the cross-correlation technique. Special care must be taken for reduction of RF interference, especially while testing 100MHz OCXO in the vicinity of strong interference caused due to noisy neighborhood. The choice of conducting the measurement in Faraday cage is welcome approach to minimize the error due to EMI.

**4.7 Factors Influence Phase Noise Measurement**

It is especially pertinent to production environment, where measurement time and accuracy of each measurement becomes critical. Several test methods and test instruments were investigated. There’s no “one size fits all” solution, but for each frequency range the optimum solutions were propose based on (1) Accuracy, (2) Repeatability, (3) Speed of Test, (4) Operating Range, (5) Cost and (6) Ease of data retrieval. The phase noise of -120dBc/Hz at 1Hz offset from the carrier and better than -190dBc/Hz at far offset from the carrier (10 MHz offset) is a challenge using existing test equipment and methods and also the measured data should be reliable and repeatable. As shown in Figure 4-29, phase noise measurement of 100 MHz OCXO using Agilent E5052B, Rohde & Schwarz FSUP 26, Holzworth, Noise XT, Anapico, for understanding the capability and limitations of the equipments for a given test condition. A survey of some of the more common topologies along with some possible trouble spots helps one to review and keep in mind the advantages and limitations of each approach. Table 4-4 describes the quick summary that addresses phase noise measurement related problems and possible remedy [2].

Table 4-4: Phase noise measurement related problems and possible remedy [2]

Sr. No	PN measurement related issue	Possible remedy
1	Reference noise compromise measurement	Obtain lower noise reference or use cross-correlation and two-independent references
2	System noise compromise measurement	Use higher drive levels and /or higher drive level mixer
3	Broadband okay, but 1/f region too high	Look at a better reference or use carrier suppression or replace mixer
4	System overall noise floor is too high	Change over to a cross-correlation topology.
5	Calibration has errors due to mixer/amplifier gain variations with offset frequency	Use AM/PM calibration standard to measure the system at each offset frequency
6	Residual detection of AM noise from Ref or DUT compromises measurement	See if a mixer with better balance will solve the problem or try to inject AM on the signal and adjust the phase balance (dc offset in the PLL loop) to minimize AM detection or switch to carrier suppression
7	Injection locking is occurring.	Improve the isolation between the sources and the mixer either by using an attenuator or an isolation amplifier. One may also need to look at power supplies or shielding.
8	PLL bandwidth compensating for phase noise close to the carrier.	Reduce the PLL gain or switch to the delay line discriminator approach or measure the amount of attenuation and compensate. This can be done using an AM/PM calibration standard.
9	PLL does not seem to be locking.	Do you have the right tuning voltage for your PLL output matched to the tuning range of your source? Does the source tune far enough to match the frequency of the other source? An external bias to the tune might be necessary to get the source close to the desired operating frequency.
10	PLL still doesn't seem to work	Frequency-divide the sources to a much lower frequency. Since the phase excursion also is divided, much less PLL gain is required and, hence, the PM bias is much less.
11	Final plot has large excursions between the peaks and valleys.	If you don't have a fairly fine line through the noise sections of the plot, the number of averages needs to be increased. See Table 1 for details.
12	Line harmonics are too high or causing excess measurement noise.	Make sure all of the equipment is on the same side of the ac line. Look at using line filters, conditioners, or batteries. Consider using an inside/outside dc block.
13	Dynamic range limitation	It is possible to insert a notch filter between the test object and the analyzing receiver (or spectrum analyzer). This way the carrier can be suppressed while the sideband noise is not much affected.

#### 4.8 Conclusion

The task was for conducting rigorous phase noise measurement using most of the equipment that claims to be measuring below the KT noise floor using cross-correlation techniques. It has been noticed that the simultaneous presence of correlated and anti-correlated signals can lead to gross underestimation of the total signal in cross-spectral analysis. Keep in view of these circumstances, the danger of fall down of cross-correlation techniques used by many equipment companies is high and must be evaluated and used very carefully. The evaluation and analysis described in this thesis was time consuming exercise and for doing so state-of-the art low noise OCXOs and VCXO (voltage controlled SAW oscillators) were developed that measure typically -147 dBc/Hz @ 100 Hz offset for 100 MHz OCXO and -153 dBc/Hz @ 10kHz offset for 1GHz SAW oscillators and exhibit noise floor -178dBc/Hz at far offset on most of the Phase noise measurement equipment. The challenging exercise was to measure better than -200dBc/Hz at 1 MHz offset from the carrier for output power of 20dBm and the measured data should be reliable and repeatable. There are many possibilities in which design engineers can be tricked into false readings or frustrated with the process of trying to achieve a good measurement.

## Chapter 5

### Resonator Dynamics and Applications in oscillators

#### 5.1 Microwave Resonators

A resonator is an element that is capable of storing both frequency-dependent electric and magnetic energy [1]. At microwave frequencies, resonators can take various shapes and forms. The shape of microwave structure affects the field distribution and hence the stored electric and magnetic energies. Potentially, any microwave structure should be capable of constructing a resonator whose resonant frequency is determined by the structure's physical characteristics and dimensions [2]-[6]. A simple example is a series or parallel combination of inductor (L) and capacitor (C), where the magnetic energy is stored in the inductance L and the electric energy is stored in the capacitance C [7]. The resonant frequency of a resonator is the frequency at which the energy stored in electric field equals the energy stored in the magnetic field. As components, resonator allows a selective transmission or blocking of signals and serve as a 1-port or 2-port frequency-determining elements for oscillator application [8].

#### 5.2 Linear Passive 1-Port

A circuit network with a single port is nomenclatured as a 1-port network. Figure 5-1 illustrates the typical schematic and equivalent representation of a 1-port network where signal at the port can be described by the complex amplitudes  $\underline{a}$  and  $\underline{b}$  of the incident and reflected or by the voltage  $\bar{V}$  and  $\bar{I}$  waves. If the relation between  $\bar{V}$  and  $\bar{I}$  or  $\underline{a}$  and  $\underline{b}$  is linear, the 1-port network is defined linear 1-port, and the complex power  $\underline{P}$  flowing into the 1-port can be given in terms of active and reactive power as [7]

$$P = \frac{1}{2} \bar{V} \times \bar{I}^* = P = \frac{1}{2} Z |\bar{I}|^2 = \frac{1}{2} Y^* |\bar{V}|^2 = P_{active} + jP_{reactive} \quad (5.1)$$

For the source-free 1-port network complex power P can be described by

$$P = P_{active} + 2j\omega(W_m - W_e) \quad (5.2)$$

where  $W_m$  and  $W_e$  are the average stored magnetic and electrical energy.

From (5.1) and (5.2) complex impedance Z and admittance Y can be characterized as

$$Z = \frac{P_{active} + 2j\omega(W_m - W_e)}{\frac{1}{2} |\bar{I}|^2} \Rightarrow X = \frac{4\omega(W_m - W_e)}{|\bar{I}|^2} \quad (5.3)$$

$$Y = \frac{P_{active} + 2j\omega(W_e - W_m)}{\frac{1}{2} |\bar{V}|^2} \Rightarrow B = \frac{4\omega(W_e - W_m)}{|\bar{V}|^2} \quad (5.4)$$

where X and B are the reactance and susceptance.

From (5.3) and (5.4)

$$\frac{dX}{d\omega} |\bar{I}|^2 = \frac{dB}{d\omega} |\bar{V}|^2 = 4(W_m - W_e) \quad (5.5)$$

$$W_e = \frac{1}{8} \left( \frac{dX}{d\omega} - \frac{X}{\omega} \right) |\bar{I}|^2 = \frac{1}{8} \left( \frac{dB}{d\omega} + \frac{B}{\omega} \right) |\bar{V}|^2, \quad W_m = \frac{1}{8} \left( \frac{dX}{d\omega} + \frac{X}{\omega} \right) |\bar{I}|^2 = \frac{1}{8} \left( \frac{dB}{d\omega} - \frac{B}{\omega} \right) |\bar{V}|^2 \quad (5.6)$$

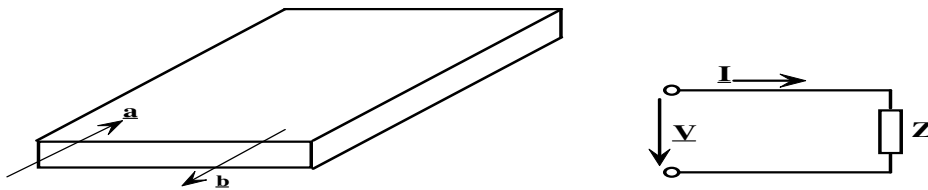


Figure 5-1: 1-port: A typical schematic drawing, and (b) equivalent representation of 1-port network

For passive lossless 1-port network,  $P_{\text{active}} = 0$ , the port is also called as reactive 1-port network, and complex power  $P$  is given by

$$P = 2j\omega(W_m - W_e) \quad (5.7)$$

Since  $W_m$  and  $W_e$  are positive values for passive lossless 1-port network, Foster [9] established the frequency dependence of a reactance as

$$\frac{dX}{d\omega} > \left| \frac{X}{\omega} \right| \quad \text{and} \quad \frac{dB}{d\omega} > \left| \frac{X}{\omega} \right| \quad (5.8)$$

From (5.8), the instantaneous values of  $W_m$  and  $W_e$  oscillate with double the resonance frequency of oscillation, and transformed their stored energy from  $W_m$  to  $W_e$  and vice versa within a quarter of the period of oscillation. However, for  $W_m \neq W_e$  a periodical energy exchange can also occur with an external circuitry (active device that generates gain or negative resistance for stable oscillation) driving the resonator tank circuit. In this case, the reactive power is flowing through the port.

### 5.3 Resonator Networks

The resonator is the core component of the filter and oscillator circuits. The selection of a resonator for oscillator or filter application involves several tradeoffs: insertion loss, Q-factor, size, cost, power-handling requirements etc. The main design considerations of resonators are the resonator size, unloaded Q, spurious performance, and power handling capability. The unloaded Q represents the inherent losses in the resonator. The higher the losses are the lower is the Q value. It is therefore desirable to use resonators with high Q values since this reduces the insertion loss of the tuned resonator and improves its selectivity performance. Microwave resonator networks are grouped into three categories: lumped-element LC resonators, planar resonators (distributed printed transmission line resonators), and three-dimensional (3D) cavity-type resonators. Figures 5-2 and 5-3 show the typical comparison between these resonators. Typically, lumped-element resonators are employed in low-frequency applications. Figure 5-4 (a) shows a lumped-element resonator constructed by using a coil inductor and a chip capacitor. The lumped-element resonator can be printed on a dielectric substrate in the form of a spiral inductor and an inter-digital capacitor as shown in Figure 5-4 (b). As shown in Figure 5-4 (a), lumped element resonators are large but can be made small at microwave frequencies and offer a wide spurious free window; however, they have a relatively low Q value. A typical Q value for lumped LC resonators is between 10 and 50 at 1GHz.

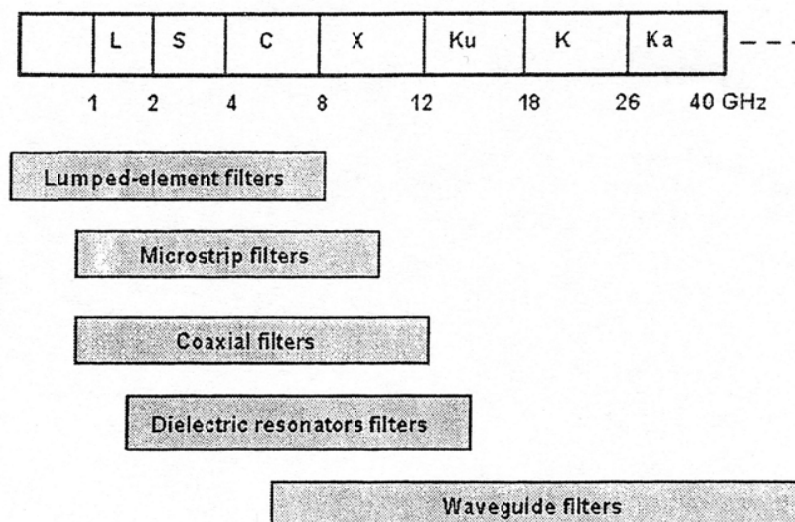


Figure 5-2: Application of the various resonator configurations [8]

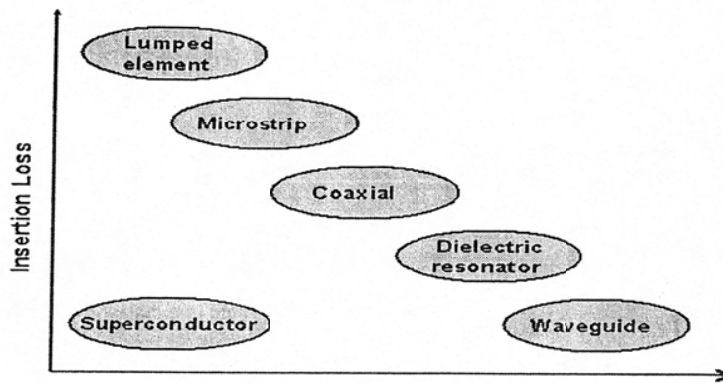


Figure 5-3: A typical relative size and insertion loss of various resonators [8]

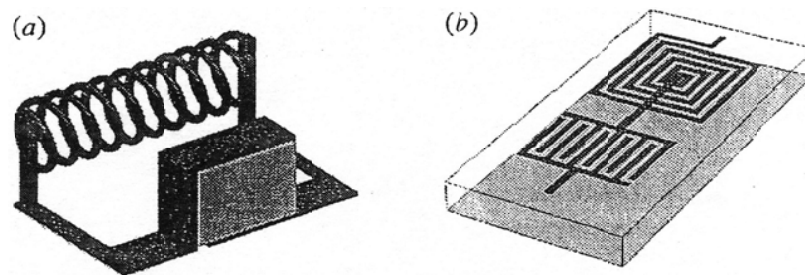


Figure 5-4: Lumped-element resonators realized by (a) coil inductor and chip capacitor, (b) Spiral inductor and inter-digital capacitor [8]

Planar resonators can take the form of a length of a microstrip transmission line, terminated in a short circuit or open circuit, or it can take the form of meander line, folded line, ring resonator, patch resonator or any other configuration [8]-[11]. Any printed structure effectively acts as a resonator whose resonant frequency is determined by the resonator's dimensions, substrate dielectric constant and substrate height, which can be used for covering both narrowband and broadband tuning characteristics of frequency source applications for current and later generation communication systems [12]. Figure 5-5 shows typical planar resonators, usually employed in wideband, compact, and low-cost signal source and filter applications. The typical Q value for planar resonators is about 50-300 at 1GHz [13]-[17]. The state-of-the-art planar resonator circuit using superconductor techniques can exhibit typical Q values ranging from 20,000 to 50,000 at 1 GHz but not a cost-effective alternative because resonator circuitry needs to be cooled down to very low temperatures, below 90 degree Kelvin [18].

In contrast to lumped LC resonators, which have only one resonant frequency, printed transmission line resonators can support an infinite number of electromagnetic field configurations or resonant modes. The spurious performance of a resonator is determined by how close the neighboring resonant modes are to the operating mode. The neighboring resonant modes act as spurious modes interfering with the fundamental resonant mode's performances. It is therefore desirable to increase the spurious free window of the resonator in order to improve the filter out-of-band rejection performance. The resonant modes in planar resonators exist in the form of a single mode representing one electric resonator or in the form of degenerate modes (i.e., modes having the same resonance frequency with different field distributions) [8]. These degenerate modes allow the realization of two electric resonators (dual-mode resonators) or three electric resonators (triple-mode resonators) within the same physical resonator. Example of dual-modes is  $TE_{11}$  modes, which exists in circular waveguide cavities [10]-[13];  $HE_{11}$  modes, which exist in dielectric resonators [14]-[15]; or  $TM_{11}$ , which exist in circular or square patch



microstrip resonators [16]. Cubic waveguide cavities and cubic dielectric resonators can support triple modes [17]. The key advantage of operating in dual-mode or triple mode configuration is size reduction. However, these modes do have an impact on the unloaded Q, spurious performance, and power handling capability of the cavity resonator. A summary of the features of each mode of operation is given in Table 5.1. Figure 5-6 shows the typical 3-D cavity resonators such as coaxial, waveguide, and dielectric resonators, offer a Q value ranging from 3000 to 30,000 at 1GHz, but not amenable for integration in RFIC/MMIC technology [19]-[20]. In addition to this, 3-D resonators are bulky in size; however, they offer very high Q values; in addition, they are capable of handling high RF power levels.

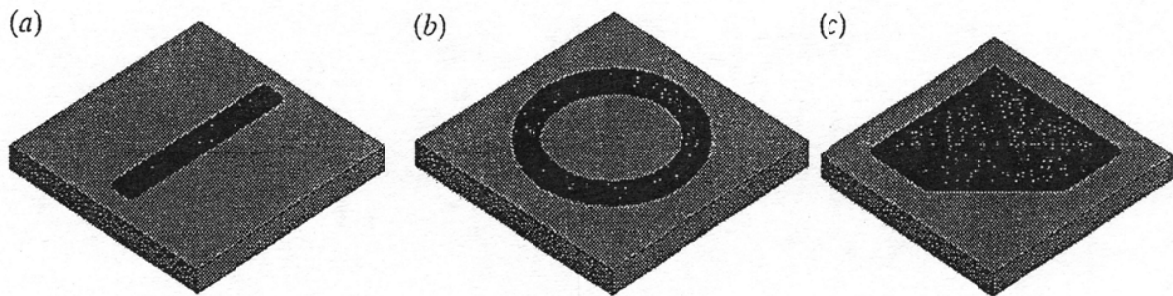


Figure 5-5: Examples of microstrip resonator configurations: (a) half-wavelength resonator, (b) Spiral inductor and interdigital capacitor [8]

Table 5.1: Comparison between various modes of operation

Parameter	Single-Mode	Dual-Mode	Triple-Mode
Size	Large	Medium	Small
Spurious Response	Good	Fair	Fair
Unloaded Q	High	Medium	Medium
Power handling capability	Low	Medium	High
Design complexity	Low	Medium	High

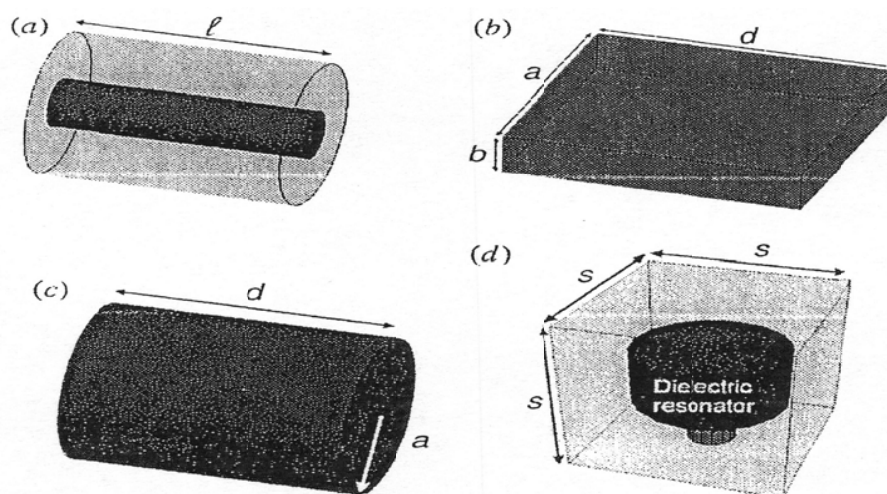


Figure 5-6: Examples of 3-D cavity resonators (a) coaxial resonator (b) rectangular waveguide resonator (c) circular waveguide resonator (d) dielectric resonator [8]

## 5.4 Resonator Q-factor

Energy dumping in electromagnetic resonance gives the definition of Q-factor for passive networks, and is  $2\pi$  times the ratio of the reactively stored energy to the energy dissipated in a unit cycle [16].

$$Q_{loaded} = 2\pi \left[ \frac{\text{average reactive energy stored}}{\text{energy dissipated in unit cycle}} \right] = \omega_o \left[ \frac{W_T}{P_T} \right] \Rightarrow \frac{1}{Q_{loaded}} = \left[ \frac{1}{Q_{unloaded}} + \frac{1}{Q_{external}} \right] \quad (5.9a)$$

$$Q_{loaded} = Q_{unloaded} \quad (\text{loosely - coupled resonator}) \quad (5.9b)$$

$$Q_{loaded} = Q_{external} \quad (\text{tightly - coupled resonator}) \quad (5.9c)$$

$$\text{where} \quad Q_{unloaded} = \omega_o \left[ \frac{W_T}{P_i} \right] \quad (5.9d)$$

$$Q_{external} = \omega_o \left[ \frac{W_T}{P_e} \right] \quad (5.9e)$$

$$P_T = P_i + P_e \quad (5.9f)$$

where  $\omega_o$  is the resonant frequency,  $W_T$  is average stored energy, and  $P_T$  is the total power loss in watts,  $P_i$  and  $P_e$  are the dissipated energies due to the resonator's internal losses and the external loadings, respectively .

From (5.9b) and (5.9c), the loaded Q-factor is equal to unloaded Q-factor ( $Q_{loaded} = Q_{unloaded}$ ) for loosely coupled resonator, the internal losses are more dominant as compared to external loss; conversely, in a tightly coupled resonator, the external loading is much more dominant, thus  $Q_{loaded} = Q_{external}$  [17]-[20]

This definition (Eq.5.9a-Eq.5.9e) is valid for circuit involving passive and active devices or energy sources until the open-loop gain approaches to unity. In positive feedback filters and multipliers or active inductors, frequency selectivity can be as sharp as desired by increasing the open-loop gain and this exceeds the limit, oscillation takes place in the circuit. In such a state, the above definition of Q factor is no longer valid because it runs into infinity. Therefore, unified definition of Q is necessary to evaluate the performance of active circuits even during the transient state of regenerative circuit (oscillators). The quality factor (Q-factor) is the most important parameter of a resonant circuit for low phase noise oscillator (signal sources) application. The Q-factor is a versatile index of resonator and oscillator performance but its definition is not unified.

Ohira [21] did rigorous analysis of the characterization of a Q-factor for general RF components and circuits. Two common definitions of Q-factor are discussed for the understanding about the dynamics of this parameter on autonomous circuit (oscillators). The first definition is based on field theory, which relates the Q-factor to frequency-selectivity, energy-storage and dissipation in resonance for stable passive circuit, whereas the second one relates to resonance for unstable active circuits (oscillators, regenerative circuits). The energy-based definition is ambiguous when a resonator has no energy storage elements, as in the case of ring or distributed oscillators. The two common definitions of Q factor (a) for passive resonant circuit and (b) for active resonant circuit (described in section 5.4.1 and 5.4.2) are explained in a step by step process by Ohira et.al [21]-[28].

### (a) Definition of Q Factor for Passive Resonant Circuit

- (i) Fractional 3-dB bandwidth
- (ii) Phase-to-frequency slope
- (iii) Stored-to-dissipated energy ratio

### (b) Definition of Q Factor for Active Resonant Circuit

- (i) Noise spectrum Basis
- (ii) Source-Pull/Push Basis
- (iii) Injection locking Basis

### 5.4.1 Definition of Q Factor for Passive Resonant Circuit

- (i) Fractional 3-dB bandwidth
- (ii) Phase-to-frequency slope
- (iii) Stored-to-dissipated energy ratio

#### 5.4.1.1 Fractional 3-dB bandwidth

Figure 5-7 shows the typical 1-port resonator and impedance versus frequency response function for the evaluation of fractional 3-dB bandwidth and quality factor, which is based on frequency selectivity of resonator, and filter networks.

Steps for Q-factor:

1. Get  $|Z(\omega)|^2$  in frequency domain
2. Find  $\omega_0$  by solving  $\frac{d}{d\omega} |Z(\omega)|^2 = 0$
3. Find  $\omega_1$  and  $\omega_2$  by solving  $|Z(\omega_1)|^2 = |Z(\omega_2)|^2 = \frac{1}{2} |Z(\omega_0)|^2$
4. Q factor from the definition of frequency selectivity:  $Q = \frac{\omega_0}{\omega_2 - \omega_1} = \frac{f_0}{f_2 - f_1}$

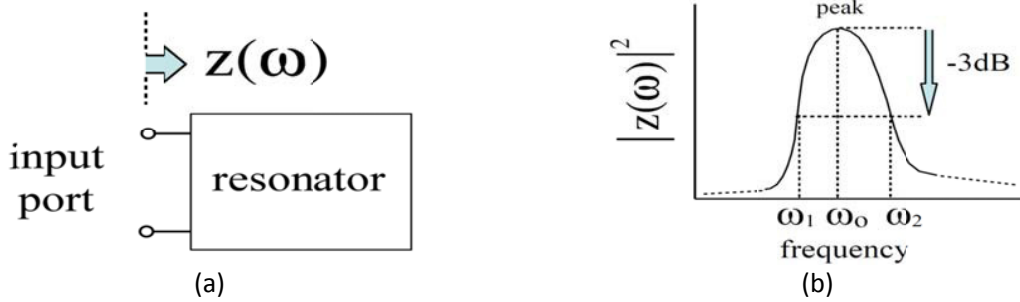


Figure 5-7: Examples of 1-port resonators (a) schematic of 1-port resonator (b) impedance versus frequency response [21]

#### 5.4.1.2 Phase-to-Frequency Slope

An alternative definition of Q-factor is based on resonator's transfer function in the frequency domain. The transfer function is a complex function which governs the relationship between the input and output as

$$H(j\omega) = A(\omega)\exp[j\phi(\omega)] \quad (5.10)$$

Where  $A(\omega)$  and  $\phi(\omega)$  are the amplitude and phase response of the resonator. The Q-factor in terms of the transfer function is given by [34]

$$Q = \frac{\omega_0}{2} \left| \sqrt{\left(\frac{\partial A(\omega)}{\partial \omega}\right)^2 + \left(\frac{\partial \phi(\omega)}{\partial \omega}\right)^2} \right|_{\omega=\omega_0} \quad (5.11)$$

$$Q \approx \frac{\omega_0}{2} \left| \frac{\partial \phi(\omega)}{\partial \omega} \right|_{\omega=\omega_0} \quad \text{for} \quad \left| \frac{\partial A(\omega)}{\partial \omega} \right|_{\omega=\omega_0} \rightarrow 0 \quad (5.12)$$

From (5.12), the approximation  $\left(\left|\frac{\partial A(\omega)}{\partial \omega}\right|_{\omega_0} = 0\right)$  is because variation in phase is more predominant as compared to amplitude variation in well-designed oscillator circuits. From (5.12), the shift in frequency ( $\Delta\omega$ ) from  $\omega_0$  can cause large rate of change in phase if the Q-factor is high, therefore forcing the frequency to return to  $\omega_0$ . Figure 5-8 shows the typical 1-port resonator and phase response function for the evaluation of rate of change of phase and quality factor.

Steps for Q-factor (neglects amplitude slope):

1. Get  $\phi(\omega)$  in frequency domain  $\phi(\omega) = \angle[Z(\omega)]$ ,  $\phi'(\omega) = \frac{d}{d\omega} \angle[Z(\omega)]$

2. Find  $\omega_0$  by solving

$$\varphi(\omega_0) = 0$$

3. Calculate  $Q$  factor from

$$Q = \frac{\omega_0}{2} \left| \frac{\partial \varphi(\omega)}{\partial \omega} \right|_{\omega=\omega_0} = \frac{\omega_0}{2} |\varphi'(\omega_0)|$$



Figure 5-8: Examples of 1-port resonators (a) schematic of 1-port resonator (b) phase versus frequency response [22]

### 5.4.1.3 Stored-to-Dissipated Energy Ratio

Electromagnetic field inside ideal resonator network stores energy at the resonant frequency, where equal storage of electrical and magnetic energies occurs. However, in reality, part of the stored energy is dissipated due to losses across the loads, thereby reducing the resonator's frequency selectivity [23]. Figure 5-9 shows the typical 1-port resonator for the evaluation of stored energy rate and quality factor.

Steps for Q-factor

1. Estimate input power and stored energy in each component

$$P(\omega) = \frac{1}{2} \text{Re}\{v_{ex} i_{ex}^*\}, \quad W_e(\omega) = \frac{1}{4} \sum_k^{cap} C_k |v_k|^2, \quad W_m(\omega) = \frac{1}{4} \sum_k^{ind} L_k |i_k|^2$$

2. Find  $\omega_0$  by solving  $W_e(\omega_0) = W_m(\omega_0)$

3. Calculate  $Q$  factor from  $Q = \omega_0 \frac{W_e(\omega_0) + W_m(\omega_0)}{P(\omega_0)}$

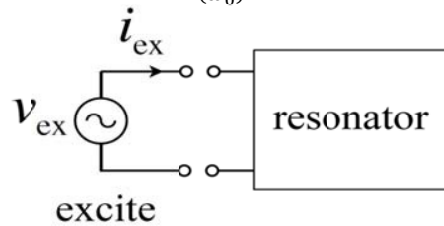


Figure 5-9: 1-port resonator (for the estimation of stored energy in each resonating component) [24]


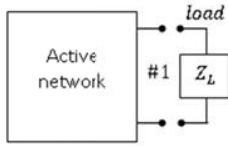
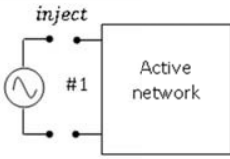
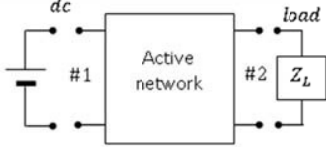
The above method for the evaluation of the Q-factor valid for massive resonator, this definition is no longer valid when the 1-port circuit is unstable and oscillates (example: regenerative active circuits) [25]. Therefore, new definition of Q-factor for active circuit is required for both analysis and synthesis of the oscillator circuits.

### 5.4.2 Definition of Q Factor for Active Resonant Circuit: Sensitive for Oscillation

Table 5.2 describes the formulation of oscillation-stability condition for active network under various conditions.

- (i) Noise spectrum Basis
- (ii) Source-Pull/Push Basis
- (iii) Injection locking Basis

Table 5.2: Types of Unstable Active Network [26]

Unstable Active Network (closed-loop gain $\geq 1$ ) Sensitive to Oscillations ( $\omega = \omega_0$ )		
Type	Scheme	condition of oscillation-stability
NINO (No Input- No Output)		Power and energy equilibrium condition stability criterion $W_e(\omega_0) = W_m(\omega_0) \rightarrow \Delta W = 0$
NISO (No Input-Signal Output)		Sideband noise load pulling
SINO (Signal Input-No Output)		Injection locking
SISO (Signal Input-Signal Output)		Source pushing

NINO (No Input-No Output) active network obeys the power and energy balance equilibrium condition. Thus, elements for NINO active network confine to inside and transact energy for equilibrium condition, the complex power  $\Psi(\alpha, \omega)$  can be defined as [27]

$$\begin{aligned} \underbrace{\Psi(\alpha, \omega)}_{\text{complex power}} &= \frac{1}{2} [v_1(\omega)i_1^*(\omega) + v_2(\omega)i_2^*(\omega) + v_3(\omega)i_3^*(\omega) + \dots + v_K(\omega)i_K^*(\omega)] \\ &= P_a - P_r + 2j\omega W_e - 2j\omega W_m = \Delta P + 2j\omega \Delta W \end{aligned} \quad (5.13)$$

From (5.13), the equilibrium state for oscillation condition of zero port (NINO) active circuit can be formulated by [28]-[29]

$$\underbrace{[\Psi(\alpha, \omega)]_{\alpha=\alpha_0, \omega=\omega_0}}_{\text{complex power}} = 0 \rightarrow \text{Equilibrium state for oscillation condition} \quad (5.14)$$

From (5.14), once equilibrium point is reached ( $\alpha = \alpha_0, \omega = \omega_0$ ), the important thing is whether the zero port active circuit (NINO) remains at steady-state at that point ( $\alpha = \alpha_0, \omega = \omega_0$ ) against the small perturbation ( $\alpha = \alpha_0 + \delta\alpha, \omega = \omega_0 + \delta\omega$ ), while maintaining the complex power balance [ $\Psi(\alpha = \alpha_0 + \delta\alpha, \omega_0 + \delta\omega) = 0$ ], i.e.

$$\frac{\partial \Psi(\alpha, \omega)}{\partial \alpha} \delta\alpha + \frac{\partial \Psi(\alpha, \omega)}{\partial \omega} \delta\omega = 0 \Rightarrow \delta\omega = \left( \frac{d\phi}{dt} - j + \frac{d\alpha}{dt} \right) \quad (5.15)$$

From (5.15), the instantaneous frequency deviation ( $\delta\omega$ ) depends not only on phase change in time but also as logarithmic amplitude change for imaginary part, can be described by [24]

$$\frac{\partial \Psi(\alpha, \omega)}{\partial \alpha} \delta\alpha + \left( \frac{d\phi}{dt} - j + \frac{d\alpha}{dt} \right) \frac{\partial \Psi(\alpha, \omega)}{\partial \omega} = 0 \quad (5.16a)$$

$$\text{Imag} \left[ \frac{\partial \Psi(\alpha, \omega)}{\partial \alpha} \left( \frac{\partial \Psi(\alpha, \omega)}{\partial \omega} \right)^{-1} \right] = \frac{1}{\delta\alpha} \frac{d\alpha}{dt} \quad (5.16b)$$

stability criterion  $\delta\alpha \frac{d\alpha}{dt} < 0$  at  $(\alpha_0, \omega_0)$

$$\underbrace{\operatorname{Im} \left\{ \frac{\partial \psi}{\partial \omega} \frac{\partial \psi^*}{\partial \alpha} \right\}_{\alpha=\alpha_0, \omega=\omega_0}}_{\text{discriminant}} > 0 \text{ Or } \underbrace{\begin{vmatrix} \frac{\partial \Delta P}{\partial \alpha} & \frac{\partial \Delta P}{\partial \omega} \\ \frac{\partial \Delta U}{\partial \alpha} & \frac{\partial \Delta U}{\partial \omega} \end{vmatrix}_{\alpha=\alpha_0, \omega=\omega_0}}_{\text{Jacobian discriminant}} > 0 \quad (5.17)$$

#### 5.4.2.1 Active NISO Circuit Q-Factor (Noise Spectrum Basis)

Fig. 5-10 shows the typical 1-port oscillator circuit model, as depicted both active and passive components are embedded in a black box, and represented by the  $Z(\omega)$  without the load (R).

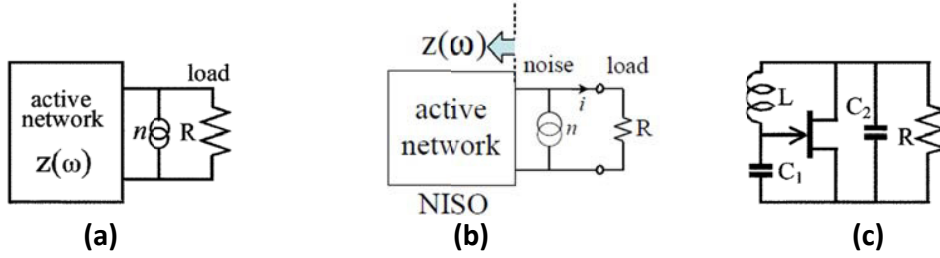


Figure 5-10: Shows the typical 1-port oscillator: (a) General model (b) Equivalent noise model of NISO, and (c) a Colpitts example representing NISO model

Assuming the noise current source in parallel, this yields single sideband (SSB) power on the spectrum. The power observed when the noise source is solely connected to load R is given by

$$P_n = \left[ \frac{R}{2} \right] |n|^2 \quad (5.18)$$

The output sideband noise power  $P_{SSB}(\omega)$  can be described by [28]

$$P_{SSB}(\omega) = \left[ \frac{R}{2} \right] \left| \frac{z(\omega)n}{R+z(\omega)} \right|^2 = P_n \left| \frac{z(\omega)}{R+z(\omega)} \right|^2 \quad (5.19)$$

$$[z(\omega) + R]_{\omega \rightarrow \omega_0} = 0 \text{ (at equilibrium state the resonance frequency } \omega = \omega_0) \quad (5.20)$$

Frequency deviation ( $\omega = \omega_0 + \delta\omega$ ) expands output impedance  $z(\omega)$  as

$$z(\omega) = z(\omega_0) + \frac{dz(\omega_0)}{d\omega_0} \delta\omega + \dots \quad (\text{Taylor expansion}) \quad (5.21)$$

$$|z(\omega)|^2 = \left| z(\omega_0) + \frac{dz(\omega_0)}{d\omega_0} \delta\omega \right|^2 \approx |z(\omega_0)|^2 \quad (5.22)$$

From (5.19)-(5.22)

$$P_{SSB}(\omega) = P_n \left| \frac{z(\omega)}{z(\omega) - z(\omega_0)} \right|^2 = P_n \left| \frac{z(\omega_0) + \frac{dz(\omega_0)}{d\omega_0} \delta\omega}{\frac{dz(\omega_0)}{d\omega_0} \delta\omega} \right|^2 = P_n \left| 1 + \frac{z(\omega_0)}{\frac{dz(\omega_0)}{d\omega_0} \delta\omega} \right|^2 \approx P_n \left| \frac{z(\omega_0)}{z'(\omega_0) \delta\omega} \right|^2 \quad (5.23)$$

From [34]

$$P_{SSB}(\omega) = \left[ \frac{\omega_0}{2Q\delta\omega} \right]^2 [P_n] \Rightarrow Q = \frac{\omega_0}{2} \left| \frac{z'(\omega_0)}{z(\omega_0)} \right| \quad (5.24)$$

From (5.24)

$$\left\{ \begin{array}{l} Q(pz) = \frac{\omega_0}{2} \left| \frac{pz'(\omega_0)}{pz(\omega_0)} \right| = \frac{\omega_0}{2} \left| \frac{z'(\omega_0)}{z(\omega_0)} \right| = Q(z) \rightarrow \text{Scaling operation} \\ Q(z^{-1}) = Q(y) = \frac{\omega_0}{2} \left| \frac{y'(\omega_0)}{y(\omega_0)} \right| = \frac{\omega_0}{2} \left| \frac{z'(\omega_0)}{z(\omega_0)} \right| = Q(z) \rightarrow \text{Inverse operation} \\ Q(z^*) = \frac{\omega_0}{2} \left| \frac{z'(\omega_0)^*}{z(\omega_0)^*} \right| = \frac{\omega_0}{2} \left| \frac{z'(\omega_0)}{z(\omega_0)} \right| = Q(z) \rightarrow \text{Conjugate operation} \end{array} \right\} \quad (5.25)$$

$P_{SSB}(\omega)$  expressed in (5.25) represent the Q-factor of oscillator that includes both active and passive devices embedded in the 1-port black box shown in Figure 5-10. In other words, the above formula is valid for any active network, regardless of oscillator topology that is comprised of types of active devices for providing closed loop gain  $\geq 1$  and compensating the loss of resonator. From (5.25), Q is invariant against the three operations (scaling, inverse, and conjugate) [29].

#### 5.4.2.2 Active NISO Circuit Q-Factor (Reflection coefficient $\Gamma(\omega)$ Basis)

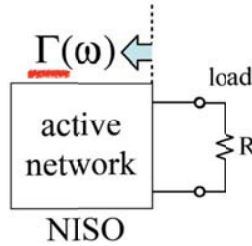


Figure 5-11: Shows the typical 1-port oscillator

$$\text{From (5.25)} \quad Q = \frac{\omega_0}{2} \left| \frac{z'(\omega_0)}{z(\omega_0)} \right|, \quad z'(\omega) = \left[ \frac{dz(\omega)}{d\omega} \right] \quad (5.26)$$

The reflection coefficient  $\Gamma(\omega)$  for 1-port network shown in Figure 5-11 can be given by [21]

$$\Gamma(\omega) = \left| \frac{z(\omega) - z_0}{z(\omega) + z_0} \right| \Rightarrow \Gamma'(\omega) = \left| \left\{ \frac{[z(\omega) - z_0] z'(\omega) - [z(\omega) + z_0] z'(\omega)}{[z(\omega) + z_0]^2} \right\} \right|, \quad \Gamma'(\omega) = \left[ \frac{d\Gamma(\omega)}{d\omega} \right] \quad (5.27)$$

$$\text{From (5.26) and (5.27)} \quad Q = \omega_0 \left| \frac{\Gamma'(\omega)}{1 - \Gamma^2(\omega_0)} \right| \quad (5.28)$$

#### 5.4.2.3 Active NISO Circuit Q-Factor (Energy Basis)

Figure 5-12 represents the general model of circuits without port for understanding the energy equilibrium dynamics, even though this kind of configuration does not have practical usefulness. Considering such a system when oscillation takes place Fig. 5-12(a) can be illustrated as zero-port closed-circuit network Fig. 5-12(b) for the analysis of equilibrium and stability criterion.

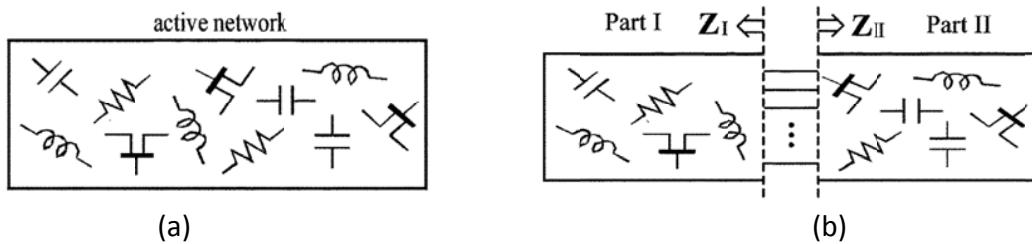


Figure 5-12: A typical Zero-port oscillator: (a) General model, and (b) Separated into two parts [26]

The total complex power of circuit represented in Figure 5-13 can be described as

$$\psi(\omega) = \frac{1}{2} (+v_1 i_1^* + v_2 i_2^* + v_3 i_3^* \dots v_k i_k^*) \quad (5.29)$$

$$\psi(\omega) = \Delta P + j2\omega \Delta E \quad (5.30)$$

$$\Delta P = P_a - P_r \quad (5.31)$$

$$\Delta E = E_e - E_m \quad (5.32)$$

where  $v_k$  and  $i_k$  are sinusoidal voltage and current, respectively, at the  $k^{\text{th}}$  branch in the system. Asterisk indicates a complex conjugate.

Active devices generate RF power  $P_a$ , and this power is dissipated in resistive elements  $P_r$ . Some portion of the energy is reactively stored in inductive ( $E_m$ ) and capacitive ( $E_e$ ) elements.  $\Delta P = 0$ ,  $\Delta E = 0$  (Energy interaction must be completed within the system, since there is no transaction between inside and outside in circuit shown in Figure 5-12). Therefore, both real and imaginary parts of  $\psi(\omega)$  must vanish, which implies need for balance in both power and energy. For circuit designers who are familiar with impedance parameters rather than with terms of energy, it is worthwhile to translate the above criterion into impedance domain. To carry this out, the zero-port oscillator is divided into two pieces as shown in Fig. 5-12(b). As illustrated in Figure 5-12, Parts I and II are interconnected in multiplex, and therefore they are each regarded as a multi-port network with impedance matrix  $[Z_I]$  or  $[Z_{II}]$  respectively. From Kirchhoff's law:

$$v = z_I i = -z_{II} i, \quad Z = Z_I + Z_{II} \Rightarrow |Z| = 0 \text{ at resonance for multi-connected active circuits} \quad (5.33)$$

From (5.29)

$$\psi(\omega) = \frac{1}{2}(v_I^T i^* - v_{II}^T i^*) = \frac{1}{2}i^T (Z_I^T + Z_{II}^T) i^* = \frac{1}{2}i^T Z^T i^* = \frac{1}{2}i^T (|Z| \tilde{Z}^{-1})^T i^* = \frac{1}{2}|Z| i^T \tilde{Z}^{-T} i^* \quad (5.34)$$

where superscripts  $^T$  and  $^{-T}$  stand for transposition and inverse transposition, and tilde  $\sim$  designates co-factor matrix. Note that term  $v_{II}^T i^*$  for part II has negative polarity due to opposite direction of currents.

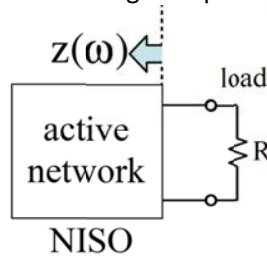


Figure 5-13: Shows the typical 1-port oscillator [21]

Loaded one-port oscillator with  $R$  can be considered as a subset of zero-port if the load  $R$  in circuit as shown in Figure 5-13 is embedded in  $Z(\omega)$  so that resulting impedance is  $Z = [Z(\omega) + R]$ . From (5.34)

$$\psi(\omega) = \frac{1}{2}|Z| i^T \tilde{Z}^{-T} i^* = \frac{1}{2}\{Z(\omega) + R\} |i|^2 = -\frac{Z(\omega)}{2} |i|^2 - P_{out}(\omega) \quad (5.35)$$

where  $P_{out}(\omega)$  is power output to the load. At the equilibrium, oscillation condition forces  $\psi(\omega_0) = 0$ . However, its frequency slope remains finite as  $z(\omega_0) \psi'(\omega_0) = -z'(\omega_0) P_{out}(\omega_0)$ . From (5.29)-(5.35), the expression of  $Q$  is given by [29]-[32]

$$Q = \frac{\omega_0}{2} \left| \frac{\psi'(\omega_0)}{P_{out}(\omega_0)} \right| = \frac{\omega_0}{P_{out}} \sqrt{\frac{1}{4} \left( \frac{\partial \Delta P}{\partial \omega} \right)^2 + \left( \frac{\omega_0 \partial \Delta W}{\partial \omega} \right)^2} \quad (5.36)$$

Considering that the power dissipation takes place only in the load and neglect frequency slope of the active devices, i.e.,  $P_{out} = P_r$  and  $\frac{\partial P_a}{\partial \omega} = 0$ , (5.36) can be written as

$$Q = \frac{\omega_0}{P_r} \sqrt{\frac{1}{4} \left( \frac{\partial P_r}{\partial \omega} \right)^2 + \left( \frac{\omega_0 \partial \Delta W}{\partial \omega} \right)^2} \quad (5.37)$$

Equation (5.37) agrees with Equation (8) in [10] and Equation (2) in [11]. Assuming  $\left| \frac{\partial P_r}{\partial \omega} \right| \ll \left| \frac{\omega_0 \partial \Delta W}{\partial \omega} \right|$ ,  $Q$ -factor can be given by [30]

$$Q \cong \frac{\omega_0^2}{P_r} \left| \frac{\partial W_e}{\partial \omega} - \frac{\partial W_m}{\partial \omega} \right| \quad (5.38)$$



This agrees with [3, eq. (31)]. If we further additionally assume special relation  $(2\omega_0 - \omega)U_m = \omega U_e$  or  $\omega U_m = (2\omega_0 - \omega)U_e$  at  $\omega = \omega_0$ . The Q equation ultimately reduces to

$$Q = \omega_0 \frac{(W_e + W_m)}{P_r} \quad (5.39)$$

Equation (5.39) concurs with the energy-dumping phenomena of Q-factor.

#### 5.4.2.4 Active SISO Circuit Q-Factor (Source-Push and Load-Pull Basis)

Figure 5-14 shows the typical 2-port oscillator model (SISO) for the derivation of Q-factor taking into account the DC source pushing and RF load pulling effect. For high performance oscillator circuit, Q-factor plays important role to make the circuit insensitive of pushing and pulling [32].



Figure 5-14: A typical 2-port oscillator model

The steady-state oscillation condition for oscillator circuit shown in Figure (5-14) can be expressed as

$$Z_{out}(\omega, V) + Z_L(\omega) = 0 \quad (5.40)$$

$$[R_{out}(\omega, V) + R_L(\omega)] + j[X_{out}(\omega, V) + X_L(\omega)] = 0 \quad (5.41)$$

From (5.41)  $R_{out}(\omega, V)$  must exhibit a negative resistance while oscillation exists because  $R_L$  is passive load and intrinsically positive resistance. The source pushing on oscillation frequency can be formulated by perturbation techniques:

$$\omega \rightarrow \omega_0 + \Delta\omega \quad \text{and} \quad V \rightarrow V_0 + \Delta V \quad (5.42)$$

where  $|\Delta\omega| \ll \omega_0$  and  $|\Delta V| \ll V_0$

With the help of Taylor series expansion, Equation (5.42) can be expanded as [31]

$$Z_{out}(\omega_0, V_0) + Z_{out}^{\omega}(\omega_0, V_0)\Delta\omega + Z_{out}^V(\omega_0, V_0)\Delta V + \dots + Z_L(\omega_0) = 0 \quad (5.43)$$

$$\text{where} \quad Z_{out}^{\omega}(\omega, V) = \frac{\partial Z_{out}(\omega, V)}{\partial \omega}, \quad Z_{out}^V(\omega, V) = \frac{\partial Z_{out}(\omega, V)}{\partial V} \quad (5.44)$$

Neglecting higher order partial differential term,

$$Z_{out}(\omega_0, V_0) + Z_L(\omega_0) = 0 \quad (5.45)$$

$$Z_{out}^{\omega}(\omega_0, V_0)\Delta\omega + Z_{out}^V(\omega_0, V_0)\Delta V = 0 \quad (5.46)$$

$$\Delta\omega = \frac{Z_{out}^V(\omega_0, V_0)}{Z_{out}^{\omega}(\omega_0, V_0)} \Delta V \quad (5.47)$$

Normalizing the frequency deviation ( $\Delta\omega$ ) and voltage deviation ( $\Delta V$ ) on both sides of Equation (5.48) by their original values ( $\omega_0, V_0$ ):

$$\frac{\Delta\omega}{\omega_0} = \frac{1}{\omega_0 V_0} \frac{Z_{out}^V(\omega_0, V_0)}{Z_{out}^{\omega}(\omega_0, V_0)} \Delta V \quad (5.48)$$

$$\left| \frac{\Delta\omega}{\omega_0} \right| = \frac{V_0}{\omega_0} \left| \frac{Z_{out}^V(\omega_0, V_0)}{Z_{out}^{\omega}(\omega_0, V_0)} \right| \left| \frac{\Delta V}{V_0} \right| = \frac{1}{Q} \left| \frac{\Delta V}{V_0} \right| \quad (5.49)$$

$$\left| \frac{\Delta\omega}{\omega_0} \right|_{SSB} = \frac{1}{Q} \left| \frac{\Delta V}{V_0} \right| \quad (5.50)$$

$$\left| \frac{2\Delta\omega}{\omega_o} \right|_{DSB} = \frac{1}{Q} \left| \frac{\Delta V}{V_o} \right| \quad (5.51)$$

On the left-hand side of (5.51) frequency deviation is doubled to measure double sideband (upper and lower sideband frequency from the carrier). The coefficient shown in (5.51) can be expressed as 1/Q because the frequency deviation ( $\Delta\omega$ ) must be inversely proportional to a certain figure of merit for sustained oscillation condition. From (5.47) and (5.51), the constant Q can be defined as a dimension free positive scalar quantity [32]

$$Q_{source-pull} = \frac{\omega_o}{2V_o} \left| \frac{Z_{out}^{\omega}(\omega, V)}{Z_{out}^V(\omega, V)} \right|_{(\omega=\omega_o, V=V_o)} \quad (5.52)$$

From the duality and superposition theorem,

$$Q_{source-pull} = \frac{\omega_o}{2V_o} \left| \frac{Y_{out}^V(\omega, V)}{Y_{out}^{\omega}(\omega, V)} \right|_{(\omega=\omega_o, V=V_o)} \quad (5.53)$$

Equation (5.52) and (5.53) is nomenclature as a source-pull Q-factor of oscillator circuit. Similarly, load-pull Q-factor can be formulated to estimate the frequency stability due to load variation. From (5.40), the condition for stable oscillation for constant voltage V can be expressed as

$$Z_{out}(\omega, g_m) + Z_L(\omega) = 0 \quad (5.54)$$

$$[R_{out}(\omega, g_m) + R_L(\omega)] + j[X_{out}(\omega, g_m) + X_L(\omega)] = 0 \quad (5.55)$$

From (5.55),  $R_{out}(\omega, g_m)$  must exhibit a negative resistance while oscillation exists because  $R_L$  is passive load with intrinsically positive resistance. The load-pulling on oscillation frequency can be formulated by perturbation of frequency and transconductance of the active device [32]. For stable oscillation, transconductance of the active device must be adjusting to maintain the gain-to-loss equilibrium condition due to the variation in the load impedance  $Z_L(\omega)$ . These phenomena can be defined as [33]

$$Z_L(\omega) \rightarrow Z_{Lo}(\omega) + \Delta Z_L, \quad \omega \rightarrow \omega_o + \Delta\omega, \quad g_m \rightarrow g_{mo} + \Delta g \quad (5.56)$$

where  $|\Delta\omega| \ll \omega_o$  and  $|\Delta g| \ll g_{mo}$

From (5.55) and (5.56), Taylor series expansion:

$$Z_{out}(\omega_o, g_{mo}) + Z_{out}^{\omega}(\omega_o, g_{mo})\Delta\omega + Z_{out}^g(\omega_o, g_{mo})\Delta g + \dots + Z_{Lo}(\omega_o) + \Delta Z_L = 0 \quad (5.57)$$

$$\text{where } Z_{out}^{\omega}(\omega, g_m) = \frac{\partial Z_{out}(\omega, g_m)}{\partial \omega}, \quad Z_{out}^g(\omega, g_m) = \frac{\partial Z_{out}(\omega, g_m)}{\partial g} \quad (5.58)$$

Neglecting higher order partial differential term,

$$Z_{out}(\omega_o, g_{mo}) + Z_{Lo}(\omega_o) = 0 \quad (5.59)$$

$$Z_{out}^{\omega}(\omega_o, g_{mo})\Delta\omega + Z_{out}^g(\omega_o, g_{mo})\Delta g + \Delta Z_L = 0 \quad (5.60)$$

From (5.60), for a given perturbation in load  $\Delta Z_L$ , there are two unknown variants ( $\Delta\omega, \Delta g$ ), the solution of (5.60) can be formulated by applying complex conjugate function (\*)

$$Z_{out}^{\omega *}(\omega_o, g_{mo})\Delta\omega + Z_{out}^g *(\omega_o, g_{mo})\Delta g + \Delta Z_L^* = 0 \quad (5.61)$$

From (5.60) and (5.61)

$$\begin{bmatrix} \Delta\omega \\ \Delta g \end{bmatrix} = - \begin{bmatrix} Z_{out}^{\omega}(\omega_o, g_{mo}) & Z_{out}^g(\omega_o, g_{mo}) \\ Z_{out}^{\omega *}(\omega_o, g_{mo}) & Z_{out}^g *(\omega_o, g_{mo}) \end{bmatrix}^{-1} \begin{bmatrix} \Delta Z_L \\ \Delta Z_L^* \end{bmatrix} \quad (5.62)$$

$$\begin{bmatrix} \Delta\omega \\ \Delta g \end{bmatrix} = -\frac{1}{J} \begin{bmatrix} Z_{out}^g *(\omega_o, g_{mo}) & -Z_{out}^g(\omega_o, g_{mo}) \\ -Z_{out}^{\omega *}(\omega_o, g_{mo}) & Z_{out}^{\omega}(\omega_o, g_{mo}) \end{bmatrix}^{-1} \begin{bmatrix} \Delta Z_L \\ \Delta Z_L^* \end{bmatrix} \quad (5.63)$$

where [J] denotes Jacobian determinant [28]

$$J = \begin{vmatrix} Z_{out}^{\omega}(\omega_o, g_{mo}) & Z_{out}^g(\omega_o, g_{mo}) \\ Z_{out}^{\omega*}(\omega_o, g_{mo}) & Z_{out}^{g*}(\omega_o, g_{mo}) \end{vmatrix} = 2j\gamma \quad (5.64)$$

$$\gamma = \text{Im}[Z_{out}^{\omega}(\omega_o, g_{mo})Z_{out}^{g*}(\omega_o, g_{mo})] \quad (5.65)$$

$$\Delta\omega = -\frac{1}{j} [Z_{out}^{g*}(\omega_o, g_{mo})\Delta Z_L - Z_{out}^g(\omega_o, g_{mo})\Delta Z_L^*] = \frac{1}{\gamma} \text{Im}[Z_{out}^g(\omega_o, g_{mo})\Delta Z_L^*] \quad (5.66)$$

$$\Delta\omega = \frac{1}{\gamma} |Z_{out}^g(\omega_o, g_{mo})\Delta Z_L| \sin|\phi - \theta| \quad (5.67)$$

Where

$$Z_{out}^g(\omega_o, g_{mo}) = |Z_{out}^g(\omega_o, g_{mo})e^{j\phi}| \quad (5.68)$$

$$\Delta Z_L = |\Delta Z_L|e^{j\theta} \quad (5.69)$$

Figure 5-15 shows the load impedance locus on a complex plane. From (5.57), frequency shift  $\Delta\omega$  depends on the phase of the load deviation  $\Delta Z_L$ . Revolving  $\theta$  from zero to  $2\pi$  as shown on a dashed circumference in Figure 5-15, the frequency shift reaches its maximum, given by [31]

$$|\Delta\omega|_{max} = \left\{ \frac{|\Delta Z_L|}{\gamma} \right\} |Z_{out}^g(\omega_o, g_{mo}) \sin \frac{\pi}{2}|_{(\phi-\theta)=\frac{\pi}{2}} \quad (5.70)$$

Normalizing the deviations in Equation (5.70) on both sides by their original values as

$$\left| \frac{2|\Delta\omega|_{max}}{\omega_o} \right|_{DSB} = \frac{1}{Q} \left| \frac{\Delta Z_L}{Z_{Lo}} \right| \quad (5.71)$$

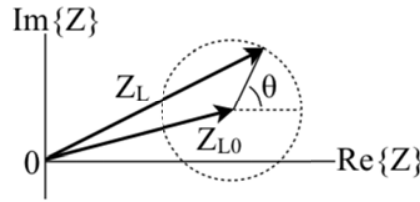


Figure 5-15: Deviated load impedance locus on a complex plane

On the left-hand side of (5.71) frequency deviation is doubled to measure double sideband (upper and lower sideband frequency from the carrier). The coefficient shown in Equation (5.71) can be expressed as  $1/Q$  because the frequency deviation ( $\Delta\omega$ ) must be inversely proportional to a certain figure of merit for sustained oscillation condition. From (5.48) and (5.52), the constant  $Q$  can be defined as a dimension free positive scalar quantity [32]

$$Q = \frac{\omega_o}{2} \left| \frac{\gamma(\omega_o, g_{mo})}{Z_{Lo}Z_{out}^g(\omega_o, g_{mo})} \right| \quad (5.72)$$

From (5.59) and (5.72)

$$Q = \frac{\omega_o}{2} \left| \frac{\gamma(\omega_o, g_{mo})}{Z_{out}^{\omega}(\omega_o, g_{mo})Z_{out}^g(\omega_o, g_{mo})} \right| = \frac{\omega_o}{2} \left| \frac{\text{Im}[Z_{out}^{\omega}(\omega_o, g_{mo})Z_{out}^{g*}(\omega_o, g_{mo})]}{Z_{out}^{\omega}(\omega_o, g_{mo})Z_{out}^g(\omega_o, g_{mo})} \right| \quad (5.73)$$

$$Q_{load-pull} = \frac{\omega_o}{2} \left| \frac{\text{Im}[Z_{out}^{\omega}(\omega, g_m)Z_{out}^{g*}(\omega, g_m)]}{Z_{out}^{\omega}(\omega, g_m)Z_{out}^g(\omega, g_m)} \right|_{(\omega=\omega_o, g_m=g_{mo})} \quad (5.74)$$

$$Q_{load-pull} = \frac{\omega_o}{2} \left| \frac{\text{Im}[Y_{out}^{\omega}(\omega, g_m)Y_{out}^{g*}(\omega, g_m)]}{Y_{out}^{\omega}(\omega, g_m)Y_{out}^g(\omega, g_m)} \right|_{(\omega=\omega_o, g_m=g_{mo})} \quad (Y \equiv Z^{-1}) \quad (5.75)$$

Equations (5.52) and (5.75) give insightful view about pushing and pulling characteristics of an oscillator for the optimization of the oscillator design for stable operation against those variations.

### 5.4.2.5 Active SIBO Circuit Q-Factor (Injection Locking Basis)

Figure 5-16 shows the typical injection-locked oscillator employing 2-port active device: (a) general model, (b) typical Colpitts oscillator, and (c) equivalent representation of (a).

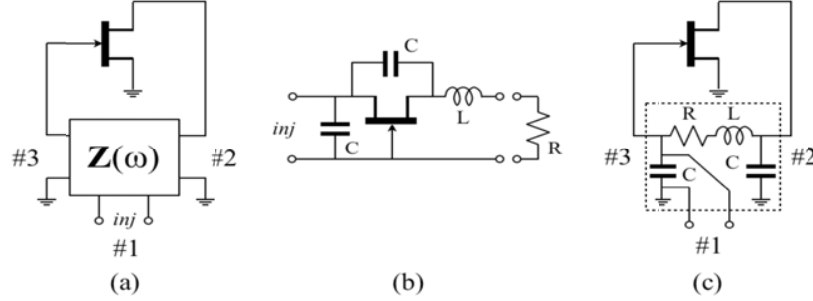


Figure 5-16: Injection-locked oscillator employing 2-port active device: (a) general model, (b) typical Colpitts oscillator, and (c) equivalent representation of (a) [26]

The impedance matrix of Figure 5-17 can be given by [27, 32]

$$Z(\omega) = \begin{bmatrix} Z_{11}(\omega) & Z_{12}(\omega) & Z_{13}(\omega) \\ Z_{21}(\omega) & Z_{22}(\omega) & Z_{23}(\omega) \\ Z_{31}(\omega) & Z_{32}(\omega) & Z_{33}(\omega) \end{bmatrix} = \begin{bmatrix} R_{11}(\omega) & R_{12}(\omega) & R_{13}(\omega) \\ R_{21}(\omega) & R_{22}(\omega) & R_{23}(\omega) \\ X_{31}(\omega) & X_{32}(\omega) & X_{33}(\omega) \end{bmatrix} + \begin{bmatrix} X_{11}(\omega) & X_{12}(\omega) & X_{13}(\omega) \\ X_{21}(\omega) & X_{22}(\omega) & X_{23}(\omega) \\ X_{31}(\omega) & X_{32}(\omega) & X_{33}(\omega) \end{bmatrix} \quad (5.76)$$

**Case I (no injected current at port 1),  $i_{inj} = i_1(\omega) = 0$**

From (5.76)

$$v_3(\omega) = R_{32}(\omega)i_2(\omega) + jX_{32}(\omega)i_2(\omega) = [R_{32}(\omega) + jX_{32}(\omega)]i_2(\omega) \quad (5.77)$$

$$i_2(\omega) = -g_m(\omega)v_3(\omega) \quad (5.78)$$

For stable oscillation to take place at  $\omega \rightarrow \omega_o$ , neither  $v_3$  nor  $i_2$  should vanish ( $v_3 \neq 0$  and  $i_2 \neq 0$ ).

From (5.77) and (5.78)

$$[1 + g_m(\omega)R_{32}(\omega)]_{\omega \rightarrow \omega_o} = 0, \quad [X_{32}(\omega)]_{\omega \rightarrow \omega_o} = 0 \quad (5.79)$$

Where  $\omega_o$  = free running oscillation frequency

**Case II [injected-locked state:  $i_{inj} = i_1(\omega) \neq 0$ ]**

$$i_{inj} = i_1(\omega) = I_1 e^{j\theta_1} \quad (\text{Current represented in exponent form}) \quad (5.80)$$

$$i_2(\omega) = -g_m(\omega)v_3(\omega) = I_2 e^{j\theta_2} \quad (\text{Current represented in exponent form}) \quad (5.81)$$

From (5.76)

$$v_3(\omega) = [R_{31}(\omega) + jX_{31}(\omega)]I_1 e^{j\theta_1} + [R_{32}(\omega) + jX_{32}(\omega)]I_2 e^{j\theta_2} \quad (5.82)$$

From (5.80), (5.81), and (5.82)

$$[R_{31}(\omega)\sin\Delta\theta + jX_{31}(\omega)\cos\Delta\theta]I_1 + X_{32}(\omega)I_2 = 0 \quad (5.83)$$

Where  $\Delta\theta = \theta_1 - \theta_2$  is the phase difference between the currents at two ports.

The injection locked state oscillation frequency  $\omega$  is slightly offset ( $\Delta\omega$ ) from the free running frequency  $\omega_o$ , the impedance matrix (8) can be expanded with the help of Taylor series.

$$R_{31}(\omega) \cong R_{31}(\omega_o) + \Delta\omega \frac{d}{d\omega} [R_{31}(\omega)]_{\omega \rightarrow \omega_o} = R_{31}(\omega_o) + \Delta\omega R'_{31}(\omega_o) \quad (5.84)$$

$$X_{31}(\omega) \cong X_{31}(\omega_o) + \Delta\omega \frac{d}{d\omega} [X_{31}(\omega)]_{\omega \rightarrow \omega_o} = X_{31}(\omega_o) + \Delta\omega X'_{31}(\omega_o) \quad (5.85)$$

$$X_{33}(\omega) \cong X_{33}(\omega_o) + \Delta\omega \frac{d}{d\omega} [X_{33}(\omega)]_{\omega \rightarrow \omega_o} = X_{33}(\omega_o) + \Delta\omega X'_{33}(\omega_o) \quad (5.86)$$

$$X_{32}(\omega) \cong X_{32}(\omega_o) + \Delta\omega \frac{d}{d\omega} [X_{32}(\omega)]_{\omega \rightarrow \omega_o} = X_{32}(\omega_o) + \Delta\omega X'_{32}(\omega_o) \quad (5.87)$$

With the help of Taylor series expansion, based on  $\omega \rightarrow \omega_o + \Delta\omega$  and free running oscillation condition  $[X_{32}(\omega)]_{\omega \rightarrow \omega_o} = 0$ ;  $|\Delta\omega| \ll \omega_o$

$$\text{From (5.76)-(5.87)} \quad \Delta\omega \cong - \left[ \frac{R_{31}(\omega_o) \sin\Delta\theta + X_{31}(\omega_o) \cos\Delta\theta}{X'_{32}(\omega_o)} \right] \frac{I_1}{I_2} \quad (5.88)$$

$$\Delta\omega \cong - \left[ \frac{\sqrt{R_{31}^2(\omega_o) + X_{31}^2(\omega_o)}}{X'_{32}(\omega_o)} \sin\phi \right] \frac{I_1}{I_2} = - \frac{|Z_{31}(\omega_o)| \sin\phi}{X'_{32}(\omega_o)} \frac{I_1}{I_2} \quad (5.89)$$

where  $\phi = \Delta\theta + \tan^{-1} \left[ \frac{X_{31}(\omega_o)}{R_{31}(\omega_o)} \right]$ , assuming phase difference  $\Delta\theta$  is not constrained i.e.  $(0 \leq \Delta\theta < 2\pi) \rightarrow 0 \leq |\sin\phi| \leq 1$ , from (5.89)

$$0 \leq |\Delta\omega| \leq \left| \frac{Z_{31}(\omega_o)}{X'_{32}(\omega_o)} \right| \frac{I_1}{I_2} \quad (5.90)$$

Eq. (5.90) is identical to Adler's injection-lock range Eq. (13b) ref [31] and Eq. (10.90) ref [33]

$$0 \leq |\Delta\omega| \leq \left[ \frac{\omega_o}{2Q} \right] \left[ \frac{I_1}{I_2} \right] \quad (5.91)$$

$$\text{From (5.90) and (5.91)} \quad Q = \frac{\omega_o}{2} \left| \frac{X'_{32}(\omega_o)}{Z_{31}(\omega_o)} \right|, \quad \text{where } X'_{32}(\omega_o) = \frac{d}{d\omega} [X_{32}(\omega)]_{\omega \rightarrow \omega_o} \quad (5.92)$$

The circuit shown in Figure 5-16(c), Q-factor can be given by

$$Q = \frac{\omega_o}{2} \left| \frac{X'_{32}(\omega_o)}{Z_{31}(\omega_o)} \right| \quad (5.93)$$

$$\text{where } Z_{31}(\omega_o) = \left\{ \frac{1}{j\omega C + \frac{1}{R + j\omega L + \frac{1}{j\omega C}}} \right\}, \quad \text{and } X_{32}(\omega) = \frac{1}{\omega C} \left\{ \frac{LC\omega^2 - 2}{\omega^2 C^2 R^2 + (LC\omega^2 - 2)^2} \right\} \quad (5.94)$$

From (5.79), (5.93) and (5.94)

$$X'_{32}(\omega_o) = \frac{d}{d\omega} [X_{32}(\omega)]_{\omega \rightarrow \omega_o} = \frac{d}{d\omega} \left[ \frac{1}{\omega C} \left\{ \frac{LC\omega^2 - 2}{\omega^2 C^2 R^2 + (LC\omega^2 - 2)^2} \right\} \right]_{\omega = \omega_o} \quad (5.95)$$

$$Q = \frac{\omega_o}{2} \left| \frac{X'_{32}(\omega_o)}{Z_{31}(\omega_o)} \right| = \frac{\omega_o L}{R} \left( \frac{L}{L + 2CR^2} \right)^{1/2} \quad (5.96)$$

## 5.5 Resonator Design Criteria for Low Phase Noise Oscillator Applications

The Leeson phase noise equation is given by [33]

$$\mathcal{L}(f_m) = 10 \log \left\{ \left[ 1 + \frac{f_o^2}{(2f_m Q_L)^2 \left(1 - \frac{Q_L}{Q_o}\right)^2} \right] \left( 1 + \frac{f_c}{f_m} \right) \frac{FkT}{2P_o} \right\} \quad (5.97)$$

where  $\mathcal{L}(f_m)$  = ratio of sideband power in a 1Hz bandwidth at  $f_m$  to total power in dB,  $f_m$  = frequency offset from the carrier,  $f_o$  = center frequency,  $f_c$  = flicker frequency,  $Q_L$  = loaded Q of the tuned circuit,  $Q_o$  = unloaded Q of the tuned circuit,  $F$  = noise factor,  $kT = 4.1 \times 10^{-21}$  at 300 K (room temperature),  $P_o$  = average power at oscillator output .

From (5.97), phase noise in oscillator is inversely proportional to the square of the resonator loaded Q-factor, indicating that insertion loss of the resonator is linked with figure of merit (FOM) as [31]-[33]

$$[Resonator]_{FOM} = 10 \log \left( \frac{I.L}{Q_L^2} \right) \quad (5.98)$$

From (5.98), for low phase noise, designer should optimize the resonator FOM. At microwave frequencies, resonators can be passive or active depends upon operating frequencies and applications.

### 5.5.1 Passive Lumped LC Resonator

Figure 5-17 shows the typical doubly loaded shunt resonator. Lumped or quasi-lumped resonator will oscillate at  $f_o = \frac{1}{2\pi\sqrt{LC}}$ .

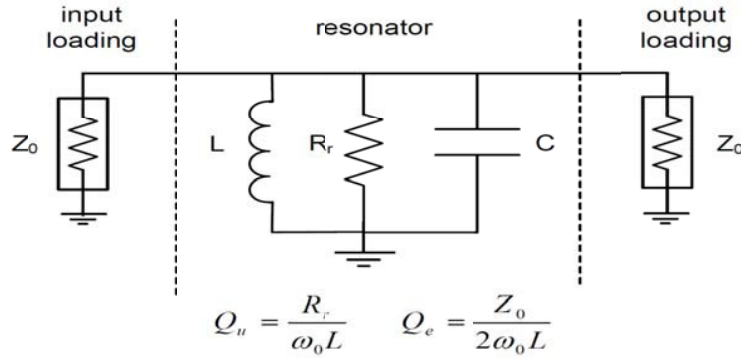


Figure 5-17: A typical doubly loaded shunt resonator [35]

The  $S_{21}$  (transmission gain) can be given for doubly loaded shunt resonator (Figure 5-17) is given by [35]

$$S_{21}(\omega) = \frac{2}{\left( \frac{Z_o}{\frac{1}{R_r} + \frac{1}{Z_o} + \frac{1}{Z_o}} \right) + jZ_o \left( \omega C - \frac{1}{\omega L} \right)} \quad (5.99)$$

$$Q = \frac{\omega_0}{2} \left| \frac{\partial \varphi(\omega)}{\partial \omega} \right|_{\omega=\omega_0} \quad \text{where } (\varphi(\omega) = \angle S_{21}) \quad (5.100)$$

$$I.L = \left| \frac{1}{S_{21}} \right|_{\omega=\omega_0}^2 = \left( 1 + \frac{Z_o}{2R_r} \right)^2 = \left( 1 + \frac{Q_e}{Q_u} \right)^2 \quad (5.101)$$

$$\text{From (5.98), } [Resonator]_{FOM} = 10 \log \left( \frac{I.L}{Q_L^2} \right) = 10 \log \left[ \left( 1 + \frac{Q_e}{Q_u} \right)^2 \left( \frac{1}{Q_e} + \frac{1}{Q_u} \right)^2 \right] \quad (5.102)$$

$$\frac{d[Resonator]_{FOM}}{dQ_e} = 0 \Rightarrow (Q_u = Q_e) \Rightarrow Q_{loaded} = \frac{Q_{unloaded}}{2} \quad (5.103)$$

### 5.5.2 Planar Transmission Line Resonator

Planar transmission line resonators are formed by using microstrip lines of various wavelengths ( $\lambda/4$ ,  $\lambda/2$ ,  $\lambda$ ), where  $\lambda$  is the guided wavelength at the fundamental resonant frequency  $f_o$ . The quarter wavelength resonator  $\lambda/4$  long resonates at the fundamental frequency  $f_o$  and at its multiple frequencies of  $f = (2n - 1) f_o$  for  $n = 2, 3, 4, 5$ . The half wavelength resonator  $\lambda/2$  long resonates at the fundamental frequency  $f_o$  and at its multiple frequencies of  $f = n f_o$  for  $n = 2, 3, \dots$  etc. This type of resonator can be shaped into open-loop resonator. The full wavelength resonator,  $\lambda$  long resonates at the fundamental frequency  $f_o$  and at other frequencies of  $f = n f_o$  for  $n = 2, 3, \dots$  etc. This type of resonator is commonly found in the form of ring or closed loop resonators with a median circumference  $2\pi r = \lambda$ , where  $r$  is the radius of the ring. Because of its symmetrical geometry a resonance can occur in either of 2 orthogonal coordinates. This type of transmission line resonator has a distinct feature; it can support a pair of degenerate modes that have the same resonant frequencies but orthogonal field distributions. This feature is utilized to design dual mode filters.

### 5.5.2.1 Microstripline Resonator

A microstrip resonator is a transmission line resonator that can have any geometrical structure that is able to contain at least one oscillating EM field [48]-[51]. There are many forms of microstrip resonators; however, its large physical size can present a drawback. Hence, there is strong interest to miniaturize such resonators particularly for oscillator applications. Miniaturization of microstrip resonators can be achieved by using either high dielectric constant substrates or meander the lines to create a folded microstrip resonator. Figure 5-18 shows the typical square open loop resonator, which can be obtained by folding a straight open resonator showed in Figure 5-18(a) [48]. Due to the corners and the fringing capacitance between the open ends, a rigorous calculation of the electromagnetic fields in the square resonator is impractical. However, it is possible to study the main characteristics of the resonant modes of the square open loop resonator by analogy to those of the straight resonator. This qualitative analysis can shed some light on the behavior of the resonator with minimum effort. Comparison of the conclusions drawn, using this approach can then be used for validation against the actual distribution of the electromagnetic fields obtained with the aid of full wave simulators.

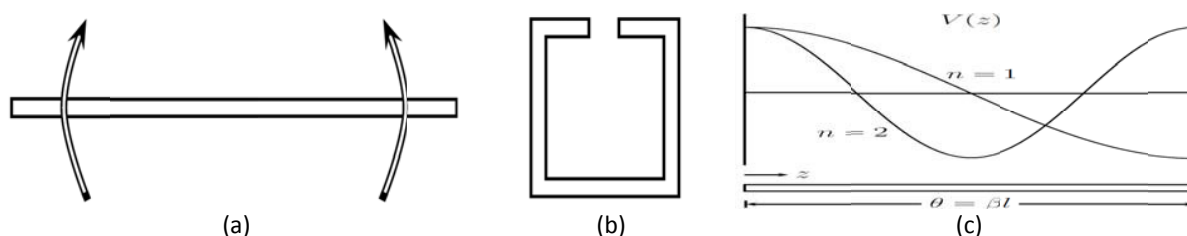


Figure 5-18: The square open loop resonator obtained by folding a straight open resonator: (a) straight open resonator, (b) square open loop resonator, and (c) voltage distribution in a straight open resonator [48, 50]

Figure 5-19 shows 2-ways of exciting square open loop resonator. As an interesting consequence, the fundamental resonance ( $n=1$ ) as shown in Figure 5-18 (c) or any other odd mode resonance cannot be excited at the center of the resonator. This phenomenon translates to the square open loop resonator as is shown in Figure 5-19. The  $Q_{ex}$  (external quality factor) of the square open loop resonator obtained by tapping into the resonator depends on the voltage level at the tapping point at resonance. If the tapping point coincides with a voltage null, then no coupling achieved between the resonator and the external circuit and the resulting quality factor is very large. Similarly, if the voltage at the tapping point is high then the external quality factor will be low. Referring to the voltage distribution of the conventional and the miniaturized resonator; it is possible to predict that in the case of the conventional resonator the external Q will decrease rapidly as the tapping point is moved away from the voltage null at the center of the resonator. The detailed analysis about square open loop resonator is discussed in the extended version of the research document as a part of this thesis [ref. 47, Ch-5].



Figure 5-19: 2-ways of exciting square open loop resonator (a) Excitation of the resonator in a null of the fundamental mode (b) Excitation of the resonator symmetrically with respect to both open ends [50]

### 5.5.3 Active Resonator

In general, Q factor of the resonator degrades with the increase in frequency because of decrease in skin depth, described by [34]-[36]

$$Q = \eta[f]^{-1/2} \quad (5.104)$$

where  $Q$  is the quality factor and  $\eta$  is the constant.

The energy dissipation in the passive resonator and radiation leads to degradation in the quality factor of the resonator tank. To facilitate desired oscillation signal, resonator is loosely coupled and loaded with the external circuit comprised of active devices and peripheral components for compensating the energy losses. Using loose coupling can reduce the loading of the resonator but results in higher attenuation. In practice, the unloaded  $Q$  factor of the resonator ' $Q_u$ ' is finite, and gets degraded after coupling to the external oscillator circuit. Therefore, even an ideal resonator with zero inner losses and  $Q_u \rightarrow \infty$  will exhibit finite loaded  $Q$  factor ' $Q_l$ '. The unloaded  $Q$  factor of the passive resonator is given by

$$Q_{u(PR)} = \frac{2\pi f_0 E}{W} = \frac{2\pi f_0 C}{G} \quad (5.105)$$

where  $f_0$ , stands for frequency,  $E$  is the energy stored in passive resonator (PR),  $W$  is energy lost in one oscillation period,  $C$  and  $G$  correspond to parallel equivalent circuit (capacitance  $C$  and conductance  $G$ ) of the PR respectively. To overcome the limitation of the  $Q$  factor of the passive resonator (PR), active resonator topology have been reported which offers promising alternative for high spectral pure signal sources [35]. The novel AR (active resonator) offers a solution for increasing  $Q_u$  and  $Q_l$  of the passive resonator (PR) by compensating the inner losses. This can be achieved by means of gain block (active circuit) coupled to the passive resonator (PR) networks. Figure 5-18 shows the typical example of AR circuit, where PR is coupled to a transmission line. As shown in Figure 5-18, active circuits create negative conductance  $-|G_n|$ , which adds to the positive conductance of the resonator  $G$ , thereby, gives effective conductance of the AR (active resonator) as

$$G_a = -|G_n| + G \quad (5.106)$$

From (5.106), unloaded  $Q$  factor ' $Q_u$ ' of the AR is given by

$$Q_{u(PR)} = \frac{2\pi f_0 C}{G_a} \Rightarrow Q_{u(AR)} > Q_{u(CPR)} \quad |G_a| < |G| \quad (5.107)$$

From (5.106) and (5.107), AR can offer high quality factor where PR suffer from losses due to loss resistance and radiations. In practical applications,  $G_a$  should be greater than zero to prevent the spurious oscillations, still keeping increased loaded  $Q$  factor  $Q_l$ .

#### **Active Resonator Oscillator Topology**

In the AR topology, normally the PR is coupled to the negative resistance generating device network so that in principle AR element is similar to the general oscillator being created [36]-[40]. A general oscillator needs both the amplitude and the phase condition to be satisfied for oscillation build up at  $f_0$ . In the case of the AR, the only phase condition for oscillation build up at  $f_0$  is required for stable and sustained oscillations and no amplitude condition is required to compensate the loss of the AR from the active device network [41]-[45]. As depicted in Figure 5-18, active amplifier works in small signal linear regime and just sufficient to compensate partially or 100% losses without creating instability [44].

Design care must be taken so that the oscillations do not build up in AR circuit and growth is restricted. Typically, amplifier's gain will compensate the inner losses of the AR circuits but 100% compensation ( $-|G_n| + G = 0$ ) of  $W$  (energy losses) will result in infinite unloaded  $Q$  (zero bandwidth). Further loading of the AR (with infinite unloaded  $Q$ ) with oscillator active circuits for obtaining desired oscillations can increase the bandwidth of the resonator for the application in tunable signal sources with improved phase noise performances [43]. However, AR based on negative resistance approach offers improved  $Q$  factors but they have drawbacks: schematic is complex and must have feedback element and the matching networks to produce the negative conductance  $-|G_n|$ , sensitive to spurious oscillation (if the oscillation start-up condition is satisfied) [46]. A normal oscillator requires the



amplitude and phase condition to be satisfied for guaranteed and sustained oscillation build up at desired frequency, whereas, for active resonator element, only phase condition is needed to be satisfied [37]-[39].

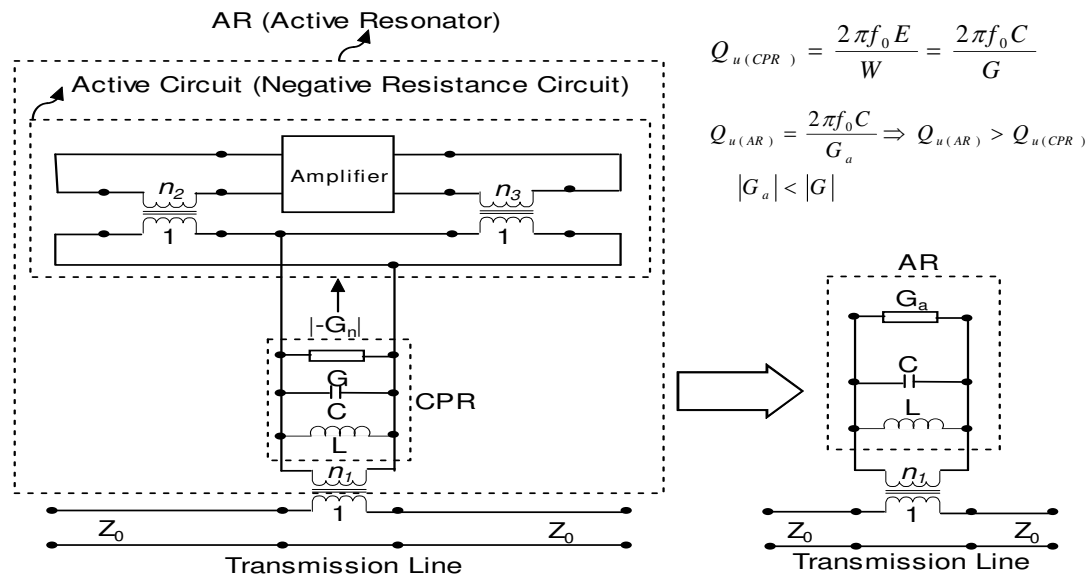


Figure 5-18: A typical AR (active resonator) with feedback arrangement [46]

Hence, oscillation will not build up across the active resonator, and therefore, active resonator module can work in the small signal regime (instead of large signal regime condition required for sustained and guaranteed oscillations), and negative resistance added to the active resonator circuit will reduce the intrinsic losses of the passive resonators used as active resonators. This approach yields high Q resonator, however, active resonator elements are sensitive to spurious oscillations that may cause generation of unwanted oscillation mode in the event of satisfying start-up oscillation condition. Printed passive resonators such as hairpin, spiral, ring, and inter-digital resonators are widely used in tunable oscillator circuits. However, printed passive resonators lack the high quality factor due to the dielectric, conductor and radiation losses, therefore limiting factor of the oscillator phase noise performance.

One possible approach for compensating these losses is an active resonator topology, thereby improved Q-factor. However, noise contributions from active resonators can be significant if design is not optimized for a given oscillator topology and a resonator figure of merit (FOM). The design philosophy of active resonators is based on active feedback loops or coupling negative resistance devices to passive resonators for compensating the losses [32]-[33]. The critical issues are the presence of excess noise added by active devices (transistors), therefore careful design methodology is required for low phase noise oscillator using active resonator networks [42]. Figure 5-19 shows the typical 3.2 GHz VCO (voltage controlled oscillator circuit) using active resonator (AR) network for the comparative analysis of the phase noise performance. As shown in Figure 5-20, the simulated Q factor of AR (active resonator) is three times larger than equivalent PR (passive resonator), the penalty is excess power budget of 60mW. The typical RF output power is +5dBm with 2.1% DC-RF conversion efficiency for a given -210.3 figure of merit (FOM) and 150mW operating DC power consumption (5V, 30mA).

Figure 5-21 shows the CAD simulated phase noise plot, the improvement in phase noise is 9dB that correlates the 3-times increase in Q-factor as compared to PR network. Different AR (active resonator) technology is described in Appendix-B for giving brief insights; unfortunately, each development design of VCO using AR technology has its price, since they occupy larger PCB area and extra power budget.

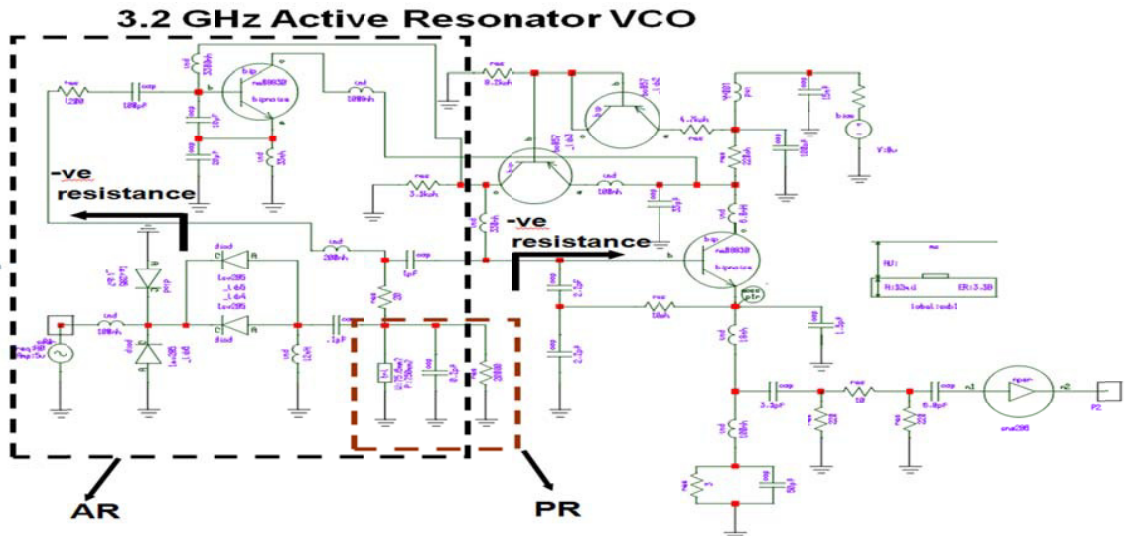


Figure 5-19: shows the typical 3.2GHz VCO using active resonator (oscillator power consumption is 150mW)

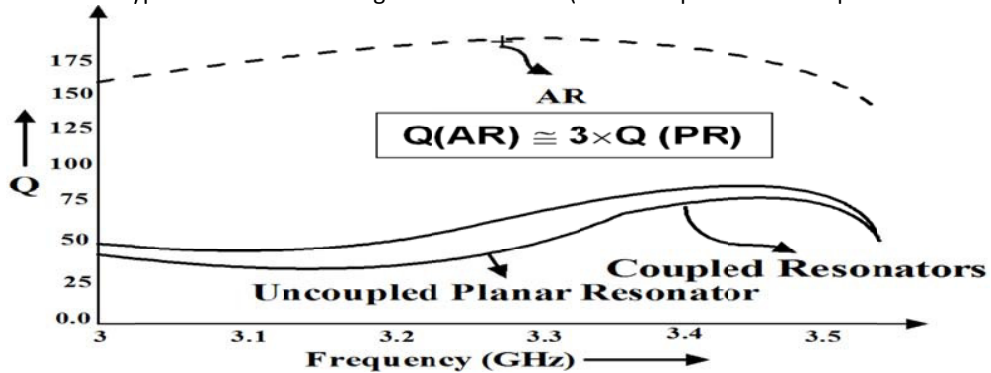


Figure 5-20: shows the typical simulated Q of passive resonator (uncoupled planar resonator and coupled planar resonator) and active resonator (AR) using negative resistance topology (as shown in Figure 5-18)

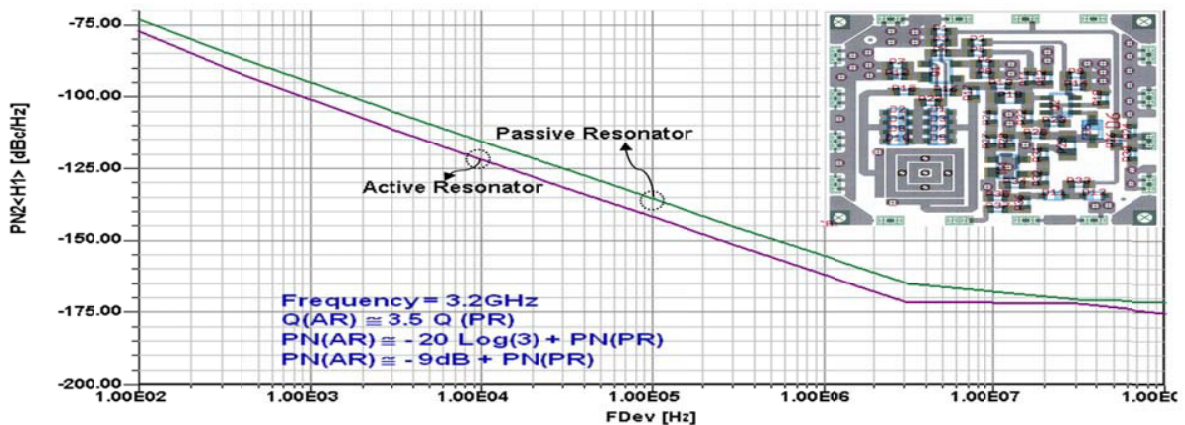


Figure 5-21: Simulated phase noise plot of 3.2 GHz VCO (voltage controlled oscillator circuit) using active resonator (AR) network (200 MHz tuning) network (FOM=-210.3,  $P_o=5\text{dBm}$ , DC-RF power conversion efficiency=2.1%)

## 5.6 Conclusion

In this Chapter, an overview of microwave resonator and its characteristics (resonator quality factor, figure-of-merit), resonator design criteria for oscillator application discussed. The detailed description discussed in the (extended version of this thesis [ref. 47, Appendix B-Appendix E].

## Chapter 6

### Printed Coupled Slow-Wave Resonator Oscillators

#### 6.1 Introduction

A printed coupled resonator network realized by slow wave dynamics is attractive due to its compact size providing a wide spurious-free band [1]. In addition to this, the physical layout of slow wave resonators enables the implementation of optimum EM (electromagnetic) couplings [2]. Printed resonator based tunable oscillator circuits are large, especially at lower operating frequencies. The physical dimension of conventional printed transmission line resonator can be reduced by incorporating slow wave propagation characteristics, thereby reducing the size of the circuits [3]. Typically, periodic shunt loading of the transmission lines can exhibit a simplified slow wave structure. This periodic shunt loading reduces the phase velocity, thereby increasing the effective electric length of the line [4]. As a result, resonators are not only compact size but due to slow wave effect also exhibit high frequency selectivity, wider stop-band resulting from the dispersion phenomena. In order to facilitate a broad yet precise description of the VCO topology, the layout of the SWR (Slow wave resonator) structure is selected in such a way that it minimizes the effect caused by temperature and mechanical stresses, and supports uniform negative resistance over wide tuning range [5]-[7].

In slow-wave propagation, the electromagnetic wave is transmitted in the guided-wave media with a slower phase velocity, namely, shorter guided wavelength, at a specified operating frequency. This is achieved by modifying electric and magnetic energy storage in the guided-wave media. SWRs are attractive due to several reasons: the slow-wave effect makes them very compact and can support evanescent mode coupling, enabling Q-multiplier effect at resonant frequency, thus providing a low phase-noise signal source solution [8]-[9]. Additionally, the geometrical configuration of SWR resonators makes the possible implementation of compact layout and is amenable for RFIC/MMIC realizations [10]-[35]. In conventional transmission lines, the phase velocity  $v_p$  is controlled only by the dielectric material and can be expressed as [3]

$$v_p = f \times \lambda = \frac{c_0}{\sqrt{\mu_r \epsilon_{reff}}} \quad (6.1)$$

where  $c_0$  is the velocity of light,  $\mu_r$  is the effective relative permeability, and  $\epsilon_{reff}$  is the effective relative permittivity. From (6.1), increasing the effective relative permittivity of dielectric material at a given operating frequency decelerates the propagation of electromagnetic (EM) waves in a guided medium. The Slow Wave Effect can be realized by adding periodical shields that decelerate the propagation of electromagnetic (EM) waves in a guided medium. From (6.1), an equivalent inductance  $L_{eq}$ , equivalent capacitance  $C_{eq}$ , and propagation constant  $\beta$  can be described as [2]

$$\beta = \omega \sqrt{L_{eq} C_{eq}} \Rightarrow V_p = \frac{1}{\sqrt{L_{eq} C_{eq}}} \quad (6.2)$$

From (6.2), both distributed inductance ( $L$ ) and capacitance ( $C$ ) along the transmission line in the guided medium can be increased for the realization of slow-wave effects owing to increase of the propagation constant  $\beta$ , consequently, reducing the loss of the resonator network [2]. Figure 6.1 shows the simplified topology of a single-coupled slow-wave resonator, which consists of a slow-wave resonator loaded at its near and far ends with series capacitors  $C_s$ .

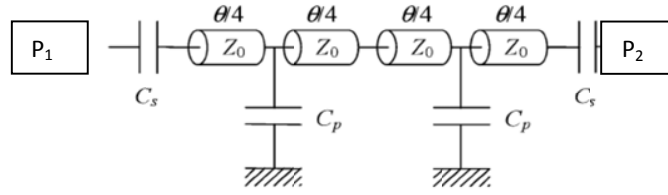


Figure 6-1: A typical topology of a single-coupled slow-wave resonator loaded at the near and far ends with series capacitors  $C_s$  [1]

The resonator itself is made up of a transmission line of characteristic impedance  $Z_0$  and electrical length ' $\theta$ ', periodically loaded by shunt capacitors  $C_p$ . The electrical length  $\theta$  of the unloaded transmission line is defined at frequency  $f$  as [1, 4]

$$\theta = \beta d = \frac{2\pi f \sqrt{\epsilon_{\text{reff}}}}{C} d \Rightarrow \theta|_{f=f_0} = \theta_0 \quad (6.3)$$

where  $\epsilon_{\text{reff}}$  is the effective relative permittivity,  $d$  is the physical length of the unloaded line, and  $C$  is the free space light velocity. At the center frequency  $f_0$ , the electrical length is  $\theta_0$ .

By using *ABCD* (cascade) matrices, the equivalent characteristic impedance  $Z_{\text{eq}}$  of a coupled slow-wave resonator can be easily extracted. As shown in Figure 6-1, the real estate of SWR (slow wave resonator) layout is quite large, therefore not suitable for the application where size is the constraint. For brief insights about the minimization of the size of slow-wave structure, the characteristics of the Lossless transmission and capacitive loaded line (CTL) are discussed.

### 6.1.1 Lossless Transmission Line

Figure 6-2 shows the typical lossless transmission line circuit, which can be characterized by  $Z_0$  (Characteristic Impedance) and  $V_p$  (Phase Velocity) as

$$Z_0 = \sqrt{\frac{L}{C}} \quad (6.4)$$

$$v_p = \frac{1}{\sqrt{\mu\epsilon_e}} = \frac{1}{\sqrt{LC}} \Rightarrow LC = \mu\epsilon_e = k \text{ (Constant depending on medium)} \quad (6.5)$$

where 
$$L = \frac{Z_0}{v_p}, \quad C = \frac{1}{v_p Z_0} \quad (6.6)$$

From (6.5),  $LC = \mu\epsilon_e$  therefore for a given  $\epsilon_e$  and  $\mu$ , it is not possible to reduce  $V_p$  by increasing inductance or capacitance per unit length because an increase in inductance  $L$  leads to a decrease in capacitance  $C$ , ( $L \uparrow \equiv C \downarrow$ ). Hence for a physically smooth transmission line, reduction in phase velocity  $v_p$  is only possible by increasing  $\epsilon_r$ .

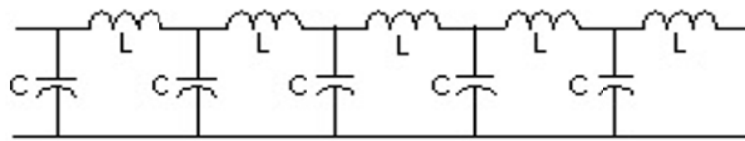


Figure 6-2: A typical lossless transmission line circuit

### 6.1.2 Capacitive Loaded Transmission Lines (CTL)

By removing the constraint that the line should be physically smooth, an effective increase in the shunt capacitance per unit length  $C$  can be obtained without a reduction in inductance  $L$ . This can be realized by loading a printed transmission line with shunt capacitance  $C_p$  at periodic intervals  $d$ . Figure 6-3 shows the typical capacitive loaded transmission (CTL) line circuit formed by loading a printed microstrip line with open stubs that exhibits shunt capacitance at periodic intervals which are shorter than the guide wavelength and causes the periodic structure to exhibit slow wave characteristics [2]-[8].

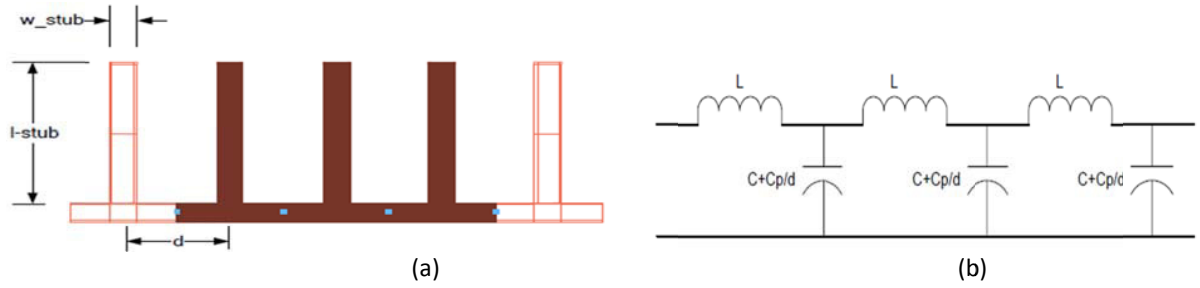


Figure 6-3: A capacitive loaded transmission line circuit: (a) printed layout, and (b) lumped equivalent network

The effective characteristic impedance and phase velocity of the CTL circuit shown in Figure 6-3 can be described by [2]-[4]

$$Z_{0CTL} = \left( \frac{L}{C + \frac{C_p}{d}} \right)^{1/2} \quad (6.7)$$

$$Z_{in} = Z_0 \frac{Z_L + jZ_0 \tan(\beta l)}{Z_0 + jZ_L \tan(\beta l)} \Rightarrow Z_{\infty}(\text{open circuit stub}) = \frac{Z_{stub}}{j \tan[\beta l]} = \frac{1}{j\omega C_p} \quad (6.8)$$

$$v_{pCTL} = \frac{1}{\sqrt{L(C + \frac{C_p}{d})}} = \left[ \frac{Z_0}{v_p} \left( \frac{1}{v_p Z_0} + \frac{C_p}{d} \right) \right]^{-1/2} \quad (6.9)$$

where  $\frac{C_p}{d}$  = lumped capacitance per unit length,  $Z_0 = \sqrt{\frac{L}{C}}$

For an m-section CTL, the equivalent electrical length in angle ( $\Phi_{CTL}$ ) and the loaded capacitance of a unit cell  $C_p$  can be given by

$$\Phi_{CTL} = \frac{2\pi m d f_0}{v_{pCTL}} = m d \omega_0 \sqrt{L \left( C + \frac{C_p}{d} \right)} \quad (rad) \quad (6.10a)$$

$$C_p = \frac{\Phi_{CTL}(Z_0^2 - Z_{CTL}^2)}{2\pi m f Z_0^2 Z_{CTL}} \quad (F) \quad (6.10b)$$

where  $f_0$  is the operating frequency.

From (6.8)-(6.10), the phase velocity  $v_{pCTL}$  can be slowed down by one or a combination of the following: (i) increase the characteristic impedance of the unloaded unit cell  $Z_0$  this is achieved by reducing the microstrip line width  $w_{TL}$ , (b) Reduce the distance between stubs  $d$ , and (c) increase the load capacitance  $C_p$  (increasing the stub electrical length  $\rightarrow \frac{\pi}{2}$ , reducing the stub characteristic impedance  $\downarrow Z_{stub}$ . This is achieved by increasing the width of the stub  $\uparrow w_{stub}$ ).

Figure 6-4 shows the typical layout of the compact capacitively coupled printed slow wave resonator. As shown in Figure 6-4, capacitive-coupling between two arms of the resonator leads to the slow-wave dynamics. The drawback of a periodically loaded line is dispersion in phase velocity; therefore phase velocity of the capacitively loaded transmission line is frequency dependent, whereas the unloaded transmission line does not exhibit dispersion in the phase velocity [9]-[24].

## 6.2 Slow Wave Resonator (SWR)

Slow wave resonator (SWR) using stepped impedance hairpin printed transmission line structure can exhibit larger group-delay in compact size, resulting in improved Q-factor [3]-[6]. The hairpin resonator was first introduced to reduce the size of the conventional parallel-coupled half-wavelength resonator with subsequent improvements made to reduce its size [3].

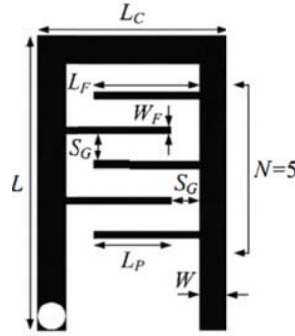


Figure 6-4: A typical slow wave coupled resonator (No. of section,  $m=5$ ) [2]

Beyond the advantage of the compact size, the spurious frequencies of the stepped impedance hairpin resonator are shifted from the integer multiples of the fundamental resonant frequency due to the effect of the capacitance-load coupled lines, including the low quality factor and high insertion loss [4]. As shown in Figure 6-5, the transmission line is periodically loaded with identical open stub elements for realization of high Q-factor SWR structure. The I/P impedance  $Z_{in2}$  for a lossless line is by [3]

$$Z_{in2} \Big|_{\tan(\beta l) \rightarrow 0} = \frac{Z_o Z_L}{Z_o} \Rightarrow Z_{in2} \propto Z_L \quad (6.11)$$

where  $L$  and  $C$  are the inductance and capacitance per unit length of the line,  $Z_o$  and  $\beta$  are the characteristic impedance and phase constant of the open stub, respectively.

From (6.11), for infinitesimal value of  $\tan(\beta l)$ , the input impedance  $Z_{in2}$  is proportional to  $Z_L$ , therefore,  $Z_{in2} \rightarrow \infty$  or  $0$  for corresponding  $Z_L = \infty$  or  $0$ . Under these cases, the slow-wave periodic structure loaded by  $Z_{in2}$  in Figure 6-5 (b) provides passband ( $Z_{in2} \rightarrow \infty$ ) and stopband ( $Z_{in2} \rightarrow 0$ ) characteristics. As depicted in Figure 6-5, the layout size is comparatively large and not attractive for VCO applications in small size, used in modern handheld portable and test equipment systems.

Figure 6-6 shows the modified version of SWR, where transmission line is loaded by a square ring resonator with a line-to-ring coupling structure [3]-[8]. As shown in Figure 6-6 (b),  $Z_{in3}$  is the input impedance looking into the transmission line  $l_b$  toward the ring resonator with the line-to-ring coupling. The input impedance  $Z_{r1}$  looks into the line-to-ring coupling structure toward the ring resonator. The input impedance  $Z_{in3}$  is given by

$$Z_{in3} = Z_o \frac{Z_{r1} + jZ_o \tan(\beta l_b)}{Z_o + jZ_{r1} \tan(\beta l_b)} \quad (6.12)$$

$$\text{Where } Z_{r1} = \frac{(Z_r + Z_g)Z_p}{(Z_r + Z_g + Z_p)}, \quad Z_g = \frac{1}{j\omega C_g \Delta l}, \quad Z_p = \frac{1}{j\omega C_p \Delta l}, \quad \omega = 2\pi f \quad (6.13)$$

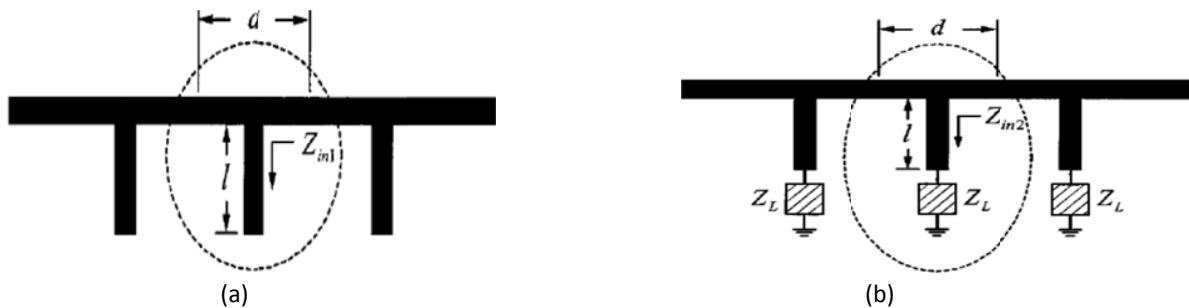


Figure 6-5: A typical slow wave structure: (a) a periodic SW structure, and (b) with loading  $Z_L$  at open end [3]

The parallel  $f_p$  and series  $f_s$  resonances of the slow wave ring resonator as shown in Figure 6-6 can be obtained by setting  $|Y_{in3}| = 0$  and  $|Z_{in3}| = 0$ . The ABCD matrix of the ring circuit (Figure 6-6a) can be described by [9]

$$\begin{aligned} \begin{bmatrix} A & B \\ C & D \end{bmatrix} &= \begin{bmatrix} \cos(\beta l_a) & jZ_o \sin(\beta l_a) \\ jY_o \sin(\beta l_a) & \cos(\beta l_a) \end{bmatrix} \begin{bmatrix} 1 & 0 \\ Y_{in3} & 1 \end{bmatrix} \begin{bmatrix} \cos(\beta l_a) & jZ_o \sin(\beta l_a) \\ jY_o \sin(\beta l_a) & \cos(\beta l_a) \end{bmatrix} \\ &= \begin{bmatrix} 1 - 2 \sin^2(\beta l_a) + jZ_o Y_{in3} \sin(\beta l_a) \cos(\beta l_a) & -Z_o^2 Y_{in3} \sin^2(\beta l_a) + j2Z_o \sin(\beta l_a) \cos(\beta l_a) \\ Y_{in3} \cos^2(\beta l_a) + j2Y_o \sin(\beta l_a) \cos(\beta l_a) & 1 - 2 \sin^2(\beta l_a) + jZ_o Y_{in3} \sin(\beta l_a) \cos(\beta l_a) \end{bmatrix} \end{aligned} \quad (6.14)$$

where  $Y_o = 1/Z_o$ . Using  $Y_{in3}(f_p)$  and  $Z_{in3}(f_s)$ , the passband and stopband of the ring circuit can be obtained by calculating  $S_{11}$  and  $S_{21}$  from the ABCD matrix in (6.14).

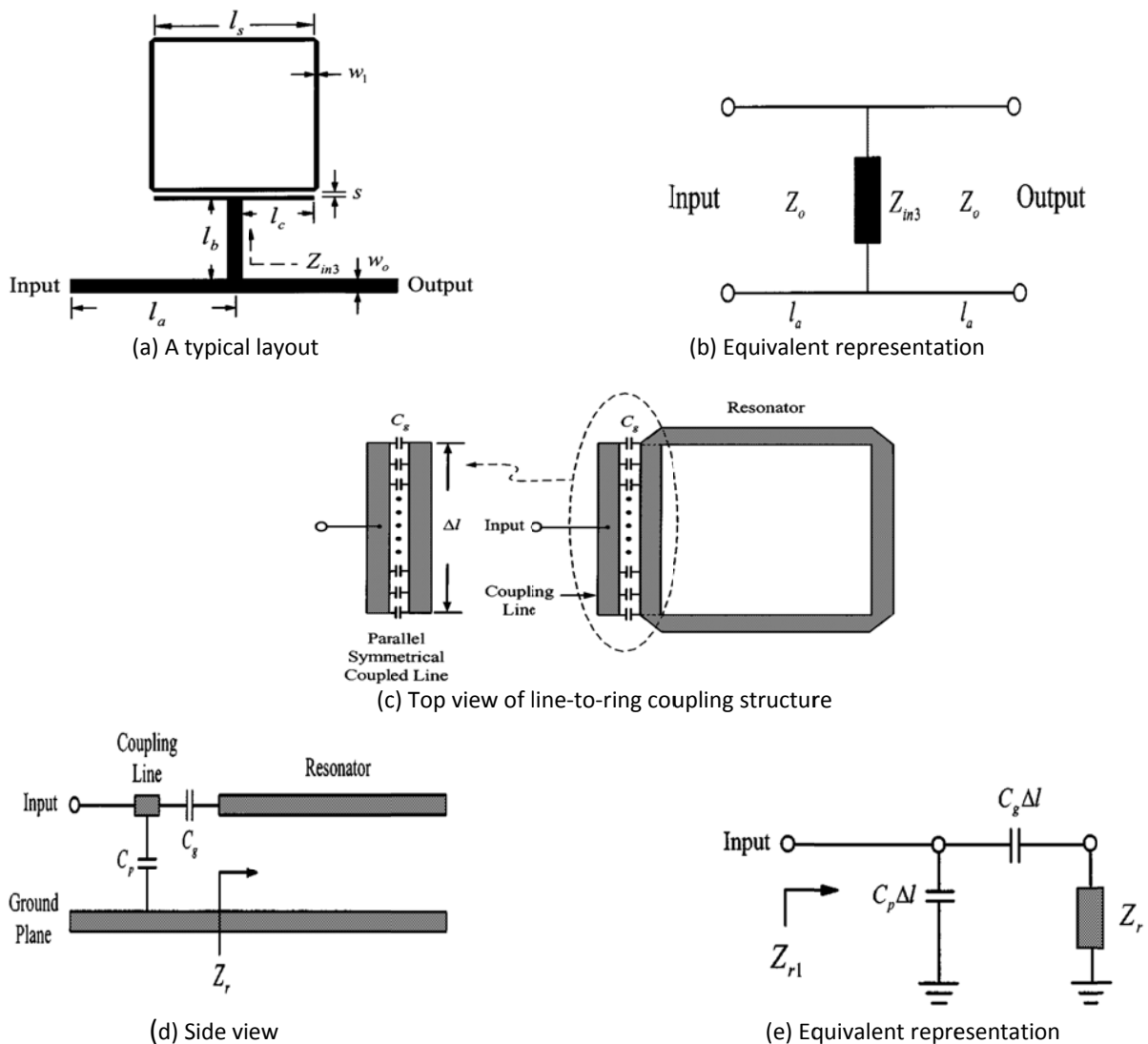


Figure 6-6: A typical slow-wave ring resonator with single edge coupling gap (slower the phase velocity, causing slow-wave effect): (a) printed layout of single edge coupled slow wave ring resonator network, (b) equivalent representation of single edge coupled slow wave ring resonator circuit, (c) top view of line-to-ring coupling structure, (d) side view of line-to-ring coupling structure, and (e) equivalent representation of circuit of line-to-ring coupling structure [3].

### 6.2.1 Slow Wave Evanescent Mode (SWEM) Propagation

The slow-wave evanescent-mode can represent surface wave propagation in planar printed resonators or the lattice waves in waveguides. In slow-wave propagation, the electromagnetic wave is transmitted in the guided-wave media with a slower phase velocity, namely, shorter guided wavelength, at a specified operating frequency [1]-[8]. This is achieved by modifying electric and magnetic storage energy by incorporating perturbation in the guided-wave media. Slow-wave resonators are attractive due to several reasons: the slow-wave effect makes them very compact and can support evanescent mode coupling for obtaining Q-multiplier effect at resonant condition, thus low phase noise signal source solutions. The wave propagation in SWEM structure can be described well using the Maxwell's equations by partitioning into (a) transmission line (TL) equations in the direction of travel, and (b) orthogonal Transverse Evanescent (TE<sub>v</sub>) wave equations [4]-[6]. For the characterization of evanescent-mode propagation, we need four pairs of separate, partially coupled TL and TE<sub>v</sub> wave equations for the four fields E, D, B, and H. The four slow-wave evanescent-mode equations for E, D, B, and H, all are radial profiles of stored energy. The seven main processes in the formation of evanescent waves are: (i) the spreading function, (ii) the self-coupling function, (iii) (radial) standing wave function, (iv) time variation of phase of stored energy components, (v) Root Sum of the Squares (RSS) combination of the four coupled equations giving dominance to the strongest field in the resonator, (vi) dissipation, radiation or absorption of energy in the resonator, (vii) exchange of energy between inter-coupled evanescent modes in SWEM resonator [4]-[10].

### 6.2.2 SWEM Resonator Modes and Noise Dynamics

In contrast to lumped LC resonators, which have only one resonant frequency, slow wave resonators (SWRs) can support an infinite number of electromagnetic field configurations or resonant modes [11]-[16]. The resonant modes in SWR structure exist in the form of degenerate modes (i.e., modes having the same resonance frequency with different field distributions). These modes allow the realization of two electric resonators within the same physical resonator (dual-mode resonators) or three electric resonators within the same physical resonator (triple-mode resonators), and n- electric resonators within the same physical resonator (n<sup>th</sup>-mode resonators).

The single-mode resonator possesses two degrees of freedom, namely, the electric and magnetic fields (voltage and current standing waves), each storing a mean thermal energy of  $kT/2$  (k: Boltzmann's constant; T: temperature), resulting in improved unloaded quality factor. The multi-mode resonator exhibits 2nd-degree of freedom, causing neighboring resonant modes which act as spurious modes interfering with the fundamental resonant mode's performances and exhibit higher noise than single-mode resonator oscillator. It is therefore desirable to increase the spurious free window of the multi-mode resonator oscillator in order to improve the stability, phase noise, and mode-jumping problems. An experimental validation supports the convergence of degenerated modes in SWR structure, resulting in improved dynamic loaded Q-factor. It is interesting to note that slow-wave propagation in SWEM structure mode-locking dynamics under large-signal drive-level condition, which is opposite the analysis because of the fact that slow-wave evanescent modes are inter-coupled together in phase for a given topology [20]-[26].

The inconsistency of multi-mode oscillator phase noise dynamics calls for a revisit to the phase noise analysis based on physics-based noise modeling in SWEM oscillator circuits. This can be physically understood in time domain: noise perturbation generated at any point  $p(x, y, z)$  in SWEM resonator affects the oscillator's phase and timing dynamics only when the respective modes pass through the point  $p(x, y, z)$ . This notion makes sense as explained above, i.e. noise at any given point  $p(x, y, z)$  in SWEM resonator structure has less chance to involve in the phase-noise dynamics for an inter-coupled mode-locked transmission line, leading to lower phase noise than the single-mode resonator oscillator [6]. The Fourier-domain phase-noise argument would predict wrong result, i.e. higher phase noise for SWEM oscillator that has a large number of harmonic modes than the single-mode oscillator circuits. Thus, the general phase



noise theory cannot be applied to the inter-coupled mode-locked resonator oscillator circuits. It is to note that SWEM design parameters (coupling coefficient, multi-mode sensitivity, and Q factor) can be obtained using full wave EM simulation. It has been found that degenerate modes play important role in improving the Q-factor, therefore, rigorous mathematical treatment is necessary for the minimization of the spurious and jitters in pass-band. The theoretical treatment and experimental validation suggests the possibility of low cost high performance synthesizer using SWEM VCO for low jitter and low phase noise applications.

### 6.3 Slow-Wave Resonator Oscillator

Figures 6-7(a), 6-7 (b), and 6-7 (c) show the typical block diagram and layout of the VCO using mode-coupled SWR, which validate a novel SWR (Slow Wave Resonator) approach, using a SiGe Hetro-junction-bipolar-transistor (HBT) active device fabricated on low loss RF dielectric substrate material with a dielectric constant of 3.38 and thickness of 22 mils printed structure [24].

The SWR structure is modeled in 3-D EM (Electromagnetic) CAD simulator and incorporated into optimized nonlinear oscillator circuit to enable configurable and low phase noise operation over the band. This enables SWR structure to set up optimum standing waves (within the resonator) and the noise impedance transfer function over the tuning range by controlling  $m_{opt}$  (by optimizing injection locking) and  $\beta_{opt}$  (by optimizing mode tuning) [17]-[23]. The nonlinear circuit contains the oscillator's active device, with S-parameters. This partitioning of the oscillator into its modeled component parts works quite well, and the combination of the S-parameters and the nonlinear circuit model agrees closely with the measured data in the circuits we already built [25]. The S-parameters used for these transistors are large-signal S-parameters, which improve the optimization cycles using commercial CAD tools such as ADS 2013 (Agilent), AWR, and Ansys (Nexxim) to the limits allowed by physics [26]-[31].

#### 6.3.1 Slow-Wave Resonator Coupling Characteristic and Q-factor

The Q (quality) factor of the printed transmission line resonator can be enhanced by introducing coupling mechanism related to the relative orientation of the neighboring resonators (electric/magnetic/hybrid). Figure 6-8 illustrates the layout of the typical electric, magnetic, hybrid-coupling planar resonator networks, and oscillator circuits for comparative analysis [32]-[37]. As described in Figure 6-8, the coupling dynamics can be characterized by proximity effect through the fringing fields, which exponentially decays outside the region; E and H field intensity concentrate near the side having maximum field distribution.

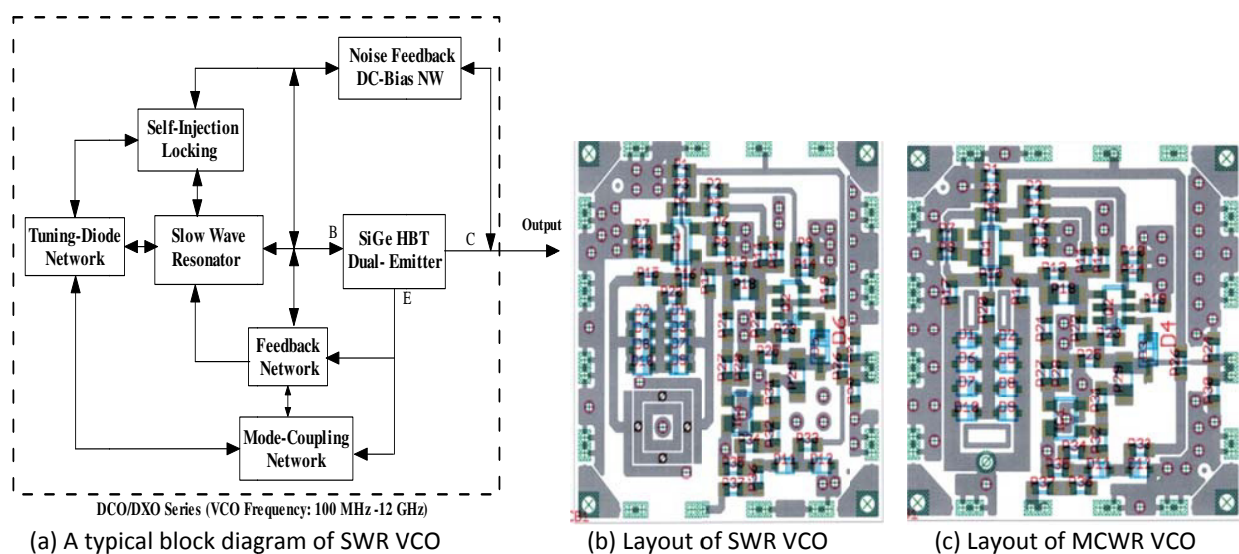


Figure 6-7: (a) A typical Block diagram of SWR VCO, (b) layout of SWR VCO and (c) layout of mode-coupled SWR VCO

The coupling coefficient ' $\beta_j$ ' depends upon the geometry of the perturbation, and it can be given by

$$\beta_j = \left[ \left( \frac{\int \epsilon E_a \cdot E_b dv}{\sqrt{\int \epsilon E_a^2 dv \int \epsilon E_b^2 dv}} \right)_{\text{electrical-coupling}} + \left( \frac{\int \mu H_a \cdot H_b dv}{\sqrt{\int \mu H_a^2 dv \int \mu H_b^2 dv}} \right)_{\text{magnetic-coupling}} \right] \quad (6.15)$$

where  $E_a$  and  $H_a$  are, respectively, the electric and magnetic fields produced by the square loop ring resonator, and  $E_b$ ,  $H_b$  are the corresponding fields due to the perturbation ( $d \neq 0$ ) or nearby adjacent resonator (second square loop resonator). From (6.15), the first term represents the coupling due to the interaction between the electric fields of the resonators and the second term represents the magnetic coupling between the resonators. Depending on the strength of interaction, multi-mode dynamics exist related to electrical, magnetic, and hybrid coupling. The configuration of Figure 6-8a produces an electric coupling since the electric field is maximum near the open ends, maximizing the numerator of the first term of Equation 6.15. As depicted in Figure 6-8c, when the resonators are operating near their first resonant frequency, the pair of resonators interacts mainly through their magnetic field, this is because the magnetic fields is maximum near the center of the resonator opposite to its open ends, maximizing the numerator of the second term of Equation 6.15. The coupling produced by the two configuration (open loop resonator # 1 and open loop resonator #2) as shown in Figure 6-8f are referred as mixed coupling or hybrid coupling because neither the electric fields nor the magnetic fields dominate the interaction between the resonators.

The definition of ' $\beta_j$ ' given in (6.15) involves complex mathematical analysis and is not suited for practical calculation since it requires the knowledge of the electromagnetic fields everywhere. A useful alternative expression for ' $\beta_j$ ' can be obtained from a well-known fact in physics when multiple resonators are coupled to each other they resonate together at different distinct frequencies ( $f_{ee}$ ,  $f_{em}$ ,  $f_{eh}$ ,  $f_{mh}$ ) which are in general different from their original resonant frequency  $f_0$ . Furthermore, these frequencies are associated with corresponding to their normal modes of oscillation of the coupled system (electric/magnetic/hybrid), and their difference increases as the coupling ' $\beta_j$ ' ( $\beta_e$ : electric,  $\beta_m$ : magnetic and  $\beta_h$ : hybrid) between the resonators increases [31]-[37]. The main interaction mechanism between resonators is proximity coupling and can be characterized by a coupling coefficient ' $\beta_j$ ' that depends upon the ratio of coupled energy to stored energy, described by

$$\beta_e \cong \frac{\text{coupled-electrical energy}}{\text{stored-energy of uncoupled-resonator}} \cong \frac{f_{me}^2 - f_{ee}^2}{f_{me}^2 + f_{ee}^2} \cong \frac{C_{me}}{C} \quad (6.16)$$

$$\beta_m \cong \frac{\text{coupled-magnetic energy}}{\text{stored-energy of uncoupled-resonator}} \cong \frac{f_{em}^2 - f_{mm}^2}{f_{em}^2 + f_{mm}^2} \cong \frac{L_{mm}}{L} \quad (6.17)$$

$$\beta_h \cong \frac{\text{coupled-electro-magnetic energy}}{\text{stored-energy of uncoupled-resonator}} \cong \frac{f_{eh}^2 - f_{mh}^2}{f_{eh}^2 + f_{mh}^2} \cong \frac{CL_{mh} + LC_{mh}}{LC + L_{mh}C_{mh}} \quad (6.18)$$

$$\text{Where } f_{ee} = \frac{1}{2\pi\sqrt{L(C + C_{me})}}, \quad f_{me} = \frac{1}{2\pi\sqrt{L(C - C_{me})}}, \quad C_{me}: \text{Mutual Capacitance} \quad (6.19)$$

$$f_{em} = \frac{1}{2\pi\sqrt{C(L - L_{mm})}}, \quad f_{mm} = \frac{1}{2\pi\sqrt{C(L + L_{mm})}}, \quad L_{mm}: \text{Mutual Inductance} \quad (6.20)$$

$$f_{eh} = \frac{1}{2\pi\sqrt{(L - L_{mh})(C - C_{mh})}}, \quad f_{mh} = \frac{1}{2\pi\sqrt{(L + L_{mh})(C + C_{mh})}}, \quad L_{mh}: \text{Hybrid Inductance} \quad (6.21)$$

$$f_0 = \frac{1}{2\pi\sqrt{LC}}, \quad f_0: \text{fundamental resonance frequency of uncoupled resonator} \quad (6.22)$$

The time average loaded Q-factor of slow wave resonator:  $\overline{Q_{swr}(\omega)}_{\omega \rightarrow \omega_0}$  can be described by

$$\overline{Q_{swr}(\omega)}_{\omega \rightarrow \omega_0} = \left[ \frac{\omega}{2(I_{max} - I_{min})} \int_{I_{min}}^{I_{max}} Q_{swr}(\omega, i) di \right]_{\omega \rightarrow \omega_0} \quad (6.23)$$

where  $I_{min}$  and  $I_{max}$  are the minimum and maximum resonator currents of the SWR network associated with the fundamental modes of the coupled resonator networks, the  $Q_{swr}(\omega, i)$  is the instantaneous quality factor at frequency  $\omega$  and current  $i$  provides an effective means to quantify the Q-multiplier effect of SWR when operated in an evanescent-mode coupling condition, especially in printed coupled resonator based oscillator circuits.

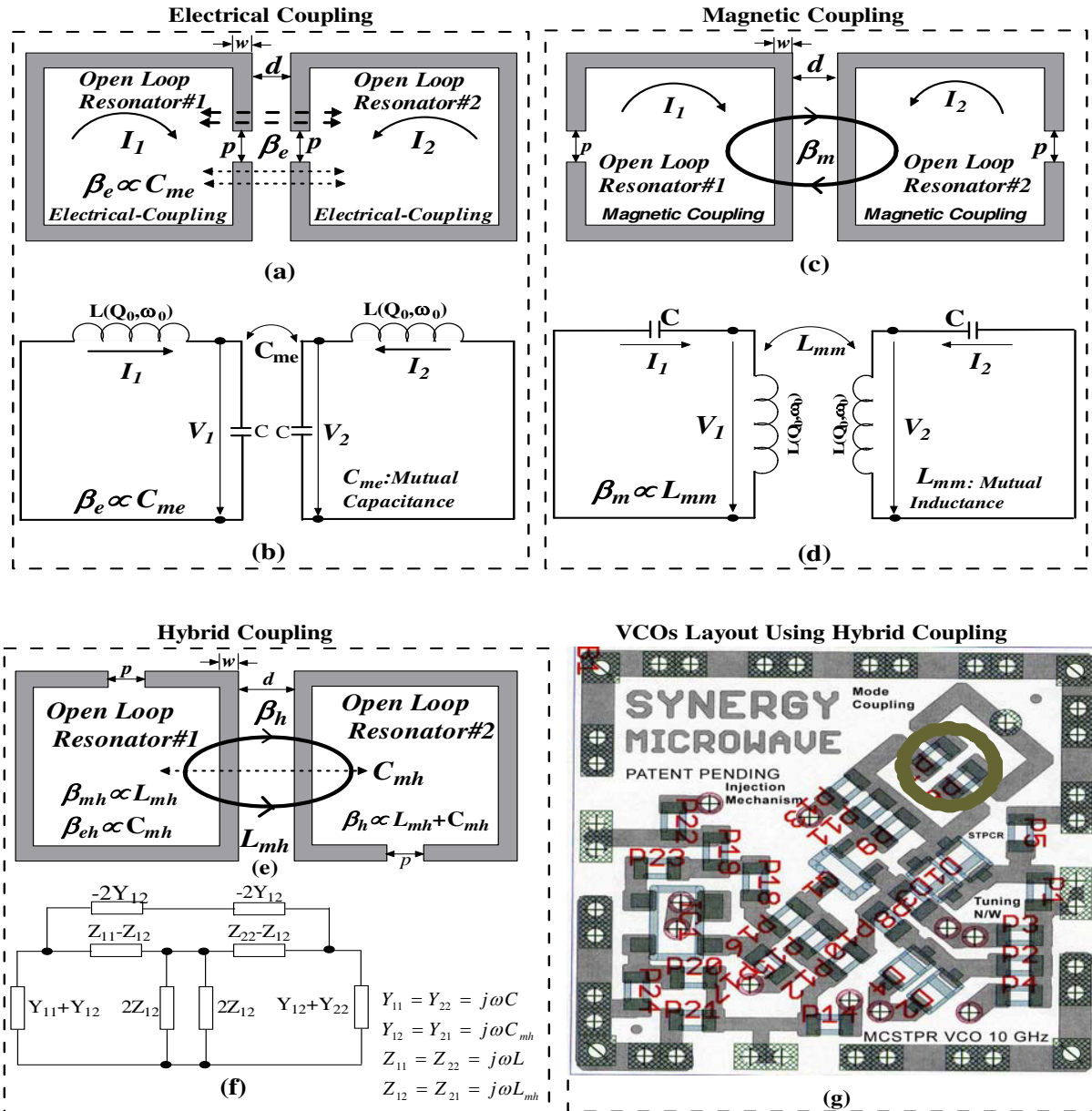


Figure 6-8: A typical simplified structure of open loop microstrip line coupled resonator networks:(a) Electrical coupling, (b) Equivalent lumped model of electrical coupling, (c) Magnetic coupling, (d) Equivalent lumped model of magnetic coupling, (e) Hybrid coupling, (f) Equivalent lumped model of hybrid coupling and (g) Layout of VCO using electric and magnetic coupling.

From (6.23), the loaded Q-factor  $Q_L$  of the coupled resonator is given in terms of unloaded Q-factor  $Q_0$  as

$$Q_L(\omega_0) = \frac{\omega_0}{2} \left[ \frac{\partial \phi}{\partial \omega} \right] \quad (6.24)$$

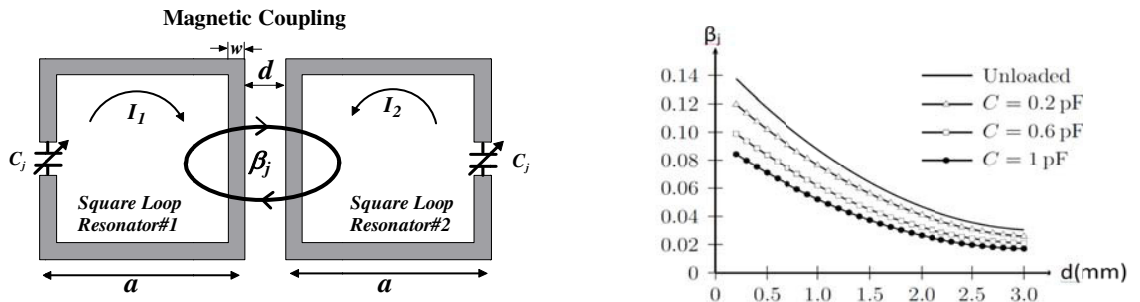
$$[Q_L(\omega_0)]_{\text{electrical-coupling}} \cong 2 \left[ \frac{Q_0}{(1 + \beta_e)} \right]_{\beta_e \ll 1} \cong 2Q_0 \quad (6.25)$$

$$[Q_L(\omega_0)]_{\text{magnetical-coupling}} \cong 2[Q_0(1 + \beta_m)]_{\beta_m \rightarrow 1} \cong 2Q_0 \quad (6.26)$$

$$[Q_L(\omega_0)]_{\text{hybrid-coupling}} \cong 2 \left[ Q_0 \frac{(1 + \beta_{mh})}{(1 + \beta_{eh})} \right]_{\beta_e \ll 1, \beta_m \rightarrow 1} \cong 2Q_0 \quad (6.27)$$

where  $\frac{\partial \phi}{\partial \omega}$  is the rate of change of the phase, and  $Q_0$  is the unloaded Q-factor of the uncoupled single open loop microstrip line resonator. From (6.25)-(6.27), there is trade-off between improving the Q factor and the permissible attenuation required (which is compensated by active device for oscillation build up).

The coupling mechanism described in Figure 6-8 shows improvement in quality factor in comparison to single uncoupled planar resonator but drawback is limited tuning range (less than 1%). By introducing tunable capacitor across the open end of uncoupled planar open loop resonator, dynamic unloaded Q-factor can be improved but limited tuning range (<25%). This is due to minimization of the radiation losses from the open ends of the resonator because of capacitive loading, causing dielectric polarization in the capacitor since most of the electric field resides inside it [38]-[42]. Therefore, a high Q capacitor could actually increase the unloaded quality factor of the whole resonator. This is analogous to the case of dielectric resonators where the fields are constrained to a small volume dielectric with high permittivity and low loss tangent resulting in a high overall Q [43]-[49]. For wideband tunability (>100% tuning), adjacent coupled open loop resonator network is preferred but at the cost of large real estate area. In general, the miniaturization of the open loop resonator reduces its capacity to couple to adjacent structures. This is because smaller resonator size represents a smaller volume of electromagnetic interactions between its coupled arms; reason being a smaller size represents a smaller volume of electromagnetic interaction between coupled resonators. The fact that the majority of the electric field that existed in the volume surrounding the open ends of a resonator is now confined to the interior of a capacitor limiting its possibility to interact with a neighboring resonator. It can be seen from the Figure 6-9 that the effect on the magnetic and mixed coupling is less severe than for the electric coupling, where the magnetic coupling coefficient is plotted against the separation between resonators for different loading capacitors [43]-[49].



(a) Capacitive loaded magnetic coupled resonator

(b) plot of magnetic coupling  $\beta_j$  as a function "d"

Figure 6.9: A typical capacitive loaded magnetic coupled square loop resonator characteristics: (a) Printed layout, (b) plot of magnetic coupling ' $\beta_j$ ' as a function of the distance between resonators for a given capacitive ( $C_j$ ) loading with resonator physical dimension  $w = 2\text{mm}$  and  $a = 26\text{mm}$ , fabricated using Roger RO4003c substrate with a dielectric constant of 3.55 and a thickness of 60mil [43]

The microstrip square open loop resonator is one of the most used structures for multi-mode oscillator resonator applications due to its compact size ( $a = \lambda/8$ ). For low phase noise multi-octave band tunability, the loaded quality factor ( $Q_L$ ) as described in (6.24)-(6.27) can be maximized by either lowering the value of mutual capacitance ( $C_m$ ) and inductance ( $L_m$ ) or maximizing the self-capacitance ( $C$ ) and inductance ( $L$ ), therefore, upper limit of the loaded  $Q$ -factor is dependent on the coupling ' $\beta_j$ ' ( $\beta_e$ : electric,  $\beta_m$ : magnetic and  $\beta_h$ : hybrid) that can be optimized by controlling the width of the transmission line ( $w$ ), gap of the open line resonator ( $p$ ), and spacing between the two open line resonators ( $d$ ) [50]-[55].

For low phase noise tunable oscillator, the coupling coefficient  $\beta_j$  should be dynamically tuned over the operating frequency band. However, dynamic controlling and tuning of the parameters ( $w$ ,  $p$ ,  $a$ , and  $d$ ) as shown in Figure 6-8 at high frequency is challenging task. The alternative tuning mechanism is capacitive loading by incorporating tuning diodes [38]-[44]. Figure 6-10 shows the typical tunable square open loop resonator in compact size ( $\lambda/8$  by  $\lambda/8$ ) for the applications in oscillator circuits. As shown in Figure 6-10 (c), the goal is to minimize the real estate area by using meander line into inner part of the resonator. To optimize the geometry of the coupled resonator they are excited with a pair of loosely coupled feed lines to obtain a transmission parameter  $S_{21}(\omega)$  from which the two resonant frequencies  $f_1$  and  $f_2$  can be obtained for a given geometry and values of  $d$  between resonators. The resonator shown in Figure 6-10 (d) offers compact size and exhibits two independent modes (dual-modes), the coupling between them can be optimized by the geometry of the inner structure. This tunable dual mode resonator can then function as two independent tunable resonators providing an immediate size reduction of 50%. For brief insights about the tuning capability of square open loop resonator (Figure 6-11), a simple equivalent circuit model of the varactor diode loaded resonator as shown in Figures 6-11(a) to 6-11(c) is used to derive its multi-mode tuning dynamics and regime.

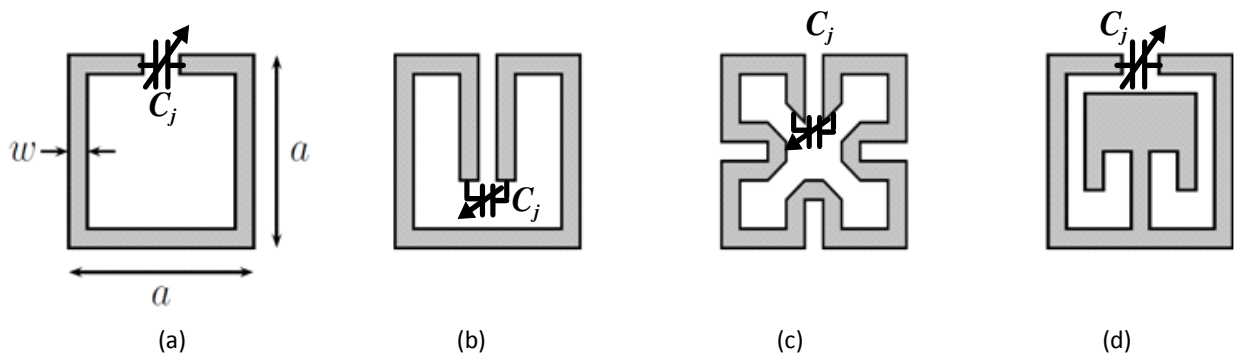


Figure 6-10: A typical layout of tunable square open loop resonator: (a) Conventional square open loop hairpin resonator, (b) Folded arms square open loop resonator, (c) Meander line square open loop resonator, (d) Dual mode square open loop resonator [43]

The voltage and current distribution at resonance can be described by using transmission line theory and the shunt equivalent model of Figure 6-11 (c) as:

$$V(\theta) = \left[ \cos(\theta) - \frac{\sin(\theta)}{\tan(\theta_T/2)} \right] \quad 0 < \theta < \theta_T \quad (6.28)$$

$$I(\theta) = \frac{j}{Z_0} \left[ \frac{\cos(\theta)}{\tan(\theta_T/2)} + \sin(\theta) \right] \quad 0 < \theta < \theta_T \quad (6.29)$$

where  $\theta = \beta z$  is the electrical length measured from one open end of the resonator, and  $\theta_T$  is the total electrical length of the resonator.

Figure 6-12 show the plots of  $V(\theta)$  and  $I(\theta)$  for loaded and unloaded square open loop resonator network. As shown in Figure 6-12, the current never goes to zero but remains near its maximum value along the

resonator and the voltage varies almost linearly between open ends (Assumptions: these typical plots are just to compare the distribution of the voltages and currents between the loaded and unloaded resonators, but not their amplitudes; they are normalized with respect to their respective maxima and they have either different frequencies or different resonator sizes) [56].

Using Miller's theorem, tunable square loop open resonator (SLOR) shown in Figure 6-11a can be equivalently represented as Figure 6-11c, if the following conditions are satisfied:

$$Y_1(\omega) = Y(\omega) \left(1 - \frac{V_2(\omega)}{V_1(\omega)}\right) \rightarrow Y_1(\omega) = Y(\omega)[1 - A(\omega)] \quad (6.30)$$

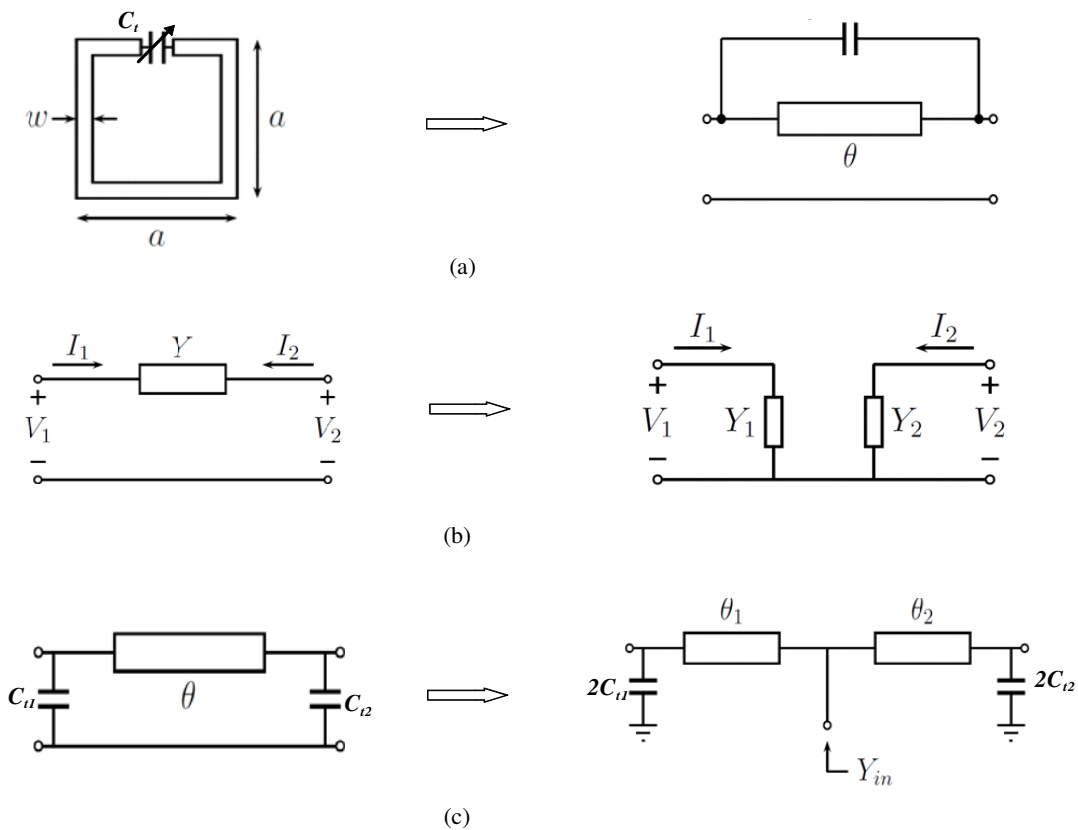


Figure 6-11: A square open loop resonator loaded with a tunable series capacitor: (a) simplified equivalent circuit model for square open loop resonator, (b) Miller-transformed equivalent circuit model, and (c) equivalent circuit of square open loop resonator with two tunable shunt capacitors at open ends [43].

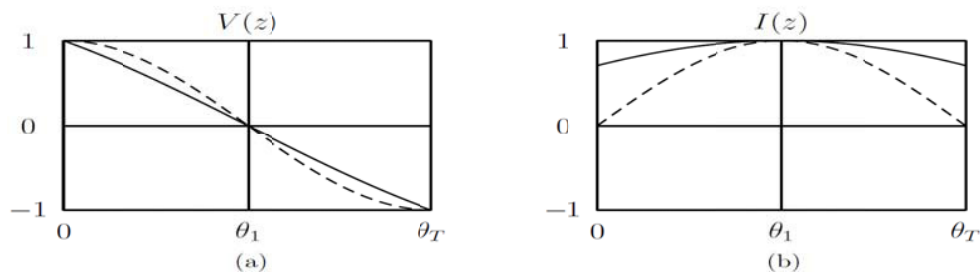


Figure 6-12: Voltage and current distribution at resonance of square loop open resonator (SLOR) shown in Figure 6-10: (a) Voltage distribution in a loaded and unloaded open loop resonator, and (b) current distribution in loaded and unloaded open loop resonator (Dashed lines are for the unloaded case) [43].

$$Y_1(\omega \rightarrow \omega_0)|_{A=-1} = 2Y(\omega_0) = j\omega_0 C_{t1} = j2\omega_0 C_t \quad (6.31)$$

$$Y_2(\omega) = Y(\omega) \left(1 - \frac{V_1(\omega)}{V_2(\omega)}\right) \rightarrow Y_2(\omega) = Y(\omega) \left(1 - \frac{1}{A(\omega)}\right) \quad (6.32)$$

$$Y_2(\omega \rightarrow \omega_0)|_{A=-1} = 2Y(\omega_0) = j\omega_0 C_{t2} = j2\omega_0 C_t \quad (6.33)$$

where  $A = V_2/V_1$  is the voltage gain from node 1 to node, near resonance ( $\omega \rightarrow \omega_0$ ), both voltages ( $V_1, V_2$ ) are in opposite phase ( $V_1 = -V_2$ ), gain  $A = -1$  (odd-mode resonance). From Figure 6-11 (c), the input admittance can be described by

$$Y_{in}(\omega) = jY_0 \left[ \frac{(2\omega C_t + Y_0 \tan \theta_1)}{(Y_0 - 2\omega C_t \tan \theta_1)} + \frac{(2\omega C_t + Y_0 \tan \theta_2)}{(Y_0 - 2\omega C_t \tan \theta_2)} \right] \quad (6.34)$$

From (6.34), at fundamental odd-mode resonance ( $V_1 = -V_2$ ),  $Y_{in}(\omega \rightarrow \omega_0) = 0$

$$Y_{in}(\omega \rightarrow \omega_0) = 0 \Rightarrow jY_0 \left[ \frac{(2\omega C_t + Y_0 \tan \theta_1)}{(Y_0 - 2\omega C_t \tan \theta_1)} + \frac{(2\omega C_t + Y_0 \tan \theta_2)}{(Y_0 - 2\omega C_t \tan \theta_2)} \right] = 0 \Rightarrow \tan(\theta_1 + \theta_2) = \frac{4Z_0 \omega_0 C_t}{4Z_0^2 \omega_0^2 C_t^2} \quad (6.35)$$

$$\tan(\theta_1 + \theta_2) = \tan(\theta_T)|_{\theta_T=(\theta_1+\theta_2)} = \frac{4Z_0 \omega_0 C_t}{4Z_0^2 \omega_0^2 C_t^2} = \frac{1}{Z_0 \omega_0 C_t} \quad (6.36)$$

$$Y_{in}(\omega \rightarrow \omega_0) = \infty \Rightarrow Z_{in} = 0 \Rightarrow (Y_0 - 2\omega C_t \tan \theta_1) \Rightarrow \tan(\theta_1)|_{(\theta_1=\theta_2)} = \frac{1}{2Z_0 \omega_0 C_t} \quad (6.37)$$

where  $\theta_T = \theta_1 + \theta_2$  is the total length of the resonator.

From (6.36), the electrical length ( $\theta_T = \theta_1 + \theta_2$ ) is calculated for a given resonance frequency  $\omega_0$  and loading capacitance  $C_t$ . From (6.37), for  $\theta_1 = \theta_2$ ,  $Z_{in} = 0$  the center of the resonator is a voltage null at the first resonant frequency. This implies that for  $\theta_1 = \theta_2$ ; Equations (6.36) and (6.37) are equivalent and there will be a voltage null at the center of the resonator whenever the resonance condition exists in square open loop resonator structure. From (6.30)-(6.37), the resonant condition of the loaded square open loop resonator structure is valid only near an odd mode resonance ( $V_1 = -V_2$ ), where the parameter 'A' of the Miller effect is -1. Away from these voltage condition ( $V_1 = -V_2$ ) at odd-mode resonant frequencies the voltage relation among the open ends changes, causing change in equivalent admittances  $Y_1$  and  $Y_2$  as shown in Figure 6-11 (b). This leads to difference between the behavior of the series and shunt loaded resonators away from the odd resonant frequencies. The two most important differences are the performance near the even resonant mode and the existence of anti-resonance for the case of series loading [43]-[54].

For even-mode ( $V_1 = V_2$ ), the capacitor ( $C_{t1}$  and  $C_{t2}$ ) as shown in Figure 6-11c is virtually open circuited caused by Miller effect ( $A = 1$ ). Therefore, the series capacitor ( $C_t$ ) as shown in Figure 6-10a does not have any effect on the behavior of the resonator near even mode resonances; these resonant frequencies are unchanged by the presence of the capacitor.

### 6.3.2 Loaded Open Loop Printed Resonator Coupling and Mode-Characteristics

Figure 6-13 shows the typical set up used for measurement of the  $S_{21}(\omega)$  for deriving the coupling characteristics of the tunable open loop resonator loaded with the varactor diode [44]-[49]. The parameter of interest is the transmission coefficient  $S_{21}(\omega)$ , where the resonant frequencies are manifested as peaks of maximum transmission between ports. Figure 6-14 shows CAD simulated (Ansoft Designer) plot of the varactor loaded open square loop printed resonator with  $\omega = 2\text{mm}$  and  $a = 26\text{mm}$ , fabricated using Roger RO4003c substrate with a dielectric constant of 3.55 and a thickness of 60mil (1.524 mm) [51]-[55]. As shown in Figure 6-14, the first resonant frequency is shifted down with different values of C, whereas the second resonance frequency remains at same location. Nevertheless, as varactor diode capacitance increases beyond certain value (for example, 1.4 pF), a couple of frequencies where the transmission coefficient  $S_{21}$  is zero appears between the first and second resonant frequencies, which is observed in Figure 6-14 for  $C = 2\text{pF}$ .

As shown in Figure 6-14, the physical size of the resonator ( $\omega = 2\text{mm}$  and  $a = 26\text{mm}$ ) is kept constant while  $C$  is varied causing a shift in the first resonant frequency. This frequency shift can be capitalized into miniaturization if we let the size of the resonator vary and is minimized while keeping the fundamental resonance fixed.

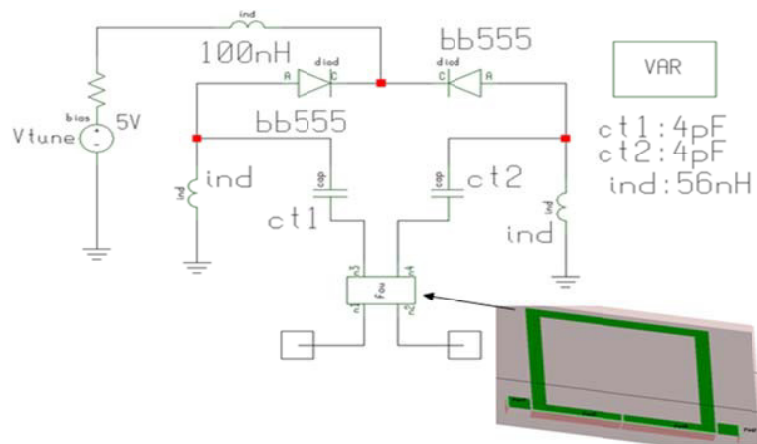


Figure 6-13: A typical setup for carrying out the measurement of the transmission coefficient  $S_{21}(\omega)$  for analyzing the coupling characteristics of the varactor loaded tunable open loop resonator [44].

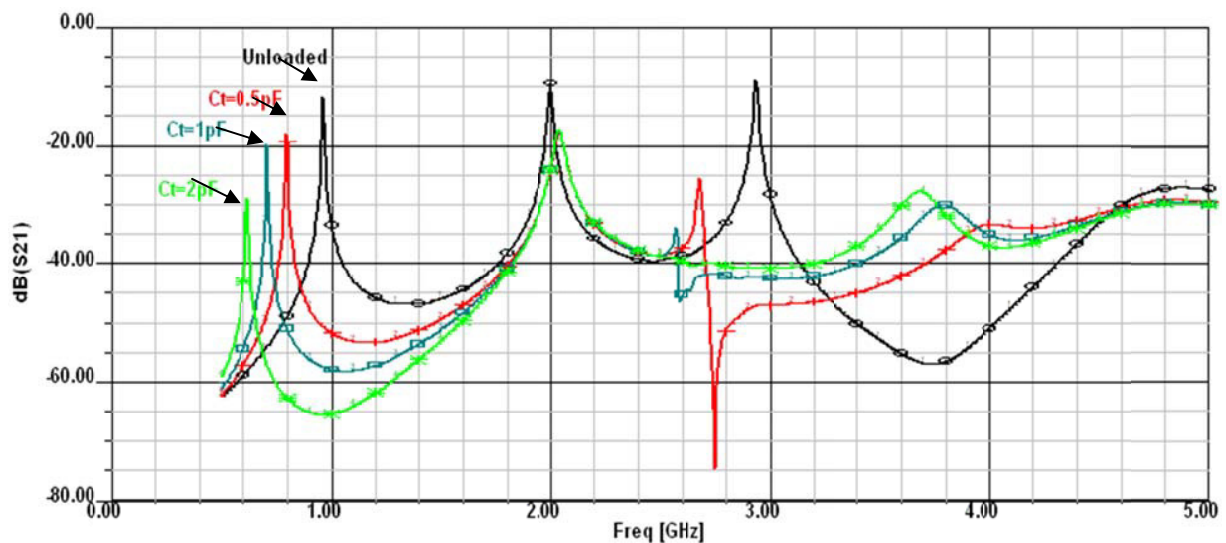


Figure 6-14: Simulated (Ansoft Designer) plot of  $S_{21}(\omega)$  of a varactor loaded SLOR for different capacitance values [45].

Table 6.1 describes a summary of the results obtained by fixing the resonant frequency at 1 GHz using the same substrate as before [52]-[56]. As shown in Table 6.1, the ratio of  $f_1/f_0$  increases as the loading increases, when the loading capacitance is 1 pF the last row of Table 6.1 indicates that the area of the miniaturized resonator is 36% that of the conventional resonator (shown in 4<sup>th</sup> column of Table 6.1).

Table 6.1: Resonator characteristics as a function of loading capacitance

$C_i$ (pF)	$a$ (mm)	$A_m$ (mm <sup>2</sup> )	$A_m/A_c$	$f_1/f_0$
0	26	676	1	2
0.2	23.2	535.92	0.79	2.23
0.6	19.5	380.25	0.56	2.66
1	17	289	0.427	3.06



where

$A_m$  : Area occupied by the varactor loaded miniaturized resonator

$A_c$  : Area of the conventional (unloaded) resonator

$w$ = width ( $w = 2$  mm in all resonators), kept constant for the simplification.

$a$ = length of the SLOR, varying for the miniaturization

$f_0$ = fundamental frequency is fixed at 1 GHz,  $f_1$ =first spurious frequency

Figure 6-15 shows the plot of area  $A(C_t)$  and frequency  $\omega(C_t)$  versus capacitive loading provided by the varactor diode in printed square open loop resonator. From (6.37), the total length of the square open loop resonator is  $\theta_T = \theta_1 + \theta_2$ , for  $\theta_1 = \theta_2$ :

$$\tan(\theta_1) \Big|_{(\theta_1 = \frac{\theta_T}{2})} = \frac{1}{2Z_0\omega_0 C_t} \quad (6.38)$$

$$\theta_1 = \frac{\theta_T}{2} = \omega \left( \frac{l}{2v_p} \right) = \frac{\beta l}{2} = \tan^{-1} \left( \frac{1}{2Z_0\omega C_t} \right) \quad (6.39)$$

$$A (\text{Square Loop Resonator Area}) = \left( \frac{l}{4} \right)^2 = \frac{\theta_T^2}{16\beta^2} = \frac{1}{4\beta^2} \left[ \tan^{-1} \left( \frac{1}{2Z_0\omega C_t} \right) \right]^2 \quad (6.40)$$

$$A(C_t) = k_1 \left[ \tan^{-1} \left( \frac{1}{p_1 C_t} \right) \right]^2 \Rightarrow A(C_t) \propto \left[ \tan^{-1} \left( \frac{1}{p_1 C_t} \right) \right]^2 \quad (6.41)$$

$$\text{From (6.39)} \quad C_t = \frac{k_2}{p_2 \omega \tan(p_2 \omega)} \Rightarrow \omega(C_t) \propto \frac{1}{p_2 C_t \tan(p_2 C_t)} \quad (6.42)$$

Equations (6.41) and (6.42) are trigonometric functions, where ' $l$ ' represents the total physical length (perimeter) of the resonator ( neglecting the size of the gap where the capacitor is mounted,  $v_p$  is the phase velocity,  $k_1$  and  $p_1$ ,  $k_2$  and  $p_2$  are constant, and  $C_t$  is the capacitive loading provided by varactor diode.

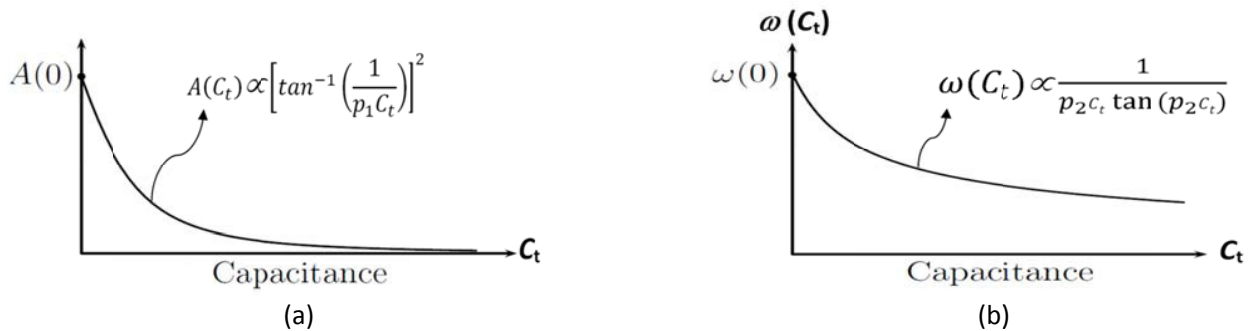


Figure 6-15: Shows the plot of area  $A(C_t)$  and frequency  $\omega(C_t)$  versus capacitive loading provided by the varactor diode in printed square open loop resonator: (a) relationship between the capacitance value and the resonator's area), and (b) resonant frequency [43]

Since the constants  $k_1, k_2$  and  $p_1, p_2$  have the effect of scaling the x and y axis respectively, any choice of them gives a good representation of the general tendency. A plot of this curve, where for simplicity  $k_1=p_1=k_2=p_2=1$ , is shown on Figure 6-15. Both curves shown in Figure 6-15 indicate that there is maximum variability for relatively small values of capacitance. It can be noticed from the Figure 6-15 that as the capacitance increases the rate of change decreases, this leads to following [43]:

- Designs with large capacitance values are more robust (less sensitive to capacitor tolerances).
- For tunable operation, small values of capacitance are better.
- Increasing the capacitance after a certain value does not provide significant advantage.

Based on above, oscillator's circuits are designed for the validation purpose.

## 6.4 Tunable Low Phase Noise Oscillator Circuits

The tunable oscillator circuits using slow wave resonator networks reported in this chapter offers cost-effective alternative to expensive high Q-factor dielectric and YIG resonator oscillators [7].

Figure 6-16 (a) shows the typical simplified schematic of an oscillator comprised of a resonator module and an external circuitry (active device that generates gain for stable oscillation) [29]-[32]. In general, resonator is described as linear model (follows the superposition theorem), ideally high Q-factor resonator used in oscillator would clean the low frequency near-carrier noise. However, in reality, the quantum dynamics of Quartz crystal, Ceramic, Dielectric, and MEMS resonator is nonlinear and drive-level dependent [57]. Therefore, nonlinearities associated with these resonators can lead to unwanted aliasing of low-frequency noise to carrier side bands as shown in Figure 6-16 (b).

The aliasing of low frequency noise can be even higher than the thermal noise floor of the expensive high Q-factor piezoelectric Quartz resonators; therefore, linearization of the resonator is needed for application in high performance signal sources [53]-[57].

Figure 6-17 shows the layout of 18.87 GHz dielectric resonator oscillator (DRO) in push-push topology for the minimization of unwanted aliasing of low frequency random fluctuation noise [46]. Although DROs in push-push topology minimize aliasing of near-carrier  $1/f$  noise it is at the cost of size, power and sensitivity to vibration [50]. One way to overcome the unwanted noise aliasing is to use linear passive printed planar resonator but planar resonator lacks with the Q-factor, and are large in size, therefore main limiting factor of the phase noise performances [17]-[21].

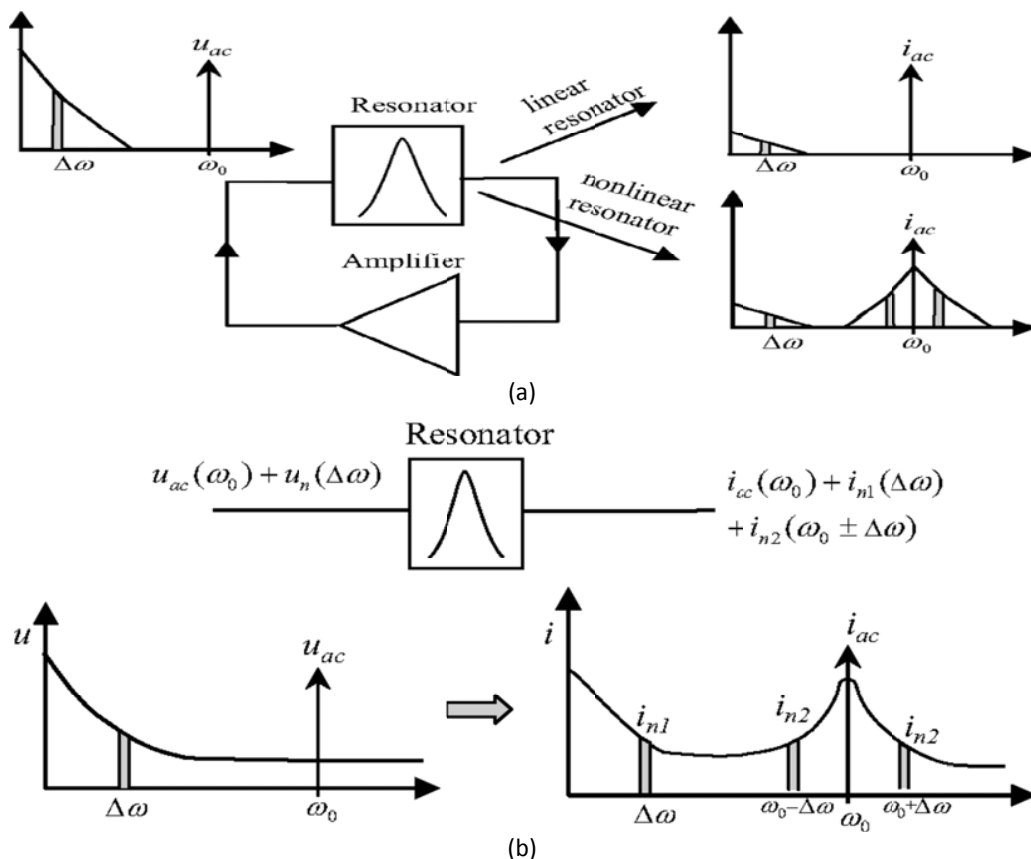
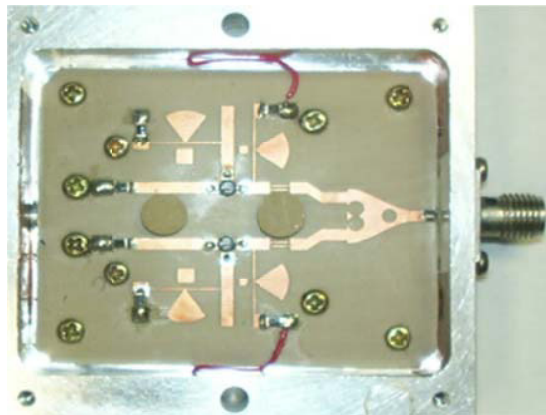
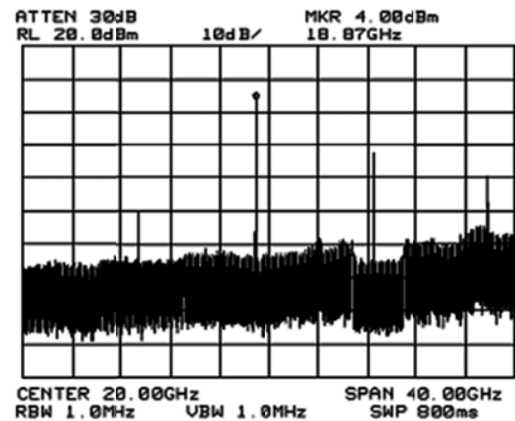


Figure 6-16: A typical noise aliasing phenomena in nonlinear resonator based oscillator circuits: (a) Schematic representation of noise aliasing in oscillator comprises of nonlinear resonator, and (b) Low-frequency noise  $u_n(\Delta\omega)$  present at filter input is aliased to carrier side-bands ( $\omega_0 + \Delta\omega$ ) due to mixing in nonlinear resonator network [57].

This thesis describes the practical examples of low phase noise oscillator circuits using novel slow wave resonator networks that supports reasonably low phase noise for a given conversion efficiency in compact size, and also amenable for integration in the integrated chip (IC) form.



(a)



(b)

Figure 6-17: (a) shows the layout of 18.87 GHz oscillator using expensive high Q-factor dielectric resonators, (b) measured phase noise plots [46]

#### 6.4.1 Examples: Slow Wave Resonator Based Tunable Oscillator Circuits

In this section, examples of tunable oscillator circuits using printed coupled resonator network in conjunction with noise minimization techniques are discussed (patented techniques) [57]-[75].

##### 6.4.1.1 Tunable (2000-3200 MHz) Oscillator Circuits [US Patent No. 7,365,612 B2] [65]

Figure 6-18 shows a slow wave resonator based tunable (2000-3200 MHz) oscillator (SWRO) circuit illustrating the critical components and layout according to the patent application [65]. As shown in Figure 6-18, the SWRO (slow wave resonator oscillator) circuit includes a noise-feedback DC bias network; noise filter in conjunction with microstripline coupled resonator for improved frequency stability under the allowable temperature fluctuations ( $-50^{\circ}\text{C}$  to  $+95^{\circ}\text{C}$ ) including the fluctuations in the supply voltage ( $< \pm 25\%$ ).

Other advantages result from the fact that it is not necessary to provide an active current source for the supply voltage. A low supply voltage is possible, and this is a major advantage in mobile communication systems, for instance. In particular, the operating point of the oscillator transistor is adjusted for a non-overdriven operating mode of the oscillator. The typical phase noise is  $-95\text{dBc}/\text{Hz}$  @ 10 KHz offset for the frequency 2000-3200MHz [60]. The circuit operates at 8Volt and 25 mA, and gives power output more than 5dBm over the tuning range. Typically, wideband oscillators undergo compound compromise, i.e. oscillator phase noise, harmonics or tuning sensitivity as a function of control tuning voltage, thereby, resulting in poor performance over the band under most of its operating condition. The problem of achieving optimum oscillator performance in terms of phase noise compounded by the fact that the optimum drive- levels and conduction angle changes with control tuning voltage [61]. These drawbacks are overcome by incorporating the circuitry that adjusts the drive level and conduction angle in response to the changes in the frequency control tuning voltage. The feedback capacitor ( $C_7$  and  $C_8$ ) as shown in Figure 6-18, is incorporated with tuning diodes in order to adaptive optimize the drive level, thereby improved phase noise performance over the band. By doing so, both phase noise performance and the tuning range of an oscillator can be extended, while simultaneously improving the harmonic contents, and over the tuning range (2000-3200 MHz), measured phase noise is  $-105\text{dBc}/\text{Hz}$  @ 10 KHz offset for the frequency 2000-3200MHz with 8 Volt and 25 mA, and power output more than 3dBm over the tuning range with harmonic rejection better than 20dBc.

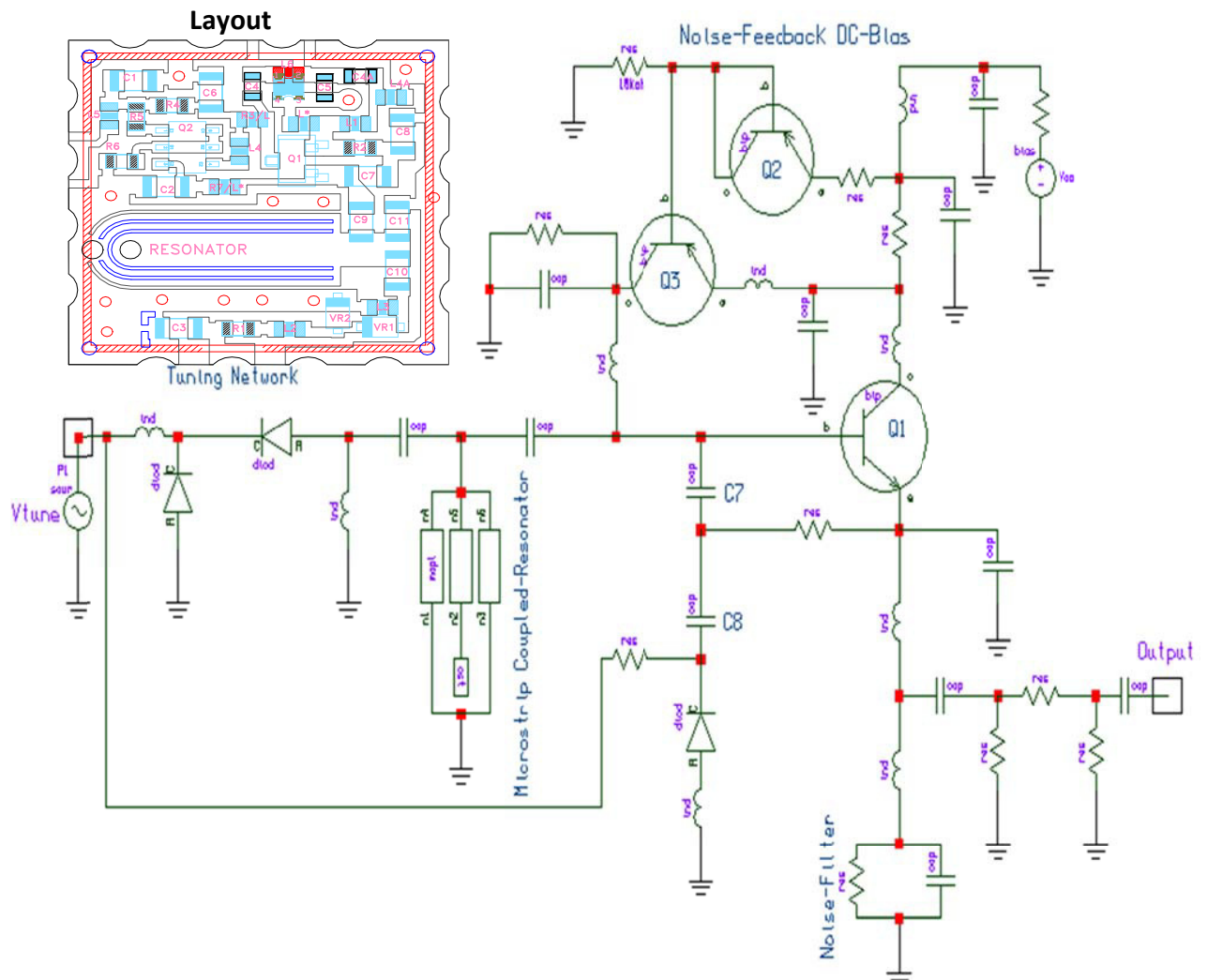


Figure 6-18: A typical schematic of oscillator and layout (32 mills substrate, Dielectric constant 3.38, 0.5 x0.5 inches size) [US Patent No. 7,365,612 B2] [65]

Figure 6-19(a) shows a circuit schematic and layout of the improved version of the SWRO circuit using novel multi-coupled line printed resonators for the improvement of the phase noise performance over the tuning range and associated phase jitter [65]. The resonator structure includes a center strip as an open transmission line in the form of an etched structure with a wavelength, which is shorter than the quarter-wavelength of the desired frequency. The resonator network includes a voltage-controlled variable-capacitance diode, and a resonator terminal connected between the voltage-controlled variable-capacitance diode of the resonator unit and the base of the 3-terminal active device. The resonator is preferably an asymmetric coupled microstripline, and the stages are disposed in a standardized housing in SMD (surface mounted device) technology. By way of example, the etched structure of the resonator may be provided as a microstrip, or as a coplanar structure or as a slot structure or embedded in a multilayer board, for instance, in other words may be made by either the monolithic technique or a hybrid technique.

This novel approach is associated with reference to a tunable ultra-low phase noise and low thermal drift oscillator at 2000-3200MHz employing dynamically tuned microstripline-coupled resonator, which is synchronized to the VCO's tuning port for low phase-jitter and better noise performance. It is especially advantageous that in this distributed resonator function; ultra-low phase noise performance is achieved

without having to use an expensive high Q resonator network with special tuning arrangement to cover wide tuning range. Figure 6-19 (b) shows the phase noise plot, the measured phase noise is better than  $-105\text{dBc/Hz}$  @10 KHz offset for the operating frequency 1900-3200MHz with 240 mW ( $V_{cc}=8\text{V}$ ,  $I_c=30\text{mA}$ ) power consumption. By means of the embodiment as an open strip in the center of the coupled-line resonator structure, a distributed resonator function is achieved while maintaining wide tunable range and higher Q factor as shown in the Figure 6-19 (c).

The measured RF output power is better than 3dBm with more than 53.1 % tuning ranges (1920MHz-3310 MHz) with sufficient margin at both lower ( $f=1650\text{ MHz}$  @  $V_t=0\text{ Volt}$ ) and upper ( $f=3250\text{ MHz}$  @  $V_t=24\text{ Volt}$ ). The measured figure of merit (FOM: defined in Ch-1, Eqn 1.1) is  $-194.49\text{ dBc/Hz}$  for a given power-frequency tuning normalized (PFTN: defined in Ch-1, Eqn 1.2) 15.08 dB.

The novel oscillator circuits shown in Figure 6-19a is stable over operating temperatures of  $-40\text{ }^\circ\text{C}$  to  $+85\text{ }^\circ\text{C}$ , providing sufficient margin for compensating the frequency drift caused due the change in operating temperature, including the package parasitics and component tolerances.

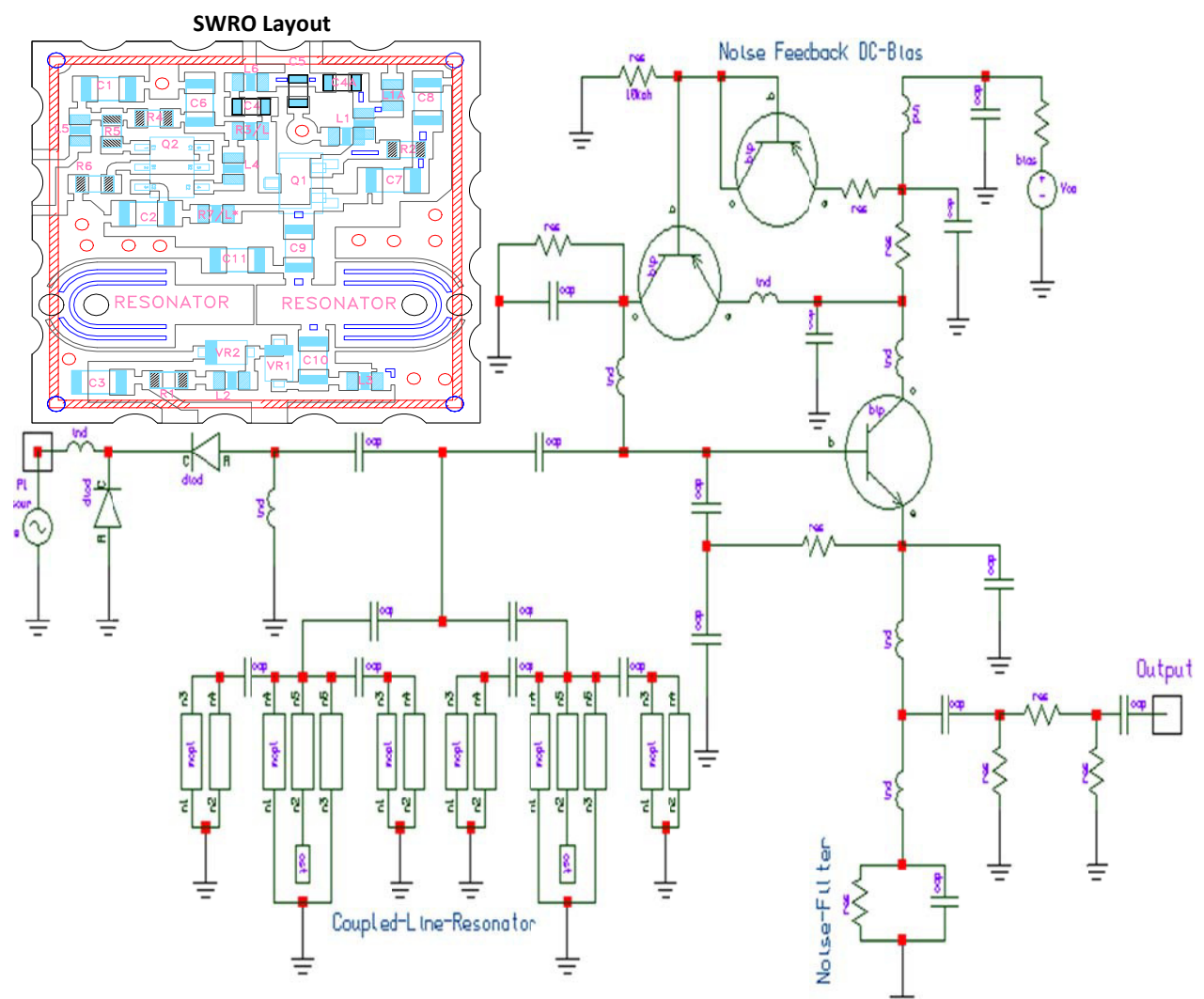


Figure 6-19 (a): An ultra-low noise wideband oscillator (1900-3200MHz) circuit schematic and layout, using inductively and capacitively coupled microstripline resonator (Layout of oscillator circuit is built on 32 mills substrate, Dielectric constant 3.38, 0.5x0.5x0.18 inches), circuit operates with 240 mW ( $V_{cc}=8\text{V}$ ,  $I_c=30\text{mA}$ ) [US Patent No. 7,365,612 B2] [65]

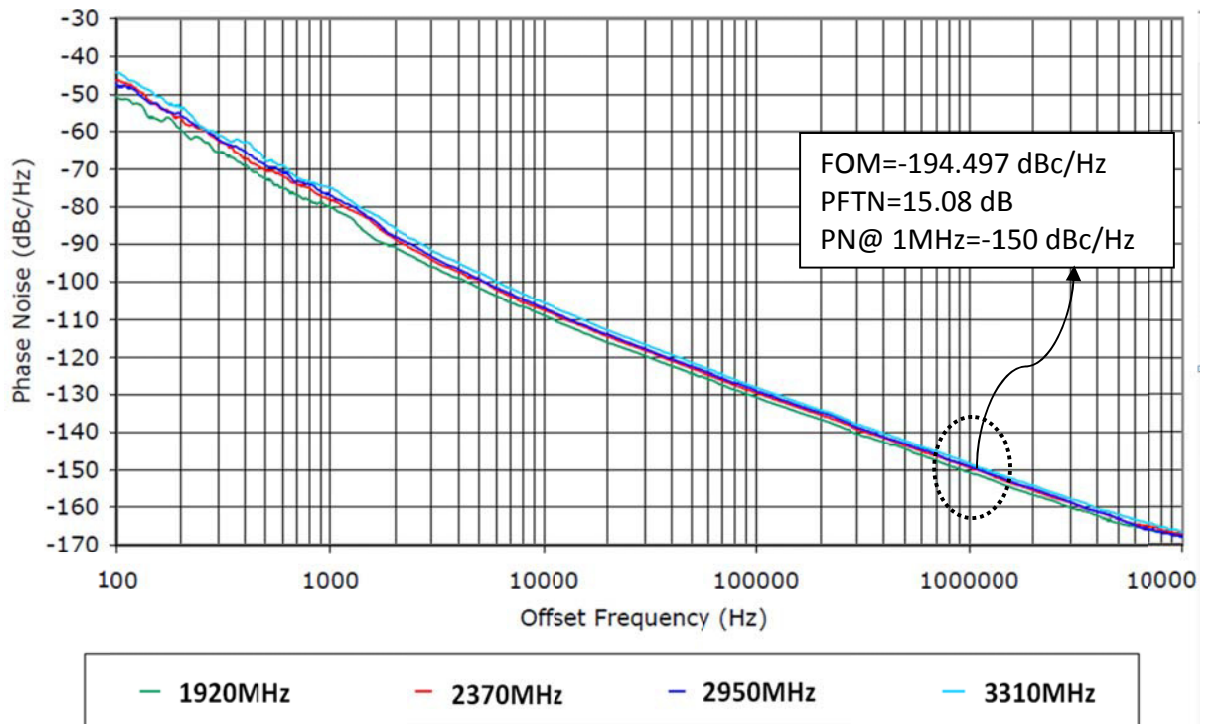


Figure 6-19 (b): Measured phase noise plot of the oscillator shown in Figure 6-19a, the measured FOM defined in Ch-1, Eq 1.1 is -194.49 for a given power-frequency tuning normalized PFTN (defined in Ch-1, Eq 1.2) is 15.08 dB.

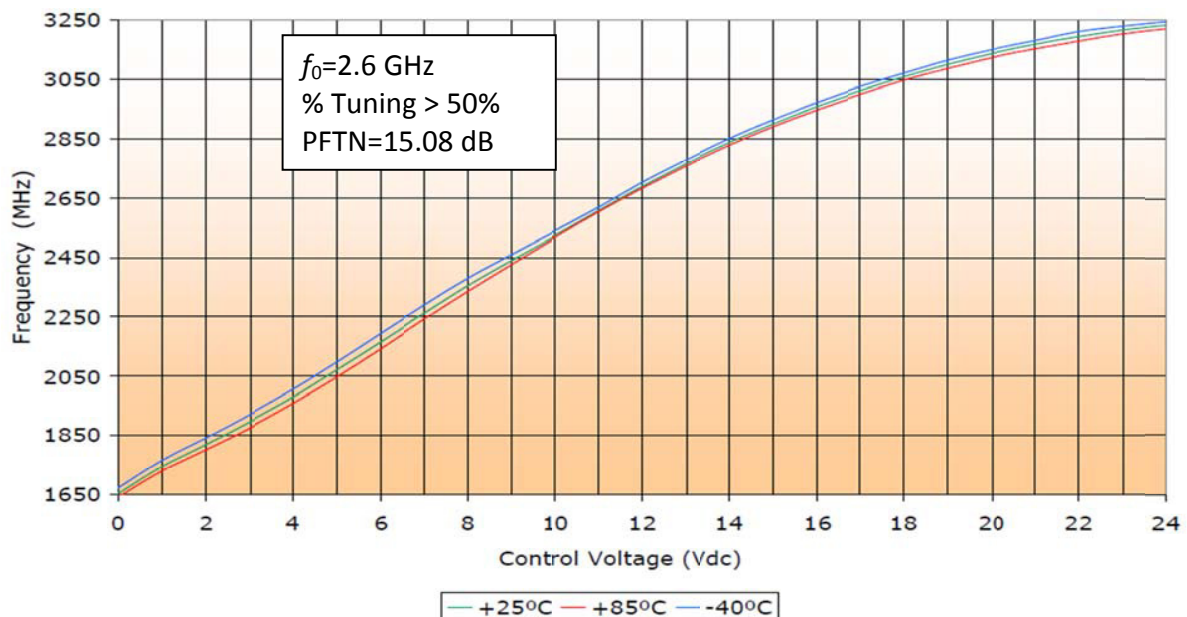


Figure 6-19(c): Measured tuning characteristics of the oscillator circuits shown in Figure 6-19a,  $f=1650$  MHz @  $V_t=0$  Volt) and upper ( $f=3250$  MHz @  $V_t=24$  Volt)

#### 6.4.1.2 Hybrid-tuned Wideband Circuit (1600-3600 MHz) with Coarse and Fine-Tuning

In an oscillator intended for fixed frequency operation, it is relatively easy to select the coupling parameter so that it gives optimum phase noise performance. However, for wideband tunability it is difficult to satisfy optimum coupling factor over the tuning range. The usual approach is to select the spacing

between the coupled lines, compromise drive level and conduction angle that permit adequate (rather than optimum) oscillator operation over the desired tuning range. By doing so, however, optimum oscillator performance is achieved at only one frequency, if at all. Further, the use of fixed structure of microstripline necessarily limits the range of possible operating frequencies, sometime preventing certain design criteria from being met. An alternative approach is to try to design oscillator circuit so that the optimum dimension changes, as a function of frequency, in exactly the same manner and magnitude as the frequency control signal changes as a function of tuning voltage. For the application in fast switching frequency synthesizer, hybrid tuned (facilitates coarse and fine-tuning) wideband oscillator circuit is required.

Figure 6-20(a) shows the schematic of the hybrid tuned (coarse/fine) design approach that facilitates coarse and fine-tuning, and maintaining low noise performance over the tuning range (1600-3600 MHz).

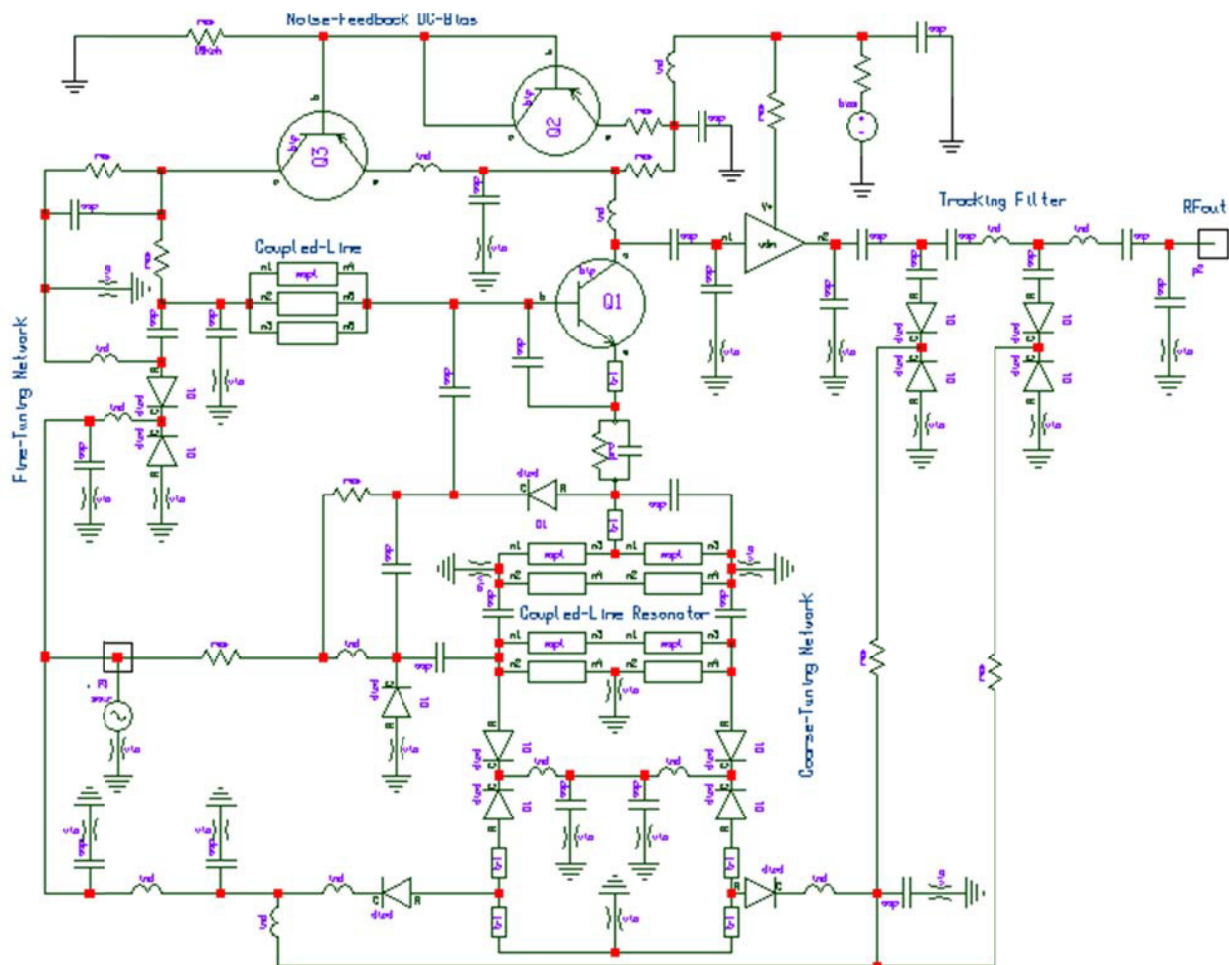


Figure 6-20(a): Schematic diagram of hybrid-tuned ultra-low noise wideband (1600-3600MHz) (SWRO) with 240 mW ( $V_{cc}=10V$ ,  $I_c=40mA$ ), tuning characteristics:  $f=1350$  MHz @  $V_t=0$  Volt  $f=3850$  MHz @  $V_t=0$  Volt [65]

Figure 6-20 (b) shows the phase noise plot, the measured phase noise is typically better than  $-90dBc/Hz$  @ 10 KHz offset for the frequency 1600-3600MHz. Figure 6-20(c) depicts the tuning characteristics; the measured coarse tuning for 1600-3600MHz frequencies is from 0.5 Volt to 16 Volts, and fine-tuning is 1-5 Volt (20-40MHz/Volt). The measured RF output power as shown in Figure 6-20(d) is better than +4 dBm with more than 75 % tuning range (1600-3600 MHz)) with sufficient margin at both lower ( $f=1350$  MHz @  $V_t=0$  Volt) and upper ( $f=3850$  MHz @  $V_t=0$  Volt) frequencies. It can be noticed that the variation in phase noise is within 1-3dB over operating ranges, shows state-of-the-art VCOs for a given class of the signal sources.

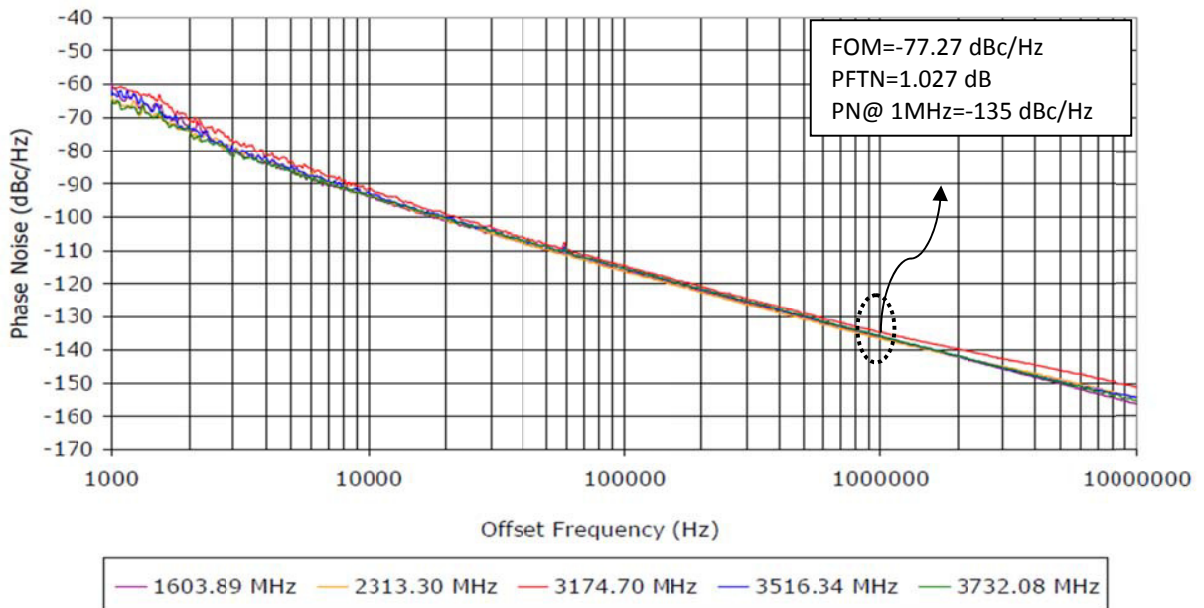


Figure 6-20(b): Measured phase noise plot of the oscillator circuit shown in Figure 6-20(a), measured figure of merit (FOM: defined in Ch-1, Eq 1.1) is -177.27 dBc/Hz for a given power-frequency tuning normalized (PFTN: defined in Ch-1, Eq 1.2) 1.027 dB.

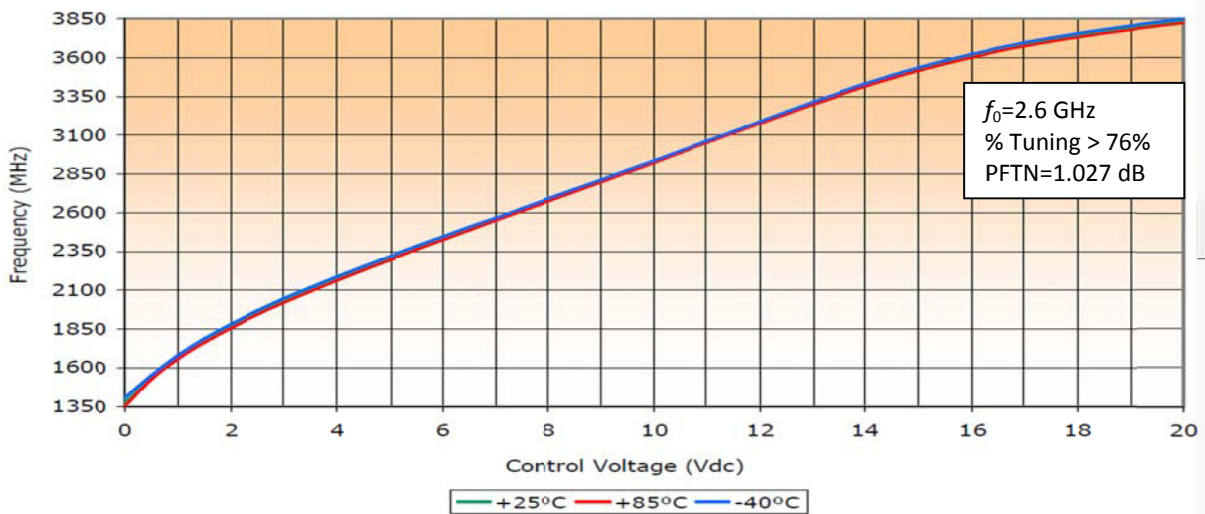


Figure 6-20©: Measured tuning characteristics of the oscillator circuits shown in Figure 6-20a,  $f=1350$  MHz @  $V_t=0$  Volt and  $f=3850$  MHz @  $V_t=24$  Volt

The measured figure of merit (FOM: defined in Ch-1, Eq 1.1) is -177.27 for a given power-frequency tuning normalized (PFTN: defined in Ch-1, Eq 1.2) 1.027 dB. The novel oscillator circuits shown in Figure 6-20(a) is stable over operating temperature  $-40$  °C to  $+85$  °C, providing sufficient margin for compensating the frequency drift caused due to the change in operating temperature, including the package parasitics and component tolerances.

Using dynamically tuned resonator network incorporated with the tracking filter at output can use the same circuit for other user defined frequency band. Furthermore, to compensate process and temperature variations, a VCO coarse-tuning (with high gain) would make the circuit more sensitive to coupling from nearby circuits and power supply noise.



To overcome this problem, fine-tuning network is incorporated at proper node of the oscillator circuit, which needs less gain to cover temperature and supply variations that minimizes the noise interference. The circuit operates at 12 Volt and 25 mA, and gives power output more than 4 dBm (Figure 6-20d) over the tuning range (1600 MHz -3600 MHz).

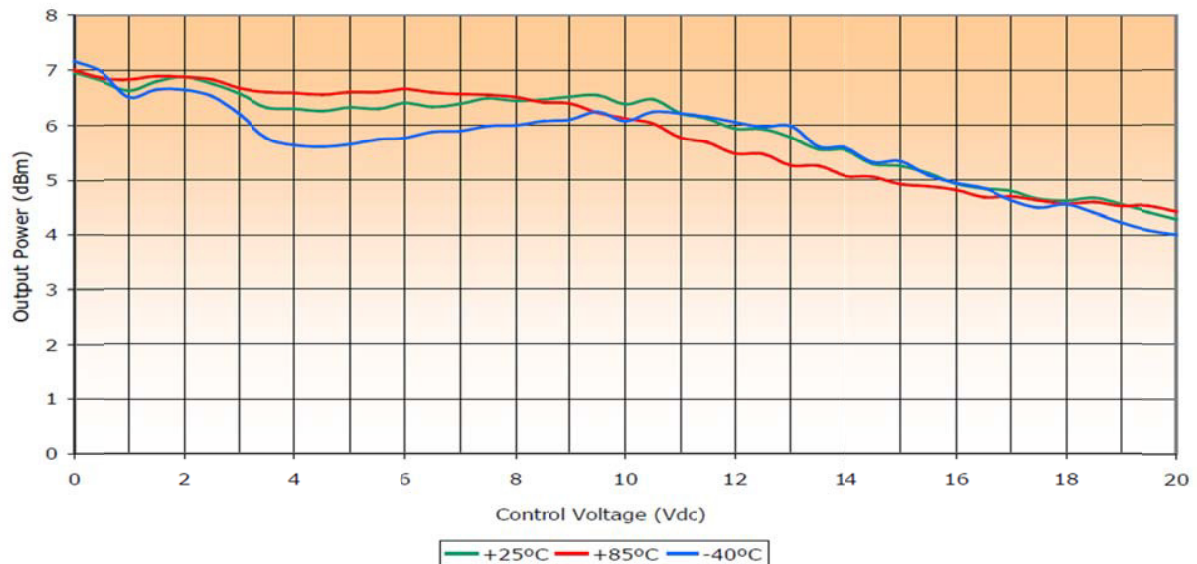


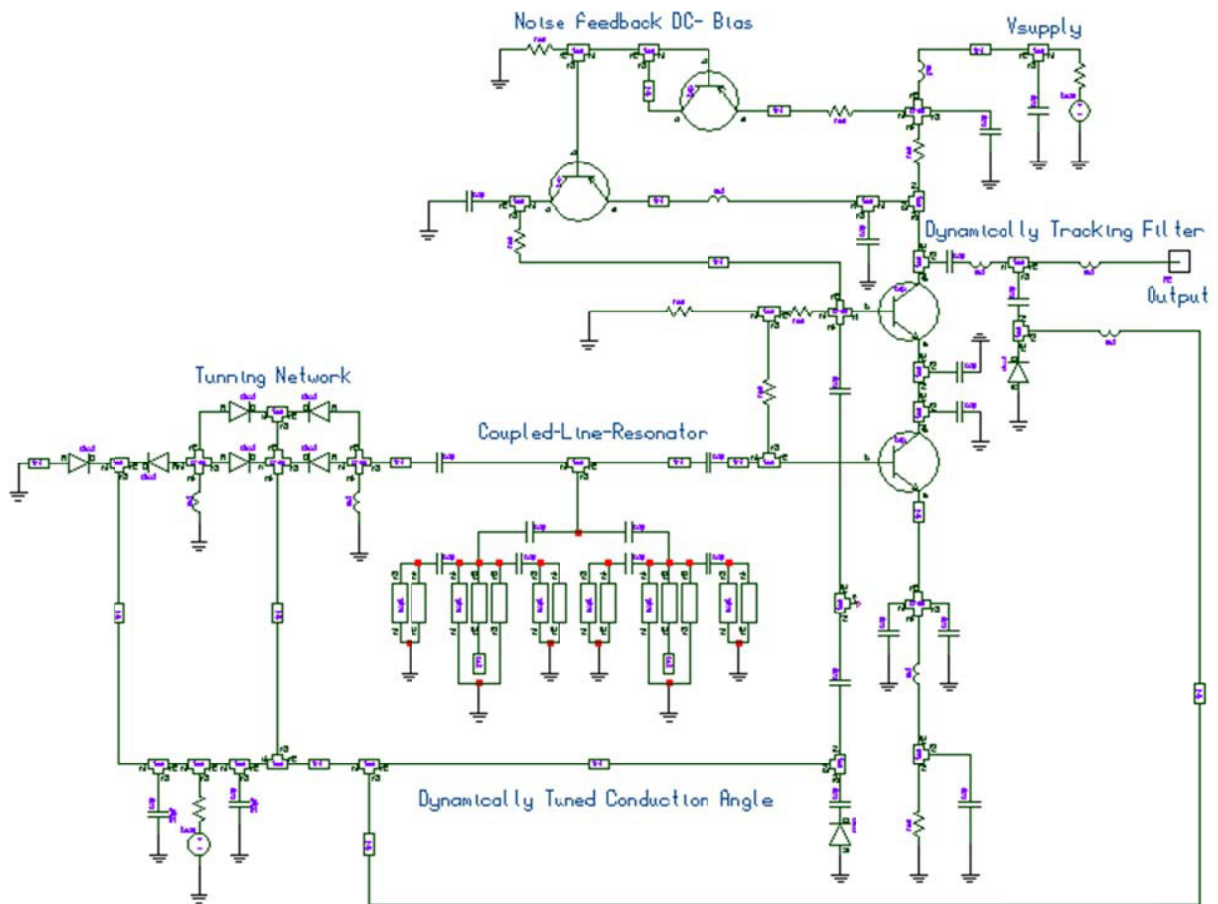
Figure 6-20(d): Measured plot of output power of the oscillator circuits shown in Figure 6-20a, The measured RF output power is better than +4 dBm with more than 75 % tuning ranges (1600-3600 MHz)) with sufficient margin at both lower (f=1350 MHz @ Vt=0 Volt) and upper (f=3850 MHz @ Vt=0 Volt).

### 6.4.1.3 Power-Efficient Wideband SWRO Circuit (2000-3000 MHz)

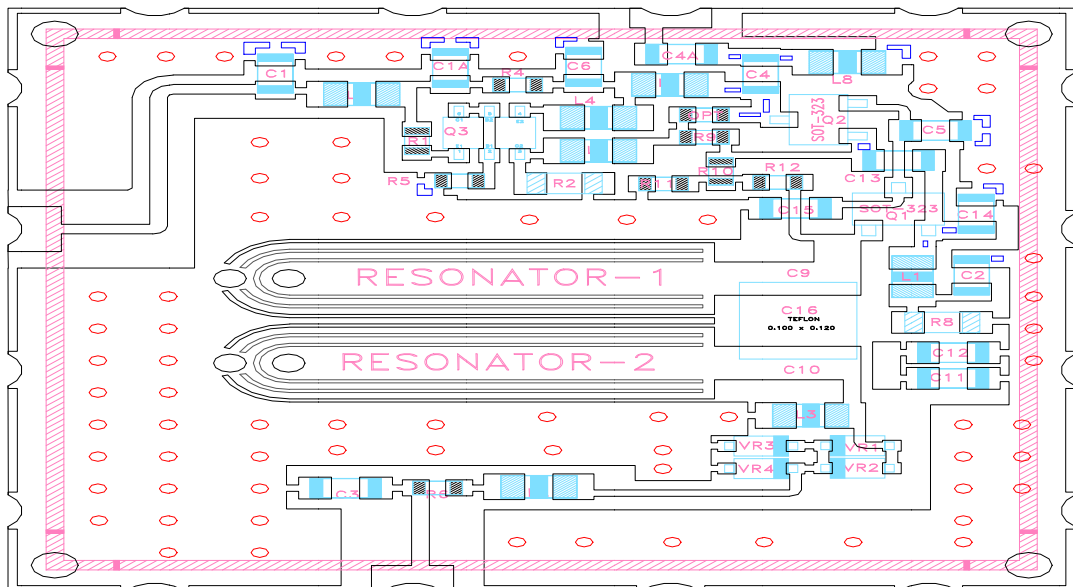
The reported oscillator circuit shown in Figure 6-21 offers the power-efficient (current effective topology), realized by incorporating two three terminal active devices (bipolar transistors) in cascode configuration so that both the devices share the same bias current. The circuit operates at 10V and 15 mA of current, and gives power output better than -3dBm.

As shown in Figure 6-21, the voltage controlled oscillator, comprising of a cascode configuration of the 3-terminal active device, is arranged in a common collector and emitter configuration for generating negative resistance under current efficient operation for wideband (2000-3000MHz) signal source applications. The applications where the phase noise performance at a lower offset from the carrier is critical, the reported novel circuit supports ultra-low noise performance over the tuning range. Figure 6-21 (c) shows the CAD simulated phase noise plot, typically better than -156 dBc/Hz at 1 MHz offset for 2000-3000 MHz tuning range.

The proposed oscillator topology as depicted in Figure 6-21(a) improves the phase noise and thermal drift and extends the operating frequency of the microstripline-based resonator to higher frequency band depending upon the coupling network. The freedom of selection of the frequency, ultra-low phase noise, wide tuning range, and stability over temperature will make this technology promising and attractive for next generation integrated high frequency mobile communication system. The novel oscillator circuits shown in Figure 6-21a is stable over operating temperature -40 °C to +85 °C, providing sufficient margin for compensating the frequency drift caused due to the change in operating temperature, including the package parasitics and component tolerances.



(a) A typical schematic of the cascode (SWRO) circuit (2000-3000 MHz) with 150 mW ( $V_{cc}=5V$ ,  $I_c=30mA$ ) [65]



(b) Layout of the cascode (SWRO) circuit (0.75x0.75x0.18 inches [US Patent No. 7,365,612 B2] [65]

Figure 6-21: A typical power-efficient wideband (SWRO) circuit (a) Schematic of the cascode configuration, and (b) Layout of oscillator circuit (32 mills substrate, Dielectric constant 3.38) [65]

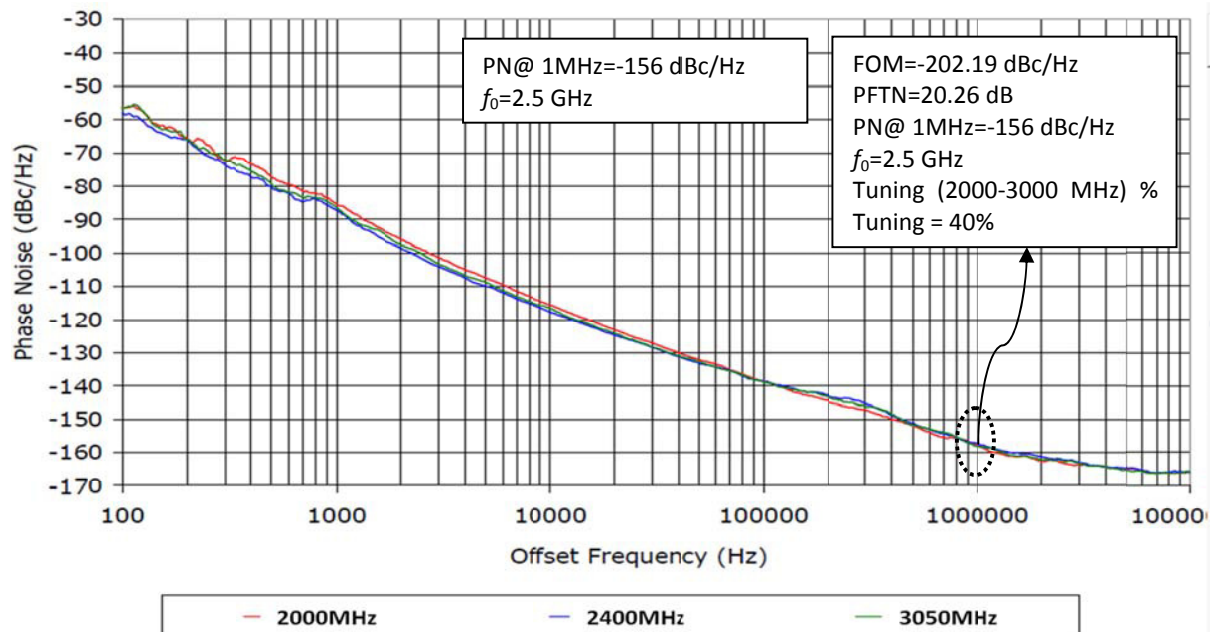


Figure 6-21(c): Measured phase noise plot of ultra low noise power efficient wideband (2-3 GHz) (SWRO), measured figure of merit (FOM: defined in Ch-1, Eq 1.1) is -202.19 dBc/Hz for a given power-frequency tuning normalized (PFTN: defined in Ch-1, Eq 1.2) 20.26 dB, with power consumption of 150mW ( $V_{cc}=10V$ ,  $I_c=15mA$ ), o/p power is 0dBm.

#### 6.4.1.4 User-Defined Ultra Low phase Noise Oscillator Circuit [U.S. Patent No. 7,586,381] [68]

The applications where the phase noise performance is most demanding parameter, proposed oscillator topology shown in Figure 6-22 offers user-defined and cost-effective alternative of expensive SAW (surface acoustic wave) and ceramic resonator based oscillators. Ceramic and SAW resonator based oscillators are used as ultra-low phase noise oscillators but these high Q resonators are expensive and their availability and performances are limited to the selected frequency and narrow operating temperature range, and these facts make them not suitable for operating in stringent temperature environment and low cost application [7]-[37]. In addition, ceramic resonators are more susceptible to noise interference, and sensitive to phase-hit in PLL applications [30]-[36]. Microstripline resonators are not without flaws, and are susceptible to noise interference, and they exhibit lower quality factor as compared to ceramic resonators. Quality factor of the resonator is the key factor for low phase noise performance but overall oscillator performance is controlled by the time average loaded Q of the oscillator circuit.

For the most part, these disadvantages have been overcome by means of novel configuration of the compact coupled planar resonator (CCPR) and act like slow wave propagation for improving group delay, thereby improving time average quality factor. The effective Q of the coupled resonator network is improved by optimizing the rate of change of the phase over the tuning range by dynamically tuning the coupling parameter. Figures 6-22(a) and 6-22(b) illustrate a layout of the user-defined high spectral purity oscillator with multi-coupled line buried slow wave resonator (SWR) constructed that configures suitable impedance transfer function of the resonator by incorporating and dynamically tuned junction capacitances ( $C_{be}$ ,  $C_{ce}$ ,  $C_{ce}$  of Q1), drive level, noise-filtering network across emitter and planar-coupled resonator [68]. They have been fabricated on low-loss 30-mil-thick dielectric material with dielectric constant of 3.38, and tested from 1 to 18 GHz for user-defined frequency sources for reconfigurable synthesizer applications.

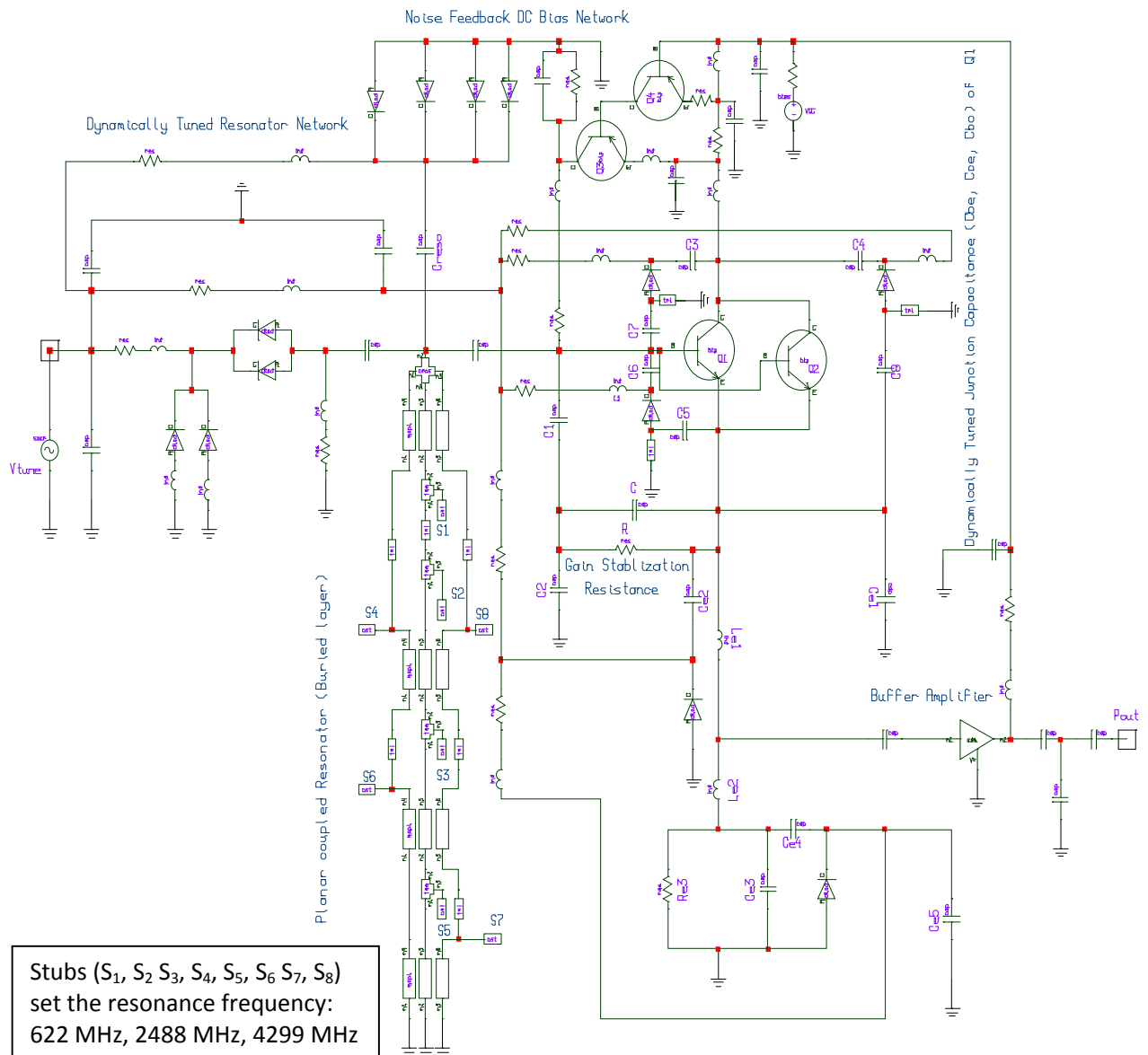


Figure 6-22(a): A typical schematic of oscillator circuit using planar multi-coupled stripline resonator constructed in accordance with the alternative of expensive non-planar SAW and Ceramic resonator based oscillator circuits, with 100 mW ( $V_{cc}=5V$ ,  $I_c=20mA$ ), RF output power is +5 dBm [U.S. Patent No. 7,586,381] [68]

As shown in Figure 6-22(b), printed multi-coupled resonators positioned parallel to each other, in such a way that adjacent resonators coupled along the guided length for the given frequencies. The layout shown in 6-22b is 6-layer board, fabricated on 64mil thick ROGER- substrate of dielectric constant 3.38 and loss tangent  $2.7 \times 10^{-4}$ . The choice of substrate depends on size, higher-order modes, surface wave effects, implementation (couplings, line length, width, spacing, and spacing tolerances), dielectric loss, temperature stability, and power handling (dielectric strength and thermal conductivity).

Figure 6-22(c) depicts the measured phase noise plot of the oscillator circuit shown in the Figure 6-22a for the typical frequency 622 MHz, 1000 MHz, and 2488 MHz; realized by arrangement of stubs-tuning ( $S_1, S_2 S_3, S_4, S_5, S_6 S_7, S_8$ ) as shown in the layout in Figure 6-22(b).

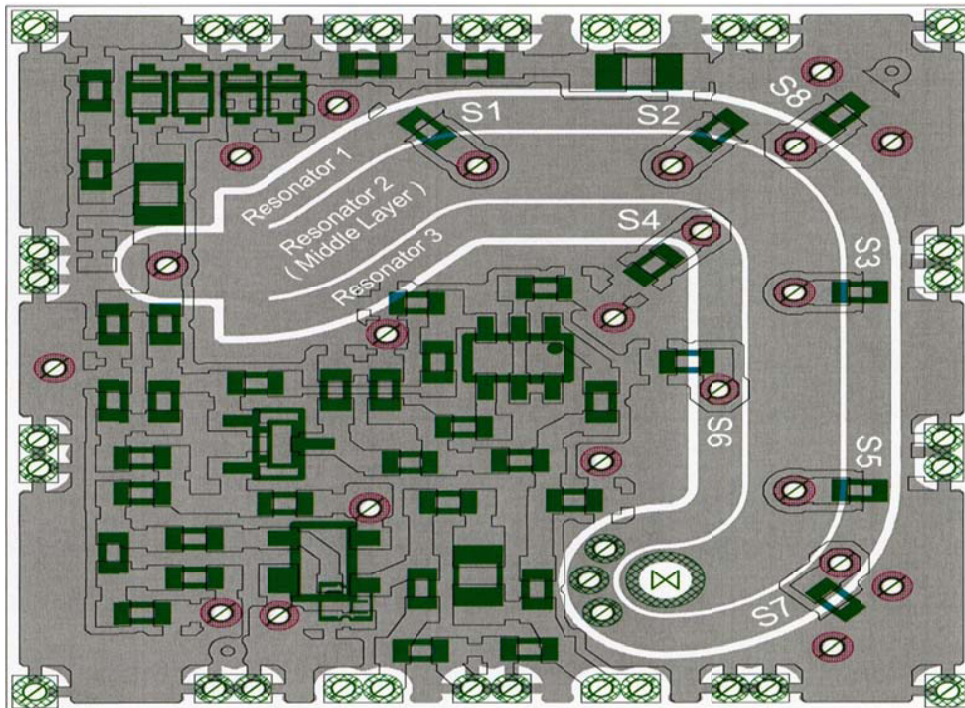


Figure 6-22(b): A layout of the user defined high spectral purity oscillator circuit with multi-coupled line buried slow wave resonator (SWR) VCO circuit (64 mills substrate, Dielectric constant 3.38) 0.75x0.75x0.18 inches, stubs ( $S_1, S_2, S_3, S_4, S_5, S_6, S_7, S_8$ ) sets the desire frequency ( 622 MHz, 2488 MHz, 4200 MHz) [U.S. Patent No. 7,586,381] [68].

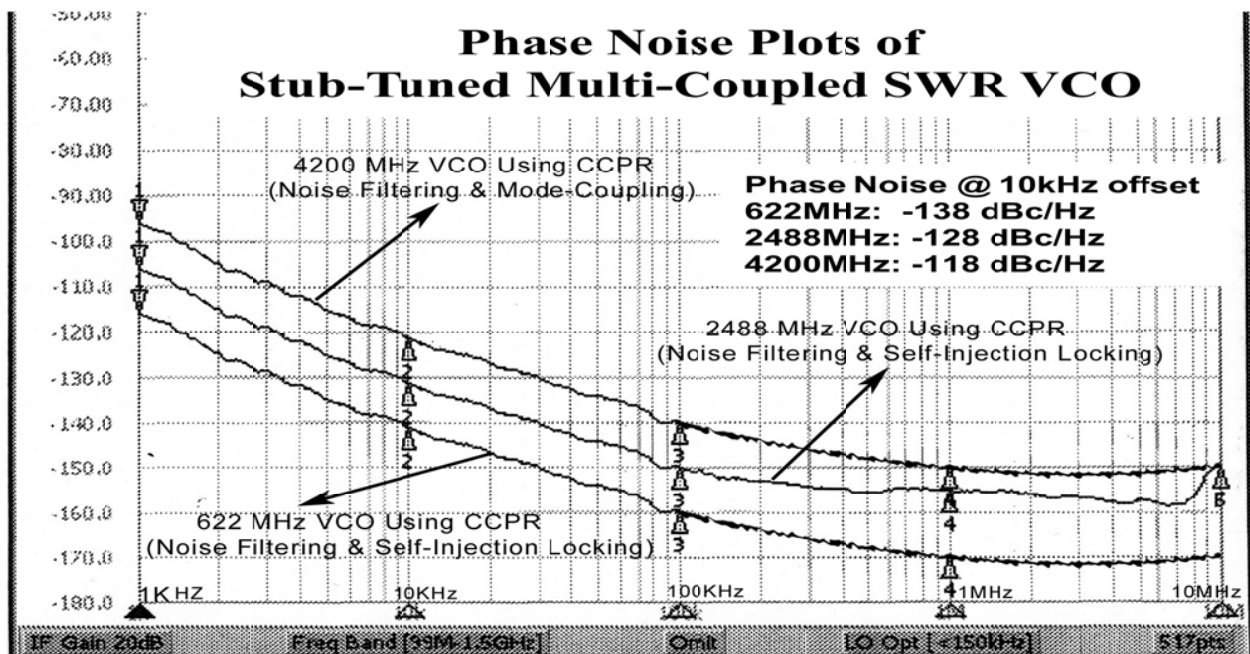


Figure 6-22(c): Depicts the measured phase noise plot of the compact coupled planar resonator (CCPR) oscillator circuit shown in the Figure 6-22a for the typical frequency 622 MHz, 2488MHz, and 4200 MHz realized by arrangement of stubs-tuning ( $S_1, S_2, S_3, S_4, S_5, S_6, S_7, S_8$ ) as shown in the layout in Figure 6-22b, measured figure of merit (FOM: defined in Ch-1, Eq 1.1) is  $-205.876$  dBc/Hz for  $f_0=622$  MHz,  $-202.9$  dBc/Hz for  $f_0=2488$  MHz,  $-205.46$  dBc/Hz for  $f_0=4200$  MHz ; with power consumption of 100mW ( $V_{cc}=5V, I_c=20mA$ ), RF o/p power is 3.3 dBm [68]

As shown in Figure 6-22c, the typical phase noise @ 10 kHz offset from the carrier, typical values: –138dBc/Hz (carrier frequency: 622MHz), –128 dBc/Hz (carrier frequency: 2488MHz), and –118dBc/Hz (carrier frequency: 4200 MHz); and is not limited to these frequencies. The circuit works at 5V, 20mA, and typical output power is 5 dBm, and second harmonic rejection is better than –20 dBc. The measured figure of merit (FOM: defined in Ch-1, Eq 1.1) is -205.876 dBc/Hz for  $f_o=622$  MHz with o/p power of +5dBm, -202.9 dBc/Hz for  $f_o=2488$  MHz with output power of +4.2 dBm, -205.46 dBc/Hz for  $f_o=4200$  MHz with output power of + 3.3 dBm. The total power consumption of the prototype oscillator circuit layout shown in Figure 6-22(b) is 100mW ( $V_{cc}=5V$ ,  $I_c=20mA$ ) with stable RF output power better than 3.3 dBm over operating temperature -40 degree C to +85 degree C.

#### 6.4.1.5 Multi-Octave Band SWRO Circuit [U.S. Patent No. 7,605,670] [69]

Modern communication systems are multi-band and multi-mode, therefore requiring an ultra-wideband low noise signal source that may allow simultaneous access to DCS1800, PCS 1900, and WCDMA networks by a single ultra-low noise wideband VCO. An ultra-low noise, low cost and power efficient VCO is reported, tuned over a wide range of frequencies while maintaining the low phase noise over the band. As a multi-coupled slow-wave (MCSWR) VCO is planar and broadband in nature, it is suited for cost-effective, monolithic-microwave-integrated-circuit (MMIC) fabrication [76]-[83]. With the potential to enable wide operational bandwidths, eliminate discrete resonator (such as a YIG sphere), and produce high-quality-factor planar resonator for low noise VCOs by means of planar fabrication process compatible with existing IC and MMIC processes, the MCSW VCO is a promising technology for present and future broadband communication requirements.

The multi-coupled distributed resonator design approach demonstrated in this work can satisfy the need for the present demand for wideband VCO, and amenable for integration in chip form. To support a uniform negative resistance over the tuning range, the varactor tuned coupled resonator shown in the Figure 6-23(a) is connected across the base and collector of the active device, and the loss resistance is compensated by the negative resistance, which dynamically adjusts in response to the change in oscillator frequency over the band, by dynamically tuning the phase shift of the negative resistance-generating network to meet the phase shift criteria for the resonance over the operating frequency band of interest.

The variable coupling capacitor  $C_c$  as shown in Figure 6-23(a) is designed for the optimum loading of the coupled resonator network across the active device, and dynamically tuned for optimum performance. The time average  $Q$  factor of the resonator has been improved by dynamically optimizing the coupling factor  $\beta$  of the multi-coupled distributed resonator over the desired tuning range. As shown in the Figure 6-23(a), the coupled resonator is connected across the base and collector of the three-terminal active device through coupling capacitor, which is electronically tuned by applying the tuning voltage to the tuning network integrated with the coupled resonator. The values of the coupling capacitor  $C_c$  are derived from the input stability circle, and it should be within the input stability circle so that the circuit will oscillate at a particular frequency for the given lowest possible value of the  $C_c$  over the band. Figure 6-23(b) depicts the layout of the Figure 6-23(a), points to a planar topology and amenable for integrated circuit solution [69]. The drawback of this topology is mode jumping; causing drop of oscillation in the desired frequency band, which can be suppressed by incorporating phase-compensating network in conjunction with progressive wave coupled resonator network [75].

Figure 6-24(a) shows a typical block diagram of multi-octave band oscillator circuit using a combination of printed multi-mode, progressive wave, slow-wave coupled resonator for ultra low phase noise and multi-octave band operation [69]. This arrangement can be characterized as a  $Q$ -multiplier effect based on evanescent-mode progressive delay that eventually improves the time average loaded  $Q$  of the planar resonator over its multi-octave operation.

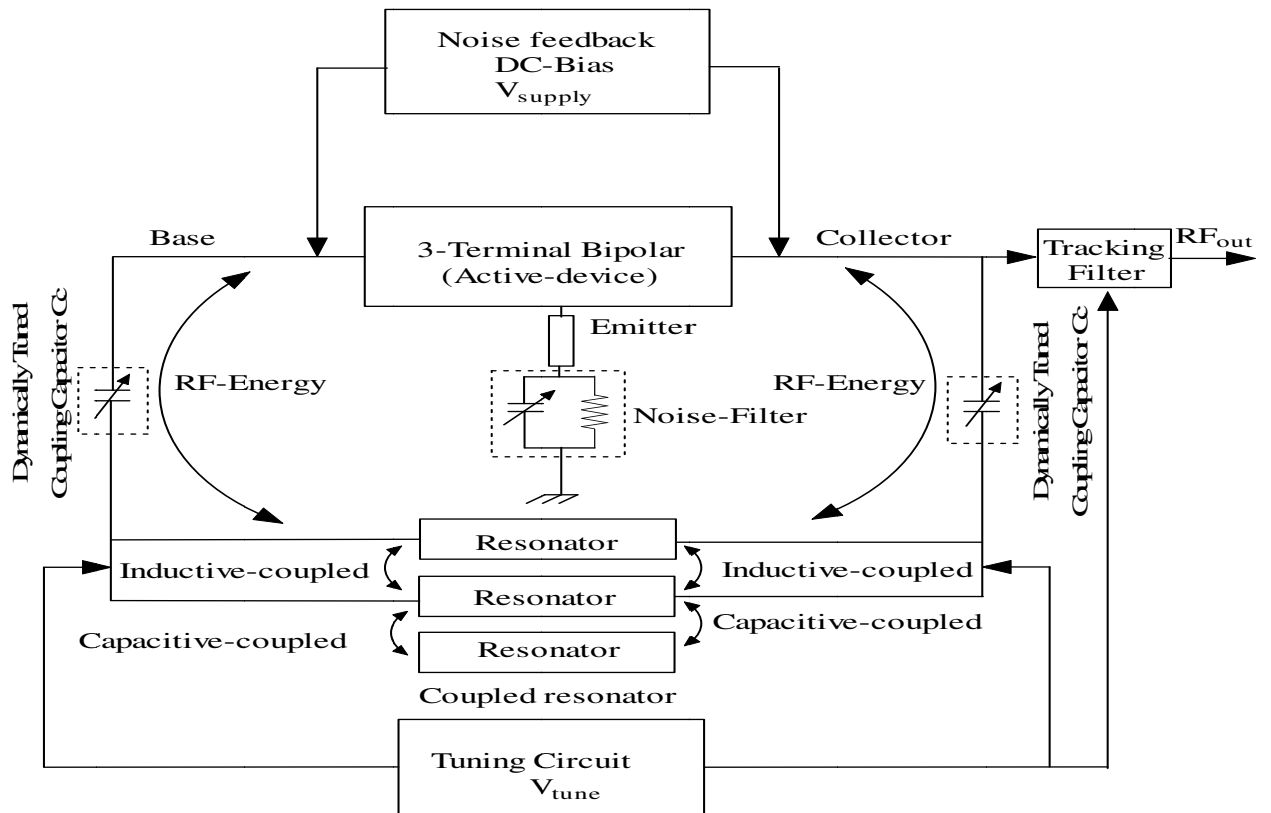


Figure 6-23(a): A typical block diagram of the wideband VCO [69]

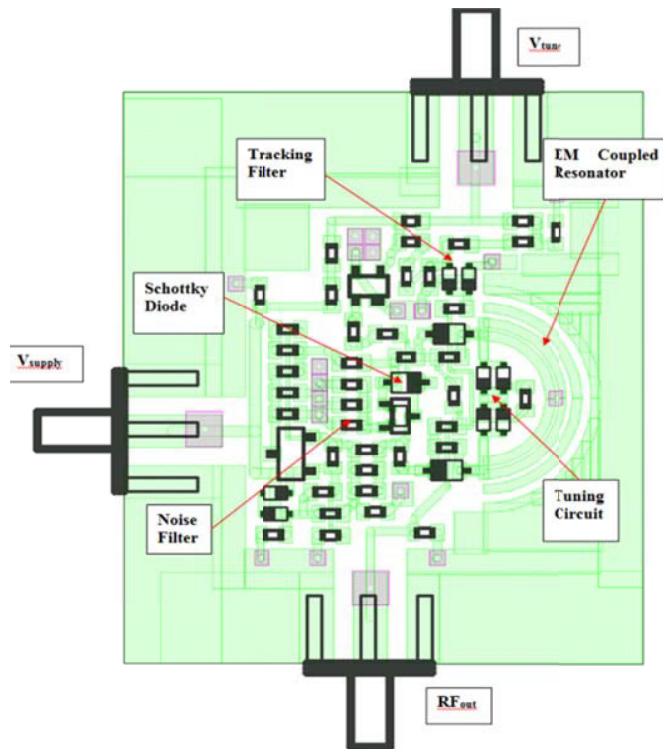


Figure 6-23(b): Shows the layout of the oscillator circuit shown in Figure 6-23a, layout is made on 32-mil substrate with Dielectric constant 3.38 in 0.75x0.75x0.18 inches size [U.S. Patent No. 7,586,381] [68]-[69].

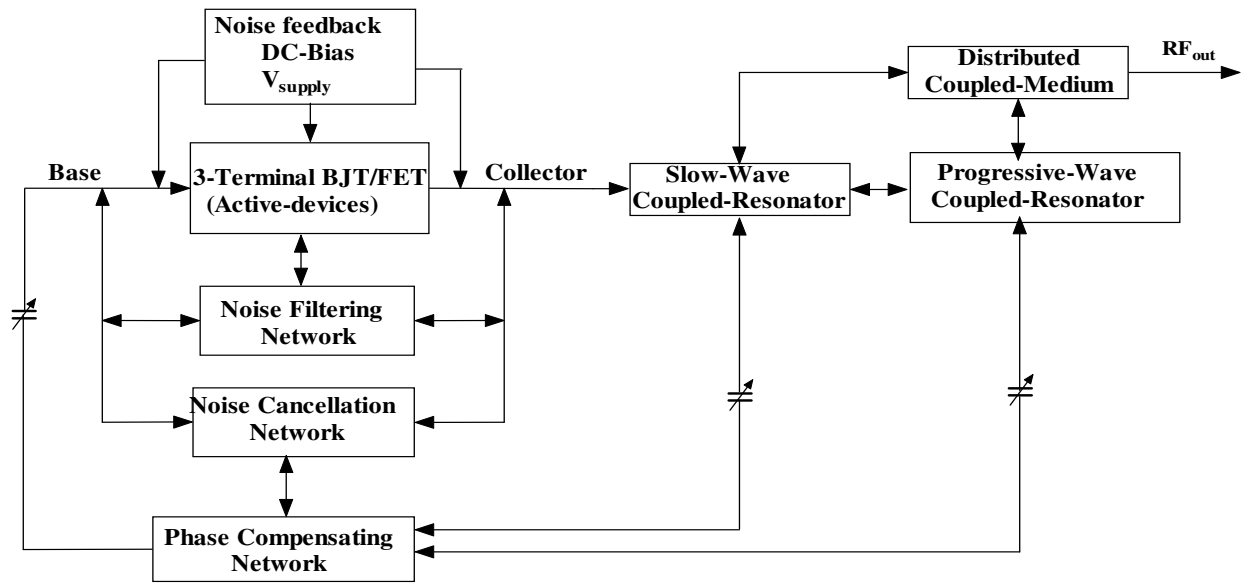


Figure 6-24(a): A functional block diagram of an oscillator using multi-mode, progressive wave, slow-wave coupled resonator for ultra low phase noise and multi-octave band operation with DC bias of 5V and 40mA.

As shown in Figure 6-24(a), the oscillator includes a 3-terminal active device (bipolar transistor NEC 68830), noise-filtering network, and a noise cancellation network connected in parallel between the base and collector terminals. Figure 6-25 shows the transistor (NE 68830) with the package parameters for the optimization of the wideband tuning characteristics. Table 6.2 shows the transistor spice and package parameters of NE68830 from manufacturer (NEC) data sheets.

A noise feedback and DC bias supply as shown in Figure 6-24(a) comprises an active feedback network that compensates for change in the DC bias power supply voltage owing to change in the operating temperature of the oscillator or its environment [64]. The active impedance created by the three-terminal device (e.g., a Bipolar or FET transistor) in a MCSWR (multi coupled slow-wave resonator) oscillator circuit exhibits a negative real part with a real magnitude and an imaginary part with an imaginary magnitude. The real magnitude is a function of the imaginary magnitude. The imaginary magnitude is selected such that the real magnitude compensates for the loss of the MCSWR network. The selection of the imaginary magnitude should also coincide with the maximum-slope inflection point of the oscillator's phase characteristics curve, in order to optimize group delay performance. Figure 6-24(b) shows the printed circuit board (PCB) layout diagrams of a VCO constructed in accordance with the description shown in block diagram (Figure 6-24a) with an aspect of multi-octave tuning characteristics in which the resonator comprised of multi-mode coupled resonator, progressive wave coupled resonator, and slow-wave coupled resonator network, including the mode-coupling and self-injection locking. Each of these resonators is planar in the form and electromagnetically coupled to each other. As explained above the electromagnetic-coupling between these resonators provide for the wideband tunability. Note that the slow-wave coupled resonator comprises a planar structure having projections that mate with openings (meander lines that support slow wave dynamics as illustrated in Figure 6-24(b)). The unified resonator structure comprised of slow wave and progressive wave resonator network depicted in Figure 6-24(b) form in combination a single high Q-factor resonator network. The combination of slow-wave resonator and progressive wave resonator enables the advantage of the wideband tunability. The limitation of spurious frequencies of the multi-mode resonator are shifted from the integer multiples of the fundamental resonant frequency, enabling multi-octave band tuning, which otherwise is not possible by using independently either the multi-mode resonator, slow-wave resonator or progressive-wave resonator [76]-[91].



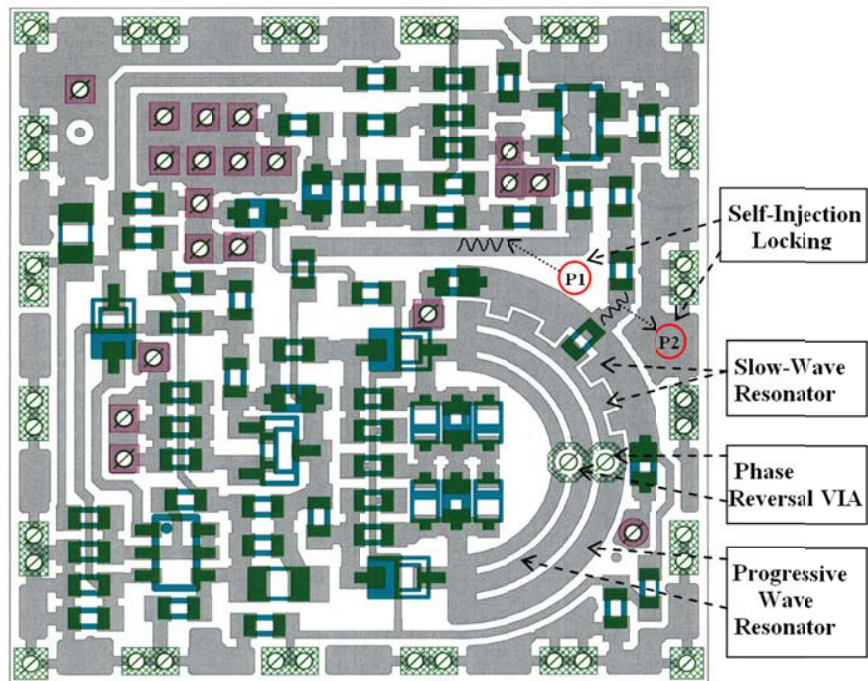


Figure 6-24(b): The printed layout diagram of an oscillator as per block diagram shown in Figure 6-24(a), points to a MMIC technology, layout is made on 32 mils substrate with Dielectric constant 3.38 in 0.75x0.75x0.18 inches.

Table 6.2: Spice parameters (Gummel-Poon Model, Berkley-Spice) [67, pp. 134]

Spice Parameters	Values	Spice Parameters	Value	Packages	NE 68830
IS	3.8E-16	MJC	0.48	C <sub>CB</sub>	0.24E-12
BF	135.7	XCJC	0.56	C <sub>CCE</sub>	0.27E-12
NF	1	CJS	0	L <sub>B</sub>	0.5E-9
VAF	28	VJS	0.75	L <sub>E</sub>	0.86E-9
IKF	0.6	MJS	0	C <sub>CBPKG</sub>	0.08E-12
NE	1.49	TF	11E-12	C <sub>CEPKG</sub>	0.04E-12
BR	12.3	XTF	0.36	C <sub>BEPKG</sub>	0.04E-12
NR	1.1	VTF	0.65	L <sub>BX</sub>	0.2E-9
VAR	3.5	ITF	0.61	L <sub>CX</sub>	0.1E-9
IKR	0.06	PTF	50	L <sub>EX</sub>	0.2E-9
ISC	3.5E-16	TR	32E-12		
NC	1.62	EG	1.11		
RE	0.4	XTB	0		
RC	4.2	KF	0		
CJE	0.79E-12	AF	1		
CJC	0.549E-12	VJE	0.71		
XTI	3	RB	6.14		
RBM	3.5	RC	4.2		
IRB	0.001	CJE	0.79E-12		
CJC	0.549E-12	MJE	0.38		
VJC	0.65				

The mode-coupling approach also includes a methodology for optimum dynamic coupling; Optimum coupling enhances the dynamic loaded Q, reduces or eliminates phase hits, diminishes susceptibility to microphonics, and minimizes phase noise while achieving a broadband linear tuning range.

Figure 6-26(a) shows the measured phase noise plots of the novel oscillator circuit layout depicted in Figure 6-24(b), the measured phase noise performance is typically better than  $-129\text{dBc/Hz}$  @  $100\text{ kHz}$  offset from the carrier frequency over the band (600-2100 MHz). The measured figure of merit (FOM: defined in Ch-1, Eq 1.1) is  $-187.5\text{ dBc/Hz}$  for a given PFTN (defined in Ch-1, Eq 1.2)  $16.02\text{ dB}$ , with power consumption of  $200\text{mW}$  ( $V_{cc}=5\text{V}$ ,  $I_c=40\text{ mA}$ ), o/p power is  $+3\text{ dBm}$ . As illustrated in Figure 6-26(a), the variation in phase noise over the operating frequency band is typically  $10\text{-}15\text{dB}$ , this variation is not acceptable in the high performance synthesized signal sources.

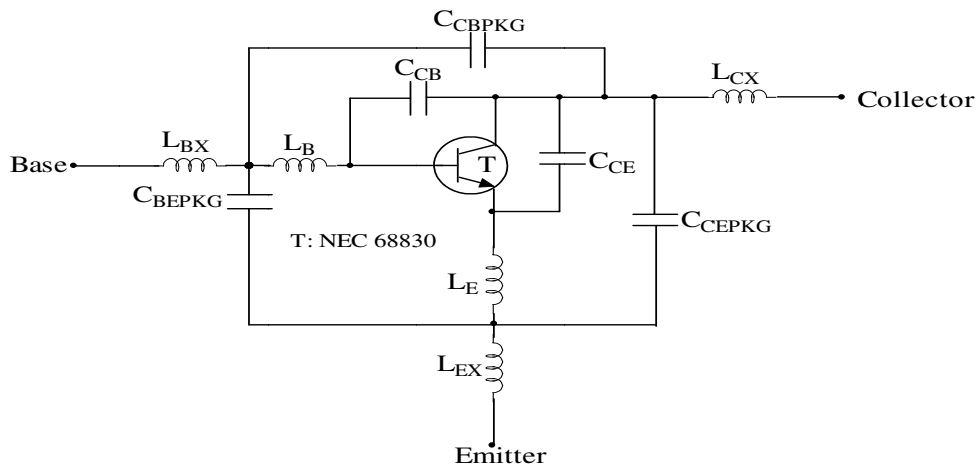


Figure 6-25: shows the transistor NE68830 with package parasitic [67, pp. 133]

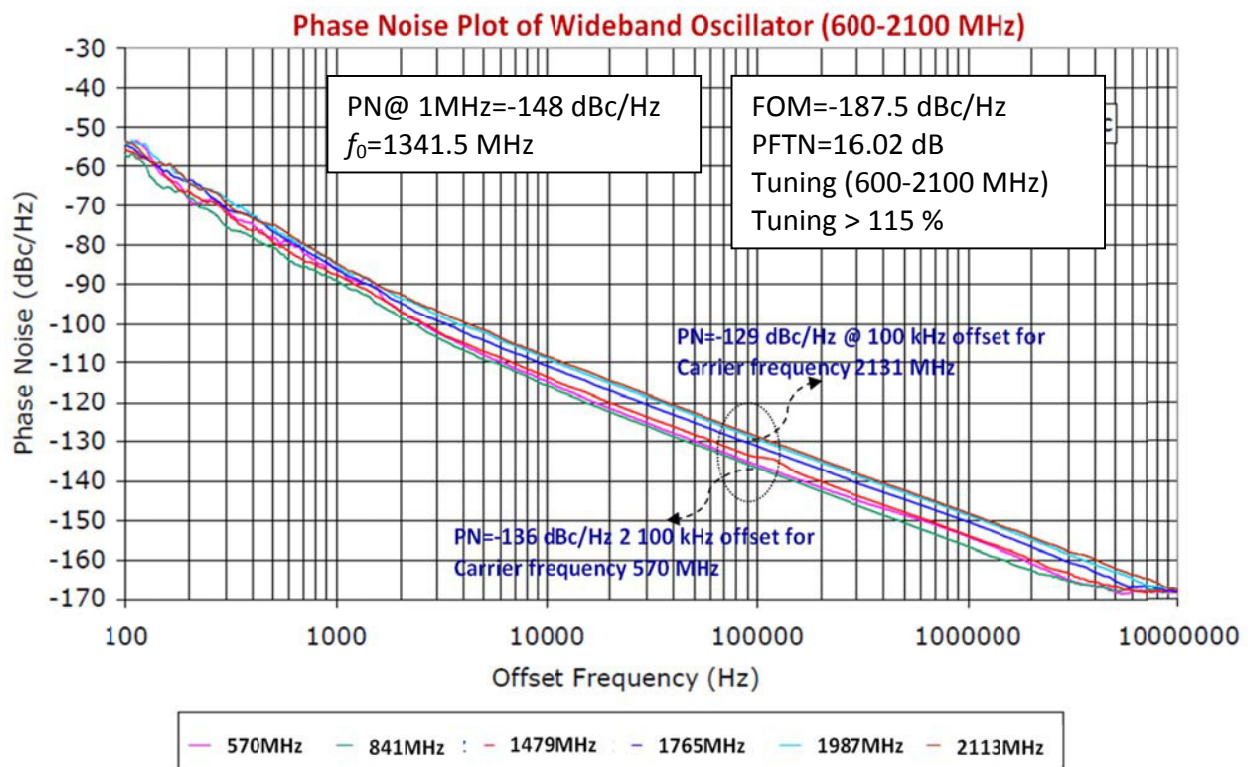


Figure 6-26(a): Measured phase noise plots of this oscillator, the measured phase noise performance is typically better than  $-129\text{dBc/Hz}$  @  $100\text{ kHz}$  offset from the carrier frequency over the band (600-2100 MHz), measured figure of merit (FOM: defined in Ch-1, Eq 1.1) is  $-187.5\text{ dBc/Hz}$  for a given power-frequency tuning normalized (PFTN: defined in Ch-1, Eq 1.2)  $16.02\text{ dB}$ , with power consumption of  $200\text{mW}$  ( $V_{cc}=5\text{V}$ ,  $I_c=40\text{ mA}$ ), O/P power is  $+3.0\text{ dBm}$ .

To overcome the variation in phase noise performance over the desired operating band, novel technique is to incorporate dynamic phase-synchronization mechanism for the suppression of multi-mode dynamics but penalty is external reference source and also require large real estate area. The innovative approach is to incorporate multi-mode phase injection locking as illustrated in Figure 6-24(b), (where signal P1 acts like as a reference input signal to RF signal P2) that is coupled through a distributed medium for broadband tuning and minimum noise performance. This approach supports multi-octave tuning in a small package, and is comparable with integrated circuit fabrication processing. In addition, the topology allows for a substantial reduction in phase noise by dynamically optimizing the impedance transfer function and coupling factor across a guided distributed medium of the planar multi-coupled network.

As illustrated in Figure 6-24(a), a phase compensating network is capacitive coupled between the base terminal and the slow-wave, and progressive-wave coupled resonator for uniform phase noise performance. The slow-wave and progressive coupled resonator network as shown in Figure 6-24a is coupled through hybrid resonance mode causing convergence effect, connected through the phase compensating network which is capacitively coupled between the base terminal and the slow-wave and progressive-wave coupled resonators, optimizes group delay dynamically for uniform and minimum phase-noise performance over the band. As the RF output signal is coupled through a distributed coupled medium, which is coupled across the slow-wave and progressive wave resonator networks, uniform output power and improved higher-order harmonic rejection throughout the operating frequency band can be achieved. Figure 6-26(b) shows the measured phase noise plots of this oscillator, the measured phase noise performance is typically  $-157\text{dBc/Hz}$  at 1 MHz offset from the carrier frequency for multi-octave-band tuning range (500-2500 MHz), the operating DC bias is 5V and 40mA. The typical variation in phase noise over the operating frequency band is typically lower than 3dB with output power varying between 3 dBm to 5.2dBm, which is acceptable limit in the high performance synthesized signal source applications.

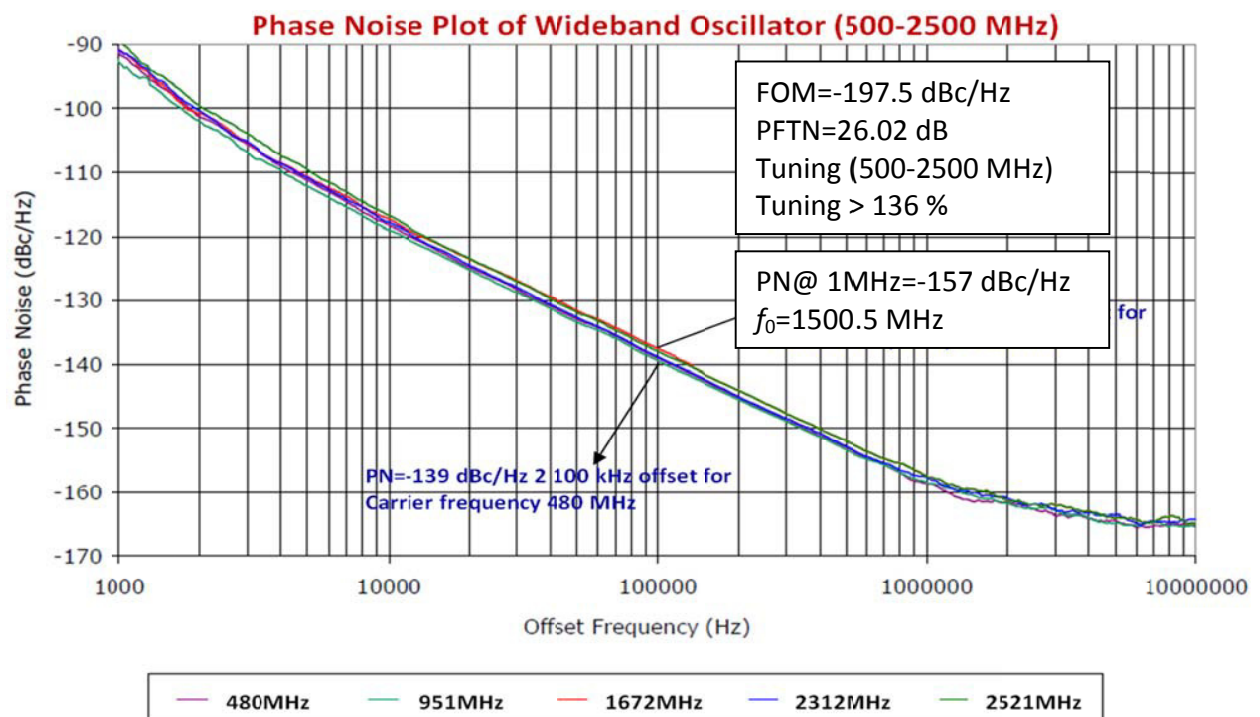


Figure 6-26(b): The measured phase noise plots of this oscillator, the measured phase noise performance is typically better than  $-136\text{dBc/Hz}$  @ 100 kHz offset from the carrier frequency over the band (500-2500 MHz), measured figure of merit (FOM: defined in Ch-1, Eq 1.1) is  $-197.5\text{ dBc/Hz}$  for a given power-frequency tuning normalized (PFTN: defined in Ch-1, Eq 1.2) 26.02 dB, with power consumption of 200mW ( $V_{cc}=5\text{V}$ ,  $I_c=40\text{ mA}$ ), O/P power is +3.2 dBm

The measured figure of merit (FOM: defined in Ch-1, Eq 1.1) is -197.5 dBc/Hz for a given power-frequency tuning normalized (PFTN: defined in Ch-1, Eq 1.2) 26.02 dB, with power consumption of 200mW ( $V_{cc}=5V$ ,  $I_c=40$  mA), output power is +3.2 dBm. The measured RF output power is better than 3dBm with more than 136 % tuning ranges (500 MHz-2500 MHz) with sufficient margin at both lower ( $f=450$  MHz @  $V_t=0.2$  Volt) and upper ( $f=2600$  MHz @  $V_t=26$  Volt) ends. The novel oscillator circuit is stable over operating temperatures of  $-40$  °C to  $+85$  °C, and provides sufficient margin for compensating the frequency drift caused due the change in operating temperature, including the package parasitics and component tolerances.

#### 6.4.1.6 High Frequency Push-Push VCO Topology (US Patent No.7, 292,113) [63]

As the frequency band for the wireless communication shifts higher, generation of the power efficient ultra-low noise wideband and thermally stable compact signal sources with low cost becomes more and more challenging due to the frequency limitations of the active devices. A high frequency signal can be generated either based on an oscillator operating at a fundamental frequency, or a harmonic oscillator. A typical oscillator operating at the fundamental frequency suffers from a low  $Q$  factor, insufficient device gain and higher phase noise at a high frequency of operation. There are two main configurations of the harmonic oscillators: cascade structure, which supports second-harmonic oscillator based on frequency-doubler approach and parallel structure, which supports  $N^{\text{th}}$  harmonic oscillator ( $N$ -push/push-push oscillator topology as a  $N^{\text{th}}$  harmonic oscillator) based on coupled-oscillator approach. The frequency doubler and other means of up conversion can be a practical and quick solution to generate high frequency signal from the oscillators operating at lower frequency but it introduces distortions and have poor phase noise performances. This limitation has created interest among the microwave community to develop alternative high frequency low cost sources. The push-push topology has several advantages over single-ended versions other than improvement in phase noise. The usable frequency range of the transistors can be extended, and this can be exploited, for instance, using transistors that are larger than usual and have lower  $1/f$  noise due to reduced current density [ref. 111, Appendix-A]. The coupled oscillators  $N$ -Push topology improves the phase noise and extends the operating frequency beyond the limitation caused by the cut-off frequency of available active devices [74]. The novel state-of-the-art topology is based on following:

- provides constant negative resistance over octave-band
- novel tuning arrangement for wideband tunability without degrading the loaded-  $Q$  of the tuning network over the octave-band
- novel coupled-resonator structure, which will support resonance over multi-octave-band.
- optimum size ( $I_{cmax}/I_{dss}$ ) of the bipolar or FET for low phase noise
- coupled-oscillator/ $N$ -Push approach for improvement in phase noise
- dynamically tuned phase coupling network

Figure 6-27(a) shows the block diagram illustrating principle modules of the ultra low noise octave-band VCO in the frequency range of 1000-2000MHz/2000-4000MHz. As shown in Figure 6-27(a), all the modules are self-explanatory, the oscillator circuit is realized by using dynamically tuned coupled-resonator network, dynamically tuned phase-coupling network and dynamically tuned combiner network for octave-band push-push operation. In push-push topology, two sub-circuits of a symmetrical topology operate in opposite phase at the fundamental frequency, and the output of the two signals are combined through the dynamically-tuned combiner network so that the fundamental cancels out, while the first harmonics interfere constructively, and are available over the tuning range. The state-of-the-art topology overcomes the limitations of the fixed frequency operation of the push-push oscillator/ $N$ -push oscillator by designing a novel tuning and phase controlling network over the desired frequency band (octave-band) [76]-[83]. Figure 6-27(b) and Figure 6-27(c) show the schematic and layout of oscillator circuit configured in push-push topology with broadband tuning characteristics (1000-2000MHz/2000-4000MHz). The various modules as

depicted in the Figure 6-27(a) are implemented in a way that allows miniaturization, and is amenable for integrated chip design. The structure and application is covered in US Patent No.7, 292,113 and 7,088189. As shown in Figure 6-27(a), each sub-circuit is designed at one-half of the desired output frequency ( $f_0$ ), and thereby the second harmonic ( $2f_0$ ) is constructively combined with the help of the dynamically tuned combiner network. Thus, separation of the two harmonics is accomplished using symmetry, which avoids space-consuming filter elements. The wideband tunability is achieved by incorporating a dynamically tuned phase coupling network so that the  $180^\circ$  phase difference, (mutually locked condition) is maintained over the tuning range for push-push operation [74].

As shown in the Figure 6-27(b), dynamically tuned coupled resonator is connected with the emitter of the transistor (NE68830) to provide a uniform loaded  $Q$  over the tuning range. The layout shown in the Figure 6-27(c) is fabricated on 32 mil thickness Rogers substrate of dielectric constant 3.38 and loss tangent  $2.7 \cdot 10^{-4}$ , 1.75x1.75x0.18 inches size of the printed circuit board (PCB). Experimental results have shown that a poor mismatch at the fundamental, resulting discontinuous tuning due to the non-uniform phase shift over the tuning range. This mismatch in phase-shift between the two sub-circuits is due to possible component tolerances, package parameters, and the phase associated with the path difference over the tuning range. Therefore, oscillator goes out of the locking range. Figure 6-27d shows the compact layout of Figure 6-27c for the minimization of the phase-shift between the two sub-circuits as shown in Figure 6-27a.

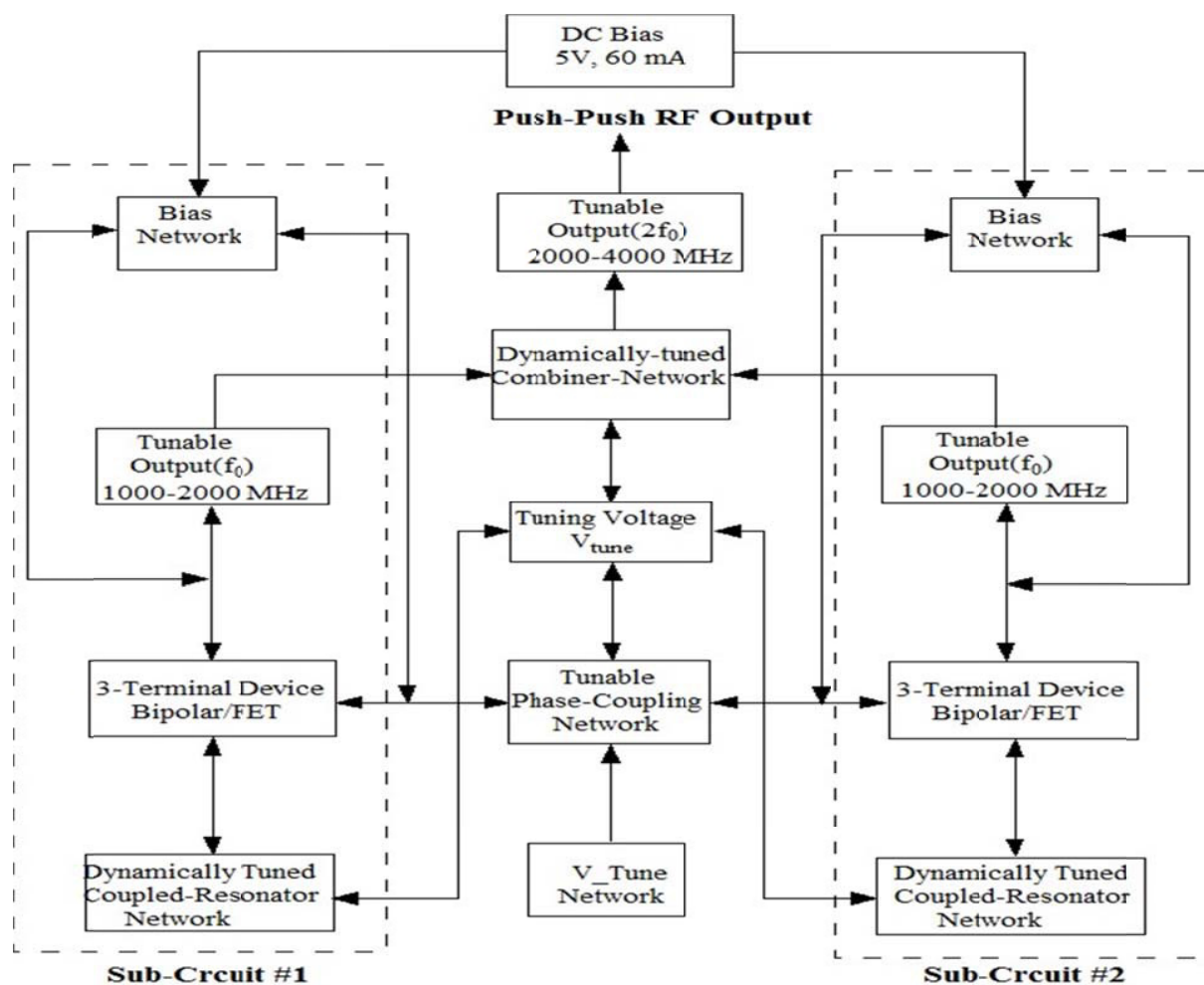


Figure 6-27(a): The block diagram illustrating principle modules of the ultra-low noise octave-band VCO in the frequency range of 1000-2000MHz/2000-4000MHz (US Patent No.7, 292,113) [60, 74]

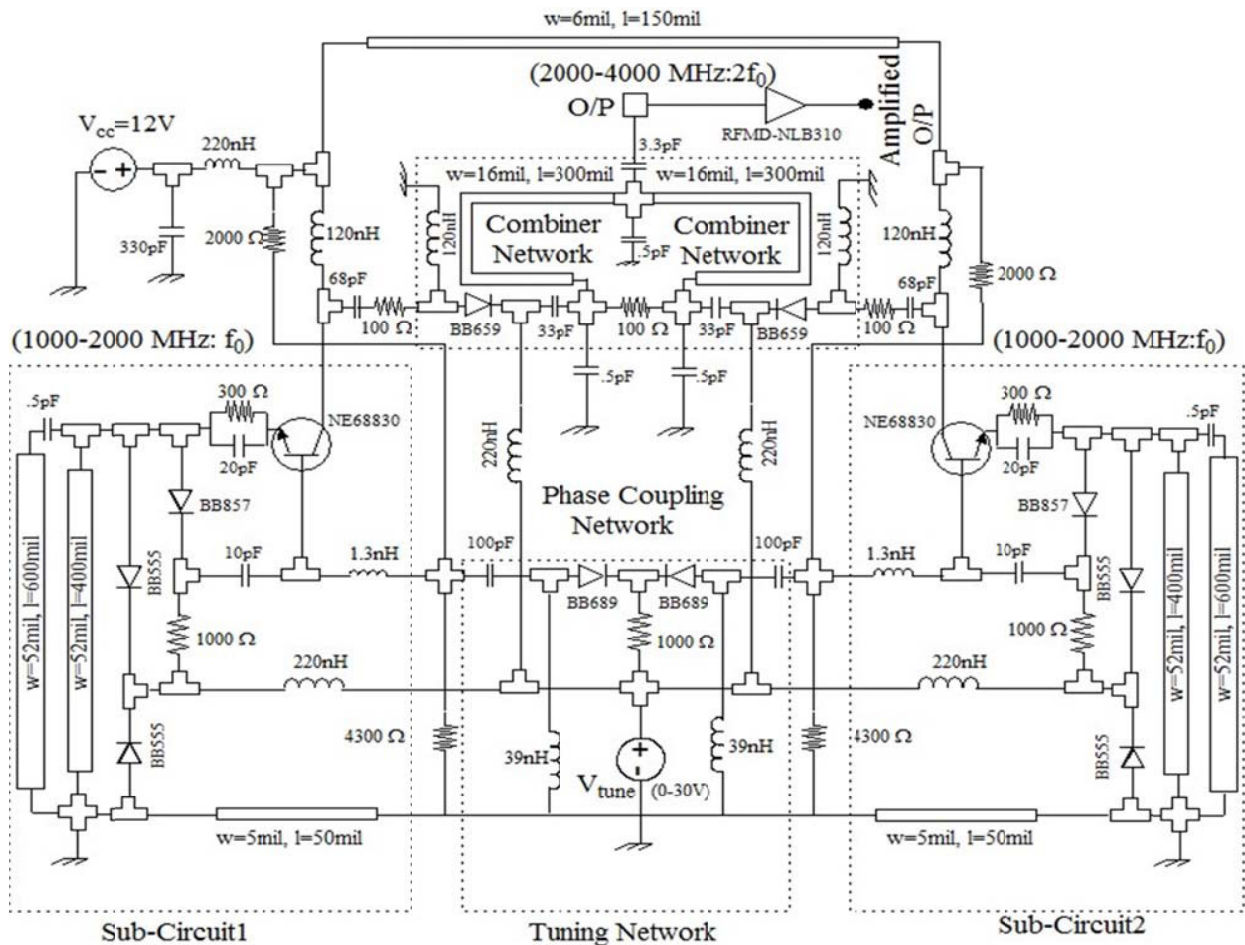


Figure 6-27(b): A typical schematic diagram of oscillator circuit comprises of printed coupled-resonator network, phase-coupling network and combiner network for octave-band Push-Push operation in accordance with the block diagram shown in Figure 6-27(a) [60]

The attempt to reduce the size of the PCB is done by combining the resonator of sub-circuit # 1 and sub-circuit # 2 as in dual horseshoe configuration as shown in Figure 6-27(d). This allows 3-times reduction in real estate area as compared to layout shown in Figure 6-27(d). An innovative dynamic tuning network integrated with coupled horseshoe microstrip resonator is incorporated to get more than octave band tunability keeping phase noise uniform throughout the band. Figure 6-27(d) shows the compact layout of integrated structure of the dynamically tuned coupled resonator of both the sub-circuits shown in Figure 6-27©, layout is built using multilayer with 64 mills substrate height and 3.38 dielectric constant of 0.75x0.75x0.18 inches size of the printed circuit board (PCB).

Figures 6-27(e) and 6-27(f) show the CAD simulated plots of oscillator output signal of sub-circuit # 1 and sub-circuit # 2 in time domain, and the phase noise plot of push-push oscillator (2000-4000MHz). As shown in Figure 6-27(f), the simulated phase noise (CAD tool: Serenade 8.71) is typically better than -109dBc/Hz @ 100 kHz offset from the carrier frequency over the band (2000-4000 MHz). Referring to Figure 6-27(e), RF-collector current of both the sub-circuits is out of phase for the fundamental (undesired frequency of the operation: 1000-2000MHz). Further increase in operating frequency and tuning range is limited by the phase shift and mode locking between two sub-circuits (sub-circuit # 1 and sub-circuit # 2) as shown in Figures 6-27(a) and 6-27(b).

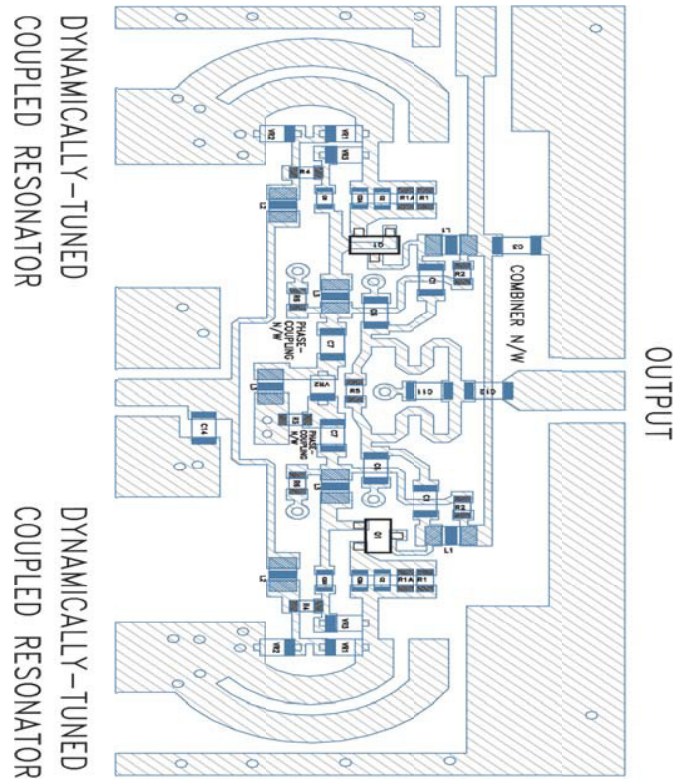


Figure 6-27(c) : The layout of the schematic of Push-Push oscillator circuit shown in Figure 6-27b (multilayer 32 mills substrate, Dielectric constant 3.38) 1.75x1.75x0.18 inches ROGERS PCB (US Copyright Reg. No: Vau-603-982) [60, 74].

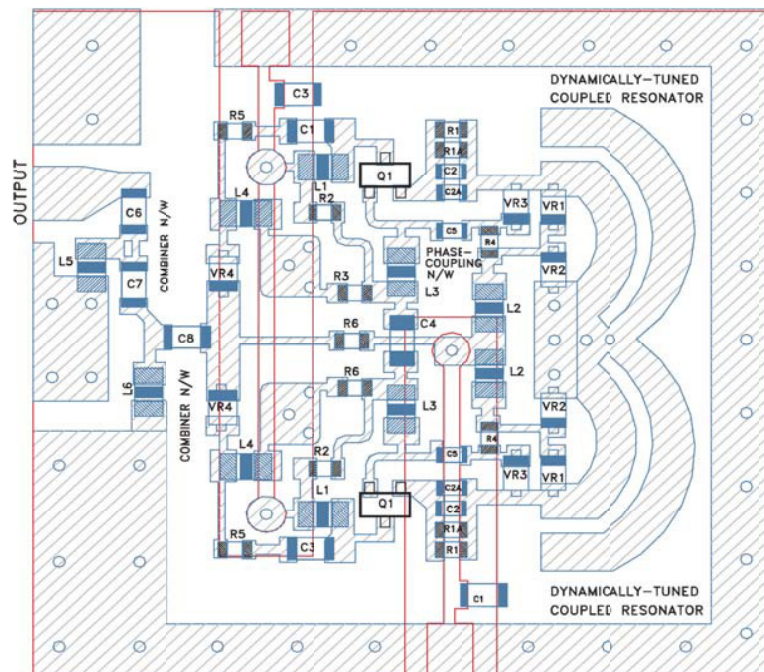


Figure 6-27(d) : The layout of compact layout of integrated structure (coupled horse-shoe microstrip resonator)of the dynamically tuned coupled resonator of both the sub-circuits shown in Figure 6-27c, layout is built using multilayer with 64 mills substrate and 3.38 dielectric constant of 0.75x0.75x0.18 inches US Copyright No: Vau-603-982 ) [60, 74].

The prototype unit shown in Figures 6-27 (c) and 6-27(d) are built by careful selection of active devices but difficult to tune to RF oscillator output of sub-circuit #1 and sub-circuit #2 in 180° out of phase across the full band (1000-2000MHz/2000-4000MHz) using discrete components.

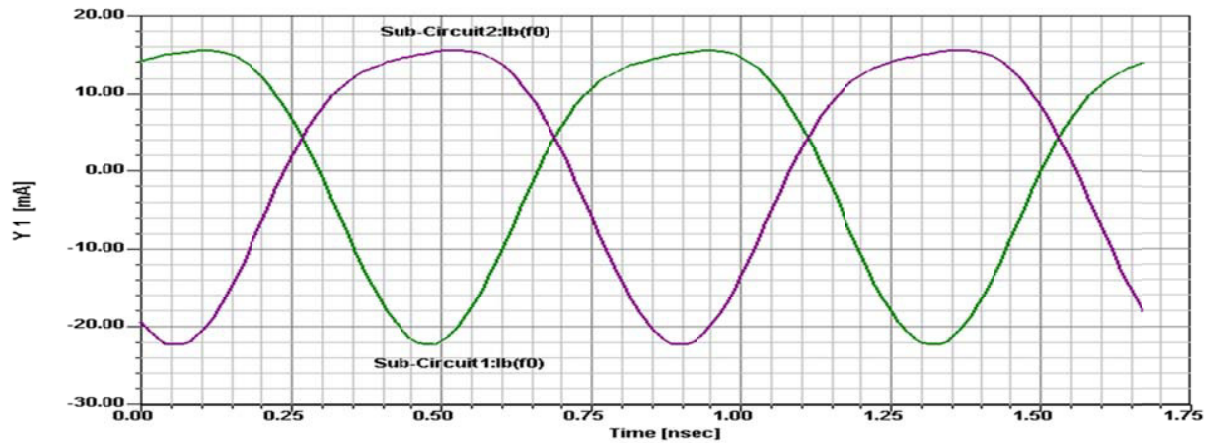


Figure 6-27(e): The plot of the RF-collector currents  $Y_1$ (mA) of sub-circuit #1 and sub-circuit #2 (Figure 6-27b)

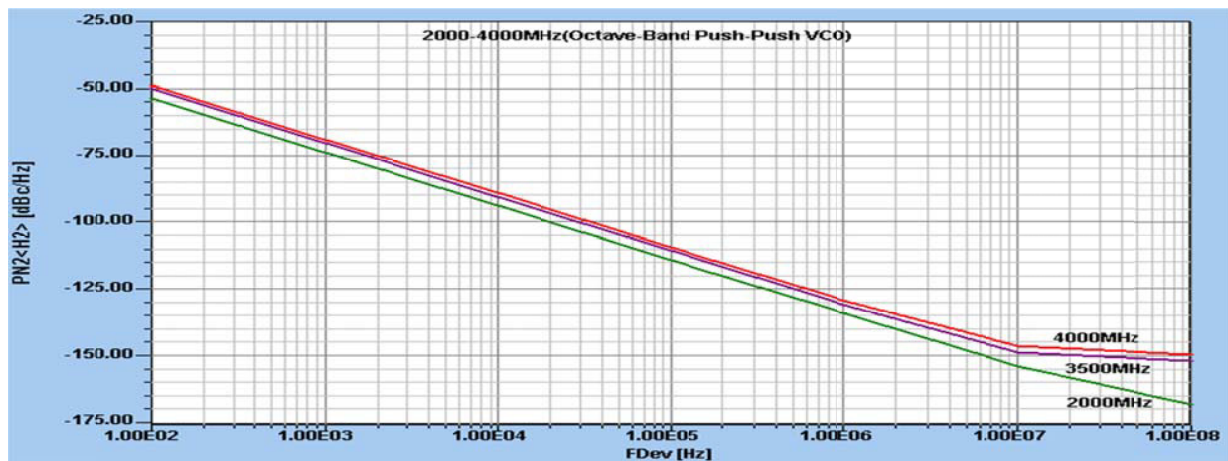


Figure 6-27(f): Simulated phase noise plot for oscillator configured in push-push topology as shown in Figure 6-27d.

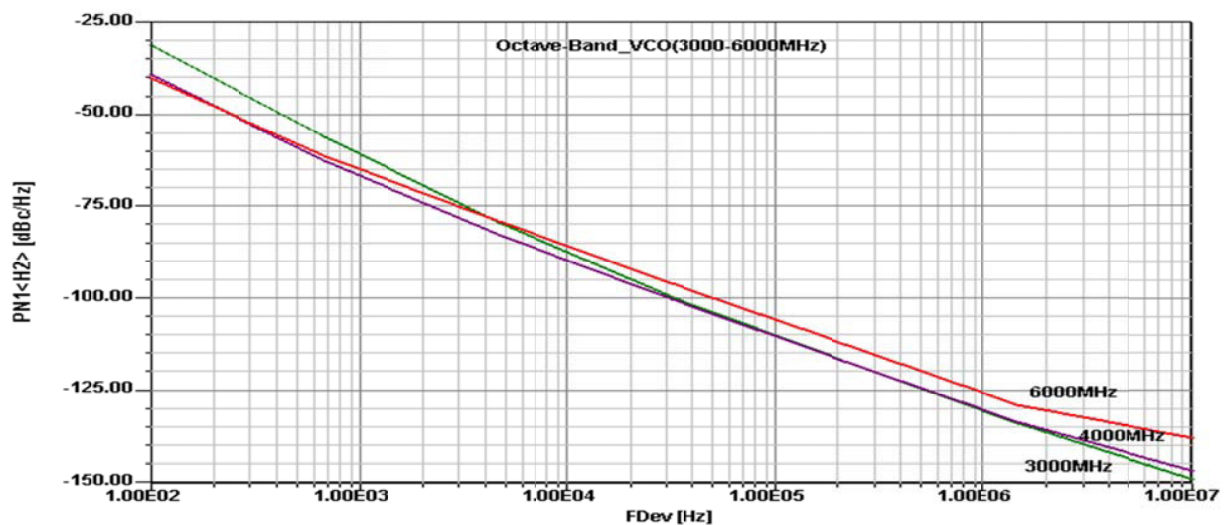


Figure 6-27(g): The phase noise plot for 3000-4000MHz, configured in push-push topology as shown in Fig. 6-27(d)



By optimizing the tuning network, up to 25 % increase in tuning range is obtained but at the cost of increase in level sub-harmonics (due to poor matching), mode-jumping, and degradation in phase noise, which is obvious due to increase in tuning sensitivity [83]. Figure 6-27(g) shows the CAD simulated phase noise plots of 3000-6000MHz push-push oscillator circuit. The variation in phase noise performance across the band is typically 10dB. The layout shown in Figure 6-27(d) minimizes the phase-shift due to the path difference between the two sub-circuits over the tuning range, but still shows discontinuous tuning at some point over the band due to the package parasitics and component tolerances associated with the discrete components of the circuit. The problem of discontinuous tuning can be overcome by incorporating a phase detector, allows multi-octave band tuning and improved phase noise performances. The objective is to identify the effects, which limits the wideband tuning range and development of unique topology, which can minimize the phase shift and support the broadband tunability without degrading the phase noise performance. With regard to the state of the art push-push/N-push oscillator, the phase-synchronization techniques using phase detector (PD) provides the general implementation of the wideband dynamically tunable coupled oscillator for the extended frequency range of operation.

#### **6.4.1.7 Multi-Octave Band Push-Push VCO Topology (US Patent No.7, 292,113) [63]**

The free running frequencies of the two oscillators in the coupled oscillator system shown in Figures 6-27(c) and 6-27(d) are not identical because of tolerances in their respective circuit component values. However, a phenomenon known as injection locking takes place and can be insured that the frequencies of the two oscillators are locked to each other. The maximum frequency range over which injection lock can occur is inversely proportional to the external Q of the oscillators. Therefore, in the case of oscillators having low values of external Q, injection locking occurs even with a large discrepancy in their free running frequencies. The circuit principle usually requires a large-signal analysis to verify the odd-mode operation of the sub-circuits and the bias network has to be properly designed with respect to two critical frequencies.

Figure 6-28(a) shows the typical block diagram illustrating principle modules of the ultra-low noise multi-octave-band push-push VCO in the frequency range of 1-5 GHz/5-10 GHz [63]. Figure 6-28(b) shows the typical schematic diagram in accordance to the block diagram shown in Figure 6-28(a). It shows a dynamically tuned coupled-resonator network, dynamically tuned phase-coupling network, dynamically tuned combiner network and dynamically tuned phase detector network for wideband push-push operation, amenable to commercially available MMIC technologies. As shown in Figure 6-28(a) and 6-28(b), by incorporating a phase detector network integrated with the tuning diode for compensating the phase error, extended operating frequency range is 1-5GHz/5-10 GHz operation.

As shown in Figure 6-28(a), the divider may comprise MC10EL32, made by ON Semiconductor, Inc., and the amplifier OPAMP TL071 from Texas Instruments and mixers available from Synergy Microwave. The phase detector network dynamically compensates for phase errors between each oscillator during wideband operation. The phase detector network detects random fluctuations in the free-running frequency and translates those fluctuations into phase errors. The phase errors are then fed back to the combiner network and used to control the phase and frequency of the buffered signal during tuning operation. The phase errors are fed back to the dynamically tuned coupled resonator networks and used to tune the oscillating frequencies of each of the three terminal devices.

Figures 6-28 (c), 6-28(d), 6-28(e) show the CAD simulated and measured phase noise plots of multi-octave-band VCO (1-5GHz/5-10GHz), configured in push-push topology as shown in Figure 6-28(a) and Figure 6-28(b). As shown in Figures 6-28(c), 6-28(d), 6-28(e), the simulated and measured phase noise agree within 3-5 dB for 1-5 GHz operation in push-push configuration, however measured phase noise for 5-10 GHz is 5-8 dB inferior as compared to simulated data. This could be due to component tolerances and phase dispersion across the higher band (5-10 GHz).

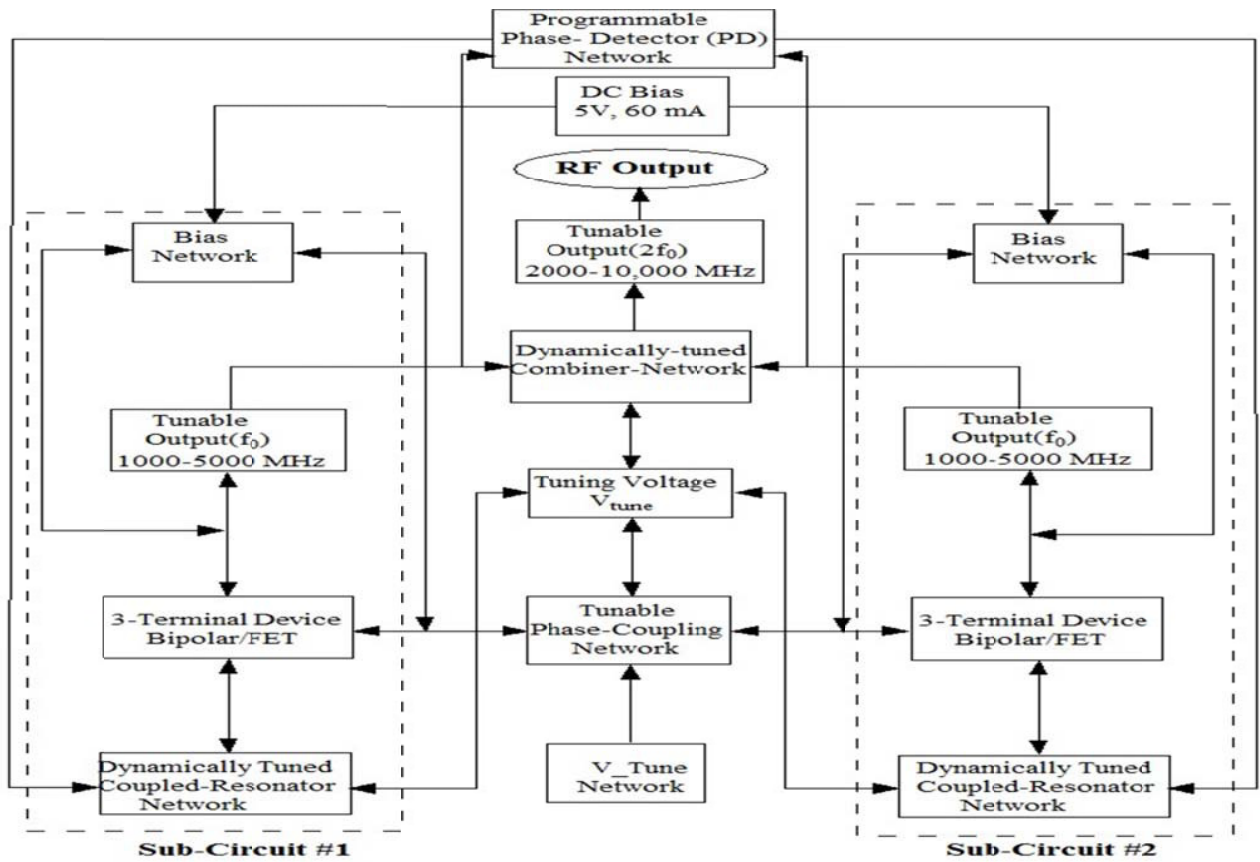


Figure 6-28(a): AI block diagram of multi-octave-band push-push VCO in the frequency range of 1-5 GHz/5-10 GHz [63]

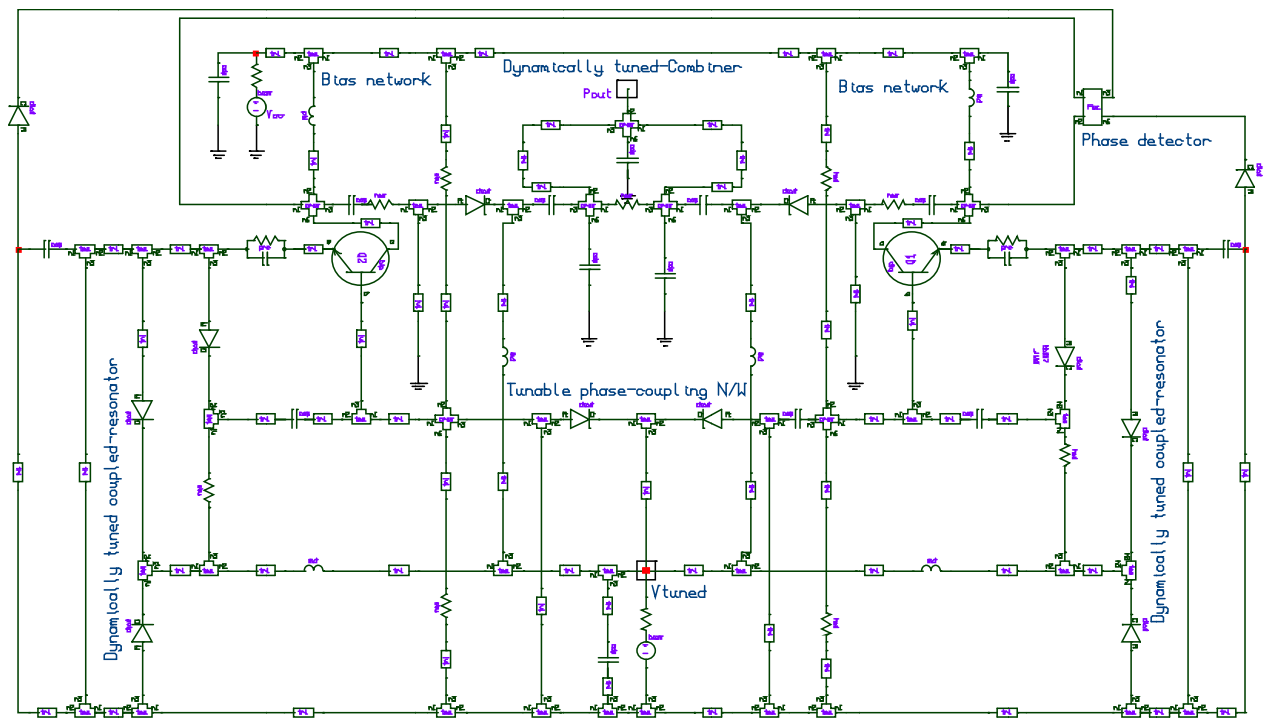


Figure 6-28(b): The schematic (of the multi-octave push-push VCO (1-5GHz/5-10GHz), DC Bias: 5V, 60mA [63].

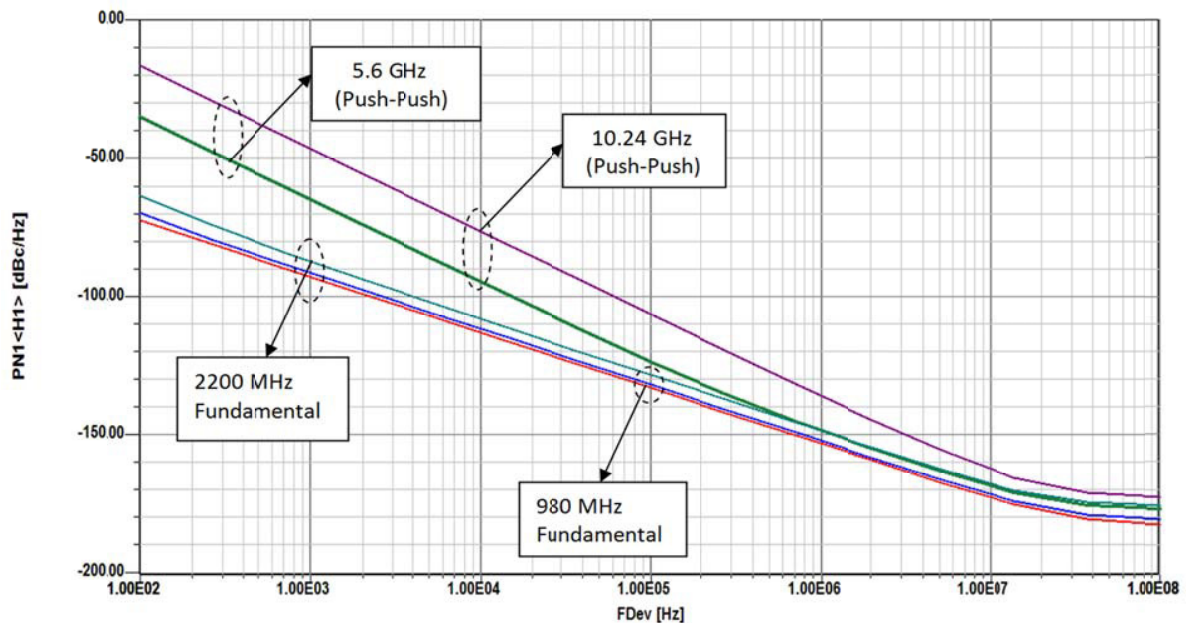


Figure 6-28(c): CAD simulated phase noise plot of multi-octave-band VCO (1-5GHz/5-10GHz), configured in push-push topology as shown in Figure 6-28(b)

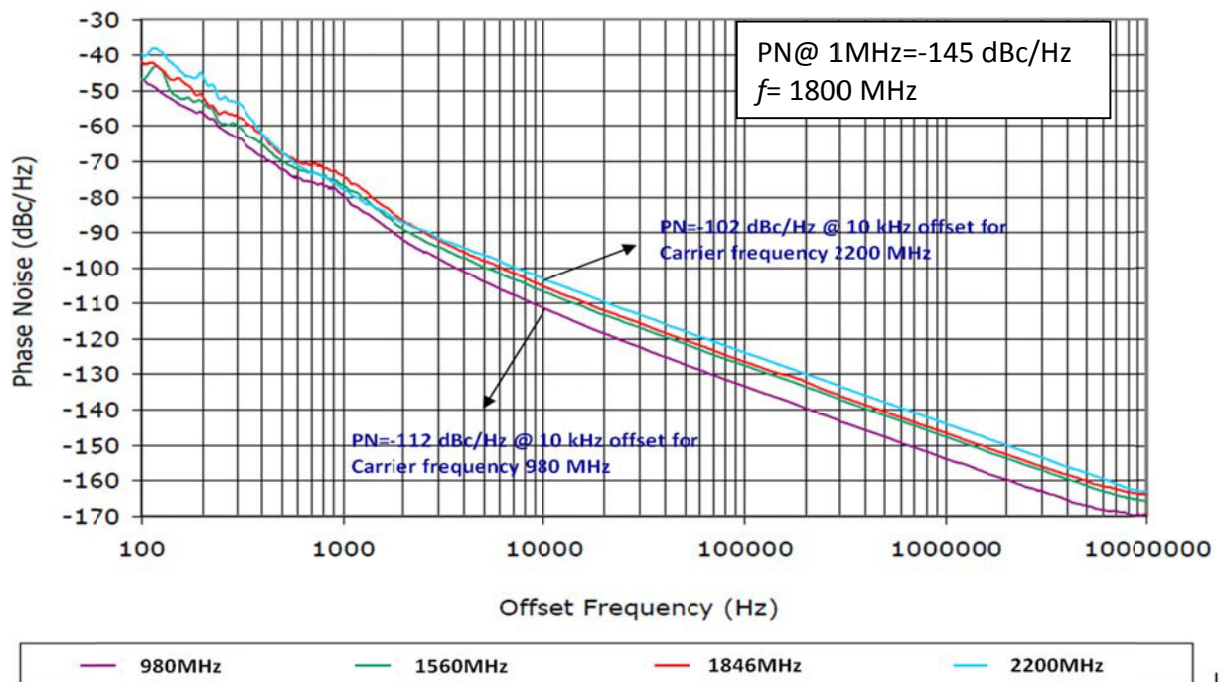


Figure 6-28(d): The measured phase noise plot of multi-octave-band VCO (1-5GHz/5-10GHz), configured in push-push topology as shown in Figure 6-28b, with power consumption of 300mW ( $V_{cc}=5V$ ,  $I_c=60$  mA), O/P power is -3.0 dBm.

#### 6.4.1.8 Substrate Integrated Waveguide (SIW) Resonator Based Oscillators

For portable communication systems, oscillator's DC-RF conversion efficiency and phase noise play important role. Toward this end, substrate integrated waveguide (SIW) based resonator have drawn attention in microwave communities due to the low radiation losses, high quality factor, and capability of making waveguide-like structures using planar printed circuit board (PCB) technology [98].

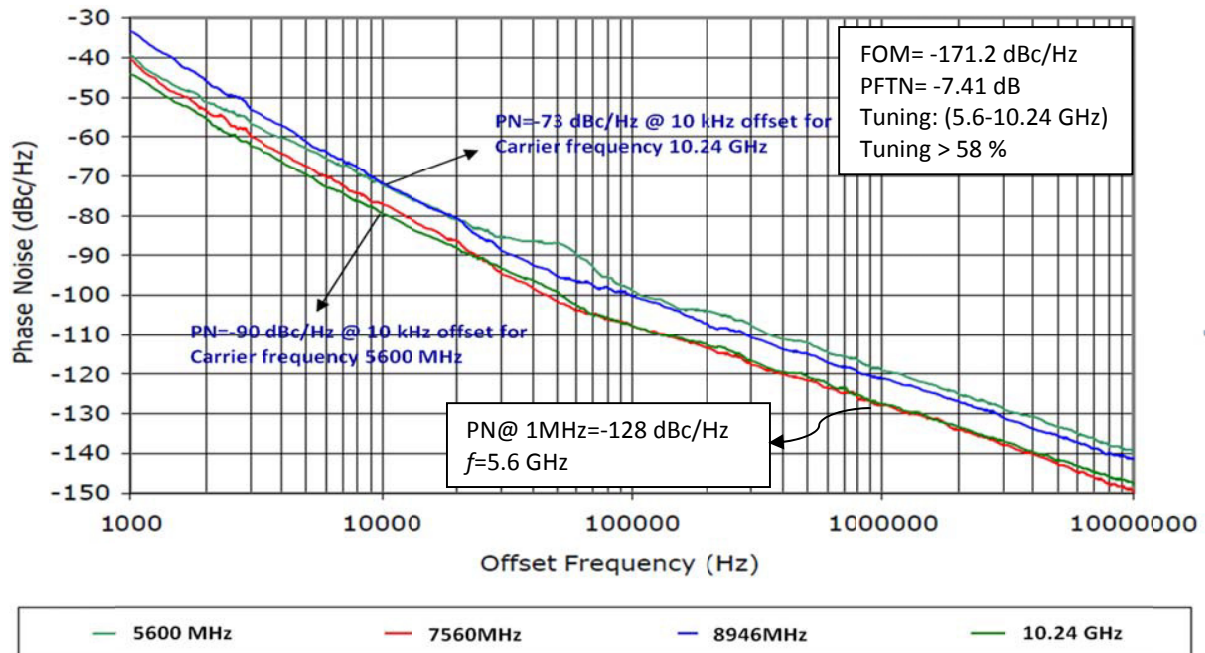


Figure 6-28(e): The measured phase noise plot of multi-octave-band VCO (1-5GHz/5-10GHz), configured in push-push topology as shown in Figure 6-28b, measured figure of merit (FOM: defined in Ch-1, Eq 1.1) is -171.2 dBc/Hz for a given power-frequency tuning normalized (PFTN: defined in Ch-1, Eq 1.2) -7.41dB, with power consumption of 300mW ( $V_{cc}=5V$ ,  $I_c=60$  mA), O/P power is -3.0 dBm

Recent publications on tunable or switchable SIW resonators [99]-[101] offer tuning or switching mechanism by connecting a varactor/PIN diodes to a floating metal on top of the SIW cavity with jump wires, causing unwanted radiation loss due to the closed-loop slots surrounding the floating metal, and therefore reduces quality (Q) factor. In addition, the jump wires used for DC bias will increase fabrication complexity and may introduce some extra parasitics as well.

To overcome these problems, a new type of tunable resonator is reported based on complementary coupled resonators (CCRs) using SIW technologies [102]-[103]. The proposed complementary coupled resonator is essentially a complementary version of a conventional microstrip coupled line resonator [67, pp. 358]. Incorporated with SIW, the complementary coupled resonators can be excited at its differential mode. In this case, the equivalent magnetic currents on the slots flow in the opposite direction; therefore, radiation loss is minimized and the quality factor of SIW Q resonator improves.

To illustrate, Figure 6-29 shows the geometry of a conventional microstrip coupled line resonator and the proposed complementary structure at about 5 GHz. The conventional coupled line resonator shown in Figure 6-29(a) is excited at its differential mode and its electric ( $E$ ) field is plotted in Figure 6-29(b). Using the principle of duality, the coupling mechanism for the proposed complementary coupled resonator is through magnetic ( $H$ ) field as shown in Figure 6-29d) and has a similar distribution as  $E$  field in the conventional one. Unlike the conventional coupled resonator where the differential mode needs to be excited by a pair of inputs with opposite polarity, the proposed complementary coupled resonator is excited by itself at differential mode due to the nature of the fundamental mode in the waveguide. As a result, the equivalent magnetic currents on the slots of the complementary coupled resonator flow in opposite directions at the symmetrically opposite edges on the SIW resonator, and therefore the radiation can be minimized, which in turn generates a high Q factor of the resonator.

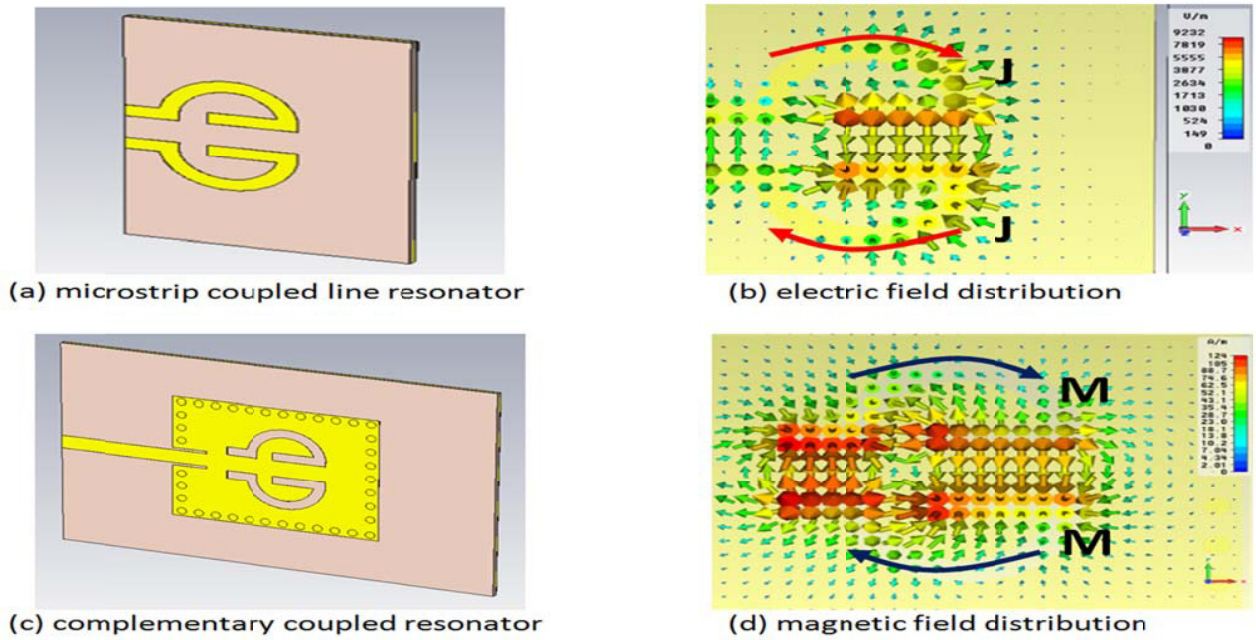


Figure 6-29: The geometry of coupled planar resonator:(a) A microstrip coupled line resonator, (b) its electric field distribution and electric current flow under differential excitation, (c) a complementary coupled resonator and (d) its magnetic field distribution and equivalent magnetic current flow under the fundamental mode of SIW cavity [102]

The calculated unloaded Q factor can be given by [Ch-5, Equation 5.25]

$$Q(\omega_0) = \frac{\omega_0}{2} \left| \frac{Z_{11}(\omega_0)'}{Z_{11}(\omega_0)} \right|_{f_0=5.34\text{GHz}} \approx 287 \quad (6.45)$$

where  $Z_{11}(\omega_0)$  and  $Z_{11}(\omega_0)'$  signify the impedance and its derivative respectively of the SIW resonator structure at frequency of  $\omega_0$ . Figure 6-30 shows the CAD simulated plots of  $[S_{11}]$  of the 1-port CCR depicted in Figure 6-29(c) for the application in Colpitts oscillator configuration where resonator is used as 1-port network. The resonant frequency for this fixed frequency resonator is 5.34 GHz, and the calculated unloaded Q-factor using fractional 3-dB bandwidth from  $[S_{11}]$  is 290, which agree closely with the simulated data from (6.43). For giving brief insights about the radiation loss characteristics of this structure (Figure 6-29c), the 3-D EM simulated radiation efficiency is 6.96% and the radiation gain is -4.64 dB, indicating a low radiation loss [103].

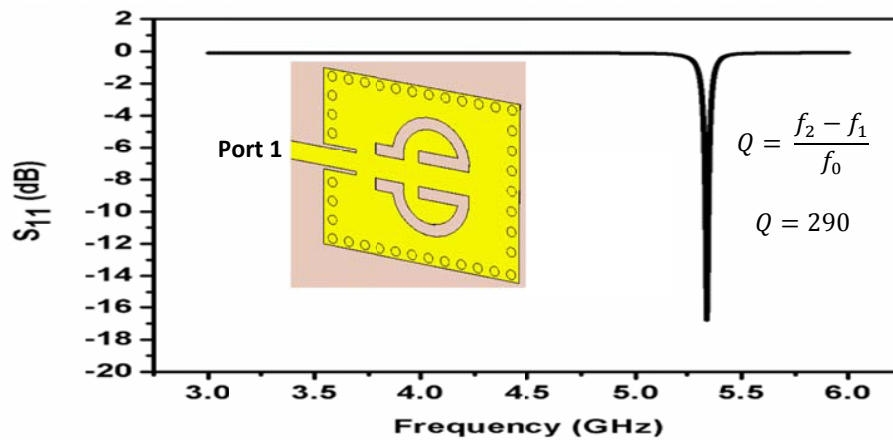


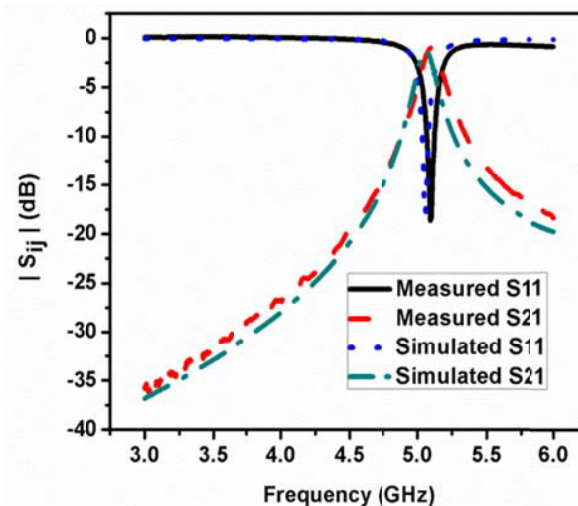
Figure 6-30: CAD simulated  $[S_{11}]$  plot of the 1-port CCR depicted in Figure 6-29c [102]

Figure 6-31 shows the typical 2-port complementary coupled resonator for the application in feedback oscillator configuration where resonator is used as a 2-port filtering network. Figure 6-32 shows the CAD simulated and measured plots of  $[S_{11}]$ ; there is a good agreement. The measured insertion loss is less than 1 dB at 5.1 GHz; the unloaded Q of the 2-port resonator can be described by [Ch-5, Equation 5.25]

$$Q(\omega_0) = \frac{\omega_0}{2} \left| \frac{Z_{21}(\omega_0)'}{Z_{21}(\omega_0)} \right|_{f_0=5.1\text{GHz}} \approx 312 \quad (6.44)$$



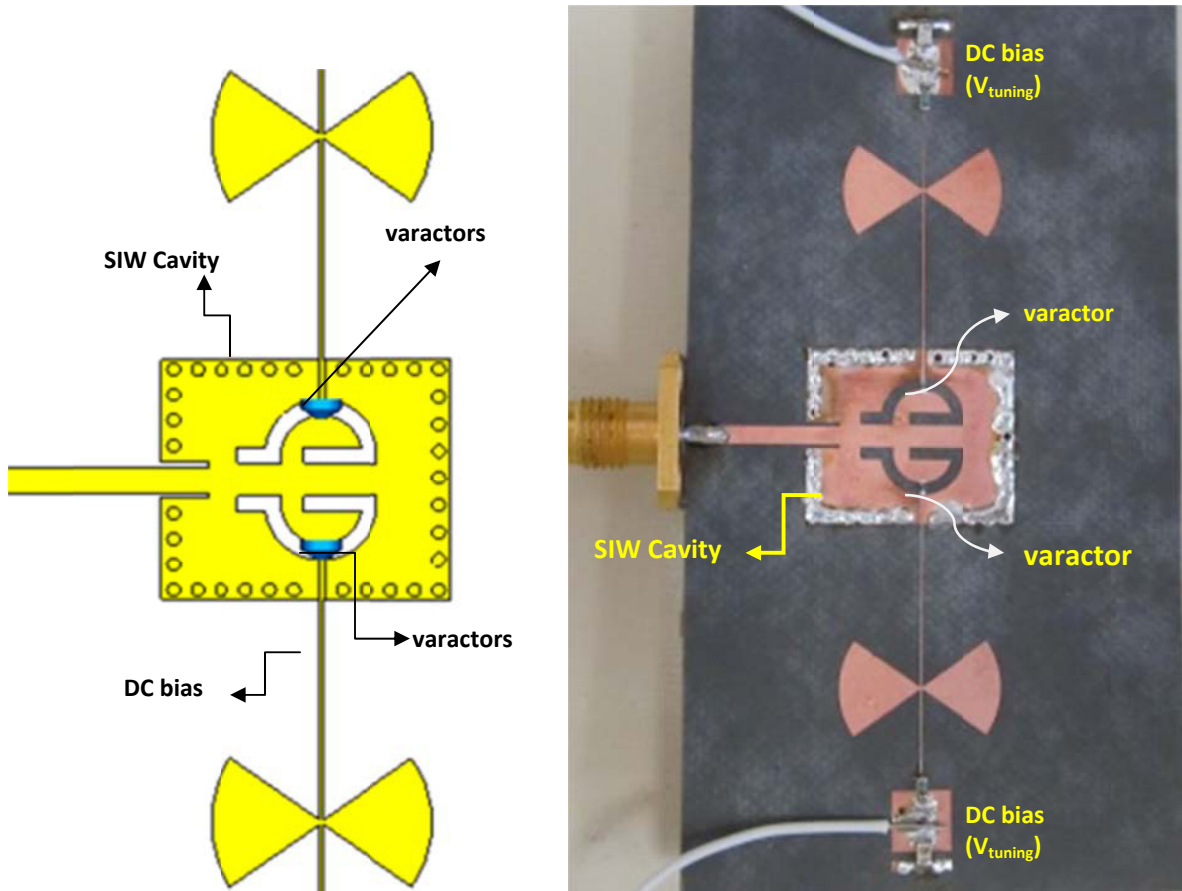
(a) 2-port complementary coupled resonator (CCR) fabricated using RT/Duroid 5880 substrate with a thickness of 0.508 mm and dielectric constant of 2.2 [103]



(a) Fabricated prototype of 2-port CCR

Figure 6-31: Two-port resonator structure (a) Fabricated prototype of 2-port CCR (complementary coupled resonator) and (b) its S-parameters [103].

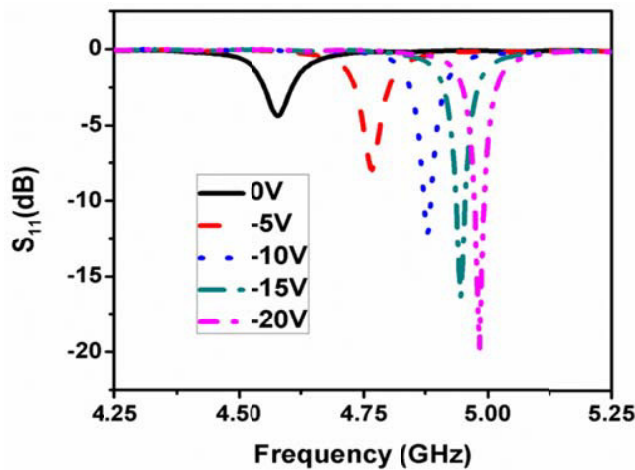
As shown in Figures 6-29 and 6-31, these resonators are not tunable, tuning mechanism is realized by incorporating tuning diodes (varactors) at the location where the  $E$  field on the slot is maximum (shown in Figure 6-32) for achieving broadband operation. Figure 6-32 shows the prototype of the 1-port CCTR (complementary coupled tunable resonator tunable resonator) using varactor diodes (MA/COM MA46H120). Figure 6-33 shows the measured  $S_{11}$  plots as a function of reverse bias voltages of both varactors from 0 V to 20 V, indicating that the resonant frequency can be tuned from 4.579 GHz to 4.984 GHz, or 8.84% of relative bandwidth. Further tuning range can be increased by reducing the gap between the DC bias line and SIW cavity, adding a coupling capacitor between the bias line and the resonator, and selecting the hyper-abrupt varactor diodes for broadband filtering and oscillator applications. It can be seen that the measured unloaded Q varies from 50 to 220 (as shown in Figure 6-33 (b)).



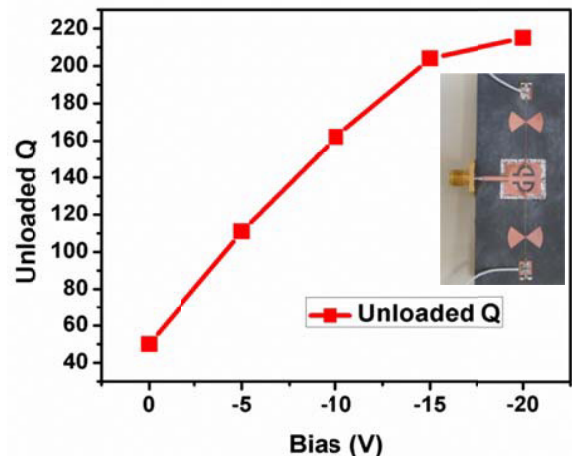
(a) Schematic of varactor-tuned 1-port port CC

(b) Fabricated prototype of 1-port CCR

Figure 6-32: Tunable 1-port resonator structure (a) schematic of varactor-tuned 1-port port CCR (complementary coupled resonator), and (b) prototype of 1-port CCR fabricated using RT/Duroid 5880 substrate with a thickness of 0.508 mm and dielectric constant of 2.2 [103]



(a) Measured  $S_{11}$  plots of 1-port resonator



(b) Measured Q of the tunable 1-port resonator

Figure 6-33: Measured data (a) measured  $S_{11}$  plots of tunable 1-port resonator structure shown in Figure 6-32, and (b) measured unloaded Q of the proposed tunable resonator with various reverse bias voltages [103]

Figure 6-34 shows the photo of the fabricated prototype of 1-port CCTR (complementary coupled tunable resonator tunable resonator), where adding a coupling capacitor between the bias line and the resonator, increases the tuning range from 8.84% (4.579 GHz to 4.984 GHz) to 66% (2.73GHz to 4.535GHz). Figure 6-35 (a) shows the tuning characteristics of the 1-port CCTR, the resonant frequency varies from 2.73 GHz (marker m16) to 4.535 GHz (marker m15) for change in the bias voltage from 0V to -15V. The increase in tuning range comes at price, Q factor degrades from 10-130 as shown in 6-35 (b), this is due to the additional losses and loading from the coupling capacitors. Multilayer capacitor with lower loss used to improve the resonator quality factor up to some degree. However, there is a design challenge to achieve multi-octave band tuning range without degradation of Q-factor. In this thesis, different approaches discussed toward maximization of both Q-factor and tuning ranges for the application in high performance signal sources. It has been shown that the resonator's loss can be compensated using the negative resistance provided by active devices, thereby enhancing the Q factors (see Ch-5, section 5.5.4.1) [104]-[106].

In order to optimize the Q of the CCTR shown in Figure 6-34, active device (HJ FET NE3210S01 from NEC), is embedded into the resonator network, powered by DC voltage, for compensating the losses over the desired operating tuning band. The novelty of this design is the compact size with improved Q factor, used for the realization of a low phase noise oscillator operating at X-band for RADAR applications.

Figures 6-36 and 6-37 show the simplified schematic representation and layout of the SIW-ACCTR (active substrate wave-guide complementary coupled tunable resonator), fabricated using RT/Duroid 5880 substrate with a thickness of 0.508 mm and dielectric constant of 2.2 [110].

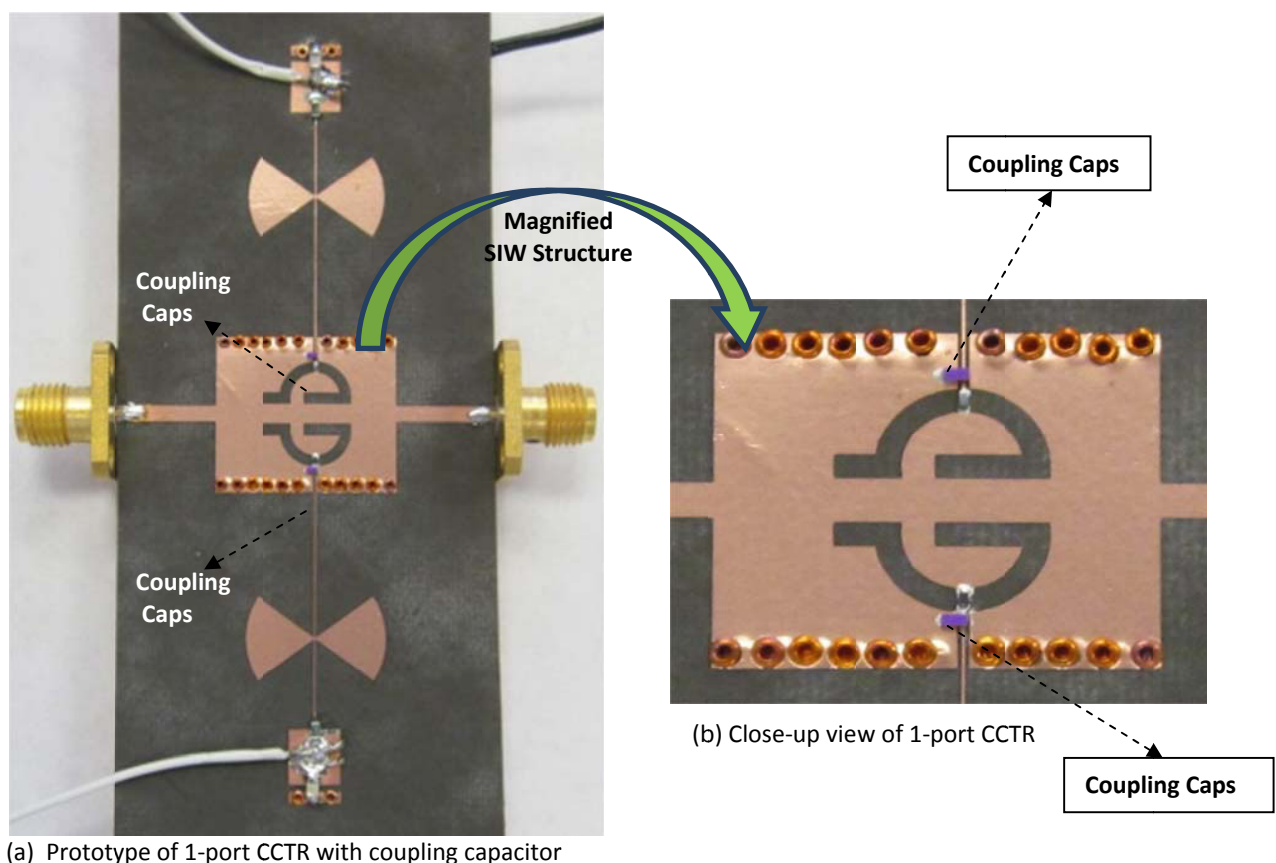


Figure 6-34: Photo of the fabricated prototype of 1-port CCTR (complementary coupled tunable resonator tunable resonator) (a) Shows additional capacitor between the bias line and the resonator, and (b) close-up view [110].



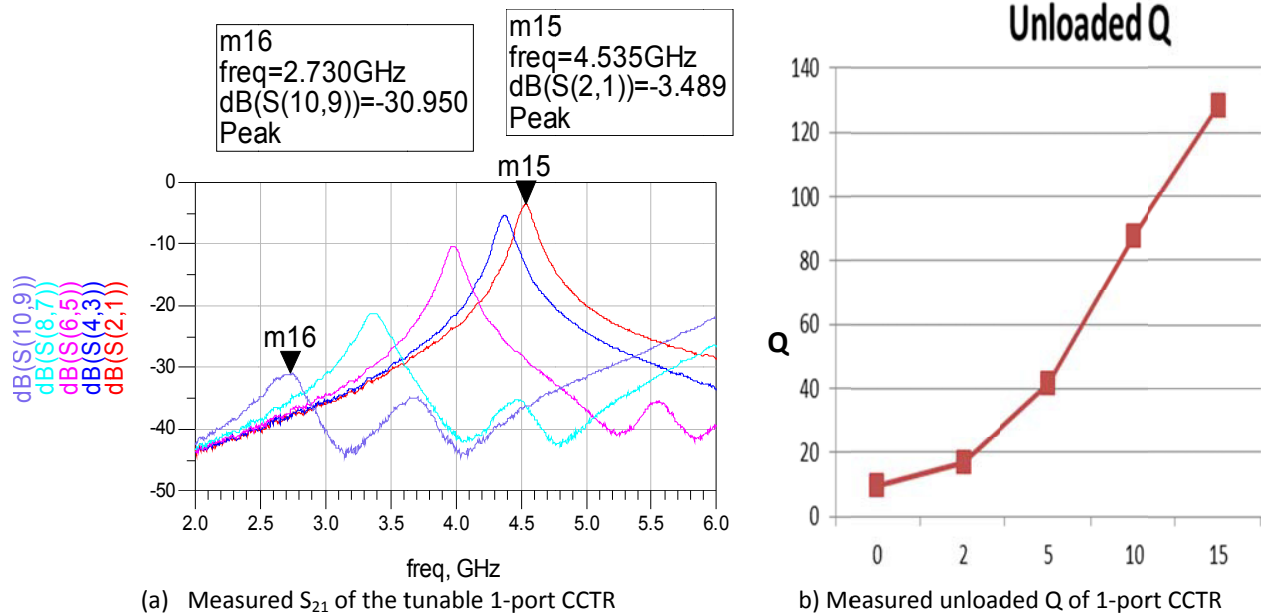


Figure 6-35: Measured data: (a) measured  $S_{21}$  of the tunable resonator shown in Figure 6-34, and (b) measured unloaded Q versus reverse bias voltage

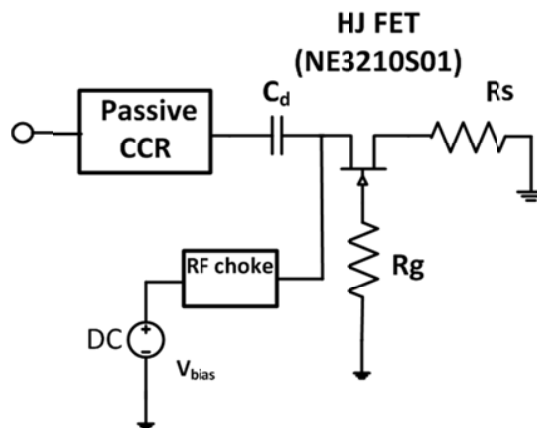


Figure 6-36: A typical schematic of active complementary coupled resonator ( $C_d=0.3$  pF,  $R_g=50$  ohm,  $R_s=127$  ohm)

Table 6.1 summarizes measured unloaded Q from (6.43), it can be seen that the highest unloaded Q measured is 21172 when the transistor is drain biased at 1.8 V, thereby confirming that the unloaded Q can be maximized by properly optimizing the DC bias operating condition, enhanced by compensating the losses using active devices [110].

Table 6.1 Measured unloaded Q

$V_{bias}$	0V	0.65V	1V	1.2V
Unloaded Q	130.7	95.6	706.3	1913.1
$V_{bias}$	1.4V	1.6V	1.8V	2.0V
Unloaded Q	3390	7249	21172	6938.5

Figures 6-38 and 6-39 show the layout and photo of the tunable oscillator using SIW-CCTR (substrate waveguide complementary coupled tunable resonator) network shown in Figure 6-34, fabricated using on RT/Duroid 5880 substrate with a thickness of 0.508 mm and dielectric constant of 2.2. As shown in Figure 6-38, NEC's Hetero-Junction FET NE3210S01 is chosen to be used for low power consumption, the transistor is drain-biased at  $V_d = 1.5$  V,  $I_{ds} = 22$  mA, and both of the varactors are reverse-biased at the same  $V_{tune}$  voltage.

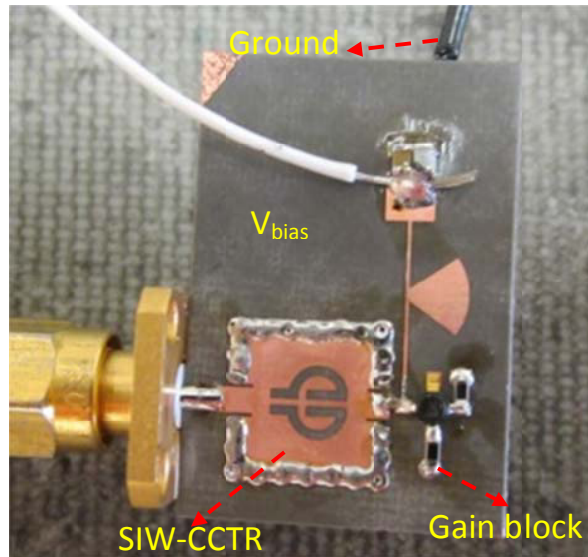
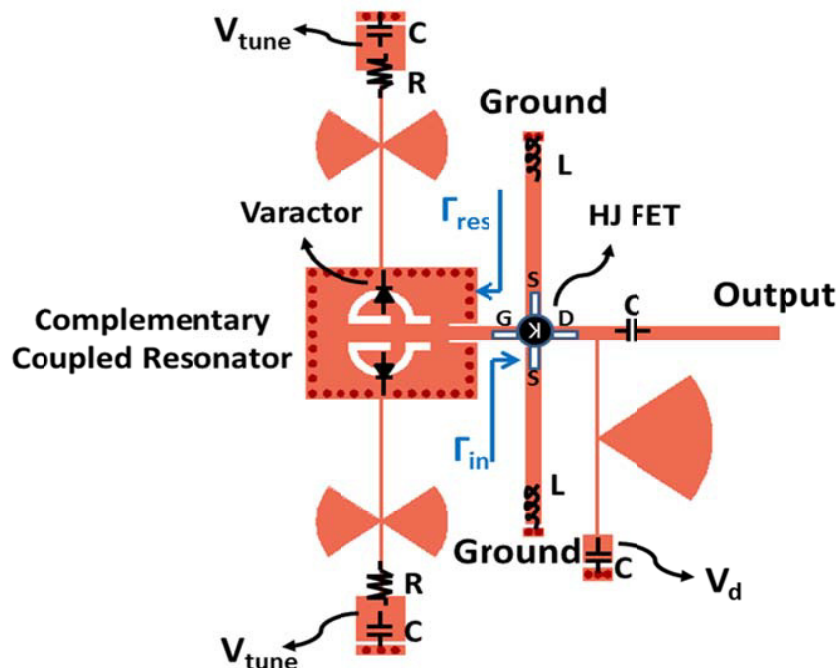
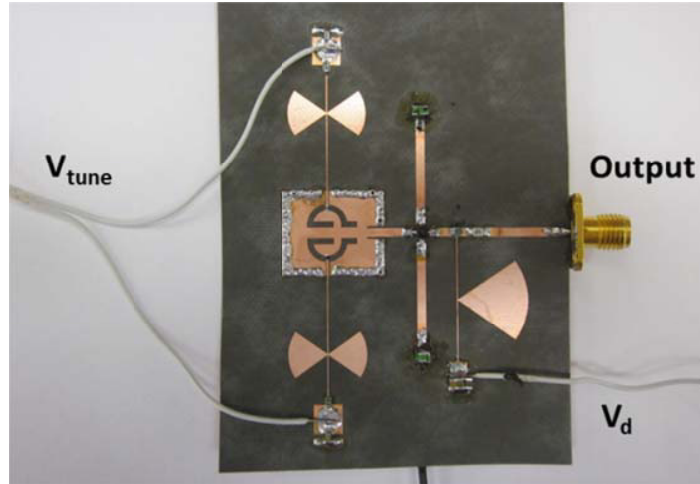


Figure 6-37: The fabricated prototype of SIW-ACCTR (active substrate wave-guide complementary coupled tunable resonator) fabricated using RT/Duroid 5880 substrate with a thickness of 0.508 mm and dielectric constant of 2.2.

The gate of the transistor (Hetero-Junction FET NE3210S01) is connected to SIW-CCTR (Figure 6-34) is DC grounded ( $V_g = 0V$ ) through inductive load supported by SIW structure. A DC decoupling capacitor is placed on the output path to prevent DC leakage. For stable oscillation,  $\Gamma_{in}$  should be greater than unity [102]. In order to make  $\Gamma_{in}$  greater than unity, two stubs in series with inductors shorted to ground and connected to the sources of the transistor to increase its instability in the desired frequency band. The lengths of the stubs are chosen so that  $R_{res} = -R_{in}/3$ ,  $X_{res} = -X_{in}$  to fulfill the oscillating conditions [103]. The oscillating frequency and output power after calibrating the cable loss plotted versus the bias voltage as shown in Figure 6-40.



Figures 6-38: A typical layout of the tunable oscillator using SIW-CCTR (substrate wave-guide complementary coupled tunable resonator) network shown in Figure 6-34 [103]



Figures 6-39: A photograph of the fabricated tunable oscillator using SIW-CCTR (substrate wave-guide complementary coupled tunable resonator) network shown in Figure 6-34 [103]

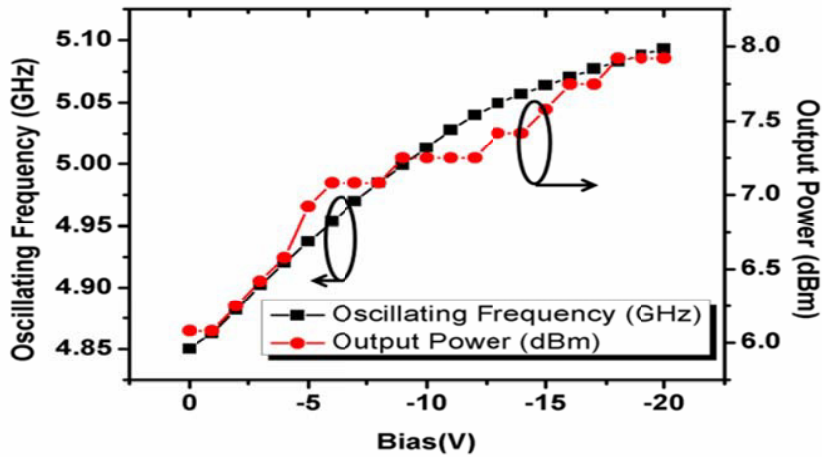


Figure 6-40: Measured performance of the tunable oscillator shown in Figure 6-39 with different bias voltage [103]

As shown in Figure 6-40, the oscillating frequency can be continuously tuned from 4.85 GHz to 5.1 GHz while reverse biased from 0 V to 20 V, which provides a tuning range of 5.15%. In addition, the output power varies from 6-8 dBm in the tuning range. The measured output spectrum of the tunable oscillator at 5.09 GHz is shown in Figure 6-41, measured phase noise is -115.2dBc/Hz at an offset frequency of 1 MHz. The figure of merit (FOM) given by (1.1)

$$FOM|_{f_{offset}} = \left[ \mathcal{E}(f_{offset}) - 20 \log_{10} \left( \frac{f_0}{f_{offset}} \right) + 10 \log_{10} \left( \frac{P_{DC}}{1mW} \right) \right] \left( \frac{dBc}{Hz} \right) \quad (6.45)$$

where  $\mathcal{E}(f_{offset})$  is the phase-noise at the offset frequency  $f_{offset}$ ,  $f_0$  is the oscillating frequency,  $f_{offset}$  is the frequency offset in MHz, and  $P_{DC}$  is the total consumed DC power in milli-watts.

From (6.45)

$$FOM|_{f_{offset}=1MHz} = -174.1 \left( \frac{dBc}{Hz} \right) \quad (6.46)$$

Figures 6-42 and 6-43 show the layout and photograph of tunable X-band oscillator topology using active resonator as shown in Figure 6-37, fabricated using RT/Duroid 5880 substrate with a thickness of 0.508 mm and dielectric constant of 2.2. As shown in Figure 6-42, NEC's Hetero-Junction FET NE3210S01 is selected for low power consumption and higher DC-RF conversion efficiency, and a shunt stub is added at its source to increase instability at the desired frequency.

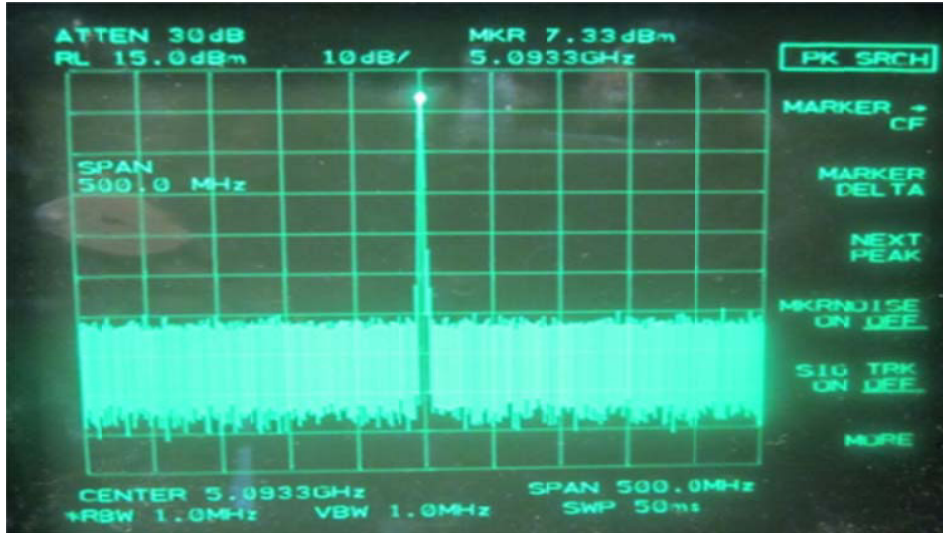


Figure 6-41: Measured output spectrum of the oscillator (Figure 6-39) at 5.09GHz [103]

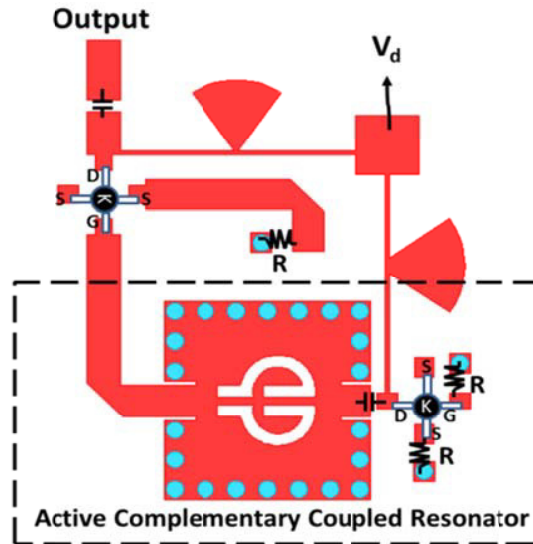


Figure 6-42: A typical layout of tunable X-band oscillator topology using active resonator as shown in Figure 6-37.

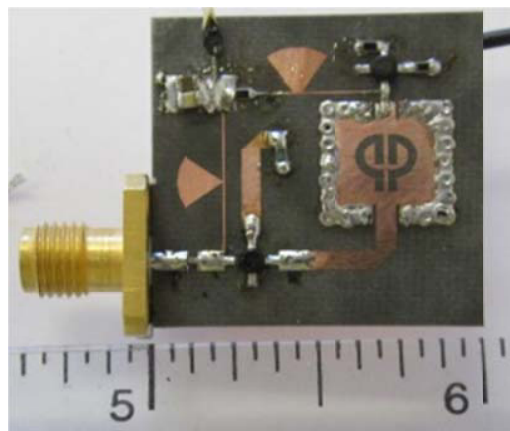


Figure 6-43: Photo of the fabricated tunable X-band oscillator topology (shown in Figure 6-42) fabricated using RT/Duroid 5880 substrate with a thickness of 0.508 mm and dielectric constant of 2.2.

The DC bias is chosen to be  $V_d=2.5$  V and  $I_d=6$  mA in the measurement in order to have optimized result for DC-RF conversion efficiency and FOM. It is to note that the entire circuit is biased with one single bias ( $V_d$ ), thus enables miniaturization. The oscillator design is based on the negative-resistance method [67]. The length of the stub for the main oscillating transistor is also chosen so that  $R_{res} = -R_{in}/3$ ,  $X_{res} = -X_{in}$ , to fulfill the starting condition for oscillation, where  $R_{res}$  and  $R_{in}$  are the real parts of  $Z_{res}$  and  $Z_{in}$ , respectively, and  $X_{res}$  and  $X_{in}$  are the imaginary parts of  $Z_{res}$  and  $Z_{in}$ , respectively. The required DC biasing is done by adding lumped passive components (resistors) in order to self-bias the two transistors at their appropriate biasing points. Two capacitors are used to decouple the DC components from the transistors.

Figure 6-44(a) shows RF output spectrum of the oscillator circuit depicted in Figure 6-43, the fundamental tone of the designed oscillator is at 9.93 GHz and it has an output power of 2.36 dBm. The second harmonic is -18.33 dBm at 19.86 GHz, as shown in Figure 6-44(b).

The phase noise measurement is carried out by using two different set-ups. The first measurement is done by using R&S FSUP26 Signal Source Analyzer, in which the measured phase noise is -93.96 dBc/Hz and -123.86 dBc/Hz at 100 kHz and 1 MHz offset as shown in Figure 6-45 (a).

The phase noise measurement is repeated on Agilent 5052B Signal Source Analyzer along with E5053A Microwave Down-converter, in which the measured phase noise is -97.65dBc/Hz and -127.01 dBc/Hz at 100 kHz and 1 MHz offset as shown in Figure 6-45 (b), respectively. Table 6.2 summarizes the measured results of using the two sets of equipments.

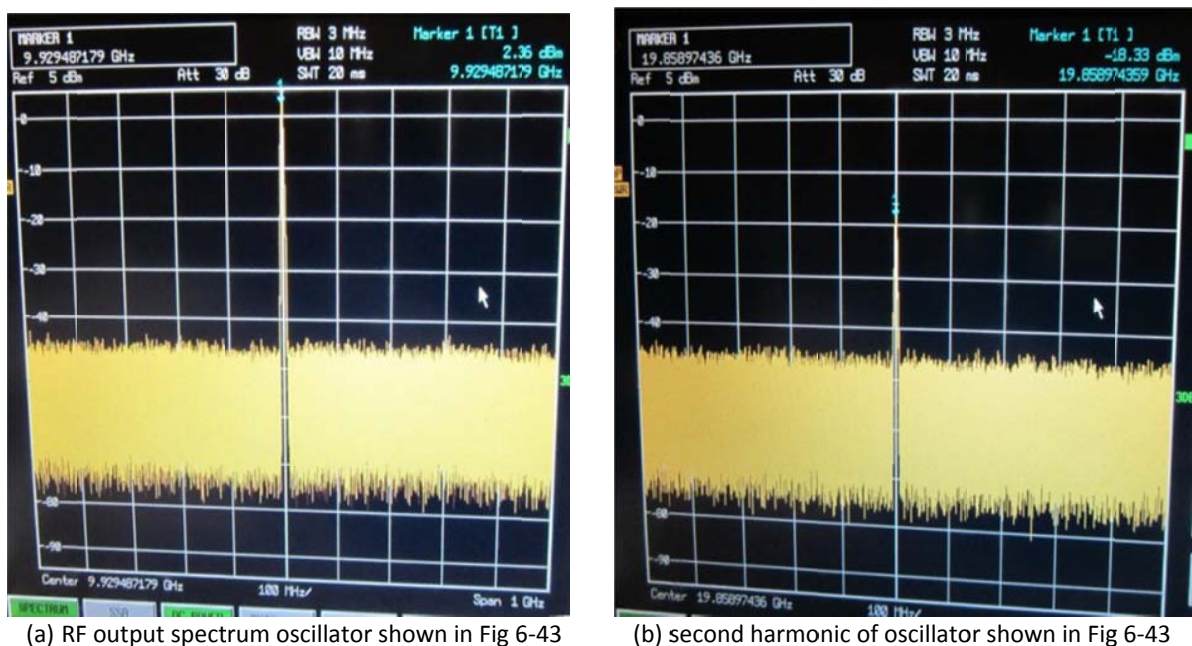


Figure 6-44: Measured data (a) shows RF output spectrum of the oscillator circuit depicted in Figure 6-43, and (b) shows second harmonic -18.33 dBm at 19.86 GHz of oscillator circuit depicted in Figure 6-43.

Table 6.2 [102]

	Oscillating Frequency	Output Power	Phase Noise@ 100 kHz	Phase Noise@ 1MHz	DC Power Consumption	FOM@ 100 kHz	FOM@ 1 MHz
<b>R&amp;S FSUP</b>	9.904GHz	2.02dBm	-93.96dBc/Hz	-123.86dBc/Hz	15mW	-182.2	-192.1
<b>Agilent 5052B</b>	9.883GHz	3.02dBm	-97.65dBc/Hz	-127.01dBc/Hz	15mW	-185.89	-195.25

As shown in Figure 6-45, the close-in phase noise (<100 kHz offset) performance is very poor because of higher 1/f noise for HJ FET device. By incorporating SiGe HBT device in place of HJ FET, the influence of 1/f noise or flicker noise can be reduced [67].



(a) Measured phase noise plot on R&S FSUP26 [102]



(b) Measured Phase noise plot on Agilent 5052B+5053A [102]

Figure 6.45: The phase noise measurement is carried out by using two different set-ups (R&S FSUP and Agilent 5053) (a) measured phase noise plot on R&S FSUP26 Signal Source Analyzer, and (b) measured phase noise plot on Agilent 5052B+5053A.

Figure 6-46 (a), and 6-46 (b) show the oscillator circuit schematic using SiGe HBT device, and the measured phase noise plot. It can be seen that measured phase noise plot as depicted in Figure 6-46 (b) shows stable behavior over temperature (-40 degree C to +85 degree C), the novel bias stabilization circuit incorporated in this research work allows optimum phase noise performance over desired operating temperature (-40 degree C to +85 degree C). The oscillator circuit delivers 4.75-dBm O/P power with DC bias of 5V and 12 mA.

As illustrated in Figure 6-46(a), 10 GHz oscillator circuit uses a SiGe Hetrojunction-bipolar-transistor (HBT) active device (NEC), fabricated on Rogers substrate material with a dielectric constant of 3.38 and thickness of 32 mil-microstripline medium. The reported paper [8, 10, and 13] by authors use BFP 540 SiGe HBTs from Infineon shows the significant improvement of more than 40 dB in phase noise performance at 10 kHz offset from the carrier frequency 10 GHz but at the cost of the increase in DC power consumption.

In this research work, SIW-CCR oscillator topology as shown in Figure 6-39 and 6-43 operating at C-band and X-band, can be easily scaled to a higher frequency such as Ku- and Ka- bands.

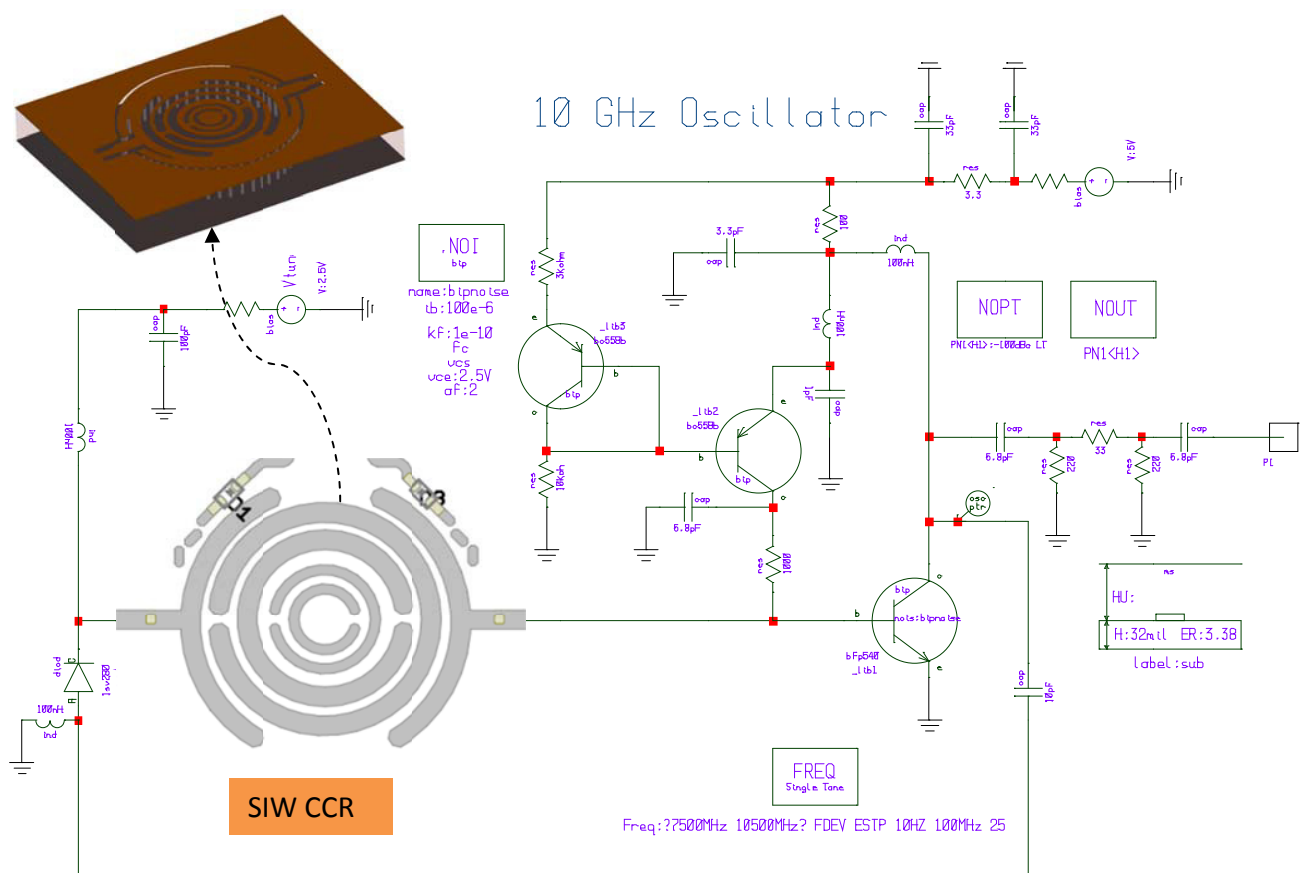


Figure 6-46 (a): A typical circuit schematic of the novel 10 GHz oscillator using printed resonator using 32 mil Roger R4003C, Dielectric constant=3.38 (size of the board 0.5x0.5 inches), with DC bias (5V, 12mA)

Figure 6-47 shows the CAD simulated layout of a Ku-band SIW-CCR with a size of 7.2 mm by 6 mm, whose center frequency is around 16 GHz. CAD Simulated results using HFSS show that the unloaded Q of Ku band CCR is around 350.

Similarly, the CCR scaled to Ka-band with a size of 3.6mmx 3mm that has a center frequency around 32 GHz, and the simulated unloaded Q is around 330. In addition to SIW CCRs, Mobius inspired resonators using slow-wave structures are discussed in Ch-7 and Ch-8 for the realization of low phase-noise oscillator circuit.

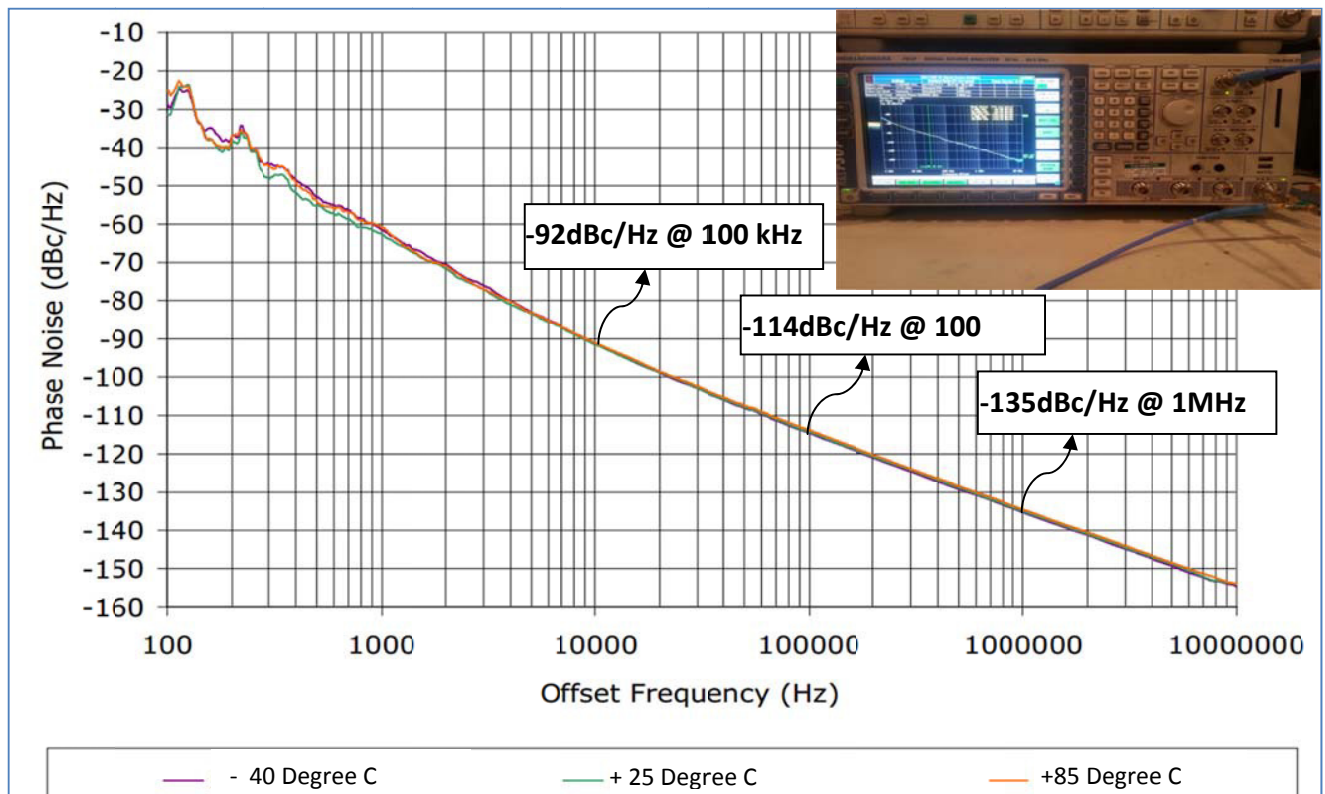


Figure 6-46 (b): Measured phase noise plot of 10 GHz oscillator circuit shown in Figure (6-45 a). It can be seen that phase noise plot shows stable behavior over temperature, the novel bias stabilization circuit helps for optimum phase noise performance over desired operating temperature (-40 degree Celsius to +85 degree Celsius)

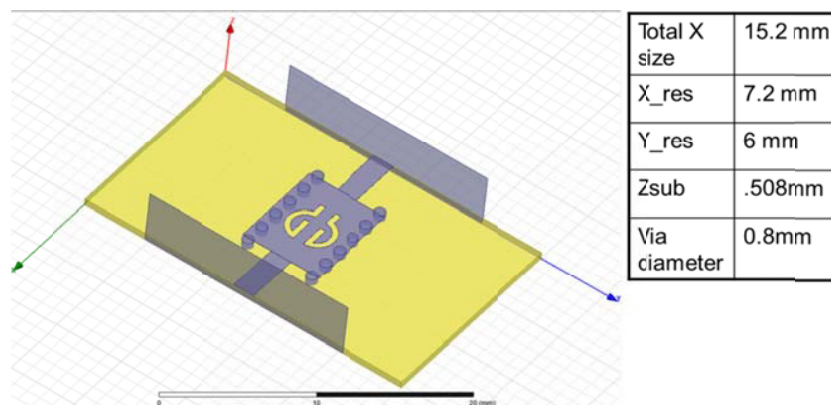


Figure 6-47: A typical CAD schematic of *Ku*-band SIW-CCR

#### 6.4.1.9 Opto-Electronic Oscillator (OEO) using Metamaterial Resonator

In the past several decades, great efforts have been made in the development of various techniques for generation of low phase noise Opto-electronic oscillator (OEO) because extremely high Q optical resonator is achieved by utilizing the low loss in optical fibers [84]-[89]. Figure 6-48 shows the block diagram that describes the novel push-push topology in conjunction with an evanescent mode metamaterial resonator combiner network. The unique properties of the metamaterial resonator are that it has a negative permittivity and negative permeability that enables amplification of an evanescent mode wave.



There are two practical methods for Q-factor measurement: (i) Reflection method for reflection mode resonators [107], and (ii) Transmission Mode Q- Factor Technique [108]-[110].

Figure 6-49 depicts the unloaded Q (quality factor) of the evanescent mode resonator and multi coupled planar resonator, plotted against a range of operating frequencies from about 2 GHz to about 16 GHz. The estimation of Q (quality factor) is done by experimental measurement of [S]-parameter using vector network analyzer. As shown in Figure 6-49, the evanescent mode resonator is capable of achieving a quality factor above 1000 at operating frequencies ranging from about 2 GHz to about 15 GHz.

As shown in Figure 6-48, the metamaterial evanescent-mode resonator combiner network is coupled (capacitively) to each of the dynamically tuned resonator networks. This acts as an evanescent mode (EM) buffer, storing a portion of the excess radio frequency (RF) energy coupled into the resonator network for a given period of a signal cycle so that the conduction angle of the device can be reduced, thereby reducing the average noise performance for a given period of time.

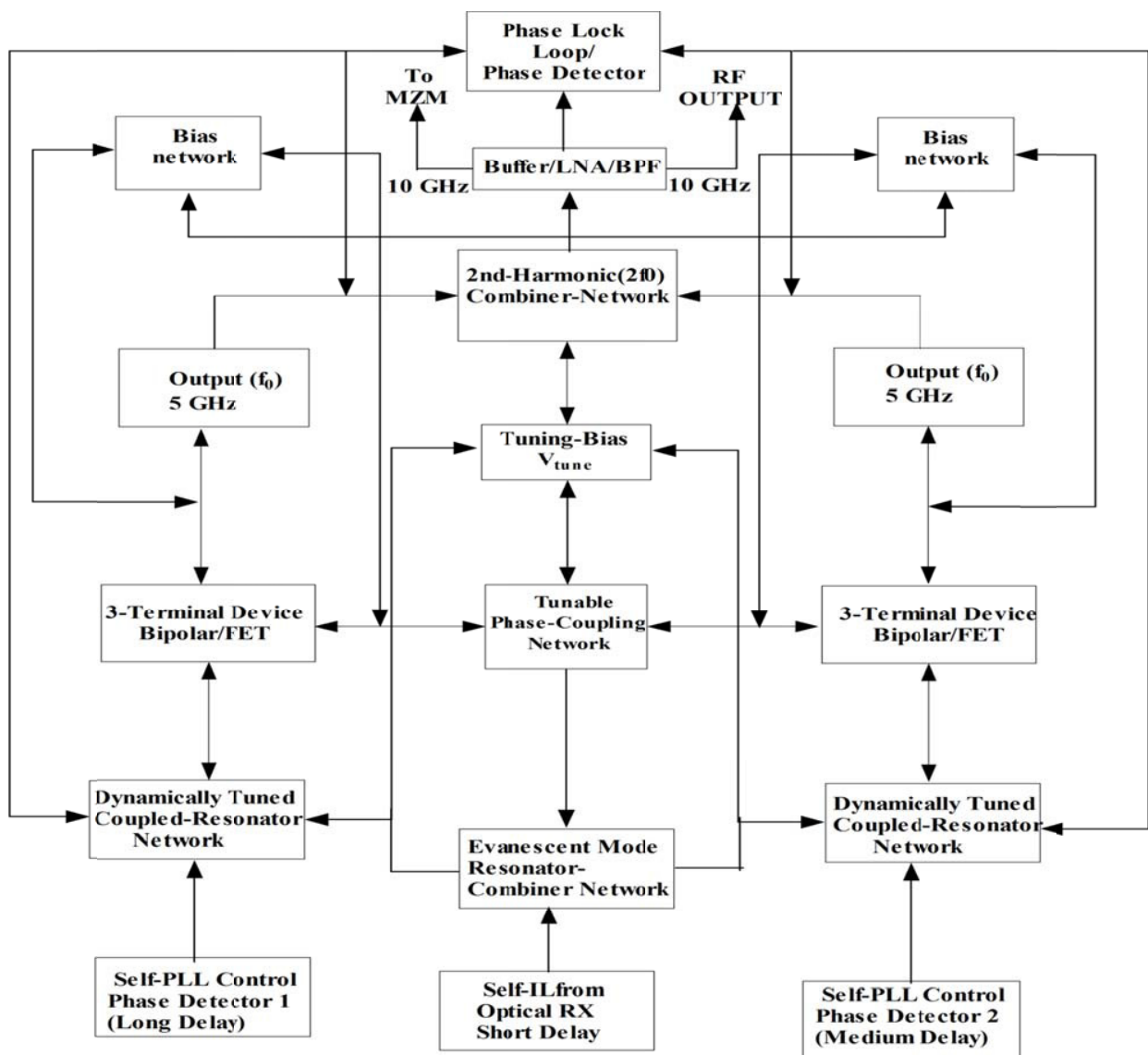


Figure 6-48: The block diagram Integrated realization of a highly stable self ILPLL RF Oscillator (US Patent application No.: 61/746, 919; filed on Dec 28, 2012 and US Patent application no. 13/760767; filed on Feb 06, 2013) [84]-[85]

The spectral pure signal is generated by locking the optical phase modulation to a free spectral range resonator in conjunction with metamaterial evanescent-mode resonator combiner network. The microwave carrier at X-band and higher frequencies is generated by locking the optical phase modulation to a free spectral range resonator in conjunction with metamaterial evanescent mode resonator combiner network that offers -160 dBc/Hz @ 10 kHz offset from the carrier, the phase noise performance is best to date for the given figure of merit (FOM) and the class of oscillator topology [84]-[86]. The brief description of optical fiber delay based frequency sources discussed in Ch-10 (The detailed description in ref. 111).

## 6.5 Conclusion

The oscillator circuits using different novel and inventive resonator networks discussed in this Chapter allow clear understanding about oscillator performance metrics in terms of size, power consumption and frequency tunability [91]-[109]. The state-of-the-art OEOs technology is disclosed in public domain, and protected by copyrights and is patented [84]-[85]. The detailed descriptions and validation examples of OEO design methodology and optimization techniques described in e-book [Ref. 111, Chapter 10].

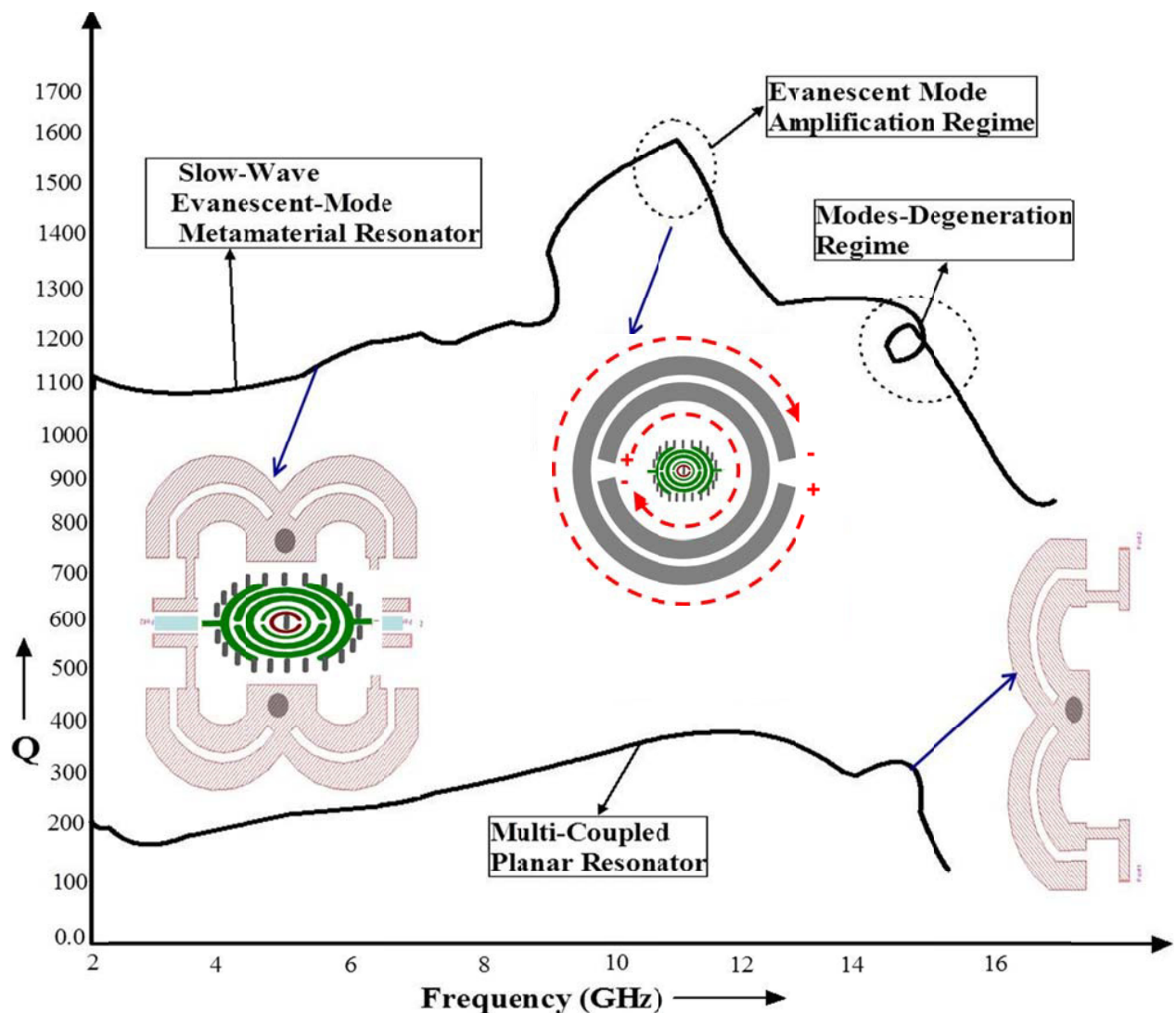


Figure 6-49: Shows the typical measured plot of unloaded quality factor (Q-factor) of novel resonators (Multi-Coupled resonator, Slow-wave evanescent-mode metamaterial resonator, Evanescent-mode amplified resonance regime).

## Chapter 7

### Printed Coupled Möbius Resonator Oscillators

#### 7.1 Introduction

Geometrical phenomenon of anholonomy depends on failure of a quantity to recover its original value, when the parameters on which it depends are varied round a closed circuit. Möbius strip provides one of the simplest examples of anholonomy, as the normal to the surface of the strip does not return to its original direction even though the radius vector does. The strip therefore deforms in such a way that its metrical properties are barely changed, some nanostructures have the same elastic properties. A necessary and sufficient condition for a Möbius surface to be developable is that its Gaussian curvature must vanish everywhere. Given a curve with non-vanishing curvature, there exists a unique flat ruled surface (the so-called rectifying developable) on which this curve is a geodesic curve (Figure 7-1) described by [1]

$$\vec{x}(s, t) = \vec{r}(s) + t[\vec{b}(s) + \eta(s)\vec{t}(s)] \quad (7.1)$$

$$\tau(s) = \eta(s)k(s), \quad s = [0, L], t = [-w, w] \quad (7.2)$$

Where  $\vec{r}$  is a parameterization of a strip with  $r$  as centerline and of length  $L$  and width  $2w$ , where  $\vec{t}$  is the unit tangent vector,  $\vec{b}$  the unit binormal,  $k$  the curvature and  $\tau$  the torsion of the centerline, the parameterized lines  $s = \text{const.}$  are the generators, which make an angle  $\beta = \text{arc}[\text{Tan}(1/\eta)]$  with the positive tangent direction. The unique properties of Möbius strips, the shape minimizes the deformation energy, which is entirely due to bending, can be described by

$$V = \frac{1}{2}D \int_0^L \int_{-w}^w k_1^2(s, t) dt ds \quad (7.3)$$

where  $D = 2h^3E/[3(1-\nu^2)]$ , with  $2h$  the thickness of the strip, and  $E$  and  $\nu$  Young's modulus and Poisson's ratio of the material.

In this section, a planar Möbius-coupled resonator is described, and the method for miniaturization can be applied to tunable oscillator circuits and memory devices used for receivers, filters, antenna, and matching networks.

#### 7.2 Planar Möbius strip Resonator

A typical Möbius is a surface with only one side and only one boundary component, the mathematical property of being non-orientable (Figure 7-1). A unified system of differential-algebraic equations that describes models of this type are published in 2007 together with its numerical solution and many technical applications [1].

The concept of the Möbius strips is based on the fact that a signal coupled to a strip shall not encounter any obstruction when travelling around the loop, the loop shall behave like an infinite transmission line, enabling compact high Q-factor resonators [2]. This characteristic enables many radio and microwave applications including: (i) a compact resonator with the resonance frequency which is half that of identically constructed linear coils [2], (ii) Tesla Coil for global transmission of electricity without wires [3], and (iii) high temperature superconductors [4] to name a few.

Recent publication describes the Möbius strip resonator [2]-[7] but the surface is non-planar 3-dimensional structure (Figure 7-2), not suitable for integration and surface mounted device (SMD) technology applications. Printed resonators are a special class of transmission lines of finite extent with well-defined boundary conditions. The particular interest here is a 1-dimensional printed ring resonator, which can be equivalently represented by the simple lumped L-C network shown in Figure 7-3.

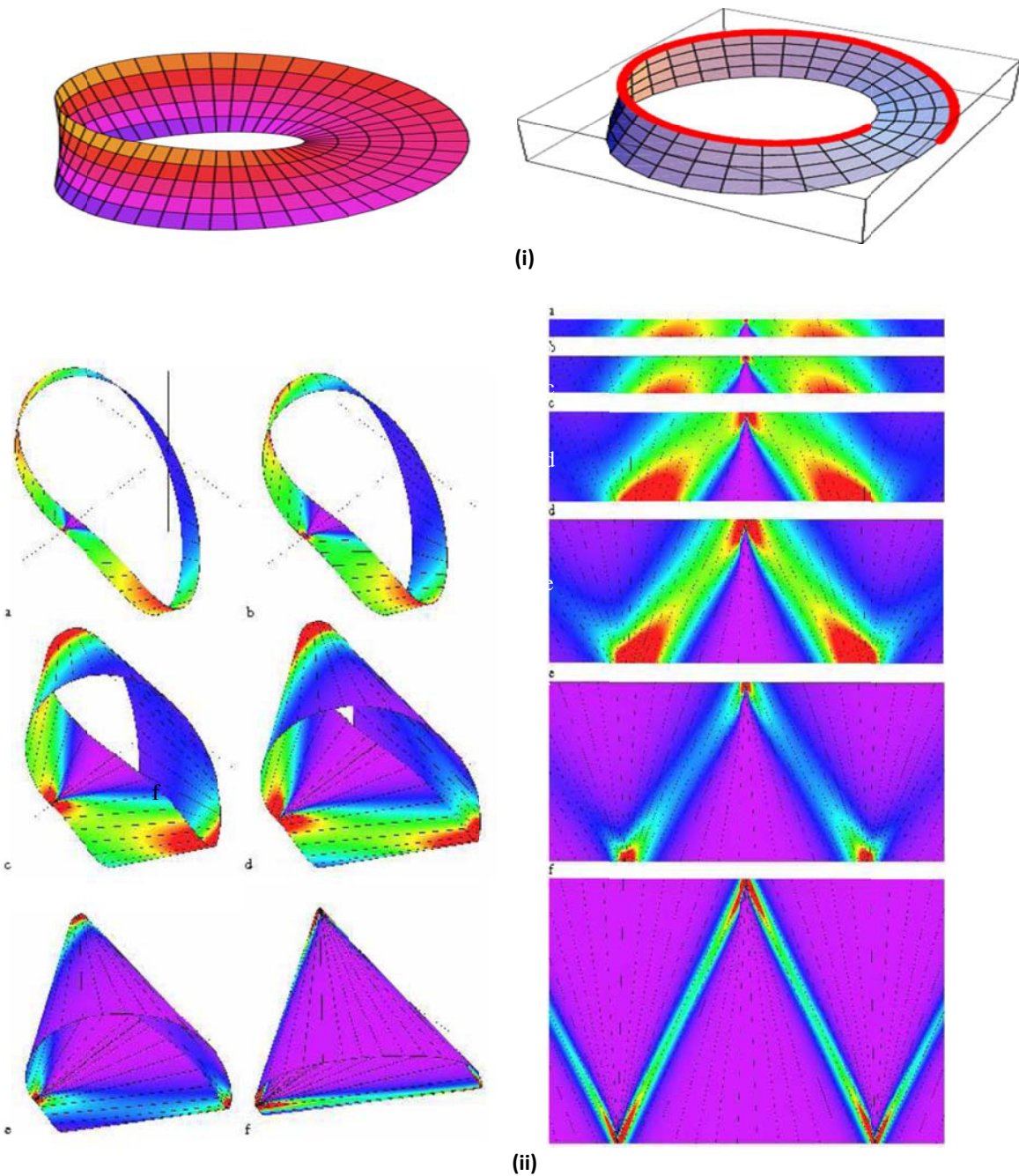


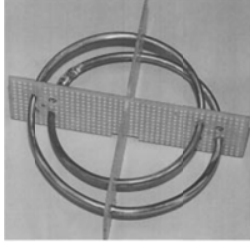
Figure 7-1 (i): A typical Möbius strip, one can move along the length of the strip, return to its starting point having traversed the entire length of the strip without ever crossing an edge, and (ii) Computed Möbius strips (coloring changes according to the local bending energy density, from violet for regions of low bending to red for regions of high bending). The left panel shows their 3D shapes for  $w = 0.1$  (a),  $0.2$  (b),  $0.5$  (c),  $0.8$  (d),  $1.0$  (e) and  $1.5$  (f), and the right panel the corresponding developments on the plane [1].

In solving, the electric currents on the resonator can be formulated by a periodic boundary condition of the form described by [8]

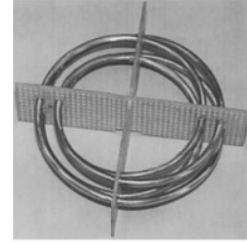
$$I_{j+k} = I_j \quad (7.4)$$

where  $I_k$  represents the electric current around the  $n^{\text{th}}$  closed loop on the periodic ladder structure of  $k$ -elements.

The boundary condition of the general form shown in (7.4) governs that  $I_k$  is a conserved quantity that gives invariance of solutions under a  $2\pi$  rotation with a definite handedness.



(a) Dual Mode



(b) Quad-Mode

Figure 7-2 Photograph of the non-planar 3-D Möbius wire resonator [3]

From the circuit theory, Kirchhoff's voltage relation for the  $k^{\text{th}}$  element is given by (assuming equivalent low pass ladder network is driven across any equivalent lumped inductor L or capacitor C):

$$\left(\omega^2 - \frac{1}{LC}\right)I_k - \gamma\left(\omega^2 - \frac{1}{2\gamma LC}\right)(I_{k+1} + I_{k-1}) = 0 \quad (7.5)$$

where  $\gamma$  is mutual coupling coefficient (Mutual inductance ' $M'=2\gamma L$ ') between nearest neighbor elements shown in Figure 7-3, and  $k$  is number of element structure. Equation (7.5) is a 1-dimensional non-dissipative wave equation of the LC network (assuming zero resistive loss and electromagnetic wavelength is much larger than the linear dimensions of the network) with a discrete rather than continuous spatial variable [8]. The solution for the ring resonator shown in Figure 7-4 (a) with the periodic boundary condition given in (7.4) can be given in the form

$$I_k = A_1 e^{\left(\frac{i2\pi j p}{k}\right)} + A_2 e^{-\left(\frac{i2\pi j p}{k}\right)} \quad (7.6)$$

where  $p$  is an integer specifying the normal mode and  $k$  is number of element structure. From (7.5) and (7.6), the dispersion relation for the allowed frequency spectrum can be described by [8]

$$\omega^2 = \left\{ \frac{2\sin^2\left(\frac{p\pi}{k}\right)}{LC\left(1-2\gamma\cos\frac{2p\pi}{k}\right)} \right\} \quad (7.7)$$

where  $p$  is an integer specifying the normal mode,  $\gamma$  is mutual coupling coefficient (Mutual inductance ' $M'=2\gamma L$ ') between nearest neighbor elements shown in Figure 7-3, and  $k$  is number of element structure. From (7.5)-(7.7), for even value of  $k$ , there are  $k-1$  eigenvalues, including  $(k-2)/2$  degenerate doublets and one singlet. A typical ring resonator, whose Eigen function satisfies (7.4), defines a distinct inner and outer surface of the ring, shown in Figure 7-4(a). Figure 7-4(b) shows a topological transformation resulting in a Möbius strip resonator, whose current dynamics can be formulated by applying twisted boundary condition as

$$I_{j+k} = -I_j \quad (7.8)$$

From (7.8), a simple topological transformation on the resonator ring (Figure 7-4) results in a sign reversal of current ( $I_j$ ) upon a  $2\pi$  rotation of the solutions, and a  $4\pi$  rotation is now required for invariance of the Eigen functions [6]-[16]. Note that the eigenfunctions satisfying the condition for twisted boundary are of the same form as (7.5) provided that the mode indices are given half-integral values ( $p = 1/2, 3/2, 5/2, \dots, (k-1)/2$ ) relative to a ring consisting of identical components. The dispersion relation for Möbius ring is same as (7.7), however, the wave-vectors are shifted by

$$\Delta\lambda = -\left(\frac{\pi}{k}\right) \quad (7.9)$$

The two distinct topologies shown in Figures 7-4(a), 7-4(b) can be considered as a complementary pair related by a single transformation.

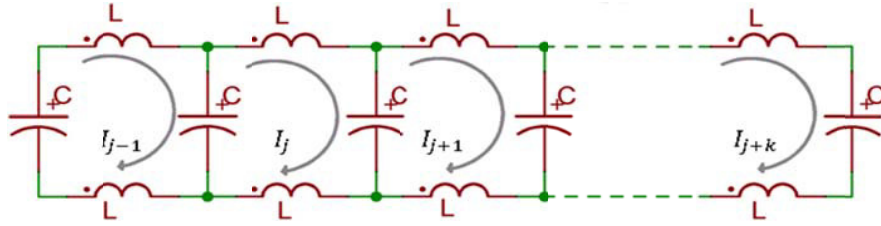
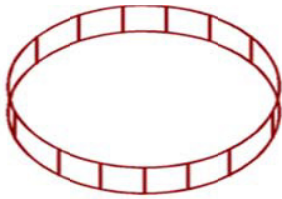
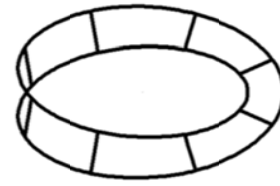


Figure 7-3: A typical low-pass ladder network consisting of a series of inductances  $L$  and capacitances  $C$  along the transmission line (Printed resonators are a special class of transmission lines of finite extent with well-defined boundary conditions, the 1-DI printed ring resonator is represented by the simple lumped L-C network) [8].



(a) Closed loop ring resonator



(b) Möbius strip resonator

Figure 7-4: shows the orientation of typical closed loop resonator: (a) the ring resonator (b) the Möbius strip resonator (a topological transformation of ring resonator into a Möbius strip resonator) [8]

From (7.4) and (7.8), it is evident that there is no additional structure associated with the Möbius ring resonator, since a second topological half-twist transformation on the Möbius resonator leads back to the boundary condition of (7.4). Their description divides into half-integral and integral normal mode indices. The Eigen functions of the Möbius resonator form an orthogonal basis set; presents an interesting possibility for the design of metamaterial for the application in tunable oscillators, antenna, and filter circuits [6]. The oscillator's loaded Q factor  $Q_L$  is described by [15]

$$Q_L = \frac{\omega_0}{2} \left| \frac{d\varphi(\omega)}{d\omega} \right|_{\omega=\omega_0} = \frac{\omega_0}{2} \tau_d; \quad \tau_d = \left| \frac{d\varphi(\omega)}{d\omega} \right|_{\omega=\omega_0} \quad (7.10)$$

$$\tau_d = \left. \frac{d\varphi(\omega)}{d\omega} \right|_{\omega=\omega_0} = \frac{\varphi(\omega_0 + \Delta\omega) - \varphi(\omega_0 - \Delta\omega)}{2\Delta\omega} \quad (7.11)$$

where  $\varphi(\omega)$  is the phase of the oscillator's open loop transfer function at a steady state and  $\tau_d$  is the group delay of the resonator. From (7.10),  $Q_L$  is proportional to the group delay; therefore, for low phase noise application, the design goal is to maximize the group delay of Möbius strip resonator by incorporating phase-injection techniques. The eigenfunctions of the Möbius resonator form an orthogonal basis set, therefore all eigenfunctions of the pair are mutually orthogonal; exhibits minimal electromagnetic interactions [8]. This presents an interesting possibility for incorporating phase-injection along the mutually coupled surface of the strips, resulting in higher quality factor for a given size of the printed transmission line resonator [12]. The Möbius strips resonator show an interesting possibility, for example if the arbitrary structure is composed of an array of typical Möbius strips as its basis, complementary strips could in principle be introduced without much disturbance the coupling dynamics for microwave component ( sensors, resonators, antenna, and filter) applications [13]-[15].

### 7.3 MCPR Oscillator: Inexpensive Alternative of DRO

Dielectric resonators (DRs) exhibit high Q-factor, are used in high-spectral-purity signal sources at RF and microwave frequencies. However, the DR requires precise machining for fabrication, careful placement of the dielectric puck for optimal coupling, and involves manual mechanical tuning of the DR for desired frequency operation [7]-[16]. The printed coupled resonator based oscillator can overcome

problem associated with DRO, except the poor phase noise performance due to inherent low Q-factor associated with printed transmission line resonator [17]-[19]. The Q (quality) factor of the coupled planar resonator network can be enhanced by introducing slow wave propagation dynamics as discussed in Ch-6, however large physical size and mode jumping restricts the application especially at lower frequencies. The loaded quality factor  $Q_L$  of the coupled resonator network is given in terms of unloaded quality factor  $Q_0$  as [Ch-6, Figure 6-8]:

$$[Q_L(\omega_0)]_{\text{electrical-coupling}} \cong 2 \left[ \frac{Q_0}{(1 + \beta_e)} \right]_{\beta_e \ll 1} \cong 2Q_0 \quad (7.12)$$

$$[Q_L(\omega_0)]_{\text{magnetical-coupling}} \cong 2[Q_0(1 + \beta_m)]_{\beta_m \rightarrow 1} \cong 2Q_0 \quad (7.13)$$

$$[Q_L(\omega_0)]_{\text{hybrid-coupling}} \cong 2 \left[ Q_0 \frac{(1 + \beta_{mh})}{(1 + \beta_{eh})} \right]_{\beta_e \ll 1, \beta_{mh} \rightarrow 1} \cong 4Q_0 \quad (7.14)$$

where coupling factor  $\beta$  ( $\beta_e$  for electric field,  $\beta_m$  for magnetic field, and  $\beta_h$  for hybrid field). From (7-12)-(7.14), hybrid coupling ( $\beta_h$ ) shown in Figure 6-8(f) (Chapter-6) acts as a Q-multiplier effect, but this phenomena holds good for fixed frequency operation only and very difficult to realize broadband Q-multiplier dynamics which is necessary for wideband oscillators. In addition to this, mode jumping caused by undesirable higher order mode generation in hybrid coupling makes this structure not suitable for tunable wideband VCO (voltage-controlled oscillator) applications. The alternative approach is to tune the coupling factor  $\beta_j$  over the desired operating frequency band in conjunction with higher order mode-suppressing network. However, broadband mode-suppression is not an easy task in multi-mode resonator structure. A novel approach is to use injection-locking and phase-synchronization techniques for broadband applications. The Möbius strip resonator topology described in Figure 7-1 can offer promising solution for broadband oscillator circuits in compact size, integrable and inexpensive alternative of expensive DROs [12]. Figure 7-5 shows the typical layout of 10 GHz Möbius resonator based oscillator. As shown in Figure 7-5, Möbius strips resonator is formed by connecting the outer and inner strips by via hole for the realization of planar structure. It can be seen that two concentric rings inside the Möbius loop minimize the spurious modes, thereby stable oscillation.

Figure 7-6 shows the measured plot of unloaded Q-factor of the printed resonator structures (electrical coupled, magnetic coupled, hybrid or mixed coupled, and Möbius coupled) for giving brief insight about the improvement in quality factor in planar domain. As shown in Figure 7-5, the Möbius coupled printed resonator (MCPR) structure and hybrid coupled resonator (Figure 6-8, Ch-6) act like a Q-multiplier, peaking at 8.6 GHz due to the convergence of evanescent- modes. It can be seen in Figure 7-6 that Möbius resonator exhibits the undesired multi-mode resonant characteristics because of non-uniform coupling across the strips (ideally Möbius strip is 3-Dimensional structure (Figure 7-1)), and care must be taken to suppress these spurious modes for low jitter in RADAR applications. The drawback of this approach is multi-mode frequencies and mode-jumping (encircling the resonator characteristics), restricts the broadband operations. To overcome this problem, mode stabilization (injection of higher order modes into the resonant cavity with proper phase shift that improves the stability factor) control circuit is incorporated. This degrades the Q factor by 10-20% resulting in degradation of phase noise performances by 3-6 dB but overcomes the problem of mode jumping, hence achieving stable operation and inexpensive alternative of 10 GHz DROs (Dielectric resonator oscillator) for X-Band RADAR applications. Figure 7-7 shows the typical block diagram of 10 GHz Möbius coupled resonator VCOs using a SiGe Hetro-junction-Bipolar-transistor (HBT) active device, built on 20mils substrate material with a dielectric constant of 2.2 for the validation of the new approach. Figure 7-8 shows the measured phase noise plot ( $-110$  dBc/Hz @ 10 kHz offset) from the carrier frequency of 10 GHz, offers promising performances for a given size in planar configuration [19]-[22].

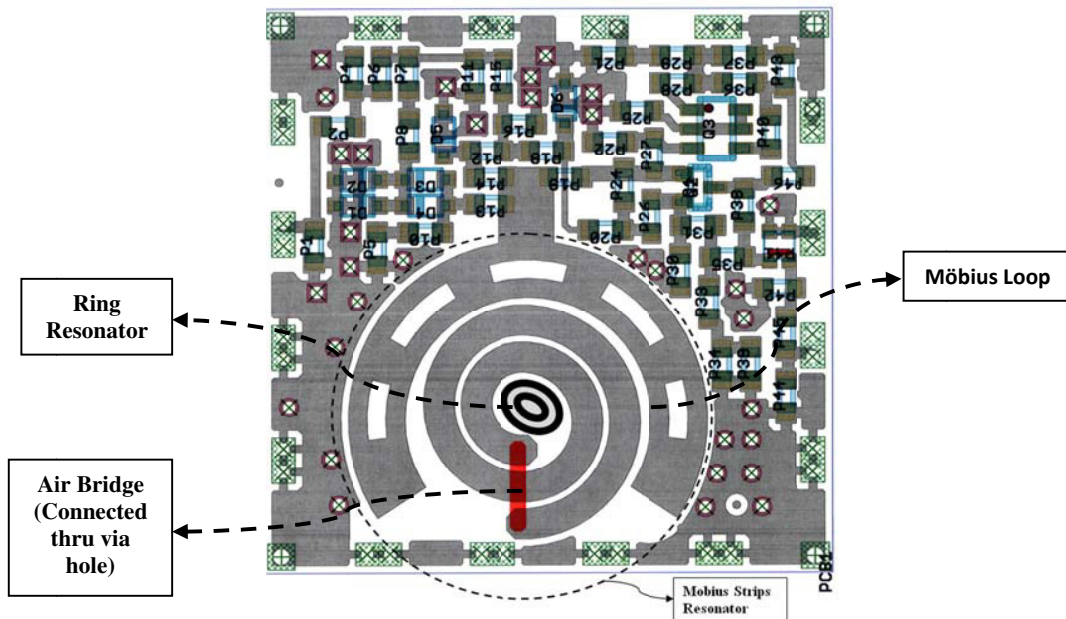


Figure 7-5: Shows the layout of 10 GHz oscillator (depicts the Möbius strips resonator sued for high Q-factor resonator (PCB layout is done with 22-mil substrate thickness with 3.38 dielectric constant, 0.5x0.5x0.18 inches)

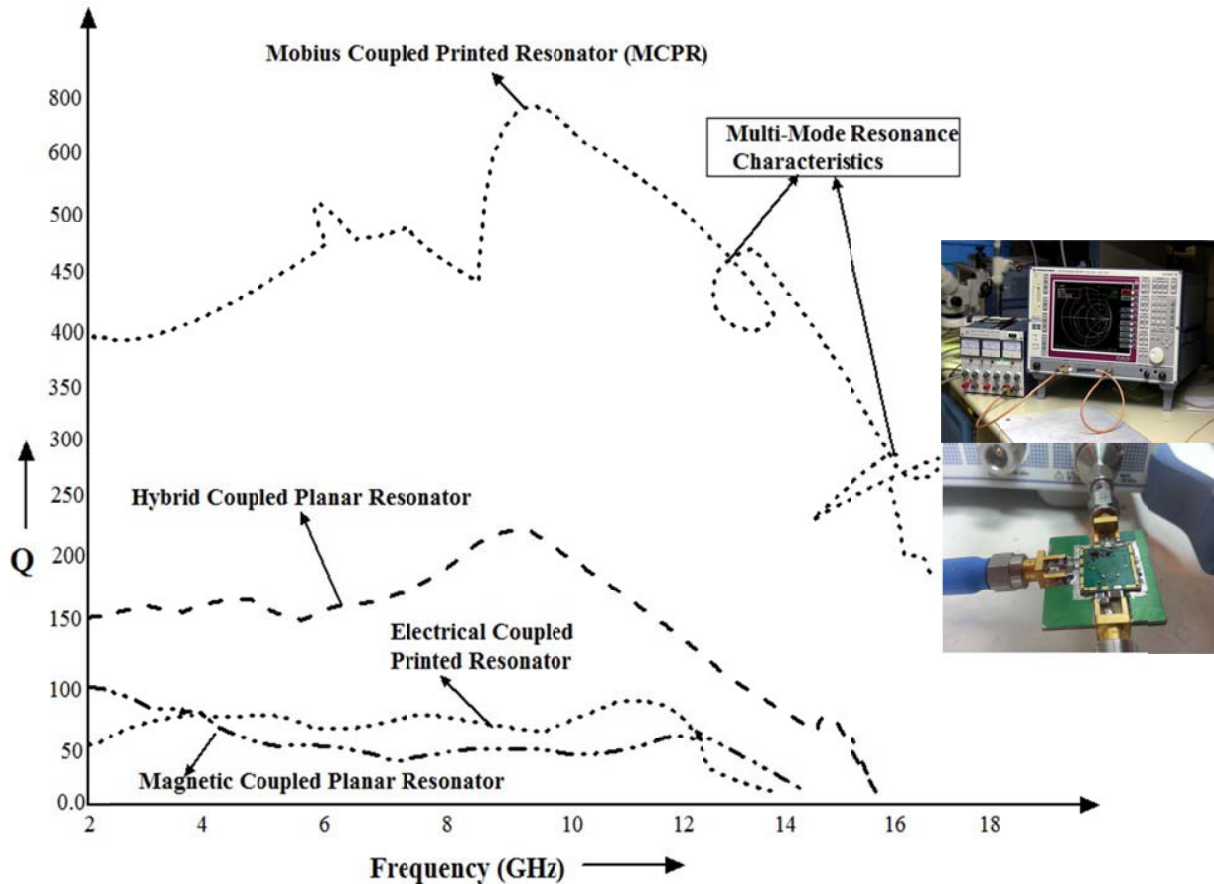


Figure 7-6: The measured plot of unloaded Q-factor of the printed resonator structures (electrical coupled, magnetic coupled, hybrid or mixed coupled, and Möbius coupled) (PCB layout for these resonators built with 20 mil substrate thickness with 2.22 dielectric constant and PCB size: 0.5x0.5x0.18 inches).



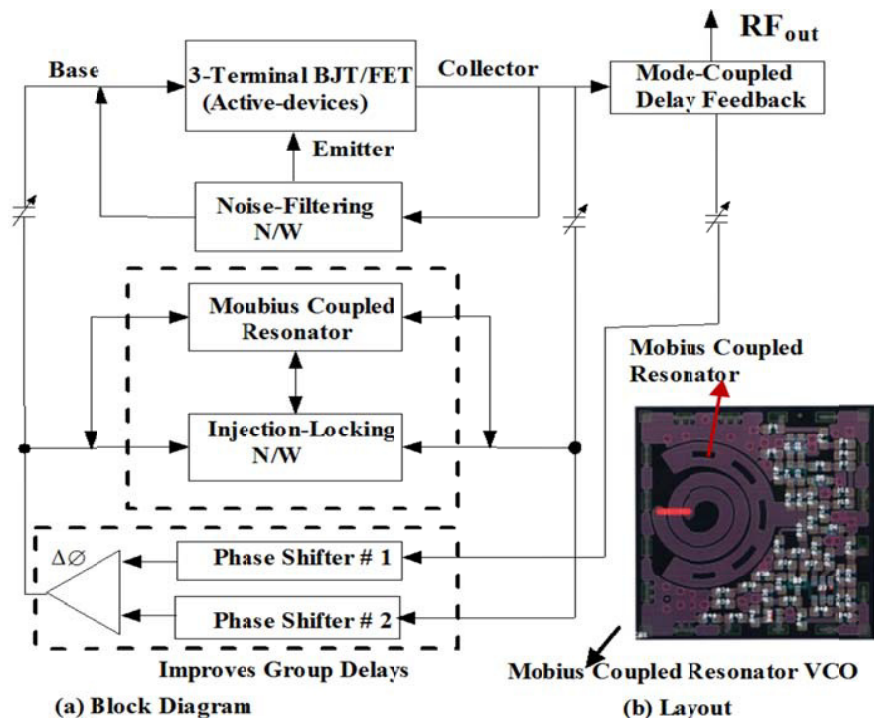


Figure 7-7: Shows the typical block diagram 10 GHz Möbius coupled resonator VCOs using a SiGe Hetro-junction-Bipolar-transistor (HBT) active device, built on 20mils substrate material with a dielectric constant of 2.2 for the validation of the new approach, PCB size: 0.75x0.75x0.18 inches [15]

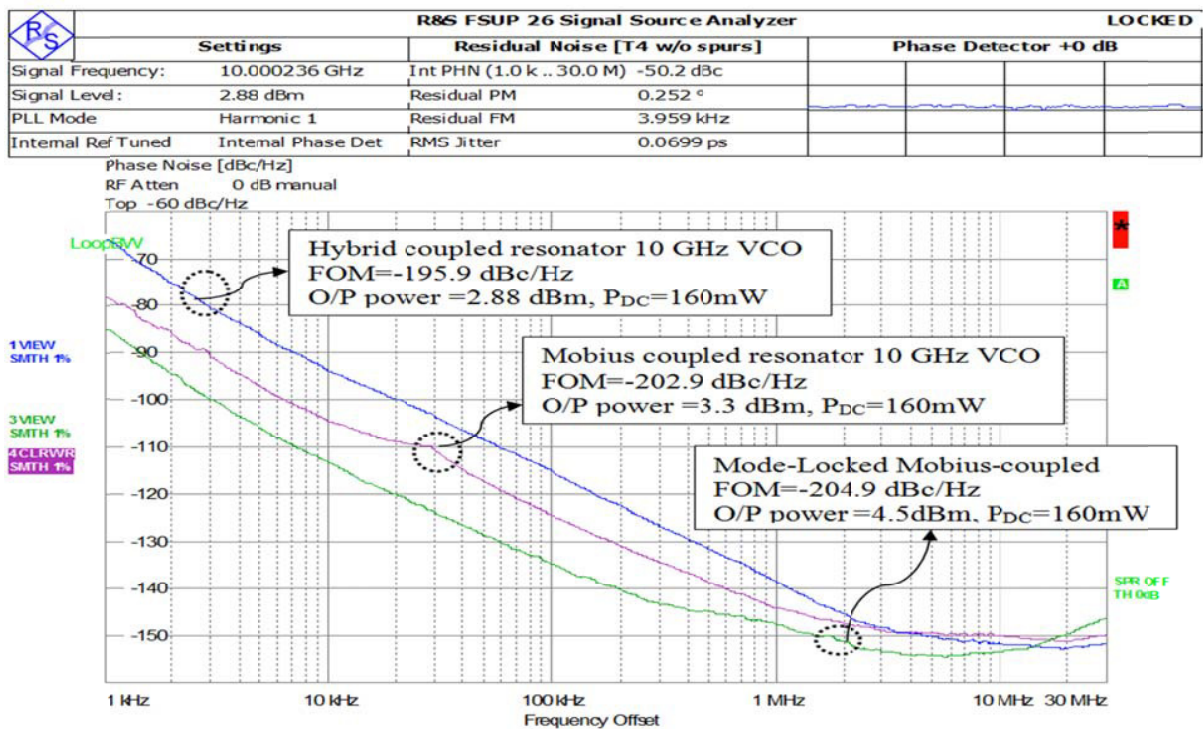
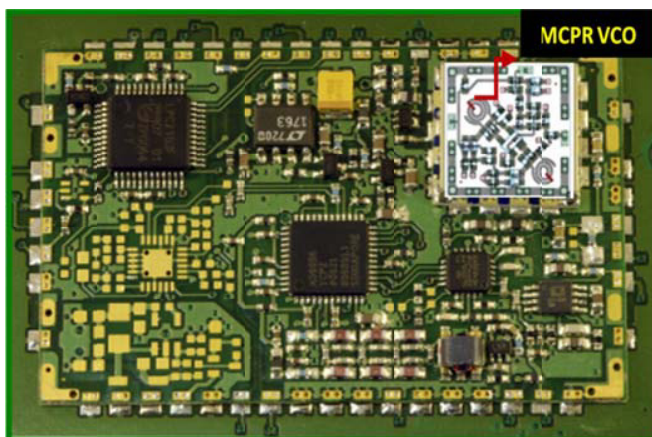


Figure 7-8: The measured phase noise plots of the 10GHz oscillators: Hybrid coupled resonator, Möbius coupled resonator, Mode-locked Möbius coupled resonator. FOM: defined in Ch-1, Eq. 1.1) is -195.9 dBc/Hz for hybrid coupled resonator, -202.9 dBc/Hz for Möbius coupled resonator, -204.9 dBc/Hz for Mode-locked Möbius coupled resonator network; with power consumption of 160mW ( $V_{cc}=5V$ ,  $I_c=32mA$ ).

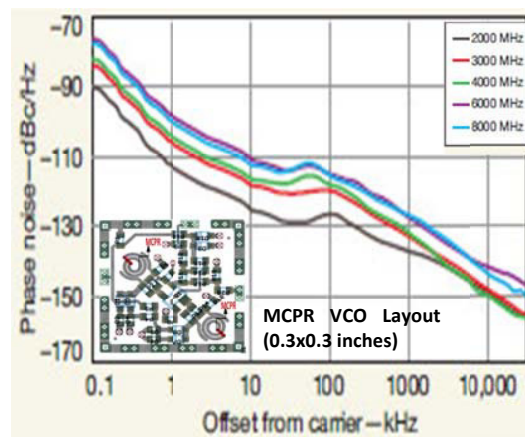
As shown in Figure 7-8, the measured figure of merit (FOM: defined in Ch-1, Eq 1.1) is -195.9 dBc/Hz for hybrid coupled resonator, -202.9 dBc/Hz for Möbius coupled resonator, -204.9 dBc/Hz for Mode-locked Möbius coupled resonator network; with power consumption of 160 mW ( $V_{cc}=5V$ ,  $I_c=32mA$ ). The DC-RF conversion efficiency is 1.2% for hybrid coupled resonator, 1.3% for Möbius coupled resonator, 1.7% for Mode-locked Möbius coupled resonator; with 160 mW ( $V_{cc}=5V$ ,  $I_c=32mA$ ).

### 7.3.1 Synthesized Frequency Sources using MCPR (Möbius Coupled Resonator) VCOs

Figure 7-9 (a) shows the layout of 2-8 GHz broadband synthesizer using wideband (2-10 GHz) tunable MCPR VCO (Layout of VCO is shown in Figure 7-9 b), offers a viable cost-effective solution for expensive YIG resonator oscillator with less susceptibility to thermal drift, vibrations, and microphonics. As shown in Figure 7-9(a), the synthesizer circuit draws typically 200 mA current from a 5-V supply, uses multi-band/multi-mode MCPR VCO (operating at 5V, 32mA) resulting in low-cost power-efficient configurable synthesizer. As shown in Figure 7-9, MCPR VCO is compact in 0.3x0.3x0.18 inches size, built on 22 mils substrate and dielectric constant of 2.2. Figure 7-9 (b) shows the typical measured phase noise plot of the mode stabilized synthesizer circuit as illustrated in Figure 7-9(a) using MCPR VCO. The measured phase noise is typically better than -108dBc/Hz @ 10 kHz offset for 2-8 GHz operations. The reported synthesizer module shown in Figure 7-9(a) offers wide bandwidths with excellent performance in terms of phase noise, harmonics ( $> -20dBc$ ), settling time (less than 1millisecond), and sideband spurious content (better than -60dBc), with low power consumption in compact size (1x1x0.2 inches) built on 22 mils substrate material with a dielectric constant of 2.2 for the validation of the new approach.



(a) Synthesizer Layout (1x1x 0.2 inches) using MCPR VCO



(b) The measured phase noise plot of synthesizer

Figure 7-9: Shows high performance wideband synthesized signal sources for modern communication systems: (a) PCB Layout of 2-8 GHz Configurable Synthesizer Module and (b) phase noise plot of synthesizer Figure 7-8(a)

The new approach to designing tunable oscillators with Möbius strips resonators yields compact VCOs with excellent phase-noise performance and in configurations that can be readily adapted to modern RF integrated circuit (RFIC) and MMIC semiconductor manufacturing processes. These compact tunable oscillators provide performance levels that are comparable to those of traditional DROs and YIG oscillators, but without the temperature sensitivity, large size, and high cost.

## 7.4 Möbius Coupled Resonator: Applications

The signal retention characteristics of Möbius coupled strip resonators are useful in radiofrequency and microwave applications, including radio astronomy, medical fields and software driven radios. Conventionally, high Q-factor cavity echo box is used in Radar testing to retain the input signals but this technique has bandwidth limitation [4]. Frequency Memory Loop (FML) technique is used in Military electronics for retention of signals, this is an expensive solution with considerable digital signal

processing and invariably noisy and bandwidth limited [11]. The novel Möbius strip configuration (back-to-back coplanar waveguide) reported here shows how the characteristic is non-resonant unlike open or shorted transmission lines, which has ability to store broadband frequencies in compact size. In this section, a typical back-to-back coplanar waveguide (CPW) in the form of Möbius strip was constructed which resulted in an infinite transmission line capable of retaining a large bandwidth of frequencies that can be useful for real time signal retention device (RTRD) [14]. By providing Möbius twist to CPW, a continuous phase change reported instead of abrupt phase change by using shorting pins between two parallel transmission lines. It is observed that the device retains the injected signal in time domain over a broad band of frequencies. The signal can also be a pulsed signal as in Ultra Wide Band (UWB), or a modulated microwave signal, and can retain transient signals encountered in Radio Astronomy, Medical applications and many more exciting applications.

#### 7.4.1 Möbius Resonator Strips for (Real Time Signal Retention Device) RTRD Applications

To construct a Möbius strip, two back-to-back coplanar waveguides (CPW) with ground plane is used. Figure (7-10) shows the typical cross-section of the transmission line using two back-to-back coplanar waveguides with 50-Ohm impedances. The low loss Taconic TLY5® substrate with thickness of 0.25 mm and dielectric constant of 2.2 is used for fabrication. As shown in Figure 7-10, the partition ground planes provide the separation between back-to-back CPW to decouple the top and bottom CPWs. These back-to-back CPWs were joined together and then twisted to form a Möbius strip to close the CPWs on itself to obtain the infinite transmission line.

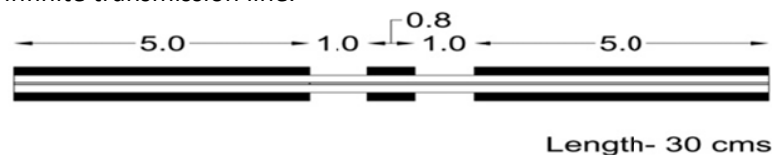


Figure 7-10: A typical cross section view of back-to-back CPW [14]

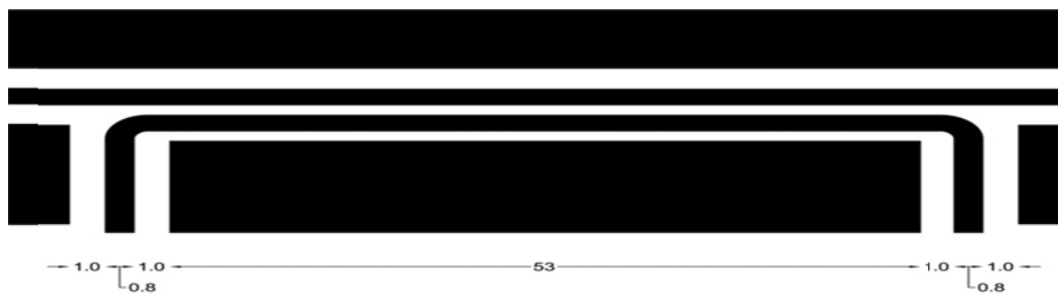


Figure 7-11: A typical layout of the Directional Coupler [14]

To inject signal into the Möbius strip, a directional coupler designed at 4 GHz was incorporated in one of the CPWs. The coupling coefficient of 10 dB was chosen to provide loose coupling to the main loop (Figure 7-11). The length of the loop was chosen as 30 cm, which corresponds approximately to one wavelength at 1000 MHz. The main function of the partition ground planes is to decouple the top and bottom CPW and it was decided that the continuity of this ground plane is not considered important. Experimental verification also confirmed this assumption. No ground-plane strapping was used to prevent any unbalanced ground loop current flow. Thus, the Möbius Twist provides a single surface for signal propagation and the central conductor provides a continuous loop along with the ground plane.

An edge coupled directional coupler at 4 GHz was designed and incorporated in one of the CPW's, the top layer as shown in Figure 7-10. SMA connectors were used at ports of the directional coupler for coupling and decoupling the signal from the device. The photograph of the finished Möbius device with the 10dB coupler is shown in Figure 7-12.



Figure 7-12: A prototype of CPW Möbius device with SMA connectors [19]

As shown in Figure 7-12, the two CPWs with ground planes are bonded back to back. The top CPW is called CPW-1 and the bottom is called CPW-2. These are then twisted and the ends are brought together manually. The CPW-2 now comes in the same plane as CPW-1. The ground planes and the center conductors of both CPWs are strap soldered to complete the Möbius configuration. The launching of the signal was done using two SMA connectors soldered to the ports of the coupler. Agilent Field Fox RF Analyzer N9912 (Figure 7-13) was used to test the proof of concept [17]-[18].



Figure 7-13: Agilent Analyzer N9912 with the device connected. The return loss test shows  $S_{11}$  parameter on Smith Chart from 2 MHz to 6 GHz. The display indicates the broadband coupling of signal into the device [19].

This instrument has a single port S-parameter testing capability (VNA) along with Cable Testing facility; in addition, it contains a Spectrum Analyzer up to 6 GHz. The Test setup is as shown in Figure 7-13. First, the return loss was tested from 2 GHz to 6 GHz with one of the ports terminated with 50 ohms. It was observed that the device has a return loss between 6 dB and 20 dB over the frequency range. This indicates that the device is exhibiting broadband behavior and the signal is being coupled to it. In other words, the continuous central conductor is getting excited over a broad band of frequencies.

Figure 7-14 shows the polar plot of S-parameter ( $S_{11}$ ) from 2MHz to 6 GHz but useful information lies in the range from 2 to 6 GHz. Figure 7-15 shows the return loss in rectangular coordinate from 2 GHz to 6 GHz, which is typically 10dB. The Smith Chart display shows the excitation of the signal to the continuous center conductor of the device over a bandwidth of 4 GHz. In this way, the device exhibits an infinite transmission line. The return loss response of more than 10 dB indicates that the energy is efficiently coupled to the device over a bandwidth of 4 GHz. The Vector Network Analyzer (VNA) was

switched to Cable and Antenna Testing Mode to check the delay response in real time. In this way, the retention of the signal can be tested. The instrument converts the measured frequency response into time domain response by performing Inverse Fast Fourier Transform (IFFT).

The results are shown in Figure 7-15, the plot is taken from 2 to 6 GHz. As expected, there is a gradual decay of the signal after every transit around the loop. Thus testing of the device has confirmed the retention of the signal in real time over broadband of microwave frequencies. The total span time is around 200 milliseconds. The physical length of the loop is 30 cm. The markers as indicated are at 0.72m, 0.89m, 0.98m, 1.05m, 1.13m and 1.46 m. This clearly indicates multiple transit of the signal around the loop. It also shows the broadband retention characteristics since it is derived from the frequency response of the device.

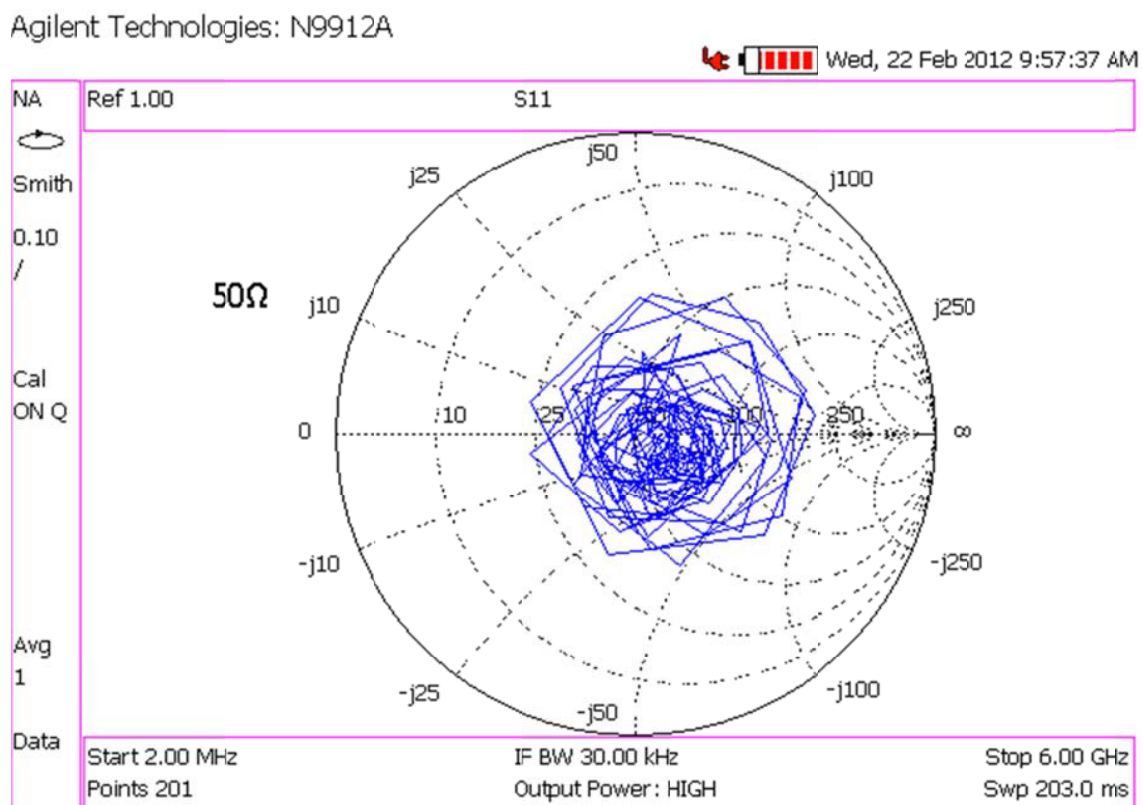


Figure 7-14: The measured  $S_{11}$  plot shown on Smith Chart, display from 2 MHz to 6 GHz [19]

The signal travels twice around the loop before arriving the feeding point, the first signal is at twice the length of the loop, which is at 72 cm. The decay of the signal over the time indicates the coupling of the power at the output port along with the losses, considering the radiation losses are minimal. This behavior calls for extensive mathematical modeling of the device. The unusual behavior could be due to the magnetic field coupling between the top and bottom layers. This will result in a distributed mutual inductance between the layers. This characteristic is similar to non-inductive resistor design [9].

The Transmission characteristics  $S_{21}$  measured at the output port indicates the coupling of the signal to the load (Figure 7-16). The frequency response of the device calls for rigorous three-dimensional mathematical modeling and analysis using Maxwell's equations and shall lead to considerable research in the field of signal retention. Möbius co-planar structure proposed in Figure 7-12 for signal retention is analogue by nature and is an economical solution for signal retention [14].

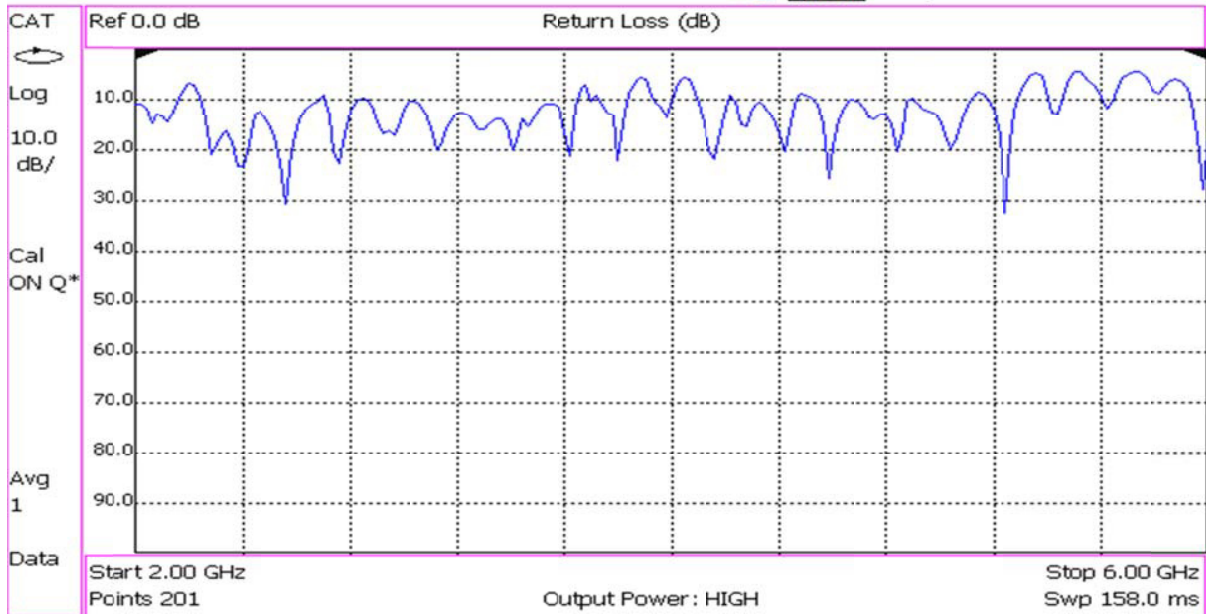


Figure 7-15: The measured return Loss display in rectangular coordinates [19]

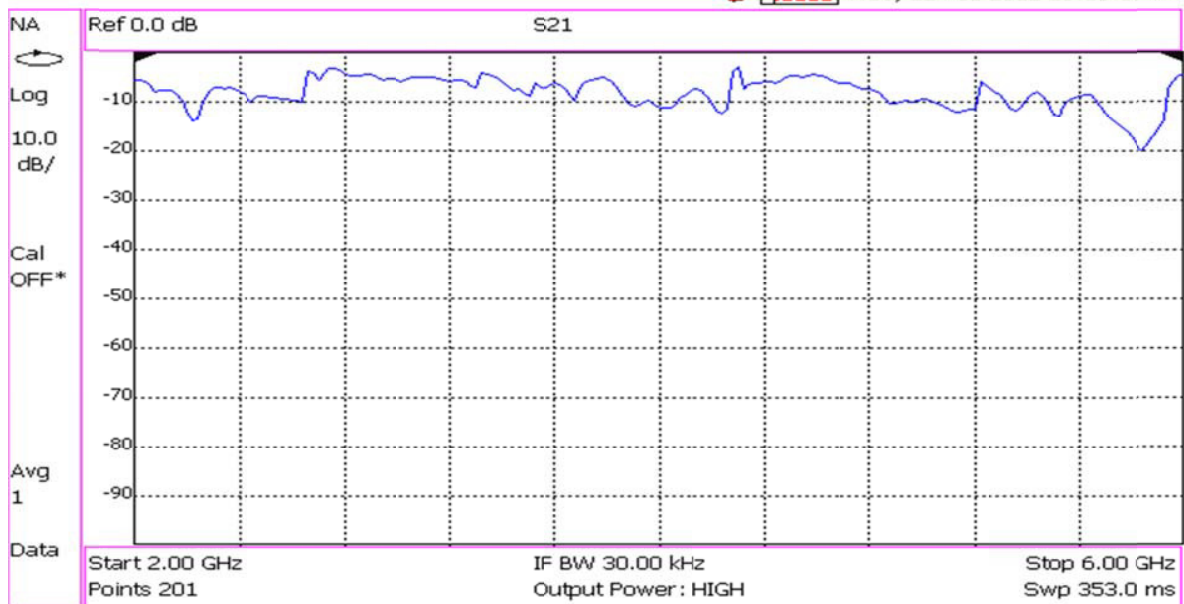


Figure 7-16: The measured transmission Characteristics (S<sub>21</sub>) of the device [19]

By providing Möbius twist to CPW as shown in Figure 7-12, a continuous phase change was reported instead of abrupt phase change by using shorting pins between two parallel transmission lines. The true Möbius strip is being created, and can achieve a gradual transition resulting in the wide band behavior of the device. It is observed that the device retains the injected signal in time domain over a broad band of frequencies. The signal can also be a pulsed signal as in Ultra Wide Band (UWB), or a modulated microwave signal. It can retain transient signals encountered in Radio Astronomy, Medical applications

and many other such applications. The device is truly an analog device, can improve the performance of Analog to Digital Converter (ADC). One can use a lower speed Digital Signal Processing (DSP) since one has the same signal available for a considerable duration of time in a repetitive manner. It is also feasible to fabricate the device using rapid proto-typing MEMS applications. This will open out many more exciting millimeter wave applications such as microwave sensors for remote sensing and detection of hidden objects, to find concealed arsenal or explosive and hazardous chemical which is of importance in our world of a growing threat.

#### **7.4.2 Möbius Coupled Resonator Strips: Discussion**

- I. GCPW- The transmission line we have used to construct the Möbius strip is CPW with ground plane, so technically the term GCPW can be used. The central partition plane acts more as a separation between top and bottom layer to prevent coupling. The spacing between the central conductor and ground plane on the coplanar side is much smaller than the thickness of the substrate leading to maximum field confinement on the surface.
- II. Higher order modes at interface: There exists a discontinuity in the partition ground planes. This characteristic is taken into account for futuristic study while developing the mathematical model for the infinite strip. Ground looping was avoided to realize the infinite transmission line at the cost of generation of higher order modes.
- III. Abnormal behavior: Unlike any resonant structure the return loss was observed to be around the center of the Smith Chart (Figure 7-6), which is non resonant behavior from 2MHz to 6 GHz. Based on our observation, any loop was exhibiting resonant nature and the response was touching the outer edge of the Smith Chart, in other words the input impedance moved from short to open.
- IV. The return loss in rectangular coordinates indicates an average of 8-10dB over the frequency sweep from 2 GHz to 6 GHz (Figure 7-6). The future research effort is to improve the return loss for good figure of merit (FOM).
- V. Testing of Loop, A CPW guide with Quadrature coupler was made into a simple loop and tested for performance. The purpose of this was to isolate the effect of the twist. It is found that the loop behaves like a resonant circuit with multiple frequencies and  $S_{11}$  touched the 0dBm axis.
- VI. To verify the effect of SRD- performance one more assembly was made with 45 cm length. A quadrature coupler designed at 4 GHz was used for coupling the power. The performance was similar to 30 cm SRD with edge-coupled input.
- VII. Video recording: The Yagi antenna was connected to the spectrum analyzer with and without the Signal retention Device. This is to check whether the device retains pulsed RF waveforms. A cell phone was kept nearby and the filming was done using a digital camera. The uplink from the cell phone is a burst signal. There is a repetitive appearance of the signal on activating the cell phone when the device was connected indicating the retention of burst signal.

#### **7.5 Conclusion**

The signal retention device developed here has the ability to store a very broad band of frequencies. It also has the ability to store a transient signal for delayed analysis. This property of the device is extremely useful in many applications including radio astronomy, medical fields and software driven radios, real time retention of signals for signal processing, and Frequency Memory Loop in Electronic Warfare (EW). This device will be less 'noisy' compared to commercially available digital storage devices; can be very useful in Software Driven Radios (SDR) and other applications.

## Chapter 8

### Printed Coupled Metamaterial Resonator Based Frequency Sources

#### 8.1 Metamaterial

Metamaterials are engineered periodic composites that have negative refractive-index characteristic not available in natural materials [1]. In 1968, Veselago reported artificial composite Left handed material (LHM), which exhibits simultaneously negative values of the electric permittivity ( $\epsilon < 0$ ) and the magnetic permeability ( $\mu < 0$ ), characterized as [2]:

- (i) Simultaneous negative permittivity ( $-\epsilon$ ) and permeability ( $-\mu$ )
- (ii) Reversal of Snell's Law (negative index of refraction), Reverse Doppler effect, and Reverse Vavilov-Cerenkov effect, Diffraction-limit breaking imaging
- (iii) Electric field, Magnetic field, and wave-vector of electromagnetic wave in a LHM form a left-handed triad
- (iv) LHMs support backward wave propagation: anti-parallel group and phase velocity
- (v) Artificial homogenous structure

The characteristics of the artificial composite metamaterial depend on the properties of the host materials, embedded material, volume of the fraction, operating frequency, and the morphology of the composite material such as the dimensions and shapes of the host structure and the guest structure [3]-[5]. Thus, when other variables are known, the important parameter is to control the dynamics of the morphology of the embedded structure that allows control over a change of the properties (permittivity, permeability and the refractive index) in the desired frequency range. In general, the refractive index of the medium, characterized by four possible sign combinations in the pair ( $\mu\epsilon$ ) [6]-[27]:

$$n = \sqrt{(+\epsilon)(+\mu)} = +\sqrt{\mu\epsilon} \rightarrow \text{(DPS-double positive material)} \quad (8.1)$$

$$n = \sqrt{(-\epsilon)(+\mu)} = j\sqrt{\mu\epsilon} \rightarrow \text{(ENG-epsilon negative material)} \quad (8.2)$$

$$n = \sqrt{(-\epsilon)(-\mu)} = -\sqrt{\mu\epsilon} \rightarrow \text{(DNG-double negative material)} \quad (8.3)$$

$$n = \sqrt{(+\epsilon)(-\mu)} = j\sqrt{\mu\epsilon} \rightarrow \text{(MNG-mu negative material)} \quad (8.4)$$

From (8.3), double negative (DNG) material is nomenclatured as metamaterial, which is broadly defined as Left-handed (LH) material with artificial homogeneous structures related to negative refractive index as

$$n = -\sqrt{\mu\epsilon} = -\sqrt{\mu_0\mu_r\epsilon_0\epsilon_r} \quad (8.5)$$

where  $\epsilon_0$  is  $8.85 \times 10^{-12}$  and  $\mu_0 = 4\pi \times 10^{-7}$ ,  $n$  is refractive index of the medium. From (8.1)-(8.4), there are four possible classes of materials, as illustrated in Figure 8-1 [28]:

- (i) DPS ( $\epsilon > 0$  and  $\mu > 0$ ): These are conventional materials, also named as double positive materials (DPS) or right handed materials (RHM) and dielectrics are its examples. The propagation of electromagnetic waves is possible in such materials.
- (ii) ENG ( $\epsilon < 0$  and  $\mu > 0$ ): These are epsilon-negative materials (ENG), having characteristic of negative value of permittivity, normally shown by many types of plasma in a particular frequency region. Metals like Gold, Silver etc., demonstrate this negative permittivity in the infrared and



visible frequency domains. The propagation of electromagnetic waves is not possible in ENG materials.

- (iii) MNG ( $\epsilon > 0$  and  $\mu < 0$ ): These materials are named as mu-negative materials (MNG), having characteristic of negative value of permeability, shown by Gyrotropic materials in certain frequency bands. The propagation of electromagnetic waves is not possible in such materials.
- (iv) DNG ( $\epsilon < 0$  and  $\mu < 0$ ): These materials are named as double negative materials (DNG) or Left-handed materials (LHM). These materials do not exist in nature but are physically realizable by making composite structures. The propagation of electromagnetic waves is possible in such material.

From (8.5) the negative refractive index referred to as left-handed (LH) material is characterized as anti-parallel phase and group velocity material that exhibits unusual properties. It can allow an electromagnetic wave to convey energy and group velocity in the opposite direction to its phase velocity, causing strong localization and enhancement of fields, thereby significant enhancement in the slew rate and group velocity of resonator resulting lower phase noise for oscillator applications [7].

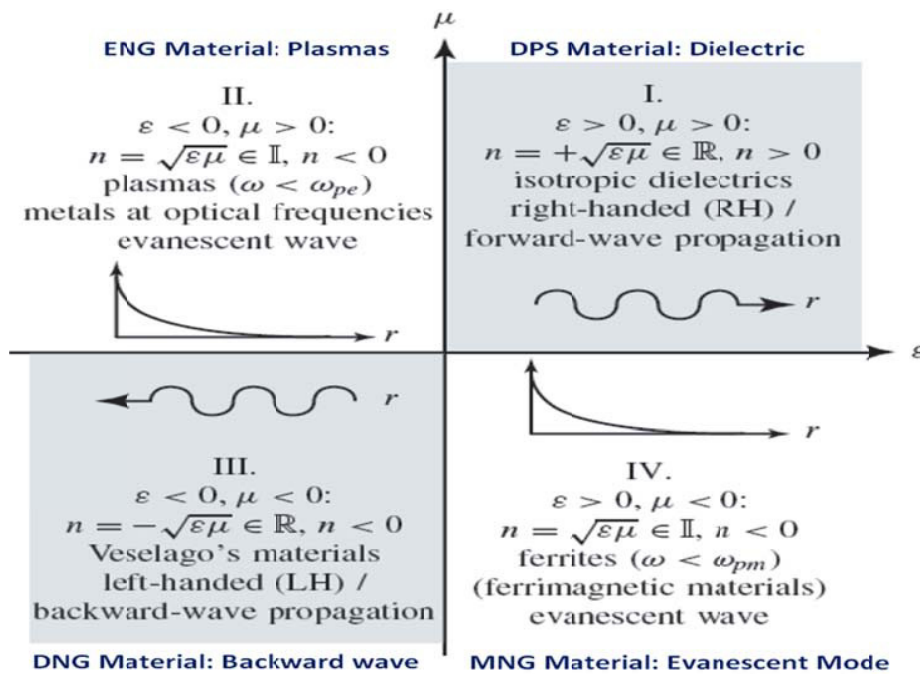


Figure 8-1 Permittivity-Permeability Diagram,  $R$  and  $I$  represents Real and Imaginary terms;  $\omega_{pe}$  and  $\omega_{pm}$  are the electric and magnetic plasma frequencies respectively [28].

These unusual characteristics of metamaterial open new degrees of freedom in resonator design for high frequency oscillator, filter, phase-shifter, antenna and other microwave applications in compact size. The artificial metamaterial components (negative value of permittivity and permeability) have been demonstrated over a large portion of the electromagnetic spectrum, from visible to radiofrequency [12]. The sign (positive or negative values) of permittivity and permeability is not restricted by any physical law, and can be positive or negative. In natural materials, negative permeability can occur during resonant condition [13]. The real part of permeability may take negative values near a resonance of sufficient strength, as for example in ferrites near the ferromagnetic resonance frequency. For artificial materials, manipulation of a negative permeability response can be realized using electrically small resonant metal inclusions of special shapes, e.g. split rings. Among metamaterial components, a split-ring resonator (SRR) is used for microwave oscillator circuits and planar microwave devices [12]-[14].

## 8.2 The Electromagnetic Wave Propagation Dynamics of Metamaterial

The Maxwell's equations can be given by [15]

$$\nabla \times \vec{E} = -\frac{\partial \vec{B}}{\partial t} - \vec{M}_s \quad (\text{Faraday's Law}) \quad (8.6)$$

$$\nabla \times \vec{H} = \vec{J} + \frac{\partial \vec{D}}{\partial t} \quad (\text{Ampere's Law}) \quad (8.7)$$

$$\nabla \cdot \vec{D} = \rho_v \quad (\text{Electric Gauss's Law}) \quad (8.8)$$

$$\nabla \cdot \vec{B} = \rho_m \quad (\text{Magnetic Gauss's Law}) \quad (8.9)$$

$$\text{Where} \quad \vec{B} = \mu \vec{H} = \mu_0 \mu_r \vec{H} \quad (8.10)$$

$$\vec{D} = \epsilon \vec{E} = \epsilon_0 \epsilon_r \vec{E} \quad (8.11)$$

$$\epsilon_r = \epsilon' - j\epsilon'' = \epsilon' [1 - j \tan(\delta_e)], \quad \tan(\delta_e) = \frac{\omega \epsilon'' + \sigma_e}{\omega \epsilon'} \quad (8.12)$$

$$\mu_r = \mu' - j\mu'' = \mu' (\delta_m), \quad \tan(\delta_m) = \frac{\omega \mu'' + \sigma_m}{\omega \mu'} \quad (8.13)$$

where  $\vec{E}$  (V/m) is the electric field intensity,  $\vec{H}$  (A/m) is the magnetic field intensity,  $\vec{D}$  (Coulomb/m<sup>2</sup>) is the electric flux density,  $\vec{B}$  (Wb/m<sup>2</sup>) is the magnetic flux density,  $\vec{M}_s$  (A/m) is the fictitious magnetic current density,  $\vec{J}$  (A/m<sup>2</sup>) is the electric current density,  $\rho_v$  (Coulomb/m<sup>3</sup>) is the electric charge density,  $\rho_m$  (Coulomb/m<sup>3</sup>) is the magnetic charge density,  $\epsilon_0$  is  $8.85 \times 10^{-12}$ ,  $\mu_0 = 4\pi \times 10^{-7}$ ,  $\epsilon_r$  is the relative permittivity, and  $\mu_r$  is the relative permeability of the medium.

From (8.6)-(8.7), conventional medium follows right hand rule, which means the electric field intensity vector  $\vec{E}$ , magnetic field intensity  $\vec{H}$  and Poynting vector  $\vec{k}$  inside medium form right handed triplet. The plane wave propagation along +z direction can be described by Helmholtz Equations [16]:

$$\nabla^2 \vec{E} + k^2 \vec{E} = 0 \quad (\text{Vector wave equation-Helmholtz Equations}) \quad (8.14)$$

$$\frac{d^2 E_x}{dz^2} + k^2 E_x = 0 \quad (\text{Simplified scalar wave equation-Helmholtz Equations}) \quad (8.15)$$

$$\vec{E}(z, t) = \hat{a}_x E_0^+ \cos(\omega t - kz) \quad (\text{Traveling wave E-field solution in time-domain}) \quad (8.16)$$

$$\vec{H}(z, t) = \hat{a}_y \frac{E_0^+}{\eta} \cos(\omega t - kz) \quad (\text{Traveling wave H-field solution in time-domain}) \quad (8.17)$$

$$\eta = \frac{|\vec{E}|}{|\vec{H}|} \quad (\text{Wave impedance}) \quad (8.18)$$

For right-handed material ( $\mu, \epsilon > 0$ ), triad  $[\vec{E}, \vec{H}, \vec{k}]$  can be illustrated by [28]

$$\vec{k} \times \vec{E} = +\omega \mu \vec{H} \quad (8.19)$$

$$\vec{k} \times \vec{H} = -\omega \epsilon \vec{E} \quad (8.20)$$

For left-handed material ( $\mu, \epsilon < 0$ ), triad  $[\vec{E}, \vec{H}, \vec{k}]$  can be illustrated by [28]

$$\vec{k} \times \vec{E} = -\omega |\mu| \vec{H} \quad (8.21)$$

$$\vec{k} \times \vec{H} = +\omega |\epsilon| \vec{E} \quad (8.22)$$

Assuming the frequency is positive quantity, the phase velocity is given by

$$\vec{v}_p = \frac{\omega}{k} \hat{k}, \text{ where } (\hat{k} = \bar{k}/|k|) \quad (8.23)$$

$$\text{LH Medium: } k < 0 (v_p < 0) \quad (8.24)$$

$$\text{RH Medium: } k > 0 (v_p > 0) \quad (8.25)$$

$$\bar{k} \times \bar{E} = s\omega|\mu|\bar{H} \quad (8.26)$$

$$\bar{k} \times \bar{H} = -s\omega|\epsilon|\bar{E} \quad (8.27)$$

$$\bar{k} = \begin{pmatrix} +1, & \text{RH} \\ -1, & \text{LH} \end{pmatrix} \quad (8.28)$$

$$\bar{E}, \bar{H} \approx e^{+j(\omega t + |n|k_0 r)} \quad (8.29)$$

$$U_n = \frac{1}{4} \{ \epsilon |E|^2 + \mu |H|^2 \} \quad (U_n: \text{Energy}) \quad (8.30)$$

where  $k = \frac{\omega}{u_p}$  (wave number or phase constant),  $v_p = \frac{1}{\sqrt{\mu \epsilon}}$  (Phase velocity),  $k = \frac{2\pi}{\lambda}$  (phase

constant in terms of wavelength). Figure 8-2 (a) illustrates the plane wave propagation characteristics in right-handed and left-handed orthogonal coordinate system. From (8.19)-(8.20),  $[\bar{E}, \bar{H}, \bar{k}]$  form a right-handed orthogonal coordinate system for positive values of  $\epsilon$  and  $\mu$ , whereas from (8.21)-(8.22),  $[\bar{E}, \bar{H}, \bar{k}]$  form a left-handed orthogonal coordinate system for negative values of  $\epsilon$  and  $\mu$  [17, 28, and 144].

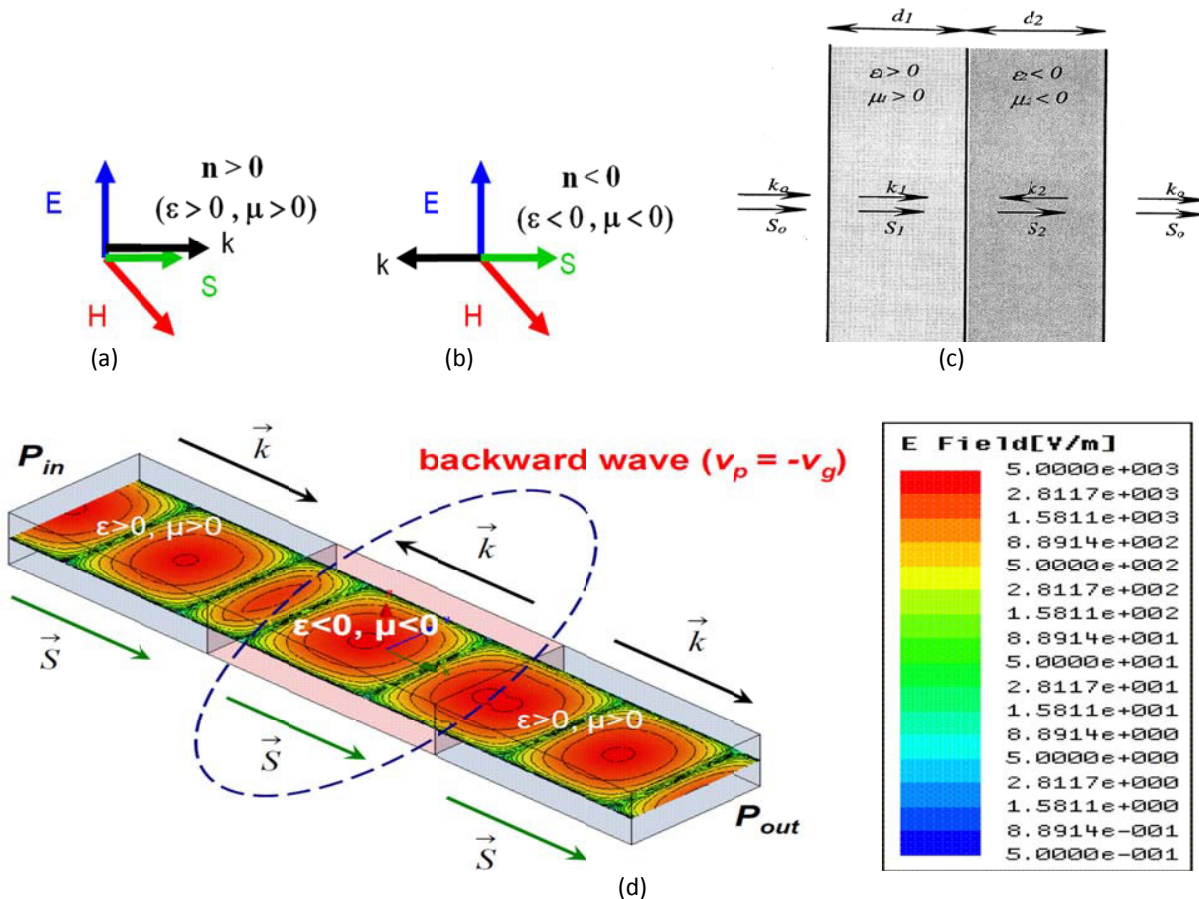


Figure 8-2: (a) Right-handed orthogonal coordinate system for materials with positive  $\epsilon$  and  $\mu$ , (b) left-handed orthogonal coordinate system for materials with negative  $\epsilon$  and  $\mu$ , (b) depicts the 2-layer structure (left layer is a DPS material and right layer is a DNG material), and (c) CAD HFSS simulation shows the plane wave propagation dynamics using effective medium [28, 144]

Figure 8-2 (b) depicts the 2-layer structure (left layer is a DPS material and right layer is a DNG material), the direction of Poynting vector  $\vec{S}$  is parallel with the direction of phase velocity or wave vector  $\vec{k}$  in DPS material but these two directions are anti-parallel in DNG material (right layer). Figure 8-2 (c) exhibits HFSS simulation showing the plane wave propagation using effective medium [28].

From (8.24) in LH (left-handed) medium phase velocity  $v_p$  propagates backward to the source in the opposite direction to that of power, related to group velocity  $v_g$  (Figure 8-2(c)). The backward propagation implies that the fields have time-space dependence. Backward-wave media are media in which the energy velocity direction is opposite to the phase velocity direction (or, the scalar product between the corresponding vectors is negative). In particular, this takes place in isotropic materials with negative permittivity and permeability (double negative media). Negative refraction takes place on interfaces between 'usual' materials and backward-wave media. Surface waves (waves propagating along a surface but exponentially decaying in the directions orthogonal to the surface) can exist on interfaces between media having material parameters of the opposite sign. The anomalous refraction at the boundary of such media and the fact that for plane wave the direction of the Poynting vector is anti-parallel with the direction of phase velocity can be advantageous in designing compact high quality factor resonator circuit. From (8.16) - (8.17), the power flow as shown in Figure 8-2 (c) is given by Poynting theorem as [29]

$$\oint_S (\vec{E} \times \vec{H}) \cdot d\vec{s} = -\frac{\partial}{\partial t} \int \left( \frac{1}{2} \epsilon E^2 + \frac{1}{2} \mu H^2 \right) dv - \int \sigma E^2 dv \quad (8.31)$$

$$\oint_S (\vec{E} \times \vec{H}) \cdot d\vec{s} = \oint_S \vec{S} \cdot d\vec{s} \quad (8.32)$$

where  $\vec{S} = (\vec{E} \times \vec{H})$  is the Poynting vector.

From (8.31)-(8.32), the propagation of energy will take place at the direction extracted from Poynting vector. The direction of Poynting vector is same for both LHM and RHM, always calculated as a right-hand-triplet from the electric and magnetic field. From (8.32), average Power density transmitted by a uniform plane wave in z direction is given as [30]-[36]:

$$\vec{S}_{av}(z) = \hat{a}_z \frac{E_0^2}{2 |\eta_c|} e^{-2\alpha z} \cos \theta_\eta \quad (\text{Lossy medium}) \quad (8.33)$$

$$\vec{S}_{av}(z) = \hat{a}_z \frac{E_0^2}{2\eta} \quad (\text{Lossless medium}) \quad (8.34)$$

$$\vec{S}_{av} = \frac{1}{2} R_e (\vec{E} \times \vec{H}^*) \quad (\text{Phasor form}) \quad (8.35)$$

The realization of true DNG material (metamaterial) is questionable! In general, it is difficult to build a material or medium simultaneously with negative permittivity and negative permeability for a broad operating frequency ranges from a set of arbitrary passive structure unit cells arranged in predefined order. This may lead to violation of energy conservation principle at the intersecting plane between a RHM (right-handed material) and LHM (left-handed material) media because of the generation of energy. However, an attempt to build the DNG material or medium based on the fact that for a specific orientation and arrangement of the passive structure, the values of permittivity and permeability reduces as the frequency increases till these material or medium initiate demonstrating negative permittivity and permeability at specific narrowband frequencies and lacks the validity for broadband operation. It is however, easy to demonstrate independently MNG (negative permeability) or ENG (negative permittivity) characteristics but achieving negative regime for permittivity and negative permeability could be challenging task and need complex and active structure to support the evidence of DNG material for broadband operation. For clear understanding, Figure 8-3 exhibits the electromagnetic wave propagation in different media [16].

### 8.2.1 Backward Wave Propagation Dynamics in Left-Handed Material

A typical material which has both negative permittivity and permeability nomenclatured as left-handed (LH) where the electric field intensity vector  $\vec{E}$ , and the magnetic field intensity  $\vec{H}$  vector forms a left-handed triplet (Figure 8-2b). From (8.24), backward wave implies that the phase traveling direction is toward source instead of away from source after electromagnetic wave enters the Metamaterial (Figure 8-3).

From (8.32) and (8.35), the energy flowing direction is always away from source irrespective of type of the medium the wave is traveling as shown in Figures 8-2 and 8-3, the main difference is which side of normal face the energy will be flowing to [21]. This property of negative phase advance in LH material exhibits the properties well suited for perfect lenses or super lenses [25].

If the electromagnetic wave propagation is in the z-axis, in order to transmit all the energy through the DNG material slab it is required that we have a propagation constant  $k'_z$  [26]:

$$k'_z = -\sqrt{\frac{\omega^2}{c^2} - (k_x^2 + k_y^2)} \quad (8.36)$$

The overall transmission coefficient for the wave entering into DNG slab ( $\epsilon=-1$  and  $\mu=-1$ ) as shown in Figure 8-4 is given by [26]

$$T = tt' = e^{-j\left[\sqrt{\frac{\omega^2}{c^2} - (k_x^2 + k_y^2)}\right]d} \quad (8.37)$$

$$T = e^{j(k'_z d)} \quad (8.38)$$

where  $t$  and  $t'$  are the transmission coefficient of DPS and DNG medium, and  $d$  is the distance the wave travels inside the DNG (Metamaterial slab).

The choice of the propagation constant  $k'_z$  is made in order to maintain causality and the required phase correction grants the DNG material capability of refocusing the image by canceling the phase of the transmitted wave as it propagates from its source [1]. This is an interesting phenomenon, which can be useful towards improving the phase-dispersion and group delay in resonator for oscillators and filters applications.

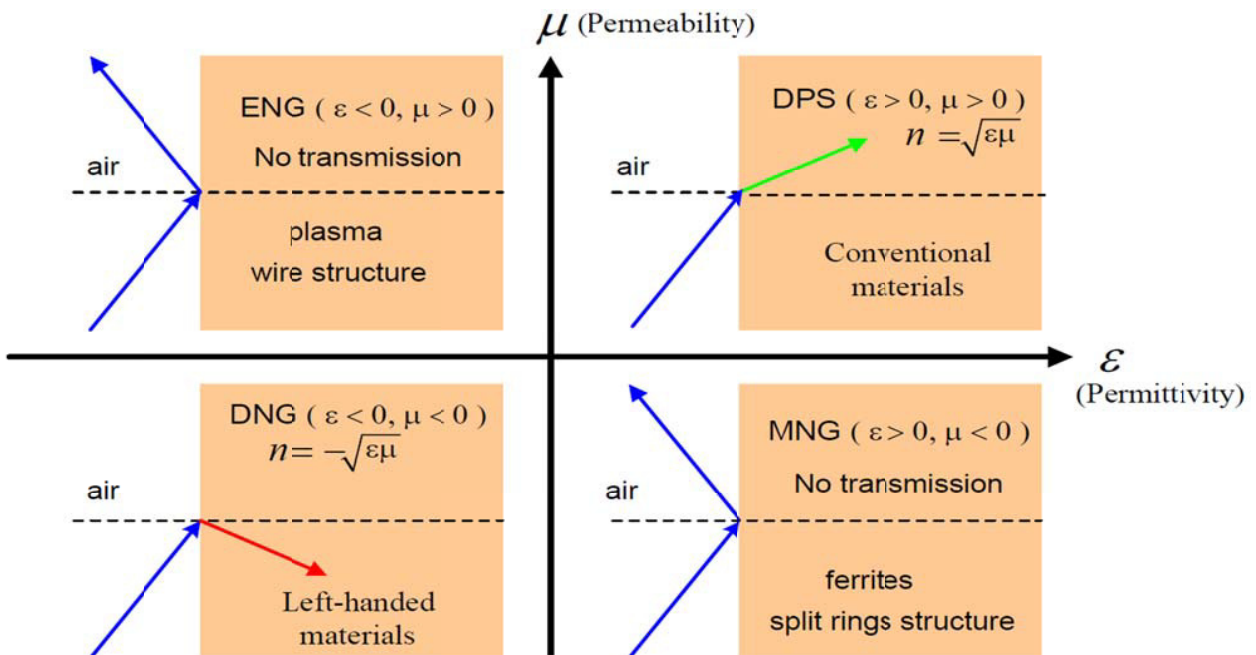


Figure 8-3: shows the electromagnetic wave propagation in different media [16]

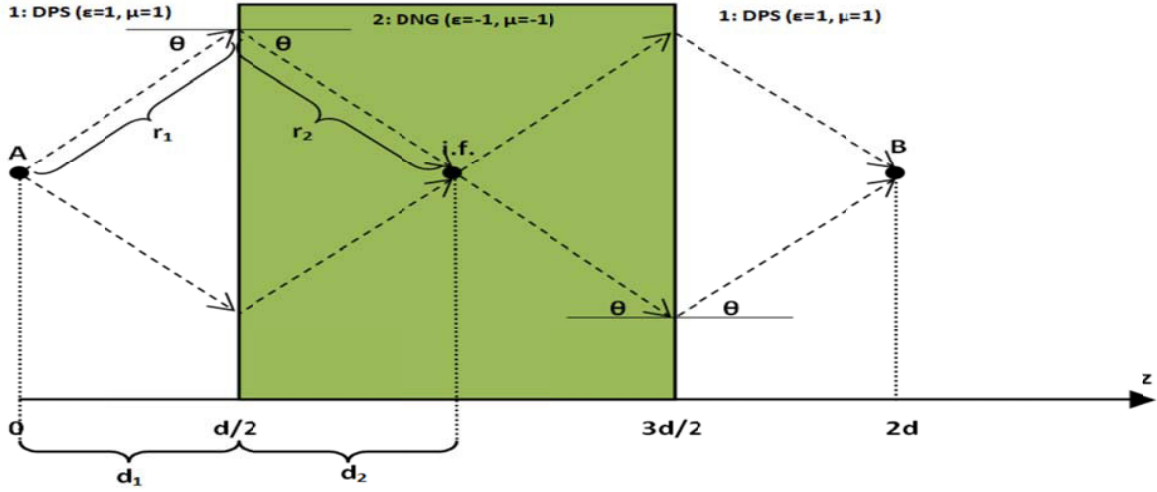


Figure 8-4: shows the wave propagation from free space (DPS) into Metamaterial slab (DNG medium) [26]

### 8.2.2 Evanescent Wave Propagation Dynamics

Considering the field expression for TE wave propagation in vacuum (medium 1) is [26]

$$\overline{E}_1 = e^{j(\bar{z}k_z + \bar{x}k_x - \omega t)} \quad (8.39)$$

$$\text{where } k_z \text{ is a propagation constant, } k_z = j\sqrt{(k_x^2 + k_y^2) - \frac{\omega^2}{c^2}} \quad \text{with } \frac{\omega^2}{c^2} < (k_x^2 + k_y^2) \quad (8.40)$$

In order to maintain the causality the field must decay as it goes away from the interface; the transmitted ( $\overline{E}_{t2}$ ) and reflected field ( $\overline{E}_{r1}$ ) can be described by

$$\overline{E}_{t2} = T e^{j(\bar{z}k'_z + \bar{x}k_x - \omega t)} \quad (8.41)$$

$$\overline{E}_{r1} = R e^{j(-\bar{z}k'_z + \bar{x}k_x - \omega t)} \quad (8.42)$$

$$\text{Where } [k'_z]_{(k_x^2 + k_y^2) > \epsilon_2 \mu_2 \frac{\omega^2}{c^2}} = j\sqrt{(k_x^2 + k_y^2) - \epsilon_2 \mu_2 \frac{\omega^2}{c^2}} \quad (8.43)$$

where  $\epsilon_2$  and  $\mu_2$  are the permittivity and permeability of the medium 2 (slab) and  $\frac{\omega^2}{c^2} < \frac{(k_x^2 + k_y^2)}{\epsilon_2 \mu_2}$ . The transmission, T, and reflection coefficients, R, can be derived by matching the electromagnetic wave fields at the interface from medium # 1 and medium #2 [26]:

$$T = \frac{2\mu k_z}{\mu k_z + k'_z} \quad (8.44)$$

$$R = \frac{\mu k_z - k'_z}{\mu k_z + k'_z} \quad (8.45)$$

The transmission, T', and reflection coefficients, R', of the transition from slab (inside medium # 2) to medium # 1 is given by

$$T' = \frac{2k'_z}{\mu k_z + k'_z} \quad (8.46)$$

$$R' = \frac{k'_z - \mu k_z}{k'_z + \mu k_z} \quad (8.47)$$

The expression of the wave transmission coefficient ( $T_e$ ) through both the interfaces can be derived by adding the multiple scattering dynamics, described by

$$T_e = \frac{\overline{E}_{transmitted}}{\overline{E}_{incident}} \quad (8.48)$$

$$T_e = TT'e^{j(k'_z d)} + TT'R^2 e^{j(3k'_z d)} + TT'R^3 e^{j(5k'_z d)} + TT'R^4 e^{j(7k'_z d)} + (\dots) \quad (8.48a)$$

$$T_e = \frac{TT'e^{j(k'_z d)}}{1-R^2 e^{j(2k'_z d)}} \quad (8.49)$$

For metamaterial (DNG medium),  $\epsilon=-1$  and  $\mu=-1$

$$[T_e]_{\epsilon \rightarrow -1, \mu \rightarrow -1} = \left[ \frac{\left( \frac{2\mu k_z}{\mu k_z + k_z'} \right) \left( \frac{2k_z'}{\mu k_z + k_z'} \right) e^{j(k'_z d)}}{1 - \left( \frac{k_z' - \mu k_z}{k_z + \mu k_z'} \right)^2 e^{j(2k'_z d)}} \right] \quad (8.50)$$

$$[T_e]_{\epsilon \rightarrow -1, \mu \rightarrow -1} = \left[ \frac{\left( \frac{-2k_z}{-k_z + k_z'} \right) \left( \frac{2k_z'}{-k_z + k_z'} \right) e^{j(k'_z d)}}{1 - \left( \frac{k_z' + k_z}{k_z - k_z'} \right)^2 e^{j(2k'_z d)}} \right] \cong e^{j(k'_z d)} \quad (8.51)$$

$$\text{where } [k'_z]_{\epsilon \rightarrow -1, \mu \rightarrow -1} = j \left( \sqrt{(k_x^2 + k_y^2) - \epsilon_2 \mu_2 \frac{\omega^2}{c^2}} \right) = j \left( \sqrt{(k_x^2 + k_y^2) - \frac{\omega^2}{c^2}} \right) = k_z \quad (8.52)$$

$$\text{From (8.51)} \quad [T_e]_{\epsilon \rightarrow -1, \mu \rightarrow -1} = e^{j(k'_z d)} = e^{j(k_z d)} \quad (8.53)$$

The overall reflection coefficient can be given by ( $R_r$ ) as [26]

$$[R_r] = \frac{\overline{E}_{reflected}}{E_{incident}} = R \left[ 1 - \frac{(1-R^2)e^{j(2k'_z d)}}{1-R^2 e^{j(2k'_z d)}} \right] = R \left[ \frac{1-e^{j(2k'_z d)}}{1-R^2 e^{j(2k'_z d)}} \right] \quad (8.54)$$

$$\text{Simplifying the Equations (8.45), (8.47) and (8.54)} \quad [R_r]_{\epsilon \rightarrow -1, \mu \rightarrow -1} \rightarrow 0 \quad (8.55)$$

From (8.55), the reflection coefficient  $R_r$  is zero in DNG medium. The consequence of having negative index ( $\epsilon \rightarrow -ve, \mu \rightarrow -ve$ ) refraction result in the wave of the form  $e^{-k_z d}$  outside the slab (DNG) that couple to waves of the form  $e^{k_z d}$  inside the slab (DNG). Therefore, even if the waves decay outside the slab, they are amplified on the inside of it, recovering an image on the opposite side of the slab, from the source, and all done by the transmission process [26]. Since the wave decay in amplitude not in phase, as they get further from the source, the DNG slab focus the image by amplifying these waves rather than correcting the phase. Figure 8-5 illustrates the evanescent field variation in DNG slab.

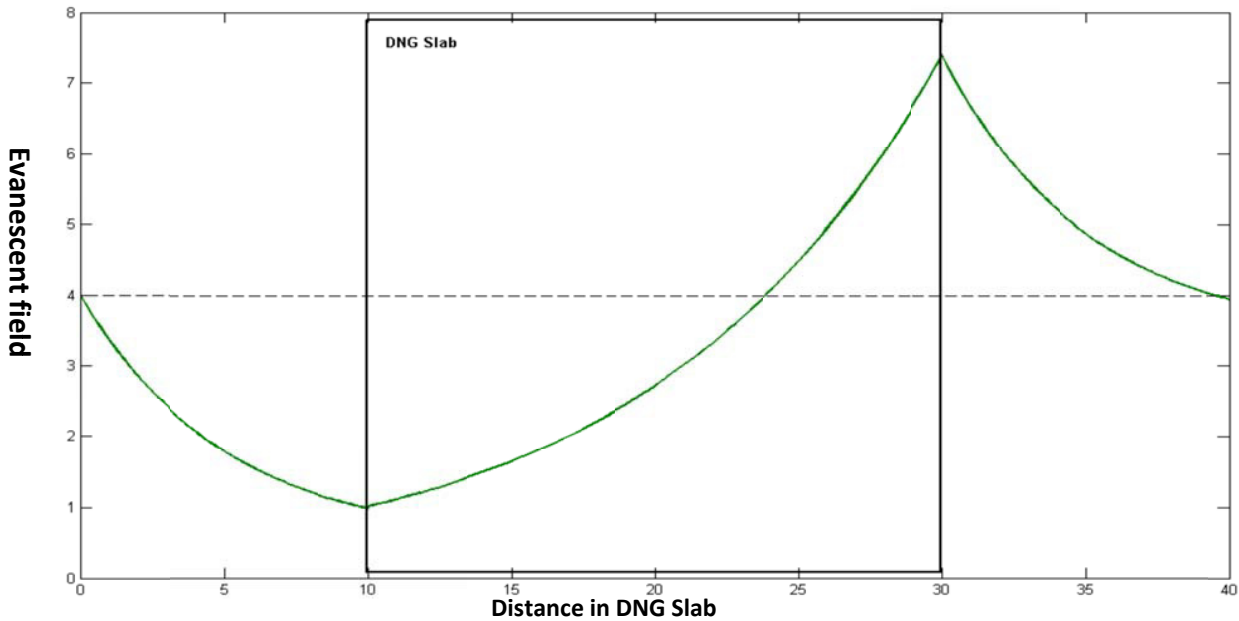


Figure 8-5: Evanescent field variation in DNG, shows amplification of evanescent wave inside the DNG slab [26]

These features can be utilized for improving the Q-factor of the evanescent mode resonator because both the propagating and evanescent waves contribute to improving the group delay. This phenomenon does not violate energy conservation law because evanescent wave does not transport the energy [27].

### 8.2.3 Phase Velocity, Group velocity, Energy Density

#### 8.2.3.1 Phase Velocity

From (8.23), the phase velocity of a wave is the rate at which the phase of the wave propagates in space or medium. The phase velocity is given in terms of the wave's frequency  $\omega$ , wavenumber  $k$ , velocity of light  $c$ , and refractive index  $n$ , given by [28]-[29]

$$v_p = \frac{\omega}{k} = \frac{c}{nk_o} \quad (k = \omega\sqrt{\epsilon\mu} = \omega n\sqrt{\epsilon_o\mu_o} = nk_o) \quad (8.56)$$

$$v_p = \frac{c}{n} = \frac{c}{\sqrt{\epsilon\mu}} \quad (8.57)$$

#### 8.2.3.2 Group Velocity

The group velocity is the rate at which the envelope of the waveform is propagating in space or medium, i.e. the rate of variation of the amplitude of the waveform. Assuming the waveform is not distorted significantly during propagation, it is the group velocity, which represents the rate at which information (and energy) is transmitted by the wave. However, if the wave is travelling through an absorptive and strongly dispersive medium, this condition no longer holds. For certain condition, it is possible to reduce the group velocity to zero, stopping the wave, or have negative group velocity, making the wave appear to propagate backwards. In isotropic media, the group velocity is given as [28]

$$v_g(\omega_o) = \frac{d\omega}{dk} = \left(\frac{dk}{d\omega}\right)^{-1} \quad (8.58)$$

where  $v_g$  is the group velocity,  $\omega$  is the wave's angular frequency,  $k$  is the wave number.

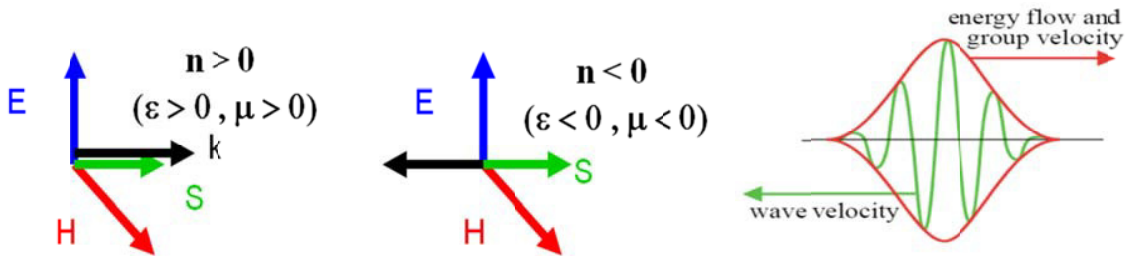


Figure 8-6: shows the typical representation of electromagnetic wave velocity

The function  $\omega(k)$ , which gives  $\omega$  as a function of  $k$ , is known as the dispersion relation. If  $\omega$  is directly proportional to  $k$ , then the group velocity is exactly equal to the phase velocity. Otherwise, the envelope of the wave will become distorted as it propagates. Figure 8-6 shows the typical pictorial representation of the electromagnetic wave velocity. From (8.56) and (8.57) [29],

$$v_g(\omega_o) = v_p + k \frac{d(v_p)}{dk} \quad (8.59)$$

$$v_g(\omega_o) = c \left[ \frac{d(n\omega)}{d\omega} \right]^{-1} = \frac{c}{n + \omega_o \left[ \frac{d(n)}{d\omega} \right]}, \quad \text{where } \frac{d(n)}{d\omega} > 0 \quad (8.60)$$

From (8.60), for positive refractive index  $n$ , the group velocity is always smaller than the phase velocity and smaller than the speed of light in vacuum.

From (8.60), for negative refractive index material ( $n < 0$ ), the group velocity can take any value because  $\frac{d(n)}{d\omega} > 0$  in a low-loss media, including materials with negative refractive index.



### 8.2.3.3 Energy Density

It is well known that any physical media other than vacuum is dispersive [28]. The expression of energy density  $U$  for non-dispersive media can be described by [30]:

$$U = \frac{1}{4}\{\epsilon|E|^2 + \mu|H|^2\} \rightarrow U = \frac{1}{4}\left\{\left[\frac{\partial(\omega\epsilon)}{\partial\omega}\right]|E|^2 + \left[\frac{\partial(\omega\mu)}{\partial\omega}\right]|H|^2\right\} \quad (8.61)$$

From (8.61), the physical requirement of the existence of the positive energy density is given by

$$\frac{\partial(\omega\epsilon)}{\partial\omega} > 0, \frac{\partial(\omega\mu)}{\partial\omega} > 0 \quad (8.62)$$

From (8.61), for Metamaterial ( $\mu, \epsilon < 0$ ) the energy density results of negative value, which yields nonphysical result. Equation (8.62) is compatible with ( $\mu, \epsilon < 0$ ), provided  $\frac{\partial(\omega\epsilon)}{\partial\omega} > \frac{|\epsilon|}{\omega}$  and  $\frac{\partial(\omega\mu)}{\partial\omega} > \frac{|\mu|}{\omega}$ . Hence, physical left-handed media is highly dispersive (Metamaterial resonator exhibits negative value of  $\epsilon$  and  $\mu$  in the highly dispersive regions just above resonances). For Metamaterial, backward-wave propagation implies opposite signs between phase and group velocities [31], can be expressed as [29]

$$\frac{\partial k^2}{\partial\omega} = 2k \left(\frac{\partial(k)}{\partial\omega}\right) = 2 \left(\frac{\omega}{v_p v_g}\right) \quad (8.63)$$

$$\frac{\partial k^2}{\partial\omega} = \omega\epsilon \left(\frac{\partial(\omega\mu)}{\partial\omega}\right) + \omega\mu \left(\frac{\partial(\omega\epsilon)}{\partial\omega}\right) < 0 \quad (8.64)$$

$$v_p v_g < 0 \quad (8.65)$$

Where  $v_p = \frac{\omega}{k}$  and  $v_g = \frac{d\omega}{dk}$  are the phase and group velocity respectively, and  $k = \omega\sqrt{\epsilon\mu}$ . Backward wave transmission line can form a non-resonant LHM (left-handed material) [28, 35].

## 8.3 Realization of Negative Refractive Index material (NRIM) Components

The refractive index is the most fundamental parameter to describe the interaction of electromagnetic radiation with matter. It is a complex  $n = (n' + jn'')$  where  $n'$  is generally being considered to be positive. While the condition of  $n' < 0$  does not violate any fundamental physical law, materials with negative index exhibit interesting properties. For example, electromagnetic wave when refracted at an interface between positive refractive index material (PRIM) and a negative refractive index material (NRIM), is bent in the "wrong" way with respect to the normal, result is group and phase velocity are antiparallel [38]. A possible-but not only-approach to achieve a NRIM in a passive medium is to design a material in which the (isotropic) permittivity  $\epsilon = (\epsilon' + j\epsilon'')$  and the (isotropic) permeability  $\mu = (\mu' + j\mu'')$  obey the inequality [35]-[41]

$$\epsilon'|\mu| + \mu'\epsilon < 0 \quad (8.66)$$

This leads to a negative real part of the refractive index  $n = (n' + jn'') = \sqrt{\mu\epsilon}$ . Equation (8.86) only holds good for passive media and the equality condition is satisfied, if  $\epsilon' < 0$  and  $\mu' < 0$ . But this is not a necessary condition, there may be magnetically active media ( $\mu \neq 1$ ) with a positive real part  $\mu'$  for which (8.66) is justified and show a negative real part of the refractive index  $n'$ .

From [100], the incorporating impedance term  $Z$  in the general relationship between the refractive index can lead to relationship [37]:

$$2 \operatorname{Re} \left(\frac{1}{Z}\right) n' = \epsilon' + \mu' \frac{|\epsilon|}{|\mu|} \quad (8.67)$$

$$2n'n'' = \epsilon'\mu'' + \mu'\epsilon'' \quad (8.68)$$

where  $Z = \sqrt{\left(\frac{\mu}{\epsilon}\right)}$ , the direction of the Poynting vector and wave vectors are governed by the sign of  $\operatorname{Re} \left(\frac{1}{Z}\right)$  and  $n'$  respectively [101]. Therefore, the sign of  $\epsilon' + \mu' \frac{|\epsilon|}{|\mu|}$  should be negative for the NRIM.

Equation (8.68) requires  $(\epsilon'\mu'' + \mu'\epsilon'')$  being negative for the absorbing effective medium and positive for a NRIM. The key to the design of the artificial NRIM resonator is to select novel geometric shape so that induced currents form loops with a relatively uniform distribution of the induced current, which produces a strong magnetic moment. In general, three types of typical geometry are used for the realization NIRM components: (i) split-ring resonators, (ii) coupled wire sets, (iii) and dielectric resonators. Figure 8-7 depicts these resonators, which exhibit negative refractive index property described in (8.66) [38]-[52].

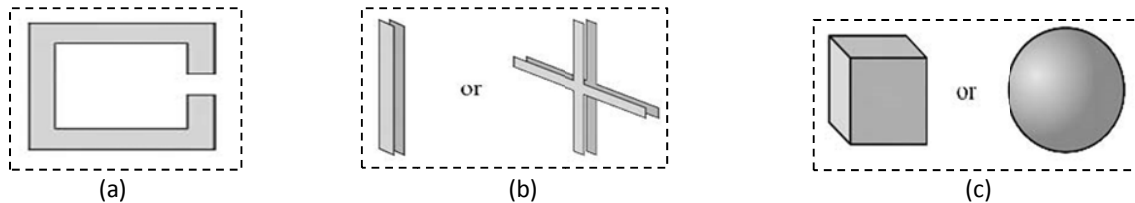


Figure 8-7 illustrates the typical resonator geometries that exhibit negative refractive index property: (a) Split ring resonator, (b) coupled wire sets, and (c) dielectric resonators [53].

### 8.3.1 Split Ring Resonator (SRR)

As shown in Figure 8-7 (a), Split-ring resonator (SRR) produces a negative permeability just above their resonant frequency, typically these structures are bi-anisotropic exhibiting coupled electric and magnetic effects [52]-[53]. A negative refractive index transmission pass-band occurs at the resonant frequency of the split ring when wires that provide a negative permittivity are aligned with their axis parallel to the plane of the loop [54]-[56]. By using concentric split rings in conjunction with diodes as shown in Figure 8-8, resonant frequency can be switched and tuned for multi-band applications [17, 46, and 57].

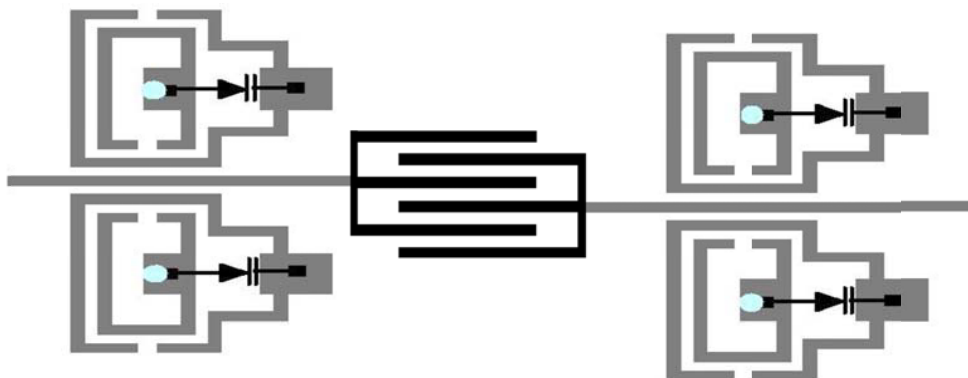


Figure 8-8: shows the typical geometries of metamaterial resonators for switchable band operation.

### 8.3.2 Coupled Wire Sets NRIM

Figure 8-7 (b) shows a typical coupled wire constructed as negative refractive index material (NRIM) that uses pairs of conducting wire strips, or other shapes, which are spaced apart in the direction of wave propagation at a distance much smaller than the wire's width [53]. As shown in Figure 8-7(b), the electric field interacts with linear elements of the structure leading to negative permittivity, whereas magnetic field interacts with the small gaps between conducting elements, exciting anti-parallel currents in the open loop of the two conducting structures, leading to negative permeability [58]-[86].

While coupled wire structures can be built as a bulk Metamaterial, since the desired properties are achieved face-on, the structure is planar by design. Thus the axis perpendicular to the material face has a different permittivity and permeability than do the axes parallel to the material face. Even though the working angle of the Metamaterial is broad, the refraction angles of different polarizations will eventually decouple because the structure is uni-axial [52].

### 8.3.3 Dielectric material resonator NRIM

Dielectric material resonator NRIMs (Figure 8-7(c)) uses a non-conductive particle with high permittivity, compared to that of the surrounding material, to create negative permeability [58]. The shape of the inclusions determines the resonant frequencies as well as the level of anisotropy. The resonances are Mie resonances (named after Gustav Mie for his theory of the electromagnetic wave scattering of spheres) for cubes and spheres: the 1st resonance is magnetic; the 2nd resonance is electric [59]-[72].

## 8.4 Metamaterial (NRIM) Model

There are different models to describe the Metamaterial behavior (negative permittivity and negative permeability), but the resonator and transmission line models are most common that uses the analogy between natural medium and artificial Metamaterial [21].

### 8.4.1 Resonator Model

Figure 8-9 shows the typical artificial metamaterial resonator model, which consists of dipole shaped thin wire for creating negative permittivity and split ring for negative permeability medium. By adjusting the spacing and dimension of dipole shaped thin wire and split ring, simultaneous negative permittivity and permeability medium in microwave frequency region can be realized, nomenclature as double negative medium (DNG).

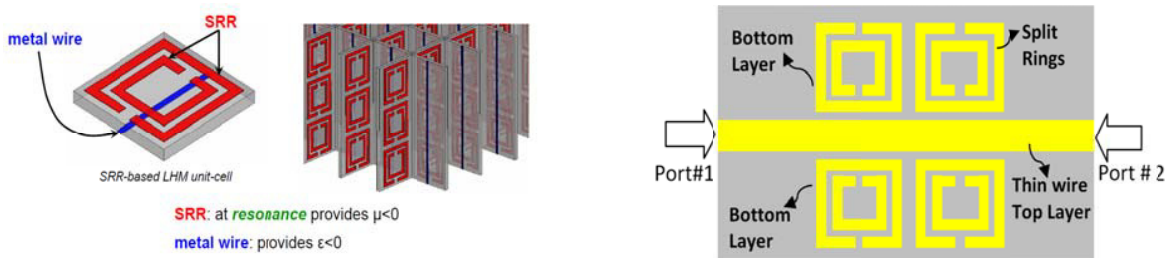


Figure 8-9: shows the typical coupled SRR, exhibits negative permittivity and permeability at resonance [35]

Figure 8-9 shows the 3-dimensional SRR-metal wire exhibiting negative refractive index properties ( $\epsilon < 0$  and  $\mu < 0$ ) for the realization of metamaterial resonator, therefore restricts the uses in planar microwave circuit applications [22]. For the application in planar microwave devices, 2-dimensional transmission-line networks can be periodically loaded with series capacitors and shunt inductors for the realization of negative refractive index, such medium makes left-handed material and supports propagating backward waves exhibiting a negative refractive index over a wide bandwidth [23]-[24].

### 8.4.2 Transmission line model (TLM)

A typical transmission line is a uniform and homogenous structure with invariant cross-section along the direction of propagation, which can transmit signals from zero to very high frequencies [29]. In general, TLM can be classified as Right-handed (printed microstripline). The Left-handed (Metamaterial) material is not available in nature, artificially created, nomenclature as CRLH (composite right/left-handed) material. Transmission line model (TLM) assumes Metamaterial as an isotropic and homogeneous medium as contrary to resonator model. A TLM can be represented by distributed series impedance ( $Z$ ) and shunt admittance ( $Y$ ) in terms of permittivity ( $\epsilon$ ) and permeability ( $\mu$ ) [22] as

$$Z'(\omega) = \frac{Z(\omega)}{d} = j\omega\mu(\omega) \Rightarrow \mu(\omega) = \frac{Z(\omega)}{j\omega d}; \quad Z' \text{ is impedance per unit length} = Z(\omega)/d \quad (8.69)$$

$$Y'(\omega) = \frac{Y(\omega)}{d} = j\omega\epsilon(\omega) \Rightarrow \epsilon(\omega) = \frac{Y(\omega)}{j\omega d}; \quad Y' \text{ is impedance per unit length} = Y(\omega)/d \quad (8.70)$$

The effective propagation constant  $\gamma(\omega)$  of right-handed (normal) material is given by

$$\gamma(\omega) = \sqrt{Z'(\omega)Y'(\omega)} \approx j\beta = j\omega\sqrt{\mu(\omega)\epsilon(\omega)} \quad (8.71)$$

The series inductance and shunt capacitance of right-handed material is given by

$$L = \mu_0 d, \quad L' = \frac{L}{d} = \mu_0, \quad C = \epsilon_0 \epsilon_r d, \quad C' = \frac{C}{d} = \epsilon_0 \epsilon_r \quad (8.72)$$

$$\beta = \omega \sqrt{\mu(\omega) \epsilon(\omega)} = \omega \sqrt{L' C'} \quad (8.73)$$

From (8.69) to (8.73), the effective permittivity is connected with series inductance and permeability is connected with shunt capacitance for right-handed material. For left-handed material (Metamaterial) that exhibits negative permittivity and permeability, change in polarity is implemented for the realization of negative series impedance for (8.69) and negative admittance for (8.70).

There exists a reverse symmetry between right handed medium and left handed medium, hence series inductor and shunt capacitor in right-handed medium is replaced by series capacitor and shunt inductor in the unit cell of the left-handed material (Metamaterial) as shown in Figure 8-10 [21-22].

$$Z'(\omega) = \frac{1/j\omega C}{d} = j\omega\mu(\omega) \Rightarrow \mu(\omega) = \frac{j\omega C}{j\omega d} = -\frac{1}{\omega^2 C'} \quad (8.74)$$

$$Y'(\omega) = \frac{1/j\omega L}{d} = j\omega\epsilon(\omega) \Rightarrow \epsilon(\omega) = \frac{1/j\omega L}{j\omega d} = -\frac{1}{\omega^2 L'} \quad (8.75)$$

From (8.74)-(8.75), the left-handed medium distributed series capacitance  $C' = C/d$  and shunt inductance  $L' = L/d$ . The effective propagation constant  $\gamma(\omega)$  of left-handed (Metamaterial) is shown in Figure 8-10 and is given by [97]

$$\gamma(\omega) = \sqrt{Z'(\omega)Y'(\omega)} \approx j\beta = j\omega\sqrt{\mu(\omega)\epsilon(\omega)} = j\omega\sqrt{\left(\frac{1/j\omega C}{d}\right) \times \left(\frac{1/j\omega L}{d}\right)} = \beta = -\frac{1}{\omega\sqrt{L'C'}} \quad (8.76)$$

From (8.76), the phase velocity and group velocity of left-handed material is given by

$$v_p(\omega) = \frac{\omega}{\gamma(\omega)} = -\omega^2\sqrt{L'C'} \quad (8.77)$$

$$v_g(\omega_o) = \frac{d\omega}{d\gamma} = \omega^2\sqrt{L'C'} \quad (8.78)$$

From (8.77) and (8.78), direction of group velocity is opposite of the phase velocity, and group velocity has positive value. This implies that phase will propagate backward and the group velocity direction (Poynting Vector) is forward as the direction of energy flowing away from the source. In an isotropic medium for right-handed medium, the phase and group velocity has same direction, therefore no dispersion phenomenon. However, in left-handed medium (LHM) the phase velocity and group velocity are 180 degree out of phase (direction is anti-parallel with group velocity direction), implies medium is dispersive. From (8.77), the negative phase velocity in LHM medium leads to the negative refractive index, which can be given by

$$n = \frac{c}{v_p(\omega)} = -\frac{\sqrt{\mu(\omega)\epsilon(\omega)}}{\sqrt{\mu_0\epsilon_0}} = -\frac{1}{\omega^2\sqrt{L'C'}\mu_0\epsilon_0} \quad (8.79)$$

$$c = \frac{1}{\sqrt{\mu_0\epsilon_0}} \quad (8.80)$$

where c is the velocity of light in free space

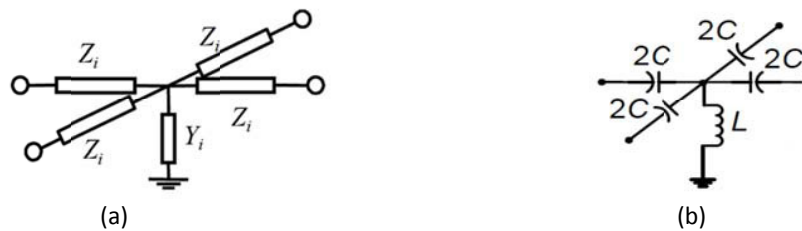


Figure 8-10: Equivalent circuit of the metamaterial unit cell (a) General model, (b) LC model (using shunt inductors for affecting  $\epsilon_r$  and series capacitors for affecting  $\mu_r$ ) [22]

### 8.5 Physical Realization of Metamaterial Component for Oscillator Circuits

Cascaded composite right/left-handed structures (CRLH) with unit dimension much smaller than the guided wavelength behave as Metamaterial, producing simultaneous negative permittivity ( $\epsilon_r$ ) and permeability ( $\mu_r$ ) properties. A CRLH-TL consists of a conventional transmission line (TL), or a right-handed (RH) TL, and its dual consisting of series capacitors ( $C_L$ ) and shunt inductor ( $L_L$ ), termed a left-handed (LH) TL as shown in Figure 8-11. CRLH structures may be realized in many different forms such as in Microstrip TL, SIW, and CPW [39]. These types of TLs can be designed to provide a nonlinear phase response with respect to frequency [136]. With proper coupling and termination (either open or short), CRLH resonators can be designed.

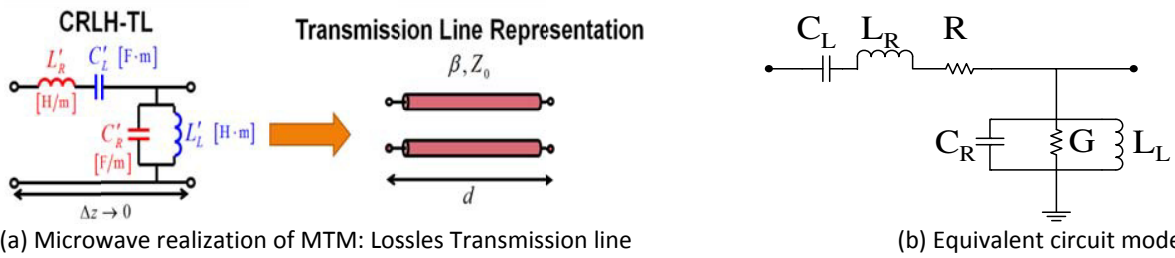


Figure 8-11: A typical equivalent circuit model of CRLH unit-cell: (a) Lossless ( $R=0$ ) transmission line representation of CRLH unit cell, and (b) Lossy circuit model of CRLH unit-cell [39]

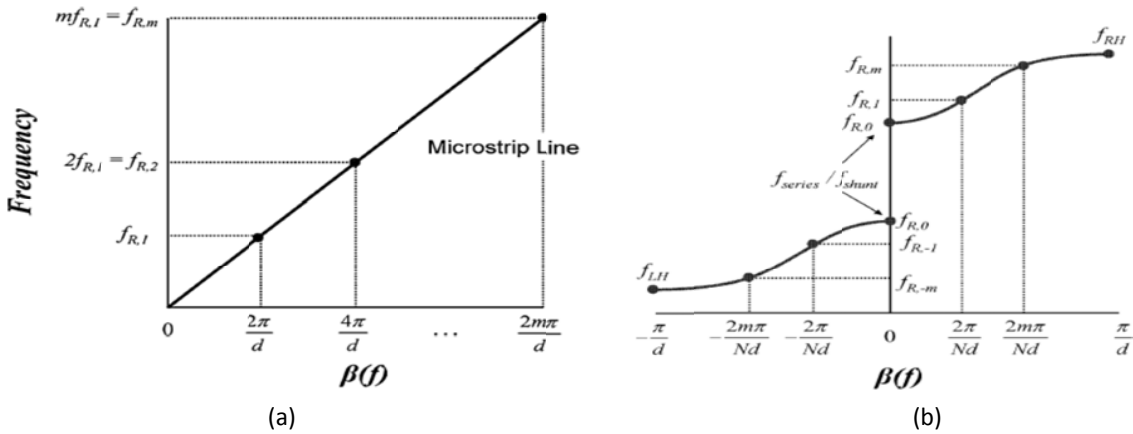


Figure 8-12: Dispersion diagram of a (a) conventional microstrip line and (b) CRLH Transmission Line [39]

Comparison between the dispersion relations of the conventional resonators and the CRLH resonator under unbalanced condition is illustrated in Figure 8-12. Note that the spurious (higher order) resonances are not at the harmonic frequencies and the mode spacing may be manipulated. Balanced condition may also be achieved by overlapping the shunt and series resonant frequencies, thereby creating smooth transition from LH to RH regions. CRLH resonator exhibits a unique resonance  $m = 0$ , at the frequencies:

$$\omega_{res}^{open} = \omega_{sh} = \frac{1}{\sqrt{L_L C_R}} \tag{8.81}$$

$$\omega_{res}^{short} = \omega_{se} = \frac{1}{\sqrt{L_R C_L}} \tag{8.82}$$

The unloaded quality factor  $Q_o$  is independent of the physical length of the structure and only depends on one of two present losses, either  $G$  or  $R$ ,

$$Q_o^{open} = \frac{1}{G} \sqrt{\frac{C_R}{L_L}} \quad (8.83)$$

$$Q_o^{short} = R \sqrt{\frac{C_L}{L_R}} \quad (8.84)$$

For instance, short-circuited format is preferred in order to avoid conductor loss of the shunt inductance  $L_L$ . In addition, unlike the conventional resonator, spurious resonances can be engineered to arbitrary frequency away from harmonic frequencies and  $Q$ -factor can be improved as compared to the conventional resonators [40].

When aforementioned zero<sup>th</sup> order resonators (ZOR) operate under balanced condition, the mode spacing and  $Q$ -factor become dependent. The phase slope of the resonant structure can be manipulated to either increased mode spacing/decreased  $Q$ -factor or decreased mode spacing/increased  $Q$ -factor. However, under unbalanced condition, the mode spacing and  $Q$ -factor become independent and it has been demonstrated where first-order mode can be considerably increased (from  $f_{mode1}/f_{mode0} = 3.5$  to 5.33), without sacrificing the  $Q$ -factor [41]. A high- $Q$  resonator based on unbalanced CRLH resonator was built using lumped components with the first-order resonance occurring at around 5 times  $f_{mode0}$ .

However, the performance was degraded due to undesired leakage when the resonator is built using distributed technology. To prevent the radiation, proper shielding may be added or lower modes such as  $n = -1, -2$ , etc. may be used to prevent leakage radiation. If the size is not the constraining factor, higher order modes such as  $n = +1, +2$ , etc. can be explored. Figure 8-13 shows the typical CRLH SIW structure, which is a good candidate for oscillator resonators because of high- $Q$  factor. In addition, CRLH substrate integrated waveguide (SIW) structure can support 0<sup>th</sup> order and negative order resonance and thereby miniaturize the circuit [43]. As shown in Figure 8-14, the one unit-cell CRLH SIW structure and miniaturized CRLH SIW antennas based on negative order resonance. The radiation through the interdigital capacitor creates radiation loss and it is difficult to use this as a guided-wave application, such as a cavity.

Shielded CRLH SIW can however eliminate the radiation by enclosing the top side with the metallic shield. The proposed structure has small size when operated in the left-handed frequency region and high quality factor due to the waveguide nature [64]-[73]. Figure 8-14 shows the proposed shielded CRLH SIW unit-cell and the dispersion relation of the structure. Even with the shield, this structure shows CRLH characteristic. Figure 8-15 shows possible candidates of shielded CRLH SIW resonators. Note that the resonators are directly excited by a strip line type feeding structure. However, we could use Microstrip line input using the transition of Microstrip line to strip line.

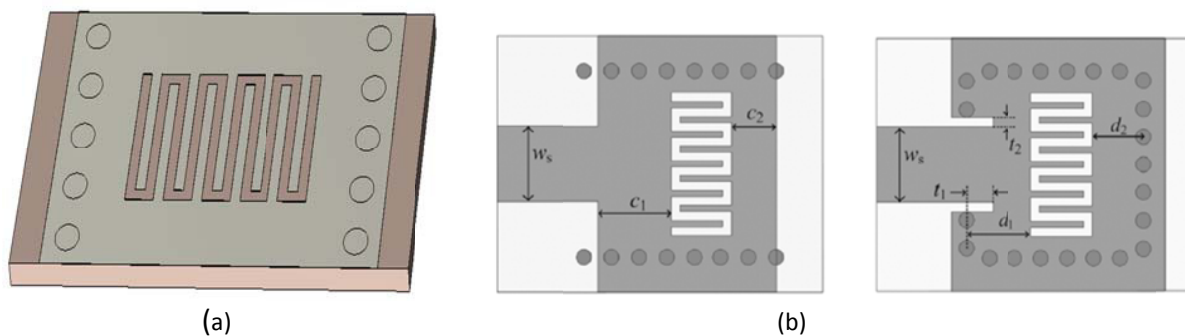
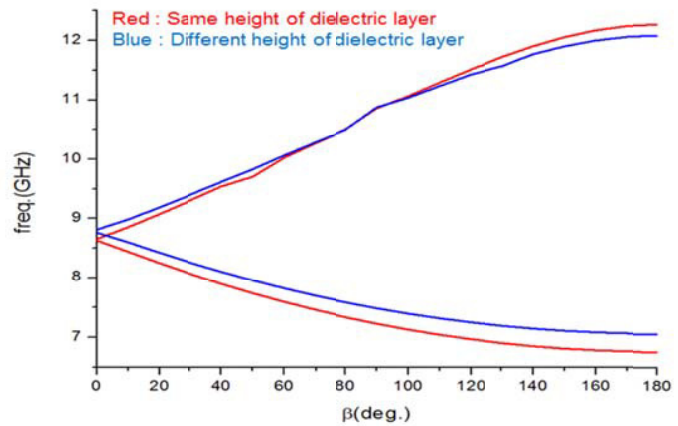
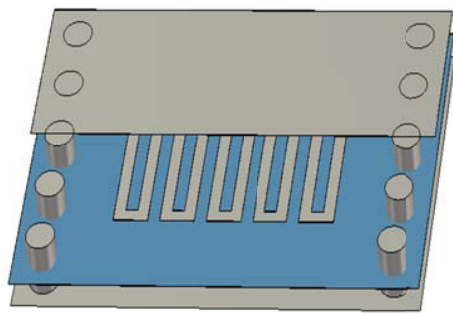


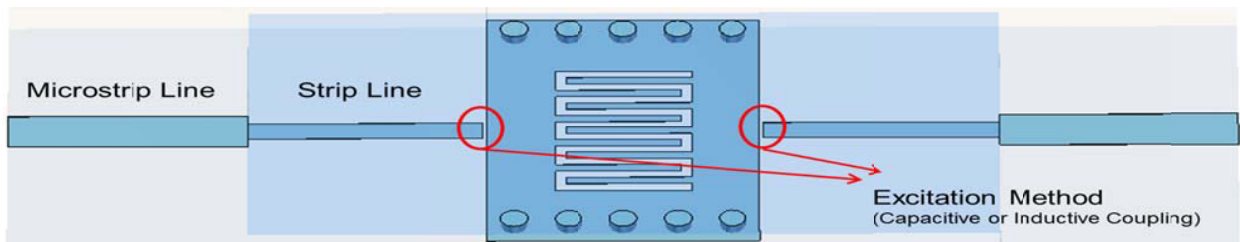
Figure 8-13 (a) The configuration of the CRLH SIW unit-cell and (b) Its applications to resonator antennas [43]



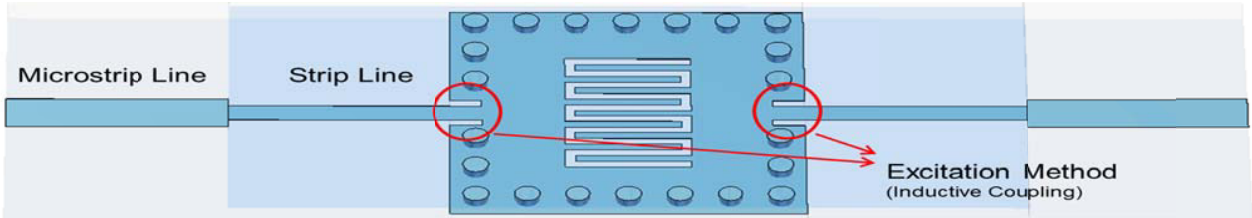
(a)

(b)

Figure 8-14: (a) The structure and (b) The dispersion relation of the shielded CRLH SIW unit-cell [a preliminary work carried out at UCLA as a joint collaboration research work with Synergy Microwave Corp.



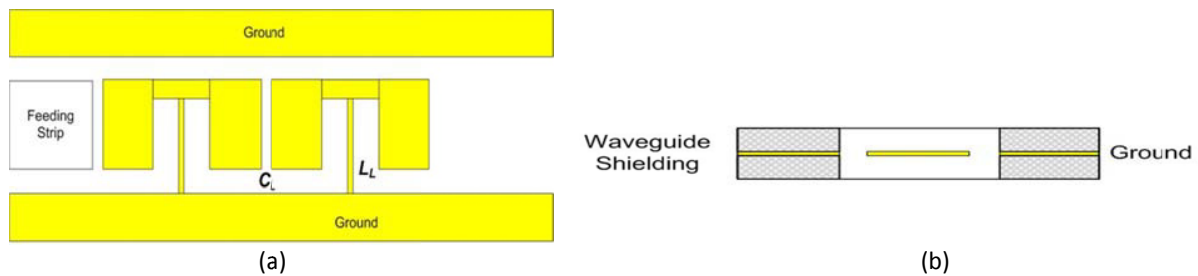
(a)



(b)

Figure 8-15: Possible resonator structures using the shielded CRLH SIW (a) Open ended and (b) Short ended [a preliminary work carried out at UCLA as a joint collaboration research work with Synergy Microwave Corp].

Figure 8-16 shows the typical layout of the CRLH CPW resonator for low phase noise oscillator applications. CRLH based ZOR using CPW technology may provide high-Q with spurious resonances far away from the harmonic resonances since this resonator dimension is not proportional to the resonant frequency as the conventional Microstrip resonator.



(a)

(b)

Figure 8-16: The shielded CRLH CPW (a) Top view and (b) Side view [a preliminary work carried out at UCLA as a joint collaboration research work with Synergy Microwave Corp. as a part of this research work]

In addition, when operated in 0<sup>th</sup>-order mode, it can also be miniaturized. CRLH based ZOR in CPW technology has been used for miniaturized band pass filter application [44]. Similarly this may be applied in designing resonator for oscillator application. However, as mentioned, one major problem with the structure may be the undesired radiation leakage [41]. It can be alleviated by enclosing the structure inside the WG shield or using MIM capacitor rather than edge coupled capacitors.

### 8.6 CSRR (Complementary Split Ring Resonator) for Oscillator Circuit Applications

Figure 8-17 shows the typical circular Split-ring resonator (SRR) that is one kind of Metamaterial provided there is effective positive permittivity ( $\epsilon$ ) and negative permeability ( $\mu$ ). As shown in Figure 8-17 (a), SRRs can induce resonating currents in the loop and thus generate equivalent magnetic dipole moments. On the other hand, complementary split-ring resonators (CSRRs), a duality form of SRRs shown in Figure 8-17 (b), behaves as electric dipoles that need an axial electric excitation and are able to exhibit negative permittivity [42].

Typically, waveguide structures are often utilized when it comes to the need of high  $Q$ -factor and high power handling capability. When these waveguide structures are loaded with MTMs such as SRRs or CSRRs, they can operate below their original cut-off frequency and thus achieve size reduction. However, main disadvantages in using conventional waveguides are high cost and the difficulty in fabrication. It is also not easy to load MTMs to the conventional waveguides. Substrate integrated waveguides synthesized in planar form by two rows of metallic vias embedded in a dielectric substrate have served as a good candidate in realizing low cost and highly integrated WG components, since SIWs can be easily fabricated using printed circuit board (PCB) technology.

Moreover, it is very convenient and efficient to create CSRRs on the surface of SIWs, which makes the structures more appealing and competitive (Figure 8-18). Figure 8-19 shows the reconfigurable dual-band oscillator at 2.675 GHz and 3.77 GHz using printed planar CSRR embedded in an SIW cavity [45]. As shown in Figure 8-19, dual band oscillator contains a diode to provide the switching capability of the oscillator. When the diode is on, it behaves as a double ring CSRR that resonates as the lower frequency (2.675 GHz), whereas if the diode is turned off, it becomes a partially single-ring CSRR that resonates at the higher frequency (3.77 GHz).

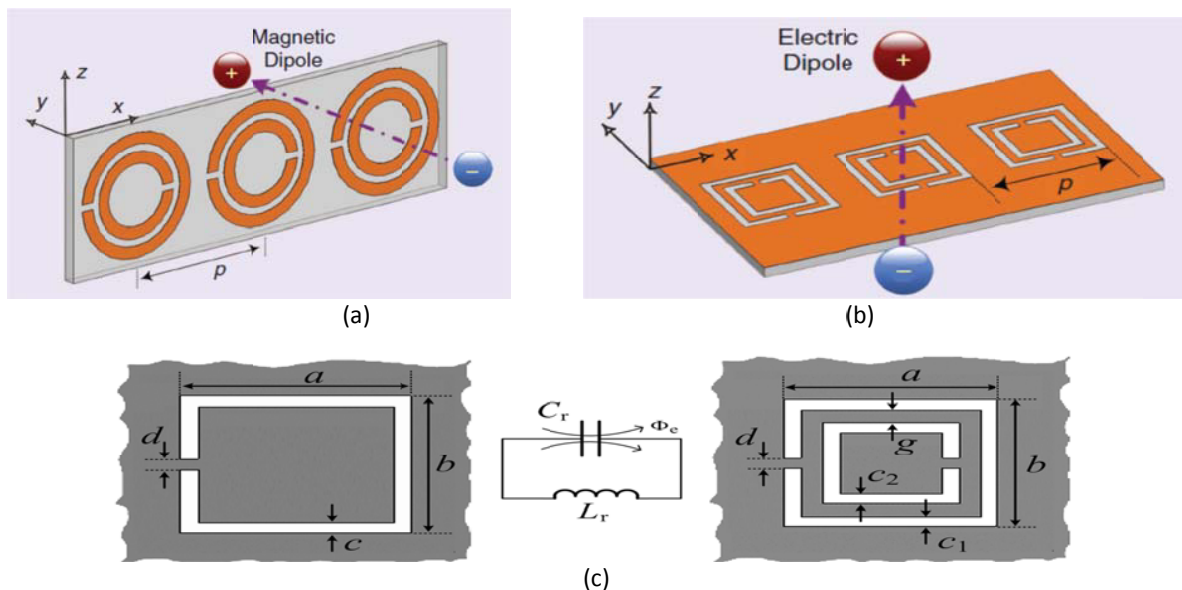


Figure 8-17: (a) SRRs, as equivalent magnetic dipoles (b) CSRRs, as equivalent electric dipoles, and (c) equivalent LC model of CSRR [42]



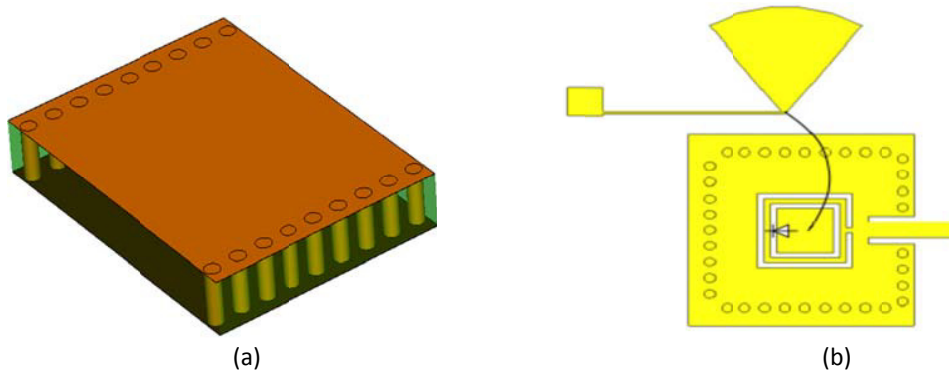


Figure 8-18: (a) a typical SIW cavity, (b) a typical layout of the SIW cavity loaded with CSRR and diode [45]

Because the SIW cavity loaded with CSRR can provide high- $Q$  and low loss, the realized oscillator had a low phase noise ( $\sim -120$  dBc/Hz @ 1MHz offset). This structure is promising to operate at even higher frequency ( $> 15$  GHz) since the dimension of the SIW can be easily scaled down. With loaded CSRR on the SIW cavity surface, it can create a very narrow band resonance below the waveguide cutoff frequency, and hence an electrically small and high- $Q$  resonator can be realized.

### 8.7 Slow Wave Metamaterial Resonator (SWMR)

Conventional Microstrip coupled lines even and odd modes exhibit different phase velocities due to the inhomogeneous dielectric medium [120]-[124]. Signals on a coupled line are the superposition of an even and odd mode and discrepancy between phase velocities of the two modes is undesirable for high quality resonator for low phase noise oscillator applications [121]. Slow wave has been demonstrated in many systems by using very different methods, such as the electromagnetic induced transparency [18] and the coupled resonator structures [19]-[20].

Slow waves on printed cascaded split ring resonators or lattices of resonant elements exhibit interesting characteristics in terms of phase velocity, group velocity, energy velocity, radiation and attenuation characteristics, quality factor, and left-handed material features (negative permittivity and negative permeability) near the resonance condition [104]. Figure 8-20 shows the typical representation of slow wave dynamics in series coupled split ring and nanoparticle resonators that exhibit left-handed and evanescent mode propagation characteristics [37]. There is significant interest in slow wave metamaterial resonator (SWMR) for the design of low phase noise oscillators. Slow wave metamaterial structure improves the group delay and equalization of the phase velocity. The Metamaterial based high- $Q$  resonators provide added advantages such as prevention of unintended generation of harmonic oscillation and structural dimensions that are not dictated by the resonant frequency.

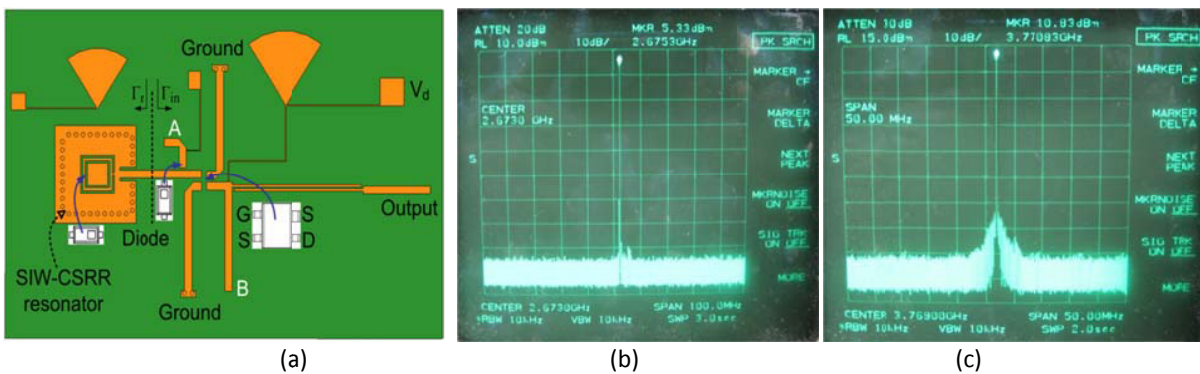


Figure 8-19: (a) A typical layout of Dual-band Oscillator with Complementary Split-Ring Resonator, (b) oscillator output at 2.675 GHz (FOM=171.8), and (c) oscillator output at 3.77 GHz (FOM=169.1) [45].

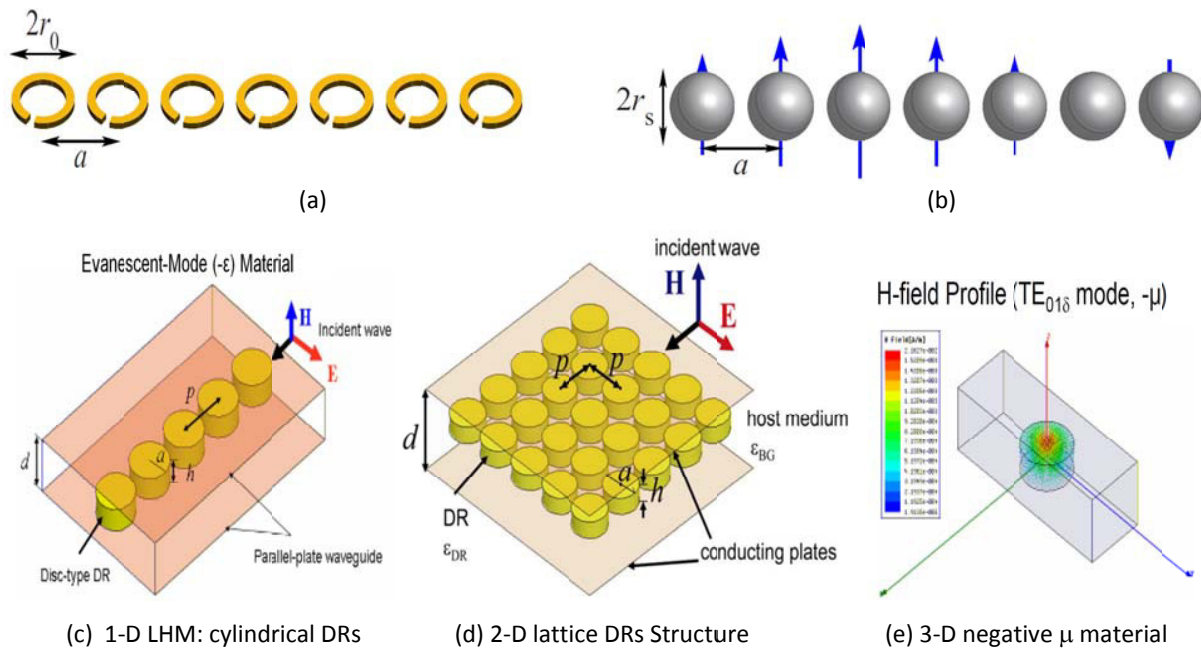


Figure 8-20: A typical representation of slow wave dynamics in (a) series coupled split ring, (b) nanoparticle resonators that exhibit left-handed and evanescent mode propagation characteristics, (c) 1-D LHM: cylindrical DRs in TE mode cutoff parallel plate waveguide ( $-\epsilon$ ) [36], (d) 2-D lattice structure for one dielectric-resonator scheme in the cutoff Waveguide, and (e) 3-Dimensional negative permeability material [37].

Metamaterial with their unique properties in conjunction with slow wave dynamics allow for the design of compact tunable oscillators, filters, phase-shifters and microwave sensors, which otherwise is difficult to achieve using conventional design approaches. To design integrated oscillator circuits, printed coupled split ring resonator structures enable readily the integration of active devices as an integral part of the resonator. Microstrip based designs are compatible with wafer-level integration and lead to the integration of active device elements as an integral part of the coupled split ring resonators. Recently, metamaterial coupled-line circuits had been attempted by placing two lines next to each other [32]-[34] with capacitor loadings to enhance coupling. The coupling is capacitive and mostly through the fringing electric fields. The edge coupling between two (coplanar) metamaterial lines is usually weak, particularly on PCB with minimum required line spacing. One would need to enhance the inductive coupling significantly to equalize the phase velocity and to obtain necessary impedance for the odd and even modes.

### 8.8 Examples: Tunable Oscillators Using Slow Wave Metamaterial Resonator (SWMR)

It has been known that the phase noise of the oscillator depends on the Q-factor of the resonator. However, the phase noise of the integrated oscillators is limited by the low Q-factor of the on chip inductors in the conventional LC based resonator tank. In general, Q-factor of the on-chip inductor ranges from 10-20 at X and Ka band. The transmission line slow wave resonators having the metamaterial property exhibits improved Q-factor, enabling lower phase noise characteristics. The main advantages of these structures are high Q-factor, easy fabrication, low radiation loss and sharp selectivity. As a possible candidate, high-Q, non-radiating composite right/left-handed (CRLH) Stripline resonator is discussed. CRLH resonators based on Microstrip and co-planar waveguide have previously been researched [40, 41, and 143]. This type of CRLH based resonator provided relatively compact size; however, only moderate Q-factors could be achieved due to undesired leaky-wave radiation loss.

In order to suppress the undesired radiation loss and further increase the Q-factor, CRLH based stripline resonator is preferred. Stripline configuration inherently has good radiation suppression; therefore, loss from radiation may be suppressed. A possible CRLH based resonator is shown in Figure 8-21 (a). The total length is less than  $\lambda_g/4$ . Therefore, the overall length can be miniaturized in comparison to the conventional  $\lambda_g/2$  stripline resonator. To facilitate the fabrication process and avoid the use of vias, we are currently using open stubs. If uses of vias are permitted, the overall dimension can be reduced further by adding vias to the stubs, thereby reducing the stub lengths. The simulated  $S_{21}$  is shown in Figure 8-21 (b). The substrate material used for the realization is RT/Duroid 5880 with  $\epsilon_r = 2.2$  and  $\tan\delta = 0.0009$ . The thicknesses for both substrate and Superstrate are 20 mils. Calculated unloaded-Q is around 300. Therefore, using CRLH based stripline resonator, higher Q-factor can be obtained in a relatively compact form. The Q-factor may be further improved after optimizations. We will also investigate other type of miniaturized/high-Q resonators.

As another candidate, a substrate-integrated waveguide (SIW) loaded with complementary coupled resonator, which is originally depicted in [77, pp. 358] has been studied to form a high-Q resonator. The structure is shown in Figure 8-21 (c) and it consists of two complementary coupled resonators facing each other side-by-side in order to reduce the radiation loss. The simulated S-parameters result is plotted in Figure 8-21 (d), using the same aforementioned substrate (RT/Duroid 5880). The dimension of the resonator itself (excluding the feed lines) is around 18mm by 12mm ( $< \lambda_g/2$ ). The simulated results show that the structure has an insertion loss of 1.34dB at 4.51GHz.

The unloaded-Q has also been calculated to be around 180. It is worth mentioning that this SIW loaded with complementary coupled resonator is analogous to the one loaded with complimentary split ring resonators (CSRRs). It can also create a pass band below the original SIW cutoff frequency and hence the size reduction can be achieved. Furthermore, the tunability of such structure has also been investigated. By inserting a varactor inside the slot of the complementary coupled resonator as shown in Figure 8-21 (e), resonance frequency can be varied; results are plotted in Figure 8-21 (f), with the varactor value changing from 1pF to 0.1pF. As a result, the center frequency of the pass band can be varied from 4.86-5.39GHz.

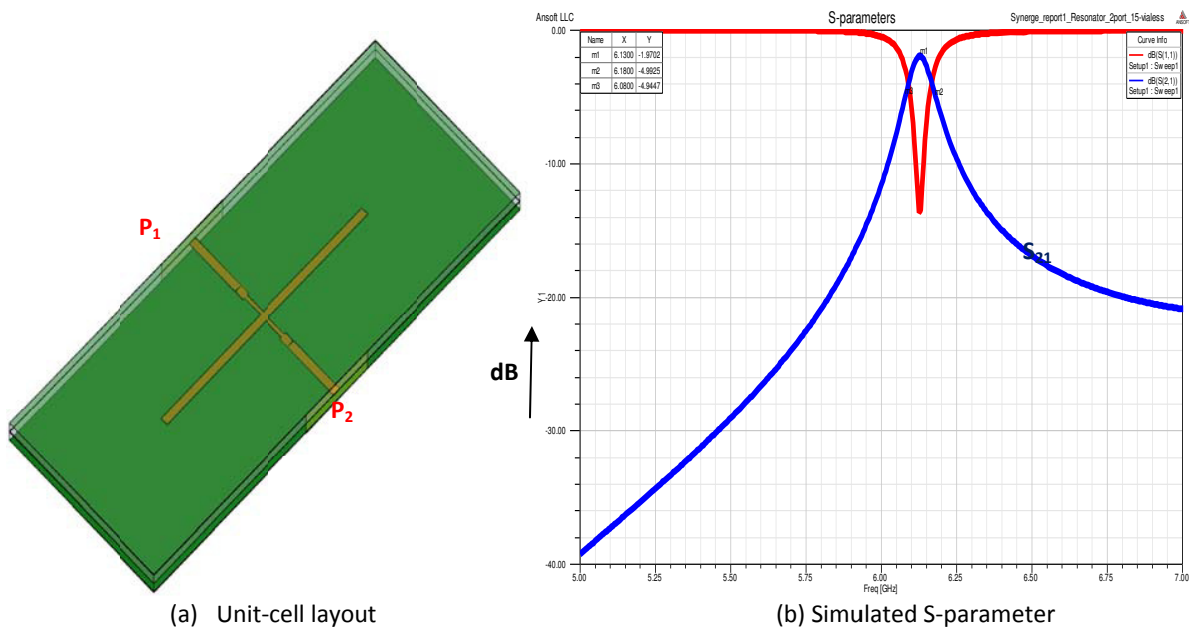
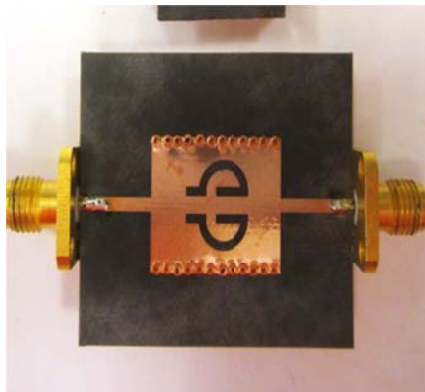
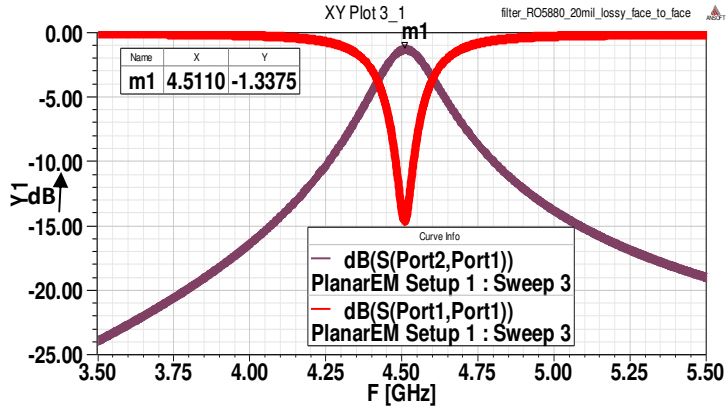


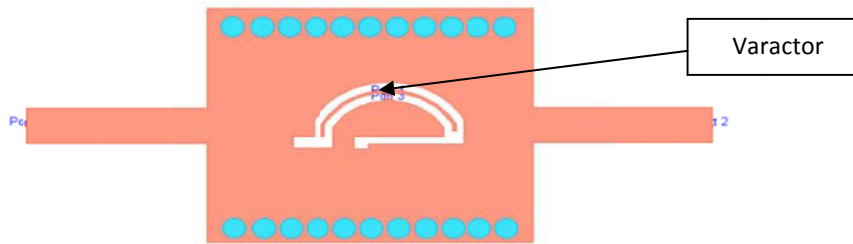
Figure 8-21: CRLH stripline resonator (a) unit-cell layout and (b) CAD simulated S-parameter results [154]



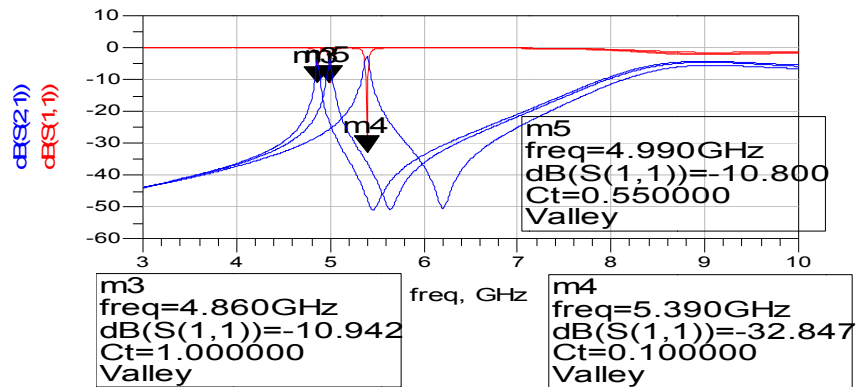
(c) CAD model of SIW loaded with CCR



(d) CAD simulated result



(e) Top view of CCR: a preliminary work carried out at UCLA as a joint collaboration work with Synergy) [154]



(f) Simulated S-parameter data

Figure 8-21: SIW loaded with complementary coupled resonator: (c) side view, (d) simulated s-parameters, (e) top view of complementary coupled resonator equipped with a varactor, and (f) measured S-parameter results

### 8.8.1 Tunable 2-4 GHz oscillator using SWMR

The novel approach is to improve the group-delay and reduce the effective dimension of the resonator by incorporating multiple concentric split-ring resonators without increasing the area occupied by the resonator [149]. They are very attractive to use in the wireless communication systems [46]-[49]. Figure 8-22 (a) shows the typical block diagram of 2-4 GHz VCO using metamaterial slow wave resonator. Figure 8-22 (b) exhibits the phase noise plot of oscillator as shown in Figure 8-22 (a).

### 8.8.2 Multi-band Oscillators using Printed Slow Wave Metamaterial Resonator

Efforts to miniaturize wireless communications hardware have led to compact radio designs with tunable oscillators, such as VCOs, to cover a number of different frequency bands. However, tunable oscillators typically exhibit tradeoffs between phase-noise performance and power consumption [106]-[119].

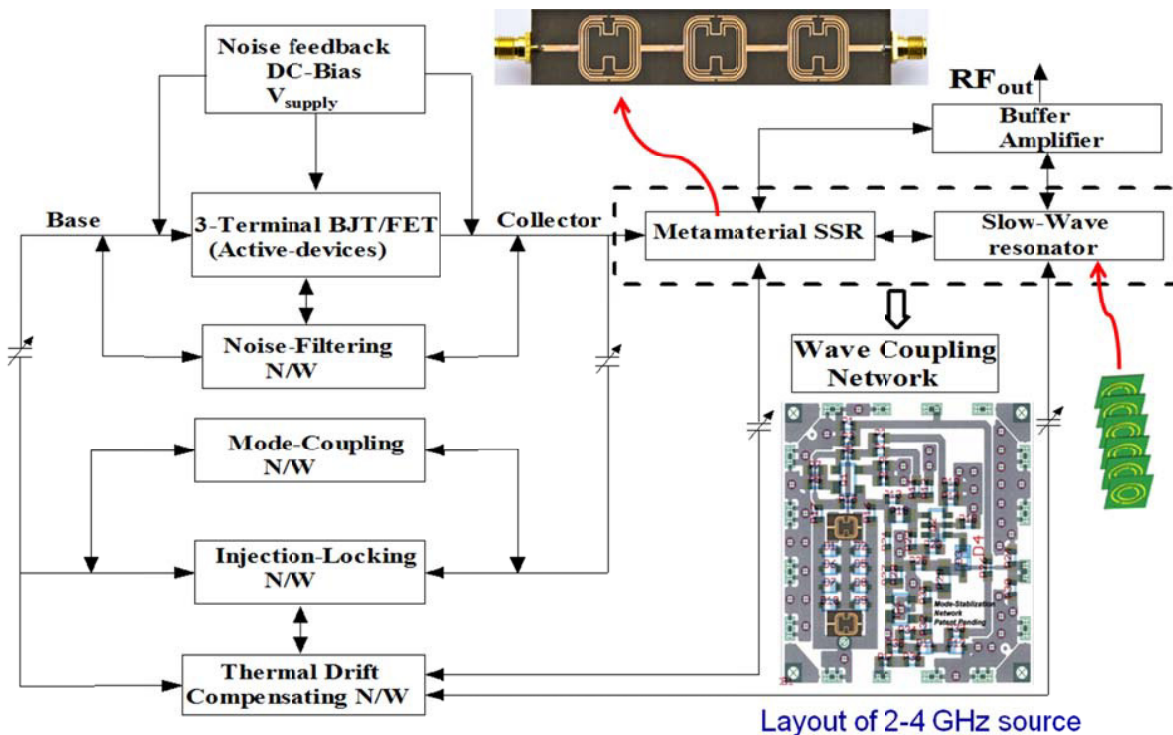
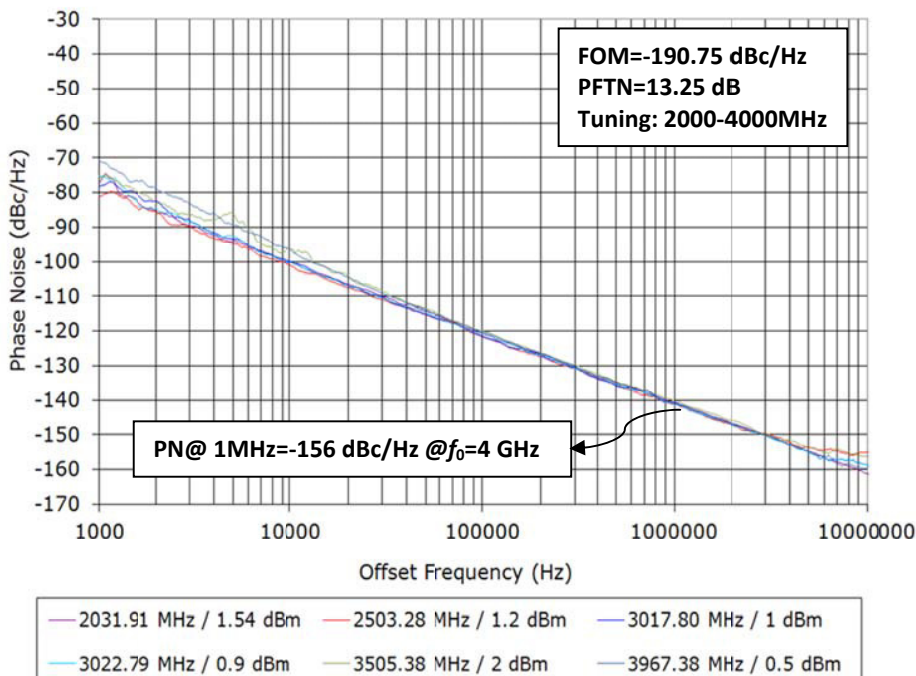


Figure: 8-22 (a): A typical block diagram of Metamaterial slow-wave resonator (SWMR) oscillator, layout of oscillator circuit is realized using 20 mils RT/Duroid 5880 with  $\epsilon_r = 2.2$ .

### Measured Phase Noise Plot of 2- 4 GHz source



### Layout of 2-4 GHz source

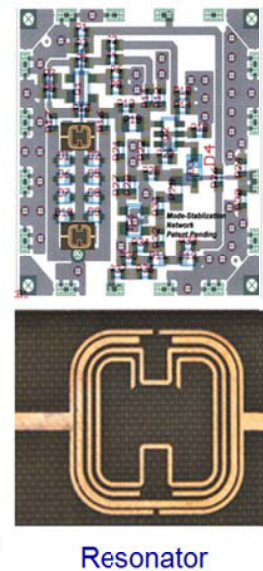


Figure 8-22 (b): Measured Phase Noise Plot of 2-4 GHz Metamaterial slow-wave resonator (SWMR) oscillator, measured figure of merit (FOM: defined in Ch-1, Eq. 1.1) is -190.75 dBc/Hz for a given power-frequency tuning normalized (PFTN: defined in Ch-1, Eq 1.2) 20.26 dB, with power consumption of 120mW ( $V_{cc}=5V$ ,  $I_c=24mA$ ), o/p power is typically better than +3dBm.

Attempts to develop multiband VCOs with low phase noise often yield large, power-hungry circuits. Numerous techniques take aim at compact source solutions for multiple-band radio designs, including switching among separate VCOs, using intermodal multiple-frequency circuits, or switching among multiple resonators [130]. However, they are inevitably large, or power hungry, or with poor phase noise. For example, switched resonators suffer from the resistive and capacitive parasitic circuit elements associated with the switches. Mode switching has been used to select among multiple oscillation modes of resonant circuits, in ways that the losses and nonlinearities of the switches do not affect the steady state and phase-noise performance of the resonators. However, this approach does not involve concurrent generation of signals, and is limited in terms of achieving reduced source size, power consumption, and design cycle time.

Traditional band-select sources have incorporated multiple resonators, VCOs, or other tunable oscillators, but any band-selection switch inevitably degrades the performance of this type of multiband source. This new class of oscillator using Metamaterial slow-wave resonator network as shown in Figure 8-23 (a) synchronously generates the signals needed for multiple-band, multimode communications. They provide the performance of separate tunable oscillators with significantly reduced size and power consumption compared to separate oscillators, for use in multiple-band, multimode wireless communications systems. The VCO circuit showed in Figure 8-23 (a) works without multipliers or switching among resonators and/or oscillators. This is why they reduce the complexity, size, and power consumption compared to other multiple-signal-generation methods along with good phase-noise performance [148].

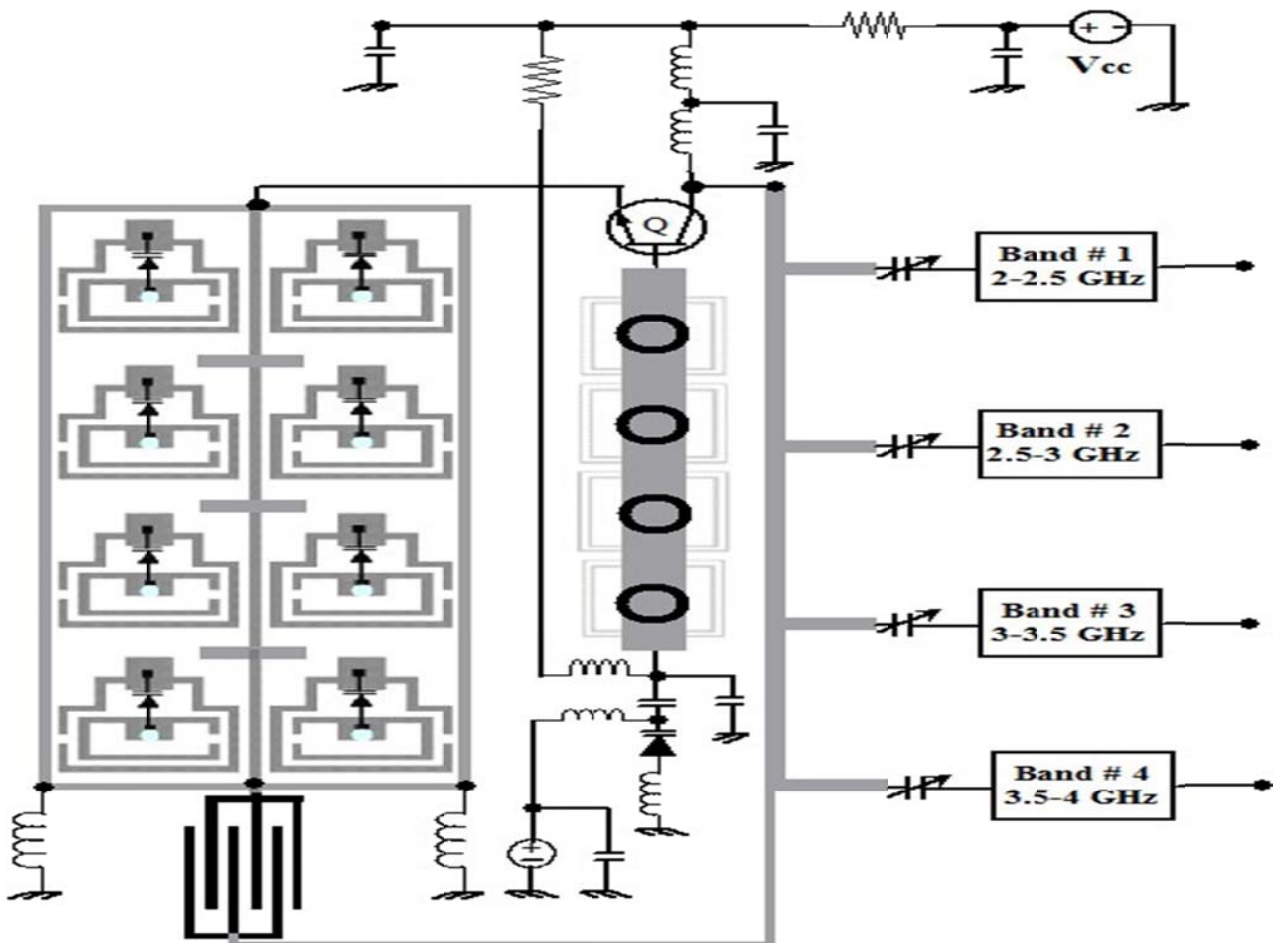


Figure: 8-23 (a): A typical layout of multi-band oscillator using evanescent mode Metamaterial resonator network realized using 20 mils RT/Duroid 5880 with  $\epsilon_r = 2.2$

The CAD simulated phase noise plots (Figure 8-23 (b)) of the prototype source (Figure 8-23 (a)) is typically better than  $-130\text{dBc/Hz}$  @  $1\text{MHz}$  from either carrier range. The measured phase noise plots shown in Figure 8-23 (c) agree with the CAD simulated data within reasonable degree of accuracy (3-5 dB variation). The multiple-band VCOs requires only  $+5\text{ VDC}$  and  $20\text{ mA}$ , and delivers  $+3\text{ dBm}$  typical output power for Band #1 (2-2.5 GHz), Band #2 (2.5-3 GHz), Band #3 (3-3.5GHz), and Band #4 (3.5-4 GHz). For multimode, multiple-frequency-band wireless equipment, this one source (Figure 8-23 (a)) may be the match of traditionally many VCOs; WLANs are the most popular of wireless applications, in home and office environments, operating within different frequency bands, notably within the Industrial-Scientific-Medical (ISM) band from 2.4-2.5 GHz and various bands from 5.15- 5.85 GHz.

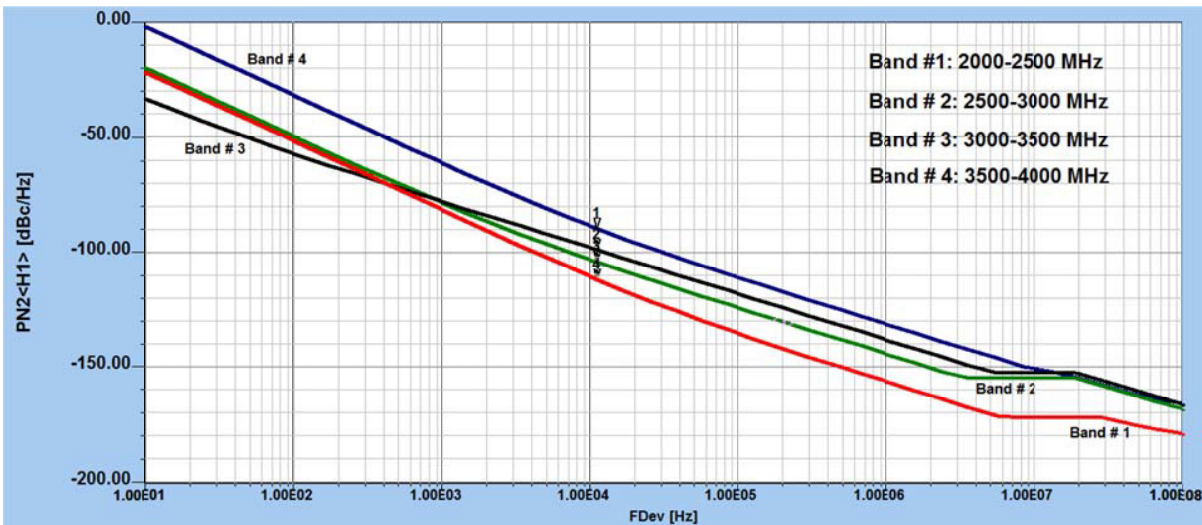


Figure 8-23 (b): CAD simulated Phase Noise Plot of multi-band Metamaterial slow-wave resonator oscillator, predicted phase noise @  $1\text{MHz}$  offset is  $-130\text{dBc/Hz}$  for Band #1 (2-2.5 GHz), Band #2 (2.5-3 GHz), Band #3 (3-3.5GHz), and Band #4 (3.5-4 GHz)

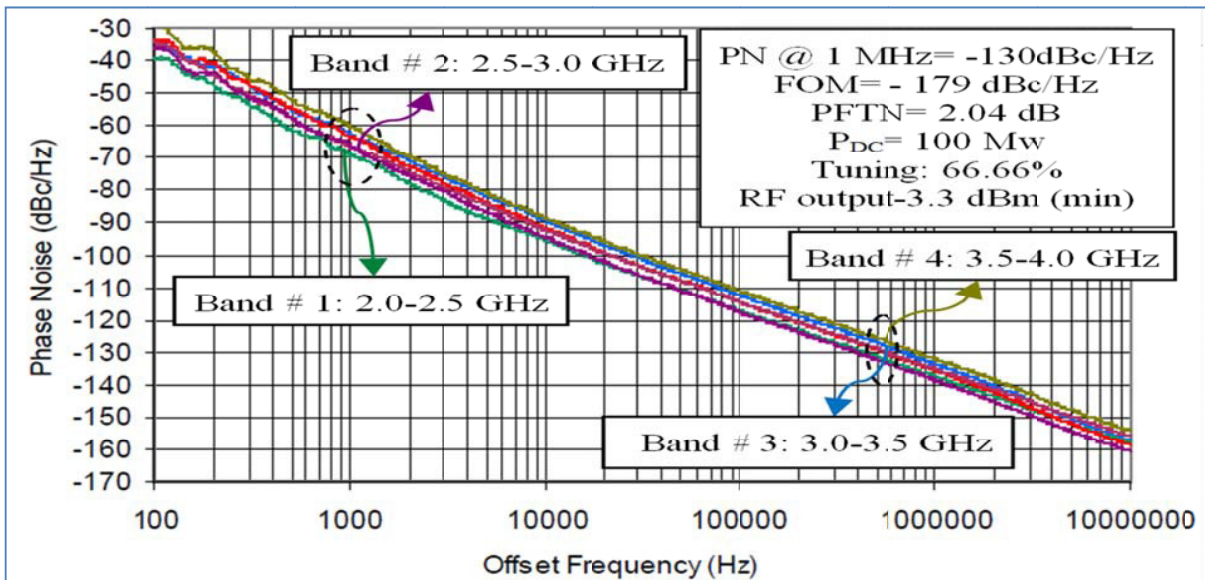


Figure 8-23 (c): Measured Phase Noise Plot of multi-band Metamaterial slow-wave resonator based oscillator circuit, measured figure of merit (FOM: defined in Ch-1, Eq. 1.1) is  $-179\text{ dBc/Hz}$  for a given power-frequency tuning normalized (PFTN: defined in Ch-1, Eq.1.2)  $2.04\text{ dB}$ , with power consumption of  $100\text{ mW}$  ( $V_{cc}=5\text{V}$ ,  $I_c=20\text{mA}$ ), o/p power is typically  $3.3\text{ dBm}$ .

The basic principle of a multimode radio is to process two or more signals of differing frequencies at the same time, using only one transmit/receive signal-processing chain. Figure 8-24 shows a frequency plan for a dual-band, 2.4-GHz/5-GHz WLAN transceiver system. It is based on a single 8-GHz VCO with a divide-by-two divider in a frequency synthesizer to generate a 4-GHz signal. This is followed by divide-by-four divider to reach 1 GHz. These in-phase (I) and quadrature (Q) signals are mixed in a quadrature single-sideband (SSB) mixer to produce the 5-GHz signal, which is further divided to obtain the 2.4-GHz signal. This approach requires multiple buffer, divider, and filter stages to produce signals for a dual-band WLAN radio. The multiple signals could also be generated by starting with lower-frequency signals and adding multipliers. Nevertheless, in cases where quadrature frequency converters are used, multiplication is rarely used for the final stage of frequency conversion, given the difficulty of working with differential outputs at higher frequencies.

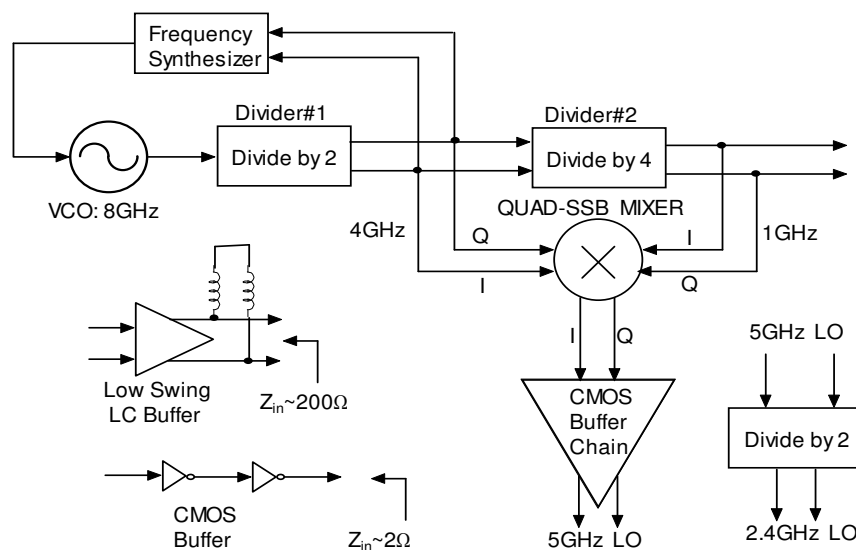


Figure 8-24: Frequency plan for a 2.4/5 GHz WLAN transceivers

Conventional single-output oscillators generate periodic waveforms, essentially a single frequency and its harmonic signal components. Tunable oscillators based on higher-order resonators can provide multiple modes of oscillation and can generate multiple, independent frequencies, individually or simultaneously [75]-[101]. A single-output tunable oscillator is a good starting place to design a multiple-band oscillator. A single-frequency tunable wideband oscillator incorporates a varactor-tuned second-order resonator network to generate a signal at a desired frequency. It employs an active device, such as a bipolar transistor, terminated in a parallel or series inductive-capacitive (LC) resonant-tuned circuit. A parallel LC resonator network exhibits a high parallel resistance (or anti-resonance) while a series LC resonator network provides a low series resistance (or resonance). Such a design will inevitably be limited by the capabilities of the transistor, the electrical contributions of its package, and the large change in capacitance needed to tune the oscillator over a broad frequency range [69]-[89].

A multimode, multiple-frequency oscillator will require more than a simple parallel LC network and an active device. An oscillator circuit that can produce two simultaneous frequencies must be capable of simultaneous negative resistance values at two distinct frequencies, and a higher-order resonator is needed for that purpose. The order of the resonator is dependent upon the number of different frequency signals/bands desired. Whereas a simple second-order resonator network produces one frequency, a fourth-order resonator network can produce two simultaneous frequencies. The trick in designing such an oscillator is learning the values of negative resistance needed to support the multiple separate frequency bands, and this information can be found by performing network analysis. Such analysis contributed to the



design of the multimode, multiple-frequency oscillator unveiled in Figure 8-23 (a). The filters employed in the multimode oscillator are meant to assist with mode leakage, such as when the oscillator circuit oscillates in dual modes. The amount of mode leakage from a given design will depend on the spectral selectivity of the succeeding filter for that portion of the circuit and the design requirements for VCO.

### 8.8.3 MCSWMR (Mode-Coupled Slow-Wave Metamaterial Resonator) VCO

It is important to achieve low phase noise in various applications. The phase noise increases a bit error rate in telecommunication links, degrades stability of beam in particle accelerators and decreases sensitivity of radars. DROs represent an interesting solution to improve the stability by reducing the bit error rate because high quality factor of a Dielectric Resonator (DR) allows for achieving an excellent phase noise performance at microwave and millimeter wave frequencies. Dielectric resonators are ceramic materials, which have high dielectric permittivity, high quality factor, and high temperature stability, have a much smaller size compared to cavity resonators; therefore, they are frequently employed in the design of frequency stable RF circuits, especially in oscillators. When high data-rates have to be transferred, as with M-QAM modulation in LTE, LMDS, and fixed frequency point-to-point digital radio and satellite-links, these systems need low phase noise signal sources either free running or phase-locked. RADAR systems and Research Laboratories also require ultra-low noise sources to generate ultra-low noise carrier signals.

A wide range of military, industrial, medical, test and measurement markets demand these very stable frequency sources with enhanced phase noise performance and low thermal drift. A popular solution in the range of 3 to 30 GHz frequency spectrum is the dielectric resonator oscillator (DRO), recognized for its superiority in ultimate noise floor and spectral purity when compared to other competing solutions such as multiplied lower frequency fundamental sources. A novel mode-coupled self-injection locked VCO is developed in response to replacing expensive DRO (Dielectric Resonator Oscillator) for reference signal sources for modern communication systems. One of the problems related to the Dielectric Resonator (DR) is fabrication in integrated circuit (IC) form due to its 3-D structure. Mode-coupled slow-wave metamaterial resonator approach described in this thesis offers cost-effective and integrable alternative for DRO circuits. For example, the typical measured phase noise for 10.21 GHz carrier frequency at 10 kHz offset is  $-109$  dBc/Hz with 300 MHz tuning in  $0.75 \times 0.75 \times 0.18$  inch circuit board size. The reported topology is not limited to this frequency, and can be extended to other frequency bands (2 GHz to 24 GHz with 500 MHz or more tuning range) by dynamically controlling mode-coupling mechanism.

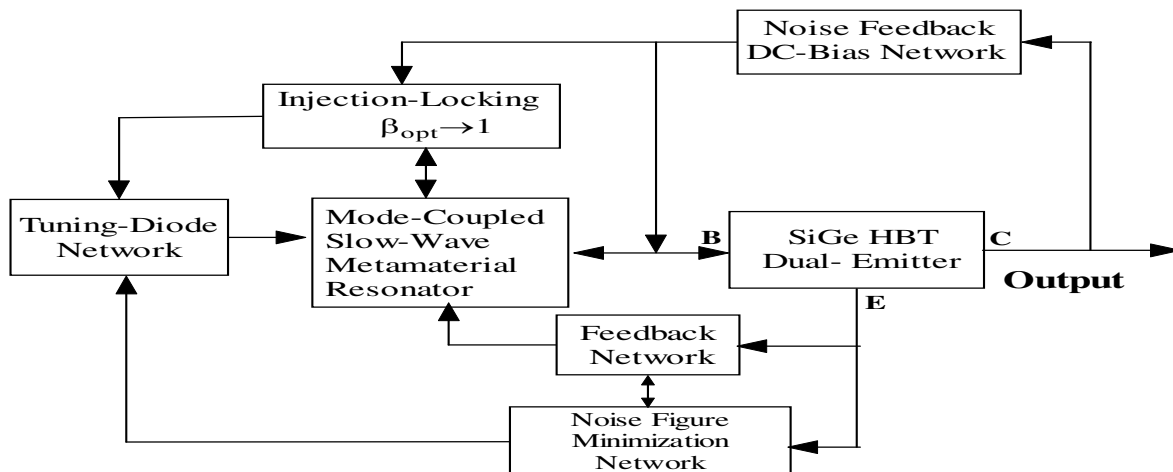


Figure: 8-25: shows block diagram of 10.2GHz MCSWMR (Mode-Coupled Slow-Wave Metamaterial Resonator) VCO

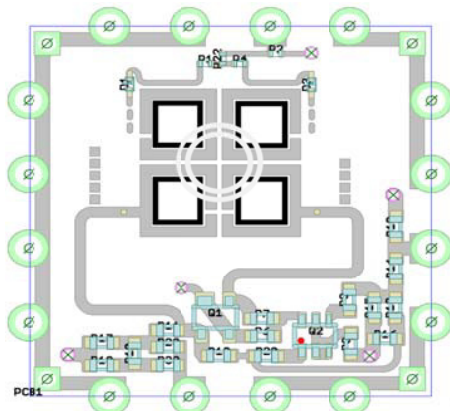


Figure: 8-26: A typical layout of 10.2GHz MCSWMR (Mode-Coupled Slow-Wave Metamaterial Resonator) VCO realized using 20 mils RT/Duroid 5880 with  $\epsilon_r = 2.2$ , PCB size is 0.75x0.75/0.18 inches

Figures 8-25, 8-26, and 8-27 show the typical block diagram, layout, and measured phase noise plot of the 10.2 GHz VCOs using a SiGe Heterojunction-bipolar-transistor (HBT) active device that was fabricated on Rogers substrate material with a dielectric constant of 2.2 and thickness of 20mils (microstripline/stripline) for the validation of the new approach. The oscillator topology for such applications can use supply voltage between +5 to +10 V and the internal voltage regulation gives high immunity to power supply noise. The supply-current is typically 20 mA and the temperature range is specified from -40°C to +85°C. For this particular oscillator circuit layout (Figure 8-26) a DC bias of 10 Volt and 30 mA was provided, the measured output power exceeds +5 dBm. As shown in Figure 8-27 (a), there is hump between 40 kHz and 1 MHz; and dip at 1 MHz offset from the carrier, possibly due to the resonator's multi-mode resonance and mode-jumping phenomena. By incorporating multi-mode-injection-locking, hump can be suppressed and stable oscillation can be guaranteed. Figure 8-27 (b) shows the measured phase noise plots; illustrating the clean signal (without hump in phase noise plot). The measured figure of merit (FOM: defined in Ch-1, Eq. 1.1) is -202.4 dBc/Hz for a given power-frequency tuning normalized (PFTN: defined in Ch-1, Eq. 1.2) -14.1 dB, with power consumption of 300mW ( $V_{cc}=10V$ ,  $I_c= 30$  mA), and output power of +10.05 dBm. The novel oscillator circuit is large in size (0.75x0.75x0.18 inches) but stable over operating temperature of -40°C to +85°C, providing sufficient margin for compensating the frequency drift caused due the change in operating temperature, including the package parasitic and component tolerances. For application requiring compact size VCO, different types of printed resonator using MCSWMR topology is developed and validated for current and later generation signal source applications.

#### 8.8.4 Examples: Compact Size MCSWMR VCOs

Similar to crystal oscillators, DROs (dielectric resonator oscillators) tend to be prone to vibrational noise since the dielectric resonator itself cannot be secured mechanically. Therefore, vibrations must effectively be damped by other means before they reach the dielectric resonator. The tiny MCSWMR VCO is designed with rugged construction to minimize vibration noise and microphonic effects to prevent unwanted modulation. Its excellent phase noise performance makes MCSWMR VCOs well suited for low-jitter communication systems, reference oscillators for phase noise measurement, RADAR systems, SDH/SONET, cable TV, SATCOM systems, aeronautical equipment, digital radios (QAM) and laboratory frequency references [90]-[102]. Custom frequencies and packages (hermetic) can be developed on request. Figure 8-28 (a) and (b) shows the typical layout of MCSWMR resonator for the realization of MCSWMR VCO in 0.25"x 0.25" x 0.08" inches square package. Figure 8-29 (a) to (f) shows the layout of the various SMD (surface mounted device) version of 0.5"x 0.5" x 0.18" inches square package developed for low cost signal source applications. Figures 8-30 – 8-35 shows the CAD simulated phase noise plots of oscillator circuits using different configuration of planar resonator topologies.

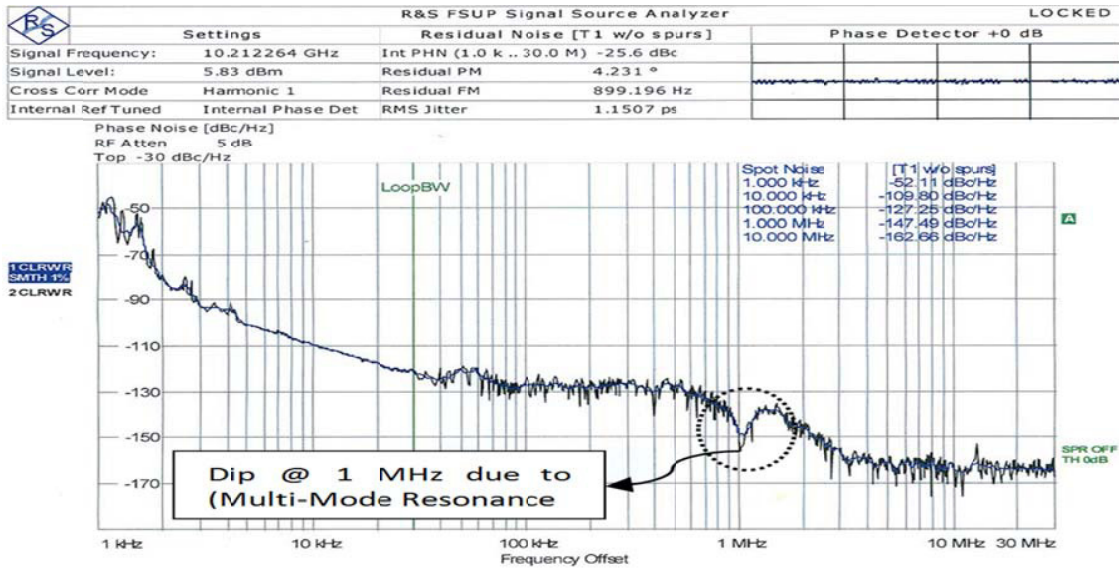


Figure 8-27 (a): Measured Phase Noise Plot of mode-coupled metamaterial slow-wave resonator oscillator

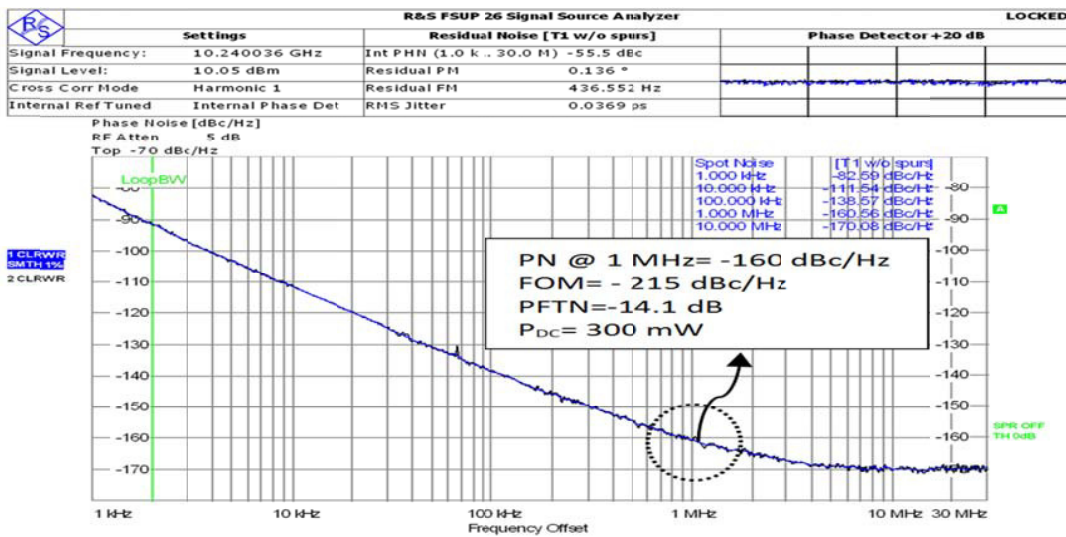
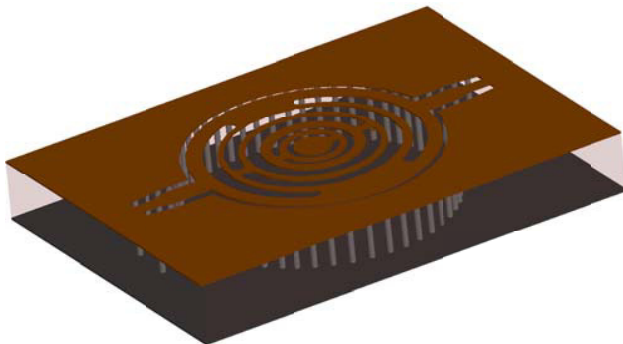
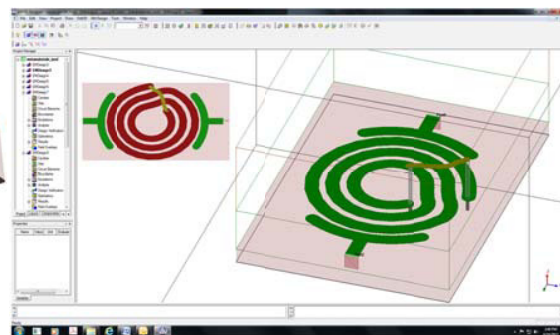


Figure 8-27 (b): Measured Phase Noise Plot mode-locked 10.2GHz oscillator (hump in Figure 8-27 (a) is suppressed)



(a) 3-D layout of planar metamaterial SWMR



(b) A screen shot of HFFS schematic of Möbius structure

Figure 8-28: A typical layout of MCSWMR in 0.25x0.25 inches size for the realization of MCSWMR VCO in 0.25" x 0.25" x 0.08" inches package (20-mil RT/Duroid 5880 with  $\epsilon_r = 2.2$ ): (a) slow wave resonator, and (b) Möbius coupled slow-wave resonator

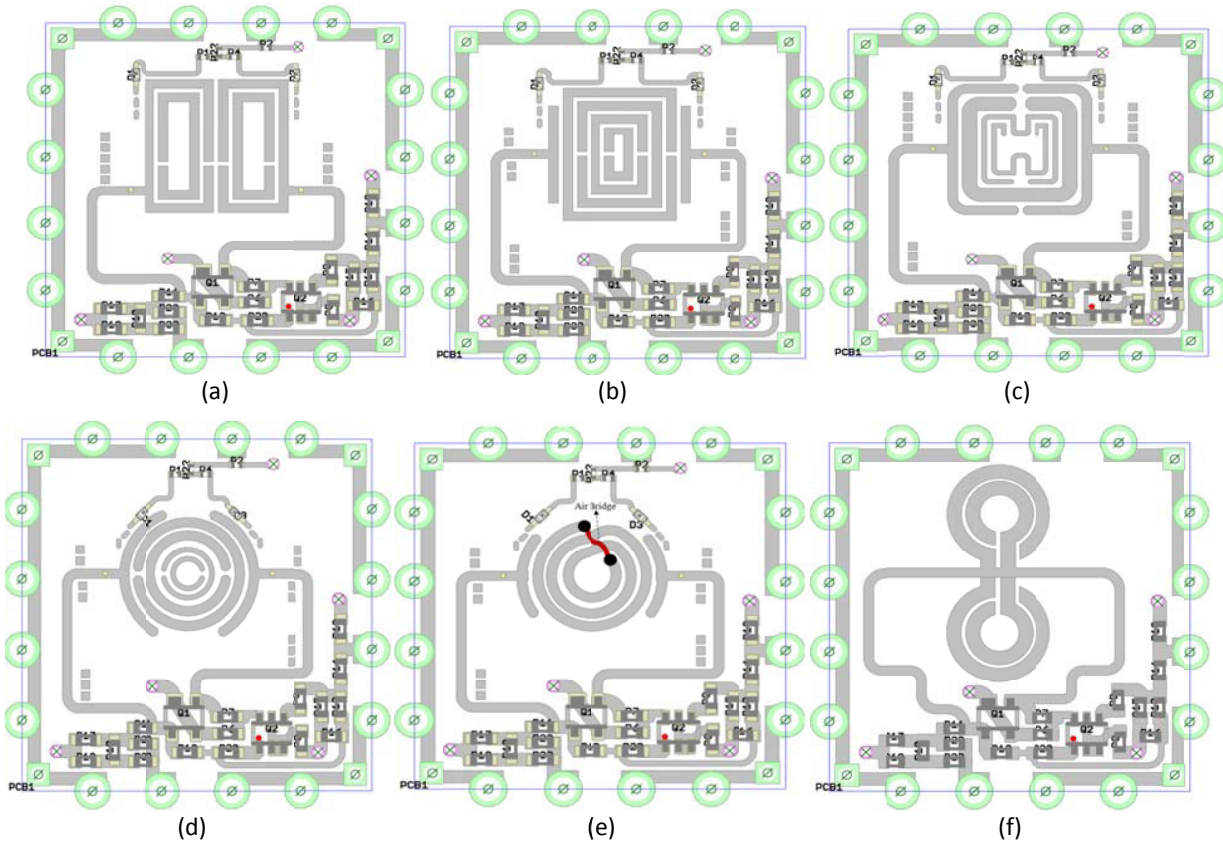


Figure 8-29: Layout of the SMD (surface mounted device) version of 0.5"x 0.5" x 0.18" inches square package are developed for low cost signal source applications: (a) 3.2 GHz Oscillator, (b) 4.7 GHz Oscillator, (c) 8.2 GHz Oscillator, (d) 12.2 GHz Oscillator, (e) 14.2 GHz Oscillator, and (f) 18 GHz Oscillator (22mils, 2.22 dielectric constant)

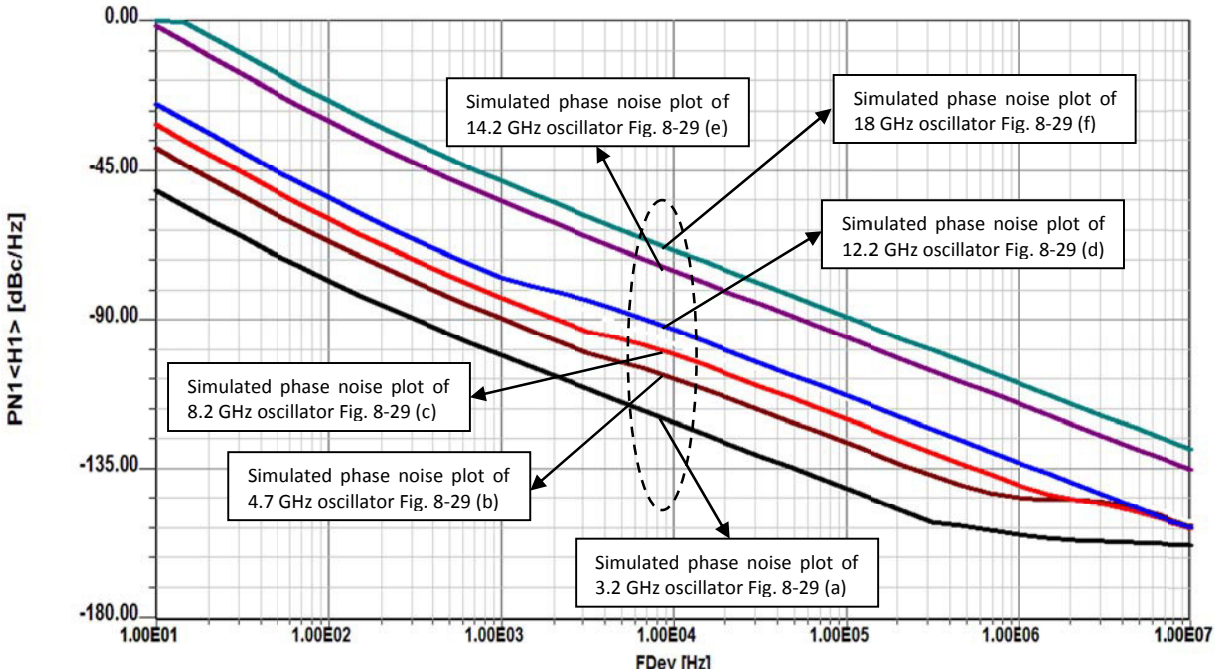


Figure 8-30: CAD simulated phase noise plot of Metamaterial Resonator Oscillator circuits as shown in Figure 8-29



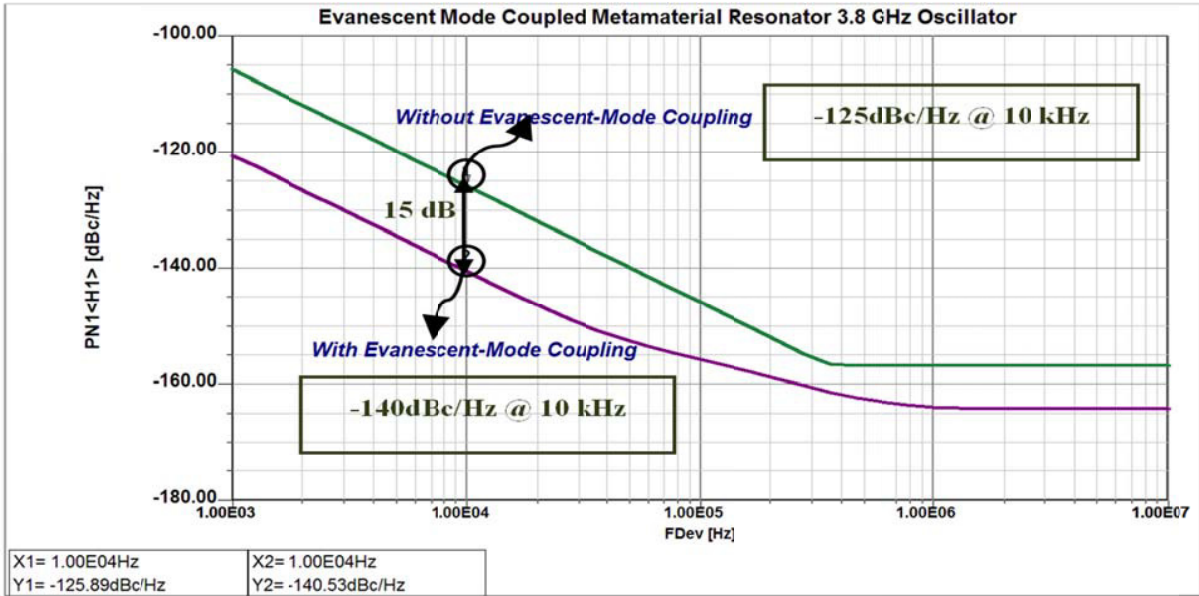


Figure 8-31 (b): CAD simulated phase noise plots of oscillator circuit shown in Figure 8-31 (a), it can be seen that evanescent mode coupling improves the oscillator phase noise by 15 dB

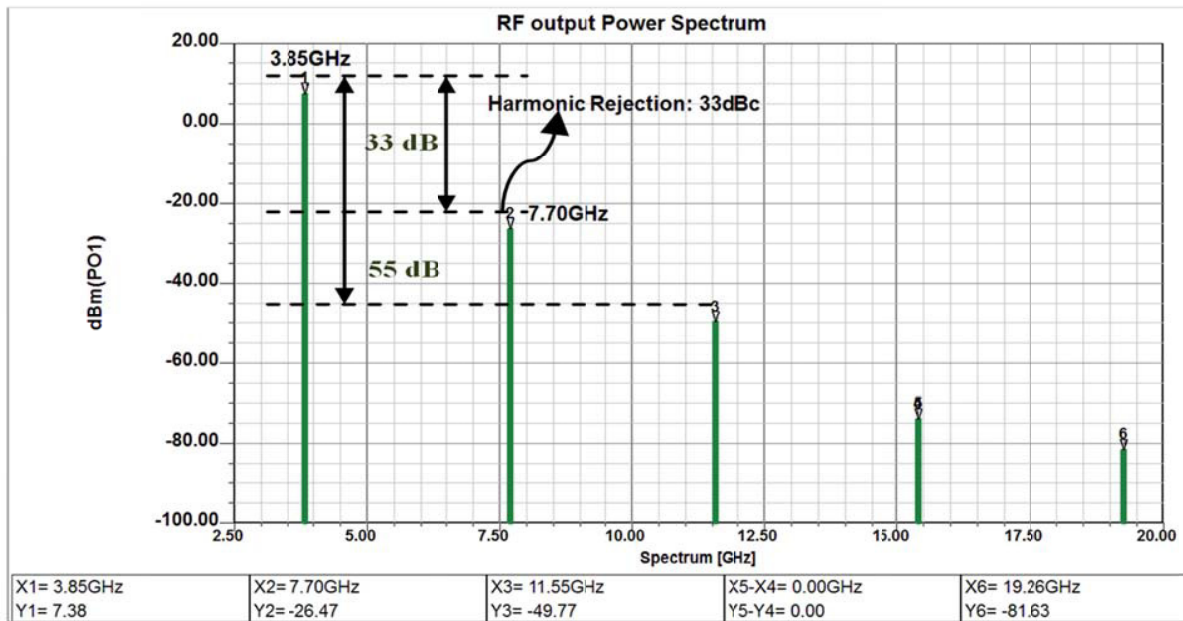


Figure 8-31 (c): Simulated RF output of oscillator circuit depicted in Figure 8-31 (a), it can be seen that evanescent mode coupling improves the 2<sup>nd</sup> and 3<sup>rd</sup> harmonic rejection level more than 33 dB and 55 dB respectively.

#### 8.8.4.2 Example: 7 GHz Evanescent-Mode Phase-Injection Mode (EMPIMC) Oscillator

Figure 8-33 (a) and 8-33 (b) show the typical 7 GHz oscillator circuit schematic of cascaded 3 and 5-resonators for the optimization of differential phase injection locking, thereby improving the phase noise and operating tuning ranges [150]. The design objective was to improve the Q value of the metamaterial resonator by cascading a progressive wave evanescent mode-coupled resonating network (to lower the phase noise without compromising the tuning range [145]-[152]. Figure 8-33 (c) shows the CAD simulated phase noise plots of oscillator circuit illustrated in Figure 8-33 (b), it can be seen that phase-injection-locking improves the oscillator phase noise by 50 dB [147].

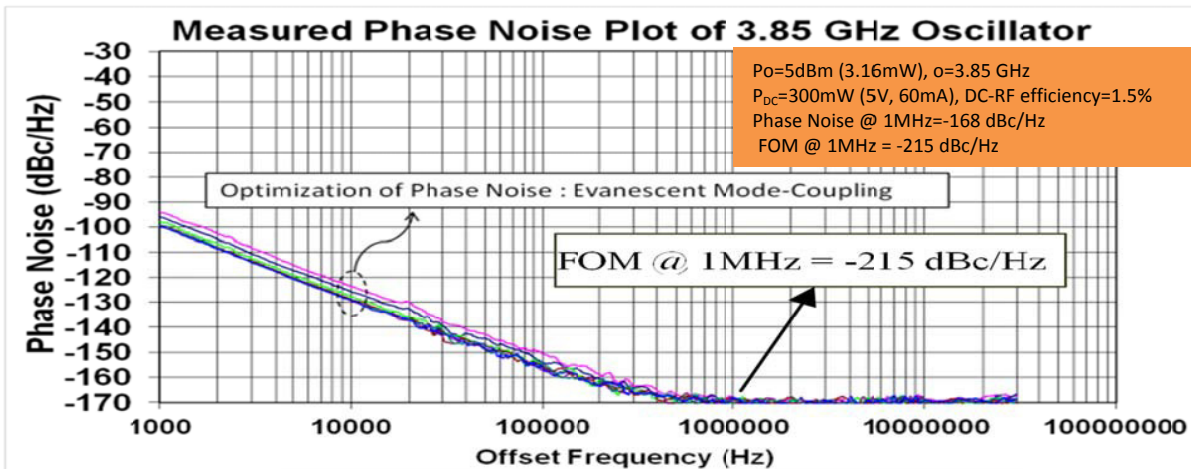


Figure 8-31 (d): The measured phase noise plots of oscillator shown in Figure 8-31 (a) phase noise plots illustrate 5-8 dB improvement depending upon of the level of coupling strength for a given phase-injection and modes.

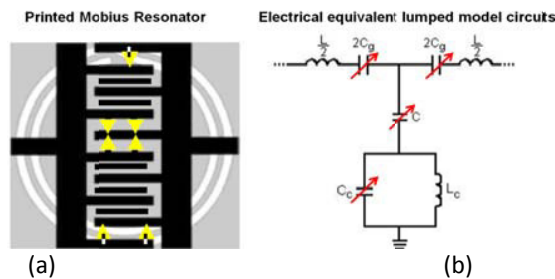


Figure 8-32: A tunable Metamaterial based Möbius resonator: (a) layout, and (b) electrical lumped model circuit [147]

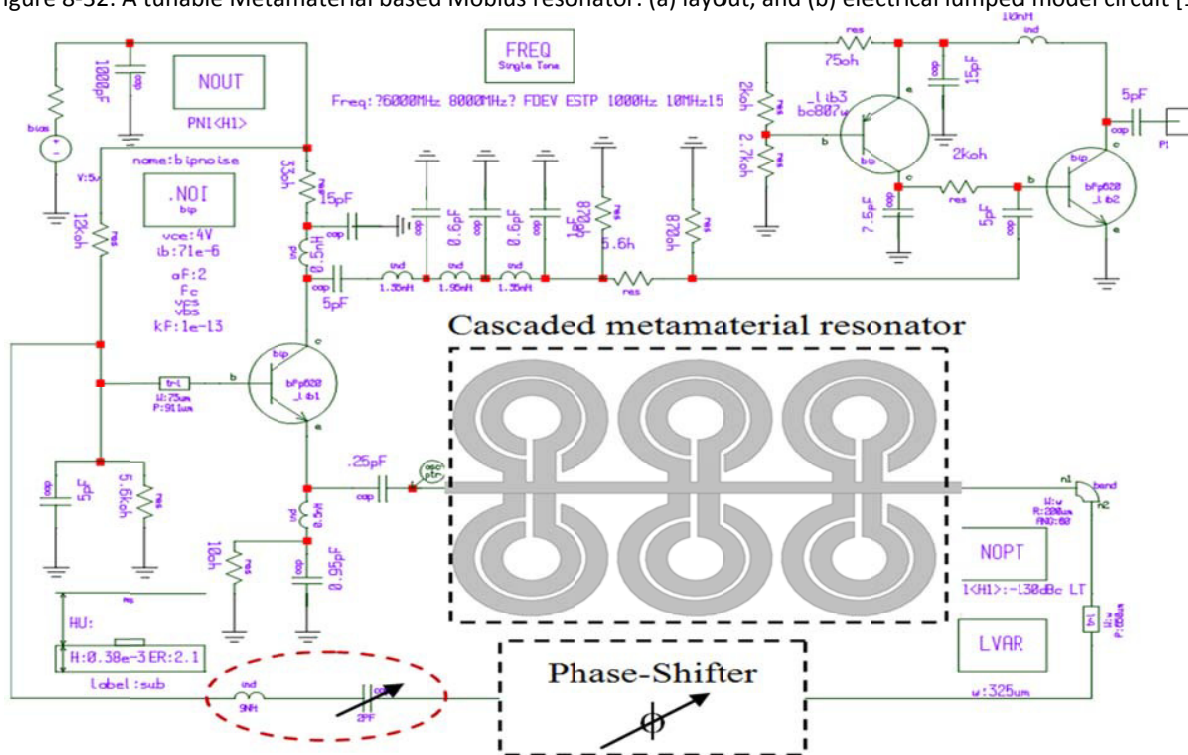
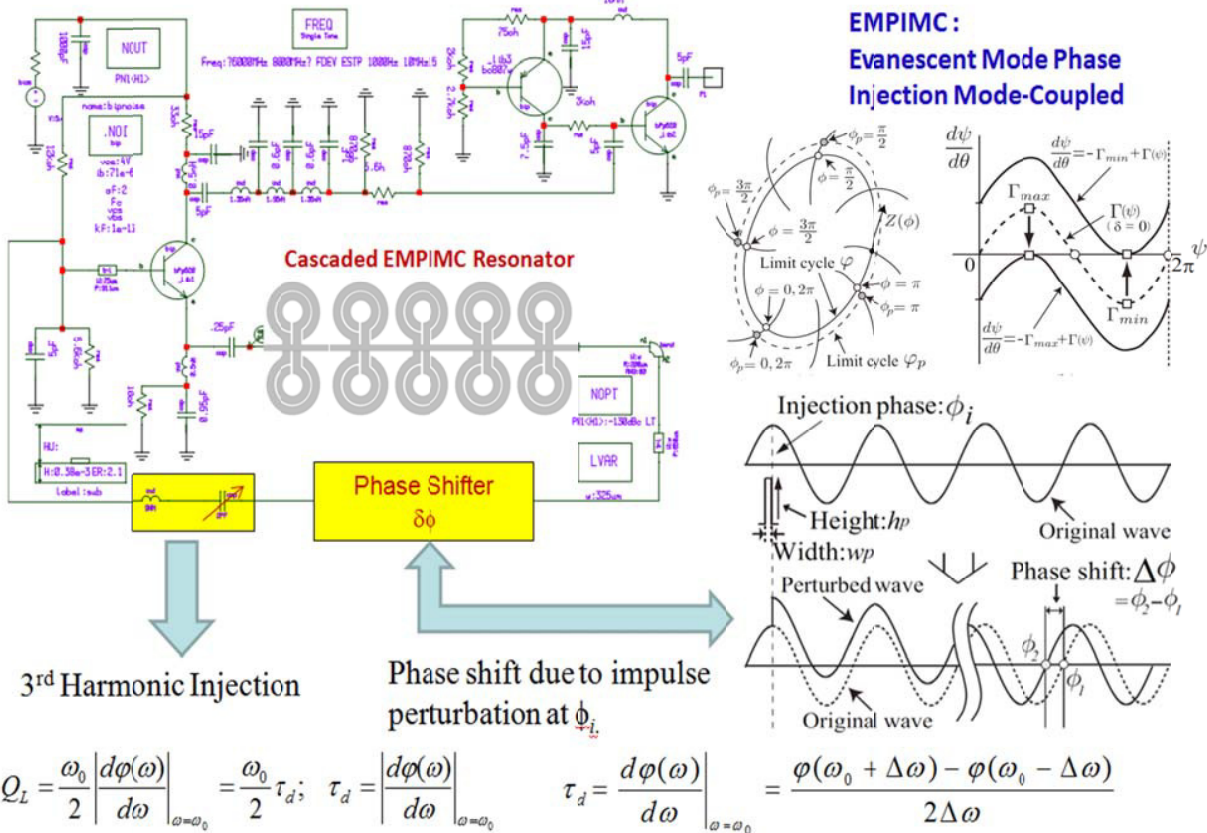


Figure 8-33 (a): A typical 7 GHz oscillator circuit schematic using 3-section cascaded evanescent mode-phase-injection-locked metamaterial resonator (Patent Pending, US Patent Application: 61976185) [145]-[148]



where  $\phi(\omega)$  is the phase of the oscillator's loop TF at steady state and  $\tau_d$  is the group delay of the metamaterial Möbius strips resonator

Figure 8-33 (b): A typical 7 GHz oscillator circuit schematic using 5-section cascaded evanescent mode-phase-injection-locked metamaterial resonator (Patent Pending, US Patent Application: 61976185) [146]-[147]

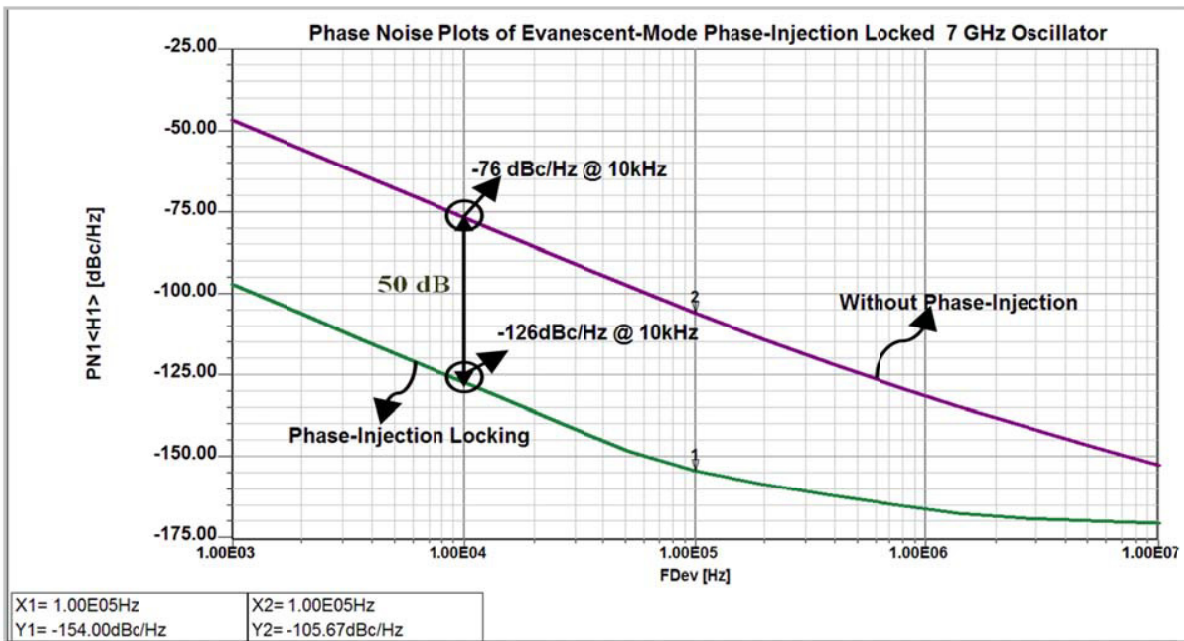


Figure 8-33 (c): CAD simulated phase noise plots; phase-injection-locking improves the phase noise by 50 dB [147].



As shown in Figure 8-33 (c), phase-injection-locking improves the oscillator phase noise by 50dB. It is to note that cascading improves the Q-factor of resonator; this is due to the fact that at resonant condition sharp change in permittivity and permeability causes significant increases in group delay, thereby Q-multiplier effect, though care must be taken to avoid or suppress the degeneration modes that limit the application below 20 GHz.

### 8.8.4.3 Example: Tunable Evanescent-Mode Phase-Injection Mode (EMPIMC) Oscillator

Figure 8-34 shows the typical circuit schematic of tunable progressive injection-locked metamaterial resonator based oscillator topology.

Figure 8-35 (a) shows the CAD simulated phase noise plots, it can be seen that phase-injection-locking technique improves the oscillator phase noise by 30 dB. Figure 8-35(b) depicts the measured phase noise plots, it can be seen that phase noise plots illustrate typically 4-6 dB variation over the tuning range from 4.25 GHz to 5.1 GHz for a  $V_{tune}$  (0-12 Volt), which otherwise can be more than 10 dB variation in phase noise performance over the tuning range for simple transmission line resonator based oscillator. Figure 8-35 (c) shows the measured tuning characteristics, the oscillator tunes from 4.25 GHz to 5.1 GHz for a tuning voltage:  $V_{tune}$  (0-12 Volt), exhibits typical RF output power better than 3dBm with DC bias of 5V, 80 mA.

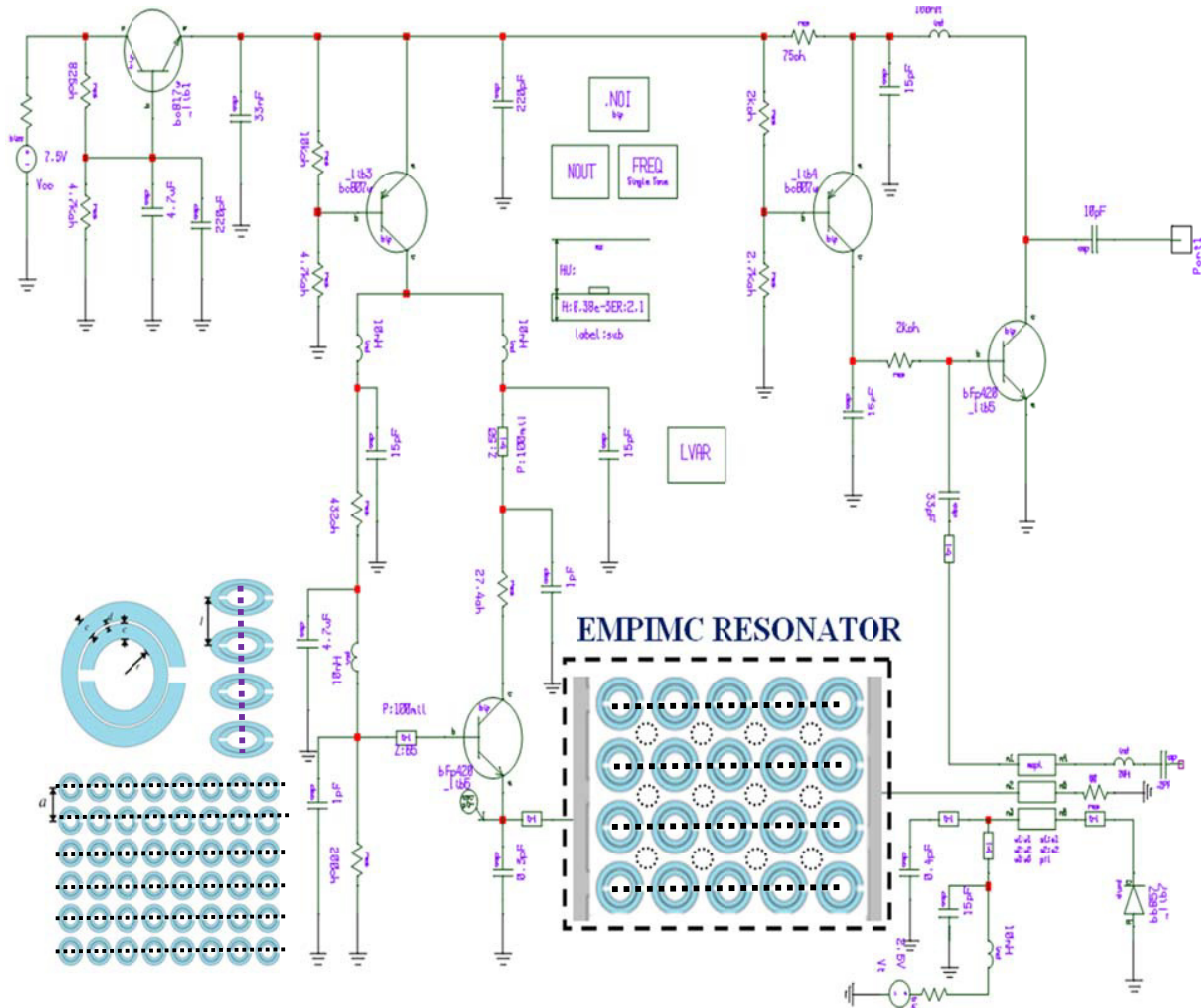


Figure 8-34(a): A typical tunable oscillator circuit using 2-dimensional cascaded injection-locked metamaterial resonator network (Patent Pending, US Patent Application: 61976185) [147]

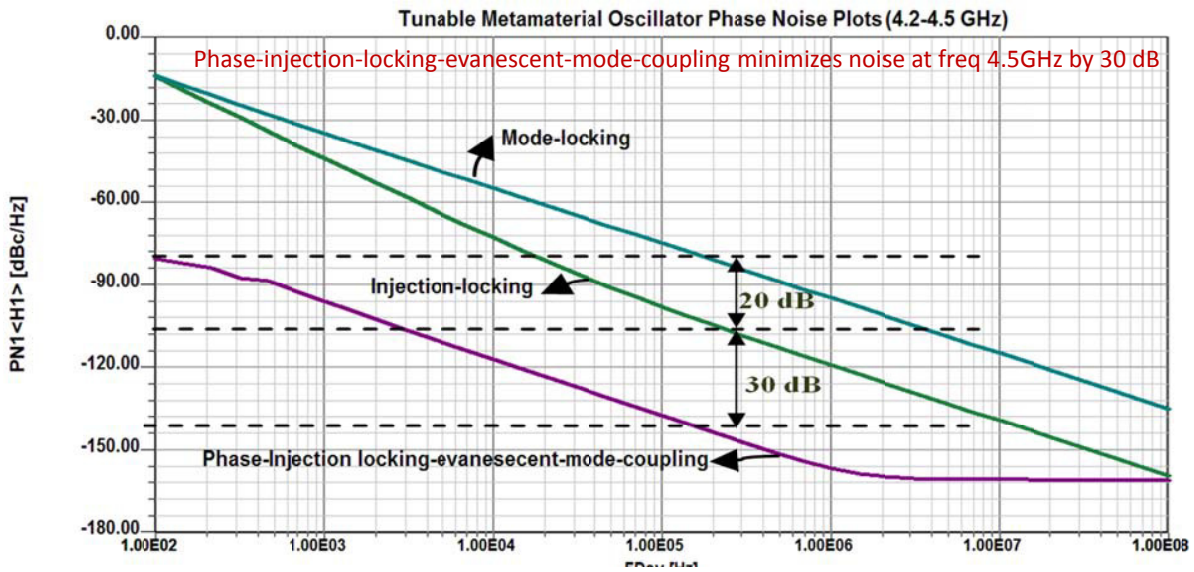


Figure 8-35(a): CAD simulated phase noise plots

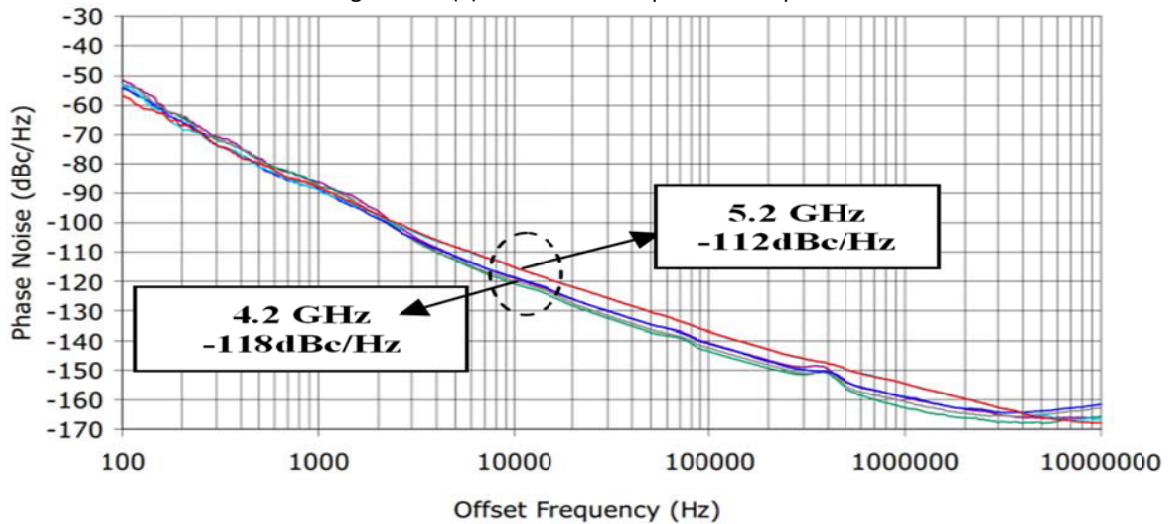


Figure 8-35(b): The measured phase noise plots, plots illustrate 4-6 dB variation from 4.25 GHz to 5.1 GHz

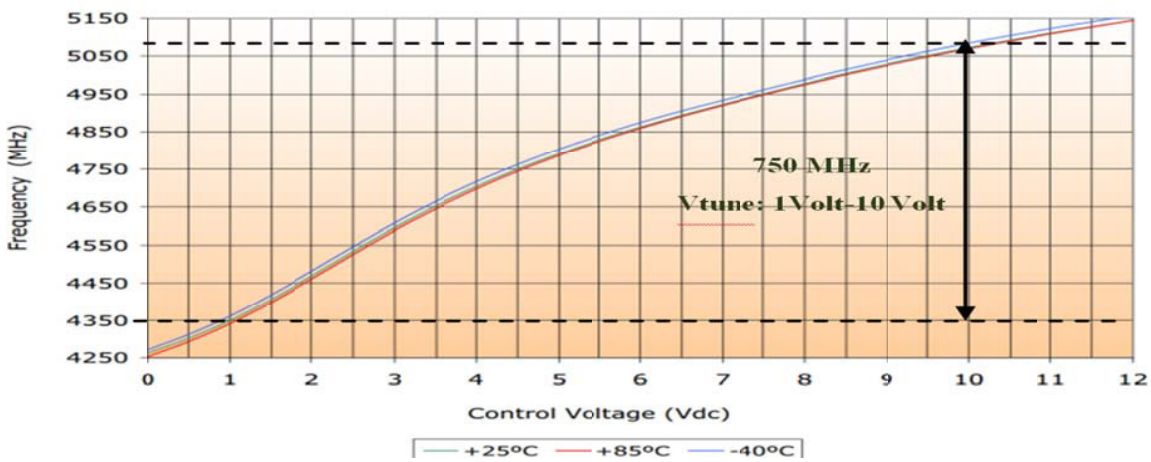


Figure 8-35(c): Measured tuning characteristics of the oscillator circuit shown in Figure 8-34 (a), the oscillator tunes from 4.35 GHz to 5.1 GHz for a  $V_{tune}$  (1-10 Volt) with DC power consumption of 5V, 80mA.

### 8.9 High Performance Frequency Synthesizer Using MCSWMR VCO

Frequency synthesizers are the essential signal sources for many high-frequency systems, from communications to test platforms. Synthesizers come in many forms, from tiny system-on-a-chip (SiC) devices to large rack-mount units [99]-[103]. The number of technologies used to implement them is almost as diverse as their package styles, relying on analog methods, digital techniques, and sometimes a combination of the two approaches [104]-[107]. For many applications, basic frequency synthesizer requirements call for a small unit with excellent spectral purity, but at an affordable price. These simple requirements drove the development of a new line of low-noise sources based on direct-digital synthesis (DDS) at a fraction of the size and cost of currently available commercial sources with comparable performance [142]. Regardless of package style and size, frequency synthesizers can be differentiated by a number of key performance specifications, including frequency tuning range (if not a fixed-frequency synthesizer), output power and output-power flatness across the tuning range, frequency switching speed, phase noise, harmonic levels, spurious levels, power consumption, and a number of other parameters [102]-[128]. Acceptable levels for these parameters are usually set by the application of interest, with something like fast switching speed, for example, being important in a frequency-agile communications system but not as important in other types of communications systems [103]. One of the more common types of synthesizer is a voltage-controlled oscillator (VCO) stabilized by a phase-locked loop (PLL). A conventional PLL-based frequency synthesizer includes a reference phase detector, loop filter, VCO, and VCO frequency divider (Figure 8-36) [104]. Equation (8.85) defines the relationship between the output frequencies,  $f_{out}$ , where N is the value of divider. From (8.35), the minimum output frequency step is  $f_{ref}/R$ . Operating the PFD and reference frequency [105]:

$$f_{out} = N \times \left(\frac{f_{ref}}{R}\right) \tag{8.85}$$

The phase-frequency detector (PFD) compares the two input signals  $f_{ref}/R$  and  $f_{out}/N$  and produces an error voltage proportional to the phase difference between them [146]. The loop filter removes the high-frequency noise components from the PFD's output and limits the bandwidth of the error signal. The filtered error voltage is applied to the tuning port of the VCO to stabilize its resulting tuned frequency; the error signal drives the VCO frequency ( $f_{out}$ ) so that the error voltage at the PFD output is zero when locked [106]. Typically, the VCO frequency divider is implemented as a dual-modulus counter to obtain large continuous division of the VCO output. To vary synthesizer output frequency,  $f_{out}$ , N is changed. From (8.85), the minimum output frequency step is  $f_{ref}/R$ . Operating the PFD at a lower frequency makes it possible to achieve a smaller step, but also increases R and N and, in increasing N, the PFD noise also increases [107]. A PLL synthesizer's close-in phase noise is estimated by adding the noise of the synthesizer,  $PN_{SYN}$  to  $20\log N$  (where N is the divider value) and  $10 \log (f_{PFD})$ :

$$PN_{TOT} = PN_{SYN} + 10\log(f_{PFD}) + 20\log(N) = PN_{SYN} + 10\log\left(\frac{f_{REF}}{R}\right) + 20\log(N) \tag{8.86}$$

$$PN_{PD}[dBc/Hz] = PLL_{FOM} + 20\log_{10}(f_{VCO}) - 10\log_{10}(f_{PD}) ; \text{ (frequencies are in Hz)} \tag{8.87}$$

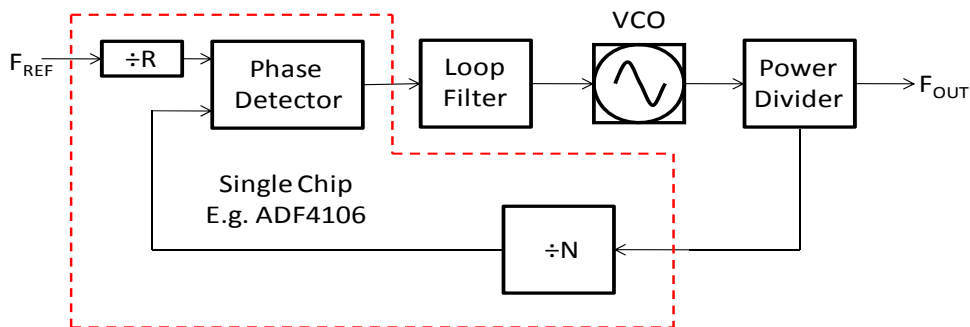


Fig.8-36: This block diagram shows a simplified PLL synthesizer module

These simple equations reveal, PLL synthesizer design is a matter of tradeoffs [108]-[142]. From [103],  $N$  should be low to minimize phase noise, but fine frequency resolution results from a PFD that is low in frequency, which leads to an increase in  $N$  and degraded noise performance. Loop filters can limit noise, but also prevent fast switching speed. A higher loop filter bandwidth yields faster switching speed, but allows noise to pass. A narrower loop filter cuts the noise level, but with slower switching speed. PLL frequency synthesizers can be implemented with integer or fractional values of  $N$ . Figure 8-37 shows the typical phase noise characteristics of integer frequency synthesizer (FSW50120-50, ref.128) that tunes from 500 MHz to 1200 MHz with the step size of 500 kHz, switching time of < 5ms. The typical spurious is -65 dB with 10 MHz reference frequency.

To improve the performance of the integer frequency synthesizer, divider “ $N$ ” can be implemented as a fractional divider instead of integer divider [131]. For example (as shown in Figure 8-38), a commercial fractional- $N$  source (LFSW160290-50, ref [128]), that tunes from 1600 to 2900 MHz in 500-kHz steps and works with a 10-MHz reference might have spurious levels of -60dBc and switching speed of 1ms. When better frequency resolution is needed, a DDS-based multi-loop synthesizer design can be used, such as in Figure 8-39. In this case the DDS clock is fed by a selectable frequency synthesizer, which provides a fixed set of frequencies based on the parallel selection lines. The DDS unit, with its resolution measured in microhertz, provides the fine frequency resolution. As with other frequency synthesizer design, a DDS has tradeoffs, notably poor spectral purity, and high spurious levels.

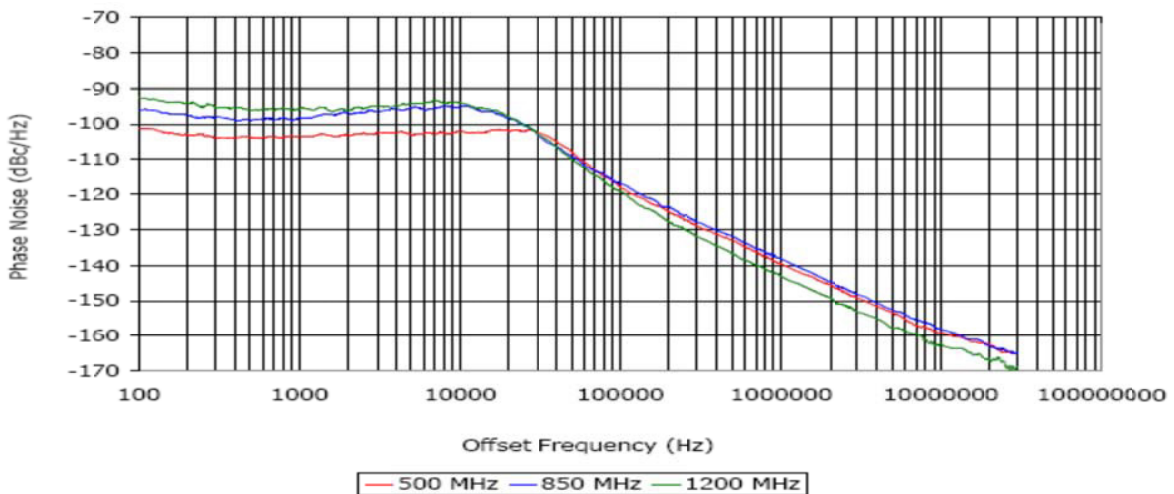


Figure 8-37: This phase-noise plot typifies the performance of an integer- $N$  PLL synthesizer

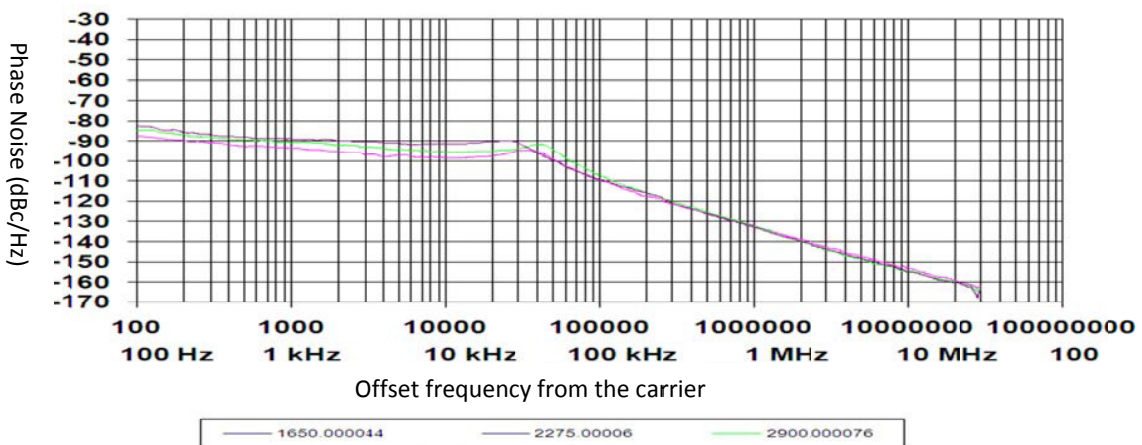


Figure 8-38: This phase-noise plot shows the typical performance of an fractional- $N$  PLL synthesizer.

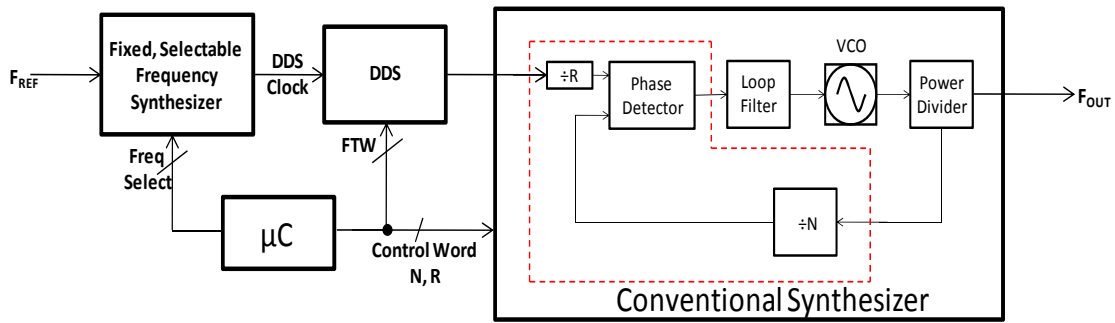


Figure 8-39: This block diagram shows a typical DDS-based dual-loop frequency synthesizer.

DDS spurious signal components that fall within the loop bandwidth are not attenuated by the loop filter. However, they can be predicted and moved in frequency by using a different DDS clock frequency [132]. With this approach, the PFD frequency of the output synthesizer can be high, improving phase-noise performance with a 10-MHz reference while still achieving 1-Hz frequency resolution. Such a design has switching speed of better than 1 ms with low phase noise and better than -70dBc spurious performance from 1.1 to 2.5 GHz. Figure 8-40 shows a typical block diagram for a DDS-based low-noise, fast-switching synthesizer based on a VCSO source. The typical synthesizer generates outputs ranging from 530 to 630 MHz with 1-MHz step size and spurious of -70 dBc or better. Since the analog phase detector has a low noise floor, the synthesizer bandwidth was kept large for faster switching time (about 200 microseconds) with low phase noise performance. With recent developments in frequency synthesizers, the DDS shown in Figure 8-40 can be replaced with a single-chip flying-adder-based synthesizer [106].

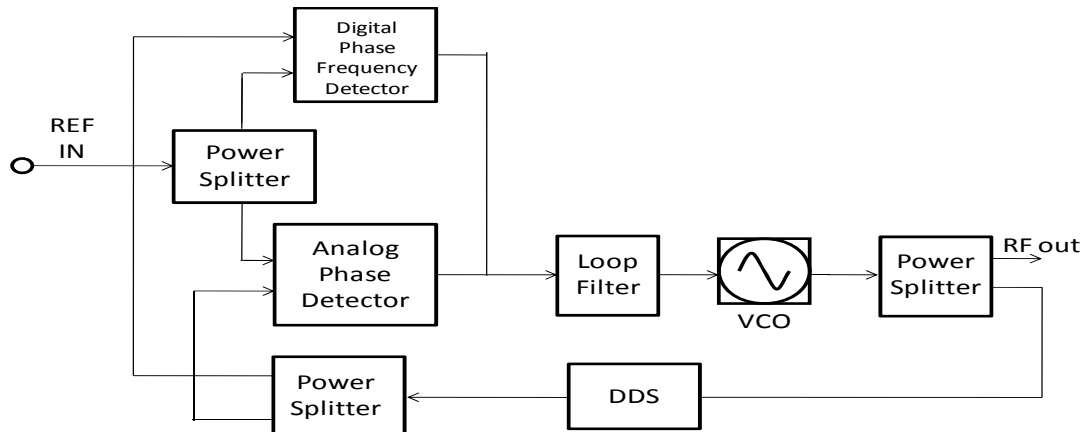


Figure 8-40: This is a block diagram of a typical fast-switching DDS-based frequency synthesizer.

A design challenge of developing a synthesizer was to provide high performance in a compact size (3.25 x 2.25 x 1.25 square in.) and be able to sell for low cost. The first consideration was to use an oscillator with octave tuning range of 4 to 8 GHz, as in ref [2]. Octave tuning allows division by two, and frequencies above 4 GHz could be successively generated. Unfortunately, process, voltage, and temperature variations would make it difficult to guarantee frequency with precision any better than a few MHz. In addition, synchronization techniques, such as locking the oscillator to a stable reference source such as an oven-controlled crystal oscillator (OCXO), would be needed for stabilization. As Figure 8-36 shows, a single-loop PLL can stabilize any frequency to the maximum oscillator's frequency. In this approach, the low-noise crystal oscillator's frequency is multiplied by the PLL to the desired output frequency. Because of frequency multiplication, a 20dB/decade degradation in phase noise is expected. For a 10-MHz crystal oscillator with phase noise of -174 dBc/Hz at 10kHz offset, the phase noise with multiplication at 8 GHz could not be better than -115 dBc/Hz. Taking advantage of PLL behavior, ideally the PLL loop bandwidth would be set to

the frequency where the -115 dBc/Hz multiplied noise floor of the crystal intersects the trace of the noise produced by the oscillator, about 400 kHz for a typical scheme [107]. This is rather idealized, since the phase detector and the frequency dividers used in this PLL can degrade the crystal noise floor by about 20 to 30 dB in commercial PLL ICs. The PLL contribution to the phase noise  $PN_{PLL}$  can be summarized as the root-mean-square addition of two components:  $PN_{PD}$ , a component determined by the phase detector comparison frequency and  $PN_{flicker}$ , a flicker component independent of the phase detector comparison frequency given in (8.86) and (8.87):

$$PN_{flicker}[dBc/Hz] = PLL_{flicker} + 20 \cdot \log_{10}(f_{VCO}) - 10 \cdot \log_{10}(f_{offset}); \text{ (freq. in Hz)} \quad (8.88)$$

In these equations, the  $PLL_{FOM}$  and  $PLL_{flicker}$  are determined by the PLL design choices, and usually provided by the PLL manufacturer, where  $f_{VCO}$  is the output frequency of the oscillator,  $f_{PD}$  is the phase detector comparison frequency, and  $f_{offset}$  is the frequency offset from the carrier used when estimating the phase noise. The noise added by the PLL circuit will then be:

$$PN_{PLL}[dBc/Hz] = 10 \cdot \log_{10} \left( 10^{\frac{PN_{PD}}{10}} + 10^{\frac{PN_{flicker}}{10}} \right) \quad (8.89)$$

A typical case with  $PLL_{FOM} = -220$ ,  $PLL_{flicker} = -250$ ,  $f_{VCO} = 8$  GHz,  $f_{PD} = 10$  MHz, and  $f_{offset} = 10$  kHz will result in  $PN_{PD} = -220 + 198 - 70 = -92$ ;  $PN_{flicker} = -250 + 198 - 40 = -92$  and the resulting  $PN_{PLL} = -89$  dBc. This is 26 dB higher than the -115 dBc/Hz contributed by the crystal oscillator considered above. For this circuit, setting the PLL bandwidth to about 20 kHz will result in the best phase-noise performance for any offset frequency. For an integer PLL, where frequency division is limited to integer numbers, the output frequency could only be set in 10-MHz increments. This is a serious limitation, since many applications require a smaller step size, say 1 Hz to 10 kHz. For an ideal noise floor of -174 dBc/Hz, with a 1 kHz comparison frequency at 8 GHz that noise multiplied results in a -36 dBc/Hz PLL noise floor. Even if such noise would be acceptable, the PLL loop bandwidth should be set to about 100 Hz, subjecting the design to high-level microphonic effects. Such a small loop bandwidth will also greatly increase the settling time of the PLL. Settling time is determined by loop bandwidth and the time needed to charge the loop filter's capacitors with limited charge pump current. A decent design with a 10-kHz loop bandwidth may use a 1-micro Farad capacitor in the loop. With a charge pump current of 5 mA, approximately 5 ms is needed to charge a 1-micro Farad capacitor to 25 V. Again, with a 10-kHz loop bandwidth, the minimum comparison frequency at the phase detector's input would be about 100 kHz limiting the step size to the same 100 kHz. This comparison frequency will ideally result in an 8-GHz output having a loop noise floor of -76 dBc/Hz when using a crystal oscillator with -174 dBm/Hz noise floor.

A fractional-N PLL helps overcome some of these limitations, dynamically changing the feedback ratio [135]. As a result, the average divide ratio becomes a fractional number. The major advantage of this technique is that the phase-detector comparison frequency does not change with step size. In the following example, the output frequency is 7999.9 MHz and the reference frequency is 10 MHz. The feedback divider divides 99 times out of 100 by 800 and divides 1 out of 100 times by 799. The average division ratio is 799.9, the output frequency is 7999.9 MHz and the phase detector comparison frequency is 10 MHz. The PLL phase noise is  $PN_{PLL} = -89$  dBc/Hz, as calculated above, a major advantage over an integer PLL which ideally would only give -76 dBc/Hz.

The drawback of this technique is the introduction of the fractional spurious product in the spectrum that has a repetition rate determined by the period needed to average the divide ratio,  $f_{spur} = 100$  kHz in the simple case presented above. Complex fractional-N PLLs will use higher-order DS modulation techniques to mitigate the spurious amplitude, while adding sub-fractional spurious content to the signal. Generally, a -40 to -60 dBc spurious amplitude is to be expected with this approach, and the PLL loop filter bandwidth must be reduced to attenuate the spurious content to an acceptable level. A PLL bandwidth of 10 kHz will impose a practical limit of about 100 kHz on the step size [101].

Spurs generated by the fractional-N PLL are caused by the inability of digital frequency dividers to position the transitions of the feedback clock with absolute accuracy in time [133]. The time resolution of the transition is equal with the period of the clock provided at the divider’s input. A DDS can overcome this limitation by adding a level of analog control to the transition [134]. By generating an analog sinusoidal wave, the position of the zero-crossings of the sine wave can be controlled with high accuracy, resulting in close-to-carrier spurious levels at -100dBc/Hz. It is worth mentioning that the DDS, or any fractional frequency divider, will exhibit a high spurious case when the input frequency of the DDS is close to a rational multiple of the output frequency. This spurious phenomenon is called “integer boundary spur” and is particularly difficult to eliminate. For frequency synthesis purpose, the DDS circuit could be considered as a low-noise frequency divider, and the output frequency of this DDS divider is given by

$$f_{DDS} = \frac{N}{2^k} f_{clk} \quad (8.90)$$

where  $f_{DDS}$  is the DDS output frequency,  $N$  is a digital number represented with a  $k$ -bit resolution and  $f_{clk}$  is the frequency of the DDS’s input clock. In practice,  $f_{DDS}$  is limited to  $0.4f_{clk}$ , or to about 400-1000MHz when using modern DDS ICs with  $f_{clk}$  as large as 1 to 2.5GHz. The resolution of the output frequency is typically set to 32 or 48 bits, allowing a sub-hertz precision of the output frequency. The availability of low-cost, low-noise VCOs [101]-[128] clears the way for small, low-noise synthesizers. Part of using these sources involves modeling surface-acoustic-wave (SAW) resonators under large-signal drive conditions for better insights about noise dynamics of close-in phase noise, then developing manufacturable methods for producing high-purity and temperature-stable oscillators in chip form can be developed [102].

Figure 8-41 shows a block diagram for a configurable user-defined multi-band low-noise VCO with 2-to-4-GHz/4-to-8-GHz/5-to-10-GHz/6-to-12-GHz tuning range. It is compact (0.3 x 0.3 x 0.08 in.), operates at 12 mA and 5 V, and exhibits phase noise -135 dBc/Hz @ 1 MHz from freq. 2GHz [128].

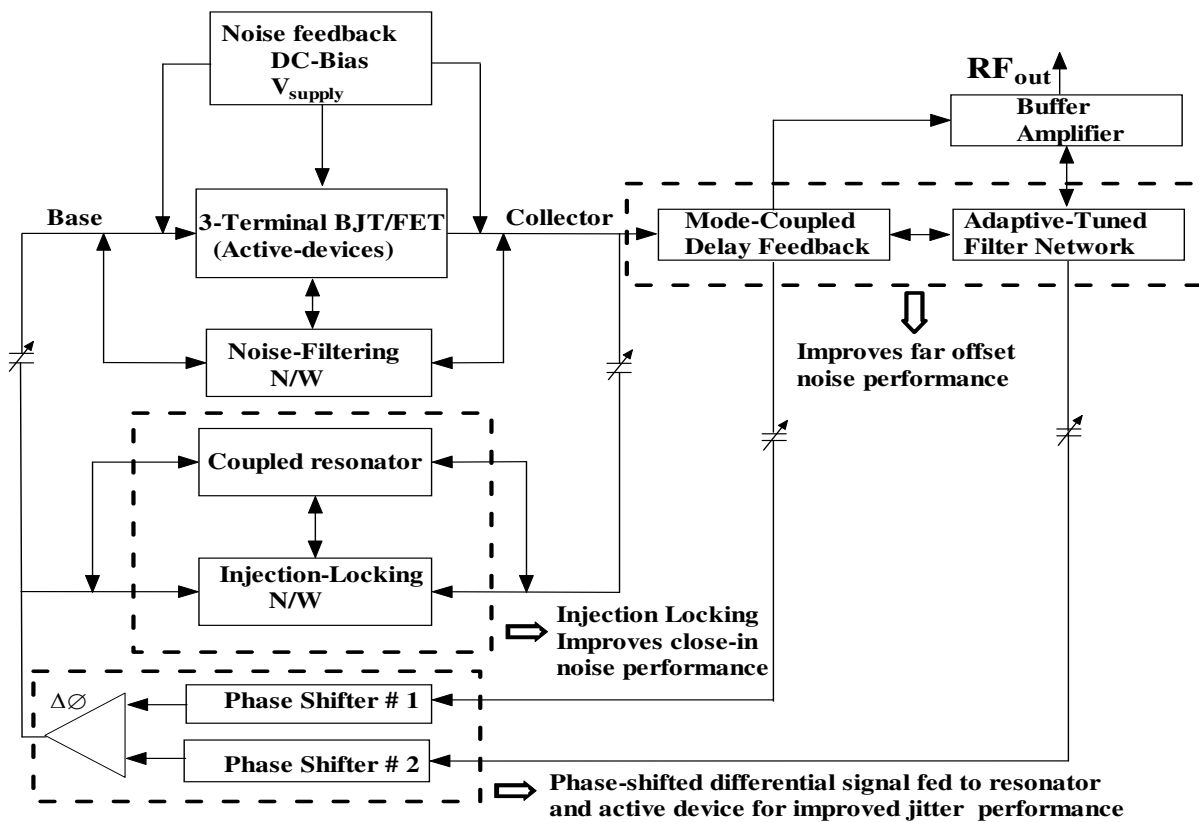
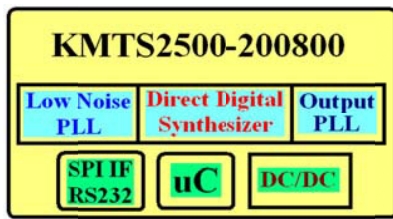


Figure 8-41: Block diagram of a low noise wideband VCO using slow-wave resonator oscillator in 0.3x0.3 inches size



(a)



(b)

Figure 8-42: shows the prototype model KMTS2500-200800-10 frequency synthesizer module, using DDS technology and slow-wave resonator oscillator: (a) Modular block diagram, and (b) prototype hardware [142].

Figure 8-42 shows prototype version of the DDS-based model KMTS2500-200800 synthesizer using high-performance adaptive dynamic mode-coupled, low-phase-noise VCO using patented techniques [114]-[122, 127]. A low-noise PLL multiplies a reference frequency to the maximum frequency allowed by the DDS circuit. The DDS output signal is then filtered and provided as a reference to a secondary PLL that will multiply the frequency to the desired range. Depending on design choices, the phase-noise performance may be limited by the primary PLL, the DDS circuit, or the secondary PLL. However, the spurious performance is determined by the frequency multiplication and division implemented by the PLL circuits and the DDS [105]. A particular example will show why the choice of frequencies is important. With this module (Figure 8-42), it is desired to generate 2000.001 MHz using a 10-MHz reference. The low-noise PLL multiplies the 10-MHz clock to 1 GHz, and the DDS uses this signal to produce the 62.50003125 MHz required by the secondary PLL. Strong integer boundary spurious products may be noticed at this point in the DDS output at 500 Hz offset from the ~62.5-MHz carrier. That 500-Hz spurious product will be amplified by 30 dB and would be practically impossible to filter out from the 2.000001-GHz output signal. The KMTS2500-200800-10 [142] employs a proprietary algorithm that selects the best combination of divide ratios, avoiding integer boundary spurious products, as well as other spurious conditions. The compact synthesizer module of Figure 8-42 (b) can generate 2-to-8-GHz outputs with a typical phase noise of -97 dBc/Hz offset 10 kHz from the carrier, and typical spurious performance of -50 dBc. Table 8-1 shows a summary of these results [153].

**Table 8-1: Summary of the phase noise performance of KMTS2500-200800**

PN [dBc/Hz]	KMTS2500-200800 (2000-8000MHz)				
Offset [Hz] ↓	2000MHz	3000MHz	4000MHz	6000MHz	8000MHz
100.00	-89.88	-83.64	-81.56	-76.32	-77.42
1000.00	-111.52	-104.51	-102.73	-97.01	-98.70
10000.00	-123.82	-116.66	-114.90	-109.51	-111.04
100000.00	-127.35	-119.99	-117.16	-114.05	-113.66
1000000.00	-137.05	-133.81	-131.95	-127.50	-126.04
10000000.00	-153.82	-153.78	-151.36	-145.79	-144.16

Figures 8-43, 8-44, 8-45, and 8-46 show the phase noise plot of 10.24 GHz synthesized signal source using novel 10.24 GHz oscillator using printed coupled resonator (slow-wave resonator, slow-wave metamaterial resonator, slow-wave mode-locked Möbius coupled metamaterial resonator, and using 128 MHz OCO locked Möbius coupled DRO ) for the application in modern Radar and communication systems. As shown in Figures 8-46, the measured phase noise @ 10 kHz offset is -139 dBc/Hz for 10.24 GHz carrier, which is best performance to date reported using this technique for a given size, power consumption and figure of



merit (FOM). The design locks a 10.24 GHz Möbius coupled 10.24 GHz VCO to the harmonics of an internal 128 MHz OCXO reference, using a low-noise PLL with double-balanced mixer serving as phase detector [153]. By using frequency multiplication from the reference, the noise performance required from the mixer and loop filter is relaxed by about 40 dB. The synthesizer typically produces +10 dBm signal at 10.239 GHz with 5V, 300 mA DC bias. The low-noise internal OCXO determines the synthesizer's performance for offset frequencies between 10 Hz and 1 kHz, with -70 dBc/Hz phase noise at 10 Hz offset, -122dBc/Hz at 1 kHz offset, -139dBc/Hz at 10 kHz offset. Above 1 MHz, the noise floor is -169dBc/Hz. To achieve full-sized performance in miniature packages, this research work describes a compact frequency synthesizers that leverage novel Möbius coupled slow-wave mode-coupled resonator (SWMCR) based (VCO) technology for the stability and low noise needed for emerging wideband, high-data-rate wireless communications systems. The advantages of this topology are: design is simple and small enabling small size packaging, performance over size ratio delivered by the architecture is very high, and architecture uses comparatively low cost components.

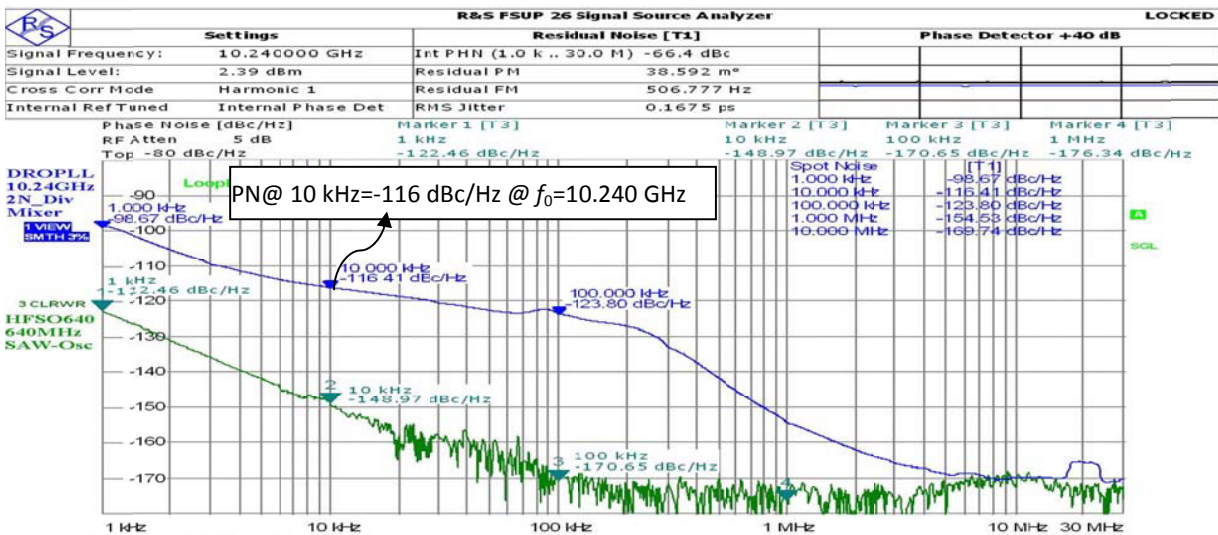


Figure 8-43: Measured phase noise of the 10.24 GHz synthesized signal source using slow-wave resonator

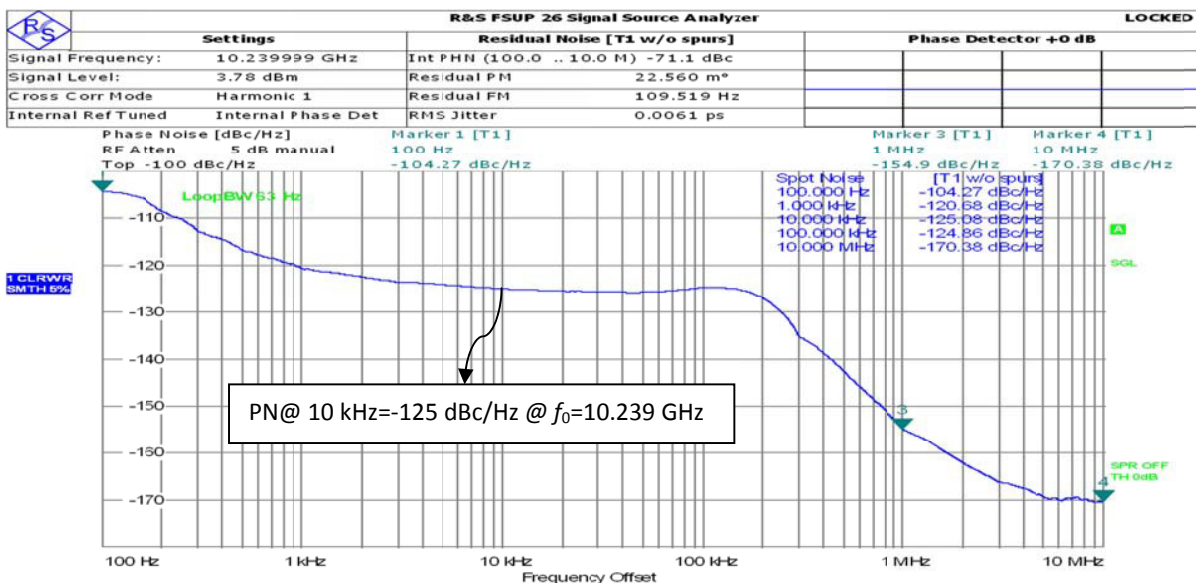


Figure 8-44: Measured phase noise of the 10.24 GHz synthesized source using slow-wave metamaterial VCO

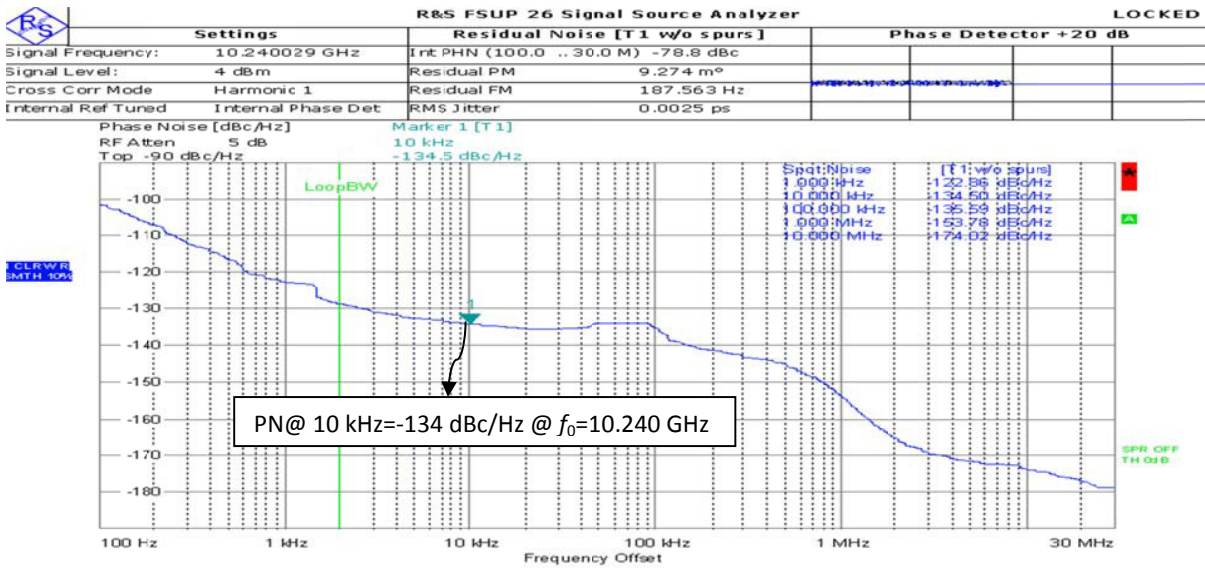
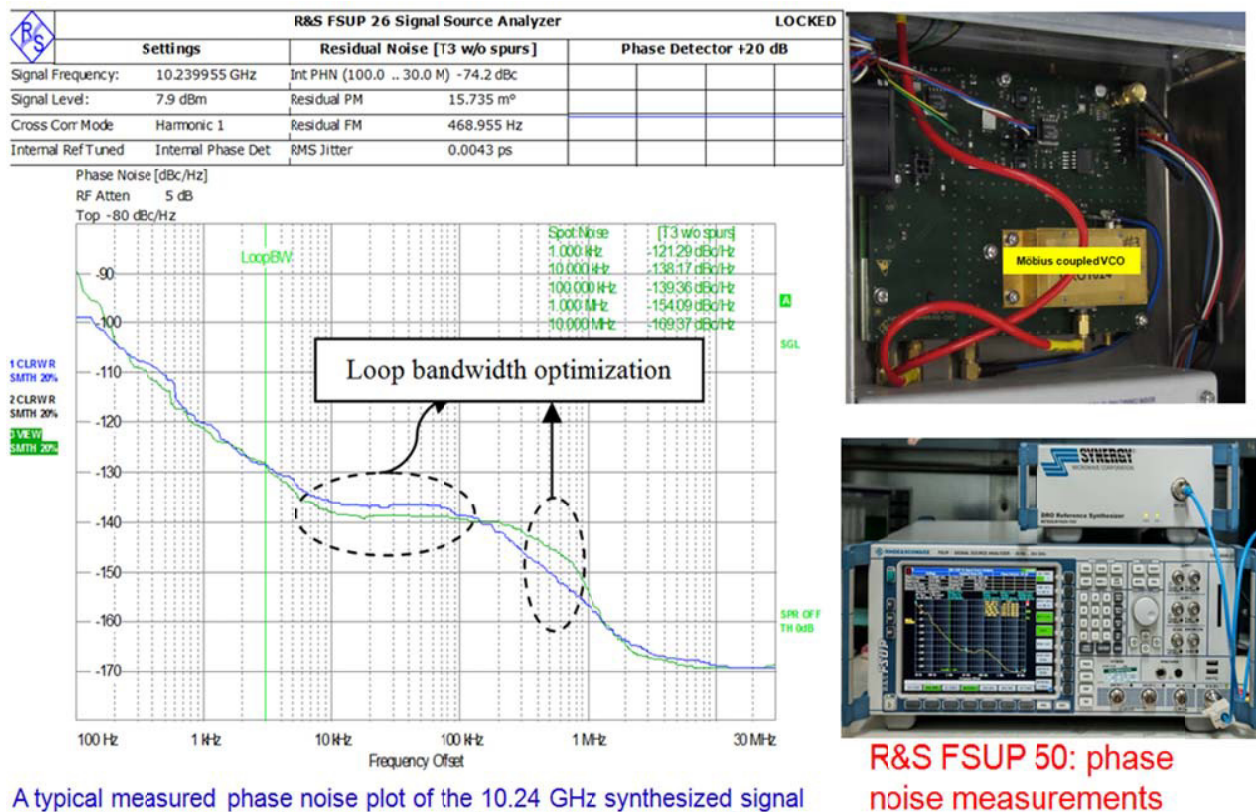


Figure 8-45: Measured phase noise of the 10.24 GHz synthesized signal source using slow-wave mode-locked Mobius coupled metamaterial resonator (uses 500 mW power consumption to produce 12 dBm output power)



A typical measured phase noise plot of the 10.24 GHz synthesized signal source (lowest phase noise source reported for a given cost and FOM)

Figure 8-46: Measured phase noise of the 10.24 GHz synthesized signal source using OXCO locked slow-wave mode-locked Mobius coupled metamaterial resonator [153]

The mode-coupled slow-wave structure based oscillator reported in this chapter has the potential to make a dramatic impact on the design of tunable oscillator using Metamaterial resonator in compact size which otherwise cannot be achieved with conventional printed transmission line resonator. Metamaterial

resonator presents several advantages in comparison with conventional planar resonator such as (i) high Q-factor, (ii) improved selectivity, (iii) easy integration in MMIC technologies, (iv) multi-band multi-mode characteristics (v) insensitive of EMI/EMC [125]-[127]. Figure 8-47 shows the CAD simulated  $S_{21}$  plots of metamaterial split ring, Möbius strips, and Metamaterial Möbius strips resonator; fabricated on substrate material of dielectric constant of 2.2 and thickness of 12 mils [148].

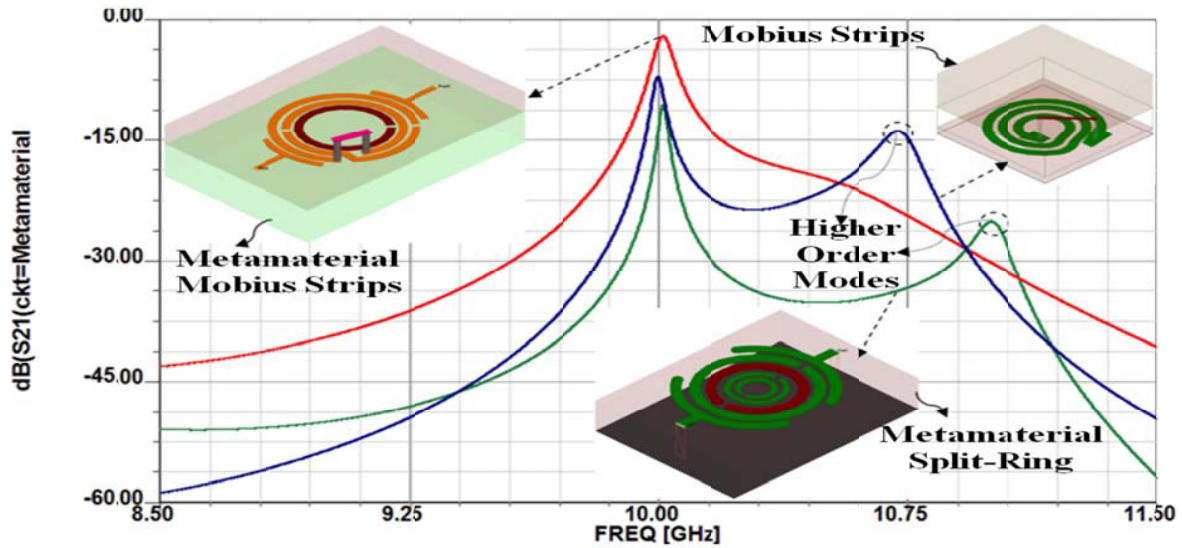
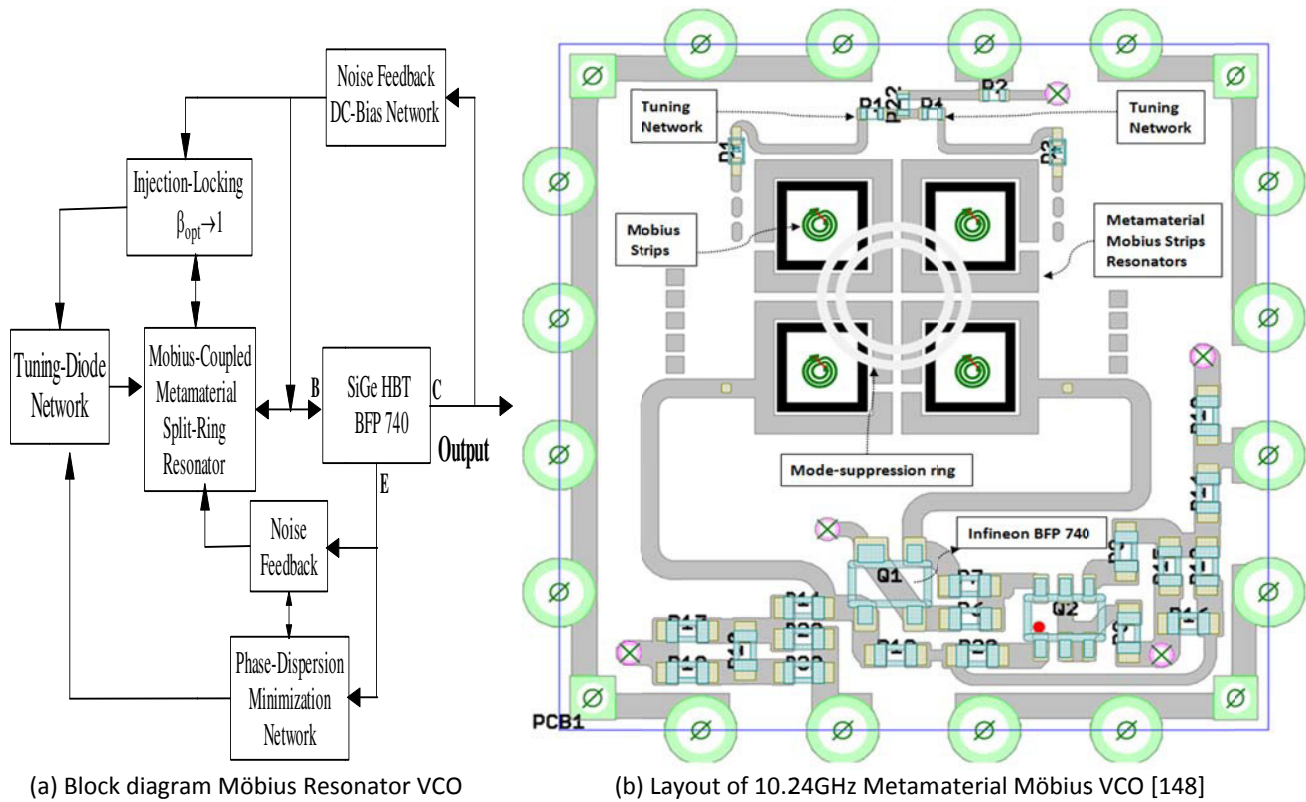


Figure 8-47: CAD simulated  $S_{21}$  plots in (dB): (a) Metamaterial split rings, (b) Möbius strips, and (c) Metamaterial Möbius strips resonator networks [148]



(a) Block diagram Möbius Resonator VCO

(b) Layout of 10.24GHz Metamaterial Möbius VCO [148]

Figure 8-48: (a) Block diagram of X-band Metamaterials Möbius Strips Resonator VCO, (b) Layout (0.9×0.9 in) [148]

As shown in Figure 8-47, Metamaterial Möbius strips (MMS) exhibit superior  $S_{21}$  characteristics resulting in improved Q-factor, suppresses the spurious resonance modes, therefore stable broadband operation as compared to metamaterial split rings and Möbius strips resonator that exhibit undesired second-order modes (marked: Blue trace-Möbius Strips; Green trace-Metamaterial Split-Rings).

To overcome mode-jumping issues and tuning problems, mode stabilization (manipulating the phase velocity by introducing **Mode-Suppression Ring** that allows multi-mode-self-injection into the Möbius Strips cavity, improves the stability) technique. A novel mode-coupled self-injection Metamaterials Möbius Strips resonator based tunable X-band oscillator for RADAR application is developed for high frequency signal sources applications [148].

Figures 8-48(a), 8-48(b), and 8-49 show the typical block diagram, layout, and the measured phase noise plot of the 10.24 GHz oscillator, using a SiGe Hetrojunction-bipolar-transistor (HBT) active device. Figure 8-49 shows the measured phase noise plot, offers superior FOM=-216dBc/Hz @ 1MHz offset calculated from Eq. 1 given in ref [45]. The O/P power is 11.3 dBm, 500MHz tuning range with 5VDC and 80mA. As shown in Figure 8-48 (b), realization of Metamaterial Möbius Strips using discrete components in planar domain is challenging task, thus future work is in progress to develop MMIC based technologies.

### 8.10 Conclusion

This chapter deals with an artificial negative index material (Metamaterials) that has been highly newsworthy for a number of years and investigates the extent to which Metamaterials can be appropriately used to implement microwave resonators with advantageous properties [139]-[143]. The printed resonators used in this Chapter are singly or multiply coupled resonators, which could also be considered without touching on the concept of Metamaterials, but developments in the implementation of Metamaterial resonator concepts, this type is the basis for achieving high quality factor, therefore discussed to closer assessment. The complex oscillator circuits using these resonators characterized with measurement results. Very impressive results from specific microwave oscillator implementations in building high performance frequency synthesizers presented [120].

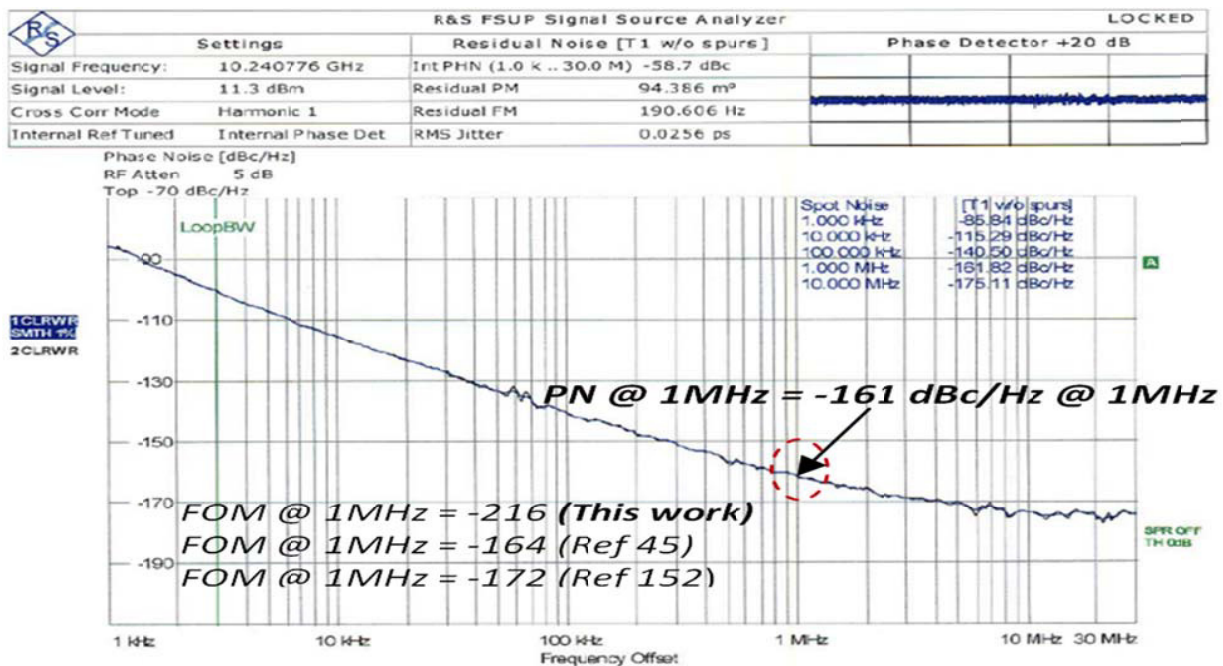


Figure 8-49: Measured phase noise plot of X-band Metamaterial Möbius VCO (layout is shown in Figure 8-48) [148]

## Chapter 9

### High Performance X-band Oscillators

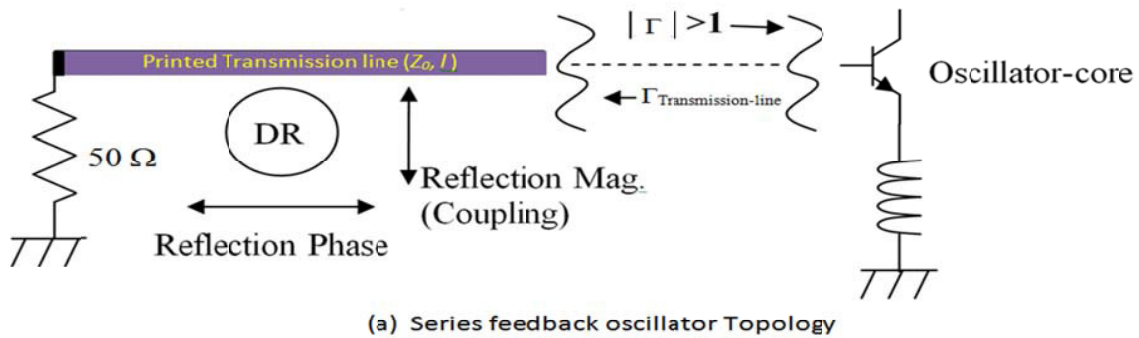
#### 9.1 Introduction

Phase noise can be a limiting factor in modern communications systems, especially those that rely on phase-based modulation. Phase noise can increase the bit error rate (BER) of a telecommunications link, degrade the stability of beams in particle accelerators, and degrade the sensitivity of radar systems [1]. The high quality factor (Q) of a dielectric resonator makes it possible to achieve oscillators with excellent phase-noise performance at microwave and millimeter wave frequencies. Dielectric resonators are fabricated on ceramic materials with high dielectric permittivity, high Q, and high temperature stability. They have much smaller size compared to cavity resonators; therefore, these resonators are frequently employed in the design of frequency stable RF circuits, especially in oscillators [2]-[5]. When high data rates must be transferred as with multiple quadrature amplitude modulation (M-QAM) schemes in Long-Term-Evolution (LTE), local multipoint distribution service (LMDS), and fixed-frequency point-to-point digital radios and satellite-communications (SATCOM) links, such systems rely on free-running or phase-locked signal sources with ultra-low phase noise performance. Such spectrally pure sources are also invaluable for radar systems and in research laboratories [6]-[23]. A wide range of military, industrial, medical, and test-and-measurement markets demand stable frequency sources with low phase-noise performance and low thermal drift. Dielectric resonator oscillators (DROs) have provided low-noise solutions in the frequency range from 3 to 40 GHz, with spectral purity that compares favorably to other competing solutions such as multiplied frequency fundamental sources [24]-[29].

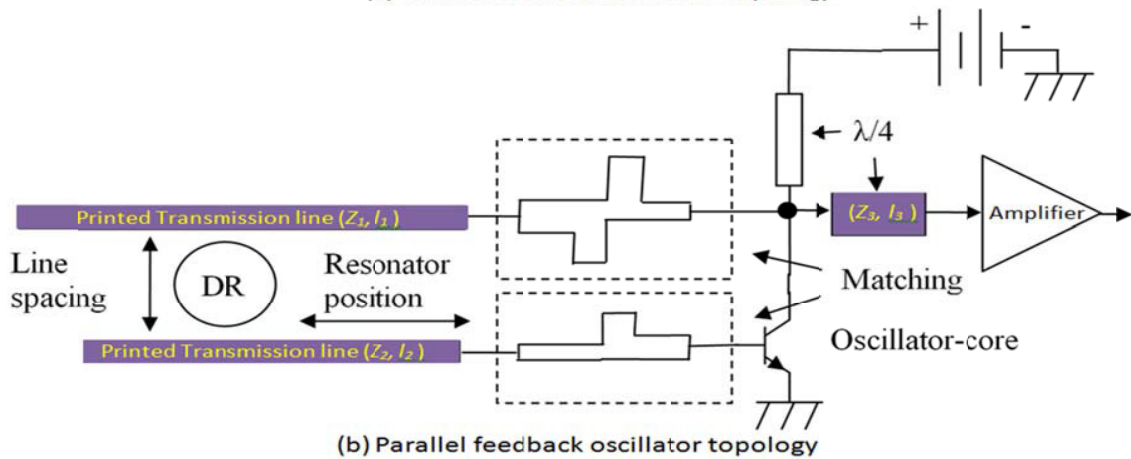
#### 9.2 DRO Circuit Topology

A typical DRO circuit uses high-Q dielectric resonator (DR) and active device in a series/parallel feedback configuration to achieve the negative resistance required for stable oscillations showed in Figure 9-1 [8, 30]. The series feedback DRO (Figure 9-1(a)) is the most common type of DRO mainly because it is easy to handle than the feedback type once the oscillator-core exhibits the required reflection-gain at the resonant frequency [25]. The oscillator core consists of an active device the input port of which does present a reflection coefficient of magnitude  $>1$  to the connected resonator arrangement. The latter is simply formed by the Dielectric Resonator (DR) placed in close proximity to a microstrip line terminated with its characteristic impedance (reaction type resonator) as shown in Figure 9-1(a). Adjustment of phase is done by moving the DR along the line at constant distance and adjustment of reflection magnitude and thus level of oscillation can be done by varying the distance between line and DR [24].

Figure 9-1(b) shows the typical parallel feedback (transmission type) DRO circuit, constructed by a set of two microstrip parallel lines mutually coupled through the interaction with a DR placed between them (transmission type resonator). The transmission lines do not require a resistive termination. In order to achieve a high  $Q_L$  it is rather preferable to use reactive terminations instead i.e. open stubs the lengths of which constitute two additional degrees of freedom. In addition to that matching structures interfacing the oscillator core's in- and output are required to maximize the loaded Q and at the same time establish the necessary round trip phase shift of  $2\pi \cdot n$  (integer n) at the target frequency. An appropriate quarter wave transformer between oscillator-core and post-amplifier may be required in order to achieve optimum performance. Since the available layout area is limited in most cases, it is desirable to have fixed positions for the resonator as well as for the core terminals. Therefore a combination of stub matching-elements and meander lines are used to realize arbitrary matching and phase shift while maintaining the mechanical length of the structures [9]-[11].



(a) Series feedback oscillator Topology



(b) Parallel feedback oscillator topology

Figure 9-1 A typical DRO circuit: (a) Series feedback (Reflection type), and (b) parallel feedback (Transmission type)

### 9.3 Dielectric Resonator (DR)

The DR is typically a piece of a dielectric material (usually manufactured in a circular shape such as a disk or cylinder) with very high (much higher than 1) relative dielectric constant,  $\epsilon_r$ , that acts like a resonant cavity by means of reflections at the dielectric/air interface. The DR can have frequencies depending on the type of material, dimensions, and the proximity and shapes of enclosures [12]. Figure 9-2 shows a typical DR in a polar coordinate system the magnetic wall at  $\rho = a$  used for providing insight into possible resonant conditions for a given physical dimension, such as  $L$ , the length of the DR, and  $a$ , the radius of the DR [13, 28]. It can be shown that by matching the tangential fields at the resonator (dielectric/air) interface, at  $|z| = L/2$  it is possible to derive following expression [14]

$$A \cos\left(\frac{\beta L}{2}\right) = B e^{-\alpha \frac{L}{2}} \quad (9.1)$$

$$-\frac{jA}{Z_d} \sin\left(\frac{\beta L}{2}\right) = \frac{B}{Z_a} e^{-\alpha \frac{L}{2}} \quad (9.2)$$

$$Z_d = \frac{\omega \mu_0}{\beta}, \quad (Z_d : \text{wave impedance within the dielectric}) \quad (9.3)$$

$$Z_a = \frac{j\omega \mu_0}{\alpha}, \quad (Z_a : \text{wave impedance within the air}) \quad (9.4)$$

where  $\alpha$  and  $\beta$  are the imaginary and real propagation constants. From (11.1) and (11.2) [28]

$$-jZ_a \sin\left(\frac{\beta L}{2}\right) = Z_d \cos\left(\frac{\beta L}{2}\right) \Rightarrow \tan\left(\frac{\beta L}{2}\right) = \frac{\alpha}{\beta} \quad (9.5)$$

By solving the transcendental equation (9.5), resonant freq. ( $f_0$ ), length ( $L$ ), and radius ( $a$ ) of the DR [28]

$$\tan \left[ \frac{L}{2} \left( \epsilon_r \left( \frac{2\pi f_0}{c} \right)^2 - \left( \frac{2.405}{a} \right)^2 \right)^{0.5} \right] = \left[ \frac{\left( \frac{2.405}{a} \right)^2 - \left( \frac{2\pi f_0}{c} \right)^2}{\epsilon_r \left( \frac{2\pi f_0}{c} \right)^2 - \left( \frac{2.405}{a} \right)^2} \right]^{0.5} \quad (9.6)$$

where  $L$  is the length of DR,  $a$  radius,  $\epsilon_r$  is the relative permittivity, and  $c$  is the speed of light.

From (9.6), the transcendental equation yields two possible solutions for resonant wavelength,  $\lambda$ , but only one of these is valid in yielding a deterministic solution within the dielectric ( $\lambda_{\epsilon_r}$ ) and air ( $\lambda_{\epsilon_0}$ ) [2]. As shown in Figure 9-2(a), an approximate frequency formula for commonly used  $TE_{01\delta}$  mode with about 2% accuracy within the ranges indicated is given by [2]

$$f_{res} = \frac{68}{D \times \sqrt{\epsilon_r}} \left( \frac{D}{2L} + 3.45 \right) (GHz), \quad 0.5 < \frac{D}{2L} < 2; \quad 30 < \epsilon_r < 50 \quad (9.7)$$

where  $D$  denotes the DR diameter and  $L$  its length (both in mm).

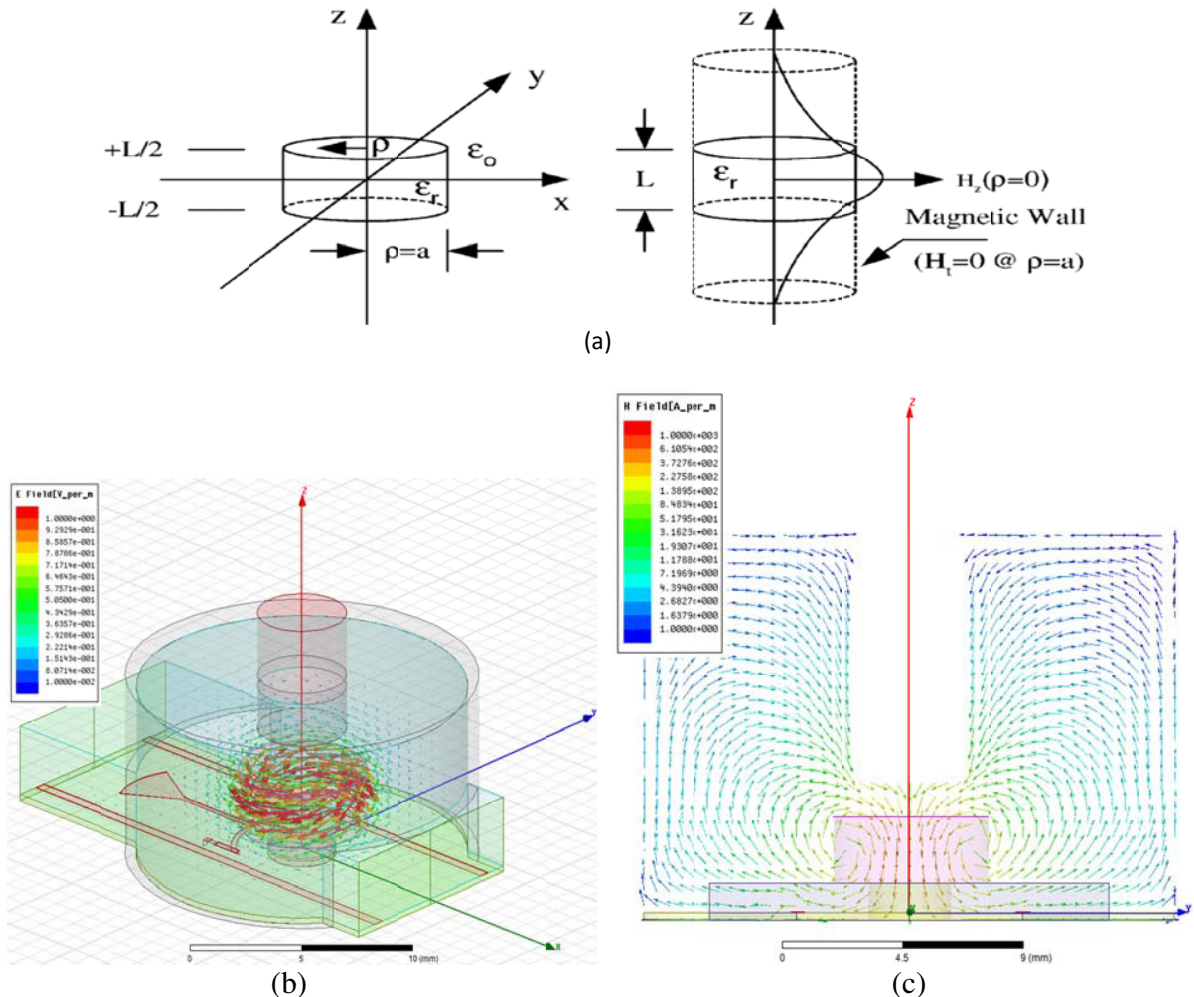


Figure 9-2: A typical dielectric disc resonator characteristics : ( a) DR  $TE_{01\delta}$  mode and  $H_z$  field distribution, (b) HFSS simulation,  $TE_{01\delta}$  E-Field vector-plot (normalized) generated from an Eigen mode solution of a DR-assembly within a conductive cavity, and (c) H Field vector plot of the  $TE_{01\delta}$  resonant mode in YZ-plane [27]

A closed conductive containment for the DR-assembly leaving openings for the ports only is recommended otherwise the unloaded quality factor ( $Q_u$ ) would be diminished by radiation loss. Since the proximity of the surrounding matter does alter the boundary conditions to some degree the resonant frequency is shifted upwards in case of metal (conductive) proximity and downwards in case of dielectric proximity for the  $TE_{01\delta}$  mode [15]. The determination of the Eigen modes of the complete resonator arrangement (DR and cavity) using CAD tool (3D-EM HFSS from Ansys; [www.ansys.com](http://www.ansys.com)) allows for verification and adjustment of the geometrical parameters of the DR, and tuning elements for a desired resonant frequency while at the same time identification of unwanted modes (modes in the vicinity of the desired one) and also giving estimation for  $Q_u$ . Designing and building low phase noise oscillator circuits based on DRs is not trivial, given the nonlinear nature of the active devices needed for the oscillators as well as the tedious task of placement of the puck and disk resonator [16]. The parallel feedback topology shown in Figure 9-1(b) offers more than six degrees of freedom plus the additional parameters of the matching networks, thus makes suitable for production.

#### 9.4 Design Methodology of Parallel Feedback 10 GHz DRO Circuit

In this section, design steps are discussed for dielectric resonator oscillators (DROs) that can deliver stable signals at microwave through millimeter-wave frequencies. With the aid of a unique Möbius coupling mechanism, these fundamental-frequency dielectric-resonator oscillators operate through 10 GHz with extremely low phase noise.

##### Design Steps:

- (i) Figure 9-3 illustrates the typical layout component with resonator interface and matching structures. The upper matching section between resonator and gain element is split to create a fixed (e.g.  $50\Omega$ ) impedance level between them to allow arbitrary phase shift to be inserted (meandered if necessary) without changing the outer impedances. Additionally this allows access to an open loop S-parameter simulation and optimization. In order to simplify the process further, the matching process is treated separately and variable reference impedances are used instead at the oscillator-core's input and the resonator-element's output respectively.
- (ii) The lower section is a cascade of a stub-matching element and a  $180^\circ$  meander transmission line allowing for adjustment of the mechanical length while maintaining the reflection coefficient of the oscillator core's output.
- (iii) Using CAD tool (ADS 2013 from Agilent; [www.home.agilent.com](http://www.home.agilent.com)) a layout-component is created with ports interfacing the resonator and the gain-element. In order to speed up the optimization-process microstrip library elements only are used and a synchronized schematic (i.e. analytical) model created. This allows a coarse optimization to be conducted using the analytical representation and a subsequent fine optimization using EM co-simulation. This may save significant computational effort if the differences between the two representations are small which unfortunately is not guaranteed depending on the actual situation and frequency.
- (iv) Figure 9-4 shows the 4-port 3D dielectric disk resonator model with port reference (shown for port 1) de-embedded to the actual interface positions. The resonator's S-parameters are taken from the results of a 4-port model 3D-EM simulation (Figure 9-5). The reference positions of the four ports required to match the corresponding positions in the layout component. The effect of the two tuning varactors has been modeled by voltage dependent lumped boundary conditions at their respective places, the tuning voltage being an additional parameter of the HFSS-model.



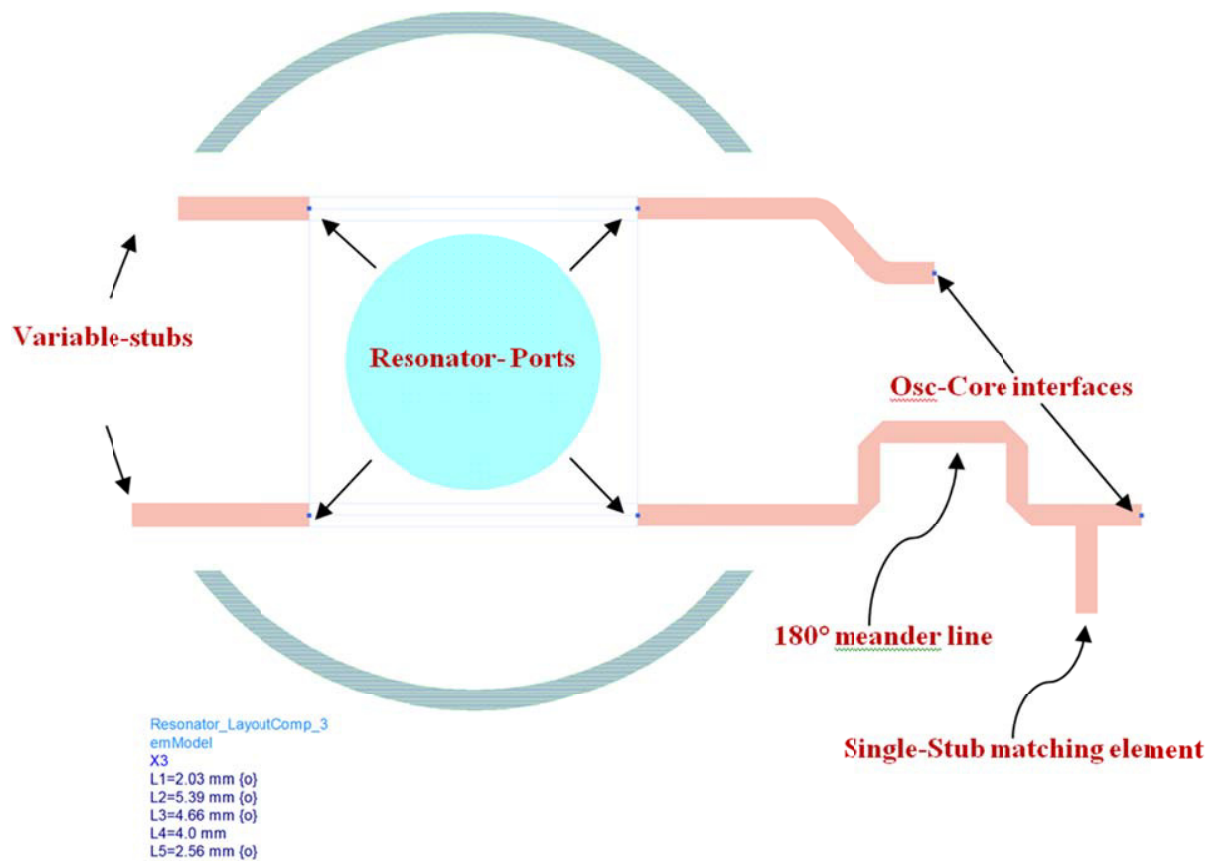


Figure 9-3: A typical layout component with resonator interface and matching structures

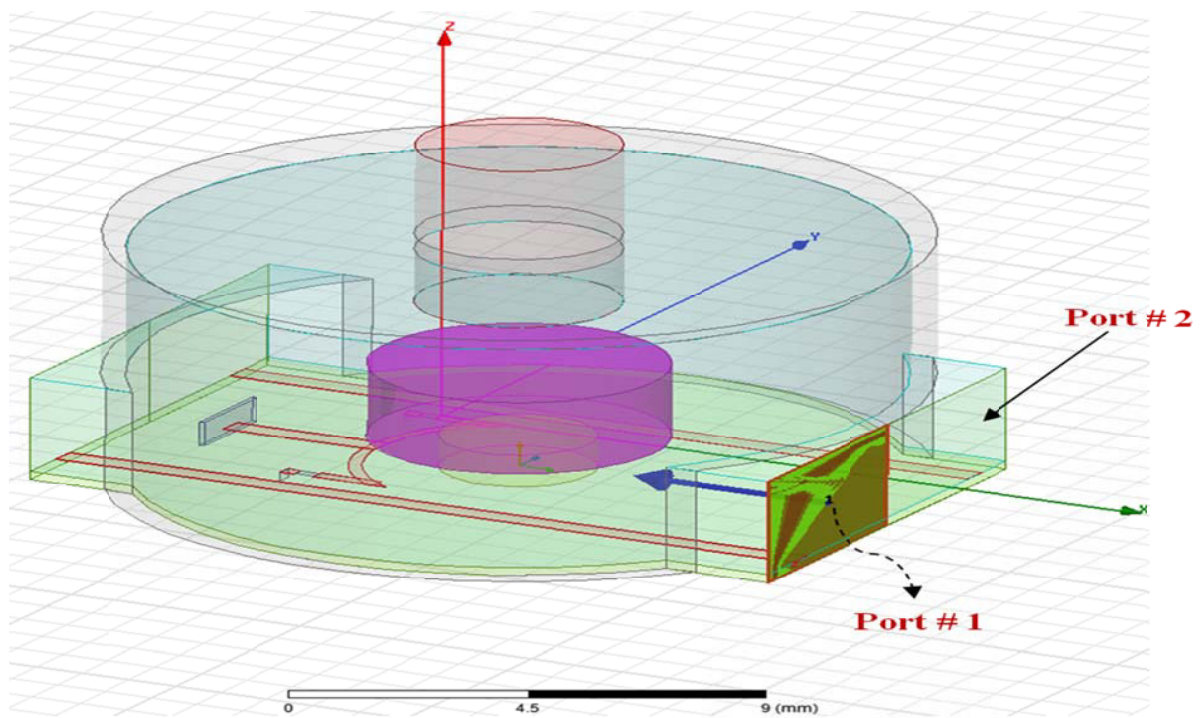


Figure 9-4: 4-port 3D resonator model with port references (shown for port1) de-embedded to interface positions.

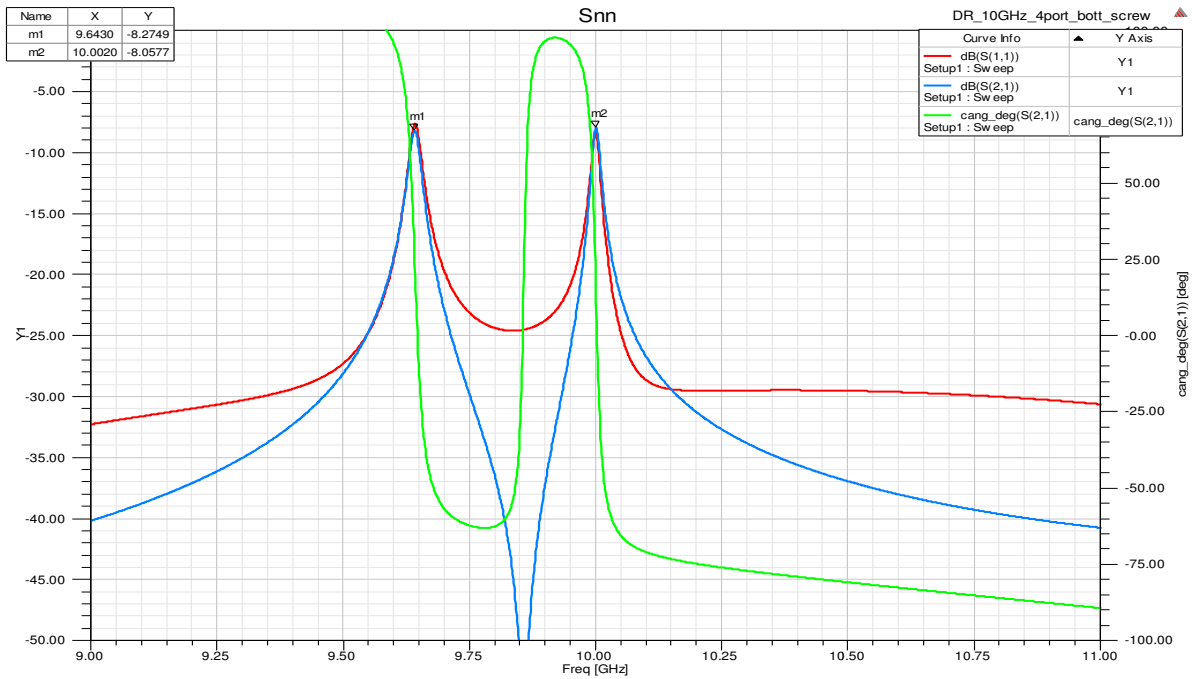


Figure 9-5:  $S_{11}$  magnitude (red) and  $S_{21}$  magnitude (blue) and phase (green) of the 4-port model above for a tuning voltage of 7 V.

- (v) Figure 9-6 shows the typical oscillator core model including bias stabilization circuitry consisting of the layout component for EM co-simulation, models for the gain element, the bias-stabilization transistors and additional lumped components. The oscillator core consists of a BFP740 transistor (from Infineon) in common emitter configuration and a bias-stabilization circuitry. The planar EM co-simulation is utilized in conjunction with substrate and pad scalable lumped component models from Modelithics as well as calibrated internal ports for them.

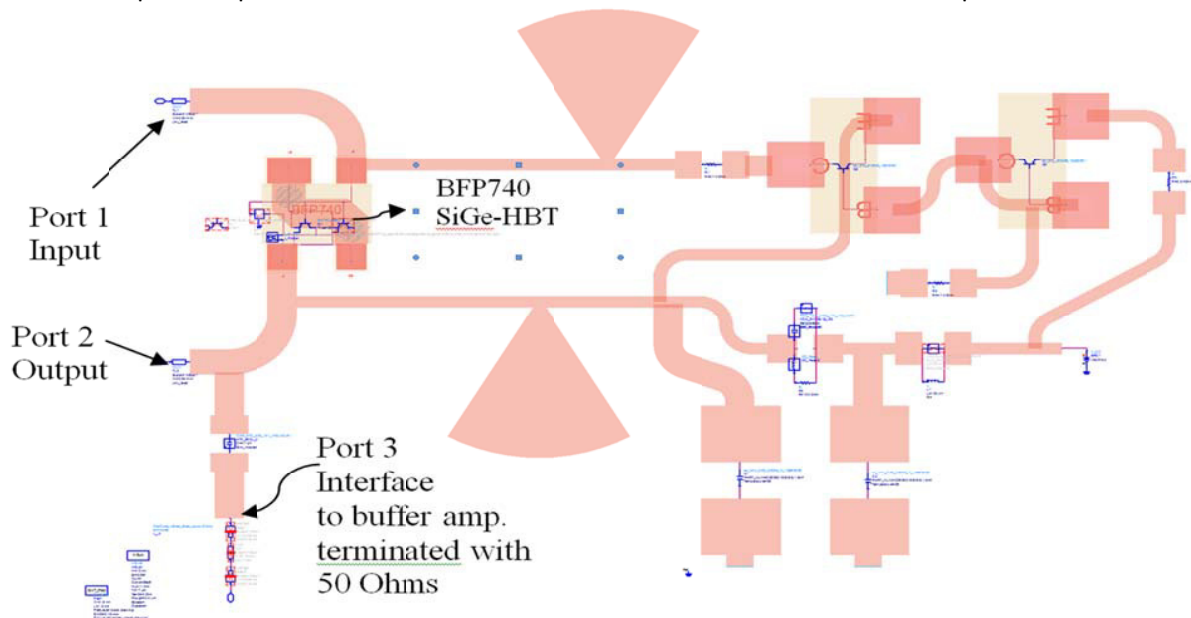


Figure 9-6: Oscillator core model including bias stabilization circuitry consisting of the layout component for EM co-simulation, models for the gain element, the bias-stabilization transistors and additional lumped components.

- (vi) A broadband S-parameter analysis of the oscillator core is recommended in order to identify potential instability issues along with available and associated gain properties. Since the regions of instability are rather small and very close to unity, it is unlikely to encounter instability since lossy matching and phase shifting elements are likely to force the terminations inside the stable region anyway, therefore additional stabilization measure is not necessary. Figures 9-7, 9-8, 9-9, 9-10 show the plots of stability factor, stability circle, gain characteristics of the oscillator core, and noise figure.
- (vii) The complete setup does allow for an open loop 2-port S-parameter simulation the reference impedances of which being additional variables of the problem. Since the S-parameter data for the resonator does not reflect DC properties ideal DC-blocks must be added if necessary while in reality an open circuit is present at 0 Hz.
- (viii) Figure 9-11 shows the CAD simulation circuit for (in ADS 2013) open loop (small signal) S-parameter simulation and optimization setup. For the coarse optimization, the random or hybrid optimizer is utilized. There is a set of four main goals:  $|S_{11}| < R$ ,  $|S_{22}| < R$ ,  $|S_{21}| > G_{min}$  and  $Q_L \geq 1k$  at or closely around the target frequency  $f_0$ . Appropriate values for the limits are  $20 \cdot \log(R) = (-20)$  dB and  $20 \cdot \log(G_{min}) = 6$  dB.  $Q_L$  is derived from the frequency of maximum gain and the corresponding 3 dB-bandwidth  $\Delta f$  according to  $Q_L = f_0 / \Delta f$ . Since the target value for the open loop gain is associated with the coupling coefficient of the resonator a higher gain may increase its value which is still below unity i.e. subcritical. In practice it was not possible to increase it much further without diminishing the other goals. On the other hand a higher gain would increase the overdrive level of the oscillator with severe impact on large signal noise figure and input reflection of the gain element.

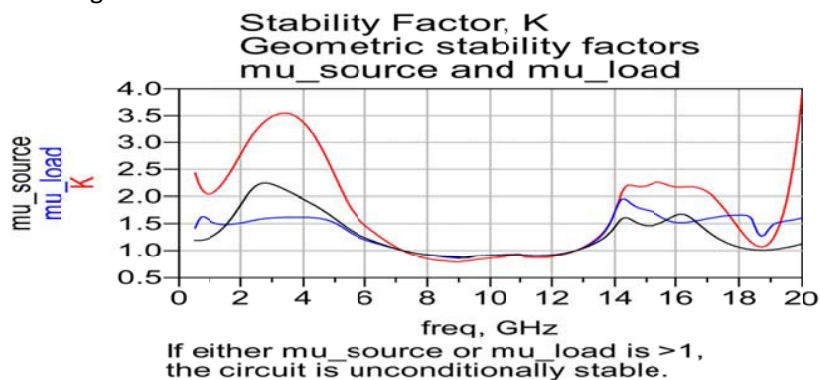


Figure 9-7: The plot of the stability factor “K” versus frequency (unconditional stability is not completely satisfied)

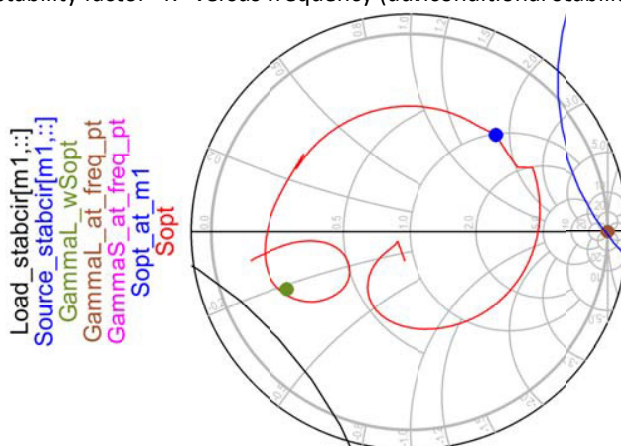


Figure 9-8: Source (blue) and load stability circles (black) at the most critical frequency (9 GHz)

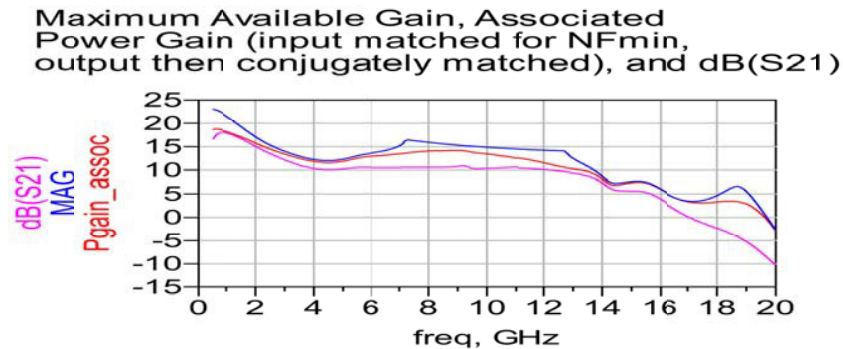


Figure 9-9: A typical gain characteristics of the oscillator core (note that the maximum available gain is invalid within the region of potential instability between 7 GHz and 13 GHz).

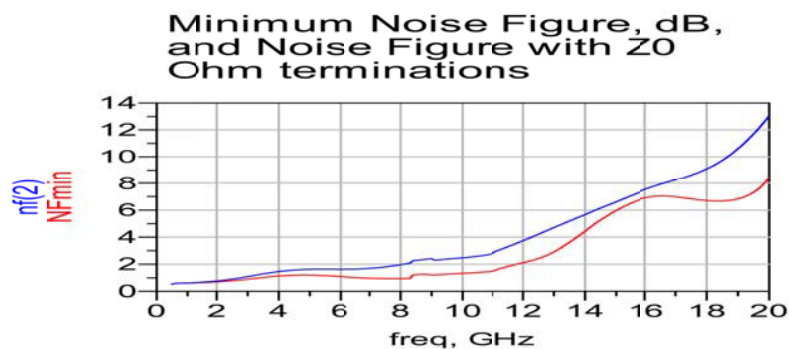


Figure 9-10: A noise figure and minimum noise figure versus frequency

- (ix) A phase goal is expendable since arbitrary phase shift may be inserted afterwards. As we will see later, the small signal phase shift is decreased significantly at higher drive levels. A large signal S-parameter simulation will yield an estimation for the additional phase shift necessary in order to arrive at  $0^\circ$  unwrapped phase for 0 dB large signal gain at  $f_0$ . Fine adjustment of the phase noise vs. phase shift will be done at a later stage. Direct optimization vs. phase noise is not recommended at this stage because potential HB convergence problems during the process for certain sets of parameters may cause the optimizer to fail.
- (x) For the fine optimization the gradient optimizer is engaged using the same set of goals but this time, invoking the EM view (-model) for the matching layout component instead of the analytical models (Figure 9-11).
- (xi) When the optimization process is accomplished, the resulting reference impedances then need to be matched to a common (e.g.  $50\Omega$ ) real impedance. This is accomplished in two steps: First two Single-Stub smart components are inserted to quickly design an electrical (ideal) transmission-line model for each matching element using the ADS-Filter/Matching Design-Guide and then a physical equivalent is created using the ADS-LineCalc or similar tools.
- (xii) Now that the small signal open-loop response and matching are well at their target values, we need to estimate the necessary additional phase shift at large signal excitation and near unity gain at the frequency of maximum gain in the small signal scenario.
- (xiii) Figure 9-12 shows the typical schematic of the parallel transmission line as a part of resonator element. Figure 9-13 shows the CAD simulated open loop S-parameters following coarse optimization using schematic - (blue) and EM-view. As the reflection coefficients and the source impedance for minimum large signal noise figure of the active device do more or less vary with increasing drive level some correction mainly to the matching element at the oscillator core's input may be required in order to establish optimal conditions w.r.t minimum phase noise.

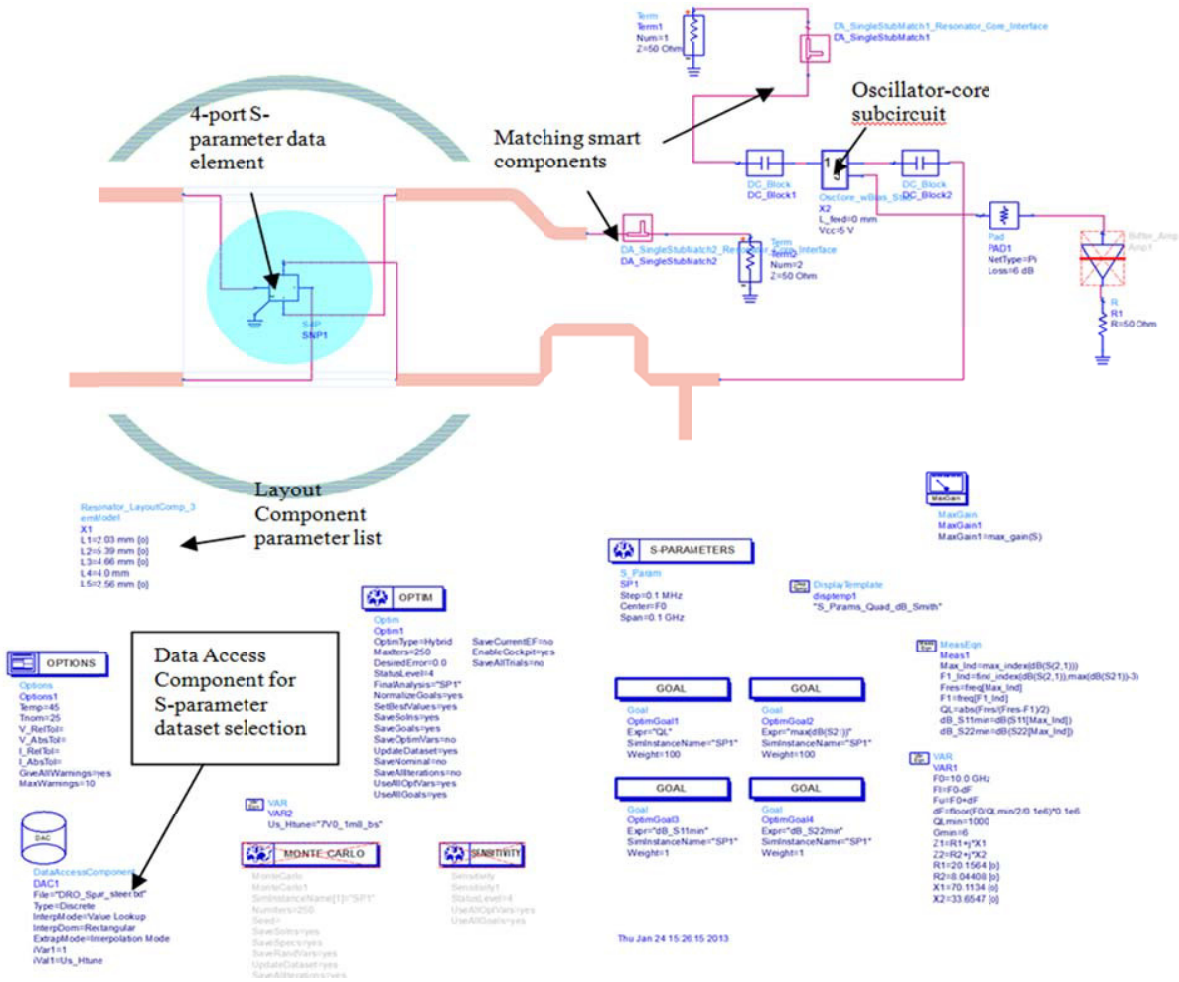


Figure 9-11: Simulation setup (ADS 2013) open loop (small signal) S-parameter simulation and optimization setup.

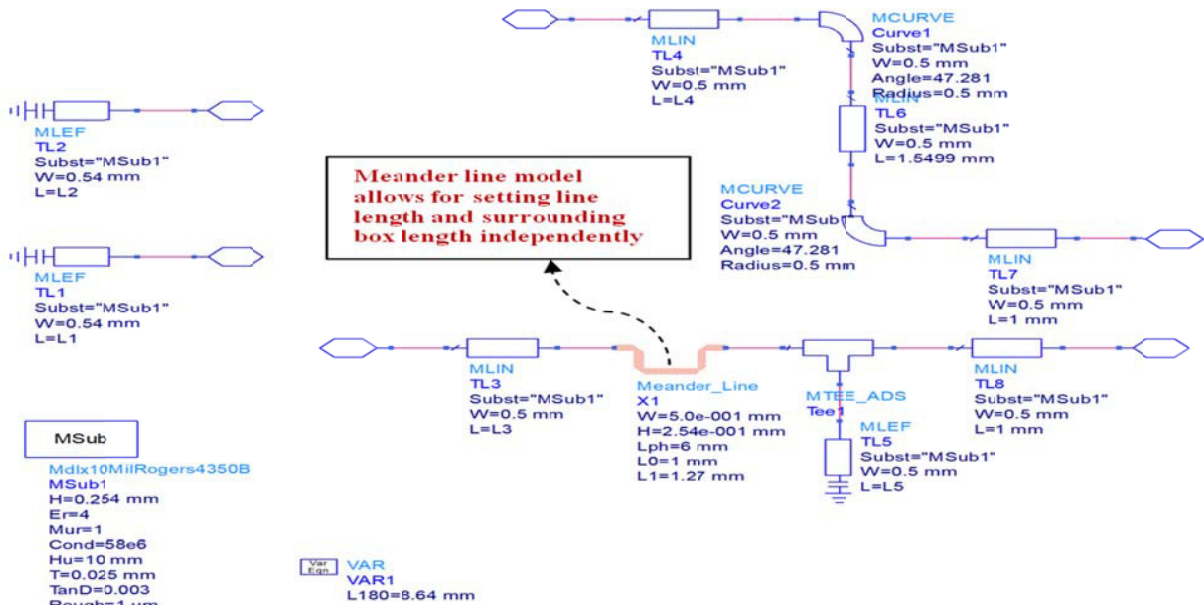


Figure 9-12: A typical schematic view of the resonator layout component

- (xiv) The result obtained in Figure 9-13 indicates an additional phase shift of  $-116^\circ$  in this case to be inserted between the two ports to arrive at the required phase shift of  $0^\circ$ . In order to save board space additional meander line as shown in Figure 9-12 of equivalent electrical length are inserted to establish the required phase shift. The surrounding box length of the meander should be set such, so as to meet the fixed layout positions of the oscillator-core if relevant. Figure 9-14 shows the equivalent physical replacement for the smart matching components as shown in the schematic (Figure 9-11)

Figure 9-15 shows the final optimization result with EM-models for the single-stub matching elements replacing the smart matching components. Note that another  $180^\circ$  meander line has been added to the lower section to compensate for the physical lengths of the matching elements. Figure 9-16 shows the CAD simulation setup (ADS 2013) for large-signal open-loop S-parameter simulation. Figure 9-17 shows the plot of large signal forward transmission at resonance frequency vs. input-power. The marker is set to near unity-gain. The corresponding phase shift is about  $116^\circ$ .

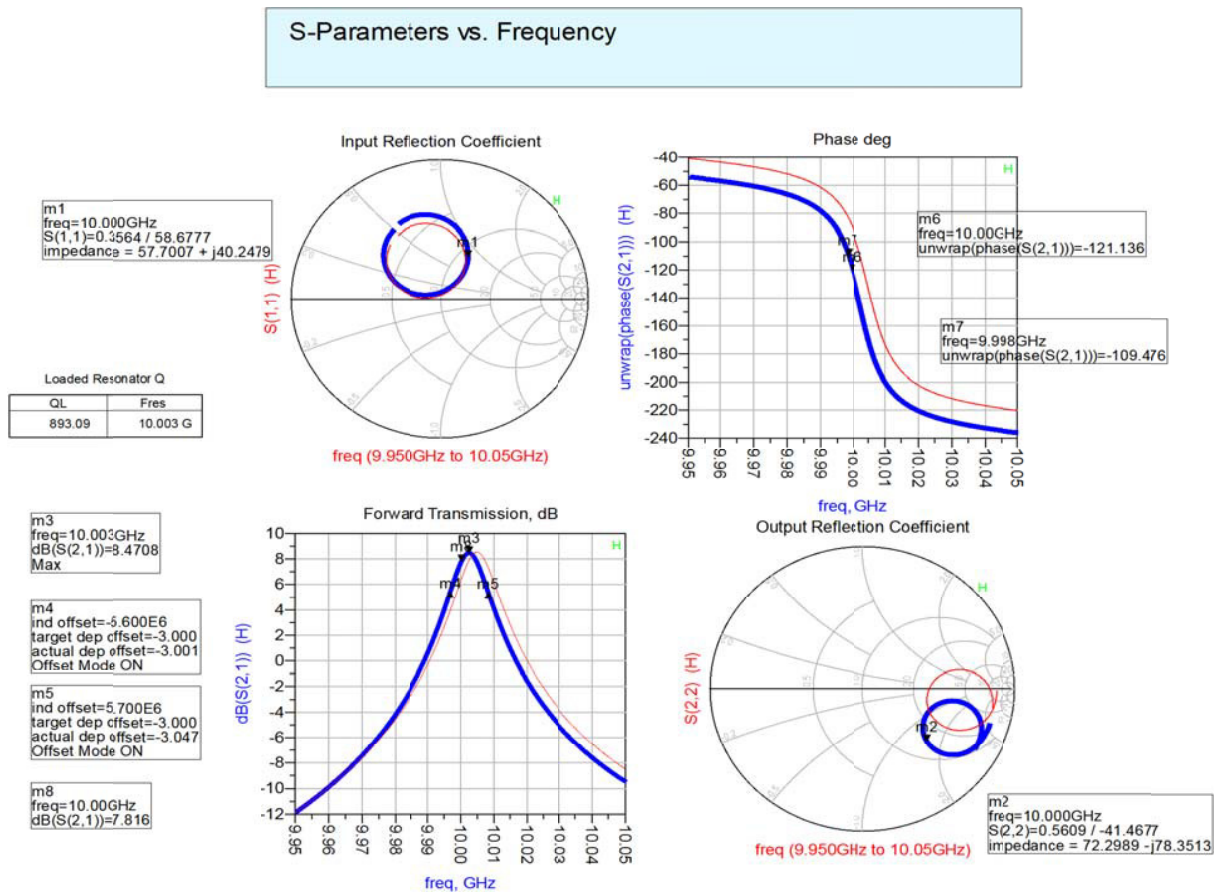


Figure 9-13: simulated open loop S-parameters following coarse optimization using schematic - (blue) and EM-view

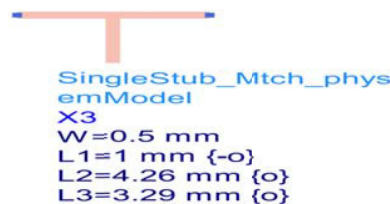


Figure 9-14: Shows the equivalent physical replacement for the smart matching components shown in Figure 9-11

## S-Parameters vs. Frequency

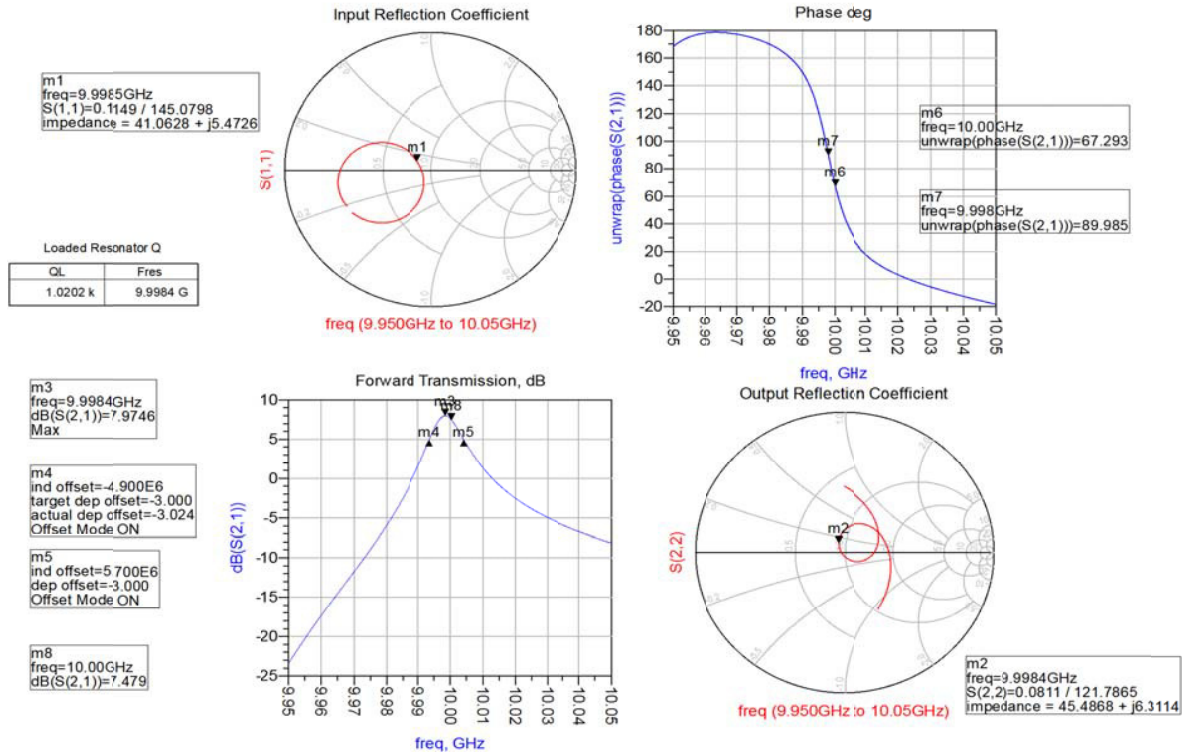


Figure 9-15: shows the final optimization result with EM-models for the single-stub matching elements replacing the smart matching components. Note that another 180° meander line has already been added to the lower section to compensate for the physical lengths of the matching elements

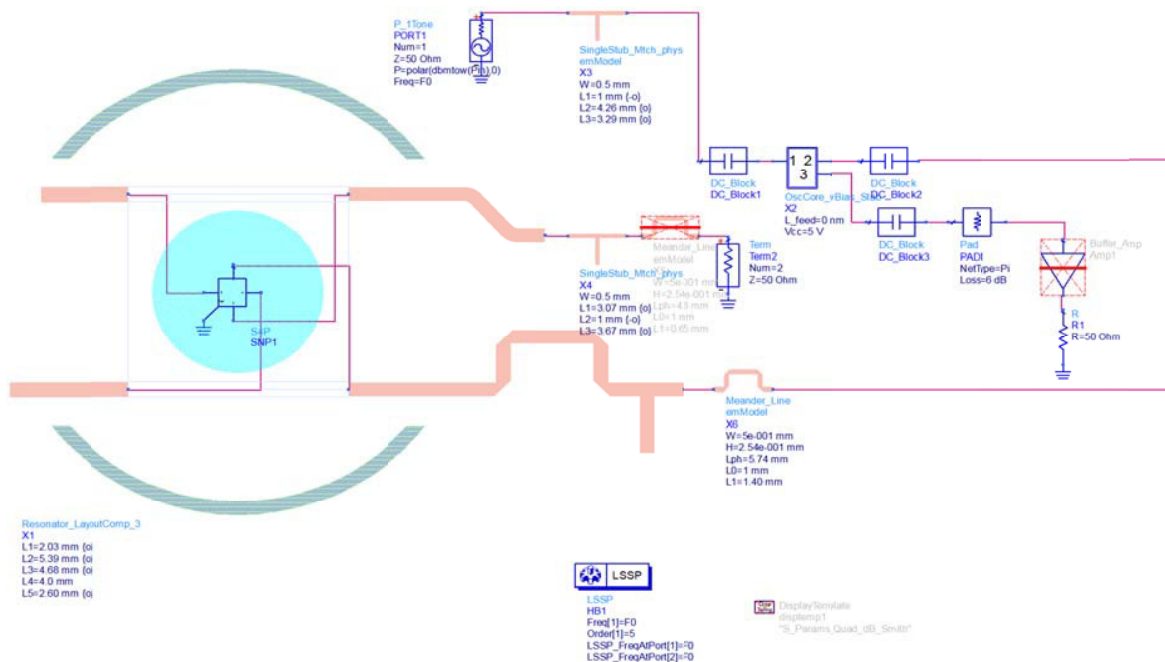


Figure 9-16: shows the CAD simulation setup for large-signal open-loop S-parameter simulation

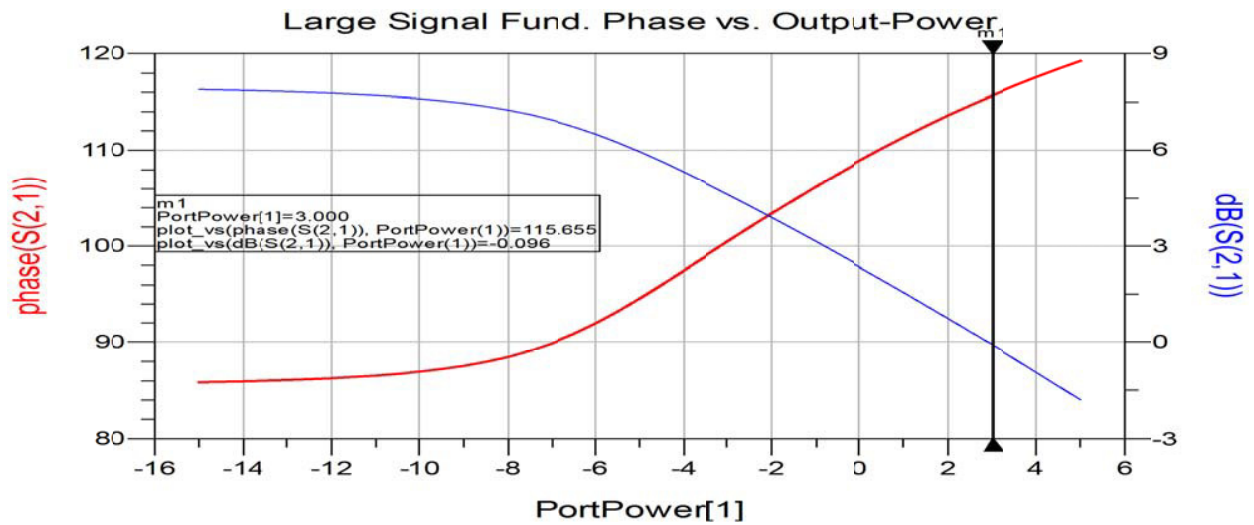


Figure 9-17: shows the plot of large signal forward transmission at resonance frequency vs. input-power. The marker is set to near unity-gain. The corresponding phase shift is about 116°.

Figure 9-18 shows the resonator matching section with delay line added and meander lines adjusted to achieve equal lateral reference positions for the interface ports to the oscillator core. Figure 9-19 shows measured amplitude and phase noise before (blue) and after (red) minor optimization of the input matching component. From the intersection of the 20dB/dec and 0dB/dec tangent, a  $Q_L$  of approximately 1k can be derived. Figure 9-20: shows the plots corresponding to the spectral and time-domain waveforms of the voltages at the output of the buffer amplifier (blue) and at the oscillator core output. 3-prototypes, namely DRO100 SN65, DRO100 SN66 and DRO100 SN78 are built for validation of the novelty of designing low phase noise DRO circuit described above.

CAD simulated data (DRO100) matches closely, agree within 2-3 degrees of accuracy with measured data of 3-prototypes (DRO100 SN65, DRO100 SN66, DRO100 SN78).

The measured phase noise plot is -112 dBc/Hz @ 10 kHz, -137 dBc/Hz @ 100 kHz and <-170 dBc/Hz @ >10 MHz; shows good agreement with the phase noise plots shown in Figure 9-19 and Figure 9-21.

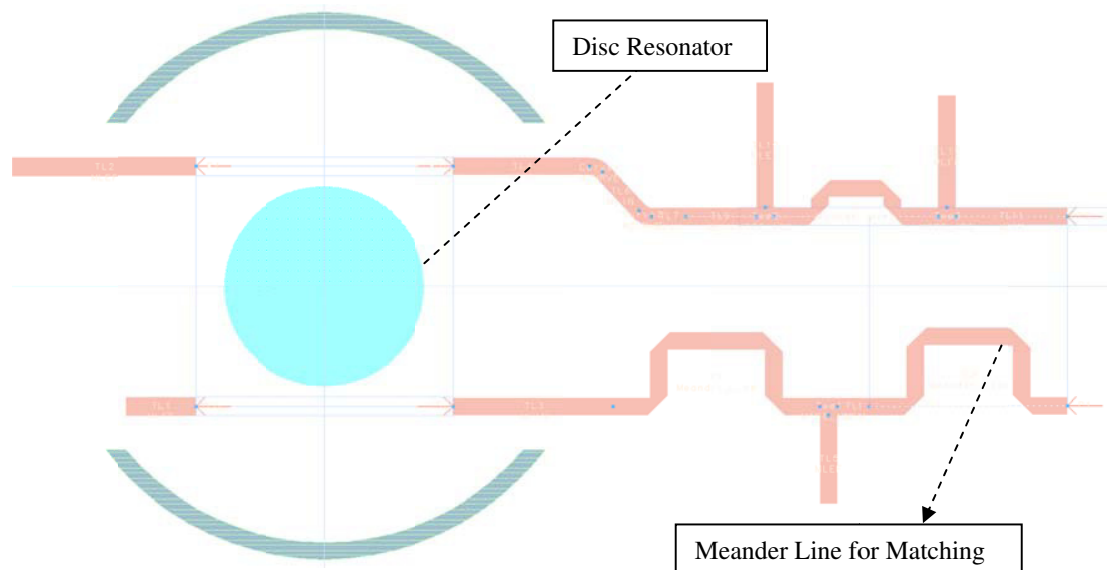


Figure 9-18: Resonator matching section with delay line added and meander lines adjusted to achieve equal lateral reference positions for the interface ports to the oscillator core.



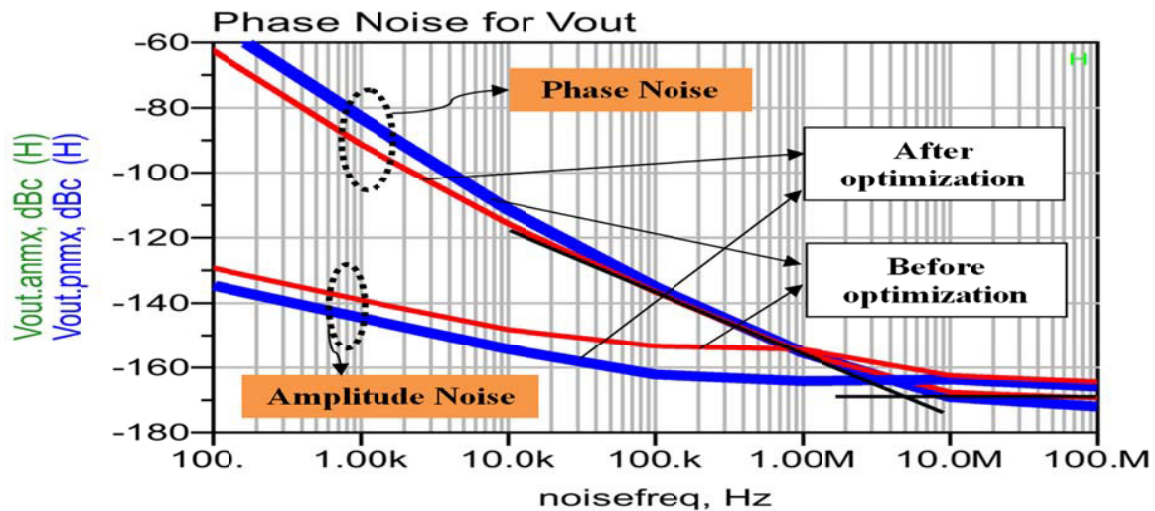


Figure 9-19: Measured amplitude and phase noise before and after minor optimization of the input matching component. From the intersection of the 20dB/dec and 0dB/dec tangent a  $Q_L$  of approximately 1k can be derived assuming that the Leeson formula does adequately reflect the situation.

#### FixedFreqOsc

Spectra and waveforms at oscillation frequency = 9.99836 GHz

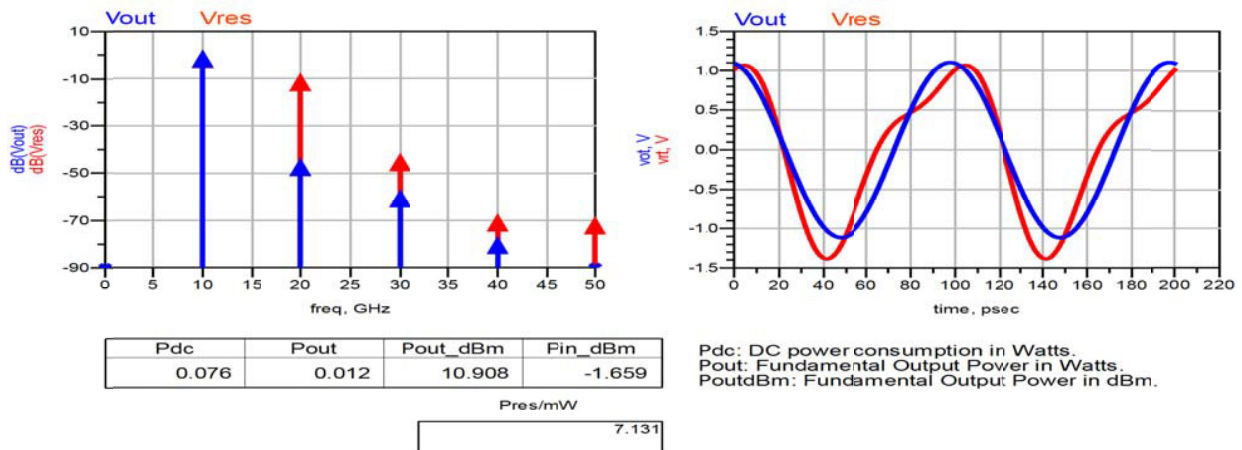


Figure 9-20: shows the plots corresponding spectra and time-domain waveforms of the voltages at the output of the buffer amplifier (blue) and at the oscillator core output.

Figure 9-22 shows the complete housing of 10 GHz DRO module ready for production, fabricated internal view of the DRO without dielectric resonator (Disc resonator bottom tuning screw is slightly elevated), and resonator cavity and dielectric disc resonator (DR not visible) added. Figure 9-23 shows the (a) Mechanical drawing of the 10 GHz DRO, and (b) a photograph of a 10 GHz DRO circuit, which is ready for production [27]. The DRO supply voltage can vary between +7 to +10 V and the internal voltage regulation gives high immunity to power supply noise. The supply-current is typically 50 mA and the temperature range is specified from -25°C to +70°C. The output-power exceeds +8dBm. The actual package size is approximately 3.1" × 1.34" × 0.788," including mounting flaps.

## 9.5 Conclusion

The step-by-step procedure of high performance X-band DRO is presented. The reported design methodology of ultra-low noise 10 GHz DRO circuit including the Möbius Coupled DRO improves the tuning range without degradation of phase noise performances [27].

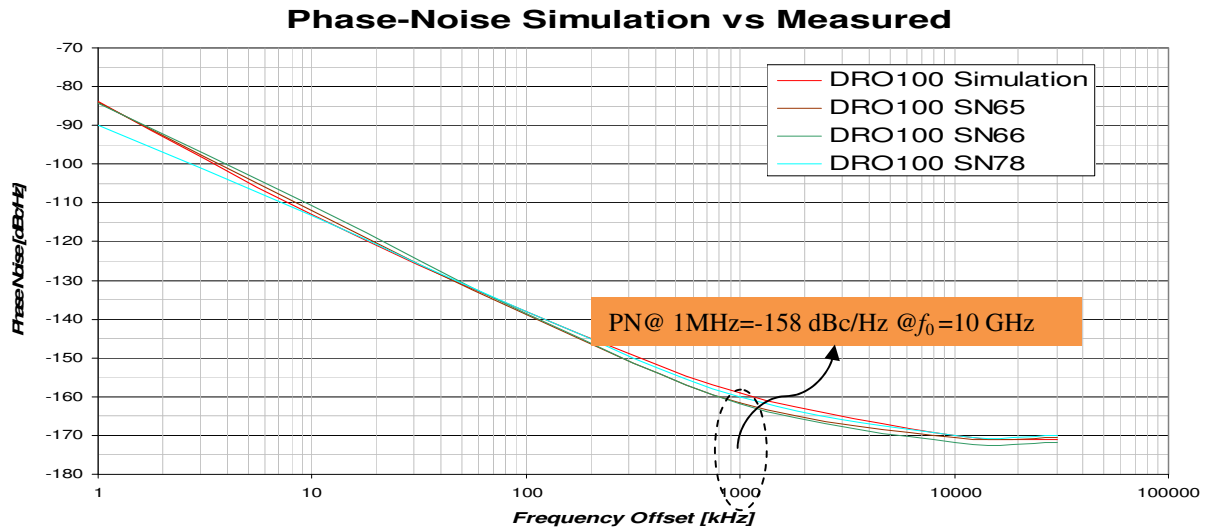


Figure 9-21: shows the CAD simulated and measured phase noise plots (3-prototypes: DRO100 SN65, DRO100 SN66, DRO100 SN78 is built for validation). CAD simulated data (DRO100) matches closely, agree within 2-3 degree of accuracy with measured data of 3-prototypes (DRO100 SN65, DRO100 SN66, DRO100 SN78).

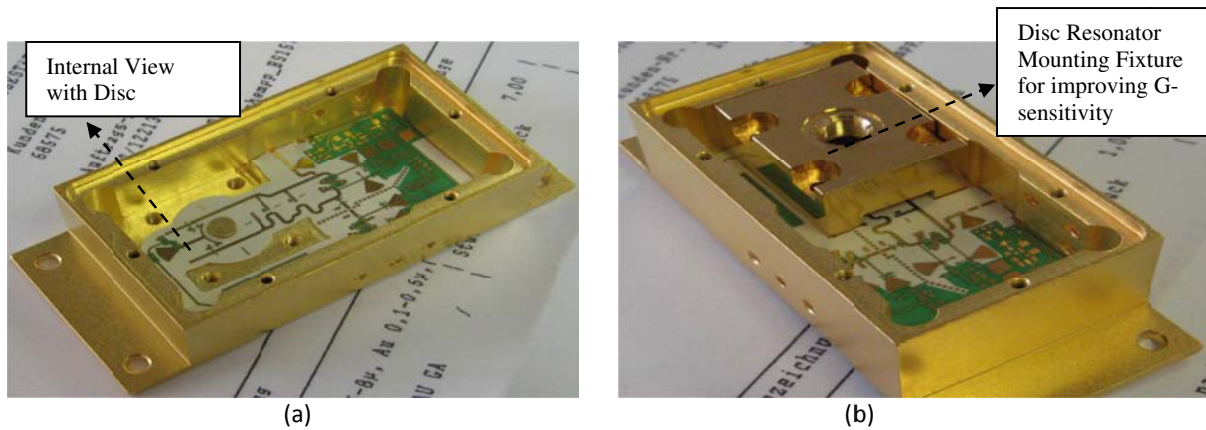


Figure 9-22: (a) Fabricated internal view of DRO housing without components, and (b) resonator cavity and dielectric disc resonator (DR not visible) not added [27]

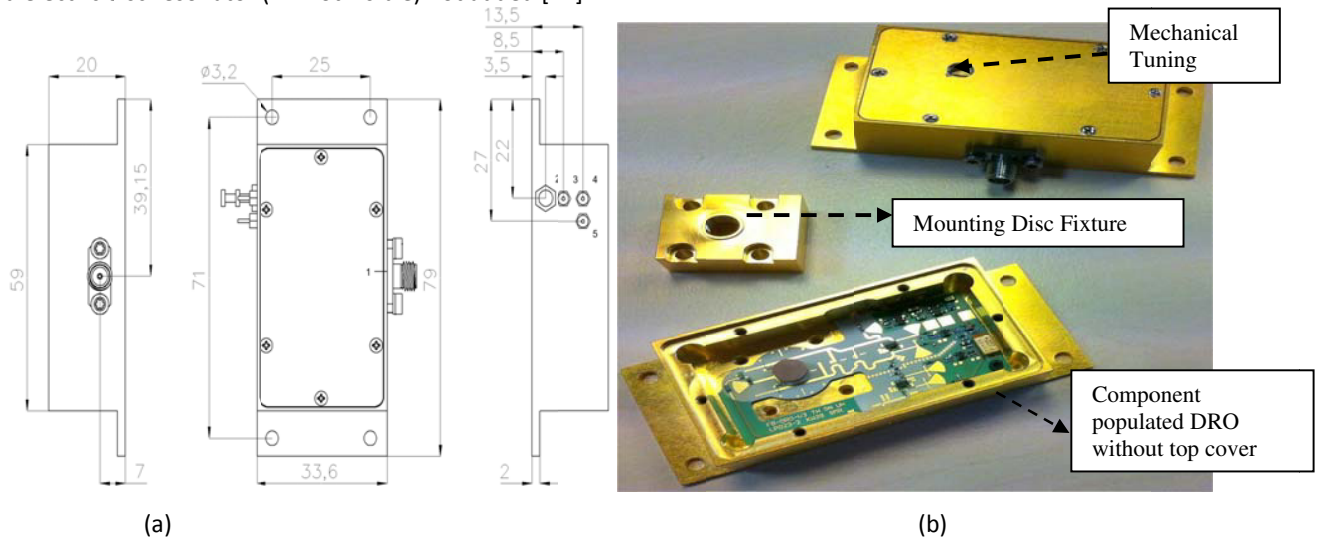


Figure 9-23: DRO module: (a) Mechanical drawing, and (b) a photograph of a 10 GHz DRO circuit [27]

## Chapter 10

### High Performance Opto-Electronic Oscillators (OEOs)

#### 10.1 Introduction

A typical OEO uses fiber delay that acts as a resonator in electronic oscillator circuits in 1 GHz-100 GHz ranges; frequency multiplication stages are not needed for achieving high frequencies (X, Ka, Ku band and above) [1]. The fundamental improvement in phase noise achievable in an OEO is attributable to direct frequency generation from an optical source rather than through electronic multiplication. Typical components of OEO circuits are assembled from discrete devices, especially optoelectronic photonic components require a large volume, high power consumption, and require a great deal of real estate and cost. Additionally, due to the assembly of a large number of discrete parts, application of OEO as reference frequency sources are generally subject to vibration and G-sensitivity problems [1]-[2]. The biggest challenge is to develop low cost and reliable integrated photonic components using Silicon CMOS, BiCMOS technology, eliminating the need for bulky and/or discrete microwave components. In this thesis, a novel high performance, low cost, and integratable OEOs system is developed based on metamaterial evanescent mode-locked resonator dynamics in conjunction with SILPLL (self injection locked phase locked loop) techniques [US Patent application No.: 61/746, 919; filed on Dec 28, 2012 and US Patent application no. 13/760767; filed on Feb 06, 2013] [3]-[4]. The detailed design examples described in extended version of this thesis [5]

#### 10.2. Opto-Electronic Oscillator (OEO) System

Figure 10-1 shows the typical block diagram of OEO system using SILPLL techniques for the realization of stable frequency source for high performance application in modern communication systems.

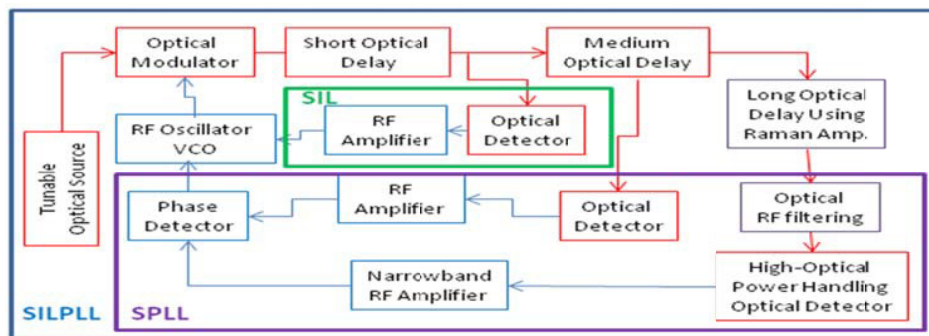


Figure 10-1: Block diagram of OEO using SILPLL (US Patent applications: 61/746, 919 and. 13/760767) (The color arrangement of various modules in the block diagram exhibits the SIL, SPLL, and SILPLL techniques) [3]-[4]

Following are the key features added for the realization of novel OEO circuits:

- Use of five port RF oscillator to have ease of self-injection, RF reference for self- phase locking (PLL), RF access for optical modulator, and output in RF domain and frequency control required in self-PLL using low frequency control as VCO port.
- Use of low loss, temperature stable, optimum length of fiber delay based on fiber loss as shown in Figure 10- 2 and Figure 10-3 [4].
- Use of optical “Nested Loop” and “Transversal Filter” in place of narrow band RF filter, the characteristics of nested loop and transversal filter shown in Figures 10-4 and 10-5.
- Realization of frequency tunable OEO when dispersive PBG optical fibers combined with tunable optical source as demonstrated in Figure 10-6.

- (e) Compensation of loss using distributed Raman amplifier to compensate and reduce fiber loss in PBG fibers as shown in Figure 10-7 and Table 10.1.
- (f) Inclusion of optical mode-locking by using the phase error comparator to adjust DC bias current of tunable semiconductor laser as optical source for both externally and directly modulated optical links and/or adjusting the DC bias condition on optical modulator in externally modulated optical links (for Mach-Zhender modulator or Electro-absorption modulators).

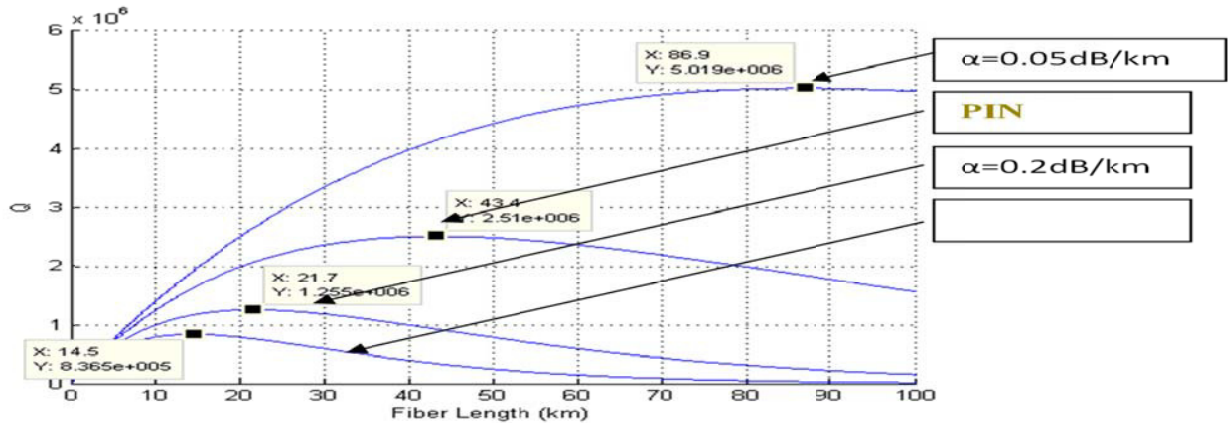


Figure 10-2: The plot of Q-factor and optimum length of fiber optic delay line for a 10 GHz oscillator using different fiber attenuations ranging from 0.05dB/km to 1dB/km [3]-[4].

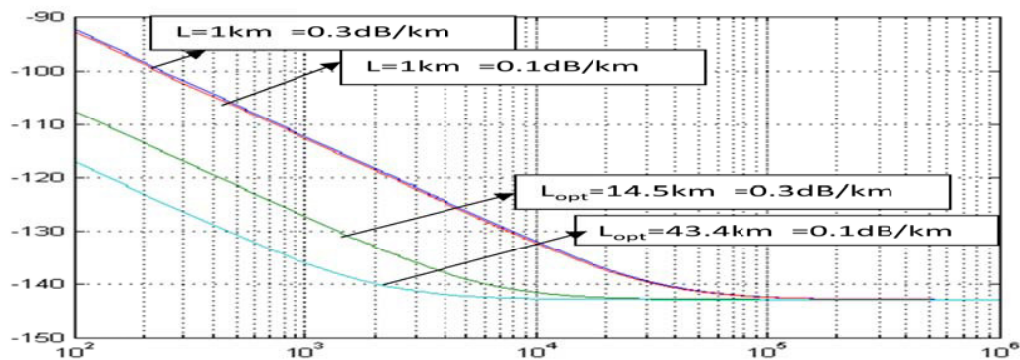
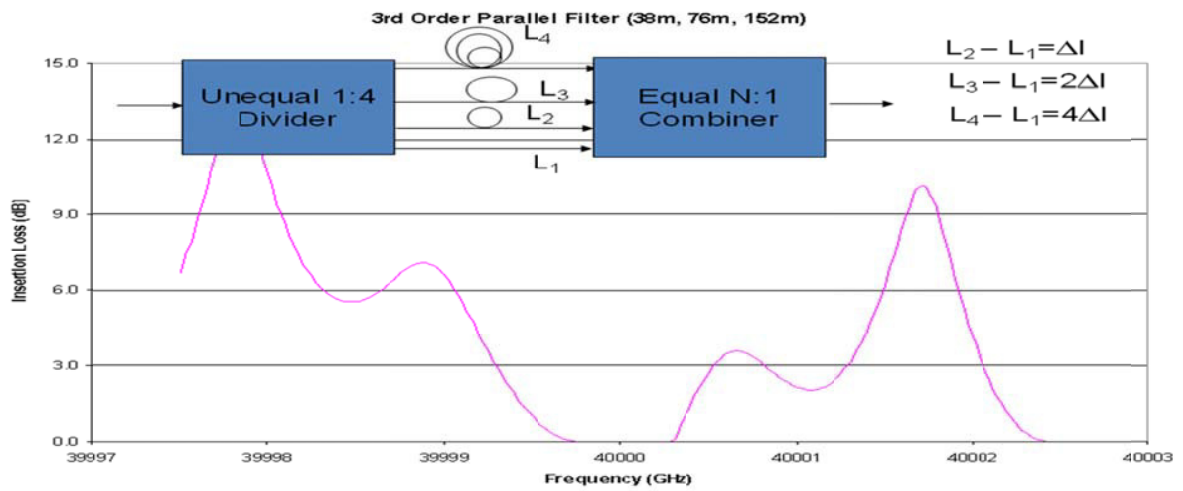


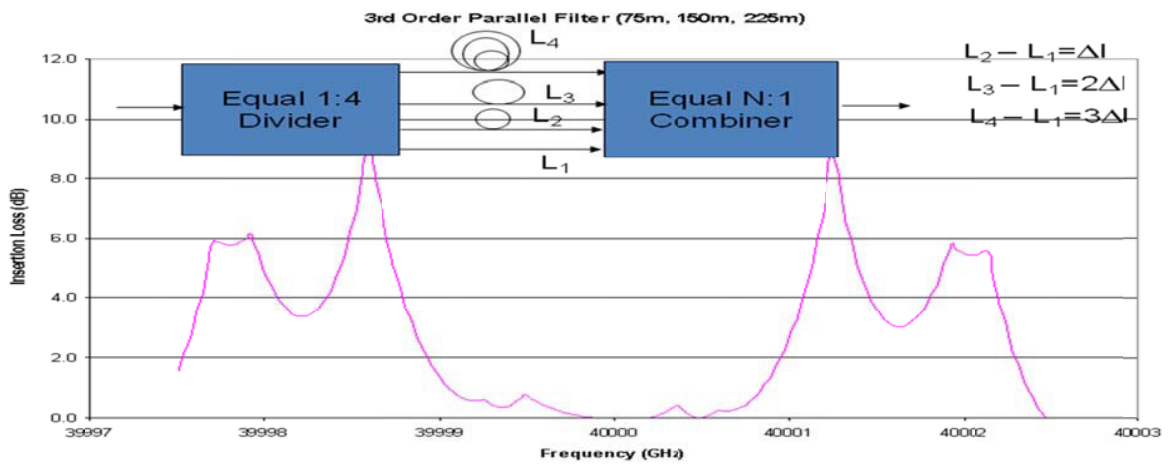
Figure 10-3: The plots show the comparison of achieved close-in to carrier phase noise of 10 GHz OEO using optimum and non-optimum lengths for fiber attenuation of 0.1dB/km versus 0.3dB/km [3]-[4].

Table 10.1: Effective Q and PN Comparison of SMF-28 and Composite Fibers before and after Raman Amplifier

	Fiber Delay Length (km)/ Pump power (dbm)	Att. without RA ( $\alpha_p$ in dB/km, $\alpha_s=0.33$ dB/k)	Effective Att. with RA ( $\alpha_p$ in dB/km, $\alpha_s=0.33$ dB/k)	Relative Q Before RA	Relative Q After RA	Phase Noise Degradation Before RA	Phase Noise Degradation After RA	Phase Noise (dBc/Hz) @ 1kHz Before RA	Phase Noise (dBc/Hz) @ 1kHz After RA	Phase Noise (dBc/Hz) @ 10kHz without RA	Phase Noise (dBc/Hz) @ 10kHz with RA
SMF-28	10/NA	-	-	$Q_s$	-	-	-	-123	-	-143	-
Composite fibers with passive Temperature Compensation of $L_{p1LS} = 38:1$	10/30	3	0.06	$\frac{Q_s}{12.6}$	$3.5Q_s$	21.9	-10.9	-101.1	-133.9	-121.1	-153.9
	3/35	10	0.04	$\frac{Q_s}{41.8}$	$4.9Q_s$	32.4	-13.8	-90.6	-136.8	-110.6	-156.8
	1.23/3 5	15	0.002	$\frac{Q_s}{62.6}$	$22.4Q_s$	35.9	-27.0	-87.1	-150.0	-107.1	-170.0



(a) Unequal 1:4 power splitter and combiners



(b) Equal 1:4 power splitter and combiners

Figure 10-4: CAD simulated insertion loss of 3<sup>rd</sup> order nested loop filter realized by parallel combination of delay lines at  $\lambda=1550\text{nm}$  as a narrowband RF filter at about 40,000MHz. (a) Unequal 1:4 power splitter and combiners, and (b) Equal 1:4 power splitter and combiners. Note measured 3dB bandwidth of this filter is  $\sim 2\text{MHz}$  [3]-[4].

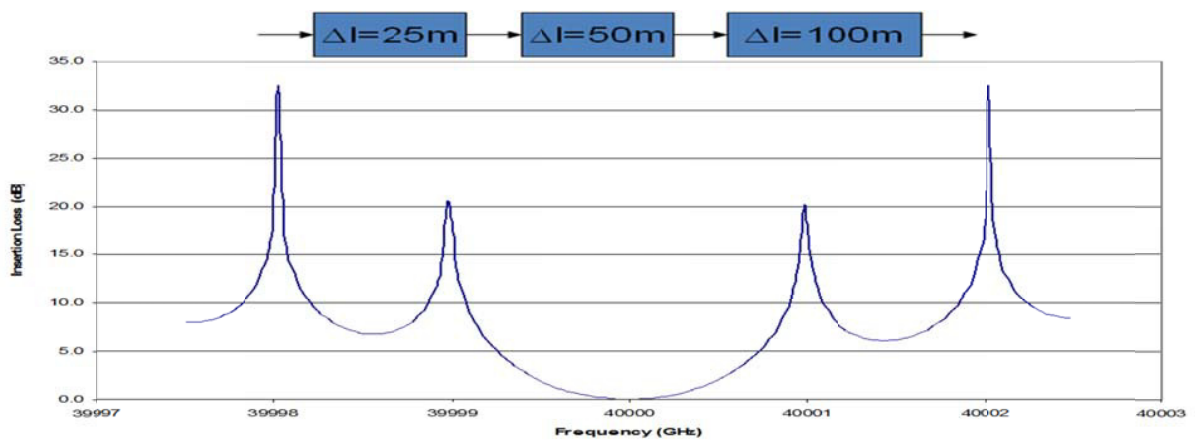


Figure 10-5 Design and simulated insertion loss of 3<sup>rd</sup> order transversal filter as nested loop RF filter at 40.000GHz. Note 3dB bandwidth is under 1MHz [3]

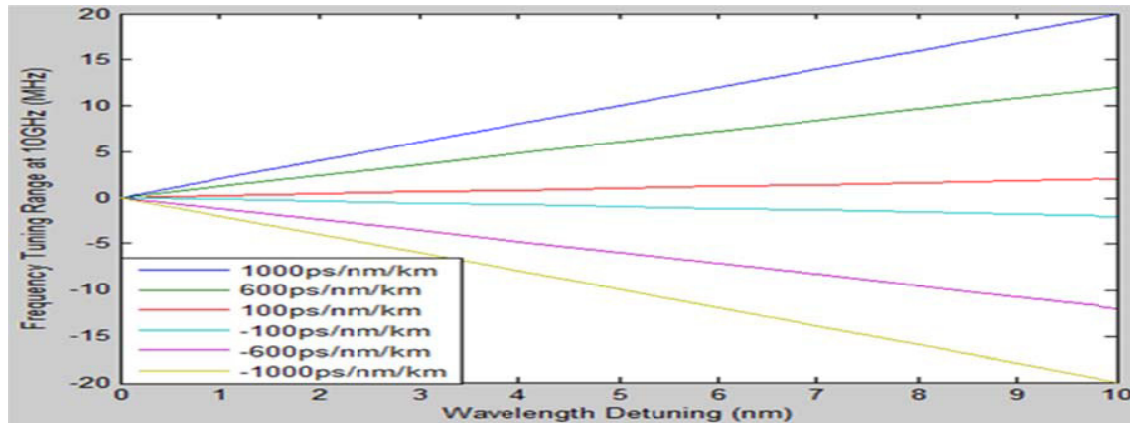


Figure 10-6: The plots show the frequency tuning range at 10 GHz as a function of Fiber Dispersion at 1550 nm for 1km Long Fiber  $\frac{\Delta f}{f} = \frac{\tau_D}{\tau}$

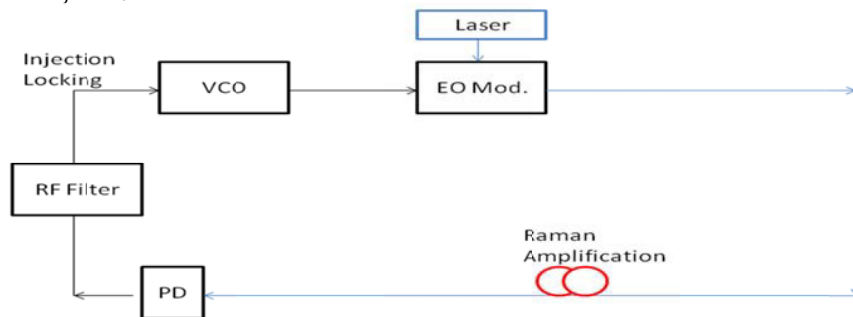


Figure 10-7: Block diagram describes the distinct features of Raman amplification [20].

### Realization of Low Phase Noise and Passive Temperature Stable OEO Circuits

Figure 10-8 shows the illustrative block diagram of “passive temperature stable ultra low phase noise and optoelectronic oscillator circuits”. As shown in Figure 10-8, the different modules explain their characteristic as follows [3]-[4]:

1. Use of self-ILPLL for phase error corrections to a free-running 5 port VCO as the nucleating seed source for OEO using a loop filter bandwidth of few MHz, phase control, efficient self-injection (this component is novelty of design), where
  - (a) Self- injection locking is used for cleaning close-in to carrier phase noise of the VCO at far away from carrier ( $\Omega > 1\text{MHz}$ ) by improving on locking range due to low Q electrical oscillator and higher injected signal using 5 port VCO
  - (b) Self-phase locking is used to improve close-in to carrier phase noise for close to carrier ( $\Omega < 1\text{MHz}$ ) of VCO using a higher natural resonance frequency of loop filter amplifier to the five port VCO using the control port
  - (c) Combining IL and PLL to achieve self-ILPLL topology to reduce close-in to carrier phase noise by optimizing combination of locking range, gain of loop filter amplifier, and fiber delay
  - (d) Ability to maintain phase locking to any phase between -90 to +90 for fundamental frequency and -180 to 180 degrees for 2<sup>nd</sup> sub-harmonic locking by setting the voltage reference of the operational amplifier in the loop filter amplifier from negative to positive voltage corresponding to a phase detuning close to -85 to +85 degrees, while still maintain a clean close-in to carrier phase noise for a phase detuning of 0 degrees

2. Use of specialized fiber optic delay line providing reduced temperature sensitivity for the optical Fabry Perot resonator and enhanced dispersion characteristics (this component is a significant novelty of the proposed OEO design), which will provide
  - (a) Low-loss and passive temperature compensation using a right combination of standard optical fibers and suffers from as much as  $-10\text{ppm/C}$  change in index of refraction in silica fibers by  $+2.5\text{ppm/C}$  of HC-PCF or a reduced temperature sensitivity of  $-3\text{ppm/C}$  of SC-PBG fibers
  - (b) Provide distributed optical amplification to actively reduce light attenuation based on principle of Raman amplification using a pump source appropriately selected with respect to the source wavelength based on Stimulated Raman Scattering
  - (c) Changing oscillation frequency of OEO by adjusting phase shift introduced in the optical delay element using high dispersion of PBG fibers to as much as  $-500\text{ps/nm km}$  from  $-17\text{ps/nm km}$  of standard fibers
  - (d) Frequency synthesis of OEO by tuning of the optical source wavelength where the oscillation frequency is being controlled by satisfying Barkhausen oscillation condition in a passively temperature compensated low loss dispersive PBG fibers.

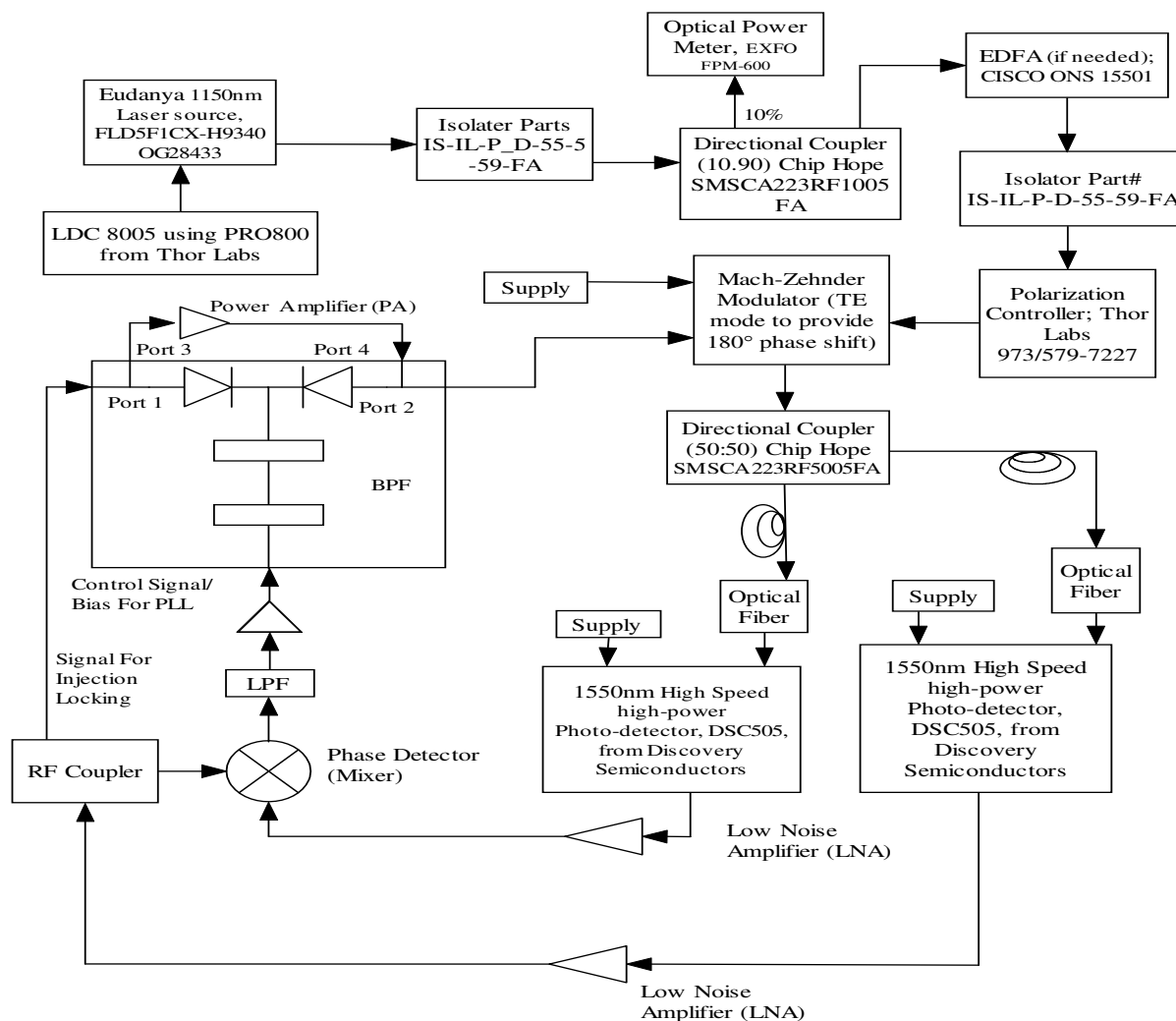


Figure 10-8: Shows the illustrative block diagram of “ultra low phase noise and passive temperature stable optoelectronic oscillator circuits” [3]-[5]

3. Use of multiple loops to perform phase comparison of different references provided through multiple fiber optic delay lines (use of many control feedback loops and phase locking is novelty of this OEO design), where
  - (a) Self-ILPLL made to a reference of 1 us (200m) delay that is fast and minimizes the oscillation frequency of VCO's drift by synchronizing every 1us;
  - (b) Self-ILPLL is being also augmented by delays of 5  $\mu$ s (1km) that is minimizing the VCO frequency drift, which in turn is to be augmented by 50 $\mu$ s (10km) to make sure that the overall frequency drift is limited to shifts limited within 1 $\mu$ s as the VCO oscillation is locked to an equivalent reference of oscillation delay of 50 $\mu$ s (10km long fiber delay)
4. Use of temperature compensated nested loop RF filters for the OEO frequency mode selection in a multi-mode system of long delays (every 20kHz for 10km long or 50 $\mu$ s delays, every 200kHz for 1km fiber delays, and every MHz for 200m long fiber delays), which
  - (a) Adjusts passband frequencies by selecting long fiber optic delay
  - (b) Avoids the need for extremely large size and insertion loss in high order RF metallic filters
  - (c) Achieves a much higher order optical fiber based Nested Loop RF filters for even similar size RF metallic filters
  - (d) Employs Hi-Bi fibers for fully integrated small size structures
  - (e) Maintain higher frequency selectivity using high order parallel or series combination of 1<sup>st</sup> order transversal optical filters
  - (f) Implement temperature compensated narrow band optical nested loop RF filter by use of PBG fibers
5. Exploring multi-modal locking in the OEO by optical phase locking (this component is novelty of OEO design) using the concepts of mode-locked OEO by establishing optical mode locking of OEO using variable changes to biasing conditions of
  - (a) Mach-Zehnder modulator DC bias in fiber optic links
  - (b) Optical phase delay shift of an integrated optical delay line using EA modulator
  - (c) Change in index of refraction of the directly modulated fiber optic delay element

Figure 10-9 shows the CAD simulated phase noise plot of SILPLL VCO. In the simulation setup, a self-injection mechanism is applied to a VCO with dual DLFD SPLL, the short and long delays are 1 $\mu$ s and 10 $\mu$ s respectively. The injection strength is  $\rho=0.316$  and the injection delay is 10 $\mu$ s. The green curve represents the phase noise of the VCO incorporating SILPLL. The phase noise of SILPLL reaches the noise floor at around 100 kHz offset while the phase noise of double loop SPLL reaches the noise floor at 100 kHz. For comparison, phase noise of a single SPLL with 10 $\mu$ s delay and a dual SPLL with 1 $\mu$ s and 10 $\mu$ s delay are also provided. The improvement in phase noise for SILPLL is significant. Phase noise of SILPLL VCO is -165 dBc/Hz @ 20 kHz offset from the carrier is predicted. It can be seen that there is hump & dip after 20 kHz offset from the carrier in Figure 10-9, the reason of degradation in phase noise performance is due to higher order modes prevalent in the fiber delay line. To suppress the hump, mode-locking technique has been incorporated using metamaterial evanescent-mode-coupling and enabling dynamic mode spacing of the optical delay line to achieve a zero or minimum frequency drift. Since the optical fiber may be intrinsically temperature sensitive, causing change in effective length and refractive index over temperature, the oscillator needs a control circuit to regulate the effective fiber length to prevent mode-jumping phenomena and thereby degradation from close-in to carrier phase noise. The active degenerative feedback, in conjunction with the self-injection and mode-locking techniques, produces uniformly fixed mode spacing, reducing frequency drift due to operating temperature changes [2].



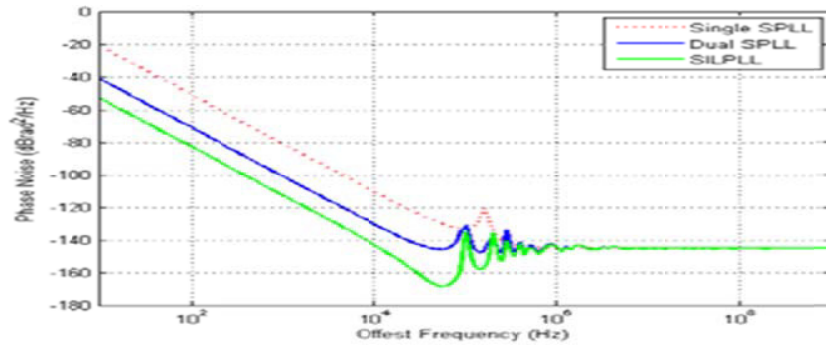


Figure 10-9: The plots show the comparison of predicted phase noise of 10 GHz OEO using SPLL & SiLPLL [3]

Figure 10-10 shows the typical block diagram of low phase noise OEO circuit. As shown in Figure 10-10, the evanescent mode resonator combiner network (206) acts as an evanescent mode (EM) buffer, storing a portion of the excess radio frequency (RF) energy coupled into the resonator network for a given period of a signal cycle so that the conduction angle of the device can be reduced, thereby reducing noise for a given period of time. The phase detector network (260) dynamically compensates for phase errors between each oscillator during wideband operation. The phase detector network (260) detects random fluctuations in the free-running frequency and translates those fluctuations into phase errors. The phase errors are then fed back to the combiner network (232) and used to control the phase and frequency of the buffered signal (250) during tuning operation. Figure 10-11 shows the printed circuit board (PCB) realization, readily amenable for monolithic integration using Si fabrication technology [5].

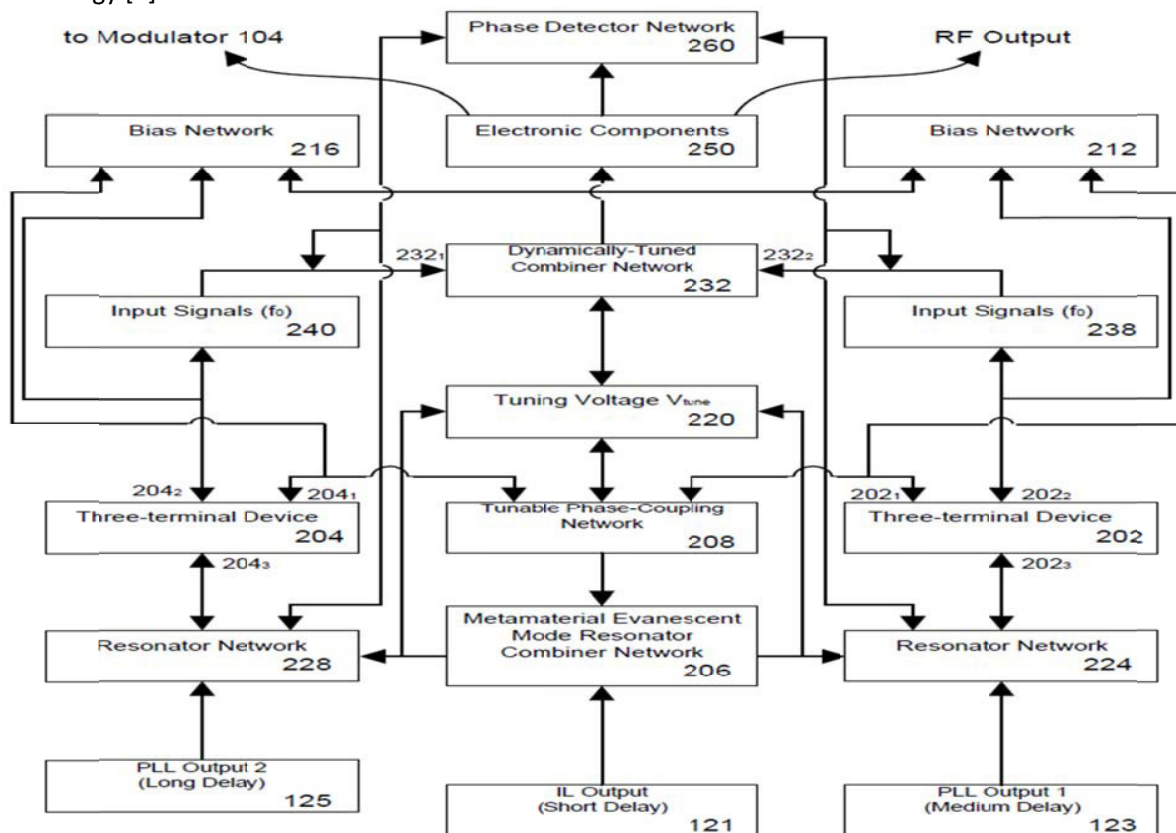


Figure 10-10: Block diagram of 10 GHz source using self ILPLL RF Oscillator (US Patent application No.: 61/746, 919; filed on Dec 28, 2012 and US Patent application no. 13/760767; filed on Feb 06, 2013) [3]-[5]

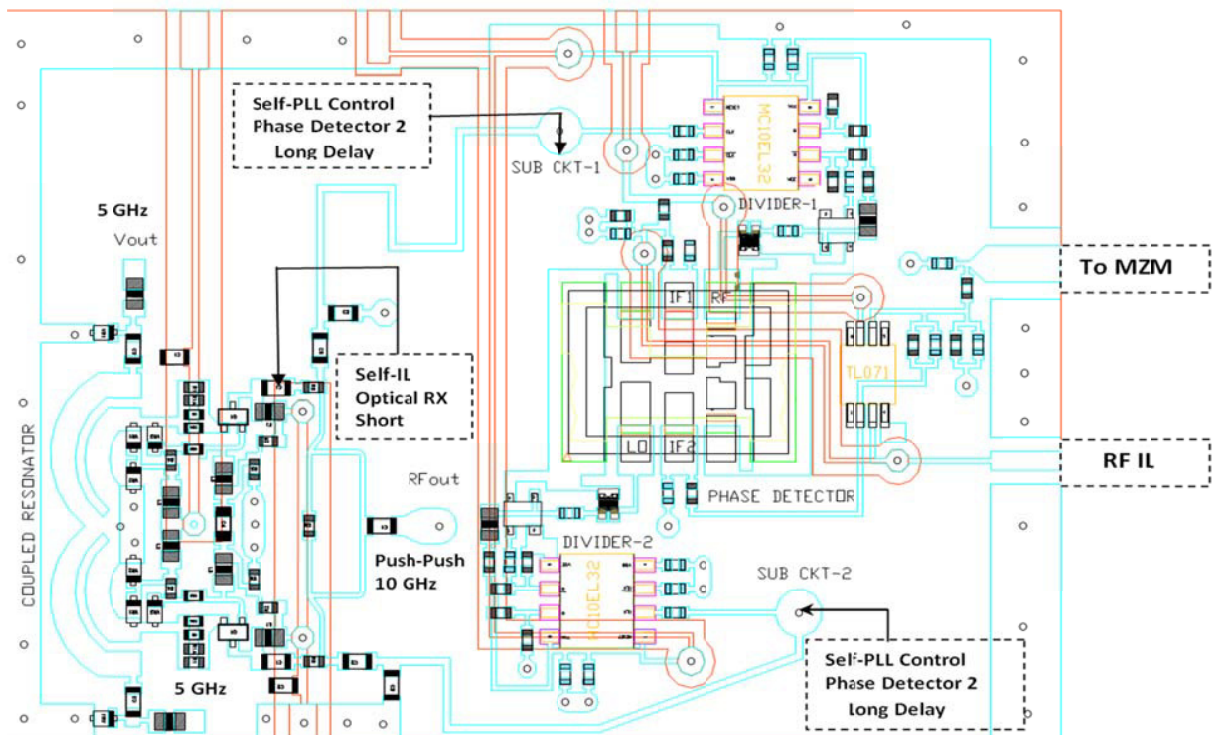


Figure 10-11: shows the layout of stable 10 GHz signal sources as per US patent applications No.: 61/746, 919; filed on Dec 28, 2012 and US Patent application no. 13/760767; filed on Feb 06, 2013 [3]-[5].

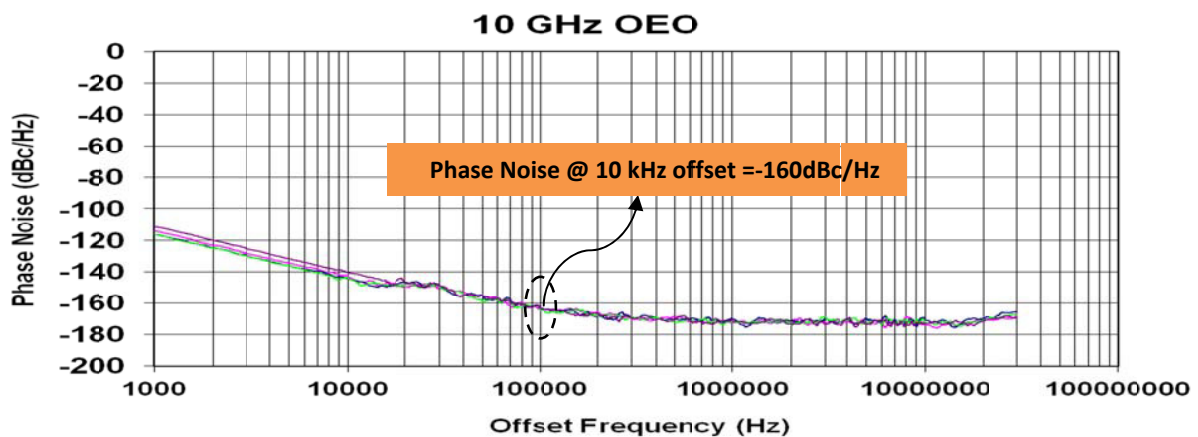


Figure 10-12: The measured phase noise plots of 10 GHz OEO circuit [3]-[4]

Figure 10-12 shows the measured phase noise plot, note that the hump & dip are suppressed. The reported phase noise plot shown in Figure 10-10 is the best performance to date reported for the given figure of merit (FOM) and this class of oscillator topology [3]-[4]. The integrated OEO solution shown in Figures 10-10 and 10-11, offers cost effective, power efficient platform in silicon (CMOS/BiCMOS/HBTs). The detailed design examples described in extended version of this thesis [ref. 5, Appendix F-I]

### 10.3 Conclusion

The reported OEO configuration shown in Figure (10-10) and (10-11) is amenable for MMIC in silicon, enabling compact, low noise and low cost solution in which it is possible to synthesize any precise RF frequency by adjusting the optical source wavelength, leading to satisfying stable oscillation conditions for a new RF frequency in highly dispersive photonic bandgap fibers.

## Chapter 11

### Conclusion

#### 11.1 Conclusion

Modern communication systems require two kinds of signal sources: (i) ultra low phase noise fixed frequency reference signal sources, and (ii) low phase noise tunable frequency signal sources. But the common denominator for both sources is identical, which is low cost, low power consumption, and compact size. Intrinsically, high Q-factor resonators (Crystal, SAW-Surface Acoustic Wave, BAW-Bulk Acoustic Wave, Ceramic, Dielectric, MEMS, and Optical Fiber) based oscillator circuits exhibit low phase noise characteristics for fixed frequency or narrow band ( $< 1\%$ ) solutions but they are power hungry, vibration sensitive, and expensive. Historically, broadband oscillators are realized by using either YIG resonator or transmission line resonator network. YIG resonator based oscillators exhibit wide tuning capability and low phase noise characteristics but sensitive to vibration, lighting, electromagnetic interference (EMI), microphonics, and frequency modulation; all of which have a detrimental effect in designing modern communication systems. Printed resonator based oscillators can offer broadband tunability and insensitive to vibration but at the cost of poor phase noise performances and larger size.

During the last decades, design engineers and research communities have been improving the phase noise performance and also exploring the optical resonator based signal source solutions. This development has taken place in two distinct lines of approach. The first one dealt with the reducing the size and improving the Q-factor of the printed resonator and the second is related with the exploring different oscillator topologies using self-injection locking, phase-locking, mode-locking, evanescent-mode coupling, mutual-injection-locking, and noise-filtering for ultra low phase noise performances. This thesis presents novel techniques to design signal sources using crystal resonator, dielectric resonators, printed transmission line resonator and optical fiber resonator networks for current and later generation communication systems. A novel "Slow-Wave Möbius Coupled Resonator Topology" discussed for superior performance, can partly or fully meet the criteria of new requirement posed by 4<sup>th</sup> generation communication systems. A quality-factor enhancement technique based on employing slow-wave resonator is discussed and experimentally verified by designing frequency synthesizer using oscillator employing mode-coupled slow-wave metamaterial resonators. The methodology discussed can be applied to design miniaturized very low phase-noise voltage-controlled-oscillators at microwave and mm-wave frequencies. The intended application is the development of multi-band low phase noise signal source solutions for current and later generation communication systems.

#### 11.2 Futuristic Work

The slow-wave metamaterial based Möbius resonators have received increasing attention for integrated oscillator design; these resonators can provide high quality-factors while occupying a small area due to small wavelengths at mm-wave frequencies. The Metamaterial Möbius technology discussed in this thesis can open new era in the field of imaging and sensors applications. Following research work as futuristic technology is in under progress:

- Telecom, Biomedical, and Sensors application
- Energy Harvesting, Solar Cells, Go Green Solution
- Subdiffraction Imaging, Superlens
- High Resolution 3-D printers
- Antenna, Invisibility Cloak

## Symbols

<u>Symbol</u>	<u>Description</u>
<i>LTV</i>	Linear time variant
<i>NLTV</i>	Nonlinear time variant
<i>LTIV</i>	Linear time invariant
<i>ATI</i>	Active tunable inductor
<i>AI</i>	Active Inductor
<i>TI or TAI</i>	Tunable inductor or Tunable active inductor
<i>TAIO</i>	Tunable Active Inductor Oscillator
<i>ATIO</i>	Active tunable inductor oscillator
<i>AIO</i>	Active inductor oscillator
<i>VCO</i>	Voltage controlled oscillator
$G_m/g_m(t)$	Large-signal transconductance
$g_m$	Small-signal transconductance
$a_n(x)$	Fourier coefficient
$I_n(x)$	Modified Bessel function of order n
$I_e(t)$	Emitter current
$I_c(t)$	Collector current
$I_{cob}$	Collector reverse current
$V_{n(total)}$	Total noise voltage
$V_{sn}$	Noise due to source
$V_{n(network)}$	Noise due to network
$Y_g$	Generator admittance
$Y_{opt}$	Optimum noise admittance
$F_{min}$	Minimum achievable noise figure
$R_n$	Noise resistance
$[C_Y]$	Y-parameter noise correlation matrix
$[C_A]$	ABCD Correlation Matrix
$Y_{cor}$	Correlation factor
$\overline{i_{bn}^2} = 2qI_b\Delta f$	Mean square value of noise due to base current

$\overline{i_{cn}^2} = 2qI_c\Delta f$	Mean square value of noise due to collector current
$\overline{i_{con}^2} = 2qI_{cob}\Delta f$	Mean square value of noise due to reverse collector current
$\overline{v_{bn}^2} = 4kTR_b\Delta f$	Mean square value of noise voltage due to base resistance
$S(i_{cn}) = 2kTg_m$	Noise power spectral densities due to collector current
$S(i_{bn}) = \frac{2kTg_m}{\beta}$	Noise power spectral densities due to base current
$S(v_{bn}) = 4kTR_b$	Noise power spectral densities due to base resistance
$S(v_{sn}) = 4kTR_s$	Noise power spectral densities due to source resistance
$\overline{i_d^2} = 4kTg_mP\Delta f$	Mean square value of noise due to drain current
$\overline{i_g^2} = \frac{4kT(\omega C_{gs})^2 R}{g_m} \Delta f$	Mean square value of noise due to gate current
$P = \left[ \frac{1}{4kTg_m} \right] \overline{i_d^2} / \text{Hz}$	FET noise coefficient
$R = \left[ \frac{g_m}{4kT(\omega C_{gs})^2} \right] \overline{i_g^2} / \text{Hz}$	FET noise coefficient
$C = -j \left[ \frac{\overline{i_g i_d^*}}{\sqrt{\overline{i_d^2 i_g^2}}} \right]$	FET noise coefficient
$P$	0.67 for JFETs and 1.2 for MESFETs
$R$	0.2 for JFETs and 0.4 for MESFETs
$C$	0.4 for JFETs and 0.6-0.9 for MESFETs
$Z_s$	Complex source impedance
$\alpha = \left[ 1 + \frac{f^2}{f_b^2} - \alpha_\theta \right] \frac{1}{\alpha_\theta}$	Modified factor
$X$	Drive-Level
$\left( \frac{kT}{q} \right) x$	Drive-Voltage
$2 \left[ \frac{I_1(x)}{I_0(x)} \right]$	Fundamental component of current
$\left[ \frac{I_2(x)}{I_1(x)} \right]$	Second harmonic component of current
$\varphi$	Conduction angle
$n$	Transformation factor
$n_{opt}$	Optimum transformation ratio
$R_p$	Parallel loss resistance

$Q_L$	Loaded quality factor
$f_0$	Center frequency
$f_c$	Flicker corner frequency
$f_m$	Frequency offset
$P_{sav}$	Average power at oscillator output
$K_0$	Oscillator voltage gain
$F = \frac{\overline{i_L^2}}{i_{LO}^2}$	Noise factor
$NF$	Noise Figure
$\mathcal{L}(f_m)$	Ratio of sideband power in a 1 Hz bandwidth at $f_m$
$E_B, E_H$	Vector of harmonic-balance (HB) errors
$E$	Vector of real and imaginary parts of all HB errors
$X_B, X_H$	Vector of state variable (SV) harmonics
$J_B, J_H$	Vector of forcing terms
$\delta X_B, \delta X_H$	Perturbation of the circuit state
$M$	Jacobian matrix of the HB errors
$\delta \omega_0(\omega)$	Phasor of the pseudo-sinusoidal components
$N_k(\omega)$	Noise power spectral density
$C_k(\omega)$	Normalized correlation coefficient
$J_p(\omega)$	Side-band noise sources
$U_p(\omega)$	Side-band noise sources
$I_k^{SS}$	Noise power spectral density
$S_{\Delta\theta}(\omega)$	Power spectral density of the input phase error
$\theta_d$	Peak phase deviation
$e_N(t)$	Noise signal voltage
$R_N(t)$	Time variant negative resistance
$k$	Boltzmann's constant (1.38E-23 J/K)
$kT$	$4.1 \times 10^{-21}$ at 300 K <sub>0</sub> (room temperature)
$R$	Equivalent noise resistance of tuning diode
$G$	Compressed power gain of the loop amplifier
$TF(j\omega)$	Closed loop transfer function
$H(j\omega)$	Open loop transfer function
$\langle  \delta\varphi_{ck}(\omega) ^2 \rangle$	PM noise at $k^{\text{th}}$ harmonic
$\langle  \delta\varphi_{mk}(\omega) ^2 \rangle$	PM noise due to contribution of modulation

$\langle  \delta A_{ck}(\omega) ^2 \rangle$	AM noise to carrier ratio at $k^{\text{th}}$ harmonic
$\langle \delta \varphi_{ck}(\omega) \delta A_k(\omega)^* \rangle$	PM-AM correlation coefficient for the $k^{\text{th}}$ harmonic
$\langle  J_H(\omega) J_H^\otimes(\omega)  \rangle$	Correlation matrix
$T_F^\otimes$	Conjugate-transpose
$T_{Ak}$	Row-matrix
$T_F$	Frequency transfer matrix
$Y_R(k\omega_\theta)$	Trans-admittance matrix
$ I_k^{SS}  \exp(j2\varphi_k^{SS})$	$k^{\text{th}}$ harmonic of the steady-state current through the load
$C_{k,-k}^*(\omega)$	Correlation coefficient of the upper and lower sidebands
$m(t)$	Modulating signal
$K_p$	Phase sensitivity
$\beta = \frac{\Delta f}{f_m}$	Modulation index of the modulating signal
$SNR$	Signal to noise ratio
$A_{SSB}$	Sideband amplitude of a phase modulation
$C_0$	Coefficient of Fourier series, $0^{\text{th}}$ order of the ISF
$\Delta f$	Noise bandwidth
$\omega_{1/f}$	1/f noise corner frequency of the device/transistor
$q_{max}$	Maximum charge on the capacitors in the resonator
$NFT_{inr}(\omega)$	Noise transfer function due to resonator loss resistance
$NFT_{vbn}(\omega)$	Noise transfer function due to transistor base resistance
$NFT_{ibn}(\omega)$	Noise transfer function due to the transistor base current
$NFT_{ifn}(\omega)$	Noise transfer function due to flicker noise
$NFT_{icn}(\omega)$	Noise transfer function due to collector current
$K_f$	Flicker noise constant
$AF$	Flicker noise exponent
$\sigma(t)$	Complex envelope of the frequency modulated signal
$\Gamma_{rms}/\Gamma(x)$	Impulse sensitivity function
$EMF$	Electromotive force
$\beta^+$	Large-signal current gain
$Y_{11}^+$	Large-signal input admittance
$Y_{21}^+$	Large-signal transconductance
$\Delta A(t)$	Amplitude fluctuation
$\Delta \varphi(t)$	Phase fluctuation

$\Delta\theta$	Steady state phase difference
$Y_n$	Normalized noise admittance
$Y_e$	Even mode admittance
$Y_o$	Odd mode admittance
$\lambda_e$	Even mode
$\lambda_o$	Odd mode
$G_n$	In-phase component of noise source
$B_n$	Quadrature component of noise source
$m$	Ratio of loaded and unloaded Q
$m_{opt}$	Optimum value of m for minimum phase noise
$Q_o$	Unloaded quality factor
$\beta_{ij}$	Coupling parameter
$\alpha_i$	Free-running amplitude of the $i^{\text{th}}$ oscillator
$A_i(t)$	Instantaneous amplitude of the $i^{\text{th}}$ oscillator
$\varphi_i(t)$	Instantaneous phase of the $i^{\text{th}}$ oscillator
$\omega_i$	Free-running frequency of the $i^{\text{th}}$ oscillator
<b>MEMS</b>	Micro-electro-mechanical-system
<b>SMD</b>	Surface mounted device
<b>SRF</b>	Self resonance frequency
<b>MSL</b>	Microstripline
$e_{inj}(t)$	Injected signal voltage
$\Delta\omega_{lock}$	Locking bandwidth
$\omega_{inj}$	Injected signal frequency
$\lambda_{ij}$	Magnitude of the coupling coefficient
$\varphi_{ij}$	Phase of the coupling coefficient
$r$	Capacitance ratio of the tuning diode
$C_{V0}$	Capacitance of tuning diode at zero bias voltage
$C_{VB}$	Capacitance of tuning diode at breakdown bias voltage



$P_n$	Average power dissipated by the network
$\mu$	Empirical nonlinear parameter
$R_n(t)$	Time variant negative resistance
$C_n$	Fourier series coefficient
$[\overline{C}]$	Matrix representation of arbitrary coupling topology
$C$	Coefficient of correlation
$\theta_n$	Phase of the $n^{\text{th}}$ harmonic
$W_e$	Average stored electrical energy
$W_m$	Average stored magnetic energy
$\omega_{diff}$	Modulation frequency
<b>VNA</b>	Vector network analyzer
<b>VDP</b>	Van der Pol
<b>SWR</b>	Slow-Wave resonator
<b>DR</b>	Dielectric Resonator
<b>MCPR</b>	Möbius coupled printed resonator
<b>RTRD</b>	Real Time Signal Retention Device
<b>IFFT</b>	Inverse Fast Fourier Transform
<b>DPS</b>	Double Positive substrates
<b>ENG</b>	Epsilon Negative Substrate
<b>MNG</b>	Mu Negative Substrate
<b>DNG</b>	Double Negative substrates
<b>NRIM</b>	Negative Refractive Index material
<b>SRR</b>	Split-ring resonator
<b>TLM</b>	Transmission line model
<b>CRLH</b>	composite right/left-handed structures
<b>SWMR</b>	Slow Wave Metamaterial Resonator
<b>SIW</b>	substrate integrated waveguide
<b>CSRR</b>	complimentary split ring resonators
<b>MCSWMR</b>	Mode-Coupled Slow-Wave Metamaterial Resonator

<i>OEO</i>	Opto-Electronic Oscillator
<i>B</i>	Injection locking loop gain
<i>DRO</i>	Dielectric resonator oscillator
<i>DSIL</i>	Dual loop Self-injection locking
<i>DSILPLL</i>	Dual loop Self-injection locked and phase locked loop
<i>DSPLL</i>	Dual loop Self-phase locked loop
$f_m$	Fourier frequency
$f_{osc}$	Oscillation frequency
<i>G</i>	Phase locking loop gain
<i>IL</i>	Injection locking
<i>ILPLL</i>	Injection locked phase locked loop
$K_d$	PLL phase detector gain
$K_h$	PLL low pass filter gain
$K_o$	PLL VCO tuning sensitivity
$L(fm)$	Single sideband phase noise
<i>MMS</i>	Metamaterial Mobius Strip
<i>PLL</i>	Phase locked loop
<i>SIL</i>	Self-injection locking
<i>SILPLL</i>	Self-injection locked and phase locked loop
<i>SLC</i>	Sapphire loaded cavity
<i>SPLL</i>	Self-phase locked loop
$S_\varphi(fm)$	Power spectral density of phase
$\zeta$	Damping factor of PLL loop
$\theta_e$	Phase error between input and VCO
$\theta_i$	Phase angle of input signal
$\theta_o$	Phase angle of VCO
$\tau$	Time delay associated with an optic fiber
$S_\varphi(fm)$	Power spectral density of phase
$\theta_i$	Phase angle of input signal

$\theta_o$	Phase angle of VCO
$\theta_e$	Phase error between input and VCO
$\phi_i$	Instantaneous phase of input signal
$\phi_o$	Instantaneous phase of VCO signal
$\zeta$	Damping factor of PLL loop
$\omega_n$	Natural frequency of PLL loop
$f_{osc}$	Oscillation frequency
$f_m$	Fourier frequency
$\tau$	Time delay associated with an optic fiber
$\tau_i$	Time delay of the fiber used in self-injection locking
$\tau_d$	Time delay of the fiber used in self-phase locked loop

# References

## Chapter 1

- [1] U. L. Rohde, "A New Efficient Method of Designing Low Noise Microwave Oscillators," Dr.-Ing. Dissertation, Faculty IV, EEC (Electrical Engineering and Computer Sciences), TU- Berlin, Germany, Feb. 2004.
- [2] A. K. Poddar, U.L. Rohde, D. Sundarrajan", A Novel Möbius-Coupled Printed Resonator Based Signal Sources", 2013 IEEE MTT-S Digest, pp. 1-3, June 2013
- [3] A. K. Poddar and U. L. Rohde, "Slow-Wave Evanescent-Mode Coupled Resonator Oscillator", 2012 IEEE FCS, pp. 01-07, May 2012.
- [4] U. L. Rohde and A. K. Poddar, "Oscillators Cover Multiple Bands", *Microwaves & RF*, pp.122-126, May 2013.
- [5] D. Hamand A. Hajimiri, "Concepts and Methods in Optimization of Integrated LC VCOs", *IEEE Journal of Solid-State Circuits*, Vol. 36, No. 6, pp. 896-909, June 2001
- [6] P. Vryonides, S. Nikolaou, and H. Haralambous, "24 GHz low phase noise HBT dielectric resonator oscillator," *IEEE 11th annual Wireless and Microwave Technology Conference*, pp. 1-4, April 2010.
- [7] C. Perez, D. Floriot, P. Maurin, P. Bouquet, P. M. Guitierrez, J. Obregon, and S. A. Delage, "Extremely low noise InGaP/GaAs HBT oscillator at C-band," *IEE Electronics Letters*, vol. 34, no. 8, pp. 813-814, April 1998.
- [8] Hittite Microwave Corporation, "HMC-C200 Dielectric resonator oscillator module", Datasheet, [http://www.hittite.com/content/documents/data\\_sheet/hmcc200.pdf](http://www.hittite.com/content/documents/data_sheet/hmcc200.pdf).
- [9] L.-H. Hsieh, and K. Chang, "High-efficiency piezoelectric-transducer tuned feedback microstrip ring-resonator oscillators operating at high resonant frequencies", *IEEE Trans. Microwave Theory Tech.*, vol. -51, no. 4, pp. 1141-1145, April 2003
- [10] L. Dussopt, D. Guillois, and G. M. Rebeiz, "A low phase noise silicon 9 GHz VCO and 18 GHz push-push oscillator", *IEEE MTT-S Dig.*, vol. 2, pp. 695-698, June 2002.
- [11] K. B. Ostman, S. T. Sipila, I. S. Uzunov, N. T. Tchamov, "Novel VCO architecture using series above-IC FBAR and parallel LC resonance," *IEEE J. Solid-State Circuits*, vol. 41, no. 10, pp. 2248-2256, October 2006.
- [12] D. Ham, and W. Andress, "A circular standing wave oscillator," *IEEE SSC Conference*, February 2004.
- [13] I. Hilborn, A. P. Freundorfer, J. Show, M. G. Keller," Design of a Single Chip GaAs MESFET Dielectric Resonator Oscillator at 26 GHz", *IEEE CCECE*, pp. 671-674, 2007
- [14] D. Ozis, N. M. Neihart, and D. J. Allstot, "Differential VCO and passive frequency doubler in 0.18 mm CMOS for 24 GHz applications," in *IEEE RF IC Symp. Dig.*, 2006
- [15] S. Ko, J.-G. Kim, T. Song, E. Yoom, and S. Hong, "20 GHz integrated CMOS frequency sources with a quadrature VCO using transformers," in *IEEE RF IC Symp. Dig.*, 2004
- [16] H. H. Hsieh and L. H. Lu, "A Low-Phase-Noise K-Band CMOS VCO," in *IEEE Microwave & Wireless Components Lett.*, Vol. 16, No. 10, pp.552-554, Oct. 2006.
- [17] C. m. Yang, H. L. Kao, Y. C. Chang, and M. T. Chen," A Low phase noise 20 GHz Voltage control oscillator using 0.18 $\mu$ m CMOS Technology", *IEEE 13<sup>TH</sup> International Symposium on Design and Diagnostics of Electronic Circuits and Systems (DDECS)*, pp. 185-188, 2010.
- [18] J.-C. Chien and L. -H. Lu, "40 GHz wide-locking-range regenerative frequency divider and low-phase-noise balanced VCO in 0.18 m CMOS," in *IEEE Int. Solid-State Circuits Conf. Tech. Dig.*, pp. 544–545, Feb. 2007
- [19] Y. Wachi, T. Nagasaku, and H. Kondoh, "A 28 GHz low-phase-noise CMOS VCO using an amplitude redistribution technique," in *IEEE SSC Conf. Tech. Dig.*, pp. 482–483, Feb. 2008.
- [20] H.-Y. Chang and Y. -T. Chiu, "K-band CMOS differential and quadrature voltage-controlled oscillators for low-phase-noise and low-power applications," *IEEE Trans. on MTT*, vol. 60, no. 1, pp. 46–59, Jan. 2012.
- [21] T. -P. Wang, "A-band low-power Colpitts VCO with voltage-to-current positive-feedback network in 0.18 m CMOS," *IEEE MWCL*, vol. 21, no. 4, pp. 218–220, Apr. 2011.
- [22] S.-L. Liu, K. -H. Chen, T. Chang, and A. Chin, "A low-power-band CMOS VCO with four-coil transformer feedback," *IEEE MWCL*, vol. 20, no. 8, pp. 459–461, Aug. 2010.
- [23] J. Kim *et al.*, "A 44 GHz differentially tuned VCO with 4 GHz tuning range in 0.12 m SOI CMOS," in *IEEE International Solid-State Circuits Conf. Dig.*, pp. 416–417, Feb. 2005.
- [24] O. Richard, A. Siligaris, F. Badets, C. Dehos, C. Dufis, P. Busson, P. Vincent, D. Belot, and P. Urard, "A 17.5-to-20.94GHz and 35-to-41.88 GHz PLL in 65 nm CMOS for wireless HD applications," in *IEEE Int. Solid-State Circuits Conf. Dig.*, pp. 252–253, Feb. 2010.

- [25] S. Choi, Y. Jeong, and K. Yang, "Low DC-Power Ku-Band Differential VCO Based on an RTD/HBT MMIC Technology", *IEEE MWCL*, Vol. 15, No. 11, pp. 742-744, Nov 2005
- [26] H. Li, H.-M. Rein, R. Kreienkamp, and W. Klein, "47 GHz VCO with low phase noise fabricated in a SiGe bipolar production technology," *IEEE MWCL*, vol. 12, no. 3, pp. 79–81, March 2002.
- [27] T. Nakamura, T. Masuda, N. Shiramizu, A. Nakamura, and K. Washio, "A 11.1-V Regulator-Stabilized 21.4-GHz VCO and a 11.5% Frequency-Range Dynamic Divider for K-Band Wireless Communication", *IEEE Trans. on MTT*, Vol. 60, No. 9, pp. 2823-2832, Sept. 2012.
- [28] M. Hossain, A. Kravetsm U. Pursche, C. Meliani, W. Heinrich, "A Low voltage 24 GHz VCO in 130nm CMOS for localization purpose in sensor networks", 7<sup>TH</sup> German Microwave Conference (GeMiC), pp. 1-4, 2012.
- [29] S. Kuhn, W. Heinrich, "GaN large-signal oscillator design using Auxiliary Generator measurements", German Microwave Conference (GeMiC) 2010, pp. 110-113.
- [30] J. Hilsenbeck, F. Lenk, W. Heinrich, and J. Würfl, "Low phase noise MMIC VCOs for Ka-band applications with improved GaInP/GaAs-HBT technology," in *IEEE GaAs IC Symp. Digest*, pp. 223–226, 2003.
- [31] A. K. Poddar, U. L. Rohde, "The Pursuit for Low Cost and Low Phase Noise Synthesized Signal Sources: Theory & Optimization", *IEEE UFFC Symposia*, May 19-22, 2014
- [32] A. K. Poddar, U. L. Rohde, "Evanescent-Mode Phase-Injection Mode-Coupled (EMPIMC) Metamaterial Resonator Based Tunable Signal Sources", *IEEE Wamicon*, June 06, 2014
- [33] A. K. Poddar, "Slow-Wave Resonator based Tunable Multi-Band Multi-Mode Injection-Locked Oscillators", Research Report, RF and Microwave Techniques Brandenburg University of Technology Cottbus-Senftenberg 2014", [https://www-docs.tu-cottbus.de/mikrowellentchnik/public/poddar\\_report\\_long\\_ebook.pdf](https://www-docs.tu-cottbus.de/mikrowellentchnik/public/poddar_report_long_ebook.pdf)

## Chapter 2

- [1] Byeong-Ha Park, "A Low-Voltage, Low Power, CMOS 900 MHz Frequency Synthesizer," Ph.D. Dissertation, Georgia Institute of Technology, December 1997
- [2] U. L. Rohde, D. P. Newkirk, "RF/Microwave Circuit Design for Wireless Applications", Wiley & Sons, pp. 205.
- [3] U. L. Rohde, "A New and Efficient Method of Designing Low Noise Oscillators," Dr.-Ing. Dissertation, Technical University of Berlin, Faculty IV, EEC (EECS), 12 February 2004.
- [4] A. K. Poddar, "A Novel Approach for Designing Integrated Ultra Low Noise Microwave Wideband Voltage Controlled Oscillator", Dr.-Ing. Dissertation, Technical University of Berlin, Faculty IV, EEC (Electrical Engineering and Computer Sciences), 14 December, 2004
- [5] U. L. Rohde, "A Novel Approach for Generating Active Inductors for Microwave Oscillators," Dr.-Ing. Habil, Dissertation, Technical University of Berlin, 2011.
- [6] G.R. Basawapatna, R. B. Stancliff, "A Unified Approach to the Design of Wide- Band Microwave Solid-State Oscillators," *IEEE Trans. MTT*, Vol. 27, pp. 379-385, May 1979.
- [7] U. L. Rohde, A. K. Poddar, and G. Boeck, *Modern Microwave Oscillators for Wireless Applications: Theory and Optimization*, John Wiley & Sons Inc., ISBN 0-471-72341-8, 2005.
- [8] R. Mukhopadhyay, S. W. Yoon, Y. Park, C.-H. Lee, S. Nuttinck, and J. Laskar, "Investigation of Inductors for Digital Si-CMOS Technologies", pp. 3750-3753, ISCAS 2006.
- [9] S-Li Eun, C. Sik Cho, J. W. Lee and J Kim, " A low power VCO using inductor for low phase noise and wide tuning range", *Proceeding of the 39<sup>th</sup> European Microwave Conference*, pp. 1255-1258, Rome, Italy, 2009.
- [10] S. Mons, M.A. Perez, R. Quere, J. Obregon, "A Unified Approach for the Linear and Nonlinear Stability Analysis of Microwave Circuits Using Commercially Available Tools," *MTT-S Digest*, Vol .3, pp. 993-996, 1999.
- [11] Alper Demir, Amit Mehotra, and Jaijeet Roychowdhury, "Phase Noise in Oscillators: A Unifying Theory and Numerical Methods for Characterization," *IEEE Tran. on Circuits & Systems*, Vol. 47, pp.655-674, May 2000.
- [12] A. Grebennikov, "Microwave Transistor Oscillators: An Analytic Approach to Simplify Computer-Aided Design," *Microwave Journal*, pp 292-299, May 1999.
- [13] U. L. Rohde and A. K. Poddar, "Miniaturized VCOs Arm Configurable Synthesizers", *IEEE IMS 2009*, pp. 1281-1284, June 7-12, 2009,
- [14] U. L. Rohde and A. K. Poddar, "Hybrid Coupled Planar Resonators Arm Miniaturized Synthesizers", 2009 European Frequency & Time Forum & IEEE Int'l Frequency Control Symposium (EFTF-IFCS 2009), Besançon, France, pp. 949-955, April 20-24 2009.

- [15] U. L. Rohde and A. K. Poddar, "Mode-Coupled VCO Replaces Expensive DRO (Dielectric Resonator Oscillator) 2008 IEEE Int'l FCS, pp. 296-304, 18-21, Hawaii, USA, May 2008.
- [16] U. L. Rohde and A. K. Poddar, "Mode-Coupled Stubs-Tuned Planar Resonator Offers Promising And Integrable Alternatives Of DRO(Dielectric Resonator Oscillator)", IEEE Sarnoff Symp, pp. 1-7, 2008.
- [17] U. L. Rohde and A. K. Poddar, "STPCR Offers Integrable Alternatives of DRO", Microwave Symposium Digest, 2008 IEEE MTT-S, pp. 233-236, Atlanta, USA, June 15-20, 2008.
- [18] U. L. Rohde and A. K. Poddar, "Injection-Tuned Coupled Oscillators" IEEE Radio Wireless Symposium 2008, pp. 367-370, 22-24, Orlando, FL, USA, January 2008.
- [19] U. L. Rohde and A. K. Poddar, "Reconfigurable Concurrent Oscillator (RCO)" IEEE Radio Wireless Symposium 2008, pp. 371-374, 22-24 Orlando, FL, USA, January 2008.
- [20] A. P. S Khanna, " Review of Dielectric Resonator Oscillator Topology", IEEE, Int, Frequency Control Symposium, pp. 478-486, 1987.
- [21] J-Francois Gravel and J. S. Wight, "On the Conception and Analysis of a 12-GHz Push-Push Phase Locked DRO" IEEE Trans. on MTT, Vol. 54, No. 1, pp. 153-159, Jan. 2006.
- [22] U. L. Rohde and A. K. Poddar, "Noise Minimization Techniques for RF & MW Signal Sources (Oscillators/VCOs)", Microwave J., page 136, Sept. 2007.
- [23] J Choi and A. Mortazawi, " A New X-Band Low Phase-Noise Multiple-Device Oscillator Based on the Extended-Resonance Technique", IEEE Trans. on MTT, Vol. 55, No. 8, pp. 1642-1648, Aug. 2007.
- [24] C. Florian, P. Andrew, G. Vannini, and F. Filicori, " Design of Low Phase Noise Dielectric Resonator Oscillators with GaInP HBT devices exploiting a Non-Linear Noise Model", 2007 IEEE MTT-S In. Microwave Symposium Dige., pp. 1525-1528, June 2007.
- [25] K. Hosoya, S. Tanaka, Y. Amamiya, T. Niwa, and H. Shimawaki, and K. Honjo, " A low phase-noise 38-GHz HBT MMIC oscillator utilizing a  $(\lambda/4 \pm \delta)$  open stubs resonator," APMC, pp. 64-67, Singapore, 1999.
- [26] J. Choi, M-Hung Chen, and A. Mortazawi, " An X-band Low Phase Noise Oscillator Employing a Four-Pole Elliptic-Response Microstrip Bandpass Filter" IEEE-MTT-S, Digest, pp. 1529-1532, 2007.
- [27] A, P. S. (Paul) Khanna, "Microwave Oscillators: The State of The Thechnology", MWJ, pp. 22-42, April 2006.
- [28] J. Everard and K. Theodoropoulos, " Ultra-Low Phase Noise Ceramic Based Dielectric Resonator Oscillators," IEEE International FCS, pp. 869-874, Florida, USA, June 4-7 2006.
- [29] V. Walkar and I. C. Hunter, Design of triple mode TE<sub>01</sub> resonator transmission filters, IEEE MWC Lett., vol. 12, pp. 215-217, June 2002.
- [30] U. L. Rohde, A. K. Poddar, and R. Rebel," Integrated Low Noise Microwave Wideband Push-Push VCO", US Patent No. 7,088189, August 8, 2006
- [31] U. L. Rohde and A. K. Poddar, "Low Cost Signal Source for Multi-Band Multi-Mode Wireless Systems", 6<sup>th</sup> international conference on antenna theory and techniques, pp. 167-169, Sept 2007.
- [32] J S. Kim, W. Wu, J. Lin, A. Verma, S. Jang, F. Ren, S. Pearton, and J. Gillespie, " A High-Efficiency GaN/AlGaIn HEMT Oscillator Operating at L-Bnad" Proc. of APMC 2006, pp.631-634, Yokohama, Japan, Dec. 12-15, 2006.
- [33] S. Romisch and R. Lutwak, " Low-Power, 4.6-GHz, Stable Oscillator for CSAC," IEEE International Frequency Control Symposium, pp. 448-451, Florida, USA, June 4-7 2006.
- [34] S. Hamano, K. Kawakami, and T. Takagi. " A Low Phase Noise 19 GHz-bnad VCO using Two Different Frequency Resonators", IEEE-MTT-S, Digest, pp. 2189-2192, 2003.
- [35] W.-M. Lance Kuo, J. D. Cressler, Yi-Jan Emery Chen, and A. J. Joseph, " An Inductorless Ka-band SiGe HBT ring oscillator", IEEE MWCL, Vol., 15, no., 10, pp. 682-684, Oct. 2005.
- [36] J. K. A. Everard and C. D. Broomfield, " High Q Printed Helical Resonators for Oscillators and Filters". IEEE Trans., on UFFC, Vol., 54, No. 9, PP. 1741-1750, September 2007.
- [37] C.-G. Hwang and N.-H. Myung, " An Oscillator Incorporating a Planar Helical Resonator for Phase Noise Reduction and Harmonic Supression", JKEES, Vol. 6, No.3, pp. 160-164, Sept 2006.
- [38] D. Y. Jung, K. C. Eun, and C. S. Park, "A system-on-Package Structure LTCC Resonator for a Low Phase Noise and Power Efficient Millimeter-Wave Oscillation", IEEE Radio Wireless Symposium 2008, pp. 391-394, 22-24, Orlando, FL, USA, January 2008.
- [39] S.-G. Park, J.-H. Kim, and S.-W. Kim, K.-S. Seo, W.-B. Kim, and J.-In Song, "A Ka-band MMIC Oscillator utilizing a labyrinthine PBG resonator", IEEE MWCL, Vol., 15, no., 11, pp. 727-729, November 2005.
- [40] H. K. Gummel and R. C. Poon," An integral charge control model of bipolar transistor, "Bell Syst. Tech. J., vol. 49, pp. 827-852, May-June 1970.

- [41] Gettreu, Modeling the Bipolar Transistor, Tektronix, 1976.
- [42] Infineon Datasheet: <http://www.infineon.com>
- [43] A. K. Poddar, "Slow-Wave Resonator based Tunable Multi-Band Multi-Mode Injection-Locked Oscillators", Research Report , RF and Microwave Techniques Brandenburg University of Technology Cottbus-Senftenberg 2014", [https://www-docs.tu-cottbus.de/mikrowellentechnik/public/poddar\\_report\\_long\\_ebook.pdf](https://www-docs.tu-cottbus.de/mikrowellentechnik/public/poddar_report_long_ebook.pdf)

### Chapter 3

- [1] D. B. Leeson, "A Simple Model of Feedback Oscillator Noise Spectrum", IEEE Proc. pp. 329-332, 1966.
- [2] U. L. Rohde, A. K. Poddar, and R. Rebel," Integrated Low Noise Microwave Wideband Push-Push VCO", US Patent No. 7,088189, Aug 2006.
- [3] K. Hosoya, S. Tanaka, Y. Amamiya, T. Niwa, and H. Shimawaki, and K. Honjo, "A low phase-noise 38-GHz HBT MMIC oscillator utilizing a  $(\lambda/4 \pm \delta)$  open stubs resonator," APMC, pp. 64-67, Singapore, 1999.
- [4] U. L. Rohde, A. K. Poddar, and G. Boeck, Modern Microwave Oscillators for Wireless Applications: Theory and Optimization, John Wiley & Sons Inc., 2005.
- [5] A. P. S. Khanna, "Microwave Oscillators: The State of the Technology", MWJ, pp. 22-42, April 2006.
- [6] J.C. Nallatamby, M. Prigent, M. Camiade, and J. Obregon, "Phase noise in oscillators – Leeson formula revisited". IEEE Trans. on MTT, Vol. 51, No. 4, pp. 1386-1394, April 2003.
- [7] A. Suárez, S. Sancho, S. Ver Hoeye, and J. Portilla, "Analytical comparison between time- and frequency-domain techniques for phase-noise analysis". IEEE Trans. on MTT, Vol. 50, No. 10, pp. 2353-2361, Oct. 2002.
- [8] S. Ver Hoeye, A. Suárez, and J. Portilla, "Techniques for oscillator nonlinear optimization and phase-noise analysis using commercial Harmonic-Balance software", IEEE MTT-S Digest, pp. 95-98, 2000.
- [9] V. Rizzoli, F. Mastri, and D. Masotti, "General noise analysis of nonlinear microwave circuits by the piecewise Harmonic Balance technique". IEEE Trans. on MTT, Vol. 42, No. 5, pp. 807-819, May 1994.
- [10] S. Sancho, A. Suárez, J. Dominguez, and F. Ramirez, "Analysis of near-carrier phase-noise spectrum in free-running oscillators in the presence of White and colored noise sources". IEEE Transactions on Microwave Theory and Techniques, Vol. 58, No. 3, March 2010, pp. 587-601.
- [11] Jia-Sheng Hong and M. J. Lancaster, "Aperture-Coupled Microstrip Open-Loop Resonators and Their Applications to the Design of Novel Microstrip Bandpass Filters", "IEEE Tran. MTT, Vol. 47, No. 9, pp. 1848-1855, September 1999.
- [12] Jia-Sheng Hong and M. J. Lancaster, "Coupling of Microstrip Square Open-Loop Resonators for Cross-Coupled Planar Microwave", "IEEE Trans. on MTT, Vol. 44, No. 12, pp. 2099-2109, December 1996.
- [13] Sheng Sun and Lei Zhu, "Guided-Wave Characteristics of Periodically Non uniform Coupled Microstrip Lines-Even and Odd Modes" "IEEE Transaction on MTT, Vol. 53, No. 4, pp. 1221-1227, April 2005.
- [14] U. L. Rohde and A. K. Poddar, "Tunable Frequency, Low Phase Noise and Low Thermal Drift Oscillator", US Patent No.7196591, March 01, 2007.
- [15] U. L. Rohde and A. K. Poddar, "Wideband voltage controlled oscillators employing evanescent mode coupled resonators," US Patent No. 71803812, Feb 2007.
- [16] U.L. Rohde, "A New Efficient Method of Designing Low Noise Microwave Oscillators," Dr.-Ing. Dissertation, TU-Berlin, Germany, Faculty IV, EEC (EECS), 12 February 2004.
- [17] U. L. Rohde, A. K. Poddar, Juergen Schoepf, Reimund Rebel, and Parimal Patel, "Low Noise Low Cost Wideband N-Push VCO," IEEE, IMS Symposium, USA, MTT-S 2005,.
- [18] A. K. Poddar, "A Novel Approach for Designing Integrated Ultra Low Noise Microwave Wideband Voltage-Controlled Oscillators", Dr.-Ing. Dissertation, TU- Berlin, Germany, Faculty IV, EEC (Electrical Engineering and Computer Sciences), 14 December 2004.
- [19] U. L. Rohde, A. K. Poddar, and R. Rebel, "Ultra Low Noise Low Cost Octave-Band Hybrid-Tuned VCO," 18th IEEE CCECE05, Canada, 2005.
- [20] U. L. Rohde and A. K. Poddar, "Ultra Low Noise Low Cost Multi Octave Band VCO", IEEE Sarnoff Symposium, Princeton, USA, April 2005.
- [21] A. K. Poddar and K. N. Pandey, "Microwave Switch Using MEMS-Technology", 8th IEEE International Symposium on High Performance EDMA Applications, November 2000.
- [22] U. L. Rohde and A. K. Poddar, "Configurable Ultra Low Ultra Wideband Power Efficient VCOs", 11th European Wireless, Conference, Cyprus, 10-13 April 2005.

- [23] U. L. Rohde, K. J. Schoepf and A. K. Poddar, "Low-Noise VCOs Conquer Wide Bands", *Microwave & RF*, pp. 98-106, June 2004.
- [24] U. L. Rohde and A. K. Poddar, "Configurable Adaptive Ultra Low Noise Wideband VCOs," *Proc. IEEE Int. Conf. Ultra-Wideband*, Switzerland, pp 452-457, Switzerland, September 5-8, 2005.
- [25] U. L. Rohde and A. K. Poddar, "Reconfigurable Wideband VCOs," *IEEE, PIMRC2005*, Germany, September 11-14, 2005.
- [26] U. L. Rohde and A. K. Poddar, "Ultrawideband (UWB) RF Signal Source," *IEEE, ISWCS2005*, Italy, September 5-7, 2005.
- [27] To-Po Wang, Zuo-Min Tsai, Kuo-Jung Sun, and Huei Wang, "Phase-Noise Reduction of X-Band Push-Push Oscillator with Second-Harmonic Self-Injection Techniques", *IEEE Trans. MTT*, vol. 55, No. 1, pp. 66-77, Jan 2007.
- [28] K. Hoffmann and Z. Skvor, "Active resonator", *EUROCON 2001 proceeding*, IEEE, Vol.1; pp. 164-166, Bratislava, 2001.
- [29] A. K. Poddar and U. L. Rohde, "Techniques Minimize the Phase Noise in Crystal Oscillators", *2012 IEEE FCS*, pp. 01-07, May 2012.
- [30] A. K. Poddar, "Expert Tips, Tricks and Techniques", *Microwave Journal*, pp.22, July 2012
- [31] A. K. Poddar and U. L. Rohde, "Latest Technology, Technological Challenges, and Market Trends for Frequency Generating and Timing Devices", *IEEE Microwave Magazine*, pp.120-134, October 2012.
- [32] Dorin Calbaza, Chandra Gupta, Ulrich L. Rohde, and Ajay K. Poddar, "Harmonics Induced Uncertainty in Phase Noise Measurements", *2012 IEEE MTT-S Digest*, pp. 1-3, June 2012.
- [33] U. L. Rohde and A. K. Poddar, "Noise Minimization Techniques for Voltage Controlled Crystal Oscillator (VCXO) Circuits", *IEEE Radio Wireless Symposium*, SAN Diego, CA, USA, Jan 18-22, 2009.
- [34] W.P. Robins, "Phase Noise in Signal Sources" London: *IEEE Telecommunications Series 9*, 1982.
- [35] T. H. Lee, A. Hajimiri, "Oscillator phase-noise: a tutorial," *IEEE JSSC*, vol. 35, pp. 326-336, March 2000.
- [36] A. Hajimiri and T. H. Lee, "A general theory of phase noise in electrical oscillators," *IEEE J. Solid-State Circuits*, vol. 33, no. 2, pp. 179-194, Feb. 1998.
- [37] D.B. Sullivan, "Characterization of Clocks and Oscillators" *National Bureau of Standards Tech. Note*, TN-1337, Feb 28, 1990.
- [38] A. Demir, A. Mehrotra, and J. Roychowdhury, "Phase noise in oscillators: a unifying theory and numerical methods for characterization," *IEEE Trans. Circuits Syst. I*, vol. 47, pp. 655 – 674, May 2000.
- [39] M. Nick, "New Q-Enhanced Planar Resonators for Low Phase-Noise Radio Frequency Oscillators", PhD Dissertation, Electrical Engineering, University of Michigan, 2011
- [40] M. Odyniec, Editor, *RF and Microwave Oscillator Design*, Chapter 5: Modern Harmonic-Balance Techniques for Oscillator Analysis and Optimization, by V. Rizzoli, A. Neri, A. Costanzo, F. Matri, Artech House, 2002.
- [41] B. Razavi, "A study of phase-noise in CMOS oscillators," *IEEE JSSC*, vol. 31, pp. 331-343, March 1996.
- [42] A. Demir, A. Mehrotra, and J. Roychowdhury, "Phase noise and timing jitter in oscillators" *IEEE Custom Integrated Circuits Conference Proceeding*, pp. 45-48, May 1998.
- [43] Hajimiri A and Lee T.H., *Design Issues in CMOS Differential LC Oscillators*, *IEEE Journal of Solid-State Circuits*, 34(5), May 1999.
- [44] Hajimiri A and Lee T.H. The, "Design Of Low Noise Oscillators", Kluwer Academic Publishers, 1999.
- [45] A. Hajimiri, S. Limotyrakis, and T. H. Lee, "Jitter and Phase Noise in Ring Oscillators," *IEEE Journal of Solid-State Circuits*, vol. 34, no. 6, pp. 790-04, Jun. 1999.
- [46] Kaertner F X. *Analysis of White and f- $\alpha$  Noise in Oscillators*. *International Journal of Circuit Theory and Application*, Vol. 18, pp-485-519, October 1990.
- [47] Demir A., "Phase Noise And Timing Jitter in Oscillators With Colored-Noise Sources", *IEEE Transactions on circuits and systems-1*, 49(12):1782.1791, Dec 2002.
- [48] G.J. Coram. A simple 2-d oscillator to determine the correct decomposition of perturbations into amplitude and phase noise. *Circuits and Systems I: Fundamental Theory and Applications*, *IEEE Transactions on*, 48(7):896 –898, Jul 2001.
- [49] *Agilent Phase Noise Measurement Solution*, ([www.home.agilent.com/application](http://www.home.agilent.com/application)), 2012
- [50] W. F. Walls, "Cross-correlation phase noise measurements", *IEEE Frequency Control Symposium*, 46th Proceedings of the 1992 IEEE, pp. 257-261, May 1992.



- [51] A. L. Lance, W. D. Seal, F. G. Mendoza and N. W. Hudson, "Automating Phase Noise Measurements in the Frequency Domain," *Proceedings of the 31<sup>st</sup> Annual Symposium on Frequency Control*, 1977
- [52] W. F. Walls, "Cross-Correlation Phase Noise Measurements", IEEE FCS, pp. 257-261, 1992
- [53] W. F. Walls, "Practical problems involving phase noise measurements, 33th annual precise time interval (PTTI) meeting, pp. 407-416, 2001
- [54] F.L. Walls et al. Extending the Range and Accuracy of Phase Noise Measurements, Proceedings of the 42nd Annual Symposium on Frequency Control, 1988.
- [55] Noise XT, DCNTS manual, [http://www.noisext.com/pdf/noisext\\_DCNTS.pdf](http://www.noisext.com/pdf/noisext_DCNTS.pdf), (2013)
- [56] Agilent E5052A Signal Source Analyzer 10 MHz to 7, 26.5, or 110 GHz – Datasheet", Agilent document 5989-0903EN, p. 12, May 2007
- [57] Frequency Extension for Phase Noise Measurements with FSUP26/50 and Option B60 (Cross-Correlation)", Rhode & Schwarz Application Note 1EF56, p. 3, Jan 2007
- [58] M. Jankovic, "Phase noise in microwave oscillators and amplifiers" , PhD thesis, Faculty of graduate School of the University of Colorado, Department of Electrical, Computer and Energy Engineering, 2010
- [59] Hewlett Packard, *RF and Microwave phase Noise Measurement Seminar*] Available at: [http://www.hparchive.com/seminar\\_notes/HP\\_PN\\_seminar.pdf](http://www.hparchive.com/seminar_notes/HP_PN_seminar.pdf), April 2010
- [60] Stephan R. Kurz, *WJ Tech note – Mixers as Phase Detectors* Available at: [http://www.triquint.com/prodserv/tech\\_info/docs/WJ\\_classics/Mixers\\_phase\\_detectors.pdf](http://www.triquint.com/prodserv/tech_info/docs/WJ_classics/Mixers_phase_detectors.pdf), May 2011.
- [61] Agilent Technologies, "Phase Noise Characterization of Microwave Oscillators – Phase Detector Method", Product Note 11729B-1, Available at: <http://tycho.usno.navy.mil/ptti/ptti2001/paper42.pdf>, May 2010
- [62] Aeroflex, Application Note #2 – PN9000 automated Phase Noise Measurement System Available at: <http://www.datasheetarchive.com/datasheet-pdf/010/DSA00173368.html>, April 2010
- [63] Hewlett Packard.). *HP 3048A Phase Noise Measurement System Reference Manual* [online]. Available: <http://cp.literature.agilent.com/litweb/pdf/03048-90002.pdf>, (1989, Sept 01
- [64] E. Rubiola and F. Vernotte.. *The cross-spectrum experimental method* [online]. Available: <http://arxiv.org/>, document arXiv:1003.0113v1 [physics.ins-det], Feb 2010
- [65] Hewlett Packard. *HP 3048A Phase Noise Measurement System Operating Manual* [online]. Available: <http://cp.literature.agilent.com/litweb/pdf/03048-61004.pdf>, June 1990.
- [66] *HP 11848A Phase Noise Interface Service Manual*, 1st ed., Hewlett-Packard Company, Spokane., Washington, 1987.
- [67] M. Sampietro, L. Fasoli, and G. Ferrari, "Spectrum analyzer with noise reduction by cross-correlation technique on two channels," *Rev. Sci. Instrum.*, vol. 70, no. 5, May 1999.
- [68] Abidi, A. A., and R. G. Meyer, "Noise in relaxation oscillators," *IEEE Journal of Solid-State Circuits*, vol. SC-18, no. 6, pp. 794-802, Dec. 1983.
- [69] Stuck, B. W., "Switching-time jitter statistics for bipolar transistor threshold crossing detectors," M. S. thesis, Massachusetts Institute of Technology, 1969.
- [70] A. Abidi, " How phase noise appears in oscillators", [http://www.rfdh.com/ez/system/db/pds\\_tn/upload/271/phase\\_noise.pdf](http://www.rfdh.com/ez/system/db/pds_tn/upload/271/phase_noise.pdf), Nov 1997
- [71] R. Navid, T. H. Lee, and R. W. Dutton, "Minimum Achievable Phase Noise of RC Oscillators", *IEEE JSSC*, VOL. 40, NO. 3, pp. 630-637, March 2005
- [72] L. DeVito, J. Newton, R. Croughwell, J. Bulzacchelli, and F. Benkley, "A 52 MHz and 155 MHz clock-recovery PLL," in *IEEE ISSCC Dig. Tech. Papers*, pp. 142–143, Feb. 1991.
- [73] I. A.Young, J. K. Greason, and K. L.Wong, "APLL clock generator with 5 to 110 MHz of lock range for microprocessors," *IEEE J. Solid-State Circuits*, vol. 27, no. 11, pp. 1599–1607, Nov. 1992.
- [74] A. Hajimiri, S. Limotyrakis, and T. H. Lee, "Jitter and phase noise in ring oscillators," *IEEE J. Solid-State Circuits*, vol. 34, no. 6, pp. 790–804, Jun. 1999.
- [75] R. Navid, T. H. Lee, and R. W. Dutton, "Lumped, inductorless oscillators: How far can they go?" In *Proc., IEEE Custom Integrated Circuits Conf.*, pp. 543–546, Sep. 2003.
- [76] A. A. Abidi and R. G. Meyer, "Noise in relaxation oscillators," *IEEE JSSC*, vol. 18, pp. 794–802, Dec. 1988.
- [77] B. Oksendal, *Stochastic Differential Equations*. Berlin, Heidelberg, Germany: Springer-Verlag, 1998.
- [78] R. L. Stratonovich, *Topics in the Theory of Random Noise*. New York: Gordon and Breach, Translated from Russian by R. A. Silverman, 1963.

- [79] R. Navid, T. H. Lee, and R. W. Dutton, "An analytical formulation of phase noise of signals with Gaussian distribution jitter," *IEEE Trans. Circuits Syst. II*, Vol. 52, Issue 3, pp 149-153, March 2005
- [80] B. Razavi, "A study of phase noise in CMOS oscillators," *IEEE JSSC* vol. 31, no. 3, pp. 331-343, Mar. 1996.
- [81] J. G. Snee and C. J. M. Verhoeven, "A new low-noise 100-MHz balanced relaxation oscillator," *IEEE J. Solid-State Circuits*, vol. 25, no. 6, pp. 692-698, Jun. 1990.
- [82] F. Herzel, M. Pierschel, P. Weger, and M. Tiebout, "Phase noise in a differential CMOS voltage-controlled oscillator for RF applications," *IEEE Trans. Circuits and Syst. II*, vol. CAS2-47, no. 1, pp. 11-15, Jan. 2000.
- [83] Y. P. Tividis, *Operation and Modeling of MOS Transistors*. New York: McGraw-Hill, 1999.
- [84] J. G. Maneatis and M. A. Horowitz, "Precise delay generation using coupled oscillators," *IEEE J. Solid-State Circuits*, vol. 28, no. 12, pp. 1273-1282, Dec. 1993.
- [85] H. Chang, X. Cao, U. K. Mishra, and R. A. York, "Phase noise in coupled oscillators: Theory and experiment," *IEEE Trans. Microwave Theory Tech.*, vol. MTT-45, no. 5, pp. 604-615, May 1997.
- [86] R. Navid and R. W. Dutton, "The physical phenomena responsible for excess noise in short-channel MOS devices," in *Int. Conf. SISPAD Dig. Tech. Papers*, pp. 75-78, Sep. 2002.
- [87] B. H. Leung, "A Novel Model on Phase Noise of Ring Oscillator Based on Last Passage Time", *IEEE Trans. on CS-I*, Vol. 51, No. 3, pp. 471-482, March 2004
- [88] B. Leung, "A Switching Based Phase Noise Model for CMOS Ring Oscillators Based on Multiple Thresholds Crossing", *IEEE Transactions on Circuits and Systems I*, Vol. 57, Issue 11, pp 2858-2869, Nov 2010
- [89] B. Leung, D. Mcleish, "Phase Noise of a Class of Ring Oscillators having Unsaturated Outputs with Focus on Cycle to Cycle Correlation", *IEEE Trans. on Circuits and Systems I*, vol. 56, no. 8. pp.1689-1707, August, 2009
- [90] N. Lam, B. Leung, "Dynamic Quadrant Swapping Scheme Implemented in a Post Conversion Block for I, Q, Mismatch Reduction in a DQPSK Receiver", *IEEE Journal of SSC*, Vol. 45, Issue 2, pp 322-337, Feb 2012
- [91] B. Leung, "Comparison of Phase Noise Models on a Class of Ring Oscillators Using Low Voltage Swing Fully Differential Delay Cells", *Analog Integrated Circuits and Signal Processing*, vol. 61, pp. 129-147, Nov. 2009
- [92] Z. Shu, K. Lee, B. Leung, "A 2.4 GHz ring oscillator based CMOS frequency synthesizer with a fractional divider dual PLL architecture", *IEEE Journal of Solid State Circuits*, vol 39, pp. 452-463, March 2004
- [93] B. Leung, "A Novel Model on Phase Noise in Ring Oscillator Based on Last Passage Time", *IEEE Transactions on Circuits and Systems I*, vol. 51, pp. 471-482, March 2004
- [94] B. Leung, D. Mcleish, "Investigation of phase noise of ring oscillators with time varying current and noise sources by time scaling thermal noise", *IEEE Trans. on Circuits and Sys-I*, vol. 51, pp. 1926-1939, Oct. 2004
- [95] M. Haidi and B. Leung, "PLL based frequency discriminator using the loop filter as an estimator", *IEEE Transactions on Circuits and Systems II*, pp.721-727, November, 2002
- [96] A. A. Abidi, "Phase Noise and Jitter in CMOS Ring oscillators," *IEEE JSSC*, vol. 41, pp. 1803-1816, Aug 2006.
- [97] M. M. Driscoll, "Modeling Phase Noise in Multifunction Subassemblies", *IEEE Transactions on Ultrasonics, Ferroelectrics, and Frequency Control*, vol. 59, no. 3, pp. 373-381, March 2012
- [98] U.L. Rohde, "A New Efficient Method of Designing Low Noise Microwave Oscillators," Dr.-Ing. Dissertation, Faculty IV, EEC (Electrical Engineering and Computer Sciences), TU- Berlin, Germany, February 2004.
- [99] Ajay Poddar, Ulrich Rohde, Anisha Apte, "How Low Can They Go, Oscillator Phase noise model, Theoretical, Experimental Validation, and Phase Noise Measurements", *IEEE Microwave Magazine*, Vol. 14, No. 6, pp. 50-72, September/October 2013.
- [100] Ulrich Rohde, Ajay Poddar, Anisha Apte, "Getting Its Measure", *IEEE Microwave Magazine*, Vol. 14, No. 6, pp. 73-86, September/October 2013.
- [101] U. L. Rohde, A. K. Poddar, Anisha Apte, "Phase noise measurement and its limitations", *MWJ*, April 2013.

#### Chapter 4

- [1] Agilent Phase Noise Measurement Solution ([www.home.agilent.com/agilent/application](http://www.home.agilent.com/agilent/application)), 2012
- [2] W. F. Walls, "Practical problems involving phase noise measurements, 33th annual precise time interval (PTTI) meeting, pp 407-416, Nov 2001.
- [3] U.L. Rohde, A.K. Poddar, and G. Boeck, "The Design of Modern Microwave Oscillators for Wireless Applications: Theory and Optimization", Wiley, New York, 2005
- [4] U. L. Rohde, "Microwave and Wireless Synthesizers, Theory and Design", Wiley, New York, 1997
- [5] U. L. Rohde, M. Rudolph, "RF/Microwave Circuit Design for Wireless Applications", Wiley 2013
- [6] U. L. Rohde, "Crystal oscillator provides low noise", *Electronic Design*, 1975

- [7] G. D. Vendelin and A. M. Pavio, U. L. Rohde, "Microwave circuit design using linear and nonlinear techniques", Wiley, New York, 2005
- [8] A. L. Lance, W. D. Seal, F. G. Mendozo and N. W. Hudson, "Automating Phase Noise Measurements in the Frequency Domain," *Proc. of the 31<sup>st</sup> Annual Symp. on Freq. Control*, 1977
- [9] Agilent Phase Noise Selection Guide, June 2011
- [10] Dorin Calbaza, Chandra Gupta, Ulrich L. Rohde, and Ajay K. Poddar, "Harmonics Induced Uncertainty in Phase Noise Measurements", 2012 IEEE MTT-S Digest, pp. 1-3, June 2012.
- [11] U. L. Rohde, H. Hartnagel, "The Dangers of Simple use of Microwave Software" [http://www.mes.tudarmstadt.de/media/mikroelektronische\\_systeme/pdf\\_3/ewme2010/proceedings/sessi\\_0nvii/rohde\\_paper.pdf](http://www.mes.tudarmstadt.de/media/mikroelektronische_systeme/pdf_3/ewme2010/proceedings/sessi_0nvii/rohde_paper.pdf), 2010
- [12] "Sideband Noise in Oscillators", <http://www.sm5bsz.com/osc/osc-design.htm>, 2009
- [13] Jeff Cartwright, "Choosing an AT or SC cut for OCXOs, [http://www.conwin.com/pdfs/at\\_or\\_sc\\_for\\_ocxo.pdf](http://www.conwin.com/pdfs/at_or_sc_for_ocxo.pdf), 2008
- [14] Benjamin Parzen, "Design of Crystal and Other Harmonic Oscillators", John Wiley & Sons, 1983
- [15] U. L. Rohde and A. K. Poddar, "Crystal Oscillators", Wiley Encyclopedia of Electrical and Electronics Engineering", pp.1-38, October 19, 2012.
- [16] U. L. Rohde and A. K. Poddar, "Crystal Oscillator Design", Wiley Encyclopedia of Electrical and Electronics Engineering, pp. 1-47, October 2012
- [17] U. L. Rohde and A. K. Poddar, "Latest Technology, Technological Challenges, and Market Trends for Frequency Generating and Timing Devices", IEEE Microwave Magazine, pp.120-134, Oct. 2012.
- [18] U. L. Rohde and A. K. Poddar, "Techniques Minimize the Phase Noise in Crystal Oscillators", 2012 IEEE FCS, pp. 01-07, May 2012.
- [19] M. M. Driscoll, "Low Frequency Noise Quartz Crystal Oscillators", Instrumentation and Measurement, IEEE Trans. Vol 24, pp 21-26, Nov 2007,
- [20] M. M. Driscoll, "Low Noise Crystal Controlled Oscillator", US Patent No. US4797639A, Jan 10, 1989
- [21] M. Driscoll, "Reduction of quartz crystal oscillator flicker-of-frequency and white phase noise (floor) levels and acceleration sensitivity via use of multiple resonators", UFFCC, vol. 40, pp 427-430, Aug 2002.
- [22] [www.mentby.com/bruce-griffiths/notes-on-the-driscoll-vhf-overtone-crystal-oscillator.html](http://www.mentby.com/bruce-griffiths/notes-on-the-driscoll-vhf-overtone-crystal-oscillator.html), Dec 28, 2009
- [23] U. L. Rohde, A. K. Poddar, "Technique to minimize phase noise in crystal oscillator", Microwave Journal, pp132-150, May 2013
- [24] O. Rajala, "Oscillator Phase Noise Measurements using the Phase Lock Method", MS thesis, Department of Electronics, Tampere University of Technology, June 2010.
- [25] W. F. Walls, "Cross-Correlation Phase Noise Measurements", IEEE FCS, pp. 257-261, 1992
- [26] J. Breitbarth, "Cross Correlation in phase noise analysis", Microwave Journal, pp 78-85, Feb 2011.
- [27] F. L. Walls et al. Extending the Range and Accuracy of Phase Noise Measurements, Proceedings of the 42nd Annual Symposium on Frequency Control, 1988.
- [28] Noise XT, DCNTS manual, [http://www.noisext.com/pdf/noisext\\_DCNTS.pdf](http://www.noisext.com/pdf/noisext_DCNTS.pdf), (2013)
- [29] Agilent E5052A Signal Source Analyzer 10 MHz to 7, 26.5, or 110 GHz – Datasheet", Agilent document 5989-0903EN, p. 12, May 2007
- [30] Frequency Extension for Phase Noise Measurements with FSUP26/50 and Option B60 (Cross-Correlation)", Rhode & Schwarz Application Note 1EF56, p. 3 Jan 2007.
- [31] M. Jankovic, "Phase noise in microwave oscillators and amplifiers" , PhD thesis, Faculty of graduate School of the University of Colorado, Dept. of ECE, 2010
- [32] Hewlett Packard, *RF and Microwave phase Noise Measurement Seminar*, Available at: [http://www.hparchive.com/seminar\\_notes/HP\\_PN\\_seminar.pdf](http://www.hparchive.com/seminar_notes/HP_PN_seminar.pdf), June 1985.
- [33] Stephan R. Kurz, *WJ Tech note – Mixers as Phase Detectors*, Available at: [http://www.triquint.com/prodserv/tech\\_info/docs/WJ\\_classics/Mixers\\_phase\\_detectors.pdf](http://www.triquint.com/prodserv/tech_info/docs/WJ_classics/Mixers_phase_detectors.pdf), [WWW][Cited 2010-05-11]
- [34] Agilent Technologies, *Phase Noise Characterization of Microwave Oscillators – Phase Detector Method–Product Note 11729B-1*, May 2010
- [35] Aeroflex, Application Note #2 – PN9000 automated Phase Noise Measurement System Available at: <http://www.datasheetarchive.com/datasheet-pdf/010/DSA00173368.html>, April 2010.

- [36] Hewlett Packard. *HP 3048A Phase Noise Measurement System Reference Manual* [online]. Available: <http://cp.literature.agilent.com/litweb/pdf/03048-90002.pdf>, (1989, Sept 01).
- [37] E. Rubiola and F. Vernotte. *The cross-spectrum experimental method* [online]. Available: <http://arxiv.org/document/1003.0113v1> [physics.ins-det], (2010, Feb 27)
- [38] Hewlett Packard *HP 3048A Phase Noise Measurement System Operating Manual* [online]. Available: <http://cp.literature.agilent.com/litweb/pdf/03048-61004.pdf>, (1990, Jun 01)
- [39] *HP 11848A Phase Noise Interface Service Manual*, 1st ed., HP- Spokane, Washington 1987.
- [40] M. Sampietro, L. Fasoli, and G. Ferrari, "Spectrum analyzer with noise reduction by cross-correlation technique on two channels," *Rev. Sci. Instrum.*, vol. 70, no. 5, May 1999.
- [41] Samuel J. Bale, David Adamson, Brett Wakley, Jeremy Everard, "Cross Correlation Residual Phase Noise Measurements using Two HP3048A Systems and a PC Based Dual Channel FFT Spectrum Analyzer", 24<sup>th</sup> European Frequency and Time Forum, pp 1-8, (April 13-16, 2010)
- [42] Jeremy Everard, Min Xu, Simon Bale, "Simplified Phase Noise Model for Negative-Resistance Oscillators and a Comparison With Feedback Oscillator Models", *IEEE Transactions on Ultrasonics, Ferroelectrics, and Frequency Control*, Vol. 59, No. 3, March 2012
- [43] Jeremy Everard, Min Xu, "Simplified Phase Noise Model for Negative-Resistance Oscillators", *IEEE Frequency Control Symposium, 2009 Joint with the 22nd EFTF*, pp. 338-343, April 2009
- [44] Time Domain Oscillator Stability Measurement Allan variance, application note, Rohde & Schwarz, pp. 1-16, <http://www.crya.unam.mx/radiolab/recursos/Allan/RS.pdf>, 2009.
- [45] M. M. Driscoll, "Modeling Phase Noise in Multifunction Subassemblies", *IEEE Transactions on Ultrasonics, Ferroelectrics, and Frequency Control*, vol. 59, no. 3, pp. 373-381, March 2012
- [46] Ajay Poddar, Ulrich Rohde, Anisha Apte, "How Low Can They Go, Oscillator Phase noise model, Theoretical, Experimental Validation, and Phase Noise Measurements", *IEEE Microwave Magazine*, Vol. 14, No. 6, pp. 50-72, September/October 2013.
- [47] Ulrich Rohde, Ajay Poddar, Anisha Apte, "Getting Its Measure", *IEEE Microwave Magazine*, Vol. 14, No. 6, pp. 73-86, September/October 2013.
- [48] U. L. Rohde, A. K. Poddar, Anisha Apte, "Phase noise measurement and its limitations", *MWJ*, April 2013.
- [49] E. N. Ivanov and F. L. Walls, "Effect of anomalously low voltage noise in measurement systems with cross-correlation signal processing," in *Conference on Precision Electromagnetic Measurements. Conference Digest. CPEM 2000 (Cat. No.00CH37031)*, Sydney, NSW, Australia, pp. 447-448.
- [50] E. N. Ivanov and F. L. Walls, "Interpreting anomalously low voltage noise in two-channel measurement systems," *IEEE Trans. UFFC*, vol. 49, no. 1, pp. 11-19, Jan. 2002.
- [51] Rubiola et al, "The cross-spectrum experimental method," arXiv e-print 1003.0113, Mar. 2010.
- [52] E. Rubiola, *Phase Noise and Frequency Stability in Oscillators*. Cambridge University Press, 2010.
- [53] G. Cibiel, M. Regis, E. Tournier, and O. Llopis, "AM noise impact on low level phase noise measurements," *IEEE Trans. of UFFC*, vol. 49, no. 6, pp. 784-788, 2002.
- [54] E. Rubiola and R. Boudot, "The effect of AM noise on correlation phase-noise measurements," *IEEE Trans. of UFFC*, vol. 54, no. 5, pp. 926-932, May 2007.
- [55] E. Rubiola, "Primary calibration of AM and PM noise measurements," arXiv e-print 0901.1073, Jan. 2009
- [56] C. W. Nelson, A. Hati, and D. A. Howe, "Collapse of the Cross-spectral Function", *IEEE Frequency Control Symposium*, FCS proceedings 2014, pp.590-591, Taipei May 2014
- [57] C.W. Nelson, A. Hati, and D.A. Howe, "A Collapse of the Cross spectral Function in Phase Noise Metrology," *Electronics Letters.*, vol. 49, no. 25, pp. 1640-1641, Dec. 2013
- [58] C. W. Nelson, A. Hati, and D. A. Howe, "A collapse of the cross spectral function in phase noise metrology," *Rev. Sci. Instrum.*, vol. 85, pp. 024705-7, Feb. 201

## Chapter 5

- [1] G. D. Vendelin, A. M. Pavio and U. L. Rohde, *Microwave Circuit Design Using Linear and Nonlinear Techniques*, New York: John Wiley & Sons, 1990.
- [2] K. L. Kotzebue, 'A Technique for the Design of Microwave Transistor Oscillators', *IEEE Trans. Microwave Theory Tech.*, MTT-32, pp. 719-721, 1984.
- [3] Cohn and Mitchel, 'Design of Microstrip Transistor Oscillators', *Int. J. Electronics*, 35, pp. 385-395, 1973.
- [4] G. I. Zysman and A. K. Johnson, 'Coupled Transmission Line Networks in an Inhomogeneous Dielectric

- Medium', IEEE Trans. MTT, 17, pp. 753–759 1969.
- [5] K. C. Gupta, R. Garg and R. Chadha, Computer-Aided Design of Microwave Circuits, Artech House, 1981.
  - [6] H. Howe, Stripline Circuit Design, Dedham: Artech House, 1974.
  - [7] P. Russer, Electromagnetics, Microwave Circuit and Antenna Design for Communication Engineering” 2nd Edition, Artech House, Inc. ISBN 1-58053-907-6, 2006
  - [8] R. J. Cameron, C. M. Kudsia, and R. R. Mansour, “Microwave Filters for Communication Systems” Fundamentals, Design, and Applications, John Wiley & Sons, Inc, 2007.
  - [9] R. M. Foster, “A reactance theorem,” Bell System Tech. J., vol. 3, pp. 259-267, 1924.
  - [10] R. E. Collin, Foundation for Microwave Engineering, McGraw-Hill, New York, 1966.
  - [11] D. Pozar, Microwave Engineering, 2nd ed., Wiley, New York 1998.
  - [12] A. E. Atia and A. E. Williams, Narrow Bandpass waveguide filters, IEEE Tran. MTT, Vol. 20, pp. 238-265, 1972.
  - [13] A. E. Atia and A. E. Williams, New types of waveguide Bandpass filters for satellite transponders, COMSAT Tech. Rev. 1 (1), 21-43 (1971).
  - [14] S. J. Fiedziusko, Dual-mode dielectric resonator loaded cavity filter, MTT Trans, Vol. 30, pp. 1311-1316, 1982.
  - [15] D. Kajfez and P. Guilon, Dielectric Resonators, Artech House, Norwood, MA, 1986.
  - [16] R. R. Mansour, Design of superconductive multiplexes using single-mode and dual-mode filters, IEEE Trans. MTT, Vol. 42, pp. 1411-1418, 1994
  - [17] V. Walkar and I. C. Hunter, Design of triple mode TE<sub>01</sub> resonator transmission filters, IEEE Microwave Wireless Component Letters, vol. 12, pp. 215-217, June 2002.
  - [18] R. R. Mansour, Microwave superconductivity, IEEE Trans. MTT, Vol. 50, pp. 750-759, 1972.
  - [19] E. O. Hammerstad and O. Jensen, Accurate models for microstrip computer-aided design, IEEE-MTT-S Digest, pp. 407-409, 1980.
  - [20] I. Bahl and P. Bhartia, Microwave Solid State Circuit Design, 2nd ed., Wiley, New York, April 2003.
  - [21] T. Ohira and K. Araki, "Dimensional extension of Kurokawa's stability criterion for general multi-port device oscillators," IEICE Electronics Express, vol. 3, pp. 143-148, April 2006.
  - [22] T. Ohira and K. Araki, "Oscillator frequency spectrum as viewed from resonant energy storage and complex Q factor," IEICE Electronics Express, vol. 3pp. 385-389, Aug. 2006.
  - [23] T. Ohira, "Theoretical essence of stable and low phase noise microwave oscillator design (tutorial)," European Microwave Conf., SC2-1, Manchester, Sept. 2006.
  - [24] T. Ohira and K. Araki, "Active Q factor and equilibrium stability formulation for sinusoidal oscillators" IEEE Trans. Circuit Systems II, vol. 54, issue 9, pp. 810-814, Sept. 2007.
  - [25] T. Ohira and T. Wuren, "Pseudolinear circuit theory for sinusoidal oscillator performance maximization (invited)" IEICE Trans. Electron., vol. E91-C, issue 11, pp. 1726-1737, Nov. 2008.
  - [26] T. Ohira, "Extended Adler's injection locked Q factor formula for general one - and two -port active device oscillators" IEICE Electronics Express ELEX, vol. 7, issue 19, pp. 1486-1492, Oct. 2010.
  - [27] T. Ohira, "Dedicated Q factor formulas stemming from oscillation frequency stability against source and load deviations" Toyohashi Univ. Tech. Tutorial Lecture 2012.
  - [28] T. Ohira, "Rigorous Q factor formulation for one- and two-port passive linear networks from an oscillator noise spectrum viewpoint," IEEE Trans. Circuits Systems II, vol. 52, issue 12, pp. 846-850, Dec. 2005.
  - [29] D.B.H. Tellegen, "A general network theorem with applications," Proc. IRE Australia, pp. 265-270, Nov. 1953
  - [30] K. Kurokawa, "Some basic characteristics of broadband negative resistance oscillator circuits," Bell System Technical Journal, pp. 1937-1955, July 1969
  - [31] R. Adler, "A study of locking phenomena in oscillators", Proc. IRE, vol. 34, pp. 351-357, June 1946
  - [32] T. Ohira, "Dedicated Q factor formulas stemming from oscillation frequency stability against source and load deviations" Toyohashi Univ. Tech. Tutorial Lecture 2012.
  - [33] U. L. Rohde, A. K. Poddar, and G. Boeck, "Modern Microwave Oscillators for Wireless Applications: Theory and Optimization", John Wiley & Sons Inc., 2005.
  - [34] Leeson, "A simple model of feedback oscillator noise spectrum," Proc. IEEE, vol. 54, pp. 329–330, Feb. 1966
  - [35] K. Hoffmann, and Z. Skvor, "Active resonator", Int. Conf. Trends, Communications, EUROCON'2001, vol. 1, pp. 164-166, July 2001.
  - [36] P. Alinikula, R. Kaunisto, and K. Stadius, " Monolithic active resonators for wireless application", in IEEE MTT-S Dig., vol. 2, pp. 1151-1154, May 1994.

- [37] C.-Y. Chang, and T. Itoh, "Microwave active filters based on coupled negative resistance method", *IEEE Trans. on MTT*, vol.-38, no. 12, pp. 1879-1884, Dec 1990.
- [38] U. Karacaoglu, and I. D. Robertson, "MMIC Active bandpass filters using varactor-tuned negative resistance elements", *IEEE Trans. Microwave Theory and Techniques*, vol.-43, no. 12, pp. 2926-2932, Dec 1995
- [39] Y. Ishikawa, S. Yamashita, and S. Hidaka, "Noise design of active feedback resonator BEF," *IEEE Trans. Microw. Theory Tech.*, vol. -41, no. 12, pp. 2133- 2138, Dec. 1991
- [40] H. Ezzedine, L. Billonnet, B. Jarry, and P. Guillon, "Optimization of noise performance for various topologies of planar microwave active filters using noise wave techniques," *IEEE Trans. Microw. Theory Tech.*, vol. -46, no. 12, pp. 2484-2492, Dec. 1998
- [41] M. Nick, "New Q-Enhanced Planar Resonators for Low Phase-Noise Radio Frequency Oscillators", PhD Dissertation, Electrical Engineering, University of Michigan, 2011
- [42] P. Gardner, and D. K. Paul, "Optimum noise measure configurations for transistor negative resistance amplifiers," *IEEE Trans. Microw. Theory Tech.*, vol. -45, no. 5, pp. 580-586, May 1997.
- [43] A. Grebennikov, "RF and microwave transistor oscillator design," New York: John Wiley & Sons, 2007.
- [44] H. A. Haus, and R. B. Adler, "Circuit theory of linear noisy networks," New York: Wiley, 1959.
- [45] J.-S Hong and M. J. Lancaster, *Microwave Filter for RF/Microwave Application*. New York: Wiley, 2001.
- [46] U. L. Rohde and A. K. Poddar, "Active Planar Coupled Resonators Replace Traditional High Q-Resonators in Low Phase Noise Oscillators/VCOs, *IEEE RWS 2007*, pp. 39-42, CA, USA, 09-11 January 2007.
- [47] A. K. Poddar, "Slow-Wave Resonator based Tunable Multi-Band Multi-Mode Injection-Locked Oscillators", Research Report , RF and Microwave Techniques Brandenburg University of Technology Cottbus-Senftenberg 2014", [https://www-docs.tu-cottbus.de/mikrowellentechnik/public/poddar\\_report\\_long\\_ebook.pdf](https://www-docs.tu-cottbus.de/mikrowellentechnik/public/poddar_report_long_ebook.pdf)
- [48] K. Chang and L.-H. Hsieh, *Microwave ring circuits and related structures*, Wiley-IEEE, 2004.
- [49] Ledezma, "A study on the miniaturization of microstrip square open loop resonators", MS. Thesis 2011,
- [50] H. Yabuki, M. Sagawa, and M. Makimoto, "Voltage controlled push-push oscillators using miniaturized hairpin resonators", in *IEEE MTT-S, Dig.*, pp. 1175-1178, 1991.
- [51] L-Hwa Hsieh, "Analysis, Modeling and Simulation of Ring Resonators and their applications to Filters and Oscillators", PhD Dissertation, Texas A&M University, 2004.

## Chapter 6

- [1] Pistono et al, "Compact Fixed and Tune-All Bandpass Filters Based on Coupled Slow-Wave Resonators," *IEEE Trans. on MTT*, Vol. 54, No. 6, June 2006, pp. 2790-2798.
- [2] Chang et. al, "Compact Microstrip Bandpass Filters Using Miniaturized Slow-Wave Quarter-Wavelength Resonators", *Proceedings of Asia-Pacific Microwave Conference 2010*, pp. 1958-1961.
- [3] Lung-Hwa Hsieh and Kai Chang, "Slow-Wave Bandpass Filters Using Ring or Stepped-Impedance Hairpin Resonators," *IEEE Tran. on MTT*, Vol. 50, No. 7, pp. 1795-1800, July 2002.
- [4] Hsiu-Ying Cho, et. al., "High-Performance Slow-Wave Transmission Lines With Optimized Slot-Type Floating Shields," *IEEE Trans. on Electron Devices*, Vol. 56, No. 8, August 2009.
- [5] T. Masuda, N. Shiramizu, T. Nakamura, and K. Washio, "Characterization and Modeling of Microstrip Transmission Lines with Slow-wave Effect," *SMIC in RF Systems*, pp.55-158, 2008.
- [6] H. wang et. al., "A 60 GHz Wideband Injection-Locked Frequency Divider with Adaptive-Phase-Enhancing Technique", *RFICS*, pp. 75-78, 2011.
- [7] A. K. Poddar, S. K. Koul and Bharthi Bhat, "Millimeter Wave Evanescent Mode Gunn Diode Oscillator in Suspended Stripline Configuration", *IR &MM Wave, 22<sup>nd</sup> Int. Conference*, pp. 265-266, July 1997.
- [8] A. K. Poddar, U. L. Rohde, "Metamaterial Möbius Strips (MMS): Application in Resonators for Oscillators and Synthesizers", *IEEE UFFC Symposia*, May 19-22, 2014
- [9] Chung-Tse M. Wu, A. K. Poddar, U. L. Rohde, T. Itoh, "A C-band Tunable Oscillator Based on Complementary Coupled Resonator using Substrate Integrated Waveguide Cavity " *EuMW 2014*
- [10] A. K. Poddar and U. L. Rohde, "Slow-Wave Evanescent-Mode Coupled Resonator Oscillator", *IEEE Frequency Control Symposium, Proceedings*, pp. 01-07, May 2012.
- [11] A. K. Poddar and U. L. Rohde, "Adaptive Mode-Coupled Harmonically Tuned High-Q Ultra Low Phase Noise Sources", *Microwave Journal*, pp. 106-120, Sept 2011.
- [12] U. L. Rohde and A. K. Poddar, "Slow-Wave Structures Slice VCO Phase Noise", *MW & RF*, May 2011.

- [13] A. K. Poddar and U. L. Rohde, "Slow Wave Resonator Based Tunable Oscillators," Proceedings of 2011 Joint Conference of the IEEE IFCS & European Frequency and Time Forum, pp. 549-558, May 2011.
- [14] U. L. Rohde and A. K. Poddar, "A Digital Frequency Synthesizer Using Adaptive Mode-Coupled Resonator Mechanism for Low Noise and Low Jitter Applications", IEEE (ISCAS), pp. 414-417, Brazil, May 15-18, 2011.
- [15] Wei-Shin Chang and Chi-Yang Chang, "A High Slow-Wave Factor Microstrip Structure With Simple Design Formulas and its Application to Microwave Circuit Design", IEEE Trans. on Microwave Theory and Techniques, Vol. 60, No. 11, pp. 3376-3383, Nov 2012.
- [16] V. K. Gupta, P. P. Kumar, and C. N. Rao, "A Novel Miniaturized, Wideband, High Directivity Microstrip Coupler on FR4", International Conference on Microwave and Photonics (ICMAP), pp. 1-4, 2013.
- [17] U. L. Rohde and A. K. Poddar, "Large-Signal Approach Yields Low-Noise VHF/UHF Oscillators, part 1, pp. 62-76, April 2008.
- [18] U. L. Rohde and A. K. Poddar, "Large-Signal Approach Yields Low-Noise VHF/UHF Oscillators, part 2, pp. 84-96, May 2008.
- [19] U. L. Rohde and A. K. Poddar, "Planar Resonators Arm Tunable Oscillators", Microwave & RF, part 1, pp. 92-96, June 2008
- [20] U. L. Rohde and A. K. Poddar, "Planar Resonators Arm Tunable Oscillators", MW & RF, part 2, July 2008.
- [21] U. L. Rohde and A. K. Poddar, "Miniature VCOs Shrink Wideband Synthesizers, MW & RF, pp. 87-92, Dec 2008.
- [22] U. L. Rohde and A. K. Poddar, "STPCR Offers Integrable Alternatives Of DRO", Microwave Symposium Digest, 2008 IEEE MTT-S, pp. 233-236, Atlanta, USA, 15-20 June 2008.
- [23] U. L. Rohde and A. K. Poddar, "Mode-Coupled Stubs-Tuned Planar Resonator Offers Promising And Integrable Alternatives Of DRO (Dielectric Resonator Oscillator)", IEEE Sarnoff Symposium, pp. 1-7, Princeton, NJ, USA, April 28-30, 2008.
- [24] U. L. Rohde and A. K. Poddar, "Injection-Tuned Coupled Oscillators" IEEE Radio Wireless Symposium 2008, pp. 367-370, Orlando, FL, USA, 22-24 January 2008.
- [25] U. L. Rohde and A. K. Poddar, "Reconfigurable Concurrent Oscillator (RCO)" IEEE Radio Wireless Symposium 2008, pp. 371-374, 22-24 January 2008, Orlando, FL, USA.
- [26] U. L. Rohde and A. K. Poddar, "Stubs-Tuned Planar Coupled Resonator Based Spectral Pure Signal Source for Wireless Communication Systems", IEEE/PIMRC 2007, pp. 01-05, Greece, Sept. 03-07, 2007.
- [27] U. L. Rohde and A. K. Poddar, "Reconfigurable Concurrent Oscillator (RCO)", IEEE/PIMRC 2007, pp. 01-05, Greece, 01-05, Sept. 03-07, 2007.
- [28] U. L. Rohde and A. K. Poddar, "Self-Injection Locked Compact Coupled Planar Resonator Based Cost-Effective Ultra Low Phase Noise VCOs For Wireless Systems", IEEE/ECCTD , pp. 998-1001, Aug 2007.
- [29] U. L. Rohde and A. K. Poddar, "Noise Cancellation and Noise Minimization Techniques for Low Cost Compact Size Configurable RF Oscillators/VCOs", IEEE/ECCTD, pp. 986-989, Aug 27-30, 2007.
- [30] U. L. Rohde and A. K. Poddar, "Concurrent, Reconfigurable and Concurrent Oscillators for Multi-Band Multi-Mode Communication Systems", EUMC 2007, pp. 1050-1053, Munich, October 09-12, 2007.
- [31] U. L. Rohde and A. K. Poddar, "Concurrent, Reconfigurable and Concurrent Oscillators for Multi-Band Multi-Mode Communication Systems", ECWT 2007, pp. 292-295, Munich, October 08-10, 2007.
- [32] U. L. Rohde and A. K. Poddar, "Low Cost Configurable RF Signal Source For Wireless Applications", European Microwave Conference, EuMiC 2007, pp. 508-511, Munich, October 09-12, 2007.
- [33] U. L. Rohde and A. K. Poddar, "Noise Reduction Techniques For Configurable RF Signal Source", 6<sup>th</sup> International Conference on Antenna Theory and Techniques, ICATT 2007, pp. 163-166, Sept. 2007.
- [34] U. L. Rohde and A. K. Poddar, "Minimization of Phase Noise in Scaled Device Coupled Mode Oscillators", 6<sup>th</sup> Int. Conf. on Antenna Theory and Techniques, IEEE/ICATT 2007, pp. 51-56 Sept 2007.
- [35] U. L. Rohde and A. K. Poddar, "Low Cost Signal Source for Multi-Band Multi-Mode Wireless Systems", 6<sup>th</sup> Int. Conf. on Antenna Theory and Techniques, IEEE/ICATT, pp. 167-169, Sept. 17-21, 2007.
- [36] Fei Shen, et. al, "A Novel V-Shaped Microstrip Meander-Line Slow-Wave Structure for W-band MMPM", IEEE Trans. on Plasma Science, Vol. 40, Mo. 2, pp. 463-469, Feb 2012.
- [37] U. L. Rohde and A. K. Poddar, "STPCR VCO Replaces Expensive DRO", IEEE/APMC 2007, pp. 1-4, Dec. 11-14, 2007, Bangkok, Thailand.
- [38] J. -S. Hong and M. J. Lancaster, "Theory and experiment of novel microstrip slow-wave open-loop resonator filters, . IEEE Trans. on MTT., vol. 45, pp. 2358-2365, December, 1997.

- [39] M. Sagawa, K. Takahashi, and M. Makimoto, "Miniaturized hairpin resonator filters and their application to receiver front-end MIC", IEEE Trans. MTT, vol. 37, pp. 1991-1997, December, 1989.
- [40] F. Rouchaud, V. Madrangeas, M. Aubourg, P. Guillon, B. Theron, and M. Maignan, "New classes of microstrip resonators for HTS microwave filters applications", IEEE MTT-S Int. Microwave Symp. Dig., Vol. 2, pp. 1023-1026, June 1998.
- [41] J. T. Kuo, M. J. Maa, and P. H. Lu, "A microstrip elliptic function filter with compact miniaturized hairpin resonators", IEEE Microwave and Guided Wave Lett., vol. 10, pp. 94-95, March, 2000.
- [42] U. L. Rohde and A. K. Poddar, "STPCR Offers Integrable Alternatives Of DRO", 2008 IEEE MTT-S, pp. 233-236, 15-20 June 2008 Atlanta, USA.
- [43] R. J. Cameron, C. M. Kudsia, and R. R. Mansour, "Microwave Filters for Communication Systems" Fundamentals, Design, and Applications, 2007 John Wiley & Sons, Inc.
- [44] L. M. Ledezma, "A study on the miniaturization of microstrip square open loop resonators", USF, MS. Thesis 2011.
- [45] J. Hong and M. Lancaster, "Microstrip Filters for RF/Microwave Applications", Wiley and Sons, 2001.
- [46] F. X. Sinnesbichler, B. Hautz and G. R. Olbrich, "A Si/SiGe HBT dielectric resonator push-push oscillator at 58 GHz", IEEE Microwave and Guided Wave Lett., vol. 10, pp. 145-147, April 2000.
- [47] L. -H. Hsieh and K. Chang, "Slow-wave bandpass filters using ring or stepped impedance hairpin resonators", IEEE Trans. on MTT., vol. 50, pp. 1795 - 1800, July 2002.
- [48] T. .Y. Yun and K. Chang, "Analysis and optimization of a phase shifter controlled by a piezoelectric transducer", IEEE Trans. on MTT, vol. 50, pp. 105-111, January 2002.
- [49] Y. M. Poplavko, Y. V. Prokopenko, V. I. Molchanov, and A. Dogan, "Frequency-tunable microwave dielectric resonator", IEEE Trans. on MTT., vol. 49, pp. 1020-1026, June 2001.
- [50] H. Yabuki, M. Sagawa, and M. Makimoto, "Voltage controlled push-push oscillators using miniaturized hairpin resonators", IEEE MTT-S IMS Symp. Dig., pp. 1175-1178, 1991.
- [51] Jia-Sheng Hong and Michael J. Lancaster "Cross-Coupled Microstrip Hairpin-Resonator Filters", IEEE Trans. Microwave Theory Tech., Vpl. 46, No. 1, Jan 1998
- [52] B. C. Wadell, Transmission Line Design Handbook, MA, Artech House, p. 321, 1991.
- [53] M. Kirschning, R. H. Jansen and N. H. L. Koster, "Measurement and computer aided modeling of microstrip discontinuities by an improved resonator method", IEEE MTT-S Dig., pp. 495-497, 1983.
- [54] S. -Y. Lee and C. -M. Tsai "New cross-coupled filter design using improved hairpin resonators", IEEE Trans. Microwave Theory Tech., vol. 48, pp. 2482- 2490, December 2000.
- [55] C. .M. Tsai, S. .Y. Lee, and C. .C. Tsai, "Hairpin filters with tunable transmission zeros", IEEE MTT-S Int. Microwave Symp. Dig., pp. 2175-2178, 2001
- [56] K. C. Gupta, R. Garg, I. Bahl, and P. Bhartia, Microstrip Lines and Slotlines, 2nd Boston: Artech House.
- [57] V. Kaajakari, J . K. Koskinen, and T. Mattila, "Phase noise in capacitively coupled micromechanical oscillators", IEEE Trans. On UFFC, Vol. 52, No. 12, pp. 2322-2331, Dec 2005.
- [58] R. M. Foster, "A reactance theorem," Bell System Tech. J., vol. 3, pp. 259-267, 1924.
- [59] U. L. Rohde, A. K. Poddar, "Wideband voltage controlled oscillators employing evanescent mode coupled resonators", US Patent No 7,180, 381 Feb 20, 2007
- [60] U. L. Rohde, A. K. Poddar, "Integrated Low Noise Microwave Wideband Push- Push VCO", US Patent No. 7,088189, Aug 2006.
- [61] U. L. Rohde, A. K. Poddar, "User-Definable Thermal Drift Voltage Controlled Oscillator", US Patent No.7, 265,642 B2, Sept 4, 2007.
- [62] U. L. Rohde, A. K. Poddar, "Low Thermal Drift Tunable Frequency Voltage Controlled Oscillatory", US Patent No.7, 262,670 B2, Aug 28, 2007.
- [63] U. L. Rohde, A. K. Poddar, "Multi-Octave Band Tunable Coupled Resonator Oscillator", US Patent No.7, 292,113, Nov. 6, 2007.
- [64] U. L. Rohde, A. K. Poddar, "Tunable Frequency Low Phase Noise and Low Thermal Drift Oscillator", US Patent No.7196591, March 2007.
- [65] U. L. Rohde, A. K. Poddar, "Low Noise, Hybrid Tuned Wideband Voltage Controlled Oscillator", US Patent No. 7,365,612 B2, April 29, 2008.
- [66] U.L. Rohde, A.K. Poddar, "Tunable Frequency Low Phase Noise and Low Thermal Drift Oscillator", U.S Patent NO. 7, 545, 229, June 09, 2009.



- [67] U.L. Rohde, A.K. Poddar, and G. Boeck, "The Design of Modern Microwave Oscillators for Wireless Applications: Theory and Optimization", Wiley, New York, 2005
- [68] U.L. Rohde, A.K. Poddar, "User-Definable, Low Cost, Low Phase Hit and Spectral Pure Tunable Oscillator", U.S. Patent No. 7,586,381 on September 08, 2009.
- [69] U. L. Rohde, A. K. Poddar, "User-Definable, Low Cost, Low noise, and phase hit insensitive multi-octave-band tunable oscillator", Phase Hit and Spectral Pure Tunable Oscillator, U.S. Patent No. 7,605,670, October 20, 2009.
- [70] M. Rohde, A. K. Poddar, "Visually Inspectable Surface Mount Device Pad", U.S. Patent No. 7,612,296, Nov 03, 2009,
- [71] U. L. Rohde, A. K. Poddar, "Low Noise and Low Phase Hits Tunable Oscillator", U.S. Patent No. 7,636, 021, Dec. 22, 2009
- [72] U. L. Rohde, A. K. Poddar, "Wideband voltage controlled oscillators employing evanescent mode coupled resonators", Canadian Patent No. 2,563, 174, July 21, 2009.
- [73] U. L. Rohde, A. K. Poddar, "User-Definable Thermal Drift Voltage Controlled Oscillator", Canadian Patent No. 2,548, 317, April 21, 2009.
- [74] U. L. Rohde, A. K. Poddar, "integrated Low Noise Microwave Wideband Push- Push VCO" Canadian Patent No.:2,548, 311, April 14, 2009.
- [75] U. L. Rohde and A. K. Poddar, "Novel Multi-Coupled Line Resonators Replace Traditional Ceramic Resonators in Oscillators/VCOs", 2006 IEEE International Frequency Control Symposium and Exposition, pp. 432-442, 5-7 June 2006, Florida, USA.
- [76] Voinigescu et. al, "A study of SiGe HBT Signal Sources in 220-330-GHz Range", IEEE JSSC, pp. 1-11, 2013
- [77] T. Tanaka, K. Takata, M. Aikawa, I. Toyoda, "A Ku band Oscillator array using positive feedback type push-push oscillators", IEEE APMC conf. proceedings, pp. 112-114, 2012
- [78] T. Sirburanon, T. Sato, A. Musa, D. Wei, K. Okada, A. Matsuzawa, "A 20 GHz push-push voltage-controlled oscillator for a 60 GHz frequency synthesizer", IEEE APMC conf. proc., pp. 205-207, 2012
- [79] S-Wein Chu, C-Kuang Wang, "An 80 GHz wide Tuning Range Push-Push VCO with gm-boosted full-wave rectification technique in 90 nm CMOS", IEEE MWCL, vol. 22, Issue 4, pp. 203-205, 2012
- [80] S. Yaoming, C. J. Scheytt, "A low phase noise 61 GHz push-push VCO with divider chain buffer in SiGe BiCMOS for 122 GHz ISM applications", 2012 IEEE RFIC symposium, pp. 79-82, 2012
- [81] Masuda et. al, "A push-push VCO with 13.9 GHz wide tuning range using loop-ground transmission line for full band 60-GHz transceive", 2102 IEEE Journal of SSC, Vol, 47, issue:6, pp. 1267-1277, 2012
- [82] M. Stuenkel, M. Feng, "A w-BAND TUNABLE Push-Push oscillator with 128X division for frequency synthesis applications", 2013 IEEE MTT-S Digest, pp, 1-3, 2012
- [83] To-Po Wang, "A fully integrated w-band push-push CMOS VCO with phase noise and wide tuning range", 2011 IEEE Trans. on UFFC, vol. 58, Issue: 7, pp. 1307-1319, 2011
- [84] A. K. Poddar, U. L. Rohde, A. S. Daryoush, "Integrated production of self injection locked self phase loop locked Opto-electronic Oscillators", US Patent application no. 13/760767 (filed on Feb 06, 2013).
- [85] A. K. Poddar, U. L. Rohde, A. S. Daryoush, "Self Injection Locked Phase Locked Looped Optoelectronic Oscillator", US Patent application No. 61/746, 919 (filed on Dec 28, 2012).
- [86] Yao, X. Steve, and Lute Maleki. "Optoelectronic oscillator for photonic systems." *Quantum Electronics, IEEE Journal of* 32.7 (1996): 1141-1149.
- [87] Moyer, Harris P., and Afshin S. Daryoush. "A unified analytical model and experimental validations of injection-locking processes." *IEEE Tran. on MTT, Vol. 48* No. 4 pp. 493-499, 2000.
- [88] C. McNeilage et al., "Review of feedback and feedforward noise reduction techniques," *Proc. IEEE Frequency Control Symp.*, Pasadena, CA, pp. 146 – 155, May 1998.
- [89] A. Suarez et al., "Analysis of Stabilization Circuits for Phase-Noise Reduction in Microwave Oscillators," *IEEE Trans. Microw. Theory Tech.*, vol. 53, No. 9, Sep. 2005
- [90] H. C. Chang, "Phase noise in self-injection locked oscillators – Theory and Experiment," *IEEE Trans. Microw. Theory Tech.*, vol. 51, no. 9, pp. 1994 – 1999, Sep. 2003
- [91] K.H. Lee et al., "A 30GHz self injection locked oscillator having a long Optical delay line for phase noise reduction," *Photonics Tech. Letters*, vol. 19, no. 24, Dec. 2007
- [92] G. Pillet et al, "Dual-frequency laser at 1.5µm for optical distribution and generation of high-purity microwave signals," *J. of Lightwave Technology*, vol. 26, no. 15, Aug. 2008

- [93] X.S. Zhou, X. Zhang, A.S. Daryoush, "A new approach for a phase controlled self-oscillating mixer," *IEEE Trans. on MTT*, vol. 45, no. 2, pp. 196-204, Feb. 1997.
- [94] D. Surzbecher *et al.*, "Optically controlled oscillators for millimeter-wave phased-array antennas," *IEEE Trans. Microw. Theory Tech.*, vol. 41, no. 6/7, Jun/Jul 1993
- [95] R. A. York *et al.*, "Analysis of oscillators with external feedback loop for improved locking range and noise reduction," *IEEE Trans. Microw. Theory Tech.*, vol. 47, no. 8, Aug. 1999
- [96] X. Zhang *et al.*, "A theoretical and experimental study of the noise behavior of subharmonically injection locked local oscillators," *IEEE Trans. Microw. Theory Tech.*, vol. 40, no. 5, May 1992.
- [97] R. E. Best, "Phase-locked loops: design, simulation, and applications, 4th ed, McGraw-Hill, New York, pp. 25-26, 1999.
- [98] F. Xu, and K. Wu, Guided-Wave and Leakage Characteristics of Substrate Integrated Waveguide, *IEEE Trans. Microwave Theory & Tech.*, vol. 53, no. 1, pp. 66-73, Jan. 2005.
- [99] Y. Dong and T. Itoh, A dual-band oscillator with reconfigurable cavity-backed complementary split-ring resonator, in *IEEE MTT-S Int. Dig.*, Jun. 1722, 2012, pp. 13.
- [100] F. F. He, K. Wu, W. Hong, L. Han, and X. Chen, A low phase-noise VCO using an electronically tunable substrate integrated waveguide resonator, *IEEE Trans. MTT*, vol. 58, no. 12, pp. 3452-3458, Dec. 2010.
- [101] S. Sirci, J. D. Martinez, M. Taroncher, and V. E. Boria, Varactor loaded continuously tunable SIW resonator for reconfigurable filter design, in *Proc. 41st Eur. Microw. Conf.*, 2011, pp. 436-439.
- [102] Chung-Tse Michael Wu, Ajay K. Poddar, Ulrich L. Rohde, and Tatsuo Itoh, "Active Complementary Coupled Resonator for Low Phase Noise X-band Oscillator," *IEEE-EFTF 2014*.
- [103] Chung-Tse Michael Wu, Ajay K. Poddar, Ulrich L. Rohde, and Tatsuo Itoh, "A C-band Tunable Oscillator Based on Complementary Coupled Resonator using Substrate Integrated Waveguide Cavity," *European Microwave Conference 2014*.
- [104] Z. Chen, W. Hong, and J. X. Chen. "High-Q planar active resonator based on substrate integrated waveguide technique." *Electronics letters* vol. 48, no. 10, pp. 575-577, May 2012.
- [105] J. Clerk Maxwell, *A Treatise on Electricity and Magnetism*, 3rd ed., vol. 2. Oxford: Clarendon, pp.68-73, 1892.
- [106] M. Nick and A. Mortazawi, "Low phase-noise planar oscillators based on low-noise active resonators", *IEEE Trans. Microw. Theory Tech.*, vol. 58, no. 5, pp. 1133-1139, May 2010.
- [107] K. Leong: "Precise measurements of surface resistance of HTS thin films using a novel method of Q-factor computations for Sapphire Dielectric resonators in the transmission mode", *Ph. D. thesis, James Cook University*, 2000.
- [108] K. Leong and J. Mazierska: "Accurate Measurements of Surface Resistance of HTS Films using a Novel Transmission Mode Q-factor Technique" *Journal of Superconductivity*, vol. 14, No. 1, pp. 93-103, 2001.
- [109] K. Leong *et al.* J. Mazierska: "Comparing Unloaded Q-Factor of a High-Q Dielectric Resonator Measured Using The Transmission Mode and Reflection Mode Methods Involving S-Parameter Circle Fitting", *Electrical and Computer Engineering, James Cook Univ. Townsville. 4811. Australia* <http://arxiv.org/ftp/arxiv/papers/1207/1207.5622.pdf>
- [110] Chun-Tse Michael Wu, "Active Integrated Metamaterial-Based Antennas and Microwaves Components", PhD Thesis June 2014, Department of Electrical Engineering, University of California, Los Angeles.
- [111] A. K. Poddar, "Slow-Wave Resonator based Tunable Multi-Band Multi-Mode Injection-Locked Oscillators", Research Report, RF and Microwave Techniques Brandenburg University of Technology Cottbus-Senftenberg 2014", [https://www-docs.tu-cottbus.de/mikrowellentechnik/public/poddar\\_report\\_long\\_ebook.pdf](https://www-docs.tu-cottbus.de/mikrowellentechnik/public/poddar_report_long_ebook.pdf)

## Chapter 7

- [1] Starostin E.L., van der Heijden G.H.M. "The shape of a Möbius strip", *Nature Materials* 6 (8): 563-7. doi: 10.1038/nmat1929.PMID 17632519, (2007).
- [2] J. M. Pond, "Möbius Dual Mode Resonators and Bandpass Filter", *IEEE. Trans. of MTT* Vol. 48, No.12, pp 2465-2471, Dec 2000.
- [3] J. M. Pond, S. Liu, and N. Newman, "Bandpass Filters Using Dual-Mode and Quad-Mode Möbius Resonators," *IEEE Trans. on Microwave Theory and Tech.* vol.49, pp.2363-2368, Dec.2001.
- [4] I. G. Wilson, C. W. Shramm & J. P. Kinzer. "High Q Resonant Cavities for Microwave Testing" *Bell System Technical Journal*, No.5, pp. 1515-1530, doi:10.1364/OPEX.13.001515, (March2005).

- [5] Honkote V., "Capacitive load balancing for Möbius implementation of standing wave oscillator", 5<sup>th</sup> IEEE MWSCAS, pp. 232-235, 2009
- [6] Hoffman, A. J. *et al.* *Nature Mater* 6, pp. 946–950 (2007).
- [7] J-Francois Gravel and J. S. Wight, "On the Conception and Analysis of a 12-GHz Push-Push Phase Locked DRO" *IEEE Trans. on MTT*, Vol. 54, No. 1, pp. 153-159, Jan. 2006.
- [8] D. J. Ballon, H. U. Voss, "Classical Möbius-Ring Resonators Exhibit Fermion-Boson Rotational Symmetry", *Physical Review Letters*: 101, 24;247701, American Physical Society, 2008
- [9] Nikola Tesla, "Coil for electromagnet", US Patent 512340, Jan 9, 1894.
- [10] R. Pérez-Enríquez, "A Structural Parameter for High Tc Superconductivity from an Octahedral Möbius Strip in BaCuO :123 type Perovskites", *Rev Mex Fis v.48 supplement 1*, p.262, 2002.
- [11] Development in FML and Miniature Millimeter Devices, Watkins Johnson, Tech Note. 1974.
- [12] A. K. Poddar, U. L. Rohde, "Evanescence-Mode Phase-Injection Mode-Coupled (EMPIMC) Metamaterial Resonator Based Tunable Signal Sources", *IEEE Wamicon*, June 06, 2014
- [13] A. K. Poddar, U. L. Rohde, "Metamaterial Möbius Strips (MMS): Application in Resonators for Oscillators and Synthesizers", *IEEE UFFC Symposia*, May 19-22, 2014
- [14] A. K. Poddar, U.L. Rohde, D. Sundararajan, "Real Time Signal Retention Device using Co-planar Waveguide (CPW) as Möbius strip", *2013 IEEE MTT-S Digest*, pp. 1-3, June 2013
- [15] A. K. Poddar, U. L. Rohde, "A Novel Evanescence-Mode Möbius-Coupled Resonator Oscillators", *IEEE joint UFFC (EFTF) and Piezo response Force Microscopy*, July 21-25, 2013
- [16] Anritsu Application Note, "Time Domain Reflectometry using Vector Network Analyzers"
- [17] Agilent "Time Domain Analysis using a Network Analyzer. Application Note 1287-12, Jan 6, 2012
- [18] Agilent "Time Domain Analysis Using a Network Analyzer", Literature No. 5989-5723EN, May 2012
- [19] U. L. Rohde, A. K. Poddar, and D. Sundararajan "Printed Resonators: Möbius Strips Theory and Applications", *Microwave journal*, pp. 24-54, Nov 2013.
- [20] A. K. Poddar, U. L. Rohde, "The Pursuit for Low Cost and Low Phase Noise Synthesized Signal Sources: Theory & Optimization", *IEEE UFFC Symposia*, May 19-22, 2014
- [21] A. K. Poddar, U.L. Rohde, T. Itoh, "Metamaterial Möbius Strips (MMS): Tunable Oscillator Circuits", *IEEE MTT-S Digest*, pp. 1-4, June 2014
- [22] U. L. Rohde, A. K. Poddar, D. Sundararajan "Printed Resonators: Möbius Strips Theory and Applications", *Microwave journal*, pp. 24-54, Nov 2013.

## Chapter 8

- [1] Veselago, V.G., "The electrodynamics of substance with simultaneously negative values of  $\epsilon$  and  $\mu$ ", *Sov. Phys. Usp.*, 10, 509–514, 1968.
- [2] Pendry *et al.*, "Magnetism from conductors and enhanced nonlinear phenomena", *IEEE Trans. on MTT*, vol. 47, 2075–2084, 1999.
- [3] Shelby R. A. Smith D.R., Schultz S., "Experimental verification of a negative index of refraction", *Science* 2001, 292, 77–79, 2001
- [4] Pendry, J.B. "Negative refraction makes a perfect lens." *Phys. Rev. Lett.* 2000, 85, 3966–3969, 2000
- [5] Jacob, Z.; Alekseyev, L.V.; Narimanov, E. "Optical hyperlens: Far-field imaging beyond the diffraction limit", *Opt. Express* 2006, 14, 8247–8256, 2006
- [6] Liu, Z.; Lee, H.; Xiong, Y.; Sun, C.; Zhang, X., "Optical hyperlens magnifying sub-diffraction-limited object", *Science* 2007, 315, 1686–1687, 2007
- [7] Smolyaninov, I.I.; Hung, Y.J.; Davis, C.C., "Magnifying superlens in the visible frequency range", *Science* 2007, 315, 1699–1701, 2007
- [8] Pendry *et al.*, "Controlling electromagnetic fields", *Science* 2006, 312, 1780–1782, 2006
- [9] Schurig, D.; Mock, J.J.; Justice, B.J.; Cummer, S.A.; Pendry, J.B.; Starr, A.F.; Smith, D.R., "Metamaterial electromagnetic cloak at microwave frequencies", *Science* 2006, 314, 977–980, 2006
- [10] Chettiar *et al.*, "Optical cloaking with Metamaterials", *Nat. Photonics*, 1, 224–227, 2007.
- [11] Pendry, J.B. "Metamaterials in the sunshine", *Nat. Mater.*, 5, 599–600, 2006.
- [12] Martin *et al.*, "Miniaturized coplanar waveguide stop band filters based on multiple tuned split ring resonators", *IEEE Microw. Wirel. Compon. Lett.* 13, 511–513, 2003.

- [13] Joan et. al, "Microwave filters with improved stopband based on sub wavelength resonators", *IEEE Trans. Microw. Theory Tech.*, 53, 1997–2006, 2005
- [14] Bonache, J.; Gil, I.; Joan, G.G.; Martin, F., "Novel microstrip bandpass filters based on complementary splitting resonators", *IEEE Trans. Microw. Theory Tech.*, 54, 265–271, 2005.
- [15] Nanostructure Metamaterials, Directorate-General for research unit G3-Vlaue-added materials, EUR 24409 EN, 2010
- [16] R. A. Shelby, D. R. Smith, and S. Schultz., "Experimental verification of a negative index of refraction", *Science*, 292(5514):77-79, April 2001.
- [17] Hou-Tong Chen, John F. O'Hara, Antoinette J. Taylor, Richard D. Averitt, "Complementary planar terahertz Metamaterials" Optical Society of America, 2007
- [18] L.V. Hau, Optical information processing in Bose-Einstein condensates, *Nat Photon* 2, 451–453, (2008).
- [19] T. Baba, Slow light in photonic crystals, *Nat Photon* 2 465–473, (2008).
- [20] M. Notomi, E. Kuramochi, and T. Tanabe, "Large-scale arrays of ultrahigh-Q coupled nanocavities", *Nat Photon* 2, 741–747, (2008)
- [21] Xiao Wang, "Simulation of Simultaneously Negative Medium Metamaterials", Master of Science in Electrical Engineering" Falls Church, Virginia, 2009
- [22] George V. Eleftheriades, Omar Siddiqui, and Ashwin K. Iyer, "Transmission Line Models for Negative Refractive Index Media and Associated Implementations Without Excess Resonators", *IEEE MWCL*, Vol. 13, No. 2, Feb. 2003
- [23] A. K. Iyer and G. V. Eleftheriades, "Negative refractive index Metamaterials supporting 2-D waves," in *IEEE MTT-S Symp. Dig.*, vol. 2, Seattle, WA, pp. 1067–1070, June 2–7, 2002.
- [24] A. Grbic and G. V. Eleftheriades, "Experimental verification of backward-wave radiation from a negative refractive index metamaterial," *J. Appl. Phys.*, vol. 92, no. 10, July 2002.
- [25] Pendry, "Negative Refraction Makes a Perfect Lens", *Phys. Rev. Lett.* vol. 85, number 18, 30 Oct 2000
- [26] Manuel et. al, "Metamaterials with Negative Permeability and Permittivity: Analysis and Application", MS thesis, UNIVERSIDADE TÉCNICA DE LISBOA INSTITUTO SUPERIOR TÉCNICO, Oct 2010.
- [27] Mohsin Nawaz, "Low Impedance Wheel Resonators for Low Voltage and Low Power Applications", Dr.-Ing Dissertation, Technischen FakultÄat der UniversitÄat Erlangen-NÄurnberg, 2009
- [28] C. Caloz, T. Itoh "Electromagnetic Metamaterials", IEEE press, Wiley, Hoboken NJ, 2006.
- [29] A. Lai, T. Itoh, "Composite Right/Left-Handed Transmission Line Metamaterials", *IEEE Microwave Magazine*, pp.34-50, Sept.2004.
- [30] J. Pacheco, T. M. Grzegorzczuk, B.-I.Wu, Y. Zhang, and J. A. Kong, "Power propagation in homogeneous isotropic frequency dispersive left-handed media", *Phys. Rev. Lett.*, 89:257401, 2002.
- [31] A. Grbic and G. V. Eleftheriades, "Experimental verification of backward wave radiation from a negative refractive index metamaterial", *J. Appl. Phys.*, 92(10):59305935, 2002.
- [32] Li et. al, "Slow-Wave Line Coupler With Interdigital Capacitor Loading," *IEEE Trans. Microwave Theory Tech.*, vol. 55, no. 11, pp. 2427-2433, November 2007,
- [33] Sun, S. and L. Zhu, "Guided-Wave Characteristics of Periodically Non uniform Coupled Microstrip Lines-Even and Odd Modes," *IEEE Trans, MTT*, vol. 53, no. 4, pp. 1221-1227, April 2005.
- [34] Liu, Z. and R.M. Weikle, "A Compact Quadrature Coupler Based on Coupled Artificial Transmission Lines," *IEEE Microwave Wireless Component Lett*", vol. 15, no. 12, pp. 889-891, December 2005.
- [35] C. Caloz and T. Itoh, *Electromagnetic Metamaterials: Transmission Line Theory and Microwave Applications*, Wiley and IEEE Press, Hoboken, NJ, 2005.
- [36] Ueda et. al, "Demonstration of negative refraction in a cutoff parallel-plate waveguide loaded with 2-D square lattice of dielectric resonators," *IEEE Trans. MTT*, vol. 55, no. 6, pp. 1280-1287, Jun. 2007.
- [37] M. Zedler, P. Russer, and C. Caloz, "Circuitual and experimental demonstration of a 3D isotropic LH metamaterial based on the rotated TLM scheme," *IEEE-MTT Int'l Symp.*, Honolulu, HI, Jun. 2007.
- [38] He et. al, "A low phase-noise VCO using an electronically tunable substrate integrated waveguide resonator," *IEEE Trans. MTT*, vol. 58, no. 12, pp. 3452-3458, Dec. 2010.
- [39] C. Caloz and T. Itoh, "Electromagnetic Metamaterials: Transmission Line Theory and Microwave Applications", New York: Wiley, 2005.
- [40] S. Abielmona, H. V. Nguyen, and C. Caloz, "CRLH zeroth order resonator (ZOR): experimental demonstration of insensitivity to losses and to size," in *Proc. APMC*, pp. 657-662, Dec. 2006.

- [41] Allen et. al, "Design of microstrip resonators using balanced and unbalanced composite right/left-handed transmission lines, *MTT Trans.*, vol. 54, no. 7, pp. 3104-3112, July 2006.
- [42] Baena et. al, "Equivalent circuit models for split ring resonators and complementary split ring resonators coupled to planar transmission lines," *MTT Trans.*, vol. 53, no. 4, pp. 1451-1461, 2005.
- [43] Y. Dong and T. Itoh, "Miniaturized substrate integrated waveguide slot antennas based on negative order resonance," *IEEE Trans. Antennas Propag.*, vol. 58, no. 12, pp. 3856-3864, Dec. 2010.
- [44] C. Li, K. Y. Liu, and F. Li, "Composite right/left-handed coplanar waveguide bandpass filter using capacitively-coupled zeroth-order resonators," *Appl. Phys. A, Mater. Sci. Process.*, vol. 87, no. 2, pp. 317-319, May 2007.
- [45] Y. Dong and T. Itoh, "A dual-band oscillator with reconfigurable cavity-backed complementary split-ring resonator," in *IEEE MTT-S Int. Microw. Symp. Dig.*, Jun. 2012.
- [46] J. Choi, and C. Seo, "Broadband and Low Phase Noise VCO Using Tunable Metamaterial Transmission Line Based on Varactor-Loaded Split-Ring Resonator," *Korea-Japan Micro. Conf.*, pp. 145-148, 2007.
- [47] S. Im, C. Seo, Jaehoon Kim, Young-wan Kim, Naesoo Kim, "Improvement of microstrip open loop resonator filter using aperture," *IEEE MTT-S International*, vol.3, pp. 1801-1804, June 2002.
- [48] E. Park and C. Seo, "Low Phase Noise Oscillator Using Microstrip square Open Loop Resonator," *IEEE MTT-S International Microwave Symposium*, June 2006.
- [49] Young-Taek Lee, Jong-Sik Lim, Jun-Seok Park, Ahn, D.; Sangwook Nam, "A novel phase noise reduction technique In Oscillators using defected ground structure", *IEEE Microwave and Wireless Components Letters*, vol. 12, Issue: 2, pp.39-41, February 2002.
- [50] Smith et al, Composite Medium with Simultaneously Negative Permeability and Permittivity," *Physical Review Letters*, vol. 84, no. 18, pp. 4184-4187, May 2000.
- [51] Smith et al, "Design and Measurement of Anisotropic Metamaterials that Exhibit Negative Refraction," *IEICE Transactions on Electronics*, vol. E87-C, no. 3, pp. 359-370, Mar. 2004.
- [52] R. Marques, F. Medina, and R. Rafii-El-Idrissi, "Role of bi-anisotropy in negative permeability and left-handed metamaterial," *Physical Review B*, vol. 65, no. 14, p. 144440, Apr. 2002.
- [53] J. Cramer, "Dielectric Resonator Fabrication and Assembly Methods for Terahertz Metamaterials", PhD. Thesis, Univ. of Massachusetts Lowell, 2011
- [54] J. B. Pendry, A. J. Holden, W. J. Stewart, and I. Youngs, "Extremely Low Frequency Plasmons in Metallic Mesostructures," *Physical Review Letters*, vol. 76, no. 25, pp. 4773-4776, June 1996.
- [55] J. B. Pendry, A. J. Holden, D. J. Robbins, and W. J. Stewart, "Low frequency plasmons in thin-wire structures," *Journal of Physics: Condensed Matter*, vol. 10, no. 22, pp. 4785-4809, June 1998.
- [56] W. Rotman, "Plasma Simulation by Artificial Dielectrics and Parallel-Plate Media," *IRE Transactions on antennas and Propagation*, vol. 10, no. 1, pp. 82-95, Jan. 1962
- [57] N. Wiwatcharagoses, K. Y. Park, and P. Chahal, "A New Metamaterial Unit Cell for Compact Microstrip Circuit Designs" *Electronic Components and Technology Conference*, pp. 169-172, 2011.
- [58] J. Zhou, L. Zhang, G. Tuttle, T. Koschny, and C. M. Soukoulis, "Negative index materials using simple short wire pairs," *Physical Review B*, vol. 73, no. 4, p. 041101(R), Jan. 2006.
- [59] Drachev et al, "Experimental verification of an optical negative index material," *Laser Physics Letters*, vol. 3, no. 1, pp. 49-55, Oct. 2006.
- [60] Kildishev et al, "Negative refractive index in optics of metal-dielectric composites," *Journal of the Optical Society of America B*, vol. 23, no. 3, pp. 423-433, Mar. 2006.
- [61] Zhang et al, , "Experimental Demonstration of Near-Infrared Negative-Index Metamaterials," *Physical Review Letters*, vol. 95, no. 13, p. 137404, Sept. 2005.
- [62] S. Zhang, W. Fan, K. J. Malloy, S. R. J. Brueck, N. C. Panouiu, and R. M. Osgood, "Near-infrared double negative Metamaterials," *Optics Express*, vol. 13, no. 13, pp. 4922-4930, June 2005.
- [63] Dolling et al, "Low-loss negative-index metamaterial at telecommunication wavelengths", *Optics Letters*, vol. 31, no. 12, pp. 1800-1802, June 2006
- [64] G. Dolling, C. Enkrich, M. Wegener, C. M. Soukoulis, and S. Linden, "Simultaneous Negative Phase and Group Velocity of Light in a Metamaterial," *Science*, vol. 312, no. 5775, pp. 892-894, May 2006.
- [65] G. Dolling, M. Wegener, C. M. Soukoulis, and S. Linden, "Negative-index metamaterial at 780 nm wavelength", *Optics Letters*, vol. 32, no. 1, pp. 53-55, Jan. 2007
- [66] Valentine et al, "Three-dimensional optical metamaterial with a negative refractive index," *Nature*, vol. 455, no. 7211, pp. 376-379, Sept. 2008.

- [67] Gustav Mie, "Beiträge zur Optik trüber Medien, speziell kolloidaler Metallösungen", *Annalen der Physik*, Vierte Folge, Band 25, 1908, No. 3, p 377-445.
- [68] Gustav Mie, "Contributions on the optics of turbid media, particularly colloidal metal solutions Translation", Sandia Laboratories, Albuquerque, New Mexico, 1978, SAND78-6018. National Translation Center, Chicago, ILL, Translation 79-21946.
- [69] L. Lewin, "The Electrical Constants of a Material Loaded With Spherical Particles," *The Proceedings of the Institution of Electrical Engineers*, vol. 94, pp. 65–68, 1947.
- [70] S. O'Brien and J. B. Pendry, "Photonic band-gap effects and magnetic activity in dielectric composites," *Journal of Physics: Condensed Matter*, vol. 14, no. 15, pp. 4035–4044, Apr. 2002.
- [71] Holloway et al, "A Double Negative Composite Medium Composed of Magneto dielectric Spherical Particles Embedded in a Matrix," *IEEE Trans, AP-S*, vol. 51, no. 10, pp. 2596–2601, Oct. 2003.
- [72] J. Baker-Jarvis, M. D. Janezic, D. Love, T. M. Wallis, C. L. Holloway, and P. Kabos, "Phase Velocity in Resonant Structures," *IEEE Transactions on Magnetics*, vol. 42, no. 10, pp. 3344–3346, Oct. 2006.
- [73] Baena, et al, "Equivalent circuit models for split ring resonators and complementary split rings resonators coupled to planar transmission line", *IEEE Trans. on MTT*, vol. 53, pp. 1451-1461, 2005.
- [74] G. SISÓ, M. GIL, M. Aranda, J. Bonache, F. Martin, "Miniaturization of Planar Microwave Devices by Means of Complementary Spiral Resonators (CSRs): Design of Quadrature Phase Shifters", *Radio Engineering* vol. 18, NO. 2, JUNE 2009
- [75] M. Tiebout, "A CMOS fully integrated 1 GHz and 2 GHz dual band VCO with a voltage controlled inductor," in *Proceeding of the IEEE European Solid-State Conference*, pp. 799-802, 2002.
- [76] A. Goel and H. Hashrmi, "Frequency Switching in Dual-Resonance Oscillators," *IEEE Journal of Solid-State Circuits*, Vol. 42, No. 3, March 2007.
- [77] U. L. Rohde, A. K. Poddar, and G. Boeck, "Modern Microwave Oscillators for Wireless Applications: Theory and Optimization", Wiley, New York, 2005.
- [78] A. D. Berny, A. M. Niknejad, and R. G. Meyer, "A 1.8 GHz LC VCO with 1.3 GHz tuning range and digital amplitude calibration," *IEEE Journal of Solid-State Circuits*, Vol. 40. No. 4, pp. 909-917. , 2005
- [79] U. L. Rohde, A. K. Poddar, "Low Noise, Low Power Consumption, Configurable, and Adaptable Ultrawideband VCOs," *IEEE -ICUWB Conference proc.* pp. 545-550, Sept. 2006.
- [80] A. Bavis, "Integrated Multi-Mode Oscillators and Filters For Multi-Bnad Radios Using Liquid Crystalline Polymer Based Packaging Technology," Ph.D. thesis, GIT- Atlanta, GA, May 2006.
- [81] Ravi et al, "A 1.4-V, 2.4/5.2-GHz, 90-nm CMOS system in a package transceiver for next generation WLAN," in *IEEE Sym. on VLSI Technology*, Digest of Technical Papers, New York, 2005.
- [82] C. Lam and B. Razavi, "A 2.6/5.2 GHz frequency synthesizer in 0.4- $\mu$ m CMOS technology," in *IEEE Journal of Solid-State Circuits*, Vol. 35, pp. 788-790, May 2000.
- [83] B. Razavi, "RF Microelectronics", Prentice-Hall, Englewood Cliffs, NJ, 2<sup>nd</sup> edition, 1998.
- [84] M-S Yim and K. K. O., "Switched resonators and their applications in a dual band monolithic CMOS LC tuned VCO," *IEEE Trans. on MTT*, Vol. 54, No. 1, pp. 74-81, January 2006.
- [85] B. Klepser, M. Punzenberger, T. Ruhlicke, and M. Zannoth, "5 GHz and 2.4 GHz dual-band RF-transceiver for WLAN 802.11a/b/g applications," in *IEEE RFIC Symp. Digest Papers*, pp. 37-40, 2003.
- [86] K. Araki et al., "Implementation and performance of a multi-band wireless configuration", pp. 207-210, 2004.
- [87] S. Wiggins, *Introduction to Applied Nonlinear Dynamics and Chaos*, Springer-Verlag, NY, 2<sup>nd</sup> edition, 1997.
- [88] B. van der Pol, "On oscillation hysteresis in a triode generator with two degree of freedom," *Philosophy Magazine*, Vol. 43, pp. 700-719, 1922
- [89] J. S. Schaffner, "Simultaneous oscillations in oscillators," *IRE Transactions on Circuit Theory*, Vol. 1, No. 2, pp. 2-8, June 1954.
- [90] T. Endo and S. Mori, "Mode Analysis of a multimode ladder oscillator," *IEEE Transactions on Circuits & Systems*, Vol. CAS-23, pp. 100-113, February 1976.
- [91] A. K. Poddar, "A Novel Approach for Designing Integrated Ultra Low Noise Microwave Wideband Voltage Controlled Oscillators," Dr.-Ing. Diss., TU- Berlin, Germany, Dec 2004.
- [92] U. L. Rohde, A. K. Poddar, and R. Rebel, "Integrated Low Noise Microwave Wideband Push- Push VCO," United States Patent No. 7,088189, August 2006.

- [93] I. Bruyland, "Simultaneous oscillations at two frequencies in RLC circuits," Proceedings of the IEEE, Vol. 1, pp. 82-83, January 1968.
- [94] A. K. Poddar, J. K. Bansal, and K. N. Pandey, "Millimeter Wave Evanescent Mode Power Combiner Gunn Oscillator in Suspended Stripline Configuration," Mathematical Methods in Electromagnetic Theory, IEEE/MMET, pp.384-386, June 1998.
- [95] N. Engheta, "Compact cavity resonators using metamaterials with negative permittivity and permeability", in Proc. Int. Conf. Electromagnetics in Advanced Applications (ICEAA), Torino, Italy, Sept. 2001, pp. 739-742.
- [96] U. L. Rohde and A. K. Poddar, "Tunable Frequency, Low Phase Noise and Low Thermal Drift Oscillator," United States Patent No.7196591, March 2007.
- [97] A. Sanada, and I. Matsuda, "Experimental Verification of Surface Waves of Metamaterials ", IMS 2005, MTT-S Digest, pp. 1737-1740, 2005.
- [98] A. K. Poddar, S. K. Koul, and Bharthi Bhat, "Millimeter Wave Evanescent Mode Gunn Diode Oscillator c Wiley-Interscience, 1997
- [99] Paul P. Sotiriadis, "Exact Spectrum and Time-Domain Output of Flying-Adder Frequency Synthesizers", IEEE Trans on UFFC, vol. 57, no. 9, September 2010.
- [100] U. L. Rohde and A. K. Poddar, "A Digital Frequency Synthesizer Using Adaptive Mode-Coupled Resonator Mechanism for Low Noise and Low Jitter Applications", IEEE International Symposium on Circuits and Systems (ISCAS), pp. 414-417, Brazil, May 15-18, 2011.
- [101] D. Calbaza and Y. Savaria, "A direct digital periodic synthesis circuit," *IEEE J. Solid-State Circuits*, vol. 37, no. 8, pp. 1039-1045, Aug. 2002.
- [102] U. L. Rohde and A. K. Poddar, "A Novel Low Cost High Performance Synthesizer", Proceedings of the IEEE EuMic, pp. 200-203, Oct 2011.
- [103] U. L. Rohde and A. K. Poddar, "A Novel High Frequency Synthesizer Using Adaptive Injection Mode-Coupled VCSO for Low Jitter and Low Noise Applications", Proceedings of 2011 Joint Conference of the IEEE IFCS & European Frequency and Time Forum, pp. 452-457, May 2011
- [104] U. L. Rohde, A. K. Poddar, and G. Boeck, *Modern Microwave Oscillators for Wireless Applications: Theory and Optimization*, Wiley, NY, 2005.
- [105] W. Egan, "Frequency Synthesis by Phase Lock", John Wiley & Sons Inc., Hoboken, NJ 2000.
- [106] U. L. Rohde and A. K. Poddar, "Wideband voltage controlled oscillators employing evanescent mode coupled resonators," *US Patent No. 7,180,381* Feb 20, 2007 .
- [107] U. L. Rohde, A. K. Poddar, and R. Rebel, "Integrated Low Noise Microwave Wideband Push- Push VCO", *US Patent No. 7,088,189*, Aug 2006.
- [108] U. L. Rohde and A. K. Poddar, "User-Definable Thermal Drift Voltage Controlled Oscillator", *US Patent No.7,265,642 B2*, Sept 4, 2007.
- [109] U. L. Rohde and A. K. Poddar, "Low Thermal Drift Tunable Frequency Voltage Controlled Oscillator", *US Patent No.7,262,670 B2*, Aug 28, 2007.
- [110] U. L. Rohde and A. K. Poddar, "Tunable Oscillator", *US Patent No.7,292,113*, Nov. 6, 2007.
- [111] U. L. Rohde and A. K. Poddar, "Tunable Frequency, Low Phase Noise and Low Thermal Drift Oscillator", *US Patent No.7196591*, March 2007.
- [112] U. L. Rohde and A. K. Poddar, "Low Noise, Hybrid Tuned Wideband Voltage Controlled Oscillator", *US Patent No. 7,365,612 B2*, April 29, 2008.
- [113] U. L. Rohde and A. K. Poddar, "Tunable Frequency. Low Phase Noise and Low Thermal Drift Oscillator", *U.S Patent NO. 7,545,229*, June 09, 2009.
- [114] U. L. Rohde and A. K. Poddar, "User-Definable, Low Cost, Low Phase Hit and Spectral Pure Tunable Oscillator", *U.S. Patent No. 7,586,381* on September 08, 2009.
- [115] U. L. Rohde and A. K. Poddar, "User-Definable, Low Cost, Low noise, and phase hit insensitive multi-octave-band tunable oscillator, Phase Hit and Spectral Pure Tunable Oscillator", *US Patent No. 7,605,670*, Oct 2009.
- [116] U. Rohde and A. Poddar, "Low Noise and Low Phase Hits Tunable Oscillator", *US Patent 7636 021*, Dec. 2009
- [117] U. L. Rohde and A. K. Poddar, "Wideband voltage controlled oscillators employing evanescent mode coupled resonators", *Canadian Patent No. 2,563,174*, July 21, 2009.
- [118] U. L. Rohde and A. K. Poddar, "User-Definable Thermal Drift Voltage Controlled Oscillator", *Canadian Patent No. 2,548,317*, April 21, 2009.

- [119] U. L. Rohde and A. K. Poddar, Integrated Low Noise Microwave Wideband Push- Push VCO, Canadian Patent No.:2,548, 311, April 14, 2009.
- [120] Low Noise VCOs product datasheet available at <http://www.synergymwave.com/products>
- [121] P. S. (Paul) Khanna, "Microwave Oscillators: The State of The Technology," *MWJ*, pp. 22-42, April 2006.
- [122] A. Chenakin, "Building a Microwave Frequency Synthesizer Part-2: Component Selection", *High Frequency Electronics*, pp. 18-26, 2008.
- [123] G. Gonzalez, "Foundations of Oscillator Circuit", Ch-IV, Artech House, Inc., London. 2007
- [124] A. Grebennikov, RF and Microwave Transistor Oscillator Design, John Wiley & Sons Ltd., UK, 2007.
- [125] J.K.A. Everard and L. Zhou. "Non Linear Effects in varactor tuned resonators" *IEEE Transactions on Ultrasonics Ferroelectrics and Frequency Control*, Vol. 53, No. 5, pp.853 – 861, May 2006
- [126] T.Ohira and K.Araki, "Active Q factor and equilibrium stability formulation for sinusoidal oscillators", *IEEE Trans.Circuits and Systems Pt II*, vol.54, no.9, pp.810-814, 2009
- [127] Nallatamby et al,"Extension of the Leeson formula to phase noise calculation in transistor oscillators with Complex tanks," *IEEE Trans. MTT*, vol. 51, issue 3, pp. 690-696, March 2003.
- [128] W. Egan, "Frequency Synthesis by Phase Lock", John Wiley & Sons Inc., Hoboken, NJ 2000.
- [129] S. Pamarti and S. Delshadpour, "A spur elimination technique for phase interpolation-based fractional-N PLLs," *IEEE Trans. Circuits Syst. I, Reg. Papers*, vol. 55, no. 6, pp. 1639-1647, Jul. 2008.
- [130] Y. Sun, et al., "Dual-path LC VCO design with partitioned coarsetuning control in 65nm CMOS," to appear in *IEEE MWCL*, Mar. 2010.
- [131] X. Yu et al., "A fractional-N frequency synthesizer with customized noise shaping for WCDMA/HSDPA applications," *IEEE JSSC*, vol. 44, pp. 2193-2201, Aug. 2009.
- [132] T. Wu, P. Hanumolu, K. Mayaram, and U. Moon, "A 4.2 GHz PLL frequency synthesizer with an adaptively tuned coarse loop," in *Proc. IEEE CICC*, pp. 547-550, Sept. 2007.
- [133] A. Chenakin, "Frequency Synthesis: Current Solutions And New Trends", *Microwave Journal*, pp. 256-266, May 2007.
- [134] J. Browne, "Frequency Synthesizers Tune Communication Systems," *Microwaves & RF*, March 2006.
- [135] Ulrich L. Rohde, Ajay K. Poddar, "Synthesizers Shave Size and Noise", *Microwave & RF*, PP. 132-164, May 2012
- [136] S.-G. Mao, M.-S. Wu, Y.-Z. Chueh, and C. H. Chen, "Modeling of symmetric composite right/left-handed coplanar waveguides with applications to compact bandpass-filters," *IEEE Trans. Microw. Theory Tech.*, vol. 53, no. 11, pp. 3460-3466, Nov. 2005.
- [137] A. K. Poddar, U. L. Rohde, "A Novel Metamaterial Resonator Based Signal Sources for applications in current and later generation radio communication systems", *IEEE BenMAS 2014*, Drexel Univ, Philadelphia
- [138] A. Apte, V. Madhavan, A. Poddar, U. Rohde, T. Itoh, "A Novel Low Phase Noise X-band Oscillator", *IEEE BenMAS 2014*, Drexel Univ, Philadelphia
- [139] Jiangpeng et al, "Metamaterial Extebds Microstrip Antenna", *Microwavws & RF*, PP. 69-73, Dec 2013
- [140] Benmostefa et al, "Metamaterials Form Miniature Bandstop Filters", *Microwavws & RF*, PP. 69-73, 2012
- [141] Katko et al, "Time-varying transistor-based metamaterial for tunability, mixing, and efficient phase conjugation", *Journal of Applied Physics*, Vol 115, Issue 14, pp. 144501 – 144506, , 2014
- [142] Tupin et al, "Near-Zero-Index Metamaterial Lens Combined With AMC Metasurface for High-Directivity Low-Profile Antennas", *IEEE Transactions on AP-S*, Volume: 62, Issue: 4, Part: 2 pp. 1928–1936, 2014
- [143] M. Gupta, J. Saxena, "Superdirective patch antenna array using metamaterial", 2014 *IEEE International Conference on Electronics, Computing and Communication Technologies (IEEE CONECCCT)*, pp. 1 – 6, 2014
- [144] N. Engheta, "An Idea for thin subwavelength cavity resonators using metamaterials with negative permittivity and permeability", *IEEE Antenna and Wireless Propagation Letters*, Vol. 1, pp. 10-13, 2002.
- [145] A. K. Poddar, U. L. Rohde, "Metamaterial Möbius Strips (MMS): Application in Resonators for Oscillators and Synthesizers", *IEEE UFFC Symposia*, May 19-22, 2014
- [146] A. K. Poddar, U. L. Rohde, "The Pursuit for Low Cost and Low Phase Noise Synthesized Signal Sources: Theory & Optimization", *IEEE UFFC Symposia*, May 19-22, 2014
- [147] A. K. Poddar, U. L. Rohde, "Evanescence-Mode Phase-Injection Mode-Coupled (EMPIMC) Metamaterial Resonator Based Tunable Signal Sources", *IEEE Wamicon*, June 06, 2014.
- [148] A. K. Poddar, U. L. Rohde, T. Itoh, "Metamaterial Möbius Strips (MMS): Tunable Oscillator Circuits", *IEEE MTT-S Digest*, pp. 1-4, June 2014



- [149] Chung-Tse M. Wu, A. K. Poddar, U. L. Rohde, T. Itoh, "A C-band Tunable Oscillator Based on Complementary Coupled Resonator using Substrate Integrated Waveguide Cavity " EuMW 2014
- [150] Li Zhang, U. A. K. Poddar, U. L. Rohde, and A. S. Daryoush, "Oscillator Phase Noise Reduction Using Self-Injection Locked and Phase Locked Loop (SILPLL), IEEE IFCS, May 2014
- [151] Chung-Tse M. Wu, A. K. Poddar, U. L. Rohde, T. Itoh, Active Complementary Coupled Resonator for Low Phase Noise X-band Oscillator ", IEEE EFTF Neuchâtel, Switzerland from June 23 – 26, 2014
- [152] W. Fei Shang et. al, "a 96-GHz oscillators by high Q-Differential Transmission Line Loaded with Complementary Split-Ring Resonator in 65-nm CMOS. IEEE Trans. on Circuits and Systems-II, Express Briefs, Vol.60, No.3, pp. 127-131, March 2013
- [153] A. K. Poddar, U. L. Rohde, "The Pursuit for Low Cost and Low Phase Noise Synthesized Signal Sources: Theory & Optimization", IEEE UFFC Symposia, May 19-22, 2014
- [154] Chun-Tse Michael Wu, " Active Integrated Metamaterial-Based Antennas and Microwaves Components" , PhD Thesis June 2014, Department of Electrical Engineering, University of California, Los Angeles.

## Chapter 9

- [1] Ulrich L. Rohde, "Microwave and Wireless Synthesizers", Wiley & Sons, pp. 86-90, 1997
- [2] D. Kajfez and P. Guillon, "Dielectric Resonators", Artech House, Dedham, MA, 1986
- [3] Jens Bischoff, Daniel Schwoch, "Entwurf eines ultra-rauscharmen Mikrowellenoszillators mit dielektrischem Resonator im S-Band", Diploma thesis, University of Applied Sciences Bremen, Germany, 2004.
- [4] Ajay Subramanian, "A low Phase Noise K-band Oscillator utilizing an Embedded Dielectric Resonator on Multilayer High Frequency Laminates", Master thesis, University of Central Florida, 2008.
- [5] Olivier Bernard, Robin Croston, "Simulate and Build a Ku-Band DRO", Microwaves &RF, May 2000.
- [6] U. L. Rohde, A. K. Poddar, and G. Boeck, "Modern Microwave Oscillators for Wireless Applications: Theory and Optimization", John Wiley & Sons Inc., 2005.
- [7] Jaechun Lee, Young-Taek Lee, and Sangwook Nam, "A Phase Noise Reduction Technique in Microwave Oscillator Using High-Q Active Filter," IEEE Microwave and Wireless Components Letters, vol. 12 pp. 424-428, November 2002.
- [8] Mahyuddin, N.M, Ain, M.F. Hassan, S.I.S, and Singh, "Modeling of a 10 GHz Dielectric Resonator Oscillator in ADS," IEEE RF and Microwave Conference, pp. 106-110, 2006.
- [9] K. Chow, "On the solution and field pattern of cylindrical dielectric resonators," IEEE Trans. Microw. Theory Tech., vol. MTT-14, no. 9, p. 439, Sep. 1966.
- [10] T. Itoh and R. S. Rudokas, "New method for computing the resonant frequencies of dielectric resonators," IEEE Trans. Microw. Theory Tech., Vol. MTT-25, no. 1, pp. 52–54, Jan. 1977.
- [11] M. W. Pospieszalski, "Cylindrical dielectric resonators and their applications in TEM line microwave circuits," IEEE Trans. Microw. Theory Tech., vol. MTT-27, no. 3, pp. 233–238, Mar. 1979.
- [12] A. M. Pavio and M. A. Smith, "A 20–40 GHz push–push dielectric resonator oscillator," IEEE Trans. Microw. Theory Tech., vol. 33, no. MTT-12, pp. 1346–1349, Dec. 1985.
- [13] F. X. Sinnesbichler, B. Haultz, and G. R. Olbrich, "An SiGe HBT dielectric resonator push–push oscillator at 58 GHz," IEEE Microw. Guided Wave Lett. vol. 10, no. 4, pp. 145–147, Apr. 2000.
- [14] J-F. Gravel and J. S. Wight, "On the conception and analysis of a 12-GHz Push-push phase locked DRO," IEEE Trans. Microw. Theory Tech., vol. 54, no. 1, pp. 153–159, Jan. 2006.
- [15] A. P. S Khanna, "Review of Dielectric Resonator Oscillator Topology", IEEE IFCS 1987.
- [16] U. L. Rohde, A. K. Poddar, "Tunable Frequency, Low Phase Noise and Low Thermal Drift Oscillator", US Patent No. 7196591, March 2007.
- [17] U. L. Rohde, A. K. Poddar, "Low Noise, Hybrid Tuned Wideband Voltage Controlled Oscillator", US Patent No. 7,365,612 B2, April 29, 2008.
- [18] U. L. Rohde, A. K. Poddar, "Tunable Frequency, Low Phase Noise and Low Thermal Drift Oscillator", U.S Patent NO. 7, 545, 229, June 09, 2009.
- [19] U. L. Rohde, A. K. Poddar, "User-Definable, Low Cost, Low Phase Hit and Spectral Pure Tunable Oscillator", U.S. Patent No. 7,586,381 on September 08, 2009.
- [20] U. L. Rohde, A. K. Poddar, "User-Definable, Low Cost, Low noise, and phase hit insensitive multi-octave-band tunable oscillator", Phase Hit and Spectral Pure Tunable Oscillator, US Patent 7605670, Oct. 20, 2009.

- [21] L. Zhou, R. Chu, Z. Wu, W.-Y. Yin, and J.-F. Mao, "Broad tuning low noise Ku band dielectric resonator oscillators", *IEEE Proc. Asia-Pacific Microw. Conf.*, pp. 1–4, Dec. 2008.
- [22] P. Stockwell, D. Green, C. Mcneilage, and J. H. Searls, "A low phase noise 1.3 GHz dielectric resonator oscillator," in *Proc. IEEE Int. Freq. Control Symp.*, pp. 882–885, May 2006.
- [23] C. Florian, P. A. Traverso, G. Vannini, and F. Filicori, "Design of low phase noise dielectric resonator oscillators with GaInP HBT devices exploiting a non-linear noise model," in *IEEE MTT-s Dig.*, pp. 1525–1528, June 2007,
- [24] U. L. Rohde and A. K. Poddar, "Mode-coupled stubs-tuned planar resonator offers promising and integrable alternatives of DRO," in *Proc. IEEE Freq. Control Symp.*, pp. 296-304, May 2008.
- [25] O. Llois, G. Cibiel, Y. Kersale, M. Regis, M. Chaubet, and V. Giordano, "Ultra low phase noise sapphire-SiGe HBT oscillator," *IEEE Microw. Wireless Component Letter*, vol. 12, no. 5, pp. 157–159, May 2002.
- [26] K. Hosoya, K. Ohata, M. Funabashi, T. Inoue, and M. Kuzuhara, "V-band HJFET MMIC DROs with low phase noise, high power, and excellent temperature stability," *IEEE Trans. MTT*, pp. 2250–2258, Nov. 2003.
- [27] U. L. Rohde and A. K. Poddar, "DRO Drops phase-noise levels", *Microwaves & RF*, pp. 80-84, Feb. 2013
- [28] D. M. Pozar, "Microwave Resonators." In *Microwave Engineering*, 2<sup>nd</sup> ed. Wiley & Sons, 1998, Ch. 6, sec. 5, pp. 323-327.
- [29] U. L. Rohde and A. K. Poddar, "STPCR Offers Integrable Alternatives of DRO", *Microwave Symposium Digest, 2008 IEEE MTT-S*, pp. 233-236, 15-20 June 2008 Atlanta, USA.
- [30] C. V. J. et al., "Design and performance of dielectric resonator oscillators with series feedback", *Electrotechnical Conference Proceedings, Integrating Research, Industry and Education in Energy and Communication Engineering*, pp. 339-342, IEEE MELECON 1989

## Chapter 10

- [1] H. C. Chang, "Phase noise in self-injection locked oscillators – Theory and Experiment," *IEEE Trans. Microw. Theory Tech.*, vol. 51, no. 9, pp. 1994 – 1999, Sep. 2003
- [2] Daryoush et al, "Optically Controlled Oscillators for Millimeter-Wave Phased-Array Antennas", *MTT* vol. 41, No. 6/7, 1993
- [3] A. K. Poddar, U. L. Rohde, A. S. Daryoush, "Integrated production of self-injection locked self phase loop locked Opto-electronic Oscillators", US Patent application no. 13/760767 (filed on Feb 06, 2013).
- [4] A. K. Poddar, U. L. Rohde, A. S. Daryoush, "Self Injection Locked Phase Locked Looped Optoelectronic Oscillator", US Patent application No. 61/746, 919 (filed on Dec 28, 2012).
- [5] A. K. Poddar, "Slow-Wave Resonator based Tunable Multi-Band Multi-Mode Injection-Locked Oscillators", *Research Report, RF and Microwave Techniques Brandenburg University of Technology Cottbus-Senftenberg 2014*, [https://www-docs.tu-cottbus.de/mikrowellentechnik/public/poddar\\_report\\_long\\_ebook.pdf](https://www-docs.tu-cottbus.de/mikrowellentechnik/public/poddar_report_long_ebook.pdf)